TOPICS IN CURRENT CHEMISTRY 285

Volume Editor P. Samorì

STM and AFM Studies on (Bio)molecular Systems

Unravelling the Nanoworld

Springer

285
Topics in Current Chemistry

Topics in Current Chemistry

Recently Published and Forthcoming Volumes

STM and AFM Studies on (Bio)molecular Systems: Unravelling the Nanoworld
Volume Editor: Samorì, P.
Vol. 285, 2008

Amplification of Chirality
Volume Editor: Soai, K.
Vol. 284, 2008

Anthracycline Chemistry and Biology II
Mode of Action, Clinical Aspects and New Drugs
Volume Editor: Krohn, K.
Vol. 283, 2008

Anthracycline Chemistry and Biology I
Biological Occurence and Biosynthesis, Synthesis and Chemistry
Volume Editor: Krohn, K.
Vol. 282, 2008

Photochemistry and Photophysics of Coordination Compounds II
Volume Editors: Balzani, V., Campagna, S.
Vol. 281, 2007

Photochemistry and Photophysics of Coordination Compounds I
Volume Editors: Balzani, V., Campagna, S.
Vol. 280, 2007

Metal Catalyzed Reductive C–C Bond Formation
A Departure from Preformed Organometallic Reagents
Volume Editor: Krische, M. J.
Vol. 279, 2007

Combinatorial Chemistry on Solid Supports
Volume Editor: Bräse, S.
Vol. 278, 2007

Creative Chemical Sensor Systems
Volume Editor: Schrader, T.
Vol. 277, 2007

In situ NMR Methods in Catalysis
Volume Editors: Bargon, J., Kuhn, L. T.
Vol. 276, 2007

Sulfur-Mediated Rearrangements II
Volume Editor: Schaumann, E.
Vol. 275, 2007

Sulfur-Mediated Rearrangements I
Volume Editor: Schaumann, E.
Vol. 274, 2007

Bioactive Conformation II
Volume Editor: Peters, T.
Vol. 273, 2007

Bioactive Conformation I
Volume Editor: Peters, T.
Vol. 272, 2007

Biomineralization II
Mineralization Using Synthetic Polymers and Templates
Volume Editor: Naka, K.
Vol. 271, 2007

Biomineralization I
Crystallization and Self-Organization Process
Volume Editor: Naka, K.
Vol. 270, 2007

STM and AFM Studies on (Bio)molecular Systems: Unravelling the Nanoworld

Volume Editor: Paolo Samorì

With contributions by

F. Cicoira · A. Ebner · S. De Feyter · C. Gerber · H. J. Gruber
T. Haselgrübler · P. Hinterdorfer · H. P. Lang · S. Lei · J. M. Mativetsky
M. Palma · J. P. Rabe · C. Rankl · F. Rosei · P. Samorì · C. Santato
H. Schönherr · E. Tocha · G. J. Vancso · L. Wildling ·R. Zhu

Springer

The series *Topics in Current Chemistry* presents critical reviews of the present and future trends in modern chemical research. The scope of coverage includes all areas of chemical science including the interfaces with related disciplines such as biology, medicine and materials science. The goal of each thematic volume is to give the nonspecialist reader, whether at the university or in industry, a comprehensive overview of an area where new insights are emerging that are of interest to a larger scientific audience.

As a rule, contributions are specially commissioned. The editors and publishers will, however, always be pleased to receive suggestions and supplementary information. Papers are accepted for *Topics in Current Chemistry* in English.

In references *Topics in Current Chemistry* is abbreviated Top Curr Chem and is cited as a journal.

Visit the TCC content at springerlink.com

ISBN 978-3-540-78394-7 ISBN 978-3-540-78395-4 (eBook)
DOI 10.1007/978-3-540-78395-4

Topics in Current Chemistry ISSN 0340-1022

Cover design: WMXDesign GmbH, Heidelberg
Typesetting and Production: le-tex publishing services oHG, Leipzig

Printed on acid-free paper

9 8 7 6 5 4 3 2 1 0

springer.com

Volume Editor

Dr. Paolo Samorì

Université Louis Pasteur
Institut de Science et d'Ingénierie
Supramoléculaires (I.S.I.S.)
8 allée Gaspard Monge
67083 Strasbourg Cedex
France
samori@isis-ulp.org

and
Istituto per la Sintesi Organica
e la Fotoreattività
Consiglio Nazionale delle Ricerche
via Gobetti 101
40129 Bologna, Italy

Editorial Board

Topics in Current Chemistry
Also Available Electronically

For all customers who have a standing order to Topics in Current Chemistry, we offer the electronic version via SpringerLink free of charge. Please contact your librarian who can receive a password or free access to the full articles by registering at:

springerlink.com

If you do not have a subscription, you can still view the tables of contents of the volumes and the abstract of each article by going to the SpringerLink Homepage, clicking on "Browse by Online Libraries", then "Chemical Sciences", and finally choose Topics in Current Chemistry.

You will find information about the

- Editorial Board
- Aims and Scope
- Instructions for Authors
- Sample Contribution

at springer.com using the search function.

Color figures are published in full color within the electronic version on SpringerLink.

To Cristiana and Emma

Preface

The invention of scanning tunneling microscopy (STM) in 1981 [1] and later atomic force microscopy (AFM) in 1986 [2] facilitated breakthroughs in various disciplines of science such as chemistry, physics and biology, and truly boosted the development of nanoscience and nanotechnology.

These two techniques made it possible to achieve a detailed understanding of chemical and biological systems as well as phenomena across multiple length scales, and in particular down to the sub-nanometer scale. In fact STM and AFM are not simply microscopy tools, but they are also extremely useful techniques to chemist and biochemists. For example AFM and STM offer synthetic chemists the chance to observe the molecules they have synthesized, how they move and dance on a surface, how they recognize and communicate with each other, thus making it possible to cast new light onto the molecular interactions [3]. Alongside their capability of generating artistic three-dimensional pictures with nanoscale resolution, they also allowed the study of molecular based architectures beyond imaging, providing quantitative insight into various physico-chemical properties [4] For instance, by manipulating molecules individually it is possible to bestow information onto their mechanical properties and to perform constructions on the nanoscale. In the last few years the application of AFM and STM to study molecular systems in various environments (e.g., liquid, gas, vacuum) is paving the way towards the unraveling of complex characteristics and phenomena of nanostructured (bio)systems.

In this volume we have selected a few of the most relevant examples of AFM and STM based experiments on (bio)molecular based systems, which offer not only a close look into the nanoworld but also provide quantitative insight into various properties of molecular and polymeric systems, and ultimately highlight some technologically relevant applications.

I was delighted and felt privileged to work with an outstanding group of contributing authors: I truly thank them for all their efforts. I am also grateful to Dr. Marion Hertel and Birgit Kollmar-Thoni for their invitation to edit this volume and for their assistance.

Strasbourg & Bologna, December 2007 Paolo Samorì

References

1. Binnig G, Rohrer H, Gerber C, Weibel E (1982) Helv Phys Acta 55:726
2. Binnig G, Quate CF, Gerber C (1986) Phys Rev Lett 56:930
3. Lehn JM (1995) Supramolecular Chemistry: Concepts and Perspectives.;CH, Weinheim
4. Samori P (ed) (2006) Scanning Probe Microscopy beyond Imaging.; Wiley-VCH, New York

Contents

Top Curr Chem (2008) 285: 1–27
DOI 10.1007/128_2007_28

Published online: 5 March 2008

Microcantilever Sensors

Hans Peter Lang (✉) · Christoph Gerber (✉)

National Competence Center for Research in Nanoscale Science, University of Basel, Institute of Physics, Klingelbergstrasse 82, 4056 Basel, Switzerland
Hans-Peter.Lang@unibas.ch, Christoph.Gerber@unibas.ch

Abstract Microfabricated cantilevers have been used in atomic force microscopy for the topography imaging of non-conductive surfaces for more than 20 years. Cantilever beams without tips have proved their applicability in recent years as miniaturized, ultrasensitive, and fast-responding sensors for applications in chemistry, physics, biochemistry, and medicine. Microcantilever sensors respond by bending due to the absorption of molecules. A shift in resonance frequency also occurs. They can be operated in different environments such as gaseous environment, liquids, or vacuum. In gas, microcantilever sensors can be operated as an artificial nose, whereby the bending pattern of a microfabricated array of eight polymer-coated silicon cantilevers is characteristic of the different vapors from solvents, flavors, and beverages. When operated in a liquid, microcantilever sensors are able to detect biochemical reactions. Each cantilever is functionalized with a specific biochemical probe receptor, sensitive for detection of the corresponding target molecule. Applications lie in the fields of label- and amplification-free detection of

DNA hybridization, the detection of proteins as well as antigen-antibody reactions, and the detection of larger entities, such as bacteria and fungi.

Keywords Artificial nose · Biosensor · Microcantilever sensor

Abbreviations

AFM	Atomic force microscopy
CMC	Carboxymethyl cellulose
CMOS	Complementary metal oxide semiconductor
DDT	Dichlorodiphenyltrichloroethane
DIMP	Diisopropyl methyl phosphonate
DMMP	Dimethylmethylphosphonate
DNA	Deoxyribonucleic acid
DNT	Dinitrotoluene
HPC	Hydroxypropyl cellulose
HPLC	High Performance Liquid Chromatography
PAAM	Poly(allylamine)
PC	Personal computer
PCA	Principal component analysis
PEEK	Poly-etheretherketone
PEI	Polyethylenimine
PEO	Poly(2-ethyl-2-oxazoline)
PETN	Pentaerythritol tetranitrate
PSA	Prostate-specific antigen
PSD	Position sensitive detector
PSS	Polystyrenesulfonate
PVP	Polyvinylpyrrolidone
PZT	Lead zirconium titanate
RDX	Hexahydro-1,3,5-triazine
QCM	Quarz crystal microbalance
SPR	Surface plasmon resonance
TNT	Trinitrotoluene
VCSEL	Vertical cavity surface emitting laser
VOC	Volatile organic compound

1 Introduction to Microcantilever Sensors

1.1 Historical Development

Measurement of adsorption-induced bending or a change in resonance frequency using beams of silicon as sensors was already described in literature in 1968, by Wilfinger et al. [1], who detected resonances in large silicon cantilever structures of 50 mm × 30 mm × 8 mm. Actuation was realized by localized thermal expansion in diffused resistors (piezoresistors) located near

the cantilever support to create a temperature gradient for driving the cantilever at its resonance frequency. Similarly, the piezoresistors could also be used to monitor mechanical deflection of the cantilever. Heng [2] fabricated in 1971 gold microcantilevers capacitively coupled to microstrip lines for the mechanical trimming of high-frequency oscillator circuits. Petersen [3] constructed in 1979 cantilever-type micromechanical membrane switches made from silicon designed to bridge the gap between silicon transistors and mechanical electromagnetic relays. Kolesar [4] suggested in 1985 the use of cantilever structures as electronic detectors for nerve agents.

Since the advent of atomic force microscopy (AFM) in 1986 [5] microfabricated cantilevers have become easily commercially available, triggering research reports on the use of microcantilevers as sensors. In 1994, Itoh et al. [6] presented a microcantilever coated with a thin film of zinc-oxide with piezoresistive deflection readout. Cleveland et al. [7] reported the tracking of cantilever resonance frequency to detect nanogram changes in mass loading when small particles are deposited onto AFM probe tips. Gimzewski et al. [8] showed the first chemical sensing applications, in which static cantilever bending revealed chemical reactions, such as the platinum-assisted catalytic conversion of hydrogen and oxygen into water at very high sensitivity. Thundat et al. [9] demonstrated that the resonance frequency as well as the static bending of microcantilevers is influenced by changing ambient conditions, such as moisture adsorption. Furthermore, they found that the deflection of metal-coated cantilevers is also thermally influenced (the bimetallic effect). Later, Thundat et al. [10] observed changes in the resonance frequency of microcantilevers due to the adsorption of analyte vapor on exposed surfaces. The frequency changes are due to mass loading or adsorption-induced changes in the cantilever spring constant. By coating cantilever surfaces with hygroscopic materials, such as phosphoric acid or gelatin, the cantilever can sense water vapor at picogram mass resolution.

1.2 Measurement Principle

1.2.1 Concept

Microcantilevers as sensors, unlike AFM cantilevers, neither need a tip at their apex nor a sample surface. The microcantilever surfaces serve as sensors, in particular, to detect the adsorption of molecules taking place on these surfaces. The generation of surface stress is monitored, eventually resulting in the bending of the microcantilever, if the adsorption preferentially occurs on one of its surfaces. Selective adsorption is controlled by coating one surface (typically the upper surface) of a microcantilever with a thin layer of a material that shows an affinity to molecules in the environment (sensor surface).

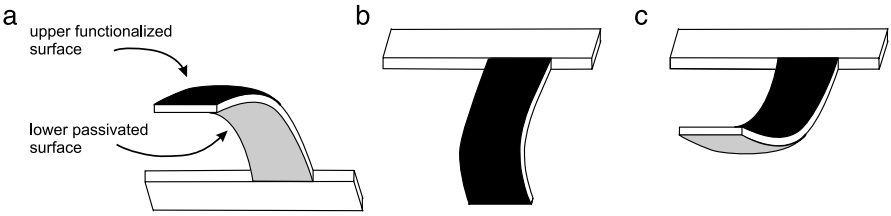

Fig. 1 **a** Schematic drawing of a microcantilever with its lower surface passivated and it upper surface functionalized for recognition of target molecules, **b** downward bending of a microcantilever due to compressive surface stress, **c** upward bending due to tensile surface stress

We call this surface the "functionalized" surface of the microcantilever (see Fig. 1a). The other surface of the cantilever (typically the lower surface) may be left uncoated or can be coated with a passivation layer, which is either inert or does not exhibit significant affinity to the molecules in the environment to be detected. To establish functionalized surfaces, often a metal layer is evaporated onto the surface designed as a sensor surface. Metal surfaces, such as gold, may be used to covalently bind a monolayer constituting the chemical surface sensitive to the molecules to be detected. Often, a monolayer of thiol molecules, offering defined surface chemistry, is covalently bound to a gold surface. The gold layer also serves as a reflection layer if the bending of the cantilever is read out optically.

1.2.2 Compressive and Tensile Stress

Adsorption of molecules on the upper (functionalized) surface will result in a downward bending of the microcantilever due to the formation of surface stress. We will call the surface stress "compressive" (see Fig. 1b), because the adsorbed layer of molecules (e.g., a monolayer of alkylthiols) produces a downward bending of the microcantilever away from its functionalized side. If the opposite situation occurs, i.e., when the microcantilever bends upwards, we would speak of "tensile stress" (see Fig. 1c). If both the upper and the lower surface of the microcantilever are exposed to surface stress changes, then the situation will be much more complex, as a predominant compressive stress formation on the lower microcantilever surface might appear as tensile stress on the upper surface. For this reason, it is extremely important to properly passivate the lower surface so that, ideally, no processes take place on the lower surface of the microcantilever. Various strategies can be used to passivate the lower surface of microcantilevers. For biochemical systems, the application of a thin layer of 2-[methoxy-poly(ethyleneoxy)propyl]trimethoxysilane will create a pegylated surface that is almost inert towards the adsorption of biological layers. For the detection of gases, coating with a gold layer will passivate the sur-

face. For the recognition of solvent vapors, coating with a fluorinated polymer layer will serve as a non-reactive layer. The actual experiment will show whether the passivation layer was really efficient, as such passivated cantilevers will not show a substantial bending response upon exposure to an analyte.

1.2.3 Differential Measurements

Single microcantilevers may bend due to thermal drift or an interaction with their environment, in particular if operated in a liquid. Furthermore, nonspecific physisorption of molecules on the cantilever surface or nonspecific binding to receptor molecules during measurements may contribute to the drift.

To exclude such influences, the simultaneous measurement of reference microcantilevers aligned in the same array as the sensing microcantilevers is crucial [11]. The difference in signals from the reference and sensor microcantilevers yields the net bending response, and even small sensor signals can be extracted from large microcantilever deflections without being dominated by undesired effects. When only single microcantilevers are used, no thermal-drift compensation is possible. To obtain useful data under these circumstances, both microcantilever surfaces have to be chemically well-defined. One of the surfaces, typically the lower one, has to be passivated; otherwise, the microcantilever response will be convoluted with undesired effects originating from uncontrolled reactions taking place on the lower surface. With a pair of microcantilevers, reliable measurements are obtained. One of them is used as the sensor microcantilever (coated typically on the upper side with a molecule layer that shows affinity to the molecules to be detected), whereas the other microcantilever serves as the reference. It should be coated with a passivation layer on the upper surface so as not to exhibit affinity to the molecules to be detected. Thermal drifts are cancelled out if difference responses, i.e., the difference in deflections of sensor and reference microcantilevers are taken (differential measurements). Alternatively, both microcantilevers are used as sensors (sensor layers on the upper surfaces), and the lower surface has to be passivated. It is best to use an array of microcantilevers, in which some are used either as sensor or as reference microcantilevers so that multiple difference signals can be evaluated simultaneously. Thermal drift is cancelled out as one surface of all microcantilevers, typically the lower one, is left uncoated or coated with the same passivation layer.

1.2.4 Deflection Measurement

The bending response of the microcantilever due to adsorption of molecules onto the functional layer is caused by stress formation at the interface be-

tween the functional layer and the forming molecular layer. Because the forces within the functional layer try to keep the distance between molecules constant, the cantilever beam responds by bending because of its extreme flexibility. The quantity describing the flexibility of the microcantilever is its spring constant k. For a rectangular microcantilever of length l, thickness t and width w the spring constant k is calculated as follows:

$$k = \frac{Ewt^3}{4l^3} , \tag{1}$$

where E is Young's modulus ($E_{\mathrm{Si}} = 1.3 \times 10^{11}$ N/m^2 for Si(100)).

The microcantilever bends as a response to the formation of surface stress caused by the adsorption of a molecular layer. In its simplest case, the shape of the bent microcantilever can be approximated as part of a circle with radius R. This radius of curvature is given by [12, 13]

$$\frac{1}{R} = \frac{6(1-\nu)}{Et^2} . \tag{2}$$

The resulting surface stress change is described using Stoney's formula [12]:

$$\Delta\sigma = \frac{Et^2}{6R(1-\nu)} , \tag{3}$$

where E is Young's modulus, t the thickness of the cantilever, ν the Poisson's ratio ($\nu_{\mathrm{Si}} = 0.24$), and R the bending radius of the cantilever.

The deflection of microcantilever sensors can be measured in various ways. They differ in the sensitivity, the effort for alignment and setup, the robustness and ease of readout, and in the potential for miniaturization.

1.2.4.1 Piezoresistive Readout

Piezoresistive microcantilevers [6, 14] are usually U-shaped and have diffused piezoresistors in both of the legs close to the fixed end. The resistance in the piezoresistors is measured using a Wheatstone bridge circuit with three reference resistors, of which one is adjustable. The current flowing between the two branches of the Wheatstone bridge is first nulled by changing the resistance of the adjustable resistor. If the microcantilever bends, the piezoresistor changes its value and a current will flow between the two branches of the Wheatstone bridge. The current is converted via a differential amplifier into a voltage, which is proportional to the deflection value. For dynamic-mode measurement, the piezoresistive microcantilever is externally actuated via a piezocrystal driven by a frequency generator. The ac actuation voltage is fed as reference voltage into a lock-in amplifier and compared with the response of the Wheatstone bridge circuit allowing to sweep resonance curves and to determine shifts in resonance frequency.

1.2.4.2 Piezoelectric Readout

Piezoelectric microcantilevers [15] are driven via the inverse piezoelectric effect (self-excitation) by applying an electric ac voltage to the piezoelectric material (PZT or ZnO). Sensing of bending is performed by recording the piezoelectric current change taking advantage of the fact that the PZT layer produces a sensitive field response to weak stress through the direct piezoelectric effect. Piezoelectric microcantilevers are multilayer structures consisting of a SiO_2 cantilever and the PZT piezoelectric layer. Two electrode layers, insulated from each other, provide electrical contact. The entire structure is protected using passivation layers. An identical structure is usually integrated into the rigid chip body to provide a reference for the piezoelectric signals from the cantilever.

1.2.4.3 Optical (Beam-Deflection) Readout

The most frequently used approach to read out microcantilever deflections is optical beam deflection [16], because it is a comparatively simple method with an excellent lateral resolution.

The actual cantilever deflection Δx scales with the cantilever dimensions; therefore, deflection responses should be expressed in terms of surface stress $\Delta\sigma$ in N/m to be able to compare cantilever responses acquired with different setups. Various strategies to convert beam deflection signals into stress are described in the literature [17, 18]. Surface stress takes into account the cantilever material properties, such as the Poisson ratio ν, Young's modulus E and the cantilever thickness t. The radius of the curvature R of the cantilever characterizes bending, see Eq. 2. As shown in the drawing in Fig. 2, the actual cantilever displacement Δx is transformed into a displacement Δd on the position sensitive detector (PSD). The position of a light spot on a PSD is determined by measuring the photocurrents from the two facing electrodes. The movement of the light spot on the linear PSD is calculated from the two currents I_1 and I_2 and the size L of the PSD by

$$\Delta d = \frac{I_1 - I_2}{I_1 + I_2} \times \frac{L}{2} \,. \tag{4}$$

As all angles are very small, it can be assumed that the bending angle of the cantilever is equal to half of the angle θ of the deflected laser beam, i.e., $\theta/2$. Therefore, the bending angle of the cantilever can be calculated to be

$$\frac{\theta}{2} = \frac{\Delta d}{2s} \,, \tag{5}$$

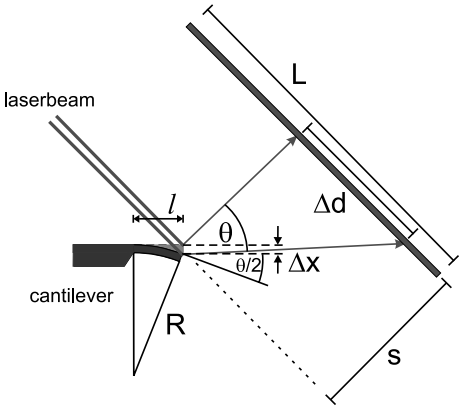

Fig. 2 Beam-deflection concept to determine microcantilever bending with an accuracy of one nanometer

where s is the distance between the PSD and the cantilever. The actual cantilever deflection Δx is calculated from the cantilever length l and the bending angle $\theta/2$ by

$$\Delta x = \frac{\theta/2}{2} \times l \,. \tag{6}$$

The combination of Eqs. 5 and 6 relates the actual cantilever deflection Δx to the PSD signal:

$$\Delta x = \frac{l \times \Delta d}{4s} \,. \tag{7}$$

The relation between the radius of curvature and the deflection angle is

$$\frac{\theta}{2} = \frac{l}{R} \,, \tag{8}$$

and after a substitution becomes

$$R = \frac{2ls}{\Delta d} \quad \text{or} \quad R = \frac{2\Delta x}{l^2} \,. \tag{9}$$

1.3 Realization of an Optical Beam-Deflection Setup

A measurement setup for microcantilever arrays consists of four main parts: 1. the measurement chamber hosting the microcantilever array, 2. an optical or piezoresistive system to detect the cantilever deflection (e.g., laser sources, collimation lenses and a PSD), 3. electronics to amplify, process, and acquire the signals from the PSD, and 4. a gas- or liquid-handling system to reproducibly inject samples into the measurement chamber and purge the chamber.

Figure 3 shows a realization of a setup for experiments performed in (a) liquid (biochemical) and (b) gaseous environment. The microcantilever sensor array is hosted in an analysis chamber of 20 μl in volume, with inlet and outlet ports for gases or liquids, respectively. The bending of the microcantilevers is measured using an array of eight vertical-cavity surface-emitting lasers (VCSELs) arranged at a linear pitch of 250 μm that emit at a wavelength of 760 nm into a narrow cone of 5 to 10°.

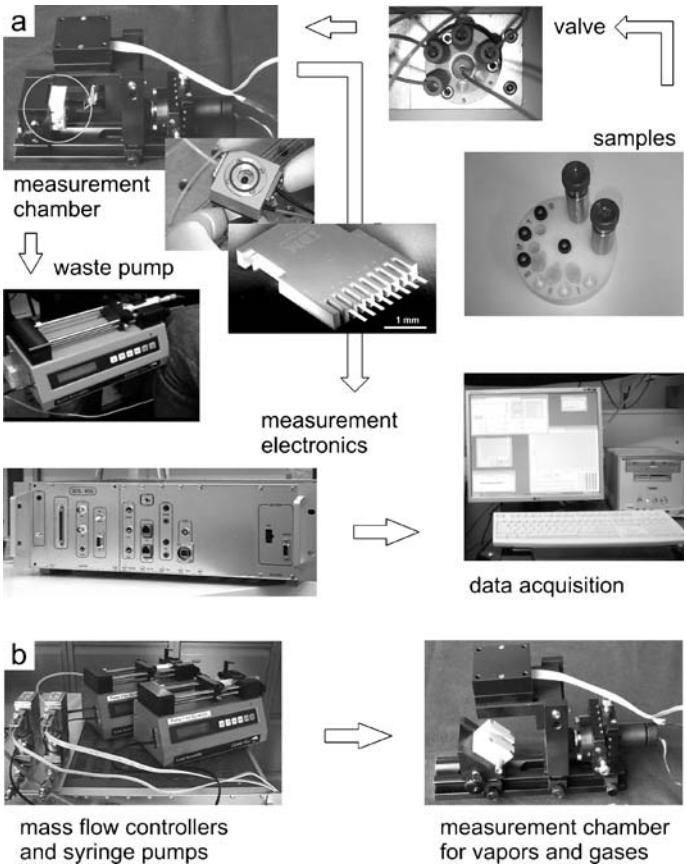

Fig. 3 **a** Realization of a static mode beam-deflection microcantilever-array sensor setup for measurements in liquids. A HPLC 6-way valve is used to select a liquid sample, which is pulled through teflon tubing into the measurement chamber hosting the microcantilever array, until it is collected in the waste pump. The microcantilever bending is measured using optical beam deflection involving VCSELs and a PSD. The location of the laser spot indicating microcantilever bending is processed and digitized using measurement electronics and a data acquisition card in a personal computer. **b** For measurements of vapors and gases the liquid handling system is replaced by a gas handling system consisting of mass flow controllers and syringe pumps for a supply of gaseous samples

The light of each VCSEL is collimated and focused onto the apex of the corresponding microcantilever by a pair of achromatic doublet lenses, 12.5 mm in diameter. This size was selected in order to make sure that all eight laser beams pass through the lenses close to its center in order to minimize scattering, chromatic, and spherical aberration artifacts. The light is then reflected off the gold-coated surface of the cantilever and hits the surface of a PSD. As only a single PSD is used, the eight lasers cannot be switched on simultaneously. Therefore, a time-multiplexing procedure is used to switch the lasers on and off sequentially at typical intervals of 10–100 ms. The resulting deflection signal is digitized and stored together with time information on a personal computer (PC), which also controls the multiplexing of the VCSELs as well as the switching of the valves and mass flow controllers used for setting the composition ratio of the analyte mixture.

The measurement setup for liquids consists of a poly-etheretherketone (PEEK) liquid cell, which contains the cantilever array and is sealed by a viton O-ring and a glass plate. The VCSELs and the PSD are mounted on a metal frame around the liquid cell. After preprocessing the position of the deflected light beam using a current-to-voltage converter and amplifier stage, the signal is digitized in an analog-to-digital converter and stored on a PC. The liquid cell is equipped with inlet and outlet ports for liquids. They are connected via 0.18 mm of i.d. teflon tubing to individual thermally-equilibrated glass containers, in which the biochemical liquids are stored. A six-position valve allows the inlet to the liquid chamber to be connected to each of the liquid-sample containers separately. The liquids are pulled through the liquid chamber by means of a syringe pump connected to the outlet of the chamber. A peltier element located beneath the microcantilever array in the PEEK chamber allows regulating the temperature within the chamber. The entire experimental setup is housed in a temperature-controlled box regulated with an accuracy of 0.01 K to the target temperature.

2 Operating Modes

A microcantilever sensor is a versatile tool for the investigation of various sample properties and allows to follow reactions occurring on its surface. Various operating modes have been presented.

2.1 Static Mode

Gradual bending of a microcantilever with molecular coverage is referred to as operation in the “static mode”. Various environments are possible, such as vacuum, ambient environment, and liquids. In a gaseous environment,

molecules adsorb on the functionalized sensing surface and form a molecular layer, provided there is affinity for the molecules to adhere to the surface. Polymer sensing layers show a partial sensitivity, because molecules from the environment diffuse into the polymer layer at different rates, mainly depending on the size and solubility of the molecules in the polymer layer. By selecting polymers among a wide range of hydrophilic/hydrophobic ligands, the chemical affinity of the surface can be influenced, because different polymers vary in diffusion suitability for polar/unpolar molecules. Thus, for detection in the gas phase, the polymers can be chosen according to the detection problem, i.e. what the applications demand. Typical chemicals to be detected are volatile organic compounds (VOCs).

Static-mode operation in liquids, however, usually requires rather specific sensing layers, based on molecular recognition, such as DNA hybridization or antigen-antibody recognition.

2.2 Dynamic Mode

If the molecules adsorb as a monolayer, the coverage and therewith the mass adsorbed can be determined from the static deflection signal. More generally, information on the amount of molecules adsorbed can be obtained by oscillating the microcantilever at its eigenfrequency. However, the surface coverage is basically not known. Furthermore, molecules on the surface might be exchanged with molecules from the environment in a dynamic equilibrium.

In contrast, mass changes can be determined accurately by tracking the eigenfrequency of the microcantilever during mass adsorption or desorption. The eigenfrequency equals the resonance frequency of an oscillating microcantilever if its elastic properties remain unchanged during the molecule adsorption/desorption process and damping effects are negligible. This operation mode is called the dynamic mode. The microcantilever is used as a microbalance, as with mass addition on the cantilever surface, the cantilever's eigenfrequency will shift to a lower value. The mass change on a rectangular cantilever is calculated [9] according to

$$\Delta m = (k/4\pi^2) \times (1/f_1^2 - 1/f_0^2)\,, \tag{10}$$

where f_0 is the eigenfrequency before the mass change occurs, and f_1 the eigenfrequency after the mass change. For the calculation of the spring constant k of the cantilever see Eq. 1.

Mass-change determination can be combined with varying environment temperature conditions to obtain a method introduced in the literature as "micromechanical thermogravimetry" [14]. The sample to be investigated is mounted onto the cantilever. Its mass should not exceed several hundred nanograms. In case of adsorption, desorption, or decomposition processes,

mass changes in the picogram range can be observed in real time by tracking the resonance-frequency shift.

Dynamic mode operation in a liquid environment poses problems, such as high damping of the cantilever oscillation due to the high viscosity of the surrounding media. This results in a low quality factor Q of the oscillation, and the resonance frequency shift is difficult to track with high resolution. The quality factor is defined as

$$Q = 2\Delta f / f_0 \,, \tag{11}$$

whereas in air a frequency resolution of below 1 Hz is easily achieved, resolution values of about 20 Hz are already to be considered very good for measurements in a liquid environment. In the case of damping or changes of the elastic properties of the cantilever during the experiment, e.g., a stiffening or softening of the spring constant by adsorption of a molecule layer, the measured resonance frequency will not be exactly the same as the eigenfrequency, and the mass derived from the frequency shift will be inaccurate. Unlike in ultrahigh vacuum conditions [19, 20], where resonance frequency is equal to eigenfrequency, these terms should be carefully distinguished for operation in a large damping environment, as described, for example, in [21].

2.3 Heat Mode

For a microcantilever that is coated with metal layers, thermal expansion differences in cantilever and coating layer will have to be taken into account, as they will further influence cantilever bending as a function of temperature. This mode of operation is referred to as "heat mode" and causes cantilever bending because of differing thermal expansion coefficients in sensor layer and cantilever materials [8]:

$$\Delta z = 1.25 \times (\alpha_1 - \alpha_2) \times (t_1 + t_2)/t_2^2 \kappa \times l^3 P/(\alpha_1 t_1 + \alpha_2 t_2) w \,. \tag{12}$$

Here α_1, α_2 are the thermal expansion coefficients of the microcantilever and coating materials, t_1, t_2 the material thicknesses, P is the total power generated on the cantilever, and κ a geometry parameter of the cantilever device.

Heat changes are either caused by external influences, such as a change in temperature, occur directly on the surface by exothermal, e.g., catalytic, reactions, or are due to material properties of a sample attached to the apex of the cantilever (micromechanical calorimetry). The sensitivity of the cantilever heat mode is orders of magnitude higher than that of traditional calorimetric methods performed on milligram samples, as it only requires nanogram amounts of sample and achieves nanojoules [9] to picojoules [22, 23] sensitivity.

These three measurement modes have established cantilevers as versatile tools to perform experiments in nanoscale science with very small amounts of material.

2.4 Photothermal Spectroscopy

When a material adsorbs photons, a fraction of energy is converted into heat. This photothermal heating can be measured as a function of the light wavelength to provide optical absorption data of the material. The interaction of light with a bimetallic cantilever creates heat on the cantilever surface, resulting in a bending of the cantilever [24]. Such bimetallic-cantilever devices are capable of detecting heat flows due to an optical heating power of 100 pW, being two orders of magnitude better than in conventional photothermal spectroscopy.

2.5 Electrochemistry

A cantilever coated with a metallic layer (a measurement electrode) on one side is placed in an electrolytic medium, e.g., a salt solution, together with a metallic reference electrode, usually made of a noble metal. Variations of the voltage between measurement and reference electrode induce electrochemical processes on the measurement electrode (cantilever), e.g., the adsorption or desorption of ions from the electrolyte solution onto the measurement electrode. These processes lead to a bending of the cantilever according to the Shuttleworth equation relating stress, surface energy, and its derivative with respect to strain [25].

3 Functionalization

It is essential that the surfaces of the cantilever are coated in a proper way to provide suitable receptor surfaces for the molecules to be detected. Such coatings should be specific, homogeneous, stable, reproducible, and either reusable or designed for single use only. For static mode measurements, one side of the cantilever should be passivated for blocking unwanted adsorption. Often, the cantilever's upper side, the sensor side, is coated with a 20 nm thick layer of gold to provide a platform for the binding of receptor molecules, for example via thiol chemistry, whereas the lower side is passivated using silane chemistry for coupling an inert surface such as poly-ethylene glycol silane. Silanization is performed first on the silicon microcantilever. Then, a gold layer is deposited on the top side of the cantilever, leaving the lower side un-

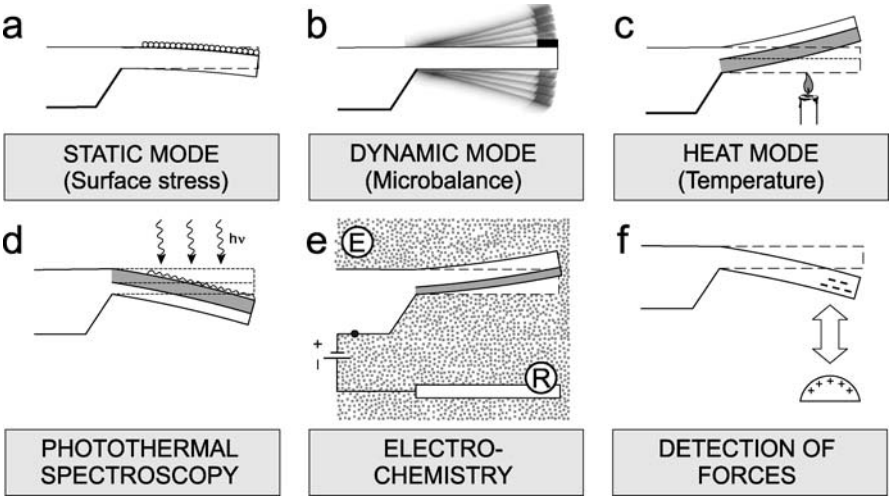

Fig. 4 Major operating modes of microcantilever sensors: **a** static mode exploiting surface stress changes, **b** dynamic mode to extract mass changes, **c** heat mode for determining phase transitions and heat capacity effects of a sample attached to the cantilever, **d** photothermal spectroscopy taking advantage of light-induced interactions with the cantilever coating, **e** electrochemistry, **f** detection of forces between the microcantilever and an external sample

changed. It is very important that the method of choice is fast, reproducible, reliable, and allows one or both cantilever surfaces to be coated separately. Various ways are reported to coat a cantilever with molecular layers. Here, two different strategies are highlighted.

3.1 Coating in Microcapillary Arrays

A convenient method to coat microcantilevers with probe molecules is the insertion of the cantilever array into an array of dimension-matched disposable glass capillaries. The outer diameter of the glass capillaries is 240 μm so that they can be placed neatly next to each other to accommodate the pitch of the cantilevers in the array (250 μm). Their inner diameter is 150 μm, allowing sufficient room to insert the cantilevers (width: 100 μm) safely (Fig. 5). This method has been successfully applied for the deposition of a variety of materials onto cantilevers, such as polymer solutions [26], self-assembled monolayers [27], thiol-functionalized single-stranded DNA oligonucleotides [28–30], and proteins [31, 32]. Incubation of the microcantilever array in the microcapillaries takes from a few seconds (the self-assembly of alkanethiol monolayers) to several tens of minutes (coating with protein solutions). The microcapillary functionalization unit may be placed in an environment of sat-

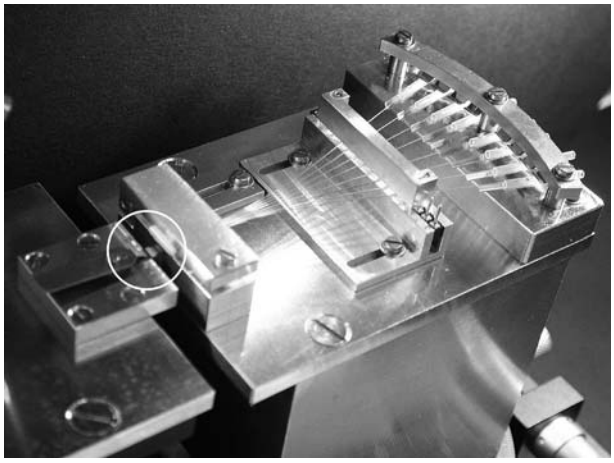

Fig. 5 Functionalization stage for coating microcantilevers with self-assembled monolayers, for example. Microcapillaries filled with the solutions containing the probe molecules transport the liquid via capillarity to the cantilevers, whereby each microcantilever is inserted into one microcapillary. Therefore, no cross-contanination of liquids will occur. The location of the microcantilever array is indicated by a circle

urated vapor of the solvent used for the probe molecules to avoid drying out of the solutions.

3.2 Coating Using an Inkjet Spotter

Coating in microcapillary arrays requires the manual alignment of the microcantilever array and the functionalization tool, and is therefore not suitable for coating large numbers of cantilever arrays. Moreover, upper and lower surface of microcantilevers are exposed to the solution containing the probe molecules. For ligands that bind covalently, e.g., by gold-thiol coupling, only the upper surface will be coated, provided the gold layer has only be applied on the upper surface of the microcantilever. For coating with polymer layers, microcapillary arrays are not suitable, because both surfaces of the microcantilever would be coated with polymer layers, being inappropriate for static mode measurements, where an asymmetry between the upper and lower surface is required.

A method appropriate for coating many cantilever sensor arrays in a rapid and reliable way is inkjet spotting [33, 34]; see Fig. 6. An x–y–z positioning system allows a fine nozzle (capillary diameter: 70 μm) to be positioned with an accuracy of approx. 10 μm over a cantilever. Individual droplets (diameter: 60–80 μm, volume 0.1–0.3 nl) can be dispensed individually by means of a piezo-driven ejection system in the inkjet nozzle. When the droplets

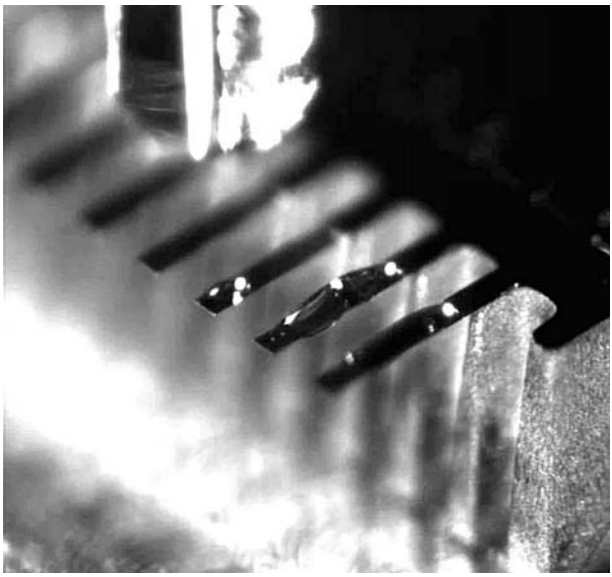

Fig. 6 Single-sided microcantilever coating using an inkjet spotter. The amount of liquid containing the probe molecules can be dosed accurately by choosing the number of drops being ejected from the nozzle

are spotted with a pitch smaller than 0.1 mm, they merge and form continuous films. By adjusting the number of droplets deposited on cantilevers, the resulting film thickness can be controlled precisely. The inkjet-spotting technique allows a cantilever to be coated within seconds and yields very homogeneous, reproducibly deposited layers of well-controlled thickness. The suc-

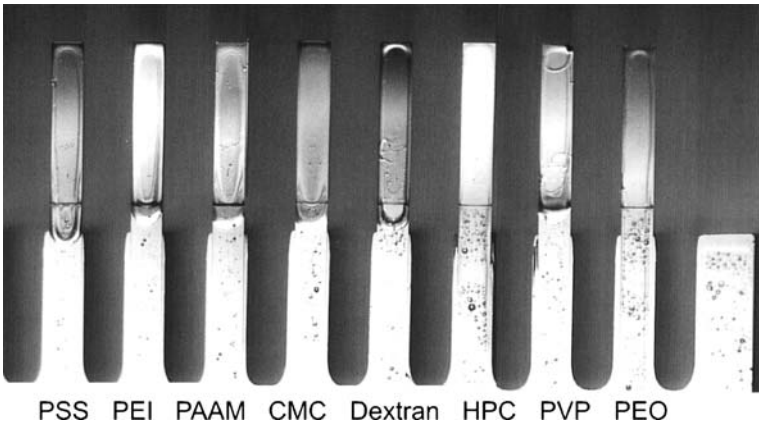

Fig. 7 Optical microscopy image of a polymer-coated microcantilever array for application as an artificial nose for solvents. The pitch between microcantilevers is 250 micron

cessful coating of self-assembled alkanethiol monolayers, polymer solutions, self-assembled DNA single-stranded oligonucleotides [34], and protein layers has been demonstrated. Figure 7 shows a polymer coated microcantilever array for the chemical vapor detection experiments described in the following section. In conclusion, inkjet spotting has turned out to be a very efficient and versatile method for functionalization that can even be used to coat arbitrarily-shaped sensors reproducibly and reliably [35, 36].

4
Applications

The applications of microcantilever sensors are manifold: gas sensing, the quality control of chemicals, food, and air as well as process monitoring and control, just to give a few examples. As an artificial nose, cantilever array sensors can characterize odors and vapors and may be used to assist fragrance design. Due to its extremely high sensitivity, the technique has a large potential to be applied for drugs and explosives detection, as well as for forensic investigations. In a liquid environment, its major applications are in biochemical analysis and medical diagnosis.

4.1
Chemical Vapor Detection

Sensors for the reliable detection of solvent vapors are important in chemical process technology, e.g., for safe handling during storage and the transport of large amounts of solvents in containers. A fast test is needed to identify solvents in transport containers. Such a test might be realized using polymer-coated microcantilever sensors. In a laboratory setup, 0.1 ml of various solvents was placed in vials, and the vapor from the headspace above the liquid was sampled using microcantilever sensors, operated in static deflection mode as a kind of artificial nose. The detection of vapors takes place via the diffusion of the vapor molecules into the polymer, resulting in a swelling of the polymer and a bending of the cantilever. Each cantilever is coated with a different polymer or polymer blend (see Fig. 7). The bending is specific for the interaction between solvent vapor and polymer time- and magnitude-wise.

Cantilever deflection traces upon subsequent injection of solvent vapor for 30 s and purging with dry nitrogen for 150 s are shown in Fig. 8 for (a) water, (b) ethanol, and (c) methanol.

The cantilever deflections at 10, 20, 30, and 40 seconds after the completion of the solvent vapor injection are extracted. They describe the time-development of the curves in a reduced data set, i.e., $8 \times 4 = 32$ cantilever deflection amplitudes ("fingerprint") that account for a measurement data set. This data set is then evaluated using principal component analysis (PCA)

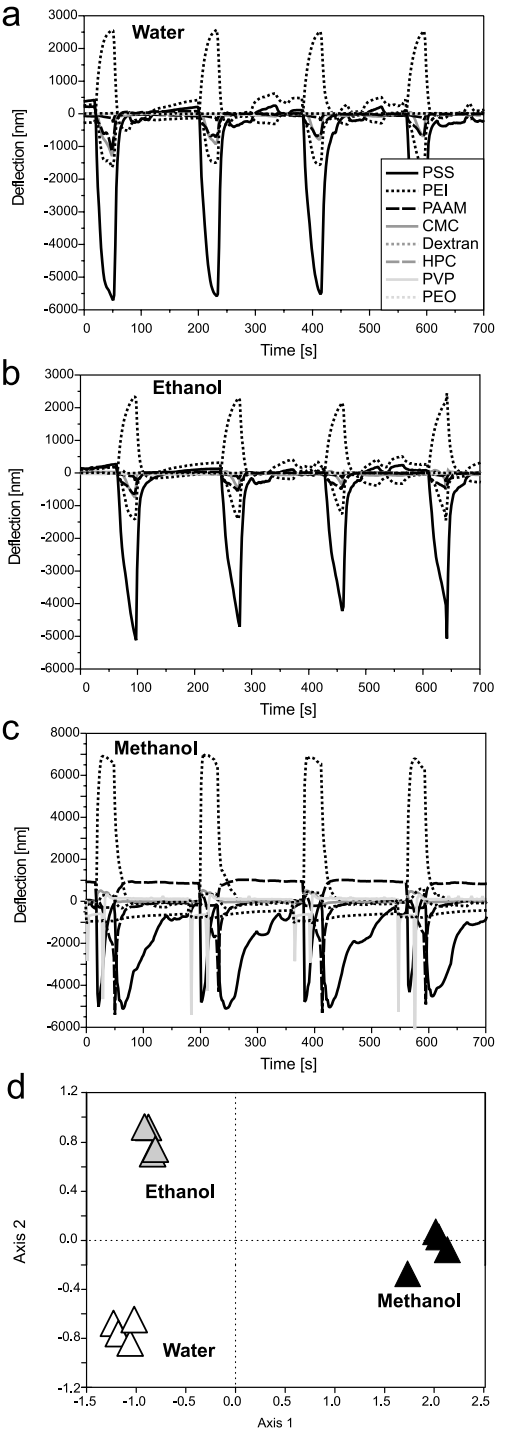
a
Water
Deflection [nm]
Time [s]
PSS
PEI
PAAM
CMC
Dextran
HPC
PVP
PEO
b
Ethanol
Deflection [nm]
Time [s]
c
Methanol
Deflection [nm]
Time [s]
d
Ethanol
Methanol
Water
Axis 2
Axis 1

◀ **Fig. 8** Application of microcantilever array sensors as an artificial electronic nose. Measurement traces of microcantilevers coated with polymers during the detection of **a** water, **b** ethanol, **c** methanol. For every solvent, four consecutive injections of vapor saturated with solvent are shown. Upon injection of solvent vapor, the microcantilevers deflect in a specific way due to the swelling of the polymer layer on exposure to the solvent vapor. Subsequent purging of the measurement chamber with dry nitrogen gas (flow rate: 100 ml/min) promotes diffusion of the solvent molecules out of the polymer layer, resulting in a bending back of the microcantilevers to the baseline. **d** Principal component analysis (PCA) of the response patterns of all eight microcantilevers upon exposure to the three different solvent vapors. Clear separation of the clusters proves the excellent distinction capability of the artificial nose setup. Each symbol in the PCA plot corresponds to one of the injections in **a**–**c**

techniques, extracting the most dominant deviations in the responses for the various sample vapors. The axes refer to projections of the multidimensional datasets into two dimensions (principal components). The labels in the PCA plot (Fig. 8d) indicate the individual measurements. The PCA plot shows well-separated clusters of measurements indicating the clear identification of vapor samples. Even vapor mixtures can be analyzed using PCA [37].

4.2 Explosives Detection

A large effort is also put into the development of inexpensive, highly selective, and very sensitive small sensors that can be mass-produced and microfabricated. Current miniaturized versions, including ion mobility spectrometers [38] or nuclear quadrupole resonance [39] are bulky. Microcantilever sensors offer sensitivities more than two orders of magnitude better than quartz crystal microbalances [40], flexural plate wave oscillators [41], and surface acoustic wave devices [42]. Several approaches to detect dangerous chemicals are already described in the literature: photomechanical chemical microsensors based on adsorption-induced and photo-induced stress changes due to the presence of diisopropyl methyl phosphonate (DIMP), which is a model compound for phosphorous-containing chemical warfare agents, and trinitrotoluene (TNT), an explosive [43]. Further explosives frequently used include pentaerythritol tetranitrate (PETN) and hexahydro-1,3,5-triazine (RDX), often also with plastic fillers [44]. These compounds are very stable, if no detonator is present. Their explosive power, however, is very large, and moreover, the vapor pressures of PETN and RDX are very low, in the range of ppb and ppt. By functionalizing microcantilevers with self-assembled monolayers of 4-mercaptobeonzoic acid (4-MBA) PETN was detected at a level of 1400 ppt and RDX at a level of 290 ppt [44]. TNT was found to readily stick to Si surfaces, suggesting the use of microcantilevers for TNT detection, taking advantage of the respective adsorption/desorption kinetics [45, 46]. The detection of TNT via deflagration on a microcantilever is de-

Table 1 Polymer coatings

Cantilever	Polymer	Full name of compound
1	PSS	Poly(sodium 4-styrenesulfonate)
2	PEI	Polyethylenimine
3	PAAM	Poly(allylamine hydrochloride)
4	CMC	Carboxymethylcellulose sodium salt
5	Dextran	Dextran from Leuconostoc spp.
6	HPC	Hydroxypropyl cellulose
7	PVP	Polyvinylpyrrolidone
8	PEO	Poly(2-ethyl-2-oxazoline)

scribed by Pinnaduwage et al. [47]. They used piezoresistive microcantilevers where the cantilever deflection was measured optically via beam deflection. TNT vapor from a generator placed 5 mm away from the microcantilever was observed to adsorb on its surface resulting in a decrease of resonance frequency. Application of an electrical pulse (10 V, 10 ms) to the piezoresistive cantilever resulted in deflagration of the TNT vapor and a bump in the cantilever bending signal. This bump was found to be related to the heat produced during deflagration. The amount of heat released is proportional to the area of the bump in the time vs. bending signal diagram of the process. The deflagration was found to be complete, as the same resonance frequency as before the experiment was observed. The amount of TNT mass involved was determined as 50 pg. The technique was later extended to the detection of PETN and RDX, where a much slower reaction kinetics was observed [48, 49]. Traces of 2,4-dinitrotoluene (DNT) in TNT can also be used for detection of TNT, because it is the major impurity in production grade TNT. Furthermore DNT is a decomposition product of TNT. The saturation concentration of DNT in air at 20 °C is 25 times higher than that of TNT. DNT was reported to be detected at the 300 ppt level using polysiloxane polymer layers [50]. The microfabrication of electrostatically actuated resonant microcantilever beams in CMOS technology for detection of the nerve agent stimulant dimethylmethylphosphonate (DMMP) using polycarbosilane-coated beams [51] is an important step towards an integrated platform based on silicon microcantilevers, which, besides compactness, might also include telemetry [52].

5 Recent Literature and Outlook

In recent years the field of cantilever sensors has been very active. Some recent developments are reviewed in [53–58]. Major topics published include the following studies: the fabrication of silicon piezoresistive [59, 60] or

polymer [61] cantilevers, detection of vapors and volatile compounds, e.g., mercury vapor [62], HF vapor [63, 64], chemical vapors [65], as well as the development of gas sensors based on the piezoresistive concept [66]. Pd-based sensors for hydrogen [67], deuterium and tritium [68] are reported, as well as sensors taking advantage of the sensing properties of hydrogels [69] or zeolites [70]. A humidity sensor is suggested in [71]. A field of growing interest is the detection of explosives [47], pathogens [72], nerve agents [73], viruses [74], bacteria, e.g., E. coli, [75], and pesticides such as dichlorodiphenyltrichloroethane (DDT) [76]. The issues of detection of environmental pollutants are discussed in [77]. A chemical vapor sensor based on the bimetal technique is described in [78]. The measurement of electrochemical redox reactions with cantilevers is reported [79]. In biochemical applications, detection of DNA [80, 81], proteins [82], prostate-specific antigen (PSA) [83], peptides using antibodies [84] and living cells [85] is possible. Medical applications involve diagnostics [86], drug discovery [87], and the detection of glucose [88]. To increase the complexity of microcantilever applications, two-dimensional microcantilever arrays have been proposed for multiplexed biomolecular analysis [89, 90].

For measurements in gaseous environment, a sensor application in dynamic mode of piezoelectric cantilevers for an ultrasensitive nanobalance is reported [91]. Micromolded plastic microcantilevers are proposed for chemical sensing [92], as well as micromachined silicon microcantilevers for gas sensing based on capacitive read-out [93]. In chemical sensing, ligand-functionalized microcantilevers for characterization of metal ion sensing are presented [94], and an array of flexible microcantilever beams is used to observe the action of rotaxane based artificial molecular muscles [95]. The importance of homeland security is discussed in [51], where electrostatically actuated resonant microcantilever beams in CMOS technology are utilized for the detection of chemical weapons. An integrated sensor platform for homeland defense based on silicon microcantilevers is described in [52]. In the field of electrochemistry, microcantilevers have been used to measure redox-induced surface stress [96], and a differential microcantilever-based system for measuring surface stress changes induced by electrochemical reactions has been presented [97].

Many publications concern biochemical applications, such as a label-free immunosensor array using single-chain antibody fragments [32] and the label-free analysis of transcription factors using microcantilever arrays [98]. Microcantilevers modified by horseradish peroxidase intercalated nano-assembly have been applied for hydrogen peroxide detection [99], and the detection of cystamine dihydrochloride and glutaraldehyde [100, 101]. Furthermore, a back-propagation artificial neural network recognition study of analyte species and concentration has been presented [102].

Cantilever sensors for nanomechanical detection have been used for the observation of specific protein conformation changes [103]. In the field of

DNA hybridization detection, the chemomechanics of surface stresses induced by DNA hybridization has been studied [104] and the grafting density and binding efficiency of DNA and proteins on gold surfaces has been characterized and improved [105]. An electrostatic microcantilever array biosensor has been applied for DNA detection [106], and microcantilever sensors for DNA hybridization reactions or antibody-antigen interactions without using external labels have been tested in dynamic mode [107].

An immunoassay of prostate-specific antigen (PSA) exploiting the resonant frequency shift of piezoelectric nanomechanical microcantilevers is reported [108], as well as phospholipid vesicle adsorption measured in situ using resonating cantilevers in a liquid cell [109]. Microcantilevers have been utilized to detect bacillus anthracis [110], and glucose oxidase multilayer modified microcantilevers can measure glucose [111].

Effort has been put into the refinement of the cantilever sensor method: a dimension dependence study of the thermomechanical noise of microcantilevers is available to determine the minimal detectable force and surface stress [112]. Furthermore, the geometrical and flow configurations for enhanced microcantilever detection within a fluidic cell have been investigated [113]. A microcapillary pipette-assisted method to prepare polyethylene glycol-coated microcantilever sensors has been suggested [114] and the role of material microstructure in plate stiffness with relevance to microcantilever sensors has been studied [115]. Double-sided surface stress cantilever sensors for more sensitive cantilever surface stress measurement have been proposed [116].

Enhanced microcantilever sensor techniques involve a biosensor based on magnetostrictive microcantilevers [117], the piezoelectric self-sensing of adsorption-induced microcantilever bending [118], the optical sequential readout of microcantilever arrays for biological detection achieved by scanning the laser beam [119], and cysteine monolayer modified microcantilevers to monitor flow pulses in a liquid [120]. The photothermal effect has been used to study dynamic elastic bending in microcantilevers [121]. For dynamic mode, temperature and pressure dependence of resonance in multi-layer microcantilevers have been investigated [122] and the inaccuracy in the detection of molecules has been discussed [123].

The influence of surface stress on the resonance behavior of microcantilevers in higher resonant modes has been studied [124] and an alternative solution has been proposed to improve the sensitivity of resonant microcantilever chemical sensors by measuring in high-order modes and reducing geometrical dimensions [125]. A modal analysis of microcantilever sensors with environmental damping is reported [126]. Furthermore, theoretical work is available on the simulation of adsorption-induced stress of a microcantilever sensor [127], the influence of nanobubbles on the bending of microcantilevers [128], the modeling and simulation of thermal effects in flexural microcantilever resonator dynamics [129], and surface stress effects related to

the resonance properties of cantilever sensors [130]. Further information about the origin of the signal in microcantilever sensors, especially diffusion properties, is found in [131]. Finally, a review on nanotechnologies for biomolecular detection and medical diagnostics appeared [132].

Cantilever array sensors might be one of the solutions to the demand for miniaturized, ultrasensitive and fast-responsive sensors for application in gas detection, and surveillance, as well as in biochemistry and medicine. For their reliable use, some technical issues have still to be resolved, e.g., the simplification of the alignment procedure, which is related to the optical beam deflection readout. Here, the integration possibilities with piezoresistive microcantilevers are much higher than for those based on optical beam-deflection. Silicon nitride coating [133] is a promising strategy to obtain the durable protection of piezoresistive microcantilevers, even in biochemical solutions.

Furthermore, the periphery for measurements with microcantilever array sensors is required to be miniaturized as well, whereby microfluidic concepts have to be integrated with the microcantilever array. Further downscaling is theoretically favorable as the sensitivity of the devices improves, but it also poses technical challenges to determine deflection signals from such tiny structures. The use of a few hundred nanometer long and a few ten nanometer thick nanocantilevers has been reported to yield a dramatical increase in performance [134, 135], but their practical use becomes very complicated, e.g., as far as the functionalization, the sample handling, and the readout are concerned. The field is open to welcome completely new ideas for efficient working procedures for nanocantilever sensors.

Acknowledgements We thank R. McKendry (University College London, London, U.K.), M. Hegner, W. Grange, Th. Braun, J. Zhang, A. Bietsch, V. Barwich, M. Ghatkesar, F. Huber, N. Backmann, J.-P. Ramseyer, A. Tonin, H.R. Hidber, E. Meyer and H.-J. Güntherodt (University of Basel, Basel, Switzerland) for valuable contributions and discussions, as well as U. Drechsler, M. Despont, H. Schmid, E. Delamarche, H. Wolf, R. Stutz, R. Allenspach, and P.F. Seidler (IBM Research, Zurich Research Laboratory, Rüschlikon, Switzerland). We also thank the European Union FP 6 Network of Excellence FRONTIERS for support. This project is funded partially by the National Center of Competence in Research in Nanoscience (Basel, Switzerland), the Swiss National Science Foundation and the Commission for Technology and Innovation (Bern, Switzerland).

References

1. Wilfinger RJ, Bardell PH, Chhabra DS (1968) IBM J Res Dev 12:113
2. Heng TMS (1971) IEEE Trans Microwave Theory Techn 19:652
3. Petersen KE (1979) IBM J Res Develop 23:376
4. Kolesar ES (1983) US Patent 4 549 427
5. Binnig G, Quate CF, Gerber C (1986) Phys Rev Lett 56:930
6. Itoh T, Suga T (1994) Appl Phys Lett 64:37
7. Cleveland JP, Manne S, Bocek D, Hansma PK (1993) Rev Sci Instrum 64:403
8. Gimzewski JK, Gerber C, Meyer E, Schlittler RR (1994) Chem Phys Lett 217:589

9. Thundat T, Warmack RJ, Chen GY, Allison DP (1994) Appl Phys Lett 64:2894
10. Thundat T, Chen GY, Warmack RJ, Allison DP, Wachter EA (1995) Anal Chem 67:519
11. Lang HP, Berger R, Andreoli C, Brugger J, Despont M, Vettiger P, Gerber C, Gimzewski J, Ramseyer JP, Meyer E, Güntherodt HJ (1998) Appl Phys Lett 72:383
12. Stoney GG (1909) Proc R Soc London, Ser A 82:172
13. von Preissig FJ (1989) J Appl Phys 66:4262
14. Berger R, Lang HP, Gerber C, Gimzewski JK, Fabian JH, Scandella L, Meyer E, Güntherodt HJ (1998) Chem Phys Lett 294:363
15. Lee C, Itoh T, Ohashi T, Maeda R, Suga T (1997) J Vac Sci Technol B 15:1559
16. Meyer G, Amer NM (1988) Appl Phys Lett 53:2400
17. Jeon S, Jung N, Thundat T (2007) Sens Actuators B 122:365
18. Godin M, Williams PJ, Tabard-Cossa V, Laroche O, Beaulieu LY, Lennox RB, Grutter P (2004) Langmuir 20:7090
19. Ekinci KL, Roukes ML (2005) Rev Sci Instr 76:061101
20. Ilic B, Craighead HG, Krylov S, Senaratne W, Ober C, Neuzil P (2004) J Appl Phys 95:3694
21. Braun T, Barwich V, Ghatkesar MK, Bredekamp AH, Gerber C, Hegner M, Lang HP (2005) Phys Rev E 72:031907
22. Bachels T, Schäfer R (1999) Chem Phys Lett 300:177
23. Bachels T, Tiefenbacher F, Schäfer R (1999) J Chem Phys 110:10008
24. Barnes JR, Stephenson RJ, Welland ME, Gerber C, Gimzewski JK (1994) Nature 372:79
25. Tabard-Cossa V, Godin M, Burgess IJ, Monga T, Lennox RB, Grutter P (2007) Anal Chem 79:8136
26. Baller MK, Lang HP, Fritz J, Gerber C, Gimzewski JK, Drechsler U, Rothuizen H, Despont M, Vettiger P, Battiston FM, Ramseyer JP, Fornaro P, Meyer E, Güntherodt HJ (2000) Ultramicroscopy 82:1
27. Fritz J, Baller MK, Lang HP, Strunz T, Meyer E, Güntherodt HJ, Delamarche E, Gerber C, Gimzewski JK (2000) Langmuir 16:9694
28. Fritz J, Baller MK, Lang HP, Rothuizen H, Vettiger P, Meyer E, Güntherodt HJ, Gerber C, Gimzewski JK (2000) Science 288:316
29. McKendry R, Zhang J, Arntz Y, Strunz T, Hegner M, Lang HP, Baller MK, Certa U, Meyer E, Güntherodt HJ, Gerber C (2002) Proc Natl Acad Sci USA 99:9783
30. Zhang J, Lang HP, Huber F, Bietsch A, Grange W, Certa U, McKendry R, Güntherodt HJ, Hegner M, Gerber C (2006) Nat Nanotechn 1:214
31. Arntz Y, Seelig JD, Lang HP, Zhang J, Hunziker P, Ramseyer JP, Meyer E, Hegner M, Gerber C (2003) Nanotechnology 14:86
32. Backmann N, Zahnd C, Huber F, Bietsch A, Plückthun A, Lang HP, Güntherodt HJ, Hegner M, Gerber C (2005) Proc Natl Acad Sci USA 102:14587
33. Bietsch A, Hegner M, Lang HP, Gerber C (2004) Langmuir 20:5119
34. Bietsch A, Zhang J, Hegner M, Lang HP, Gerber C (2004) Nanotechnology 15:873
35. Lange D, Hagleitner C, Hierlemann A, Brand O, Baltes H (2002) Anal Chem 74:3084
36. Savran CA, Burg TP, Fritz J, Manalis SR (2003) Appl Phys Lett 83:1659
37. Taurino AM, Distante C, Siciliano P, Vasanelli L (2003) Sens Actuators B 93:117
38. Ewing RG, Miller CJ (2001) Field Anal Chem Technol 5:215
39. Garroway AN, Buess ML, Miller JB, Suits BH, Hibbs AD, Barrall GA, Matthews R, Burnett LJ (2001) IEEE Trans Geosci Remote Sens 39:1108
40. O'Sullivan CK, Guilbault GG (1999) Biosens Bioelectron 14:663
41. Cunningham B, Weinberg M, Pepper J, Clapp C, Bousquet R, Hugh B, Kant R, Daly C, Hauser E (2001) Sens Actuators B 73:112

42. Grate JW (2000) Chem Rev 100:2627 (Washington, DC)
43. Datskos PG, Sepaniak MJ, Tipple CA, Lavrik N (2001) Sens Actuators B 76:393
44. Pinnaduwage LA, Boiadjiev V, Hawk JE, Thundat T (2003) Appl Phys Lett 83:1471
45. Muralidharan G, Wig A, Pinnaduwage LA, Hedden D, Thundat T, Lareau RT (2003) Ultramicroscopy 97:433
46. Pinnaduwage LA, Yi D, Tian F, Thundat T, Lareau RT (2004) Langmuir 20:2690
47. Pinnaduwage LA, Wig A, Hedden DL, Gehl A, Yi D, Thundat T, Lareau RT (2004) J Appl Phys 95:5871
48. Pinnaduwage LA, Thundat T, Gehl A, Wilson SD, Hedden DL, Lareau RT (2004) Ultramicroscopy 100:211
49. Pinnaduwage LA, Gehl A, Hedden DL, Muralidharan G, Thundat T, Lareau RT, Sulchek T, Manning L, Rogers B, Jones M, Adams JD (2003) Nature 425:474
50. Pinnaduwage LA, Thundat T, Hawk JE, Hedden DL, Britt R, Houser EJ, Stepnowski S, McGill RA, Bubb D (2004) Sens Actuators B 99:223
51. Voiculescu I, Zaghloul ME, McGill RA, Houser EJ, Fedder GK (2005) IEEE Sensors J 5:641
52. Pinnaduwage LA, Ji HF, Thundat T (2005) IEEE Sensors J 5:774
53. Majumdar A (2002) Disease Markers 18:167
54. Lavrik NV, Sepaniak MJ, Datskos PG (2004) Rev Sci Instrum 75:2229
55. Ziegler C (2004) Anal Bioanal Chem 379:946
56. Hansen KM, Thundat T (2005) Methods 37:57
57. Carrascosa LG, Moreno M, Alvarez M, Lechuga LM (2005) TRAC-Trends Anal Chem 25:196
58. Yan XD, Ji HF, Thundat T (2006) Curr Anal Chem 2:297
59. Tang YJ, Fang J, Yan XD, Ji HF (2004) Sens Actuators B 97:109
60. Forsen E, Nilsson SG, Carlberg P, Abadal G, Perez-Murano F, Esteve J, Montserrat J, Figueras E, Campabadal F, Verd J, Montelius L, Barniol N, Boisen A (2004) Nanotechnology 15:S628
61. McFarland AW, Poggi MA, Bottomley LA, Colton JS (2004) Rev Sci Instrum 75:2756
62. Rogers B, Manning L, Jones M, Sulchek T, Murray K, Beneschott B, Adams JD, Hu Z, Thundat T, Cavazos H, Minne SC (2003) Rev Sci Instrum 74:4899
63. Mertens J, Finot E, Nadal MH, Eyraud V, Heintz O, Bourillot E (2004) Sens Actuators B 99:58
64. Tang YJ, Fang J, Xu XH, Ji HF, Brown GM, Thundat T (2004) Anal Chem 76:2478
65. Abedinov N, Popov C, Yordanov Z, Ivanov T, Gotszalk T, Grabiec P, Kulisch W, Rangelow IW, Filenko D, Shirshov YJ (2003) Vac Sci Technol B 21:2931
66. Zhou J, Li P, Zhang S, Huang YP, Yang PY, Bao MH, Ruan G (2003) Microelectron Eng 69:37
67. Baselt DR, Fruhberger B, Klaassen E, Cemalovic S, Britton Jr. CL, Patel SV, Mlsna TE, McCorkle D, Warmack B (2003) Sens Actuators B 88:120
68. Fabre A, Finot E, Demoment J, Contreras S (2003) Ultramicroscopy 97:425
69. Zhang YF, Ji HF, Brown GM, Thundat T (2003) Anal Chem 75:4773
70. Zhou J, Li P, Zhang S, Long YC, Zhou F, Huang YP, Yang PY, Bao MH (2003) Sens Actuators B 94:337
71. Lee CY, Lee GB (2003) J Micromech Microeng 13:620
72. Weeks BL, Camarero J, Noy A, Miller AE, Stanker L, De Yoreo JJ (2003) Scanning 25:297
73. Yang YM, Ji HF, Thundat T (2003) J Am Chem Soc 125:1124
74. Gunter RL, Delinger WG, Manygoats K, Kooser A, Porter TL (2003) Sens Actuators A 107:219

75. Gfeller KY, Nugaeva N, Hegner M (2005) Biosens Bioelectron 21:528
76. Alvarez M, Calle A, Tamayo J, Lechuga LM, Abad A, Montoya A (2003) Biosens Bioelectron 18:649
77. Cherian S, Gupta RK, Mullin BC, Thundat T (2003) Biosens Bioelectron 19:411
78. Adams JD, Parrott G, Bauer C, Sant T, Manning L, Jones M, Rogers B, McCorkle D, Ferrell TL (2003) Appl Phys Lett 83:3428
79. Quist F, Tabard-Cossa V, Badia A (2003) J Phys Chem B 107:10691
80. Gunter RL, Zhine R, Delinger WG, Manygoats K, Kooser A, Porter TL (2004) IEEE Sensors J 4:430
81. Alvarez M, Carrascosa LG, Moreno M, Calle A, Zaballos A, Lechuga LM, Martinez C, Tamayo J (2004) Langmuir 20:9663
82. Lee JH, Kim TS, Yoon KH (2004) Appl Phys Lett 84:3187
83. Wu G, Datar RH, Hansen KM, Thundat T, Cote RJ, Majumdar A (2001) Nat Biotechnol 19:856
84. Kim BH, Mader O, Weimar U, Brock R, Kern DP (2003) J Vac Sci Technol B 21:1472
85. Saif MTA, Sager CR, Coyer S (2003) Ann Biomed Eng 31:950
86. Kumar S, Bajpai RP, Bharadwaj LM (2003) IETE Techn Rev 20:361
87. Zhang YF, Venkatachalan SP, Xu H, Xu XH, Joshi P, Ji HF, Schulte M (2004) Biosens Bioelectron 19:1473
88. Pei JH, Tian F, Thundat T (2004) Anal Chem 76:292
89. Khanafer K, Khaled ARA, Vafai K (2004) J Micromech Microeng 14:1328
90. Yue M, Lin H, Dedrick DE, Satyanarayana S, Majumdar A, Bedekar AS, Jenkins JW, Sundaram S (2004) J Microelectromech Syst 13:290
91. Shin S, Paik JK, Lee NE, Park JS, Park HD, Lee J (2005) Ferroelectrics 328:59
92. McFarland AW, Colton JS (2005) J MEMS 14:1375
93. Amirola J, Rodríguez A, Castaner L, Santos JP, Gutierrez J, Horrillo MC (2005) Sens Actuators B 111:247
94. Dutta P, Chapman PJ, Datskos PG, Sepaniak MJ (2005) Anal Chem 77:6601
95. Liu Y, Flood AH, Bonvallett PA, Vignon SA, Northrop BH, Tseng HR, Jeppesen JO, Huang TJ, Brough B, Baller M, Magonov S, Solares SD, Goddard WA, Ho CM, Stoddart JF (2005) J Am Chem Soc 127:9745
96. Tabard-Cossa V, Godin M, Grutter P, Burgués I, Lennox RB (2005) J Phys Chem B 109:17531
97. Tabard-Cossa V, Godin M, Beaulieu LY, Grutter P (2005) Sens Actuators B 107:233
98. Huber F, Hegner M, Gerber C, Güntherodt HJ, Lang HP (2006) Biosens Bioelectron 21:1599
99. Yan XD, Shi XL, Hill K, Ji HF (2006) Anal Sci 22:205
100. Yoo KA, Na KH, Joung SR, Nahm BH, Kang CJ, Kim YS (2006) Japn J Appl Phys Pt 1 45:515
101. Na KH, Kim YS, Kang CJ (2005) Ultramicroscopy 105:223
102. Senesac LR, Dutta P, Datskos PG, Sepaniak MJ (2006) Anal Chim Acta 558:94
103. Mukhopadhyay R, Sumbayev VV, Lorentzen M, Kjems J, Andreasen PA, Besenbacher F (2005) Nano Lett 5:2385
104. Stachowiak JC, Yue M, Castelino K, Chakraborty A, Majumdar A (2006) Langmuir 22:263
105. Castelino K, Kannan B, Majumdar A (2005) Langmuir 21:1956
106. Zhang ZX, Li MQ (2005) Progr Biochem Biophys 32:314
107. Tian F, Hansen KM, Ferrell TL, Thundat T (2005) Anal Chem 77:1601
108. Lee JH, Hwang KS, Park J, Yoon KH, Yoon DS, Kim TS (2005) Biosens Bioelectron 20:2157

109. Ghatnekar-Nilsson S, Lindahl J, Dahlin A, Stjernholm T, Jeppesen S, Hook F, Montelius L (2005) Nanotechnology 16:1512
110. Wig A, Arakawa ET, Passian A, Ferrell TL, Thundat T (2006) Sens Actuators B 114:206
111. Yan XD, Xu XHK, Ji HF (2005) Anal Chem 77:6197
112. Alvarez M, Tamayo J, Plaza JA, Zinoviev K, Dominguez C, Lechuga LM (2006) J Appl Phys 99:024910
113. Khanafer K, Vafai K (2005) Int J Heat Mass Transfer 48:2886
114. Wright YJ, Kar AK, Kim YW, Scholz C, George MA (2005) Sens Actuators B 107:242
115. McFarland AW, Colton JS (2005) J Micromech Microeng 15:1060
116. Rasmussen PA, Grigorov AV, Boisen A (2005) J Micromech Microeng 15:1088
117. Li SQ, Orona L, Li ZM, Cheng ZY (2006) Appl Phys Lett 88:073507
118. Adams JD, Rogers B, Manning L, Hu Z, Thundat T, Cavazos H, Minne SC (2005) Sens Actuators A 121:457
119. Alvarez M, Tamayo J (2005) Sens Actuators B 106:687
120. Tang YJ, Ji HF (2005) Instr Sci Technol 33:131
121. Todorovic DM, Bojicic A (2005) J Phys IV 125:459
122. Sandberg R, Svendsen W, Molhave K, Boisen A (2005) J Micromech Microeng 15:1454
123. Luo C (2005) J Appl Mech – Transactions of the ASME 72:617
124. McFarland AW, Poggi MA, Doyle MJ, Bottomley LA, Colton JS (2005) Appl Phys Lett 87:053505
125. Lochon F, Dufour I, Rebiere D (2005) Sens Actuators B 108:979
126. Dareing DW, Thundat T, Jeon SM, Nicholson M (2005) J Appl Phys 97:084902
127. Dareing DW, Thundat T (2005) J Appl Phys 97:043526
128. Jeon SM, Desikan R, Fang TA, Thundat T (2006) Appl Phys Lett 88:103118
129. Jazar GN (2006) J Vibration Control 12:139
130. Lu P, Lee HP, Lu C, O'Shea SJ (2005) Phys Rev B 72:085405
131. Sheehan PE, Whitman LJ (2005) Nano Lett 5:803
132. Chang MMC, Cuda G, Bunimovich YL, Gaspari M, Heath JR, Hill HD, Mirkin CA, Nijdam AJ, Terracciano R, Thundat T, Ferrari M (2006) Curr Opin Chem Biol 10:11
133. Aeschimann L, Meister A, Akiyama T, Chui BW, Niedermann P, Heinzelmann H, De Rooij NF, Staufer U, Vettiger P (2006) Microelectr Eng 83:1698
134. Yang JL, Despont M, Drechsler U, Hoogenboom BW, Frederix PLTM, Martin S, Engel A, Vettiger P, Hug HJ (2005) Appl Phys Lett 86:134101
135. Yang J, Ono T, Esashi M (2000) Sens Actuators A 82:102

Top Curr Chem (2008) 285: 29–76
DOI 10.1007/128_2007_24

Published online: 4 April 2008

Functionalization of Probe Tips and Supports for Single-Molecule Recognition Force Microscopy

Andreas Ebner · Linda Wildling · Rong Zhu · Christian Rankl · Thomas Haselgrübler · Peter Hinterdorfer · Hermann J. Gruber (✉)

University of Linz, Institute of Biophysics, Altenberger Str. 69, A-4040 Linz, Austria
hermann.gruber@jku.at

Abstract The measuring tip of a force microscope can be converted into a monomolecular sensor if one or few "ligand" molecules are attached to the apex of the tip while maintaining ligand function. Functionalized tips are used to study fine details of receptor–ligand

interaction by force spectroscopy or to map cognate "receptor" molecules on the sample surface. The receptor (or target) molecules can be present on the surface of a biological specimen; alternatively, soluble target molecules must be immobilized on ultraflat supports. This review describes the methods of tip functionalization, as well as target molecule immobilization. Silicon nitride tips, silicon chips, and mica have usually been functionalized in three steps: (1) aminofunctionalization, (2) crosslinker attachment, and (3) ligand/receptor coupling, whereby numerous crosslinkers are available to couple widely different ligand molecules. Gold-covered tips and/or supports have usually been coated with a self-assembled monolayer, on top of which the ligand/receptor molecule has been coupled either directly or via a crosslinker molecule. Apart from these general strategies, many simplified methods have been used for tip and/or support functionalization, even single-step methods such as adsorption or chemisorption being very efficient under suitable circumstances. All methods are described with the same explicitness and critical parameters are discussed. In conclusion, this review should help to find suitable methods for specific problems of tip and support functionalization.

Keywords Force microscopy · Functionalization · Recognition · Silane · Silicon nitride

Abbreviations

AFM	Atomic force microscope (or: microscopy)
Aldehyde-PEG-NHS	4-Formylbenzoyl-NH-PEG-CO-NHS
APTES	3-Aminopropyltriethoxysilane
APTMS	3-Aminopropyltrimethoxysilane
APhS	4-Aminophenyltrimethoxysilane
Biotin-PEG-NHS	Biotinoyl-NH-PEG-CO-NHS
Benzophenone-PEG-NHS	Benzophenone-4-yl-CO-NH-PEG-CO-NHS
BSA	Bovine serum albumine
DMSO	Dimethylsulfoxide
Fluorescein-PEG-NHS	Fluorescein-5-yl-NH-C(=S)-NH-PEG-CO-NHS
HOPG	Highly oriented pyrolytic graphite
ICAM	Intercellular adhesion molecule
IEP	Isoelectric pH value
IgG	Immunoglobulin G
Lysine-NTA	N_α,N_α-bis-(carboxymethyl)-lysine
Maleimide-PEG-NHS	3-Maleimidopropionyl-NH-PEG-CO-NHS
NHS-	*N*-hydroxysuccimide ester of a carboxylic group
NHS-PEG-NHS	PEG dicarboxylic acid, disuccinimidyl ester
NH_2–PEG–COOH	*O*-(2-aminoethyl)-*O*′-(2-carboxyethyl)-poly(ethylene glycol)
NTA	Nitrilotriacetic acid
OTS	Octadecyltrichlorosilane
PDP-	3-(2-Pyridyldithio)-propionyl group
PDP-PEG-NHS	PDP-NH-PEG-CO-NHS
PDP-PEG-NTA	PDP-NH-PEG-CO-lysine-NTA
PEG	Poly(ethylene glycol)
SAM	Self-assembled monolayer
SATP	*N*-succinimidyl 3-(acetylthio)-propionate
SATP-	3-(Acetylthio)-propionyl residue, introduced with SATP
SMRFM	Single-molecule recognition force microscopy
SMRFS	Single-molecule recognition force spectroscopy

ssDNA	Single-stranded DNA (synthetic oligonucleotide)
Tris-NTA	See Fig. 31
TREC	Simultaneous topography and recognition imaging
Vinylsulfone-PEG-NHS	4-Vinylsulfonylbenzoyl-NH-PEG-CO-NHS

1 Introduction

Atomic force microscopy can be conducted in aqueous solution under physiological conditions [1] and reveal fine details not resolved by electron microscopy [2]. AFM is thus well-suited for structural analysis of biomolecules and their assemblies [3–5]. In addition, the AFM tip can be upgraded into a monomolecular sensor by coupling of a "ligand" molecule, which is moved over the sample surface and recognized by complementary receptor molecules on the sample surface, yielding a map of recognition sites [3, 6]. In conventional SMRFM, local binding sites are detected by receptor–ligand rupture events, which are sensed by a vertically oscillated cantilever [7, 8]. In the TREC mode, the tip-tethered ligand remains bound to the receptor during several tip oscillation periods. Binding is nevertheless detected in each oscillation cycle because the spring-like PEG chain (~6 nm) between tip and ligand dampens the upper amplitude maxima of tip oscillation [9–11]. At the same time, the lower amplitude maxima are dampened whenever the tip apex hits the sample surface. Simultaneous readout of both top and bottom maxima therefore yield separate maps of the recognition sites and of sample topography from one X–Y scan of the sample surface [9–11].

At a fixed X–Y position of the ligand-functionalized tip above a receptor molecule, force spectroscopy of ligand–receptor interaction can be performed by measuring the unbinding forces at different force loading rates [12], interaction times before dissociation [13], biochemical modification and coassociation of third components [14], or with different mutants or truncated forms of the participating proteins [15], to name just few examples of SMRFS studies published so far (for reviews see [3–5, 16]).

The double purpose of ligand-functionalized AFM tips for recognition site mapping (X–Y scanning) and force spectroscopy (Z scanning) is unique because other force probes, such as the surface force apparatus [5, 17], the biomembrane force probe [5, 18], intermolecular force microscopy [19], tip-less cantilevers carrying a complete living cell as specific sensor element [20, 21], and light tweezer-operated nanospheres [22] are limited to the quantitation of attractive/repulsive forces, with little or no lateral resolution, for lack of a sharp measuring tip. For these reasons, the latter techniques are outside the scope of this review. Also omitted is chemical force microscopy, i.e., high resolution mapping of surface potential or hydrophobicity/hydrophilicity [6, 23, 24], measurement of polymer stretching [25, 26], as

well as protein unfolding [27], in spite of tip functionalization, because no specific recognition between ligands and receptors is involved in these applications of force microscopy.

Single-molecule recognition force microscopy and spectroscopy imply that a tip-linked probe molecule (termed ligand for simplicity) be specifically bound to its cognate target site (receptor) on the sample surface during one tip–surface encounter, giving rise to a characteristic unbinding event during subsequent tip retraction (see Fig. 1d). Different strategies have been used to achieve a low number of functional ligands on the apex of the tip, either starting from high ligand density on the tip and inactivating most of the ligands by specific block [28–33], or attaching few highly functional ligands in the first place. The latter is usually achieved with a flexible, thin PEG chain [3, 8–11, 13–15, 34–63], or amylose [50, 54, 64–71] between tip and sensor molecule.

Another important aspect is the strength of the tether between tip and ligand. For obvious reasons, the rupture force for any part of the linkage between tip and ligand should be much higher than the rupture force of the ligand–receptor complex. This is usually ensured if the tip–ligand connection consists of covalent bonds since receptor–ligand interactions are non-covalent and about one order of magnitude weaker (<0.2 nN at the typical loading rates of 1–10 nN/s) than covalent bonds ($\geq$1 nN, except for lipoate-gold binding, which is ruptured at 0.2 nN at a loading rate of 12–14 nN/s [50]).

The downside of covalent ligand linking to the AFM tip is that it requires more chemical skill than the formation of non-covalent bridges such as biotin-avidin-biotin or His_6–Ni^{2+}–NTA. For this reason, non-covalent linkages have often been used to attach ligands to the AFM tip, in spite of their relatively low rupture forces (see Sect. 3.2). Apart from these non-covalent, but specific bridges, completely non-specific adsorption has often served as a simple and effective means of tip functionalization (see Fig. 2 and Sect. 3.2).

Whether AFM is used for topographic imaging or to study binding of ligands and receptors, a minimum of vertical and/or lateral force is always exerted on the object of interest, thus firm attachment of the latter to the support is also essential. Eukaryotic cells can be attached by electrostatic adsorption to poly-L-lysine-coated coverslips [52, 53, 67, 72], specifically bound via their glycocalix to concanavalin A-coated glass [73], or simply grown in the presence of culture medium on glass [74] or in a plastic petri dish [75]. Bacteria can be adsorbed to tissue culture polystyrene or specifically bound on fibronectin-covered support [76], organelles or plasma membrane vesicles can be adsorbed to ultraflat gold [63], dense layers of viruses can be electrostatically adsorbed to mica via Ni^{2+} ions [56], and tissue thin sections are typically adsorbed to gelatin-coated coverslips [34]. Single target molecules can be attached to commercial affinity supports, e.g., to dextran-coated BIAcore chips, as used for immobilization of avidin [31], His_6 peptide [77], or NTA functions [78], or to agarose beads, as used for presentation of biotin [32, 33, 79], DNA [80], mannose [81], and synaptobrevin [82]. The

rough, and fluctuating surface of such polysaccharide supports, however, prevents imaging and restricts the information from being gained by force spectroscopy. For a more detailed analysis of target molecule structure and receptor–ligand interaction, more elaborate immobilization to ultraflat supports is required, as described below.

2 Flat Supports for Immobilization of Biological Samples and Individual Target Molecules

If cells, organelles, or other relatively large objects are being studied, then flatness of the support is not too critical. In contrast, ultraflat supports are required if single target molecules are to be imaged before/after/during measurement of specific interaction between a tip-bound sensor molecule and its cognate target sites on the support [8–11, 13, 25, 29, 36, 38, 41, 46, 55–58, 83]. Highly oriented pyrolytic graphite (HOPG) and mica are the two natural materials which provide the most planar surfaces. Moreover, cleavage of these two materials generates 2D-crystalline surfaces which are not only ultraflat but also perfectly clean. HOPG indeed proved to be the ideal support for 2D-protein crystals, which could then be imaged with high resolution [2], but no example is known in which individual biomolecules were attached to HOPG for subsequent AFM studies.

In contrast to HOPG, mica is very hydrophilic and exhibits a negative surface potential which can be exploited for firm electrostatic adsorption of target molecules (see Sect. 3.1). Moreover, mica can be aminofunctionalized for subsequent attachment of biomolecules via bifunctional crosslinkers (see Sects. 4.1, 4.2). The drawback of mica derivatization is the difficulty to adjust grafting site densities and surface properties. These problems are absent when using gold as support (see Sect. 5) because no other material can be functionalized in such versatile ways as gold [84] (see introduction of [85] for a condensed overview).

Fortunately, ultraflat gold can be prepared as a replica of the mica surface, thereby ensuring atomically flat areas of 10×10 μm [86–88]. After vapor deposition of gold onto freshly cleaved mica, some easy-to-cut plate (e.g., a silicon wafer) is glued to the top side of gold with carefully selected epoxy glue [86–88], which is subsequently hardened by baking at 140–150 °C to ensure that it becomes absolutely insoluble in organic solvent. In this form, the mica-gold-glue-silicon sandwich can be stored for many months without loss of quality. Immediately before use, the mica sheet is stripped from gold ("template-stripped gold"), preferably in tetrahydrofurane and with slight suction on the mica sheet [88], yielding a perfectly flat and clean metal surface in the moment of stripping. This surface must immediately be used, either for direct attachment of target molecules if they contain thiol/disulfide

functions (see Sects. 5.1 and 5.2), or for coating with a self-assembled monolayer (see Sect. 5.3).

The commercially available ultraflat gold is not template-stripped gold but mica covered with a layer of gold that has been flattened by flame annealing. Upon exposure to ambient conditions, these gold surfaces soon adsorb unknown material which greatly increases the contact angle and is difficult to remove [84, 89]. According to our experience, such contaminated gold can still be functionalized with simple SAMs having a high density of reactive groups [85] but not with protein-resistant SAMs [89]. Unfortunately, all rigorous cleaning procedures (with piranha, or with NH_3/H_2O_2/water = 1/1/5 by volume [90], both very hazardous [89]) were seen to detach commercial gold from mica, while UV/ozone appeared to be insufficient.

Single-crystal p(111) silicon wafers also provide an ultraflat surface, even after harsh cleaning and conversion of the top layer into silicon dioxide for the purpose of subsequent silanization. The surface roughness of the silicon dioxide layer was shown to be as low as 0.14 nm [91]. Surprisingly, the same low roughness can also be achieved on glass coverslips after proper treatment [92].

3
Functionalization of Tip and/or Support by Physisorption

Non-specific adsorption relies on non-covalent bonds such as hydrophobic interaction, stacking, hydrogen bonds, and electrostatic attraction, which are usually classified as weak bonds in comparison to covalent bonds. Biopolymers, such as proteins or nucleic acids, however, are large, flexible molecules. Thus, a single biomolecule can form many non-covalent bonds with a solid support, resulting in adhesion forces in the range of covalent bonds or even much larger [93, 94], as explained in a detailed review [95].

In general, proteins will adsorb to almost any solid surface, that has not been rendered protein-resistant by special coatings [84, 95]. In SMRFM studies, freshly cleaved mica has been the most popular support for target molecule adsorption because it is perfectly flat and clean. Fortunately, the most widely used AFM tips (silicon nitride with a superficial oxide layer) also allow for firm attachment of proteins via physisorption. Thus, many SMRFM studies could be done with physisorption as the sole mechanism of support and tip functionalization, as described in later sections.

3.1
Electrostatic Adsorption of Biomolecules Onto Freshly Cleaved Mica or Glass

Mica is a phyllosilicate which is preferentially cleaved in the plain of K^+ ions (see Fig. 3d), resulting in an atomically flat surface that has an overall negative charge but no free OH groups (silanols). K^+ ions are electrostatically bound

on the negatively charged oxide layer (see Fig. 3c,d), and these can be replaced by other buffer cations, such as H_3O^+ [96] or divalent cations [56, 97, 98]. Exchange of K^+ for Mg^{2+} of Ni^{2+} leads to a cationic surface potential which has been exploited for electrostatic adsorption of DNA [97, 98] or of whole viruses [56] in AFM studies.

Just like DNA, most proteins are negatively charged at physiological pH, thus electrostatic adsorption to freshly cleaved mica is limited to the minority of proteins, which are cationic at pH $\sim$ 7, or which carry a cluster of positive charge in one domain. The latter applies to BSA which has a net negative charge at pH $\sim$ 7 (IEP $\sim$ 4.5 [99]) but a cluster of positive charges in domain III [95], resulting in tight adsorption of BSA to mica or glass [100]. In fact, adsorption of biotin-BSA to mica [29, 101] or glass [30, 102] has frequently been used in model studies of recognition force microscopy in which the biotin residues, or subsequently bound streptavidin, served as the target sites for specific recognition (see Fig. 2b). Accordingly, in these studies, the tip was functionalized with streptavidin or with biotin residues, respectively (see Fig. 2a), in order to measure (strept)avidin–biotin interaction forces at different loading rates. In one applied study, the GroEL "barrels" could be adsorbed to mica in an upright orientation, allowing for specific interaction with tip-tethered native or denatured β-lactamase in the presence/absence of ATP [83]. Similarly, the ryanodine receptor was found to adsorb to mica with

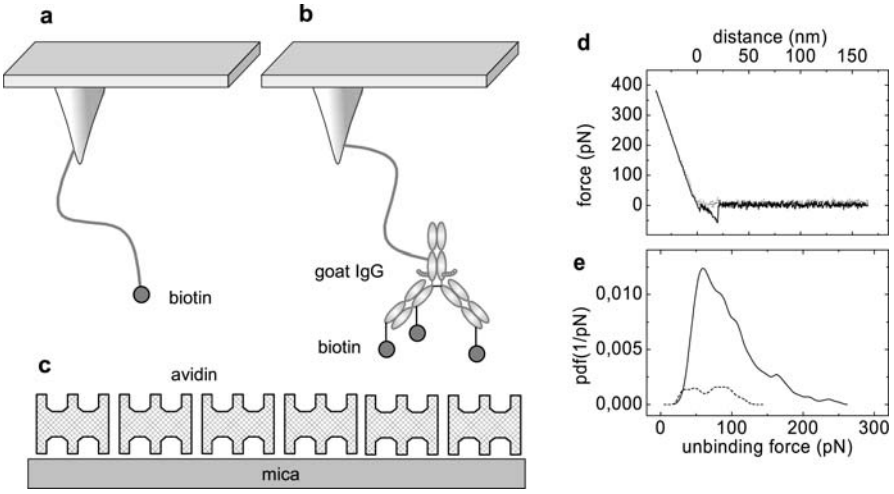

Fig. 1 Simple test systems for AFM tip functionalization with individual biotin residues (**a**) or biotinylated antibodies (**b**) that have been tethered to the tip via 6–8 nm long PEG linkers, using a dense monolayer of avidin on mica (**c**) as test sample. **d** Force-distance cycle in which a biotin-IgG on the tip binds and then unbinds from immobilized avidin. **e** Unbinding force distribution profile in the absence of biotin (*solid line*, 44% binding probability) or after block of avidin with free biotin (0.1 mg/mL, *dotted line*, 2.9% binding probability)

its sarcoplasmic side only, thus the cytoplasmic face was well-accessible for SMRFM [49].

Two proteins most popular in model studies, avidin and lysozyme, are positively charged at pH ~ 7, thus they can be immobilized on freshly cleaved mica at the desired lateral density within minutes [11, 38, 42, 46, 55, 58]. Lysozyme (IEP = 11.0–11.4 [99]) is firmly adsorbed directly from physiological buffer [58], whereas avidin (IEP ~ 10 [103]) requires a 10-fold lower ionic strength for irreversible attachment to mica. Fortunately avidin does not detach during subsequent force measurements even in physiological buffer [11, 38, 42, 46, 55]. Cleavage of mica and preparation of a dense layer of avidin takes ~30 min, the result is very reproducible, and this avidin monolayer is an ideal test sample with highly specific recognition sites (see Fig. 1c), as practically applied in many methodical optimizations of AFM tip functionalization and SMRFM [38, 42, 46, 55].

Typical recognition force data obtained with tip-tethered biotin-IgG and mica-bound avidin (depicted in Fig. 1b and Fig. 1c, respectively) are shown in Fig. 1d (data taken from [46]). In a so-called force-distance cycle, the mica support was raised towards the tip (dotted line) up to the point of contact (at *distance* = 0 nm, *X*-axis), whereafter the cantilever was bent upwards with increasing force (*Y*-axis). Upon retraction (solid line), the cantilever returned to its resting position, while further retraction pulled the cantilever downwards, until at 55 pN pulling force the cantilever suddenly jumped back to the resting position, reflecting sudden unbinding of tip-tethered biotin-IgG from mica-bound avidin. The slope of downward deflection of the cantilever was less steep than the slope of upward bending because the force constant of tip-bound PEG was smaller than the force constant of the cantilever alone. The solid line in Fig. 1e shows the unbinding force distribution from 435 force-distance cycles, with a distinct maximum at 59 pN. Higher unbinding forces in this distribution reflect the simultaneous binding/unbinding of two or more biotin residues, which are covalently attached to the same IgG molecule on the tip (see Fig. 1b) from one or two adjacent avidin molecules on mica (see Fig. 1c). The binding probability was 44%, i.e., 435 out of 999 force-distance cycles showed a specific unbinding event as in the upper panel. In the subsequent control experiment, avidin on mica was blocked by perfusion with biotin (0.1 mg/ml in the same buffer), whereupon only 29 out of 999 force-distance cycles (2.9%) showed some kind of unbinding event as in the upper panel, with no clear-cut force maximum reflecting avidin–biotin interaction.

Test experiments with dense avidin layers as in Fig. 1c allowed to quantify AFM tip functionalization by various types of linking chemistry [38, 42, 46, 55]. Similar experiments with sparse layers of avidin or lysozyme on bare mica proved useful to explore simultaneous measurement of topography and recognition [9, 11, 58], taking advantage of the uncompromised flatness and cleanness of unmodified mica.

3.2 AFM Tip Functionalization by Protein Adsorption

Irreversible adsorption of biotin-BSA to unmodified silicon nitride tips has extensively been used in SMRFM, for two distinct purposes: (1) In *model* studies on avidin–biotin interaction, either the biotin residues themselves [31, 32, 101], or subsequently bound (strept)avidin [29, 30, 32, 33, 102, 104] served as the specific ligand on the AFM tip to measure specific binding with support-bound (strept)avidin or biotin-BSA, respectively (see Fig. 2). In one of these studies [33], the biotin-BSA layer on the tip was crosslinked with glutaraldehyde, in which case many free-tangling glutaraldehyde residues on BSA must also have formed crosslinks with subsequently bound avidin, resulting in a covalently interlinked protein network with very firm attachment to the tip.

(2) In several *applied* studies, tip-adsorbed biotin-BSA [81] or avidin [105] was used as a primary anchor layer, to which (strept)avidin and/or biotinylated sensor molecules (concanavalin A [81] or P-selectin [105]) were bound in subsequent steps. As depicted in Fig. 2a, this also resulted in an interlinked protein network because (1) avidin is a tetramer with two opposed pairs of biotin-binding sites [103], (2) the biotinylated sensor proteins had an extended structure, and (3) each sensor protein carried many biotin residues. As a consequence, the detachment force of one sensor protein in these studies was much higher than a single (strept)avidin–biotin bond (~50 pN at

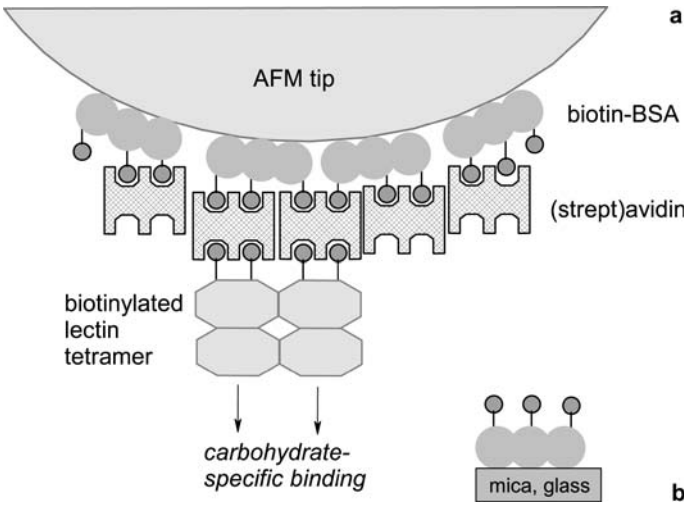

Fig. 2 Functionalization of AFM tips (**a**) and support (**b**) by non-specific protein adsorption. In model studies, biotin-BSA or subsequently bound (strept)avidin served as "ligand" or "receptor" molecules. In applied studies a triple layer of biotin-BSA, (strept)avidin, plus the biotinylated sensor molecule was sufficiently interlinked not to lose the sensor molecules during repeated contact with the complementary target molecules

typical loading rates [37, 38, 46, 55]). Although never discussed before, this must have been the basis for the very successful functionalization scheme shown in Fig. 2a. In contrast, a single (strept)avidin–biotin bond would not suffice to fix typical sensor molecules to AFM tips because antigen-antibody and many other protein–protein recognition forces are on the order of 40–200 pN [13, 22, 35, 44, 45], i.e., higher or similar to a single (strept)avidin–biotin bond at typically applied loading rates. As an exception, biotin-ssDNA with a single 5′-terminal biotin residue was also used as a sensor molecule on a streptavidin-modified tip [106]. In which case, it was assumed that the hybridization forces between tip-bound ssDNA and support-bound ssDNA were significantly weaker than the rather weak streptavidin–biotin bond.

In most of the above studies, unmodified silicon nitride tips with a freshly generated and cleaned oxide layer were used for protein adsorption, thus bonding must have been by electrostatic adsorption of positively charged protein domains to the deprotonated, i.e., negatively charged silanol groups on the silicon oxide layer (compare Fig. 3a) [107], in addition to hydrogen bonds between oxide and protein. In a minority of studies, the tip was first coated with a hydrophobic silane [72, 105] or a positively charged aminosilane [75]. In particular, avidin was non-specifically adsorbed to mercaptosilanized tips (for subsequent binding of biotin-P-selectin) [105], a ligand of CD47 was adsorbed to allyltrichlorsilan-modified tips [72], and antibodies were adsorbed to aminosilanized tips [75], in order to study the biospecific interaction with complementary proteins. As explained in a review on protein adsorption [95], hydrophobic interactions, and especially the combination of hydrophobicity and charge on an aminosilanized surface, provide for stronger protein adsorption than on unmodified silicon oxide.

It can be summarized that non-specific adsorption of sensor proteins, or of an anchor layer of BSA molecules is a legitimate, efficient, and successful method of support and/or tip functionalization, and that it can well be combined with avidin–biotin technology. However, adsorption and avidin–biotin bonds may not always be stronger than the specific interaction between tip-bound ligand and support-bound target molecules. Therefore, detailed consideration of the adsorption mechanisms and of avidin–biotin interaction forces is required to ensure practical success and proper data interpretation. These complications are avoided when using covalent bonds, as described below.

4 Covalent Functionalization of Tip and/or Support with Organosilanes or Ethanolamine Hydrochloride

Aminosilanization of AFM tips or supports has widely been used as the first of several reaction steps when ligand and/or target molecules were

immobilized by covalent bonds [10, 29, 37, 40, 49–51, 54, 55, 57, 60–62, 64, 65, 75, 83, 92, 93, 108–116]. As an alternative, AFM tips and mica support have been aminofunctionalized with ethanolamine hydrochloride [8, 9, 11, 13, 14, 22, 34–36, 38, 39, 44–46, 52, 53, 55, 56, 58, 63, 117], presumably via Si – O – C bond formation (see Fig. 8) [118]. The "ethanolamine method" is much easier to perform but has significant limitations (see Sect. 4.2), especially that it cannot be varied to accommodate different needs.

The main problem of tip aminofunctionalization is that the tip must not get sticky and that chemical derivatization must be limited to a flat, thin layer on the tip surface. In fact the ethanolamine method was developed in 1994 [44] because the then prevailing protocol with APTES [92] gave 10^2 nm long tentacles on the AFM tip, which stuck to mica support with much higher force than the wanted measurement of the antigen–antibody interaction. At that time it was not known that freshly purchased or freshly distilled APTES is required for reproducible results. Many other critical parameters were identified only later on. Nevertheless, major efforts are continuing to improve understanding and control of aminosilanization [119, 120].

In some cases, aminofunctionalization of tip [75] or support [98, 113, 114] was performed to enhance non-covalent adsorption of protein or DNA but, in most of the mentioned studies, the newly introduced amino groups were usually reacted with a homo- or heterobifunctional crosslinker in a second step, followed by attachment of a specific ligand molecule (see Sect. 4.3).

4.1 Aminofunctionalization with Aminosilanes

Various aminosilanes (Fig. 6) and diverse protocols [54, 57, 92, 93, 111, 113, 115, 116, 119, 120] have been used for aminosilanization of silicon nitride tips, monocrystalline silicon chips, mica, and glass supports [10, 29, 37, 40, 50, 51, 54, 55, 57, 60–62, 64, 65, 75, 83, 92, 93, 108–116]. Some procedures rely on vapor deposition, others operate in solution, either under rigorously dry conditions or in neat water as solvent, giving rise to the misleading impression that "anything goes". In practice, however, the experimental parameters of these diverse protocols are highly critical, and a mechanistic insight is essential for practical success, as explained in the following.

Under ambient conditions, silicon nitride tips and silicon chips are covered with a layer of silicon dioxide and most cleaning procedures include oxidative treatment that produce a continuous oxide layer [30, 44, 45, 50, 55, 57, 59, 93, 108, 111, 112, 121]. In the crystalline form of tridymite (Fig. 3b) each Si atom carries one silanol group [122]. Less regular surfaces also contain geminal silanols (two OH groups per Si atom, Fig. 3a). This irregular surface structure is similar to that of silica gel and glass, and in fact most studies on the mechanism of silanization have been performed on these two solids and on mica. The latter differs from the other substrates in that it contains no free

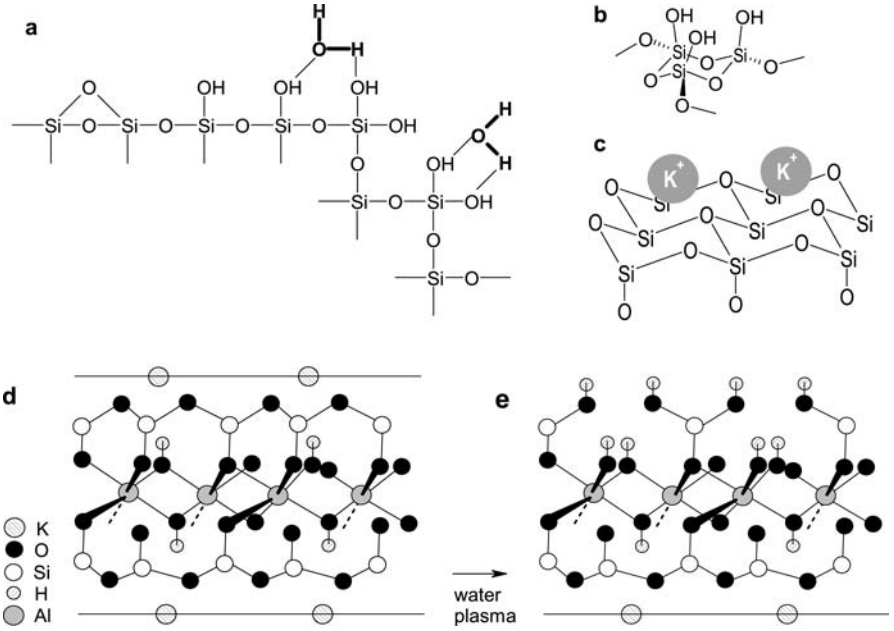

Fig. 3 Chemical structure of the silicon dioxide layer as formed on the surface of silicon or silicon nitride tips/chip under atmospheric conditions (**a**) and ideal surface structure of SiO_2 (**b**). In contrast, to SiO_2, the surface of freshly cleaved mica (**c**) does not contain reactive silanol groups but electrostatically bound K^+ ions which can be exchanged for H_3O^+ or divalent cations from aqueous solution. **d** Mica is a phyllosilicate in which two layers of condensed silicic acid are strongly held together by a layer of aluminum hydroxide. These trilayers are stacked and weakly held together by layers of K^+ ions which constitute predetermined fracture plains. **e** Water plasma activation partially fragments the silicate layer and generates reactive silanol groups. Parts **d** and **e** are reproduced from [129] with permission

silanol groups but electrostatically bound K^+ ions on the side which is exposed upon cleavage (Fig. 3c,d). The vicinal silanol groups on superficially oxidized silicon [123] or on silica gel [124] lose water above 420 °C or 600 °C, respectively, and form anhydride bonds, also called siloxane bridges (shown on the left of Fig. 3a), thereby lacking the silanol groups needed for covalent bonding of an organosilane [123, 124]. Another study indicates that siloxane bridge formation on silica already occurs between 100 and 400 °C [125]. Such disagreement is typical of all aspects of silanization whereby most authors agree on mechanisms and trends but not on the conditions under which they occur.

The siloxane bridges are re-converted into silanol groups by water, partially at room temperature and completely near the boiling point [123]. The Si – O – Si bonds on the mica surface, however, are resistant to water (Fig. 3d). Only when using water plasma (Fig. 3e), these bonds are fragmented into silanol groups [126–129], with preferential loss of K^+ and aluminum hydrox-

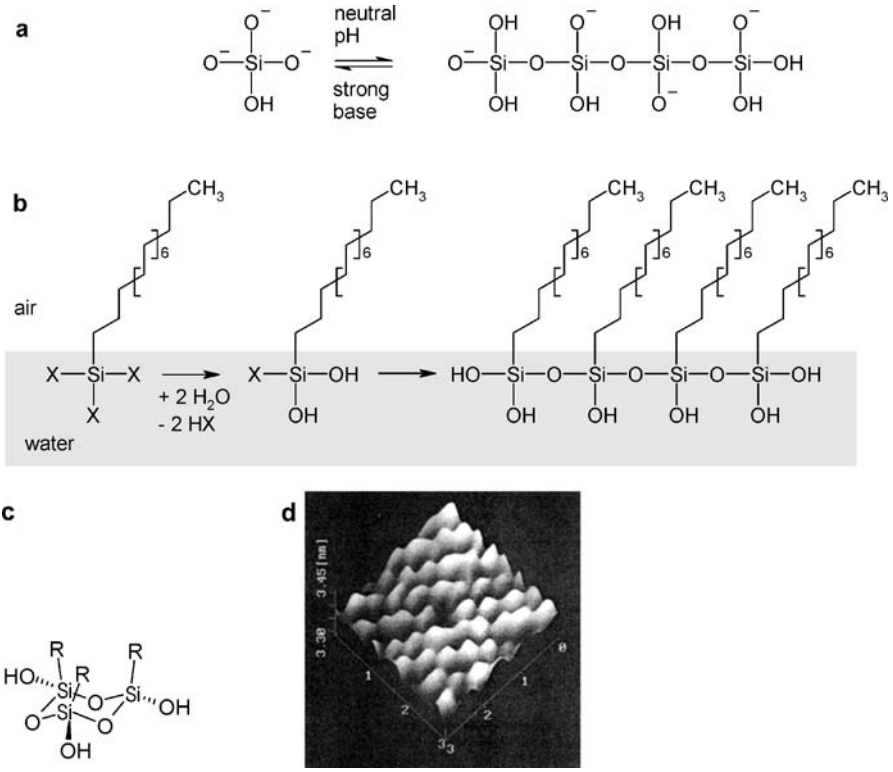

Fig. 4 Condensation of orthosilicate which is only present in a strong base by neutralization or acidification (**a**). Condensation of octadecyltrichlorosilane (OTS, X=Cl [130]) or Octadecyltrimethoxysilane (X=O – CH_3 [132]) at the air/water interface after initial hydrolysis, resulting in a two-dimensional polymeric network (**b**) that has been transfered onto silicon by Langmuir–Blodgett technique and imaged on the hydrophobic side by AFM (**c**) (reproduced with permission from [130])

ide [129]. The plasma-induced silanol groups (Fig. 3e) provide for covalent bonding of various organosilanes on mica [126–129]. Nevertheless, Carson and Granick have conclusively shown that SAMs of octadecyltrichlorosilane (OTS) formed on plasma-activated mica are much less stable than on untreated mica, if only the proper amount of water is predeposited on the mica surface, followed by exposure to OTS in rigorously water-free toluene [96, 127]. The explanation of this paradoxical finding, as well as the paradoxical need for a wet surface and a rigorously dry solution of the organosilane, provides for a profound insight into the essentials of aminosilanization, as described in the following.

Upon contact with water, OTS is quickly hydrolyzed with concomitant release of HCl (see Fig. 4b) [130]. The resulting octadecylsilanetriol has a strong tendency to form siloxane bridges under acidic conditions (Fig. 4b), just like

orthosilicic acid, which is monomeric at high pH only, but progressively forms linear and branched networks when the pH is changed to neutral or acidic conditions (Fig. 4a) [131]. If a droplet of OTS/toluene is deposited at the air–water interface, OTS hydrolyzes and condenses into a perfectly regular SAM on the water surface (see Fig. 4b–d), as demonstrated by subsequent transfer onto superficially oxidized silicon and imaging of the densely packed alkyl chains with AFM (Fig. 4d) [130]. Interestingly, a similar procedure has been used to coat AFM tip and support with SAM carrying initiator groups for living polymer formation on tip and support [121].

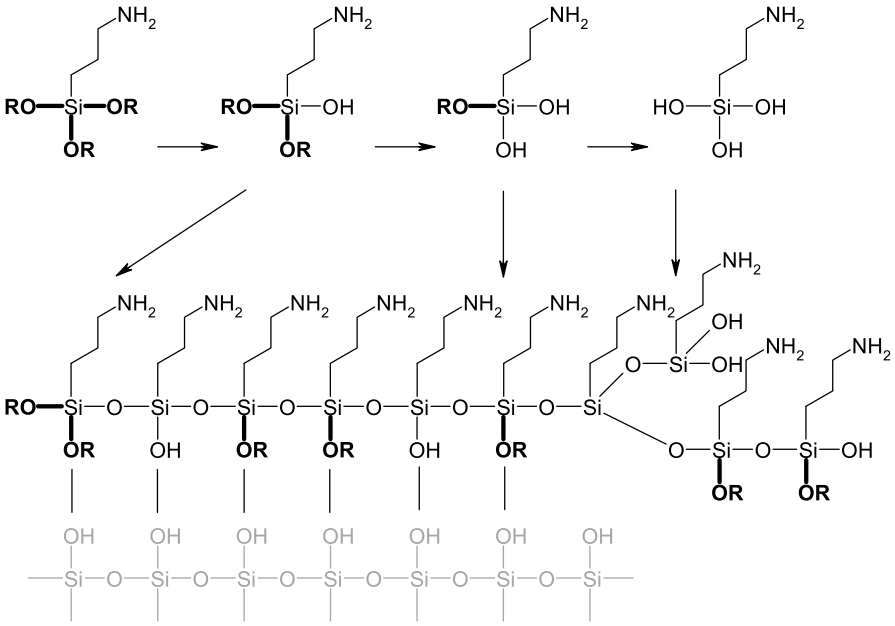

Fig. 5 Hydrolysis and condensation of APTES (R = ethyl) or APTMS (R = methyl) on the surface of hydrated silicon dioxide, resulting in a lateral network that is strongly adsorbed to the inorganic surface via hydrogen bonds. Curing (heating to 80–150 °C) is essential for irreversible binding [133], probably by driving lateral condensation to completion, possibly also by formation of siloxane bridges with the inorganic support

Like OTS, octadecyltrimethoxysilane also forms SAMs at the air–water interface, whereby the kinetics of hydrolysis and condensation is fast at pH 1, intermediate at pH 11, and very slow at pH 5.6 [132]. By analogy, aminosilanes also possess 1, 2, or 3 methoxy or ethoxy groups which need to be hydrolyzed. Fortunately, the amino group automatically affords the base catalysis which is necessary for hydrolysis of the methoxy/ethoxy functions. The downside of autocatalytic hydrolysis is the ability of aminosilanes to prematurely hydrolyze and condense into networks while stored on the shelf or when dissolved in toluene, except when water is rigorously excluded. In prac-

tice, this means that aminosilanes (especially the tri-alkoxy forms, Figs. 5 and 6) need to be stored under argon and withdrawn from the sure seal bottle with a rigorously dry syringe. Even so, the shelf life is limited to about one month (unpublished observation).

After this excursion the question can be answered why the most stable OTS-SAM was formed without plasma activation of mica, applying rigorously dry OTS/toluene to a strongly hydrated mica surface [96]. The dryness of the OTS/toluene solution was obviously needed to prevent premature hydrolysis and condensation into three-dimensional OTS networks which would adhere to mica as big OTS aggregates. Defined deposition of water on mica was achieved by exchange of mica-bound K^+ ions with H_3O^+ ions (HCl wash) and removal of excess water with a stream of nitrogen. The remaining hydrated H_3O^+ ions constituted just the right amount of water, as needed for OTS hydrolysis and condensation, the latter being completed by the indispensable "curing" step, i.e., by heating to 120 °C for 2 h, as originally discovered in aminosilanization of silica by Waddell et al. [133].

No covalent bonds are thought to have been formed between the OTS-SAM and unmodified mica, for lack of silanol functions. Nevertheless, the

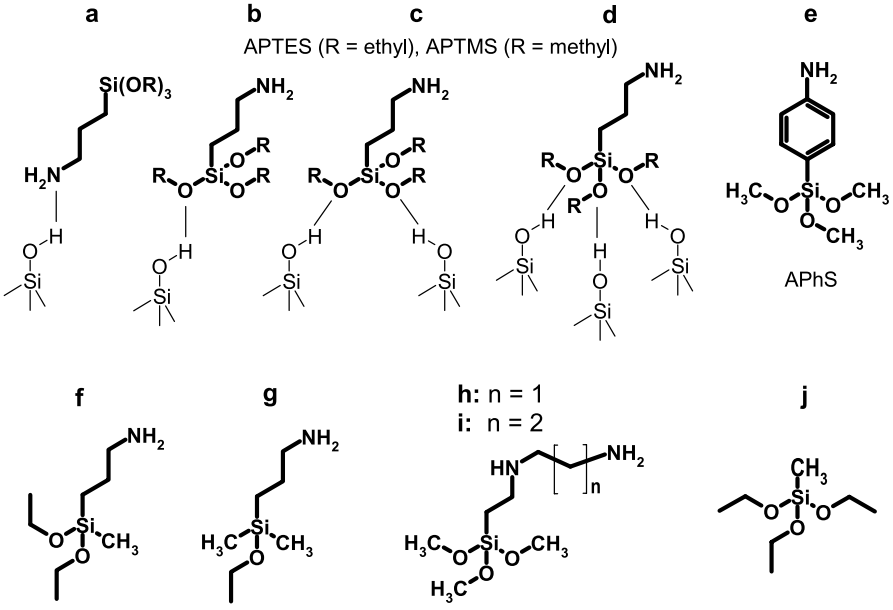

Fig. 6 Aminosilanes (**a**–**i**) and methyltriethoxysilane (**j**, for adjustment of low amino group surface densities in gas phase silanization [50, 133]). Hydrogen-bonding of APTES and APTMS to silicon dioxide surfaces, initially via their amino function (**a**), and after "flipping" [124, 134] via their alkoxy groups (**b**–**d**, reproduced from [135] with permission). APhS (**e**) and the diamines shown in **h** and **i** also possess three reactive methoxy groups, whereas 3-aminopropyl-methyl-diethoxysilane (**f**) or 3-aminopropyl-dimethyl-ethoxysilane (**g**) contain two or a single reactive ethoxy function only

OTS-SAM formed from dry OTS/toluene on water-covered mica was more stable than on plasma-activated mica which allows for covalent bonds between organosilane and surface [96, 127]. From this it follows that the main goal should be the formation of a well-condensed two-dimensional network of organosilane on the AFM tip or support (see Fig. 5). In this case, the sum of all hydrogen bonds to the solid support easily suffices to hold each individual silane molecule in place with higher force than by a single covalent Si – O – Si bond between organosilane and solid surface.

Even single aminosilane molecules form strong hydrogen bonds on surfaces with silanol groups, initially via their amino groups (Fig. 6a), and after "flipping" [124, 134] via their alkoxy functions, preferably with more than one surface silanol group (Fig. 6b–d) [135]. As first proposed by Waddell et al. [133], a monolayer of surface-bound water (or half a monolayer after drying at 140 °C [136]) is required for hydrolysis of the organosilane, which is then laterally condensed and/or vertically bound to the solid surface in the subsequent curing step. Only after prolonged drying at 200 °C, surface-bound water (Fig. 3a) is completely lost from silicon dioxide surfaces [124].

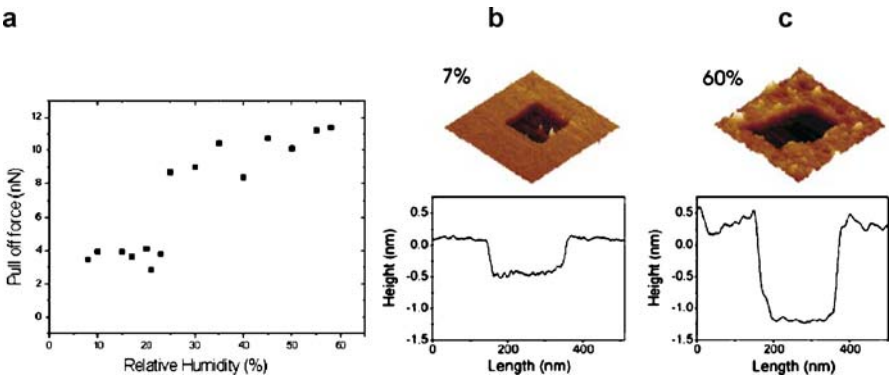

Fig. 7 Hydration state of mica and derivatization with APTES at different relative humidity (reproduced from [119] with permission). **a** The pull-off forces between bare mica and a hydrophilic AFM tip indicate that below 25% relative humidity only firmly bound water molecules are present on the tip whereas above 25% relative humidity fluid bulk water is present on mica, as independently verified by direct imaging of water with an OTS-modified AFM tip (not shown [138]). **b** At 7% or 60% relative humidity, a monolayer or a bilayer, respectively, of APTES is formed by vapor deposition

Freshly cleaved mica also strongly adsorbs water [96, 137, 138], due to its ionic nature, as directly visualized with an OTS-modified AFM tip [138]. Even at 7% relative humidity, the amount of adsorbed water appears sufficient to form a stable monolayer of APTES from the gas phase (Fig. 7b), whereas above 25% relative humidity a phase transition takes place (Fig. 7a) that yields a defined double layer of APTES (Fig. 7c) [119].

The findings in Fig. 7 [119] provide valuable proof of the high efficiency of gas phase silanization with APTES and tertiary amine as catalyst [10, 51, 55, 62, 113–116]. This is because when first applying this method it seems hard to believe that 30 μL of APTES with its relatively high boiling point (217 °C) in a 6 L desiccator can indeed form a dense layer on tip and/or mica support within 2 h. In addition, Fig. 7 confirms the importance of an argon atmosphere during gas phase silanization because only below 25% relative humidity is a defined monolayer of APTES formed (Fig. 7b). After removal of liquid APTES, the tips are stored for at least 2 days in the argon-filled desiccator, which appears to have the same curing effect as short incubation at elevated temperature.

In a quantitative study of AFM tip functionalization [55], gas phase silanization with APTES/tertiary amine has been compared to immersion in toluene/APTES (or APTMS), which has been used in many SMRFM studies [37, 40, 57, 59–61, 64, 93, 112]. Both methods generated a sufficient number of amino groups on AFM tips to perform SMRFM studies [55]. The gas phase method appeared more efficient and it has the advantage that dry conditions can instantaneously be created by using an argon atmosphere, whereas toluene must be dried with molecular sieves that have been preactivated by evacuation at <10 Pa and >100 °C. In addition, the amino group density can be downscaled in the gas phase method by adding a 250-fold [54] or a 10-fold excess [50] of methyltriethoxysilane (Fig. 7j), as needed for subsequent coupling of protein with long homobifunctional crosslinkers (Fig. 14).

None of the above methods produce sticky tentacles on the tip, provided that APTES/APTMS is fresh and silanization is under dry conditions. For this reason it is surprising that in a number of SMRFM studies a 10/90 [109–111] or 5/95 [83] mixture of APTES and water (pH 7 adjusted with acetic acid) has successfully been used for AFM tip aminofunctionalization. In these cases, however, step 2 was always reaction with glutaraldehyde, followed by attachment of protein to free-tangling aldehyde groups (Fig. 17). Thus, potentially formed APTES tentacles may have been highly crosslinked by glutaraldehyde, and dense coverage with protein may have eliminated all stickiness, as observed on sticky aldehyde surfaces (Fig. 34a) after dense coverage with IgG [85].

Besides APTES and APTMS (Fig. 6d), other aminosilanes have rarely been used for tip and support functionalization. The diamino analogs of APTES (Fig. 6h,i) were each used once [65, 139]. APhS (Fig. 6e) has been claimed to give smoother monolayers than APTES [140], but it was also found to be less efficient on AFM tips [141] and on silicon chips [142]. The latter study claims the diethoxy analog of APTES (Fig. 6g) to be the best aminosilane to give a defined monolayer on silicon [142]. One SMRFM study has successfully used the diethoxy form (Fig. 6g) for tip and support functionalization [143]. The monoethoxy form (Fig. 6f) has been found to be almost ineffective in most reported attempts [119, 123, 142, 144], with one exception [108].

In conclusion, aminosilanization with APTES or APTMS from the gas phase or from dry toluene are the best established and characterized methods for efficient aminofunctionalization of AFM tips and supports. These methods allow for versatile further functionalization with heterobifunctional linkers (Figs. 9, 10, 12, 13, 16, 18–20), in contrast to the APTES/water method, which was used with glutaraldehyde only as crosslinker between tip-NH_2 and protein.

4.2 Aminofunctionalization with Ethanolamine Hydrochloride

Aminofunctionalization with ethanolamine hydrochloride (Fig. 8b) was inspired by a preceding report [118] about a new treatment of glass with neat dodecanol at 230–250 °C, which yielded a monolayer of dodecyl chains bound via Si – O – C bonds (Fig. 8a). Aiming at aminofunctionalization, we tried ethanolamine in place of dodecanol (Fig. 8b). The base form of ethanolamine, however, was feared to also catalyze cleavage of the Si – O – C bond which we wanted to form. For this reason, ethanolamine hydrochloride was chosen. In order to obtain a liquid state at ~150 °C, DMSO was added as a non-volatile solvent, and molecular sieves were added to bind moisture. Although this attempt seemed rather optimistic, it was successful at first try [44] and proved to be a robust and simple method of aminofunctionalization [8, 9, 11, 13, 14, 22, 34–36, 38, 39, 45, 46, 49, 52, 53, 55, 56, 58, 63, 117].

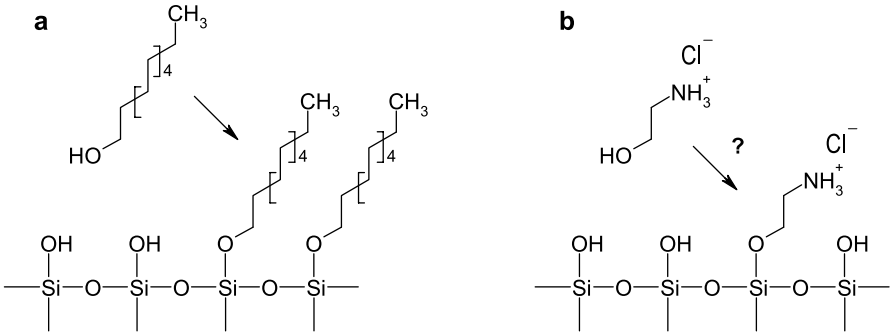

Fig. 8 Esterification of a glass surface (condensed silicic acid with embedded Na^+ counterions) with a perfect SAM of dodecanol at high temperature [118] and putative mechanism of AFM tip aminofunctionalization with ethanolamine hydrochloride in DMSO [44, 55]

Initially, the ethanolamine method was found to be incompatible with magnetic tips because the magnetic coating was lost in hot ethanolamine hydrochloride/DMSO. The problem was solved by using just enough heat to dissolve all solids in DMSO and cooling to room temperature before the precleaned AFM tips were immersed overnight [55]. Consequently, all our

SMRFM studies since 1999 [58] have used the room temperature method for tip functionalization.

In comparison to APTES/gas phase, the ethanolamine method is much simpler and somewhat more efficient [55], but it has two distinct drawbacks. The practical disadvantage is that many batches of PEG- and antibody-functionalized AFM tips (see Figs. 10 and 18) show unbinding lengths which are 10–30 nm longer than the sum of crosslinker length plus antibody length plus the height of the target molecule (see Fig. 1b,c). In contrast, no such problem is seen when using APTES/gas phase for aminofunctionalization. With any given tip, however, the discrepancy between expected and observed unbinding length appears to be constant. From this we conclude that some kind of short polymers must have been formed on the tip in ethanolamine hydrochloride/DMSO, with oxygen and/or DMSO as possible co-reactants. This vague hypothesis brings up the second disadvantage of the ethanolamine method: its chemical mechanism is essentially unknown. The initially assumed esterification mechanism (Fig. 8b) appears improbable also because ethanolamine hydrochloride/DMSO is effective at room temperature, whereas esterification with fatty alcohols requires high temperatures [118].

In practical terms, ethanolamine hydrochloride/DMSO is a convenient method for measurement of unbinding forces, whereas APTES/gas phase is preferred for explicit measurement of unbinding lengths, as well as in the TREC mode where the effective crosslinker length should not exceed 6 nm for optimal imaging conditions (S.M. Lindsay, personal communication, 2007).

4.3 Coupling of Ligands to Aminofunctionalized Tips and of Target Molecules to Aminofunctionalized Supports

Aminofunctionalization is only the first of several steps by which ligands are tethered to AFM tips. In the second step, the amino group is reacted with the amino-reactive terminus of a flexible bifunctional linker molecule. In two exceptional cases, the second end of the linker molecule already carried a biospecific ligand (Fig. 9), thus functionalization was finished at this level (Sect. 4.3.1). In all other cases, the linker carried another reactive group on its second terminus (Sect. 4.3.2). Homobifunctional linkers have two amino-reactive functions and have a high tendency to form loops between adjacent amino groups on the tip (Figs. 14, 15, 17), whereas heterobifunctional linkers have only one amino-reactive function. Thus, the linker can attach to the surface with this end only, all second termini being spared for binding of ligand molecules (Figs. 10, 12, 13, 16, 19, 20). Figure 18 shows an intermediate case in which both ends of the PEG linker are amino-reactive, yet with very different kinetics.

The majority of SMRFM studies have used long flexible linkers like PEG (6–10 nm in length, Figs. 9, 10, 12, 13, 14, 16, 18, 19) or amylose chains

(Figs. 14 and 28) which, in comparison to short linkers (Figs. 15, 17 and 20), have many advantages: (1) The long polymer chain is more elastic than the cantilever and its force constant is dependent on the applied force, giving rise to characteristic unbinding events (Fig. 1d) that are easily discriminated from direct adhesion of the tip on the support. (2) The ligand molecule is on a long leash, it can freely re-orient and "palpitate" the sample surface. Consequently, even a single antibody on the tip (Fig. 1b) was seen to recognize its target site in 44% out of 999 measured force-distance cycles (Fig. 1d,e). Moreover, the receptor–ligand complex can be formed without strain while the linker is unstretched, thus subsequent unbinding occurs with a more uniform force. (3) A sensor molecule on a long linker can more easily escape the danger of being crushed. This is concluded from the observation that tips with just one or few bound ligands can be used for hours without loss of function.

4.3.1 Single-Step Coupling of Ligand-PEG Conjugates to Aminofunctionalized Tips and Estimation of PEG Chain Density

Fluorescein-PEG-NHS has been attached to aminofunctionalized tips (Fig. 9) in order to study the mechanism of hapten–antibody interaction with nine different mutants of a single chain antibody [57, 59]. Interestingly, the unbinding forces (extrapolated to zero loading rate) closely correlated with the off-rates measured in parallel fluorescence studies, suggesting a similar unbinding pathway under force and without force.

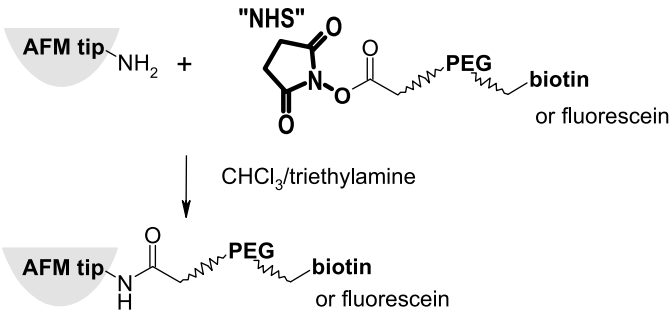

Fig. 9 Attachment of presynthesized ligand-PEG conjugates to aminofunctionalized AFM tips, with the amino-reactive NHS-esters of either biotin-PEG-COOH [11, 55] or fluorescein-PEG-COOH [57, 59]

Biotin-PEG-NHS was coupled to tip-NH_2 (Fig. 9) in order to quantitatively estimate the number of amino groups (per μm^2) that can be reacted with a PEG-NHS ester after any given method of aminofunctionalization. The number of biotin-PEG tentacles on the tip was estimated by performing the whole functionalization procedure on flat silicon nitride chips in

place of silicon nitride tips and measuring the amount of specifically bound Extravidin-peroxidase [55]. Equally functionalized tips (Fig. 1a) were tested with SMRFM on dense avidin monolayers (Fig. 1c) and characterized by the binding probability in the absence and presence of free biotin. The macroscopic method with marker enzyme and the AFM characterization agreed in that ethanolamine (at room temperature, see Sect. 4.1) and APTES/gas phase (see Sect. 4.2) were the best methods of tip functionalization [55]. The number of ~2000 Extravidin-peroxidase per μm^2 must be cautiously interpreted because more than one peroxidase and more than one avidin tetramer were part of one protein aggregate, thus many PEG-biotin could bind to one Extravidin-peroxidase aggregate. Nevertheless even a 10-fold higher lateral density of PEG-biotin would represent only a tiny fraction of the $\sim 4 \times 10^6$ alkyl chains per μm^2 present in a densely packed monolayer as shown in Fig. 4d. The reason for this low density is not known, whether a fraction of the amino groups oxidizes in air or whether the reactivity of PEG-NHS esters is too weak for most of the amino groups on the tip surface. In any case, similarly low lateral densities of PEG linkers were found in subsequent studies [38, 46] by the coupling schemes shown in Figs. 10 and 18, as well as in Fig. 19 (Wildling et al., manuscript in preparation). Moreover, a lateral density of several thousand per μm^2 agrees well with the observation that only one or few ligand molecules are active on tips with 10–20 nm tip radius [38]. Finally, the same functionalization density was also found when virus particles were linked to a cantilever with aldehyde-PEG-NHS (see Fig. 18b) and imaged with an unmodified tip [38].

4.3.2
Multi-Step Coupling of Bioligands to Aminofunctionalized Tips and Supports

Figure 10 shows tip-PEG-protein linking with PDP-PEG-NHS which has most often been used in SMRFM [8–10, 13, 22, 34, 35, 39, 44–49, 52, 53, 58, 62, 63]. The first step (amide coupling to the tip) is done in chloroform with 0.5% triethylamine [46] because in this aprotic solvent hydrolysis of the NHS ester is very slow. Crosslinker concentrations of more than 1 mg/mL gave little higher degrees of derivatization than 1 mg/mL [46]. The same rule applies to the other PEG-NHS esters (Figs. 9, 12, 19), except for aldehyde-PEG-NHS (Fig. 18, see below). The next step is coupling the protein by disulfide formation in buffer (pH 7.5). As explained in Sect. 7, protein concentrations of 1 μM or lower suffice for efficient tip functionalization. Inclusion of EDTA (1 mM) was found to be much more important than argon atmosphere to suppress oxidation of protein thiols (H.J. Gruber, unpublished observations, 2007). The same applies to the other coupling schemes involving free thiol groups (Figs. 12, 13, 16, 21, 22, 24, and 29).

The coupling scheme with PDP-PEG-NHS (Fig. 10) tends to give higher degrees of tip functionalization [46] with antibodies than the newer alter-

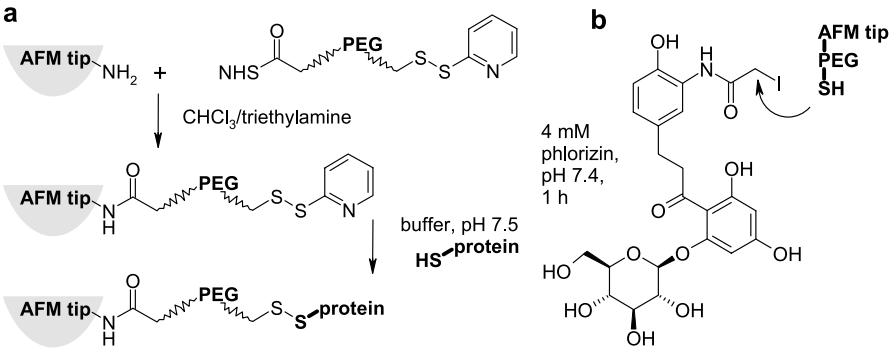

Fig. 10 Tethering of thiol proteins to aminofunctionalized tips **a** via PDP-PEG-NHS in two separate steps: amide bond formation and disulfide coupling [44–46, 145]. Alternatively, tip-PEG-*S*-*S*-pyridine can be reduced to tip-PEG-SH, followed by coupling of a thiol-reactive molecule [63]

natives (Fig. 18 [38] and Fig. 19), the downside of PDP-PEG-NHS being the need for a free thiol on the protein. In a few studies, a half-antibody [58] or a cysteine peptide [47, 48] were used which already contained a free thiol. In all other cases, antibodies were prederivatized with SATP as shown in Fig. 11a [46, 145]. The minor problem is that this seems to be a psychological barrier for non-chemists. The more significant problem is the consumption of precious protein (0.1–0.2 mg per batch) because after gel filtration (e.g., on a PD10 column, GE Healthcare) the protein is too dilute (~0.1 mg/mL) for freezing. Stabilization with albumine is forbidden because it contains a free thiol [146].

If prederivatization of antibodies is performed with periodate and pyridyldithiopropionic acid hydrazide ("SPDP hydrazide", Fig. 11b) [85, 147],

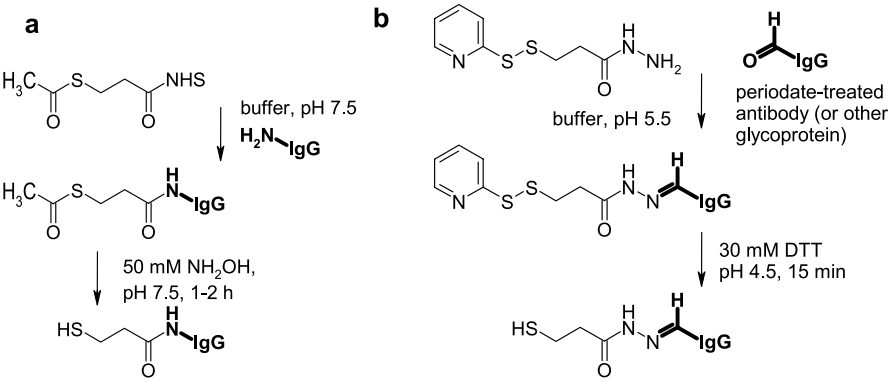

Fig. 11 Artificial introduction of thiol residues on antibody, either with SATP (**a**) [46, 145] or with pyridyldithiopropionic acid hydrazide (**b**) [147] and mild cleavage with DTT at pH 4.5 [148] in order to leave the disulfides in the protein structure intact

then the thiols are selectively introduced on the small oligosaccharide groups next to the central hinge region (see Fig. 1b). As a consequence, the PEG leash is attached to the center of the antibody which has been used to determine the pattern of cytosine methylation on DNA with AFM (Zhu et al., submitted manuscript and Austrian patent application A 170/2006, priority date February 3, 2006). As shown in Fig. 10b, tip-PEG-*S*-*S*-pyridine can be reduced with DTT to give tip-PEG-SH to which a thiol-reactive molecule can be coupled. This has been exemplified with iodoacetamido-phorizin, a potent blocker of the sodium-coupled glucose transporter in brush border membranes [63].

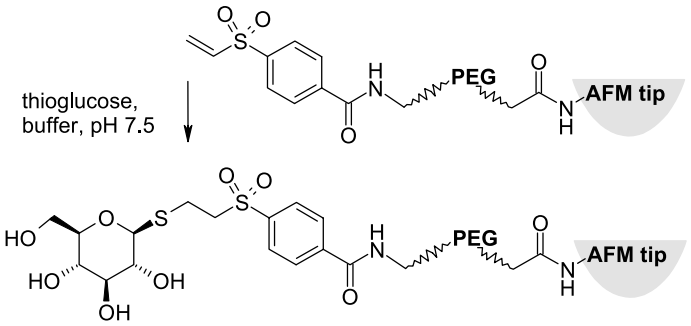

Fig. 12 Tethering of small thiol ligands to aminofunctionalized AFM tips via vinylsulfone-PEG-NHS [52, 53]. The slow kinetics of vinylsulfone-thiol coupling [149] was compensated for by high concentration (100 mM) of thioglucose [52, 53]

Figure 12 shows an alternate method for the tethering of a small molecule to the tip. Here the ligand (β-D-thioglucose) provided the thiol for coupling to the thiol-reactive vinylsulfone group on the free end of PEG. It should be mentioned that vinylsulfones are much less reactive towards thiol groups ($k_2 \sim 1\ M^{-1}\ min^{-1}$ at pH = 8 [149]) than pyridyl-*S*-*S* groups ($k_2 = 10^2 - 10^3\ M^{-1}\ min^{-1}$ at pH 7.5 [46]). In fact, tip-PEG-vinylsulfone (Fig. 12) was unable to couple de-acetylated biotin-IgG-SATP (unpublished observations) under conditions which gave excellent coupling of tip-PEG-*S*-*S*-pyridine (Fig. 10) according to testing with AFM (Fig. 1) and Extravidin-peroxidase (see Sect. 4.3.1). In contrast to biotin-IgG-SATP, thioglucose could be applied at 100 mM concentration [52, 53], thereby overcoming the problem of slow reaction of vinylsulfone with thiols.

While vinylsulfones (Fig. 12) are 10^2–10^3 times less reactive to thiols than pyridiyl-S-S groups (Fig. 10), the opposite is true for maleimides [150]). As depicted in Fig. 13, maleimide-PEG-NHS or a shorter analogue have successfully been used to tether thiolated ssDNA to aminofunctionalized tips and supports to measure the forces of double strand separation or of DNA-protein interaction [40, 51, 60, 61]. Analogous reaction conditions as in Fig. 10a were used to react maleimide-PEG-NHS with tip-NH_2 in the first step, and with thiolated DNA in the second step [51].

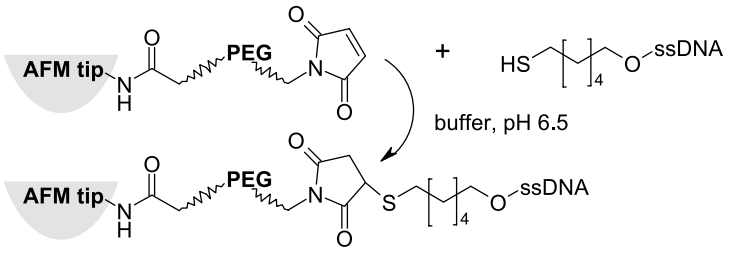

Fig. 13 Tethering of 5′-thiohexyl-ssDNA to aminofunctionalized tip via maleimide-PEG-NHS [40, 51, 60, 61] or a short heterobifunctional linker with a maleimide and NHS-ester function [134]

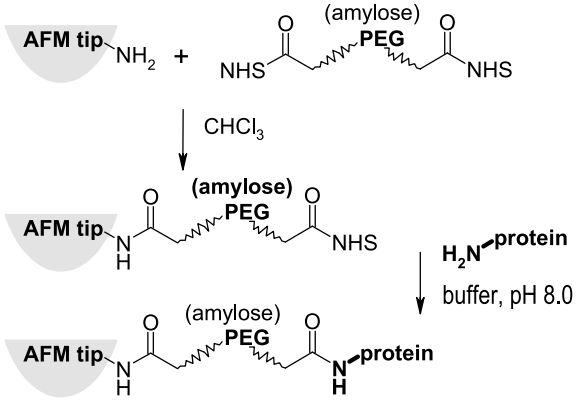

Fig. 14 Use of long homobifunctional NHS-PEG-NHS [50, 54], or long amylose with many NHS-ester functions [64, 65] for flexible tethering of unmodified protein to aminofunctionalized AFM tips

The coupling scheme in Fig. 14 differs from the previous ones by use of homobifunctional NHS-PEG-NHS [50, 56] – or of amylose chains with many amino-reactive NHS ester functions [64–68]. Since free amino groups are abundant in most proteins (80–90 lysines per antibody molecule [151]), both methods allow to couple proteins without any prederivatization. The published results indicate good performance of both methods. Nevertheless, the reader should be aware of two side reactions, the relative extent of which is critically dependent on several parameters: First, NHS-PEG-NHS has a high chance of binding two adjacent amino groups on the tip and become useless for binding of proteins. The extent of this side reaction is decreased at lower amino group density, and for this reason APTES has been mixed with ten to 250-fold excess of non-aminosilane (see Fig. 6d,j) in gas phase silanization [50, 56]. Shorter length and/or higher concentrations of NHS-PEG-NHS would also be helpful to minimize the relative extent of undesired loop formation, as observed under comparable circumstances (Fig. 18) [38]. Possibly, the

reaction in chloroform without the usual help of a tertiary amine (compare Fig. 14 with Figs. 9 and 10) also constitutes an essential parameter.

Second, NHS esters are not stable in aqueous solution [152], the rate of hydrolysis increasing by an order of magnitude when the pH is raised by one unit. Consequently, exposure of an NHS ester to buffer in the absence of the amine to be coupled dramatically lowers the yield of coupling [153], thus timing is critical. Re-activation of carboxyls with EDC/NHS could easily solve this problem, though. Carboxymethylamylose (indicated in Fig. 14) was actually activated with EDC/NHS and reacted with tip-NH_2 and protein in sequential steps [64, 65]. Although EDC/NHS activation is much more efficient in distilled water [154] or at pH 4.0–4.5 than in neutral buffer [153, 155], neutral pH was used with carboxymethylamylose, probably in order to prevent excessive activation [64–71].

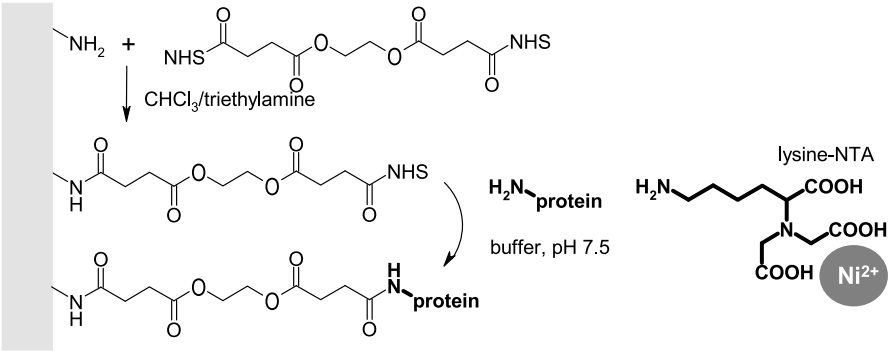

Fig. 15 Use of a short homobifunctional crosslinker to attach underivatized protein [117] or lysine-NTA [14] to aminofunctionalized mica

The above discussed parameters influence all coupling schemes in which surface-bound NHS esters are reacted with soluble amine components (Figs. 15, 26, 27, 28, 29). Working with a short bis-NHS ester (Fig. 15) is obviously less critical than with the long PEG_{3400} bis-NHS ester (Fig. 14) because the small linker can be placed at much higher lateral density and it can bridge only closely spaced amino groups on the surface. As depicted in Fig. 15, it was used to immobilize target proteins on aminofunctionalized mica [117], or to couple lysine-NTA, for subsequent capturing of His_6-tagged importin β in the presence of Ni^{2+} [14].

In the latter study [14], SMRFM was used to unravel the mechanism, and the role of GTP/GDP in the interaction of importin β with Ran, another component of the nuclear import machinery. The linking of His_6-tagged Ran protein to the tip was also by the non-covalent NTA–Ni^{2+}–His_6 bridge, albeit with a 6 nm long spacer between tip and NTA function (Fig. 16). Disulfide bond formation was used for reliable attachment of PDP-PEG-NTA to aminofunc-

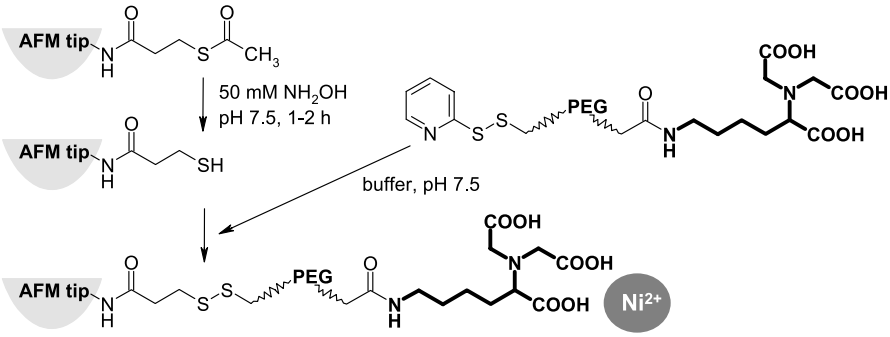

Fig. 16 Flexible attachment of NTA groups to AFM tips [14, 56]. The aminofunctionalized tip was first reacted with SATP (compare Fig. 12). Deacetylation gave a reactive thiol which was reacted with PDP-PEG-NTA to give a stable disulfide

tionalized and SATP-modified AFM tips (Fig. 16) [14, 56]. Besides His_6-Ran, His_6-tagged very-low density lipoprotein receptor constructs were also tethered to the AFM tip in order to study specific recognition by mica-bound human rhinovirus particles [56].

Tip functionalization with PEG-NTA (Fig. 16) was a side step from the series of homobifunctional linkers. It was described at this point because it nicely complemented support functionalization with lysine-NTA in the preceding figure. Figure 17 shows the most widely known homobifunctional linker, glutaraldehyde. As described in Sect. 4.1, a high extent of internal crosslinking by glutaraldehyde may even be helpful to form a compact layer from the three-dimensional networks formed in APTES/water. Evidently, a sufficient fraction of glutaraldehyde is unilaterally bound for subsequent coupling of protein. Moreover, the aldehyde residue cannot hydrolyze and thus remains reactive towards amines on a timescale of hours to days [85, 156, 157].

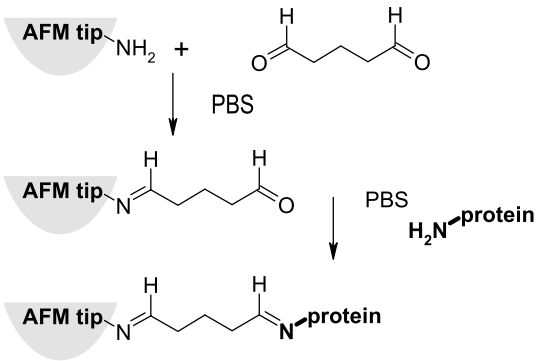

Fig. 17 Use of glutaraldehyde to attach underivatized proteins (or DNA [10, 112]) to aminofunctionalized mica [10, 51, 62, 115, 116], glass [109–111], silicon chips [108, 112], and/or AFM tips [83, 93, 108, 109, 111, 112]

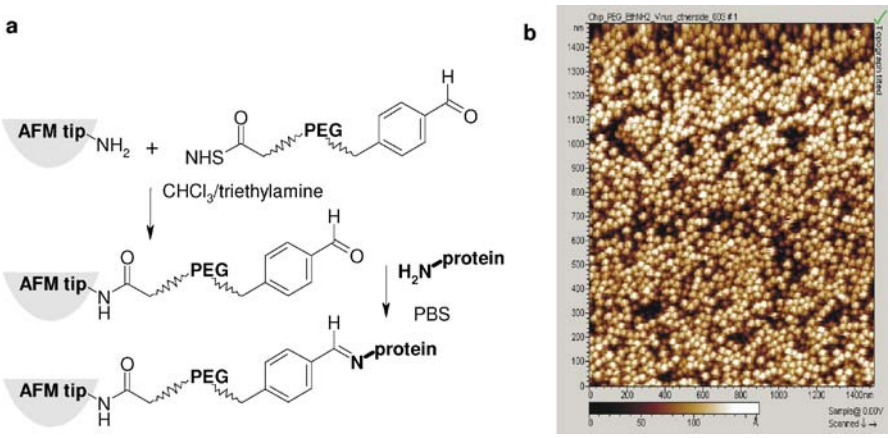

Fig. 18 **a** Use of long heterobifunctional aldehyde-PEG-NHS for flexible attachment of underivatized protein to aminofunctionalized AFM tips [36, 38]. The C = N double bond is usually fixed by reaction with sodium cyanoborohydride. **b** Human rhinovirus particles (serotype 2) were tethered to an ethanolamine-functionalized silicon nitride cantilever by use of aldehyde-PEG-NHS and imaged with an unmodified cantilever [38]. In contrast, very few virus particles were bound after benzaldehyde block with ethanolamine (see [38])

The coupling scheme in Fig. 18 also takes advantage of protein coupling to aldehydes, yet PEG was inserted as a flexible tether between tip and the benzaldehyde function [36, 38]. The other end of the linker was a NHS ester function which has a much higher reactivity for amino groups than the aldehyde function [38, 157]. This difference in reactivity helps to largely suppress undesired loop formation between adjacent amines on the tip surface. Even so, a rather high linker concentration (6.6 mg/mL) was necessary to accelerate unilateral reaction of the NHS ester function because, once attached, the PEG-benzaldehyde frequently collides with adjacent amino functions, allowing for fast reaction rates in spite of low intrinsic kinetics [38].

The most general and least critical coupling scheme is shown in Fig. 19. Benzophenone-PEG-NHS was unilaterally attached to aminofunctionalized tips (Wildling et al., manuscript in preparation), in agreement with the general notion that the ketone function of benzophenone has no significant reactivity for amino groups. Subsequent incubation with 1 μM biotin-IgG (see Fig. 1b) and illumination with UV light gave tips which had a high binding probability with avidin-covered mica (Fig. 1c) in the absence, but not in the presence of free biotin. Omission of UV light resulted in no tip functionalization and all results were confirmed by macroscopic experiments on silicon nitride chips, using Extravidin-peroxidase for quantitation.

As shown in Fig. 20, analogous coupling via an amino and photoreactive crosslinker has been used to immobilize proteins on glass [92] or mica [8] for subsequent AFM investigations. The azido linker in Fig. 20 is very effi-

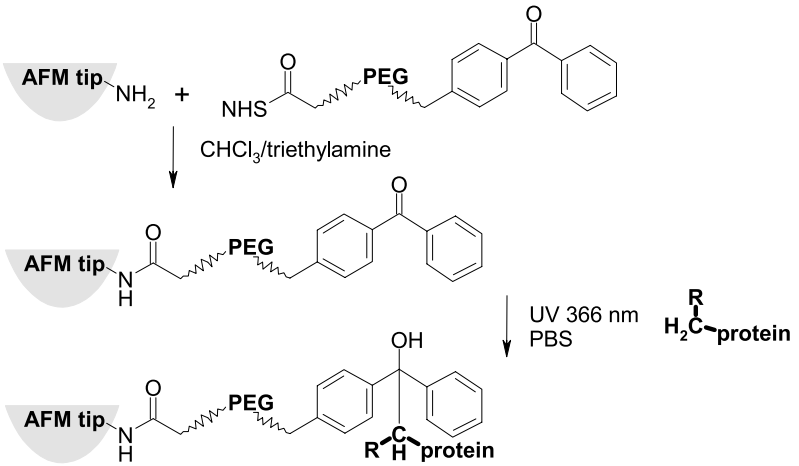

Fig. 19 Flexible tethering of underivatized proteins to aminofunctionalized AFM tips via benzophenone-PEG-NHS by amide bond formation and photolinking (Wildling et al., in preparation)

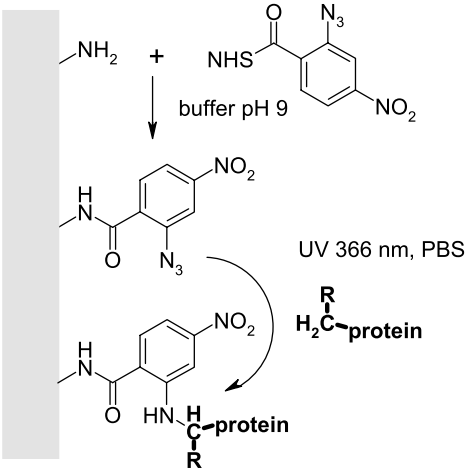

Fig. 20 Photoimmobilization of proteins on aminofunctionalized mica [8] or glass [92] by a short heterobifunctional linker

cient in coupling if the protein to be coupled is already in place (i.e., adsorbed) in the moment of N_2 release from the azide. Otherwise, the unstable nitrene will react with solvent or any other available component and be irreversibly lost. The benzophenone in Fig. 19, however, can be excited to the reactive triplet state many times before it reacts with the solvent. The latter has a lifetime of several minutes, thus the ability of coupling is maintained over a long time even during irradiation [158]. In conclusion, the coupling scheme in

Fig. 19 is applicable to protein and DNA without prederivatization (not even with NH_2 groups on DNA). It requires the least chemical expertise of all covalent methods, thus it can be recommended to the large community of non-chemists using SMRFM in nano- and bioscientific research and technology.

5 Functionalization of Gold-Coated Tips and/or Supports

Gold surfaces show unique advantages over any other inorganic solid when it comes to functionalization with well-defined monolayers of linker and ligand or target molecules: (1) After evaporation onto an inorganic support, the gold surface is perfectly clean. The same is true when a mica-gold-glue-silicon sandwich (which can be stored for a long time) is soaked in THF to strip off the mica template, yielding an atomically flat and clean gold surface (template-stripped gold [86–88]). (2) If the gold support is immediately transfered into a thiol solution, the short exposure to ambient atmosphere has no significant effect, in contrast to most other metal films. (3) The high inertness of gold allows the use of harsh cleaning conditions such as oxygen plasma, ozone, piranha (extremely hazardous), and NH_3/H_2O_2/water (extremely hazardous [89]) to remove tenaciously bound impurities after prolonged exposure to ambient condition [84, 89]. (4) Gold is inert to almost any functional group except for thiols/disulfides/thioethers [84]. Thus, densely packed SAMs are formed from a wide variety of molecules which contain sulfur atoms in such a reduced state (see Figs. 21, 22, 23, 24, 25, 26, 27, 28, 29, 30, 31 and 34). The physical and chemical properties of the SAMs can be adjusted for various needs by choosing proper functional groups (or a mixture thereof) on the top side of the SAM (see same figures). In particular, the SAMs with a layer of oligo(ethylene glycol) are highly resistant to protein adsorption [84, 159], tetra(ethylene glycol) providing the best protein resistance at minimal SAM thickness, and under more forgiving working conditions than with tri(ethylene glycol)-terminated SAMs [89].

Template-stripped gold appears to have no disadvantages compared to any other AFM support (the only exceptions are those rare cases in which a particular biomolecule adsorbs to freshly cleaved mica with just the right orientation, see Sect. 3.1). Gold-coated tips, however, have the drawback that they are prepared by evaporation of a 2–15 nm thick adhesive layer of Cr or Ti and a 25–100 nm layer of gold [69–71, 78, 160–167] onto the silicon nitride tips. As a consequence, the tip radius increases from the original 10–20 nm to much higher values, leading to much less imaging resolution. Another critical aspect of gold tips is the cleaning of the gold surface in case that SAM formation does not immediately follow gold deposition. UV/ozone has been reported to afford clean gold tips for subsequent functionalization with thiols/disulfides [70, 163]. It should be added that this is not achieved with every

type of UV/ozone cleaner, especially when highly protein-resistant SAMs are to be formed on gold [89].

Of particular importance for use in SMRFM is the strength of the gold–sulfur bond. Although classified as a weak covalent bond, its rupture force was nevertheless shown to be >1 nN [50, 66], i.e., an order of magnitude higher than antibody–antigen rupture forces [44]. Surprisingly, lipoic acid with its cyclic disulfide does not form a stronger but a fivefold weaker bond with the gold surface [50]. Also weak is the binding of *S*-acetylated alkanethiol to gold [168], yet this problem is easily abolished by de-acetylation with a primary amine (compare Fig. 11a).

5.1
Direct Chemisorption of Ligand Molecules onto Bare Gold Tips and/or Supports

As shown in Fig. 21, widely different molecules have been chemisorbed to bare gold tips and/or surfaces via their endogenous thiol or disulfide groups.

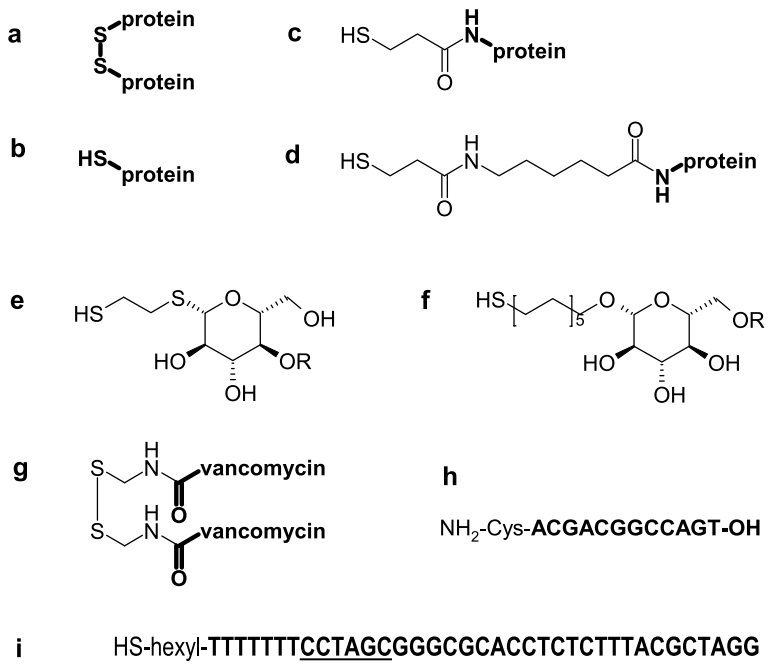

Fig. 21 Direct chemisorption onto gold-coated tips and/or supports of proteins or peptides via endogenous disulfides (**a**) [36, 76, 78, 94, 169] or thiols (**b**) [57, 110] or artificially introduced thiol groups (**c** [170] and **d** [73]). The same strategy was used for chemisorption of carbohydrates with ω-mercaptoalkyl groups (**e** [69, 70] and **f** [166, 171]), of vancomycin-cystamin (**g**) [163], of a peptide nucleic acid with an N-terminal cysteine (**h**) [172], and of 5′-thiohexyl-ssDNA with a hairpin loop sequence (**i**) [106]

Fab fragments of antibodies [169], as well as azurin [36] and fibronectin [76, 94] all possess a disulfide at their "base" (Fig. 21a), i.e., opposite their biospecific recognition sites, thus the latter was optimally accessible after chemisorption to gold. The same is true for Fab' fragments of antibodies [110] and Cys–Gly–His_6 or His_6–Gly–Cys peptide [47, 48], except that these were chemisorbed to gold via their endogenous thiols (Fig. 21b), rather than disulfides. Interestingly, direct chemisorption of Fab' onto bare gold tips resulted in much higher probability of antigen binding than with the SAM shown in Fig. 26 between the gold and the Fab' [110].

An aggrecan and a lectin, both lacking accessible disulfides or thiols have been derivatized with mercaptopropionyl groups (Fig. 21c [170]) or an extended version thereof (Fig. 21d [73]), respectively, for chemisorption to gold tip and gold support. By analogy, mono- and oligosaccharides have been extended with short or long mercaptoalkyl chains at the 1-position of the terminal monosaccharide (Fig. 21e [69, 70] and Fig. 21f [166, 171]) to study the interaction of carbohydrates with lectins or carbohydrates. Vancomycin has been attached to cystamine (Fig. 21g [163]) to study the specific interaction of this antibiotic with the dipeptide D-Ala-D-Ala (Fig. 27). Peptide nucleic acid with an N-terminal cysteine (Fig. 21h [172]) and 5′-thiohexyl-ssDNA (Fig. 21i [106]) have been chemisorbed onto gold tips [106, 172] and substrates [106] for measurement of hybridization and single point mutations by SMRFM. In conclusion, the direct chemisorption of biomolecules or synthetic molecules onto bare gold tip/support is experimentally simple and gives uniformly oriented monolayers with a high degree of functionality, except when protein has been statistically introduced with chemical reagents [73, 170].

5.2
Single-Step Functionalization of Gold Tips and/or Supports with Mixed SAMs

The ligand molecules shown in Fig. 21 were sufficiently bulky to keep the lateral density below the critical level at which mutual steric hindrance would have prevented recognition by the corresponding receptor molecules in SMRFM. This also applied to 5′-HS-hexyl-ssDNA with a hairpin segment (see underlined sequence in Fig. 21i). In general, however, thiolated ssDNAs are known to form such densely packed monolayers on gold that hybridization with complementary single strands is fully prevented [173]. This problem has been solved by formation of mixed SAMs, i.e., by inclusion of various ω-mercaptoalkanols as lateral spacers between the thiolated DNA (Fig. 22a) or RNA molecules (Fig. 22n), allowing to measure double strand rupture forces between complementary ssDNA on tip and support [164, 174]. Recently, the optimal lateral density of ssDNA and the minimal non-specific adhesion has been adjusted with a mixture of HS-undecyl-tetra(ethylene glycol) (5 μM) and 5′-HS-hexyl-ssDNA (24-mer, 0.1 μM) in 1 M KH_2PO_4 buffer, as shown by analysis of hybridization with surface plasmon resonance [175].

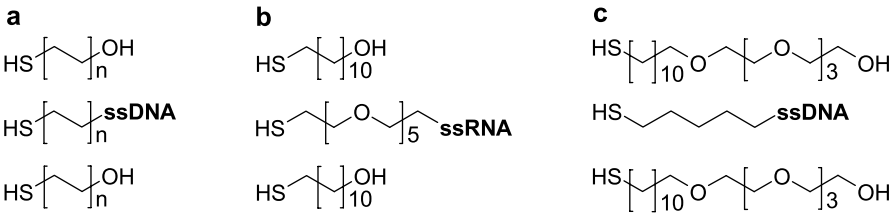

Fig. 22 Chemisorption of mixed SAMs of 5′-mercaptoalkyl-ssDNA (**a**, **c**) [164] or 5′-mercapto-PEG-ssRNA (**b**)[174] with various ω-mercaptoalkanols on gold-coated AFM tips and supports [164, 174], and adjustment of optimal lateral DNA density with a 50 : 1 mixture of spacer and ssDNA in phosphate buffer (**c**)[175]

Mixed SAMs have also been used for functionalization of gold tips with synthetic ligands to measure the interaction forces with synthetic receptors by formation of host-guest complexes in water (Fig. 23) [165, 167, 176]. Binding of cyclodextrin with its seven thioether-containing alkyl chains is one of the less common examples of thioether SAMs on gold.

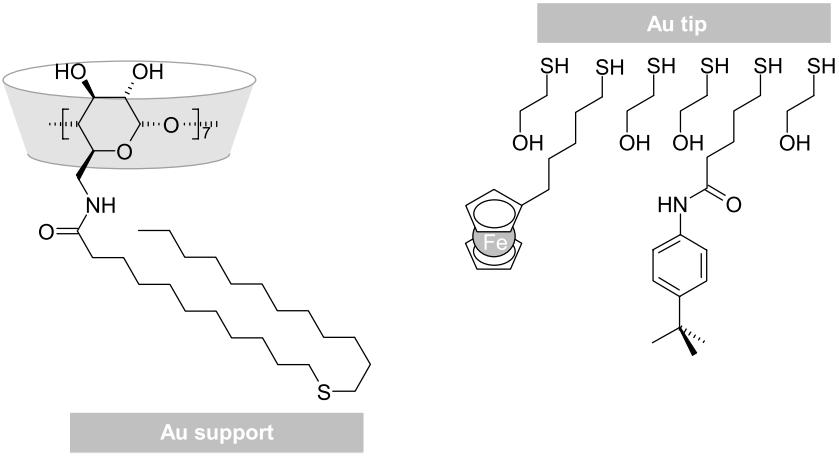

Fig. 23 Functionalization of gold-coated AFM tips with mixed SAMs presenting either ferrocene or *t*-butylbenzene as ligands and of gold support with thioether-derivatized β-cyclodextrin as receptor molecule [165, 167, 176]. Host–guest complexes were formed in water, as measured with SMRFM

Measurement of recognition forces between complementary synthetic molecules has also been performed in hexadecane medium (Fig. 24) [177]. Here, the same ligand was used on tip and support because the ligand function was self-complementary in non-polar solvent, yielding ligand–ligand dimers which were ruptured upon tip retraction from the surface. On the tip, a mixed SAM of 2-mercaptoethanol with the short HS-spacer-ligand conju-

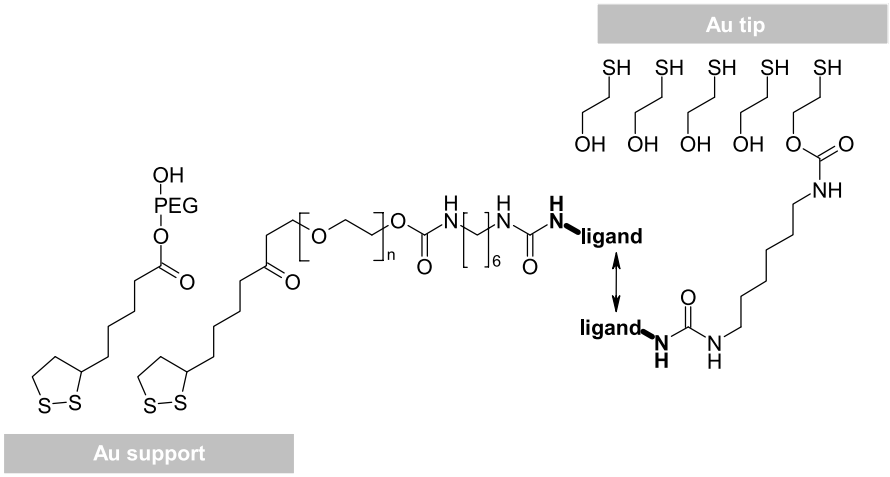

Fig. 24 Functionalization of gold-covered tip and support with mixed SAMs carrying the same ligand molecule via a short or long spacer, respectively [177]. Homophilic trans-interactions between self-complementary ligands were formed in hexadecane, as measured with SMRFM. Ligand-PEG-ligand conjugates could also be inserted between tip- and support-bound ligands

gate had to be formed for optimal lateral spacing. On the support, the low lateral density desired for SMRFM was adjusted by the bulkiness of the long PEG spacers between lipoate anchor and ligand function, as well as by use of lipoyl-PEG-OH as lateral spacer.

5.3
Modular Multi-Step Functionalization of Gold Tips and/or Supports

At first sight, direct chemisorption of thiolated ligands/receptors (Fig. 21) and of mixed SAMs with lateral spacers (Figs. 22, 23, 24) appears convenient because gold tip functionalization is achieved in a single step. However, the main effort is shifted to the steps which precede tip functionalization, i.e., elaborate synthetic chemistry (Figs. 21e–h, 22, and 23) or protein prederivatization (Fig. 21c,d) or extensive optimization of molar ratios in mixed SAMs (Figs. 22, 23, 24) are required, except when sensor proteins possess an endogenous thiol/disulfide at the desired position, i.e., opposite the recognition site (Fig. 21a,b).

Figures 25, 26, 27, 28, 29, 30, and 31 show the opposite strategy of gold tip/support functionalization, which is modular in that SAMs with a broad application range are formed on gold, followed by one or several steps which result in coupling of ligand/receptor molecules. The SAM with densely packed NHS ester functions in Fig. 25 has unique properties in that they are exceptionally resistant to hydrolysis, even at pH 12 [178]. Nevertheless, the coup-

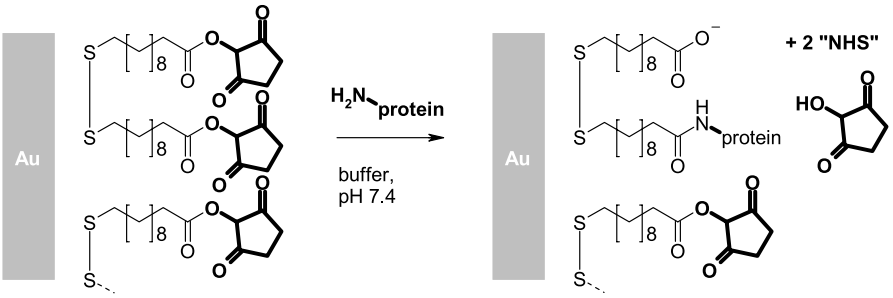

Fig. 25 Functionalization of gold-coated tips [28, 161] and/or supports [28, 37, 88, 161, 178] with a SAM of di-(*N*-succinimidyl)-11,11′-dithiodiundecanoate, the NHS ester functions of which can react with the lysine residues of native proteins. A similar amino-reactive SAM has also been formed from succinimidyl 3-(2-pyridyldithio)-propionate and used for coupling of ferritin [169]

ling of protein via endogenous lysine residues (Fig. 25) is very efficient, even at low protein concentration [28, 37, 88, 161, 178, 179]. The apparent paradox that the small hydroxide ion should have more steric problems than a protein molecule in attacking the active ester underneath the NHS residue (Fig. 25) strongly indicates that the protein is preadsorbed on, and strongly interacts with the top side of the SAM (see Sect. 7).

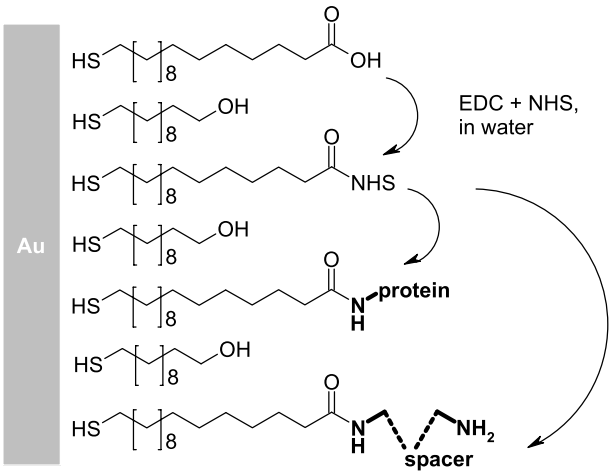

Fig. 26 Functionalization of gold-coated tips [94, 110, 162] or supports [54, 160] with mixed SAMs of ω-mercaptohexadecanoic acid and ω-mercaptoundecanol (50/50) [160, 162] or with SAMs lacking the long chain alcohol [94, 110]. The carboxyl groups on the SAM were activated as NHS-esters with EDC/NHS, providing for amide bond formation with unmodified protein [94, 160]. Alternatively, short or long chain diamines were coupled and further functionalized on the free-tangling amino group [54, 110, 162]

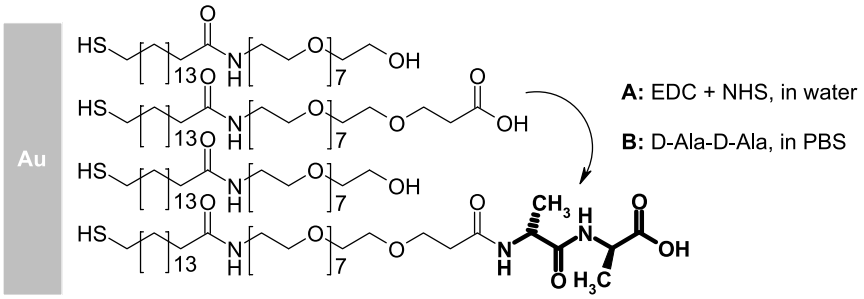

Fig. 27 Functionalization of gold-covered support with a non-adsorptive (protein-resistant) mixed SAM carrying COOH functions on 10% of the PEG chains. Activation with EDC/NHS provided for coupling of dipeptide [163]

Figures 26 and 27 also show the coupling of proteins to SAMs with NHS ester functions. However, here only a fraction of the COOH groups on the SAM is transiently activated with EDC/NHS. Moreover, the thiolated fatty acids (Fig. 26) or fatty acid-PEG conjugates (Fig. 27) are often laterally diluted by similar OH-terminated thiols to further lower the lateral density of reactive sites, thereby enhancing their accessibility, reactivity, but also sensitivity to hydrolysis. At first sight, Figs. 26 and 27 look similar. However, the two surfaces are physically very different, with strong protein adsorption and exceptionally fast protein coupling on the simple SAM (Fig. 26), whereas the protein-resistant SAM in Fig. 27 has a very moderate rate of protein coupling (see Sect. 7).

Carboxymethylamylose (Fig. 28) has extensively been used for the tethering of proteins to aminosilanized tips and supports (compare Fig. 14) [7, 50,

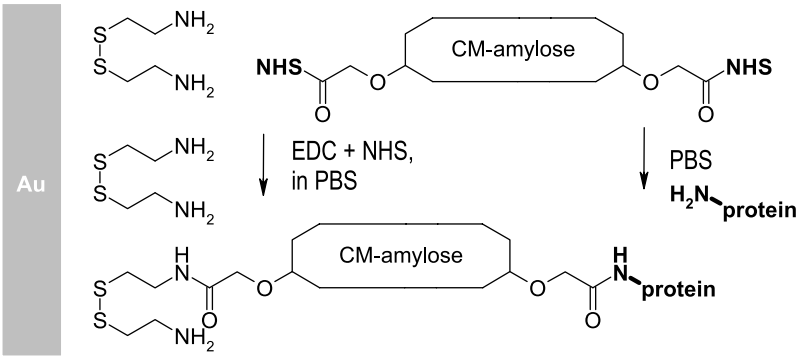

Fig. 28 Functionalization of gold-coated tips and/or supports [69, 71] with a SAM of cystamine dihydrochloride to which EDC/NHS-activated carboxymethylamylose is coupled by amide bond formation. Residual NHS ester functions on carboxymethylamylose allow for coupling of proteins via amide bonds. This scheme is analogous to derivatization of aminosilanized silicon nitride tips and of glass (Fig. 14) and also similar to the use of commercial carboxymethyldextran chips as AFM supports [31, 77, 78]

64–68]. Meanwhile it has been shown that this versatile method can easily be adapted for gold tips/supports by chemisorption of commercial cystamine dihydrochloride [69, 71]. In this way, a lectin was tethered to the gold support to study the interaction with a hexasaccharide bound to the gold tip as shown in Fig. 21e. The interaction of immunoglobulin G and protein A was also analyzed by SMRFM after tethering them to tip and support, respectively, as depicted in Fig. 28.

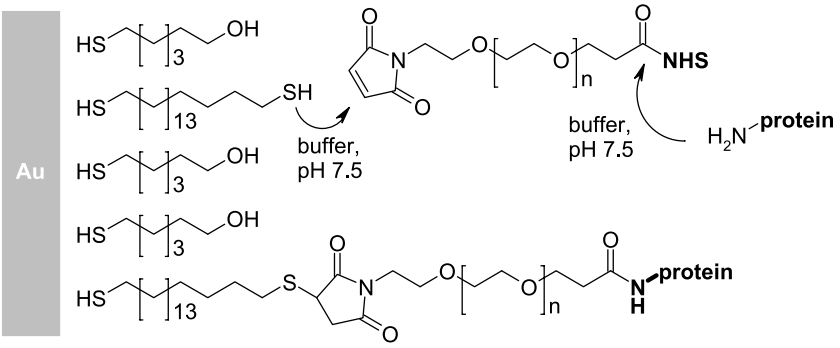

Fig. 29 Tethering of unmodified proteins to gold-coated tips and supports by (1) formation of a mixed SAM with 5% dithiol and 95% mercaptohexanol, (2) attachment of maleimide-PEG-NHS by a thioether bond, and (3) coupling of protein via amide bond formation [15, 43]

Figure 29 shows a simple and powerful method of gold tip/support functionalization in which the heterobifunctional linker, maleimide-PEG-NHS, is used in the "reverse way" (according to the chemists' preconception). The reason is that NHS esters are reactive to both NH_2 and SH groups. Only the typical thiol-reactive functions such as maleimide, pyridyl-*S*-*S*, and vinylsulfone possess a high selectivity for thiol over amine under typical crosslinking conditions. In case of maleimide-PEG-NHS, however, the exceptionally fast maleimide-thiol coupling [150] outruns the potential side reaction of NHS esters with thiols on the gold surface (see Fig. 29), just like NHS esters override benzaldehydes in the competition for tip-NH_2 (compare Fig. 18). As with aldehyde-PEG-NHS, some side reaction, i.e., loop formation will also occur by twofold reaction of maleimide-PEG-NHS with adjacent thiols on the SAM surface. The so formed loop ("SAM-*S*-maleimide-PEG-CO-*S*-SAM") can gradually hydrolyze to give "SAM-*S*-maleimide-PEG-COOH", or possibly react with NH_2-protein, resulting in "SAM-*S*-maleimide-PEG-CO-NH-protein", which is identical to the desired product, as formed by the two-step mechanism shown in Fig. 29. Whether by direct or indirect pathway, the functionalization of the dithiol SAM in Fig. 29 with maleimide-PEG-NHS allows to couple almost any protein, due to abundance of lysines in proteins. The method has been used to analyze the mechanism of homophilic

interaction between pairs of ICAM1 molecules on tip and support [15, 43]. It should be emphasized that only maleimide-PEG-NHS can safely be used in the "reversed order" shown in Fig. 29. The pyridyl-*S*-*S* group in PDP-PEG-NHS (Fig. 10) and the vinylsulfone function in vinylsulfone-PEG-NHS (Fig. 12) are $\sim 10^2$- and $\sim 10^5$-fold less reactive than maleimides [46, 149, 150] towards thiols, respectively, thus outrunning of NHS ester functions by these slow thiol-reactive groups cannot be expected.

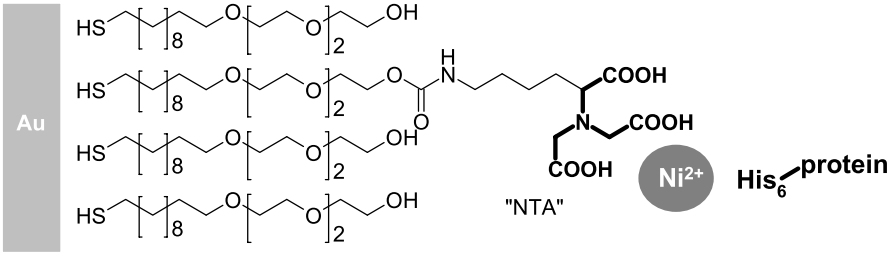

Fig. 30 Functionalization of gold-coated tips [77, 160, 185] with a protein-resistant mixed SAM to which His_6-tagged proteins were specifically bound in presence of Ni^{2+}. A similar SAM (lacking the triethylene glycol chains) was used to prepare an AFM support with NTA functions [4, 48]

Figure 30 depicts a very convenient strategy of protein immobilization which does not require any covalent chemistry and nevertheless achieves a strong and lasting attachment of proteins to the surface. It relies on the well-known specific interaction of hexahistidine peptides or His_6-tagged proteins with surface-bound NTA-Ni^{2+} complexes [180]. A decade after the invention of this method, there was a first report that one isolated NTA group on a chip surface can hold His_6 peptide or His_6-tagged protein for minutes only, whereas proteins with both N- and C-terminal His_6 tag were irreversibly bound on the timescale of days [181]. An even better solution to the problem of fast dissociation was found by synthesis of bis-NTA (not shown) and tris-NTA (Fig. 31) [87, 182–184]. The latter can accomodate two histidine residues on each NTA-Ni^{2+}, and this hexadentate complex affords irreversible binding on a timescale of days, especially with His_{10} tags where steric contraints are further reduced.

So far, only the mono-NTA (lysine-NTA) functions have been used to attach His_6-tagged proteins as ligands to gold tips (as shown in Fig. 30) [77, 160, 185] or to silicon nitride tips (as shown in Fig. 16) [14, 56] in order to measure recognition with complementary "receptor" proteins on the support. The implicit assumption in these studies was that the NTA–Ni^{2+}–His_6 bridge be stable for a long period of time and also resistant to the pulling forces needed for "receptor–ligand" separation. In the light of the preceding paragraph, however, the assumption of long-term stability seems questionable. In addition, the rupture forces measured for the NTA–Ni^{2+}–His_6 bridge

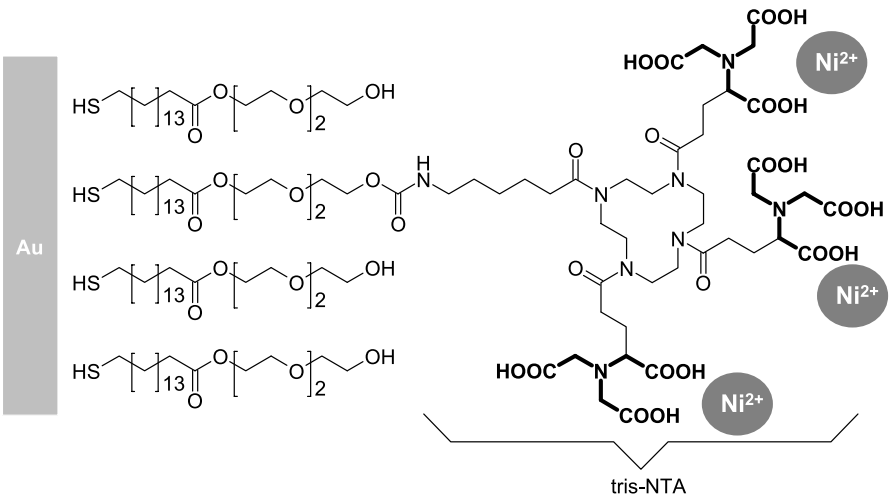

Fig. 31 Functionalization of ultraflat gold supports with a mixed SAM carrying tris-NTA functions for non-covalent, yet irreversible binding of His_6- and His_{10}-tagged proteins [87, 184]

range from 50 to 500 pN [47, 48, 77, 78], the lower values being in the range of many protein–protein interactions. Nevertheless, when actually used, tips with mono-NTA were consistently able to hold on to their His_6-tagged sensor proteins for hours, and for thousands of force-distance cycles with significant force stress [14, 56, 77, 160, 185]. Thus, an explanation is needed to reconcile predicted failure (premature loss of His_6-protein) with actual success. Most likely, His_6-tagged proteins are indeed soon lost from single NTA functions but stably bound to pairs of NTA functions on the surface. Especially with our long PDP-PEG-NTA (Fig. 16), such bis-NTA- and possibly tris-NTA-like configurations have a high chance to occur on the AFM tip. Nevertheless, the likely use of tris-NTA for tip functionalization in the near future is expected to constitute major progress in AFM tip functionalization.

6 Functionalization of Hydrogen-Terminated Silicon or Diamond and of Carbon Nanotubes

Figure 32 depicts the first example in which a hydrogen-terminated silicon tip (prepared by cleaning with 2% HF in water) was covalently coated by refluxing under nitrogen in a solution of $H_2C = CH - (CH_2)_9 - O - (CH_2 - CH_2 - O)_3 - CH_3$ in mesitylene [186]. At this level, the tip is very non-adhesive but not yet functional for SMRFM. Electrooxidation was used to selectively oxidize the chain termini at the apex of the tip [42]. The re-

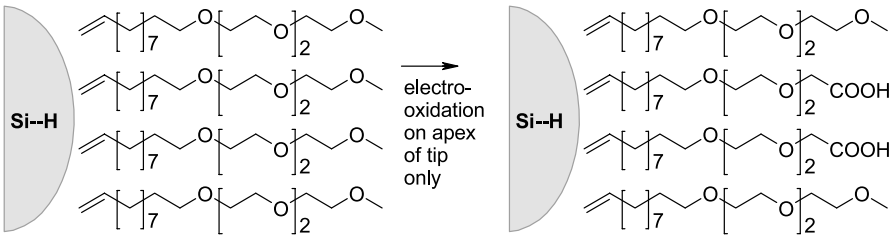

Fig. 32 Functionalization of hydrogen-terminated silicon tips with a protein-resistant SAM [186]. Carboxyl groups were generated at the apex of the tip by electrooxidation, followed by activation with EDC/NHS and coupling of NH_2-PEG-biotin, allowing for recognition force microscopy as depicted in Fig. 1a [42]

sulting COOH groups were activated with EDC/NHS. Amide bonds were formed with NH_2-PEG-NH-biotin, resulting in tip-PEG-biotin that was tested with SMRFM on avidin-covered mica as usual (compare Figs. 1a,c and 9). Hydrogen-terminated diamond is well-known to be derivatized by the very same methods as is H-terminated silicon [187]. To our knowledge, however, H-terminated diamond has not yet been used for AFM tips or supports. Carbon nanotubes have occasionally been functionalized for chemical force microscopy [6, 188], but one SMRFM model study has been reported in which terminal COOH groups on the carbon nanotube were activated with EDC and reacted with $NH_2 - (CH_2)_5 - NH$-biotin [189]. The test sample was mica with a layer of biotin-BSA and a layer of streptavidin on top of it (compare Fig. 2). Altogether, it is difficult to predict whether silicon, diamond and/or carbon nanotubes will become popular for tip/support functionalization in the near future.

7
Acceleration of Surface Attachment by Preadsorption

The mechanism of thiol protein coupling to tip-linked PEG-S-S-pyridine (see Figs. 10a and 33a) has been analyzed by imitation in bulk solution as shown in Fig. 33b [46]. The latter reaction could be followed in a spectrometer cuvette by measuring the release of 2-thiopyridone via UV absorption (ε_{343} = 8080 M^{-1} cm^{-1} [145]). The bimolecular reaction constant obtained from fitting this bulk reaction was then used to estimate the half-life for the reaction of tip-PEG-*S*-*S*-pyridine with a thiol protein at 1 μM protein concentration. Surprisingly, this predicted half-life was 5 days, thus 1 month would be required to reach 98.3% coupling probability (6 half-lives). In practice, however, the maximum yield of antibody coupling has always been reached within 1–2 h at 1 μM antibody concentration (0.15 mg/mL) and lower (0.2 μM) [8–10, 13, 14, 34–36, 38, 39, 41, 42, 44–46, 49, 51, 52, 56–58, 62, 63].

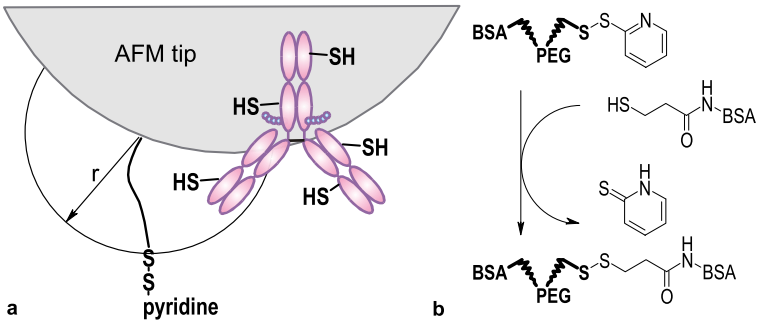

Fig. 33 **a** Preadsorption model [46] for calculating the acceleration of antibody coupling via disulfide formation when one antibody with one reactive thiol is loosely adsorbed next to a 6 nm long PEG-*S*-*S*-pyridine tentacle. The formal thiol concentration with reach of the PEG linker is 3 mM, in contrast to the typical bulk concentrations of antibody (e.g., 1 μM, 0.15 mg/mL). As determined experimentally, preadsorption reduces the time constant for coupling of 1 μM protein from 5 days in bulk solution to <1 h on the tip surface. **b** Imitation of the reaction of tip-PEG-*S*-*S*-pyridin with thiolated antibody by reaction of BSA-PEG-*S*-*S*-pyridine with $HS-CH_2-CH_2-CO-NH-BSA$ in bulk solution. The reaction was monitored by release of 2-thiopyridone ($\varepsilon_{343} = 8080\ M^{-1}\ cm^{-1}$)

The reason for at least 10^3-fold acceleration of protein coupling on the tip as compared to bulk solution results from the phenomenon that proteins generally adsorb to any solid surface, except for so-called protein-resistant surfaces which are not easily prepared [84, 89, 95, 190, 191]. Therefore, the probability is high that at least one thiol protein adsorbs next to a tip-bound PEG-*S*-*S*-pyridine tentacle (see Fig. 33a), corresponding to 3 mM protein concentration within the 6 nm reach of the crosslinker, i.e., $>10^3$ times higher than the 1 μM concentration in bulk solution.

The above hypothesis is indispensible to explain 10^3-fold faster coupling on the tip than in bulk solution, and it is plausible (proteins are known to adsorb to almost any solid). Nevertheless, positive evidence is preferred over inference. Figure 34 shows two kinds of SAM-covered gold surfaces, which have in common that 5–10% of the SAM components carry amino-reactive aldehyde functions, yet their physical properties are very different. The surface to the left has a high tendency for protein adsorption, as measured before the aldehyde functions were generated from vicinal diols with periodate [85], whereas the surface to the right is very protein resistant [156]. As predicted by the above hypothesis of preadsorption-induced coupling, the kinetics of protein coupling was $>10^3$ times faster on the surface shown in Fig. 34a as compared to Fig. 34b, with a 1 min timescale on the adsorptive surface [85] and a 1 day timescale on the protein-resistant SAM [156] for monolayer coverage at 1 mg/mL IgG concentration (6.7 μM).

Does this mean that protein-resistant SAMs as shown in Figs. 27 and 30, 31, 32 are incompatible with protein coupling to AFM tips? The answer depends

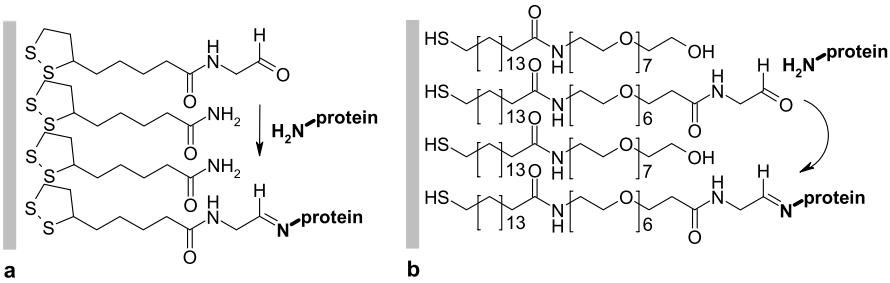

Fig. 34 Demonstration of at least 10^3-fold acceleration of covalent protein immobilization by preadsorption. A full monolayer of covalently bound protein is formed within 1 min on a simple adsorptive SAM (**a**) [85], whereas on a protein-resistant SAM (**b**) the time scale is shifted to days (10^3–10^4 min) [156]

on the type of coupling reaction between SAM and protein: Slow coupling functions such as pyridyl-*S*-*S* (Fig. 10), vinylsulfone (Fig. 12) and aldehyde (Fig. 18) are indeed dependent on the acceleration of protein coupling by preadsorption. In contrast, maleimides (Fig. 13) and, to a lesser degree, NHS esters are sufficiently reactive to efficiently couple proteins from 1–10 μM bulk solution onto a protein-resistant surface [156]. Fortunately, the same also applies to binding of His_6-tagged proteins on protein-resistant SAMs with mono-, bis-, and tris-NTA functions [87].

8
Conclusion and Perspective

The above described methods of tip and support functionalization can be grouped into two categories: case-to-case solutions and systematic/modular approaches. Spontaneous adsorption of certain suitable proteins onto mica (Sect. 3.1) or bare gold (Sect. 5.1) are examples of the first kind, and the same applies to suitably modified synthetic ligand/receptor molecules. With respect to systematic strategies, one set of methods has been developed for "silanizable materials" and the other for gold-coated tips/supports.

Silicon nitride tips, silicon chips, glass and mica have usually been functionalized in three steps: aminofunctionalization, crosslinker attachment, and ligand coupling. The two prevailing methods of aminofunctionalization, APTES/gas phase (Figs. 5, 6, 7) or ethanolamine (Fig. 8) were found to be exchangeable, APTES being superior in terms of predictable unbinding lengths. A multitude of crosslinkers with widely different lengths and coupling functions has successfully been used thus far (Figs. 10, 11, 12, 13, 14, 15, 16, 17, 18, 19, 20). On gold, the usual systematic approach has been coating with a SAM to which the ligand/receptor molecules can be coupled in a single step. In this case, linker length was rather short (Figs. 25, 26, 27, 30 and 31).

Only rarely, amylose (Fig. 28) or PEG chains (Fig. 29) have been used as long flexible linker between the SAM and the ligand molecule.

Widely different coupling functions are available for attachment of the linker molecules in the last step of tip/support functionalization. Maleimides are the fastest among the covalently reacting functions. Aldehydes and NHS esters are convenient because they can react with amino groups which are abundant in proteins and available upon demand in synthetic DNA. Benzophenone appears to be the most general of all functions, any aliphatic carbon atom being a potential target. Since most cloned proteins are nowadays expressed with a His_6 tag, the NTA and especially the novel tris-NTA function are a significant step towards "plug-and-play" functionalization methods.

Recognition force microscopy has brought forth remarkable studies which have been published in high-level journals where methodical details must be kept to a minimum. Here, we have tried to present all methods in the same explicit way, for the benefit of the reader and of AFM users interested in converting their tips into molecular sensors.

Acknowledgements The support of the Austrian Science Foundation (FWF project P15295), the Human Frontiers Science Program of the European Union (HFSP project RGP0053), the Sixth Framework Program of the European Commission (TIPS4CELLS LSHG_CT_2005_512101, NAS-SAP No. 13523, and BIO-LIGHT-TOUCH No. 028781), and the GEN-AU project of the Austrian Federal Ministry for Science and Research is gratefully acknowledged.

References

1. Hörber JK, Miles MJ (2003) Science 302:1002
2. Scheuring S, Muller DJ, Ringler P, Heymann JB, Engel A (1999) J Microsc 193:28
3. Hinterdorfer P, Dufrene YF (2006) Nat Methods 3:347
4. Kienberger F, Ebner A, Gruber HJ, Hinterdorfer P (2006) Acc Chem Res 39:29
5. Leckband D, Israelachvili J (2001) Q Rev Biophys 34:105
6. Kim C, Seo K, Kim B, Park N, Choi YS, Park KA, Lee YH (2003) Phys Rev B 68
7. Radmacher M, Cleveland JP, Fritz M, Hansma HG, Hansma PK (1994) Biophys J 66:2159
8. Willemsen O, Snel M, van der Werf KO, de Grooth BG, Greve J, Hinterdorfer P, Gruber H, Schindler H, van Kooyk Y, Figdor C (1998) Biophys J 75:2220
9. Stroh CM, Ebner A, Geretschlager M, Freudenthaler G, Kienberger F, Kamruzzahan ASM, Smith-Gill SJ, Gruber HJ, Hinterdorfer P (2004) Biophys J 87:1981
10. Stroh C, Wang H, Bash R, Ashcroft B, Nelson J, Gruber H, Lohr D, Lindsay SM, Hinterdorfer P (2004) Proc Natl Acad Sci USA 101:12503
11. Ebner A, Kienberger F, Kada G, Stroh CM, Geretschlager M, Kamruzzahan ASM, Wildling L, Johnson WT, Ashcroft B, Nelson J, Lindsay SM, Gruber HJ, Hinterdorfer P (2005) Chem Phys Chem 6:897
12. Evans E, Ritchie K (1997) Biophys J 72:1541
13. Baumgartner W, Hinterdorfer P, Ness W, Raab A, Vestweber D, Schindler H, Drenckhahn D (2000) Proc Natl Acad Sci USA 97:4005

14. Nevo R, Stroh C, Kienberger F, Kaftan D, Brumfeld V, Elbaum M, Reich Z, Hinterdorfer P (2003) Nat Struct Biol 10:553
15. Wieland JA, Gewirth AA, Leckband DE (2005) J Biol Chem 280:41037
16. Willemsen OH, Snel MME, Cambi A, Greve J, De Grooth BG, Figdor CG (2000) Biophys J 79:3267
17. Wong JY, Kuhl TL, Israelachvili JN, Mullah N, Zalipsky S (1997) Science 275:820
18. Merkel R, Nassoy P, Leung A, Ritchie K, Evans E (1999) Nature 397:50
19. Tsukasaki Y, Kitamura K, Shimizu K, Iwane AH, Takai Y, Yanagida T (2007) J Mol Biol 367:996
20. Li F, Redick SD, Erickson HP, Moy VT (2003) Biophys J 84:1252
21. Benoit M, Gabriel D, Gerisch G, Gaub HE (2000) Nat Cell Biol 2:313
22. Baumgartner W, Golenhofen N, Grundhofer N, Wiegand J, Drenckhahn D (2003) J Neurosci 23:11008
23. Duwez A-S, Poleunis C, Bertrand P, Nysten B (2001) Langmuir 17:6351
24. Frisbie CD, Rozsnyai LF, Noy A, Wrighton MS, Lieber CM (1994) Science 265:2071
25. Duwez A-S, Cuenot S, Jerome C, Gabriel S, Jerome R, Rapino S, Zerbetto F (2006) Nat Nano 1:122
26. Jerome C, Willet N, Jerome R, Duwez A-S (2004) Chem Phys Chem 5:147
27. Brockwell DJ, Paci E, Zinober RC, Beddard GS, Olmsted PD, Smith DA, Perham RN, Radford SE (2003) Nat Struct Biol 10:731
28. Dammer U, Hegner M, Anselmetti D, Wagner P, Dreier M, Huber W, Guntherodt HJ (1996) Biophys J 70:2437
29. Lee GU, Kidwell DA, Colton RJ (1994) Langmuir 10:354
30. Lo Y-S, Huefner ND, Chan WS, Stevens F, Harris JM, Beebe TP (1999) Langmuir 15:1373
31. Ludwig M, Dettmann W, Gaub HE (1997) Biophys J 72:445
32. Moy VT, Florin E-L, Gaub HE (1994) Coll Surf A Physicochem Eng Aspects 93:343
33. Wong J, Chilkoti A, Moy VT (1999) Biomol Eng 16:45
34. Avci R, Schweitzer M, Boyd RD, Wittmeyer J, Steele A, Toporski J, Beech W, Arce FT, Spangler B, Cole KM, McKay DS (2004) Langmuir 20:11053
35. Baumgartner W, Gruber HJ, Hinterdorfer P, Drenckhahn D (2000) Single Mol 1:119
36. Bonanni B, Kamruzzahan ASM, Bizzarri AR, Rankl C, Gruber HJ, Hinterdorfer P, Cannistraro S (2005) Biophys J 89:2783
37. De Paris R, Strunz T, Oroszlan K, Güntherrodt H-J, Hegner M (2000) Single Mol 4:285
38. Ebner A, Wildling L, Kamruzzahan ASM, Rankl C, Wruss J, Hahn CD, Hölzl M, Kienberger F, Blaas D, Hinterdorfer P, Gruber HJ (2007) Bioconjugate Chemistry 18:1176
39. Ebner A, Kienberger F, Huber C, Kamruzzahan AS, Pastushenko VP, Tang J, Kada G, Gruber HJ, Sleytr UB, Sara M, Hinterdorfer P (2006) Chem Bio Chem 7:588
40. Grange W, Strunz T, Schumakovitch I, Güntherodt H-J, Hegner M (2001) Single Mol 2:75
41. Gamsjaeger R, Wimmer B, Kahr H, Tinazli A, Picuric S, Lata S, Tampe R, Maulet Y, Gruber HJ, Hinterdorfer P, Romanin C (2004) Langmuir 20:5885
42. Gu J, Xiao Z, Yam C-M, Qin G, Deluge M, Boutet S, Cai C (2005) Biophys J 89:L31
43. Hukkanen E, Wieland J, Gewirth A, Leckband D, Braatz RD (2005) Biophys J 89:3434
44. Hinterdorfer P, Baumgartner W, Gruber HJ, Schilcher K, Schindler H (1996) Proc Natl Acad Sci USA 93:3477
45. Hinterdorfer P, Schilcher K, BAumgartner W, Gruber HJ, Schindler H (1998) Nanobiology 4:177

46. Kamruzzahan ASM, Ebner A, Wildling L, Kienberger F, Riener CK, Hahn CD, Pollheimer PD, Winklehner P, Holzl M, Lackner B, Schorkl DM, Hinterdorfer P, Gruber HJ (2006) Bioconjugate Chem 17:1473
47. Kienberger F, Pastushenko VP, Kada G, Gruber HJ, Riener C, Schindler H, Hinterdorfer P (2000) Single Mol 1:123
48. Kienberger F, Kada G, Gruber HJ, Pastushenko P, Riener C, Trieb M, Knaus H-G, Schindler H, Hinterdorfer P (2000) Single Mol 1:25
49. Kada G, Blayney L, Jeyakumar LH, Kienberger F, Pastushenko VP, Fleischer S, Schindler H, Lai FA, Hinterdorfer P (2001) Ultramicroscopy 86:129
50. Langry KC, Ratto TV, Rudd RE, McElfresh MW (2005) Langmuir 21:12064
51. Lin L, Wang H, Liu Y, Yan H, Lindsay S (2006) Biophys J 90:4236
52. Puntheeranurak T, Wildling L, Gruber HJ, Kinne RK, Hinterdorfer P (2006) J Cell Sci 119:2960
53. Puntheeranurak T, Wimmer B, Castaneda F, Gruber HJ, Hinterdorfer P, Kinne RKH (2007) Biochemistry 46:2797
54. Ratto TV, Langry KC, Rudd RE, Balhorn RL, Allen MJ, McElfresh MW (2004) Biophys J 86:2430
55. Riener CK, Stroh CM, Ebner A, Klampfl C, Gall AA, Romanin C, Lyubchenko YL, Hinterdorfer P, Gruber HJ (2003) Anal Chim Acta 479:59
56. Riener CK, Kienberger F, Hahn CD, Buchinger GM, Egwim IOC, Haselgrubler T, Ebner A, Romanin C, Klampfl C, Lackner B (2003) Anal Chim Acta 497:101
57. Ros R, Schwesinger F, Anselmetti D, Kubon M, Schafer R, Pluckthun A, Tiefenauer L (1998) Proc Natl Acad Sci USA 95:7402
58. Raab A, Han W, Badt D, Smith-Gill SJ, Lindsay SM, Schindler H, Hinterdorfer P (1999) Nat Biotechnol 17:902
59. Schwesinger F, Ros R, Strunz T, Anselmetti D, Guntherodt H, Honegger A, Jermutus L, Tiefenauer L, Pluckthun A (2000) Proc Natl Acad Sci USA 97:9972
60. Strunz T, Oroszlan K, Schafer R, Guntherodt HJ (1999) Proc Natl Acad Sci USA 96:11277
61. Strunz T, Oroszlan K, Schumakovitch I, Guntherodt H, Hegner M (2000) Biophys J 79:1206
62. Wang H, Bash R, Lindsay SM, Lohr D (2005) Biophys J 89:3386
63. Wielert-Badt S, Hinterdorfer P, Gruber H, Lin J, Badt D, Wimmer B, Schindler H, Kinne R (2002) Biophys J 82:2767
64. Cross B, Ronzon F, Roux B, Rieu JP (2005) Langmuir 21:5149
65. Desmeules P, Grandbois M, Bondarenko VA, Yamazaki A, Salesse C (2002) Biophys J 82:3343
66. Grandbois M, Beyer M, Rief M, Clausen-Schaumann H, Gaub HE (1999) Science 283:1727
67. Grandbois M, Dettmann W, Benoit M, Gaub HE (2000) J Histochem Cytochem 48:719
68. Kühner F, Costa LT, Bisch PM, Thalhammer S, Heckl WM, Gaub HE (2004) Biophys J 87:2683
69. Touhami A, Hoffmann B, Vasella A, Denis FA, Dufrene YF (2003) Langmuir 19:1745
70. Touhami A, Hoffmann B, Vasella A, Denis FA, Dufrene YF (2003) Microbiology 149:2873
71. Touhami A, Jericho MH, Beveridge TJ (2007) Langmuir 23:2755
72. Sen S, Subramanian S, Discher DE (2005) Biophys J 89:3203
73. Gad M, Itoh A, Ikai A (1997) Cell Biol Int 21:697
74. Afrin R, Yamada T, Ikai A (2004) Ultramicroscopy 100:187

75. Almqvist N, Bhatia R, Primbs G, Desai N, Banerjee S, Lal R (2004) Biophys J 86:1753
76. Bustanji Y, Arciola CR, Conti M, Mandello E, Montanaro L, Samori B (2003) Proc Natl Acad Sci USA 100:13292
77. Schmitt L, Ludwig M, Gaub HE, Tampe R (2000) Biophys J 78:3275
78. Conti M, Falini G, Samori B (2000) Angew Chem Int Ed Engl 39:215
79. Florin EL, Moy VT, Gaub HE (1994) Science 264:415
80. Florin E-L, Rief M, Lehmann H, Ludwig M, Dornmair C, Moy VT, Gaub HE (1995) Biosens Bioelectron 10:895
81. Chen A, Moy VT (2000) Biophys J 78:2814
82. Liu W, Montana V, Chapman ER, Mohideen U, Parpura V (2003) Proc Natl Acad Sci USA 100:13621
83. Vinckier A, Gervasoni P, Zaugg F, Ziegler U, Lindner P, Groscurth P, Pluckthun A, Semenza G (1998) Biophys J 74:3256
84. Love JC, Estroff LA, Kriebel JK, Nuzzo RG, Whitesides GM (2005) Chem Rev 105:1103
85. Hahn CD, Leitner C, Weinbrenner T, Schlapak R, Tinazli A, Tampe R, Lackner B, Steindl C, Hinterdorfer P, Gruber HJ, Holzl M (2007) Bioconjugate Chem 18:247
86. Hegner M, Wagner P, Semenza G (1993) Surf Sci 291:39
87. Tinazli A, Tang J, Valiokas R, Picuric S, Lata S, Piehler J, Liedberg B, Tampe R (2005) Chem Eur J 11:5249
88. Wagner P, Hegner M, Güntherodt H-J, Semenza G (1995) Langmuir 11:3867
89. Hahn CD, Tinazli A, Hölzl M, Leitner C, Frederix F, Lackner B, Müller N, Klampfl C, Tampé R, Gruber HJ (2007) Chem Monthly 138:245–252
90. Benesch J, Svedhem S, Svensson SCT, Valiokas R, Liedberg B, Tengvall P (2001) J Biomater Sci Polym 12:581
91. Wei ZQ, Wang C, Zhu CF, Zhou CQ, Xu B, Bai CL (2000) Surf Sci 459:401
92. Karrasch S, Dolder M, Schabert F, Ramsden J, Engel A (1993) Biophys J 65:2437
93. Chen X, Davies MC, Roberts CJ, Tendler SJB, Williams PM, Davies J, Dawkes AC, Edwards JC (1997) Langmuir 13:4106
94. Conti M, Donati G, Cianciolo G, Stefoni S, Samorì B (2002) J Biomed Mater Res 61:370
95. Andrade JD, Hlady V, Wei A-P, Ho C-H, Lea AS, Jeon SI, Lin YS, Stroup E (1992) Clin Mater 11:67
96. Carson GA, Granick S (1990) J Mater Res 5:1745
97. Bustamante C, Vesenka J, Tang CL, Rees W, Guthold M, Keller R (1992) Biochemistry 31:22
98. Feng XZ, Bash R, Balagurumoorthy P, Lohr D, Harrington RE, Lindsay SM (2000) Nucl Acids Res 28:593
99. Kondo A, Higashitani K (1992) J Colloid Interface Sci 150:344
100. Fitzpatrick H, Luckham PF, Eriksen S, Hammond K (1992) J Colloid Interface Sci 149:1
101. Chilkoti A, Boland T, Ratner BD, Stayton PS (1995) Biophys J 69:2125
102. Lo Y-S, Simons J, Beebe TP (2002) J Phys Chem B 106:9847
103. Green NM (1990) Methods Enzymol 184:51
104. Yuan C, Chen A, Kolb P, Moy VT (2000) Biochemistry 39:10219
105. Fritz J, Katopodis AG, Kolbinger F, Anselmetti D (1998) Proc Natl Acad Sci USA 95:12283
106. Jin Y, Wang K, Tan W, Wu P, Wang Q, Huang H, Huang S, Tang Z, Guo Q (2004) Anal Chem 76:5721
107. Bell DS, Jones AD (2005) J Chromatogr A 1073:99

108. Allen S, Chen X, Davies J, Davies MC, Dawkes AC, Edwards JC, Roberts CJ, Sefton J, Tendler SJ, Williams PM (1997) Biochemistry 36:7457
109. Brogan KL, Shin JH, Schoenfisch MH (2004) Langmuir 20:9729
110. Brogan KL, Schonfisch MH (2005) Langmuir 21:3054
111. Chowdhury PB, Luckham PF (1998) Coll Surf A Physicochem Eng Aspects 143:53
112. Jiang Y, Zhu C, Ling L, Wan L, Fang X, Bai C (2003) Anal Chem 75:2112
113. Lyubchenko YL, Gall AA, Shlyakhtenko LS, Harrington RE, Jacobs BL, Oden PI, Lindsay SM (1992) J Biomol Struct Dyn 10:589
114. Lyubchenko Y, Shlyakhtenko L, Harrington R, Oden P, Lindsay S (1993) Proc Natl Acad Sci USA 90:2137
115. Wang H, Bash R, Yodh JG, Hager GL, Lohr D, Lindsay SM (2002) Biophys J 83:3619
116. Wang H, Bash R, Yodh JG, Hager G, Lindsay SM, Lohr D (2004) Biophys J 87:1964
117. Klein DG, Stroh CM, Jensenius H, van Es M, Kamruzzahan ASM, Stamouli A, Gruber HJ, Oosterkamp TH, Hinterdorfer P (2003) Chem Phys Chem 4:1367
118. Trau M, Murray BS, Grant K, Grieser F (1992) J Colloid Interface Sci 148:182
119. Crampton N, Bonass WA, Kirkham J, Thomson NH (2005) Langmuir 21:7884
120. Howarter JA, Youngblood JP (2006) Langmuir 22:11142
121. Devaux C, Chapel J-P (2003) Eur Phys J E Soft Matter 10:77
122. Stevens MJ (1999) Langmuir 15:2773
123. Gauthier S, Aime JP, Bouhacina T, Attias AJ, Desbat B (1996) Langmuir 12:5126
124. Vrancken KC, van der Voort P, Possemiers K, Vansant EF (1995) J Colloid Interface Sci 174:86
125. El Shafei GMS, Mokhtar M (1995) J Colloid Interface Sci 175:518
126. Claesson PM, Cho DL, Gölander C-G, Kiss E, Parker JL (1990) Progr Coll Polym Sci 74:217
127. Carson GA, Granick S (1989) J Appl Polym Sci 37:2767
128. Gölander C-G, Kiss E (1993) Colloids Surf A 74:217
129. Parker JL, Cho DL, Claesson PM (1989) J Phys Chem 93:6121
130. Kojio K, Ge S, Takahara A, Kajiyama T (1998) Langmuir 14:971
131. Durrant PJ, Durrant B (1970) Introduction to advanced inorganic chemistry. Longman Group, London
132. Sjöblom J, Stakkestad G, Ebeltoft H (1995) Langmuir 11:2652
133. Waddell TG, Leyden DE, DeBello MT (1981) J Am Chem Soc 103:5303
134. Linde HG (1990) J Appl Polym Sci 40:613
135. Piers AS, and Rochester CH (1995) J Colloid Interface Sci 174:97
136. Trens P, Denoyel R (1996) Langmuir 12:2781
137. Park S-H, Sposito G (2002) Phys Rev Lett 89:085501
138. Wei Z, Wang C, Wang Z, Liu D, Bai C (2001) Surf Interface Anal 32:275
139. Lee G, Chrisey L, Colton R (1994) Science 266:771
140. Zhang F, Srinivasan MP (2004) Langmuir 20:2309
141. Ebner A, Hinterdorfer P, Gruber HJ (2007) Ultramicroscopy 107:922
142. Moon JH, Shin JW, Kim SY, Park JW (1996) Langmuir 12:4621
143. Otsuka H, Arima T, Koga T, Takahara A (2005) J Phys Organ Chem 18:957
144. Kallury KMR, Macdonald PM, Thompson M (1994) Langmuir 10:492
145. Haselgrübler T, Amerstorfer A, Schindler H, Gruber H (1995) Bioconjugate Chem 6:242
146. Riener CK, Kada G, Gruber HJ (2002) Anal Bioanal Chem 373:266
147. Zara JJ, Wooda RD, Boonb P, Kimc C-H, Pomatoc N, Bredehorst R, Vogel C-W (1991) Anal Biochem 194:156
148. Carlsson J, Drevin H, Axen R (1978) Biochem J 173:723

149. Morpurgo M, Veronese FM, Kachensky D, Harris JM (1996) Bioconjugate Chem 7:363
150. Gruber H, Kada G, Pragl B, Riener C, Hahn C, Harms G, Ahrer W, Dax T, Hohenthanner K, Knaus H (2000) Bioconjugate Chem 11:161
151. Dorner MM, Bassett EW, Beiser SM, Kabat EA, Tanenbaum SW (1967) J Exp Med 125:823
152. Tournier EJM, Wallach J, Blond P (1998) Anal Chim Acta 361:33
153. Walsh MK, Wang X, Weimer BC (2001) J Biochem Biophys Methods 47:221
154. Johnsson B, Lofas S, Lindquist G (1991) Anal Biochem 198:268
155. Marchand-Brynaert J, Deldime M, Dupont I, Dewez J-L, Schneider Y-J (1995) J Colloid Interface Sci 173:236
156. Hölzl M, Tinazli A, Leitner C, Hahn CD, Lackner B, Tampe R, Gruber HJ (2007) Langmuir 23:5571
157. Peelen D, Smith LM (2005) Langmuir 21:266
158. Horn R, Ding S, Gruber H (2000) J Gen Physiol 116:461
159. Prime KL, Whitesides GM (1991) Science 252:1164
160. Berquand A, Xia N, Castner DG, Clare BH, Abbott NL, Dupres V, Adriaensen Y, Dufrene YF (2005) Langmuir 21:5517
161. Dammer U, Popescu O, Wagner P, Anselmetti D, Guntherodt H, Misevic G (1995) Science 267:1173
162. Friedsam C, Del Campo Becares A, Jonas U, Gaub HE, Seitz M (2004) Chem Phys Chem 5:388
163. Gilbert Y, Deghorain M, Wang L, Xu B, Pollheimer PD, Gruber HJ, Errington J, Hallet B, Haulot X, Verbelen C, Hols P, Dufrene YF (2007) Nano Lett 7:796
164. Noy A, Vezenov DV, Kayyem JF, Meade TJ, Lieber CM (1997) Chem Biol 4:519
165. Schönherr H, Beulen MWJ, Bugler J, Huskens J, van Veggel F, Reinhoudt DN, Vancso GJ (2000) J Am Chem Soc 122:4963
166. Tromas C, Rojo J, de la Fuente JM, Barrientos AG, Garcia R, Penades S (2001) Angew Chem Int Ed 40:3052
167. Zapotoczny S, Auletta T, de Jong MR, Schonherr H, Huskens J, van Veggel FCJM, Reinhoudt DN, Vancso GJ (2002) Langmuir 18:6988
168. Skulason H, Frisbie CD (2000) J Am Chem Soc 122:9750
169. Harada Y, Kuroda M, Ishida A (2000) Langmuir 16:708
170. Dean D, Han L, Grodzinsky AJ, Ortiz C (2006) J Biomech 39:2555
171. de la Fuente JM, Penades S (2004) Glycoconjugate J 21:149
172. Lioubashevski O, Patolsky F, Willner I (2001) Langmuir 17:5134
173. Höök F, Ray A, Norden B, Kasemo B (2001) Langmuir 17:8305
174. Green NH, Williams PM, Wahab O, Davies MC, Roberts CJ, Tendler SJB, Allen S (2004) Biophys J 86:3811
175. Boozer C, Chen S, Jiang S (2006) Langmuir 22:4694
176. Auletta T, de Jong MR, Mulder A, van Veggel FC, Huskens J, Reinhoudt DN, Zou S, Zapotoczny S, Schonherr H, Vancso GJ, Kuipers L (2004) J Am Chem Soc 126:1577
177. Zou S, Schönherr H, Vancso GJ (2005) Angew Chem Int Ed 44:956
178. Wagner P, Hegner M, Kernen P, Zaugg F, Semenza G (1996) Biophys J 70:2052
179. Wang MS, Palmer LB, Schwartz JD, Razatos A (2004) Langmuir 20:7753
180. Hochuli E, Dobeli H, Schacher A (1987) J Chromatogr A 411:177
181. Nieba L, Nieba-Axmann S, Persson A, Hamalainen M, Edebratt F, Hansson A, Lidholm J, Magnusson K, Karlsson A, Pluckthun A (1997) Anal Biochem 252:217
182. Lata S, Piehler J (2005) Anal Chem 77:1096
183. Lata S, Reichel A, Brock R, Tampe R, Piehler J (2005) J Am Chem Soc 127:10205

184. Tinazli A, Piehler J, Beuttler M, Guckenberger R, Tampe R (2007) Nat Nanotechnol 2:220
185. Dupres V, Menozzi FD, Locht C, Clare BH, Abbott NL, Cuenot S, Bompard C, Raze D, Dufrene YF (2005) Nat Methods 2:515
186. Yam CM, Xiao Z, Gu J, Boutet S, Cai C (2003) J Am Chem Soc 125:7498
187. Strother T, Knickerbocker T, Russell JN, Butler JE, Smith LM, Hamers RJ (2002) Langmuir 18:968
188. Wong SS, Woolley AT, Joselevich E, Lieber CM (1999) Chem Phys Lett 306:219
189. Wong SS, Joselevich E, Woolley AT, Cheung CL, Lieber CM (1998) Nature 394:52
190. Ostuni E, Chapman RG, Holmlin RE, Takayama S, Whitesides GM (2001) Langmuir 17:5605
191. Szleifer I (1997) Biophys J 72:595

Top Curr Chem (2008) 285: 77–102
DOI 10.1007/128_2008_4

Published online: 23 April 2008

Molecular Workbench for Imaging and Manipulation of Single Macromolecules and Their Complexes with the Scanning Force Microscope

Jürgen P. Rabe

Department of Physics, Humboldt University Berlin, Newtonstr. 15, 12489 Berlin, Germany
rabe@physik.hu-berlin.de

Abstract The structure and properties of single macromolecules are key to understanding function in biological molecular systems, as well as to developing artificial functional systems. In order to systematically investigate and control the conformations of single macromolecules and their complexes a "molecular workbench" has been developed. It consists of an atomically flat, inert solid substrate such as the basal plane of highly oriented pyrolytic graphite (HOPG), coated with a layer of molecules such as alkanes or alkyl chains containing amphiphiles that control the interaction between the substrate and adsorbed macromolecules. A scanning force microscope (SFM) operated in tapping or contact mode is used to both image and manipulate the macromolecules to correlate their structure with mechanical properties, and to assemble macromolecular systems that would not form spontaneously.

Keywords Conformation · Interface · Manipulation · Scanning force microscopy · Single macromolecules

1 Introduction

Single macromolecules such as polynucleic acids and proteins are the fundamental constituents of biological systems that perform functions with efficiencies that are largely unparalleled in artificial molecular systems: our

genome is stored and replicated using single DNA strands and proteins, single molecules are detected and manipulated by the immune system with extremely high perfection, and in molecular motors, macromolecules are efficiently used to exert forces. A fundamental understanding of the physical and chemical properties of single macromolecules in controlled environments promises to lead the way to novel molecular systems exhibiting functionalities close to ultimate physical limits, which may or may not have biological analogues.

The scanning force microscope (SFM) is a formidable tool for investigating the structure and properties of single macromolecules at a resolution on the nanometer scale. At that length scale, i.e., below the Kuhn-segment lengths of common semiflexible polymers, imaging with the SFM allows analysis of macromolecular conformations in great detail [1–24], and it is these conformations and the transitions between them that determine the unique properties of macromolecules. In order to study single macromolecular chains with the SFM one has to prepare them on a solid substrate, ideally stretched out in quasi-two dimensions, and immobilized for sufficiently long times. This can be achieved systematically by adsorption from solution and the subsequent removal of the solution, provided one has precise control over the conformation in solution, the adsorption process, the removal of the solution, and the mobility in the final state. *Nota bene*, both the adsorption process and the mobility in the final state are largely determined by the interaction of the macromolecules with the substrate. For their control, we have developed a molecular workbench consisting of an atomically flat, inert solid substrate such as the basal plane of highly oriented pyrolytic graphite (HOPG), coated with a layer of molecules such as alkanes or alkyl chains containing amphiphiles. Beyond imaging, the capability to manipulate macromolecules with the SFM provides a fundamentally new dimension for the determination of both the structure and properties of single macromolecules [25–31]. The key is that it allows the preparation of well-defined nonequilibrium conformations. While the latter may be of interest in itself or for other characterization studies, one can also use subsequent SFM imaging or other techniques to follow their relaxations with time.

This paper provides an introduction to the properties of the molecular workbench and its potential to control conformations and conformational transitions of single macromolecules and supramolecular systems within a SFM, illustrated with examples stemming largely from our laboratory.

2
Imaging Single Macromolecules

Single macromolecules can be imaged on solid surfaces in vacuum as well as at interfaces with vapors and liquids. The resolution of the images depends on various parameters. While for macromolecules at (nano)crystalline sur-

faces, a resolution well below 1 and 2 nm may be achieved in contact- and tapping-mode SFM respectively [32–34], the resolution is typically lower for isolated macromolecules adsorbed to solid substrates. This is partly due to the softness of single macromolecules, which causes sizable deformations, particularly during scanning with the SFM. Also the solvents may influence tip–sample adhesion and cause swelling of the macromolecules [17]. Another limiting factor is the corrugation of the sample surface, which due to the convolution of the tip shape with the sample topography, produces images that have to be corrected by determining the tip shape from images of known objects and then deconvoluting the images of the unknown samples. For instance, the sizes of individual proteins with diameters in the range of 20 nm have been determined very precisely from images with apparent diameters around 50 nm, taking into account the tip shape [35].

A prerequisite to determine the conformation of single macromolecules from images of their contour is to stretch them out in quasi-two dimensions in a reproducible way, and then to immobilize them. It has been shown [1] that depending on the substrate and the solution, the deposition of double-stranded (ds)DNA from aqueous solution may lead to an ensemble of macromolecules with end-to-end distances corresponding to equilibrium or nonequilibrium conformations. In the wormlike chain model, a system in thermal equilibrium is characterized by an orientation correlation function of the form:

$$\langle \cos \theta(l) \rangle = \exp\left(-\frac{l}{2l_\mathrm{p}}\right)$$

with the persistence length

$$l_\mathrm{p} = \frac{k_\mathrm{bending}}{k_\mathrm{B}T}$$

determined by the bending modulus k_bending of the macromolecule and the temperature [36]. Figure 1 a displays a tapping-mode SFM image of an ensemble of dsDNA adsorbed from an aqueous electrolyte solution to mica, which allows following of the contours in two dimensions. The orientation correlation function calculated from a computerized analysis [37] of many such images (Fig. 1b) indicates that the ensemble represents a snap shot of an equilibrated system in two dimensions with a persistence length of $l_\mathrm{p} = 53$ nm, similar to what is found from scattering methods for dsDNA in solution, taking into account the difference between two and three dimensions.

With the contour analysis described above, it has been shown that single polyisocyanides with lateral hydrogen-bonding networks (Fig. 2a) are even more rigid single-strand polymers [6]. Figure 2b and c displays SFM images and Fig. 2d–f the corresponding contour-length distribution, together with the average end-to-end distances as a function of the contour lengths, and the distribution of angles θ between segments a fixed distance apart along the contour. The data reveal equilibration in two dimensions, and a resulting l_p

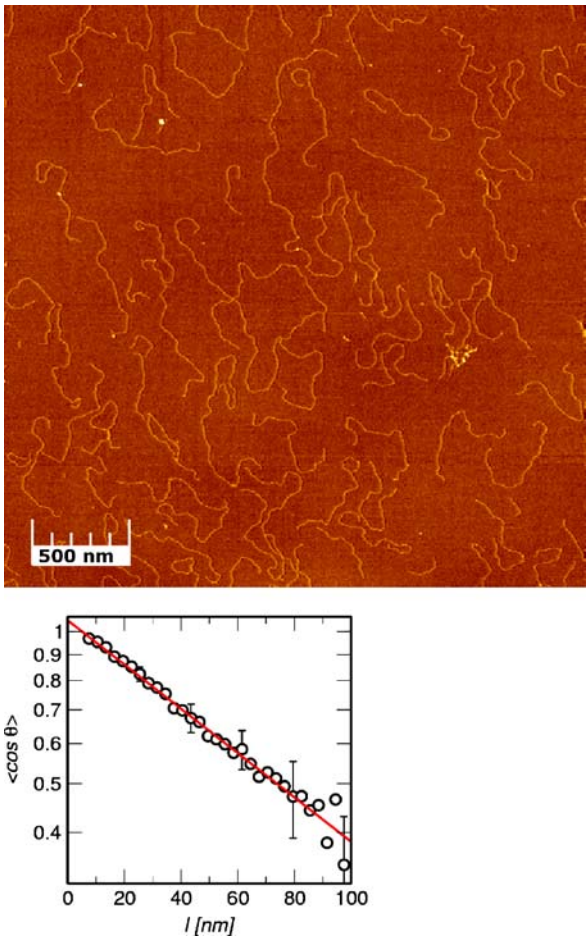

Fig. 1 **a** Scanning force microscope (SFM) image displaying an ensemble of monodisperse dsDNA, where the chains were allowed to equilibrate prior to the immobilization during the evaporation of the solvent. **b** Orientation correlation function derived from the computerized analysis of many such images, indicating a behavior according to the wormlike chain model with a persistence length in two dimensions of $l_p = 53$ nm. (See also [37])

of 76 nm. SFM has been used further to characterize the orientation of these rods through hydrodynamic flow [13]. Moreover, it has been used to characterize the conformation of single-stranded conjugated polymers thickened and isolated by the formation of rotaxanes with cyclodextrins [8].

In order to fully stretch macromolecules on a solid substrate we have complexed them with amphiphiles and adsorbed them to the basal plane of HOPG covered with an ordered monolayer of alkanes or amphiphiles. The first example is metallosupramolecular coordination-polyelectrolyte amphiphile complexes, exhibiting perfectly straight rods oriented along one of

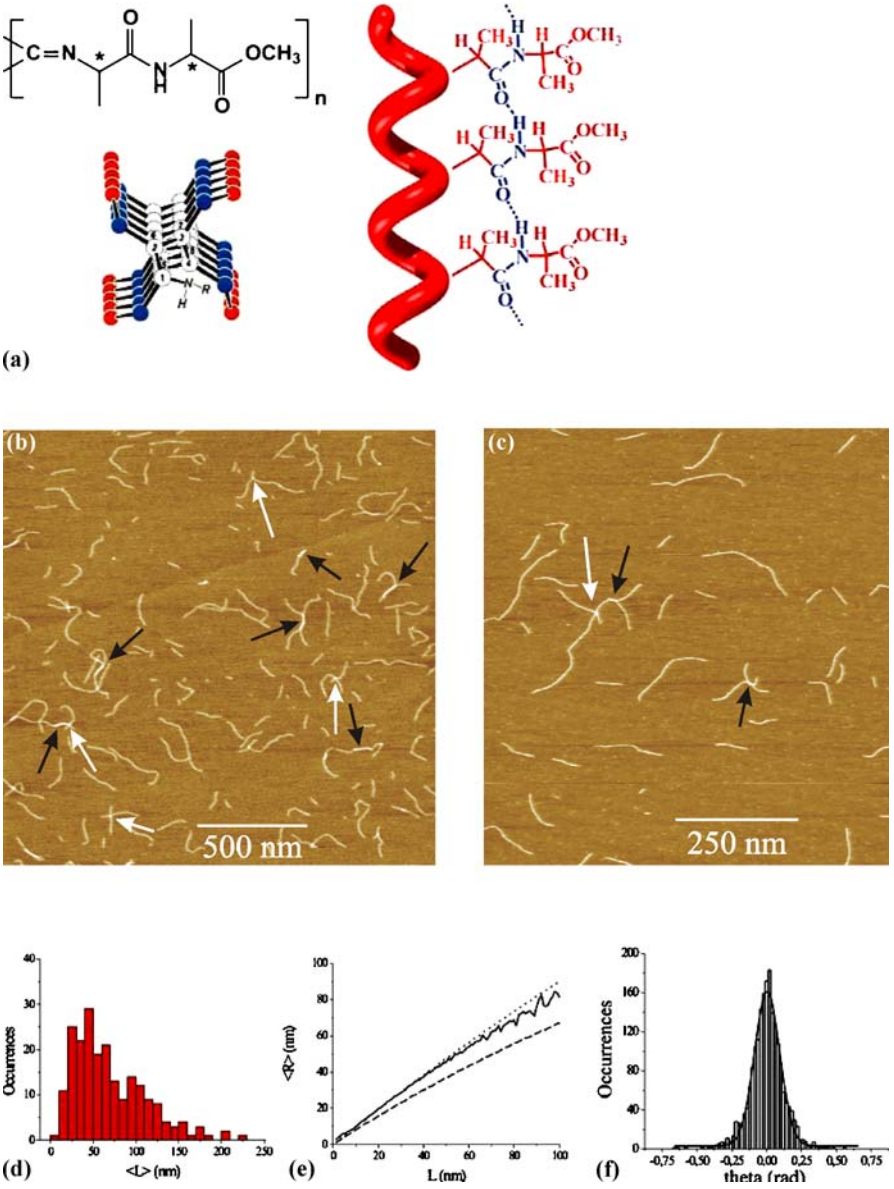

Fig. 2 **a** Structure of poly(isocyano-L-alanine-D-alanine methyl ester) with the scheme of a 4_1 helix and the hydrogen-bonded array within the sidechain of the polymer. **b,c** SFM images of single stretched out polyisocyanides. **d–f** Contour length distribution, the average end-to-end distances as a function of the contour lengths and the distribution of angles θ between segments a fixed distance apart along the contour. The *dotted line* in **e** represents the theoretically expected dependence for a persistence length of 76 nm, while the *dashed line* represents the expectation for the projection of the three-dimensional contour into two dimensions. (Reproduced from [6])

the three lattice axes of a basal plane of graphite that is covered with a crystalline alkane monolayer [7]. The method has been also applied to covalent polymers such as polystyrene sulfonate, with the amphiphiles forming both

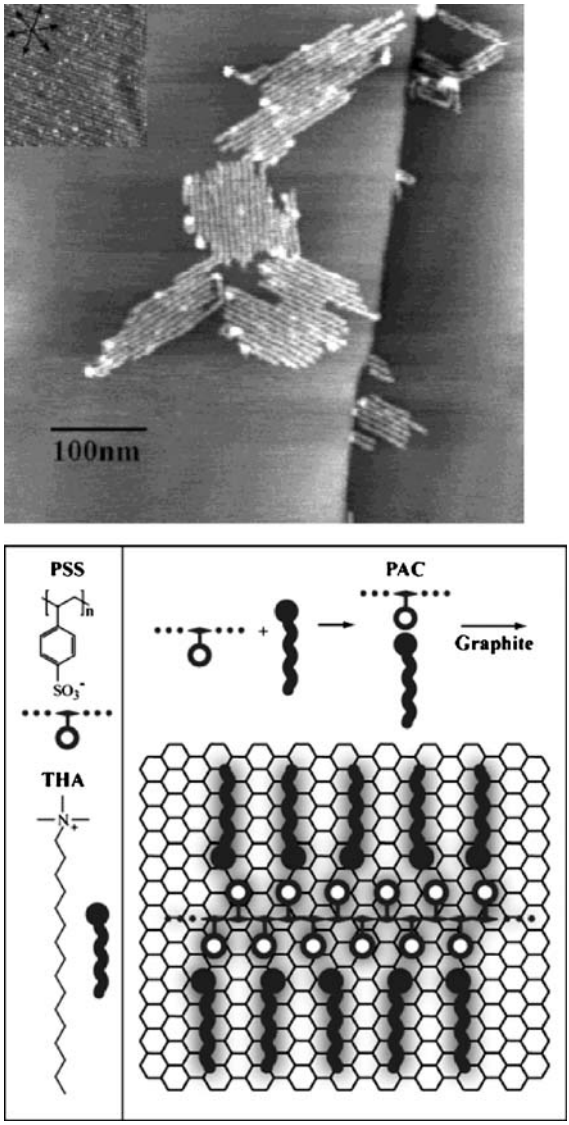

Fig. 3 **a** SFM image of fully extended complexes of atactic polystyrene sulfonate with an amphiphile (trimethylhexadecylammonium bromide) on highly oriented pyrolytic graphite (HOPG) covered with the amphiphile (see *inset*). **b** Schematic illustrating the formation of the polyelectrolyte-amphiphile complexes on HOPG. (Reproduced from [14])

polyelectrolyte–amphiphile complexes (PACs) and covering the HOPG with a monolayer [14]. Figure 3 displays a SFM image of a PAC of polystyrene sulfonate with trimethylhexadecylammonium bromide. The full extension of the macromolecules allows very accurate determination of the distribution of their contour lengths. The quantitative analysis of a fractionated sample with very small polydispersity reveals an average contour length that is about 14% shorter than in an all-trans conformation, indicating conformations with a substantial degree of helical segments.

The conformation of the adsorbate depends not only on the substrate, but also on the conformation in solution prior to adsorption [20]. Figure 4 displays SFM images of polystyrene sulfonate adsorbed from different ethanol–water mixtures to HOPG precovered with a monolayer of octadecylamine. One can easily recognize the increasing openness of single macromolecules with improving solvent quality. Moreover, from the good solvents, segments on the order of 100 nm are stretched out perfectly straight, following the

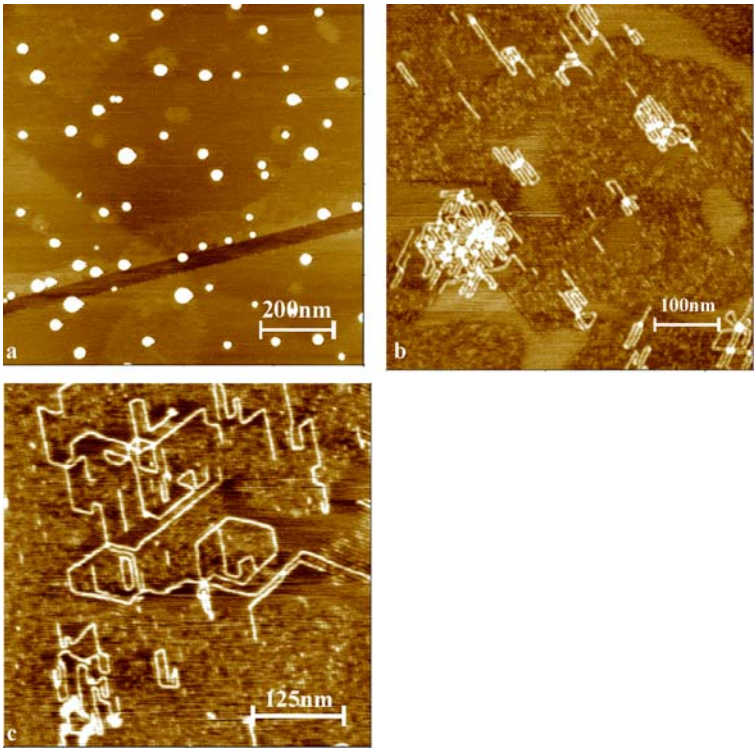

Fig. 4 SFM images of polystyrene sulfonate on a monolayer of octadecylamine on HOPG adsorbed from different ethanol–water mixtures with an ethanol content of **a** 80–100%, **b** 60–80%, and **c** 0–60%, respectively. Note the increasing openness of single macromolecules with improving solvent quality. (Reproduced from [20])

amphiphilic monolayer template. This indicates two length scales: while the global conformation of the macromolecule on the surface corresponds to a projection of the conformation in solution, the local conformation is determined by the interaction with the surface template.

Rigid rod polymers tend to aggregate more readily than flexible macromolecules. This was investigated originally with poly-*para*-phenylene ethynylene derivatives on various crystalline and amorphous substrates [38–42], which have been found to form nanoribbons with very high aspect ratios, where the long axes of the rods are oriented perpendicularly to the long axes of the ribbons.

Most interesting are more complex supramolecular polymers prepared from functionalized oligopeptides that can be polymerized [21–24]. Figure 5 displays supramolecular polymers of oligopeptide-functionalized diacetylenes that can be UV-polymerized into double helices of polydiacetylenes.

Dendronized polymers are a particularly interesting class of polymers, which allow the broad varying of the properties of a given polymer back-

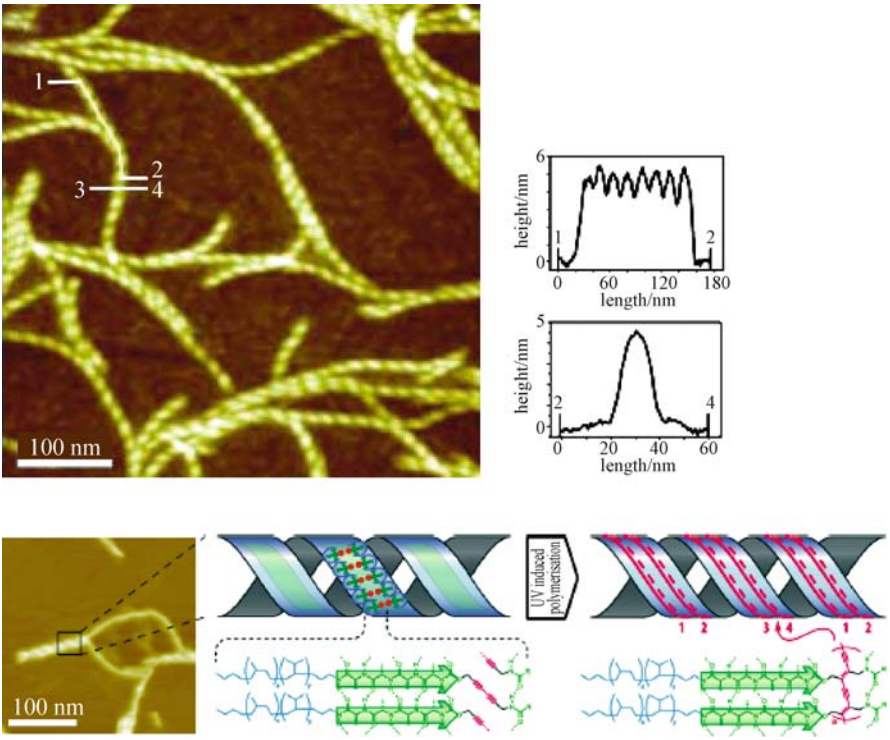

Fig. 5 SFM images with height contours and schematic structure of a supramolecular polymer of oligopeptide-functionalized diacetylenes that can be polymerized. (Reproduced from [21, 22])

bone [3, 4]. Ultrathin films of relatively short dendronized polymers on HOPG have revealed domains of highly ordered cylinders oriented parallel to the substrate surface along one of the graphite lattice axes [43, 44]. Isolated single polymers on solid substrates can be used to characterize their molar mass distributions [9, 25, 26], as well as rare topologies such as branching [19].

More difficult to understand are their conformations on mica, i.e., a strongly adsorbing substrate (Fig. 6), where undulated conformations have been observed and attributed to a rapid "zipping" adsorption process [37].

With large pending dendrons, these polymers can be turned into giant macromolecules with a peculiar wetting behavior [16] that can be investigated by SFM with submolecular resolution (Fig. 7). Owing to the control over the periphery of the backbone, a dendronized polymer can be used to form macromolecular complexes both with itself as double helices [18], or, e.g., with oppositely charged macromolecules such as dsDNA, which winds around dendronized polymers carrying amine groups [10–12].

One way to address the mechanical properties of dendronized polymers is to follow their conformation upon annealing. Figure 8 shows that locally ordered molecular arrays can be obtained upon annealing a first-generation dendronized polystyrene layer on the basal plane of graphite, indicating that a liquid-like state can be obtained, which allows the dendronized polymers to order preferentially perpendicularly to the HOPG crystal axes [15]. The onset

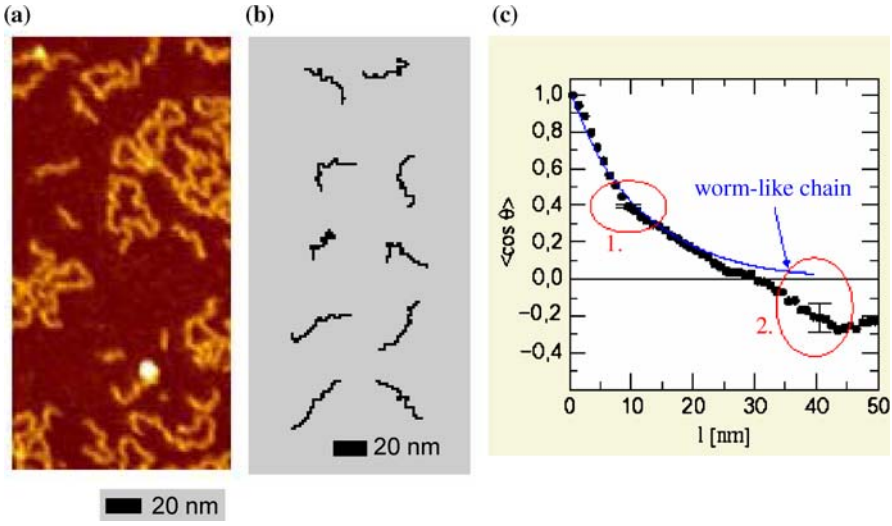

Fig. 6 **a** SFM image of a dendronized polymer on mica. **b** Result of a Monte Carlo simulation of the conformation of wormlike chains rapidly adsorbed on a strongly adsorbing substrate in a "zipping" process. **c** Orientation correlation function determined from SFM images, revealing deviations from the behavior of a wormlike chain, particularly an anticorrelation at distances larger than about 30 nm. (Reproduced from [37])

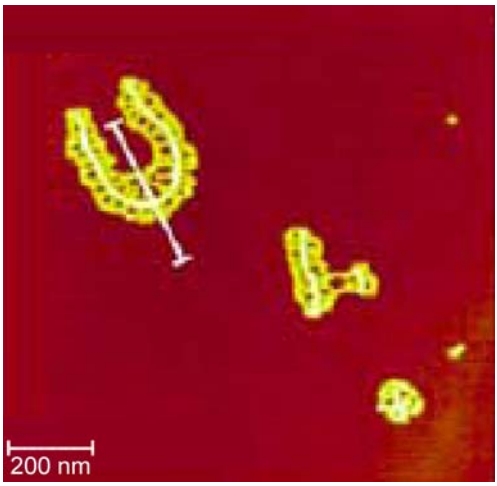

Fig. 7 SFM image of a second-generation dendronized polymer with poly(methylmethacrylate) sidechains. (Reproduced from [16])

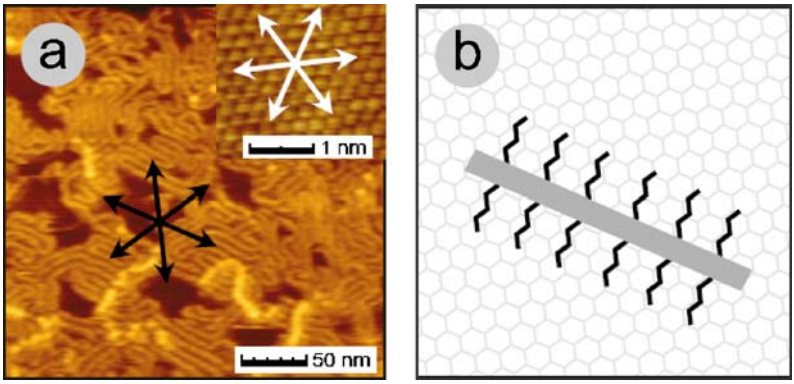

Fig. 8 Alkylated first-generation dendronized polystyrene annealed in air at 60 °C. **a** Orientation of the polymer and the graphite lattice at the same positions. The *black* and *white rosettes* are rotated by 90° indicating that the polymers are oriented perpendicular to the *zigzag axes* of the graphite. **b** Schematic view of the orientation of the dendronized polymer backbone (*grey*) and the alkyl side chains. (Reproduced from [15])

of the liquid state is generation dependent; e.g., the first-generation dendron has been oriented in air at 60 °C (Fig. 8), whereas higher generation dendrons additionally required the presence of a good solvent [15]. The dependence on the generation can be explained by the increasing influence of dendron entanglements towards higher generation numbers.

3
Manipulation

Another way to learn more about the mechanical properties of single macromolecules on solid substrates is based on their manipulation with the SFM, which, moreover, may be employed to prepare well-defined nonequilibrium conformations. The use of the molecular workbench with the SFM will be discussed for moving, bending, stretching, breaking and linking single macromolecules will be discussed here.

3.1
Manipulation in Contact Mode on Bare HOPG

Figure 9 displays SFM tapping-mode images of fourth-generation dendronized polystyrene, deposited by spin coating from sufficiently diluted solutions in tetrahydrofuran onto the basal plane of HOPG [25, 26]. The images show that the macromolecules adsorb with the molecular backbones parallel to the surface, but obviously not in a wormlike chain conformation in two dimensions. Instead, there is a tendency of the backbones to fold within

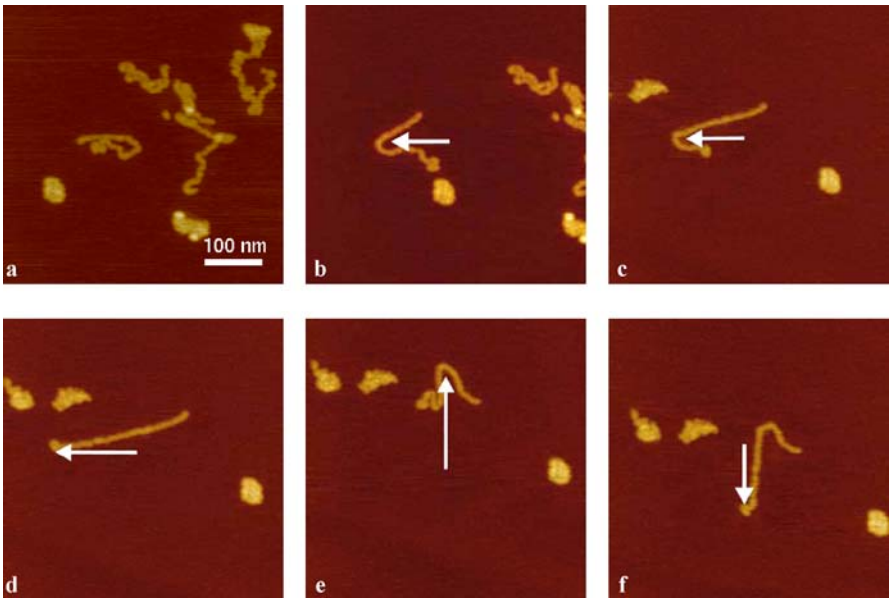

Fig. 9 Sequence of SFM height images in tapping mode of a fourth-generation dendronized polystyrene spin-coated onto HOPG. **a** After preparation. **b–d** After moving the tip in contact mode in three steps to the left. **e** After pushing it together and then moving it up. **f** After moving it down. The images in **b–f** are centered in order to fully cover the one object which has been moved. (Reproduced from [25, 26])

the plane of adsorption. This results in a characteristic smallest separation between backbones which fits well to the assumption that each monomer fills a cylindrical slice with a thickness given by the length of the repeat unit, and the diameter is calculated from a reasonable density.

Nota bene, the individual macromolecules are immobilized on the surface, which is rather surprising for the basal plane of graphite, exhibiting a rather flat potential corrugation [45, 46]. Possibly, this immobilization is due to some ultrathin layer on the order of a monolayer thickness adsorbed from the atmosphere or from the applied solution.

In order to distinguish single macromolecules from loosely bound molecular aggregates, single objects were moved across the surface by switching the SFM tip at the center of the image from tapping mode to contact mode and then moving the tip in a certain direction across the surface. Figure 9b displays a tapping-mode image after moving the single object sitting left of the center of Fig. 9a further to the left (as indicated by the arrow in Fig. 9b). The moved object remains one continuous chain that changes its conformation, while the other objects remained completely unaltered (Fig. 9b). Figure 9c and d show that the molecule can be almost fully extended (the only fold left is at the molecule's terminus), indicating a contour length of more than 260 nm which translates into at least 1000 repeat units. Figure 9e and f show that the folds can also be made and removed by manipulating with the tip, indicating that the rigidity of the molecule is not sufficient to allow its sliding across the surface without changing its shape.

Figure 10 displays a similar sequence for dendronized fourth-generation dendronized polystyrene, where each terminal dendron group was alkylated [25, 26]. Again, there are characteristic separations between backbones and also small folds, which, however, are wider than in the analogues without alkyl chains. After moving a single molecule by sliding the SFM tip from the center of Fig. 10a upwards (Fig. 10b), one recognizes that the fold structure

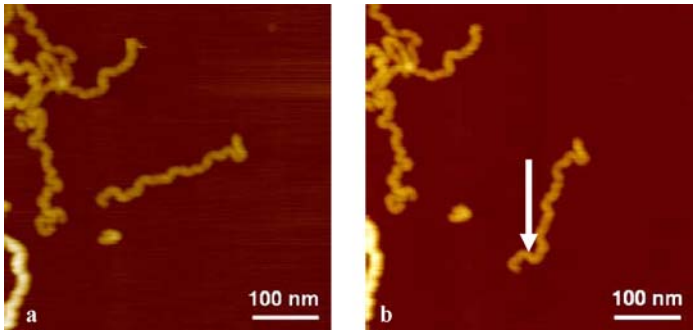

Fig. 10 Sequence of SFM height images in tapping mode of alkylated fourth-generation dendronized polystyrene spin-coated onto HOPG. **a** After preparation. **b** After moving the tip in contact mode downwards. (Reproduced from [25, 26])

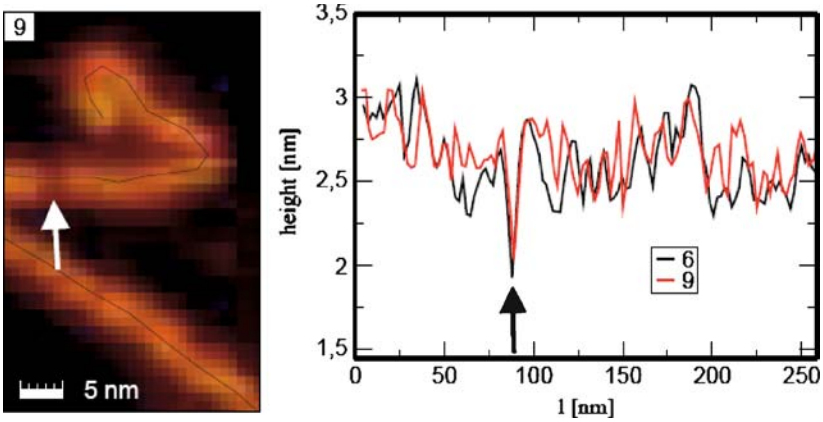

Fig. 11 Height along the contour for the manipulated fourth-generation dendronized polystyrene as shown in Fig. 9. *Left* Image showing the line at which the height was recorded. The *arrow* marks a characteristic nick which can be found in all the images of this molecule. *Right* Height structure for two images. The height scale starts from 0 nm at the substrate surface. Besides some noise, both *curves* show a clear correlation of characteristic features. The *arrow* gives the position of the nick. (Reproduced from [15])

along the backbone remains intact to a large extent. Basically, the molecule has been translated and rotated with a small localized bend at one point along the backbone. This indicates that the "heavy" alkylation (32 alkyl chains per repeat unit) enhanced the rigidity of the backbone so that it maintains its shape to a large extent upon manipulation across the surface of HOPG. This effect may be employed to obtain stiffened macromolecules.

Obviously, upon manipulating single alkylated fourth-generation dendronized polymers, the glassy state could be directly evidenced by a complete preservation of the shape of the molecule when moved on the substrate surface. For nonalkylated fourth-generation dendronized polymers, the lateral shape persistence was lower, but nonetheless the height structure was preserved (Fig. 11), indicating at least a local shape persistence. By manipulating an oriented third-generation macromolecule, it was shown that the molecule has weak locations, acting as preferred positions for kink formation. The weak locations were explained as inhomogeneities of the dendron shell that have frozen in. The switchable single polymer glass state is an interesting property which might find applications.

3.2
Manipulation in Contact Mode on Precoated HOPG

The "free" manipulation of single macromolecules on solid substrates may also be used to assemble molecular systems that would not form sponta-

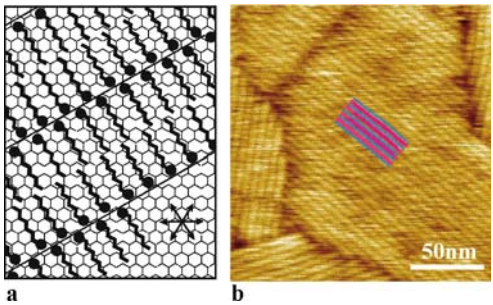

Fig. 12 **a** Schematic of a monolayer of alkyl chains containing amphiphiles on the basal plane of graphite. *Circles* denote head groups and *arrows* denote the crystallographically equivalent graphite axes with threefold symmetry. (Reproduced from [27]). **b** SFM image of a monolayer of octadecylamine on HOPG. The *blue and pink stripes* indicate the hydrophilic and hydrophobic "rails", respectively

neously. A method is described here that allows the manipulation of already-deposited single macromolecules. In particular, single polyelectrolytes such as DNA have been positioned, bent and stretched on a solid substrate. Moreover, stretching defects have been removed, and dsDNA overstretched into two parallel single strands [27].

The most critical issue for the manipulation of a macromolecule is its interaction with the substrate; this is usually either too weak, causing the molecule to diffuse rapidly across the surface [45, 46], or it is too strong, causing a long molecule to break during manipulation [47]. Long-chain alkanes and alkyl chains containing amphiphiles have been shown to self-assemble on crystalline substrates like the basal plane of graphite [48] or transition metal dichalcogenides [49] into monolayers, with the alkyl chains oriented along the substrate axes parallel to each other, while the end groups phase-separate into straight lamellae (Fig. 12). These lamellae can serve as soft nanoscopic "rails". Rows of head groups, which may be positively or negatively charged, are thereby separated by rows of hydrophobic alkyl chains. The chemical nature of the head groups and the length of alkyl chains define a surface po-

Fig. 13 SFM images of dsDNA adsorbed on a graphite surface modified with $CH_3(CH_2)_{11}NH_2$ molecules. Manipulation was performed by bringing the tip in contact with the surface and moving it in the desired direction, using homemade manipulation hard- and software. **a** ds-plasmid DNA molecules as deposited. **b** After stretching two of them (nos. 2 and 4) along the *white arrows*. **c** After manipulation of the same molecules into triangles. **d** Seven-letter word written with polydisperse sample of linear dsDNA. **e** Zoom of the *square* marked in **b**, revealing two separated single DNA strands. **f** Zoom of the *square* marked in **c**, revealing the same section as in **e**, but now with two fully extended single DNA strands. (Reproduced from [27]) ▶

tential ripple, which may be used to orient single polymer molecules on a dry surface [7].

At room temperature, any attempt to manipulate polymers with a contour length beyond 200 nm on a graphite surface coated with a monolayer of $CH_3(CH_2)_{17}R$ (R=COOH or NH_2) using an SFM tip leads to breakage of the molecules. For the shorter alkyl chains, e.g., $CH_3(CH_2)_{11}NH_2$ with

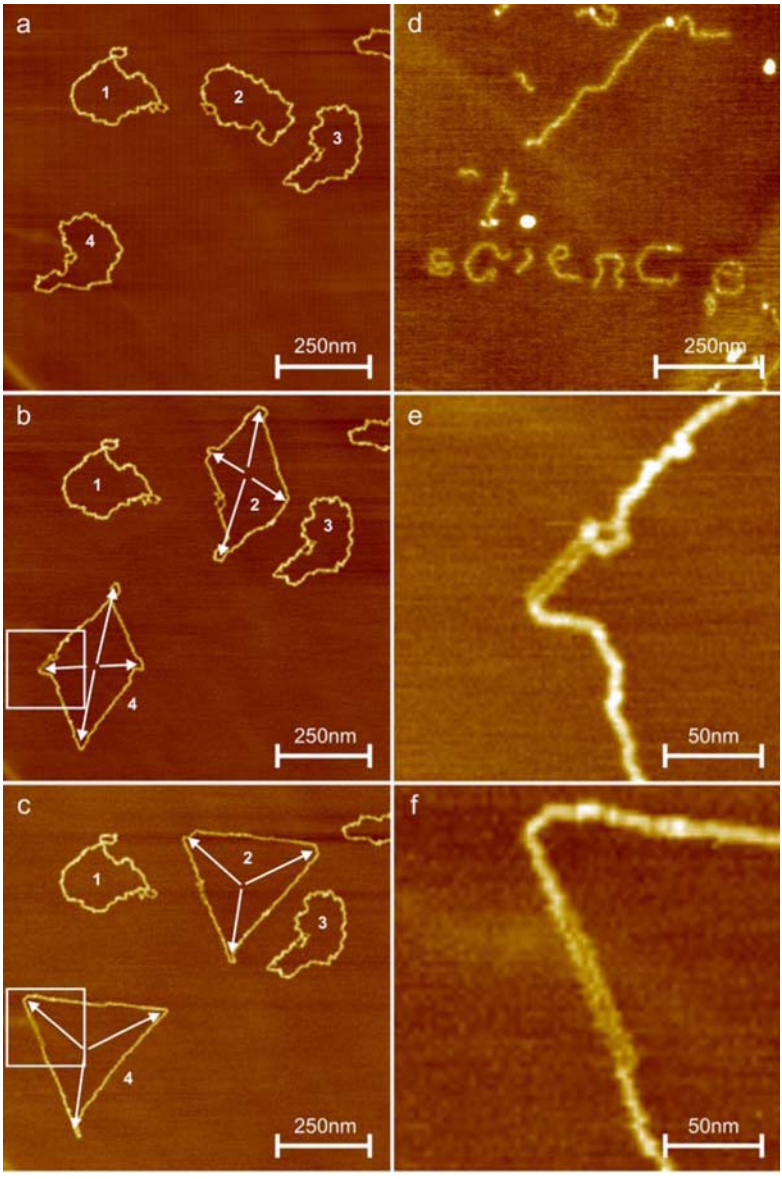

a bulk melting point of only 31 °C, we could not observe lamellae with the SFM, which may be due to an increased molecular mobility within the monolayer [50] and correspondingly to a lower two-dimensional density. Still the polyelectrolyte molecules are adsorbed individually onto the substrate and the threefold symmetry still appeared. However, the length of the straight segments was reduced. Most interestingly, manipulation with the SFM tip allows displacement of the whole molecule without its rupture, which we attribute to the softness of the short-chains monolayer near room temperature.

Figure 13 displays the image of four ds-plasmid DNA molecules adsorbed to the modified substrate. From the digitized images, their contour lengths were determined as 792, 803, 812, and 859 nm, respectively, which is a little less than the expected 913 nm (corresponding to 2686 base pairs). The difference is attributed to the nonideally flat adsorption of some segments. Moreover, there are some short sections, where the double strand has separated into two single strands, which apparently is caused by the interaction with the substrate. In order to stretch subsequently two of the molecules with the SFM, the tip was brought into contact and then moved from within a molecular ring outwards in four directions as marked in Fig. 13b. Subsequent imaging in the tapping mode revealed an increase of the contour lengths of these molecules to 1048 and 1114 nm, respectively, which is about 15 and 22% longer than the fully extended B-form dsDNA. Figure 13c displays the same molecules stretched further into a triangular shape with contour lengths of 1131 and 1220 nm, corresponding to 24 and 33% overstretching, respectively. Note the sharp curvature at the upper right edge of the lowest triangle, which indicates a radius of curvature below the resolution of the image, i.e., below 3 nm. Also note the two parallel single strands on the left side of the lowest triangle (Fig. 13c and f).

Moreover, the manipulation with the SFM tip on a properly tailored substrate allows the displacement of the whole molecule without its rupture. Free arranging and shaping of polymer molecules is evidenced in Fig. 13d, which displays the arrangement and shaping of seven dsDNA molecules of a polydisperse sample. Similarly we have manipulated ssDNA and polystyrene sulfonate (PSS) molecules. dsDNA has also been manipulated on molybdenum disulphide. Both dsDNA and PSS with contour lengths of up to 2 μm have been moved as a whole. In all these cases, we attribute the immobilization of the macromolecules to the interaction of the charged polymer backbone with an oppositely charged row of head groups in the surfactant monolayer as in a polyelectrolyte–amphiphile complex.

To summarize the manipulation on the defined ultrathin layer on HOPG, it has been demonstrated that the interaction between a solid substrate and a polymer chain can be tailored in such a way that the synthetic or naturally occurring single macromolecule is immobilized, and at the same time can be manipulated with a SFM tip without chain breakage. Combined with spec-

troscopy of fluorescently labeled single molecules [51, 52], this may provide new opportunities to correlate macromolecular conformation with spectroscopic properties. Precise positioning and stretching of DNA molecules combined with ultra high resolution methods like scanning tunneling microscopy (STM) and tip enhanced Raman spectroscopy (TERS) [53, 54] will provide intriguing new opportunities for direct sequencing of DNA. Moreover, free two-dimensional molecular shaping should provide a means to fabricate different two-dimensional molecular architectures, such as electronic circuitry from single macromolecules.

3.3
Manipulation in Tapping Mode on Precoated HOPG

A rather new method to manipulate single macromolecules on solid supports is based on transmitting forces across the surface via an ultrathin liquid film [28]. It may be used to "blow" topologically or covalently formed polymer loops embedded in an ultrathin liquid film on a solid substrate into circular "bubbles" during SFM imaging. In particular, supercoiled vector dsDNA has been unraveled, moved, stretched, overstretched to two times its B-form length and then torn apart. The blowing of the DNA bubbles can be attributed to the interaction of the tapping SFM tip with the ultrathin liquid film.

More specifically, ultrathin liquid films have been prepared by spin-coating either neat liquid amphiphiles ($C_nH_{2n+1}NH_2$ with $n = 4$ or 6) or the longer chain amphiphiles $C_{12}H_{25}NH_2$ (dodecylamine) or $C_{18}H_{37}NH_2$ (octadecylamine) onto the basal plane of HOPG. A submonolayer of a polyelectrolyte such as vector DNA was applied from a dilute aqueous solution by putting a drop on the freshly precoated substrate for a few seconds and spinning it off subsequently. Vector DNA molecules are especially suited for such experiments since they are long, monodisperse, and well-defined polymer rings. The amphiphiles provide on the one hand affinity of DNA molecules to the graphite surface and immobilize DNA sufficiently for imaging with tapping-mode SFM, and on the other, they allow manipulation of the DNA molecules across the surface [27]. The blowing effect was also observed with polymer molecules deposited on the graphite surface coated with an ultrathin solvent film only.

Figure 14a–d displays tapping-mode SFM images of an initially supercoiled vector dsDNA deposited onto graphite covered with $C_4H_9NH_2$ (butylamine) at ambient conditions. A few repeated scans of the whole image caused the two initial loops of the DNA to grow until finally two almost circular bubbles appear. DNA molecules outside the scan area remain in disordered conformations, which we demonstrate by increasing the scan area after a few scans. Analogously, loops have been formed randomly by crossings of linear DNA and PSS on the same substrates. Also, these loops could

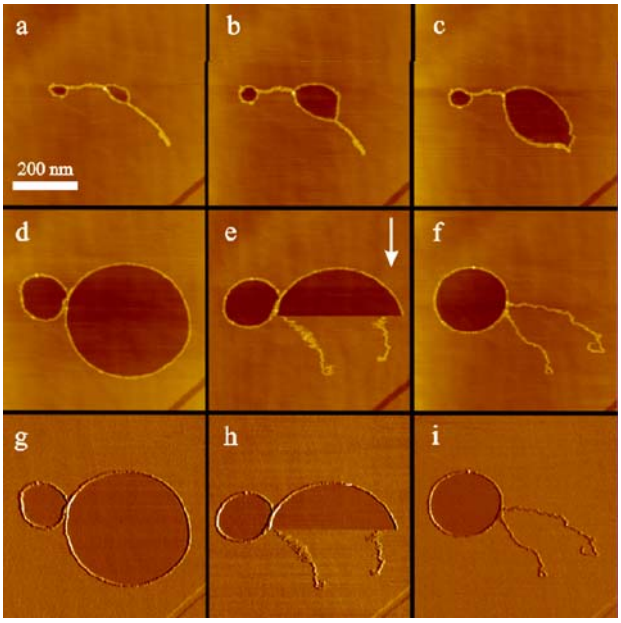

Fig. 14 **a–d** SFM tapping-mode height images, revealing the unraveling of an initially supercoiled vector dsDNA on $C_4H_9NH_2$ upon repeating SFM-scanning of the same surface area. **e** During one of the scans the largest loop breaks, the slow scan direction is indicated with the *arrow*. **f** After a few scans, the smaller loop stabilizes its size and does not grow under continues scanning. **g–i** SFM tapping-mode phase images taken simultaneously with the corresponding height images **d–f**. (Reproduced from [28])

be blown into bubbles. In all cases, SFM height and phase images reveal a difference between the inside and outside of the blowing loops. The difference between the SFM height and phase data inside and outside of the loops is identical for all loops in one scan area and does not change during growth of the bubbles (Fig. 14a–d). Linear polymer molecules that do not form loops are not affected by the scanning.

The circumference of the vector dsDNA circles can become as long as twice the contour length of B-form dsDNA, indicating that the DNA is overstretched in this state. The area enclosed by the DNA loops can increase considerably during blowing; for example, the larger loop on Fig. 14a–e increases 30 times. Large DNA circles can break, and then the height and phase for the area inside quickly level up with the area outside (Fig. 14e and h). When the molecular loop is broken, the force stretching it disappears and the DNA relaxes into a less stretched conformation, yet longer than B-form dsDNA (Fig. 14f). After a few scans, the size of the remaining bubbles stabilizes and does not grow anymore under continuous scanning (Fig. 14f). The DNA loops also grow and can break during repeated tapping in the center of the loops, which was demonstrated by zooming into the center of a DNA loop after the first scan and zooming out after a few

scans. This experimental observation implies that the DNA loops can blow in the absence of the direct interaction between the SFM tip and the DNA strand. The transmission of the influence from the tip to the molecule is attributed to the ultrathin liquid film inside the DNA loop.

The effect of expansion of polymer loops into circles can only be observed for a limited time that depends on the nature of the coating liquid and on its temperature. For example, while for neat $C_4H_9NH_2$ (b.p. 76 °C) blowing upon SFM scanning stops after roughly 50 min at room temperature (~20 °C), for $C_6H_{13}NH_2$ (b.p. 131 °C) blowing can be still observed 24 h after sample preparation. The time during which the blowing effect can be observed is referred to as the "active" time. The vanishing of the blowing effect is not abrupt, because the DNA loops blow and break more readily at the beginning of the active period. The difference in phase and height between the inside and outside of the blown loops disappears when the sample becomes inactive. For the investigated systems, the active time decreases with increasing temperature (e.g., there is no blowing for neat $C_4H_9NH_2$ after annealing at 40 °C for 20 min). The dependence of the active time on both temperature and boiling point of the liquids indicates that the vanishing of the blowing effect is due to the evaporation of the liquid coating. All samples can be repeatedly reactivated upon spin-coating organic solvents such as dichloromethane, chloroform, hexane, benzene, acetone, or toluene onto the sample.

For the liquids with high boiling points, i.e., toluene (b.p. 111 °C) and $C_6H_{13}NH_2$ (hexylamine, b.p. 131 °C) the active time starts not immediately after spin-coating the liquid but after some induction time, which can be as long as 2 h for $C_6H_{13}NH_2$ at room temperature or 10 min for toluene, indicating that some amount of liquid has to evaporate before the system becomes active. This observation indicates that the blowing effect is present only when the liquid film is very thin. Since the polymer molecule acts as boundary separating the films inside and outside of the loop, the thickness of the liquid film during the active time should be comparable or less than the diameter of the molecules. For example the diameter of dsDNA in the B-form is about 2 nm.

Blown DNA circles relax slowly after the scanning has stopped into a less stretched state. If the scanning is restarted within the active time, the loops reshape back into circles. When the sample becomes inactive, i.e., no new loops can be blown, already-blown loops relax slowly into a less stretched state both during and in the absence of scanning (Fig. 15). On graphite coated with short-chain amphiphiles the relaxed conformation tends to become less regular (Fig. 15a–c), while on long-chain amphiphiles ($C_{18}H_{37}NH_2$), it exhibits hexagons (Fig. 15d). The relaxation of circles into hexagons manifests the hexagonal symmetry of the substrate consisting of the graphite and the long chain alkylamines, which, like alkanes and many of their derivatives, adsorb on the basal plane of graphite with their long axes preferably along the crystallographic axes [34].

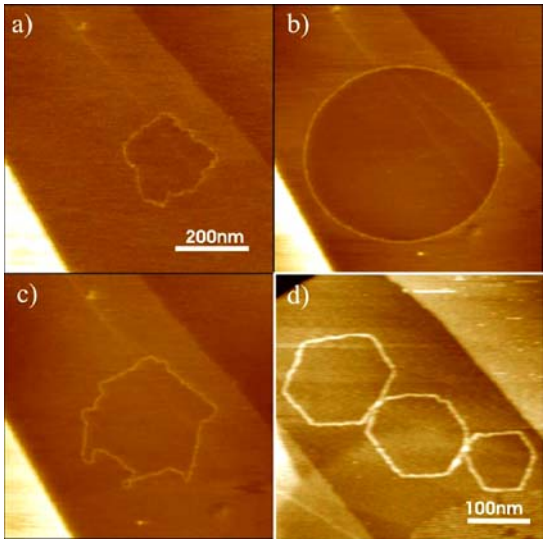

Fig. 15 SFM height images show a vector DNA on graphite coated with $C_{12}H_{25}NH_2$ and refreshed with hexane. **a** First scan; the length of the DNA molecule is 915 nm, which corresponds to the B-form **b** after a few scans, the loop blows to circle and stabilizes its shape at 1590 nm length. Next, the tip is retracted for 2 h and image **c** is made thereafter; no difference between inside and outside of the DNA loop can be detected and the DNA loop does not change its shape during scanning, which indicates the inactive state; the length of the DNA molecule is 1380 nm, which is still significantly longer than the B-form length. **d** The relaxation into hexagons of DNA blown on graphite coated with $C_{18}H_{37}NH_2$ chloroform solution. (Reproduced from [28])

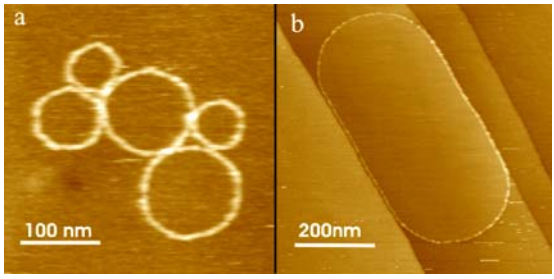

Fig. 16 **a** Several topologically formed loops of one dsDNA on $C_{12}H_{25}NH_2$ can blow independently from each other. **b** Defects on the surface like monoatomic step edges on graphite confine the motion of the polymer during blowing. (Reproduced from [28])

On the longer chain amines $C_{12}H_{25}NH_2$ and $C_{18}H_{37}NH_2$, typically more supercoiled twists remain on the surface after blowing, resulting in several touching circles of different diameters (Fig. 16a). Defects on the surface,

like monoatomic step edges on graphite, confine the motion during blowing (Fig. 16b).

Regarding the difference in the phase images between the inside and outside of the blowing loops, we recall that the phase lag between oscillations of the external force and of the position of the tip depends on the viscoelastic properties of the liquid film the tip interacts with. The phase lag mapped on the phase images reflects therefore the difference between surfaces covered with different liquid films. However it is difficult to quantify the phase and height difference exactly, due to their dependence on tip and tapping conditions. In order to characterize the phases inside and outside the loop further, the amplitude of the oscillating tip was recorded as a function of the tip–sample distance for a bare graphite surface, a graphite surface freshly coated with $C_4H_9NH_2$, and both inside and outside of DNA loops blown on a film of $C_4H_9NH_2$ during the active time of blowing [28]. For these measurements first an SFM image was taken, then the tip was moved to the desired location, the feedback was switched off and the tip oscillating at a frequency close to its resonance frequency was extended towards the surface. While the amplitude–distance dependence measured on graphite is linear over a range determined by the amplitude of the tip oscillation for both approach and retraction (which is consistent with a solid substrate and hard cantilevers), it exhibits hysteresis, similarly for both graphite with freshly spin-coated $C_4H_9NH_2$, and outside of DNA loops blown on graphite surface coated with $C_4H_9NH_2$ during active time.

The hysteresis can be explained by the formation of a meniscus connecting the tip and the fluid film. Quite noise-free images indicate that during imaging, the tip vibration prevents meniscus formation. However, when the tapping amplitude is sufficiently reduced due to the interaction with the surface, a meniscus can form and the tip jumps into contact. Upon retraction, the existing meniscus damps the tip oscillations resulting in hysteresis between approach and retraction. The amplitude–distance dependence measured inside the blown loop does not exhibit hysteresis, indicating that the meniscus does not form; however, it exhibits a glitch. After the DNA breakage the amplitude-distance dependence measured inside the loop starts to exhibit hysteresis indistinguishable from outside of the DNA loop, indicating that the liquid film outside the loop flows into the now-open area inside the loop. The hysteresis measured outside of the blown loops disappears when the samples become inactive, and the glitch appears typical for the amplitude–distance dependence measured inside a blown DNA loop. Amplitude–distance dependences measured 1 day after the application of $C_4H_9NH_2$ are linear, which is typical for bare graphite.

To summarize the manipulation in tapping mode on precoated HOPG, it has been demonstrated that pressure created by an SFM tip in an ultrathin liquid film allows exertion of a homogeneous force on a single macromolecular ring. This provides a new tool for fabricating macromolecular

nanostructures and further investigations of the mechanical properties of ds-DNA and other synthetic and biologically relevant macromolecules and their complexes. For dsDNA overstretching to twice its B-form length has been observed, followed by the rupture of the molecules. Since the surfaces can be activated by many different organic liquids, the blowing effect is a quite general phenomenon.

3.4 Covalent Linkage of Two Polymers at Predefined Sites

The first report on a covalent connection of two individual polymer chains is based on a move-connect-prove sequence under ambient conditions applied to two individual strands of dendronized polymers using a SFM [29, 30]. The connection is achieved by UV irradiation and proven by challenging its mechanical stability. For that purpose, dendronized polymers with diameters of a few nanometers and lengths of up to several hundred nanometers were used. They were equipped with 4, 8, or 16 peripheral amine groups at every repeat unit, which could be functionalized with azides that eas-

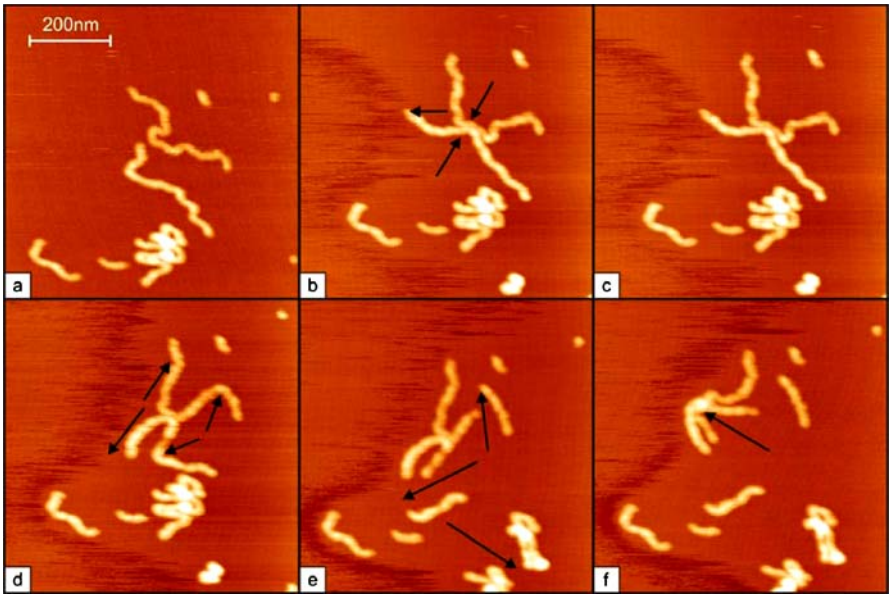

Fig. 17 Tapping-mode SFM images of two individual azide-functionalized dendronized polymers, moved towards each other ("move"; **a** → **b**, irradiated by UV light), "connect" (**b** → **c**), and challenged mechanically ("prove" **d**–**f**). The *arrows* indicate the movement of the SFM tip during manipulation (an animated version of this sequence is provided as a video in the supplementary information of [29, 30]). In addition some smaller molecules and a molecular aggregate can be recognized. (Reproduced from [29, 30])

ily decompose thermally or photochemically into nitrenes (and elementary nitrogen), which are highly reactive, short-lived intermediates undergoing various addition and insertion reactions with formation of covalent bonds. Figure 17 displays tapping-mode SFM images of such dendronized polymers on HOPG.

Figure 17a exhibits two individual azide-functionalized dendronized polymers, both with their backbone extended essentially parallel to the substrate, revealing contour lengths on the order of 400 nm. Figure 17b shows the sample after the two molecules have been moved towards each other with the previously described procedure. After irradiation of the whole sample in situ, (while the SFM is scanning) for 3 min with UV-C light, no change of the image was observed (Fig. 17c). In order to test whether the irradiation caused a stable (covalent) linking of the two adjacent molecules, the mechanical stability of the junction was challenged by pulling on each of the four chain ends with the SFM tip. Obviously the junction did not break (Fig. 17d). Upon moving through the two points of strongest bending, the molecular chains were cut at the position of impact rather than on the newly formed junction (Fig. 17e), indicating that the junction is stronger than the main chain. This can be understood, since the number of covalent bonds in the junction could be more than 100, estimating a contact length on the order of 20 nm. Also, upon dragging the whole molecule across the surface (Fig. 17f) the junction did not break. Other topologies including a full circle have been fabricated. As control, the same experiment was repeated several times without the irradiation, proving that in this case it was easy to pull the molecules apart again. It has also been concluded that there is no covalent connection between the newly formed molecule and the underlying HOPG because the molecule can be manipulated after irradiation [29, 30]. This can be understood because cycloaddition of nitrene to a graphite double layer leads to a separation between the top and the top-1 layer which lowers the dispersion interaction and direct orbital overlap between the two and is therefore energetically unfavorable.

This work demonstrates that two individual polymer chains on a surface can be manipulated until they attain a predetermined relative position in which they can be covalently connected. It was the first application of a move-connect-prove sequence under ambient conditions and opened exciting possibilities for generating and covalently fixing structurally defined, nano-sized functional units of macromolecules. The same sequence may be used to connect unaltered macromolecules if, instead of dendronized polymers, azide-terminated commercially available spherical dendrimers are used as "glue" between two nanoobjects such as nanotubes and DNA, the only condition being that they can be manipulated and imaged with the SFM. For instance carbon nanotubes (CNTs) have an increased reactivity due to the high surface curvature with respect to the inert basal plane of HOPG. The described method is a means to synthesize single macromolecules with novel,

e.g., X-, Y-, O-, or 8-shaped homo- and hybrid-structures, which are practically not accessible by conventional, flask-type synthesis.

More recently, acrylamide-based dendronized polymers with a defined number of azide groups in the periphery have been deposited on an ultrathin layer of fatty acids on HOPG to provide a better defined substrate for both polymer adsorption and manipulation. The application of the move-connect-prove sequence demonstrates that noncharged dendronized polymers can also be manipulated with this method [31].

4 Summary and Outlook

A molecular workbench has been introduced, consisting of an atomically flat, inert solid substrate such as the basal plane of HOPG, coated with a layer of molecules such as alkanes or alkyl chains containing amphiphiles that control the interaction between the substrate and adsorbed macromolecules. The workbench has been used to demonstrate that this interaction can be tailored in such a way that synthetic or naturally occurring single macromolecules are immobilized, and at the same time can be manipulated with a SFM tip without chain breakage. Combined with spectroscopy of fluorescently labeled single molecules, this may provide new opportunities to correlate macromolecular conformation with spectroscopic properties. In particular, precise positioning and stretching of DNA molecules combined with ultra high resolution methods like STM and TERS may provide new opportunities for direct sequencing of biopolymers such as DNA. Moreover, free two-dimensional molecular shaping should provide a means to fabricate different two-dimensional molecular architectures, including electronic circuitry from single macromolecules.

Acknowledgements I am indebted to my associates and students who contributed over the last decade to the work covered here, notably Frank Schabert, Wolfgang Stocker, Illdiko Gössl, Christoph Ecker, Jörg Barner, Wei Zhuang, Hua Liang, and particularly Paolo Samori and Nikolai Severin. I am grateful to D.G. Kurth, H. Frauenrath and A. Dieter Schlüter for very stimulating collaborations. The work has been supported by the DFG, particularly through Sfb 448 "Mesoscopically Organized Composites".

References

1. Rivetti C, Guthold M, Bustamante C (1996) J Mol Biol 264:919
2. Rabe JP (1998) Curr Opin Coll Int Sci 3:27–31
3. Schlüter AD, Rabe JP (2000) Angew Chem 112:860–880
4. Schlüter AD, Rabe JP (2000) Angew Chem Int Ed 39:864–883

5. Sheiko SS, Möller M (2001) Chem Rev 101:4099–4123
6. Samorí P, Ecker C, Gössl I, De Witte PAJ, Cornelissen JJJM, Metselaar G, Otten MBJ, Rowan AE, Nolte RJM, Rabe JP (2002) Macromolecules 35:5290–5294
7. Kurth DG, Severin N, Rabe JP (2002) Angew Chem Int Ed 41:3681–3683
8. Cacialli F, Wilson JS, Michels JJ, Daniel C, Silva C, Friend RH, Severin N, Samorì P, Rabe JP, O'Connell MJ, Taylor PN, Anderson HL (2002) Nat Mater 1:160–164
9. Shu L, Gössl I, Rabe JP, Schlüter AD (2002) Macromol Chem Phys 203:2540–2550
10. Gössl I, Shu L, Schlüter AD, Rabe JP (2002) J Am Chem Soc 124:6860–6865
11. Gössl I, Shu L, Schlüter AD, Rabe JP (2002) Single Mol 3:5–6
12. Gössl I, Shu L, Schlüter AD, Rabe JP (2002) Single Mol 3:315–316
13. Otten MBJ, Ecker C, Metselaar GA, Rowan AE, Nolte RJM, Samorì P, Rabe JP (2004) Chem Phys Chem 5:128–130
14. Severin N, Rabe JP, Kurth DG (2004) J Am Chem Soc 126:3696–3697
15. Ecker C, Severin N, Shu L, Schlüter AD, Rabe JP (2004) Macromolecules 37:2484–2489
16. Zhang A, Barner J, Gössl I, Rabe JP, Schlüter AD (2004) Angew Chem 43:5185–5188
17. Zhuang W, Ecker C, Metselaar GA, Rowan AE, Nolte RJM, Samorí P, Rabe JP (2005) Macromolecules 38:473–480
18. Böttcher C, Schade B, Ecker C, Rabe JP, Shu L, Schlüter AD (2005) Chem Eur J 11:2923–2928
19. Kasëmi E, Zhuang W, Rabe JP, Fischer K, Schmidt M, Colussi M, Keul H, Ding YI, Cölfen H, Schlüter AD (2006) J Am Chem Soc 128:5091–5099
20. Severin N, Okhapkin IM, Khokhlov AR, Rabe JP (2006) Nano Lett 6:1018–1022
21. Jahnke E, Lieberwirth I, Severin N, Rabe JP, Frauenrath H (2006) Angew Chem 118:5510–5513
22. Jahnke E, Lieberwirth I, Severin N, Rabe JP, Frauenrath H (2006) Angew Chem Int Ed 45:5383–5386
23. Jahnke E, Millerioux A-S, Severin N, Rabe JP, Frauenrath H (2007) Macromol Biosci 7:136–143
24. Jahnke E, Severin N, Kreutzkamp P, Rabe JP, Frauenrath H (2008) Adv Mater 20:409–414
25. Shu L, Schlüter AD, Ecker C, Severin N, Rabe JP (2001) Angew Chem 113:4802–4805
26. Shu L, Schlüter AD, Ecker C, Severin N, Rabe JP (2001) Angew Chem Int Ed 40:4666–4669
27. Severin N, Barner J, Kalachev A, Rabe JP (2004) Nano Lett 4:577–579
28. Severin N, Zhuang W, Ecker C, Kalachev AA, Sokolov IM, Rabe JP (2006) Nano Lett 6:2561–2566
29. Barner J, Mallwitz F, Shu L, Schlüter AD, Rabe JP (2003) Angew Chem 115:1976–1979
30. Barner J, Mallwitz F, Shu L, Schlüter AD, Rabe JP (2003) Angew Chem Int Ed 42:1932–1935
31. Al-Hellani R, Barner J, Rabe JP, Schlüter AD (2006) Chem Eur J 12:6542–6551
32. Stocker W, Schumacher M, Graff S, Thierry A, Wittmann JC, Lotz B (1998) Macromolecules 31:807–814
33. Kajitani T, Okoshi K, Sakurai S-I, Kumaki J, Yashima E (2006) J Am Chem Soc 128:708–709
34. Kumaki J, Kawauchi T, Okoshi K, Kusanagi H, Yashima E (2007) Angew Chem Int Ed 46:5348–5351
35. Seebeck FP, Woycechowsky KJ, Zhuang W, Rabe JP, Hilvert D (2006) J Am Chem Soc 128:4516–4517
36. Grosberg AY, Khokhlov AR (1994) Statistical Physics of Macromolecules. AIP, Woodbury

37. Ecker C (2005) Conformations of single polymer chains on surfaces – non-equilibrium, equilibrium and manipulation. Dissertation, Humboldt University Berlin, http://edoc.hu-berlin.de
38. Samorì P, Francke V, Mangel T, Müllen K, Rabe JP (1998) Opt Mater 9:390–393
39. Samorì P, Francke V, Müllen K, Rabe JP (1998) Thin Solid Films 336:13–15
40. Samorì P, Sikharudlidze I, Francke V, Müllen K, Rabe JP (1999) Nanotechnology 10:77–80
41. Samorì P, Francke V, Müllen K, Rabe JP (1999) Chem Eur J 5:2312–2317
42. Schnablegger H, Antonietti M, Göltner C, Hartmann J, Cölfen H, Samorì P, Rabe JP, Häger H, Heitz W (1999) J Coll Int Sci 212:24–32
43. Stocker W, Schürmann BL, Rabe JP, Förster S, Lindner P, Neubert I, Schlüter A-D (1998) Adv Mater 10:793–797
44. Stocker W, Karakaya B, Schürmann BL, Rabe JP, Schlüter A-D (1998) J Am Chem Soc 120:7691–7695
45. Hentschke R, Schürmann BL, Rabe JP (1992) J Chem Phys 96:6213–6221
46. Hentschke R, Schürmann BL, Rabe JP (1993) J Chem Phys 98:1756–1757
47. Jun H, Yi Z, Haibin G, Minqian L, Hartman U (2002) Nano Lett 2:55–57
48. Rabe JP, Buchholz S (1991) Science 253:424–427
49. Cincotti S, Rabe JP (1993) Appl Phys Lett 62:3531–3533
50. Askadskaya L, Rabe JP (1992) Phys Rev Lett 69:1395–1398
51. Vanden DA Bout, Yip W-T, Hu D, Fu D-K, Swanger TM, Barbara PF (1997) Science 277:1074–1077
52. Jäckel F, De Feyter S, Hofkens J, Köhn F, De Schryver FC, Ego C, Grimsdale A, Müllen K (2002) Chem Phys Lett 26:534–540
53. Hamai C, Tanaka H, Kawai T (1999) J Vac Sci Technol B 17:1313–1316
54. Stöckle RM, Suh YD, Deckert V, Zenobi R (2000) Chem Phys Lett 318:131–136

Top Curr Chem (2008) 285: 103–156
DOI 10.1007/128_2007_29

Published online: 25 April 2008

Friction and Surface Dynamics of Polymers on the Nanoscale by AFM

Holger Schönherr (✉) · Ewa Tocha · G. Julius Vancso (✉)

MESA$^+$ Institute for Nanotechnology and Faculty of Science and Technology, University of Twente, Department of Materials Science and Technology of Polymers, P.O. Box 217, 7500 AE Enschede, The Netherlands
h.schonherr@utwente.nl, g.j.vancso@utwente.nl

Abstract In this article the measurement and understanding of friction forces and surface dynamics of polymers on the one hand and the importance of molecular relaxation processes and viscoelasticity in polymers for advanced micro- and nanoscale applications on the other hand are discussed. Particular attention is paid to the nanoscale (surface)

analysis by scanned probe microscopic approaches, including atomic force microscopy (AFM), as a means to assess molecular relaxation processes that operate at a given temperature. Established AFM approaches, including lateral force and force modulation microscopy, are introduced and more recently developed techniques, such as torsional resonant modes, are briefly sketched. On the basis of the discussion of the techniques to measure friction and to probe surface dynamics of polymers on the nanoscale, illustrative examples are reviewed. The examples discussed address in particular the determination of values of the glass transition temperature (T_g) and the difference of T_g assessed in the bulk vs. at the free surface of polymers. Confinement and thin film effects on T_g, but also on sub-T_g transitions and chain dynamics, are treated in detail. Finally, the mapping of multiphase systems and anisotropic friction receive attention.

Keywords AFM · Confinement effects · Friction · Glass transition temperature · Nanotribology · Polymer viscoelasticity · Thin film effects

Abbreviations

AFM	Atomic force microscopy
FFM	Friction force microscopy
SM-FM	Shear modulation force microscopy
SVM	Scanning viscoelasticity microscopy
SLAM	Scanning local acceleration microscopy
TR	Torsional resonance
LFM	Lateral force microscopy
CFM	Chemical force microscopy
HFM	Heterodyne force microscopy
f–d	Force-displacement
T_g	Glass transition temperature
MEMS	Microelectromechanical systems
NEMS	Nanoelectromechanical systems
SFA	Surface forces apparatus
JKR model	Johnson, Kendall and Roberts model
DMT model	Derjaguin, Muller, Toporov model
PMMA	Poly(methyl methacrylate)
PMA	Poly(methyl acrylate)
PnBMA	Poly(*n*-butyl methacrylate)
PtBuA	Poly(*tert*-butyl methacrylate)
PTFE	Poly(tetrafluoroethylene)
PS	Polystyrene
PI	Polyisoprene
PE	Polyethylene
PP	Polypropylene
EP	Ethylene-propylene
PES/SAN	Poly(ether sulfone)/polyethersulfone/poly(acrylonitrile-*co*-styrene)
PVOH	Poly(vinyl alcohol)
PVP	Poly(vinyl pyridine)
OTS	Octadecyltrichlorosilane
PVME	Poly(vinyl methylether)

1 Introduction

Friction and (surface) dynamics of polymers play an important role not only in advanced applications related to adhesives, lubricants and protective coatings and in everyday life (e.g. the low adhesion and low friction properties of poly(tetrafluoroethylene), PTFE, coatings), but following the accelerating drive towards nanometer scale technology and devices, these phenomena may become limiting factors in various applications. A closer look at the state of the art in this area shows that there is, in particular in the area of tribology, despite decades of research, a wide gap in terms of length and time scales between theory (modeling), nanoscale and micro-/macroscale experimental work [1, 2].

Clearly, the mastering of the theoretical treatment and understanding of the chain dynamics of polymers in the bulk, as developed by the pioneering work of Williams, Landel, Ferry and many others [3], had an enormous impact on polymer science on the one hand and via the research and development in the polymer industry on high tech and low tech applications that are today commonplace on the other hand. With shrinking dimensions, for instance in coatings in data storage devices [4] or in fabrication processes like photoresist technology-based lithography [5], substrate and interface effects, confinement effects and thereby affected chain dynamics alter the known bulk behavior of polymers [6]. Effects include, among others, altered transport properties [7] as well as crystallization [8] and dewetting kinetics [9]. Most strikingly this is illustrated in the pronounced effect of the ultrathin film architecture (surface/interface chemistry, film thickness) of substrate-supported polymer films on the glass transition temperature (T_g) and polymer chain dynamics [10–12]. Altered T_g's of up to 50 °C have been reported [10–13].

The molecular origin for friction in polymers is, as will be pointed out below, directly linked to the molecular relaxation processes that operate at a given temperature. Near T_g friction in polymer melts shows highly cooperative dissipation phenomena, known as heterogeneous dynamics of glass formers. The associated critical length scale, over which collective molecular motion occurs, is called the size of a cooperatively rearranging region. This length scale ranges in the bulk from several monomeric segments to several molecules [14]. Such localized effects mandate the study of the underlying principles and the determination of the length scales by high-resolution techniques, i.e. by techniques that operate at the corresponding length scale.

In more general terms, in the understanding of friction, despite decadelong efforts, a gap can be identified between molecular or atomistic models on the one hand [15], and continuum (e.g. contact mechanics) approaches [17] that describe the deformation between elastic single asperities on the other hand [1]. Consequently, the understanding of fundamental aspects of friction and the mechanisms of energy dissipation remains limited on

a first-principles level. Multi-level experiments (from micrometer to nanometer scale) are clearly required to advance the understanding of tribology. The goal of the multi-level experiments is to determine the mechanism of friction, which is partly based on the atomic and molecular scale phenomena at the sliding interface, and to correlate the corresponding processes to the macroscopic scale frictional behavior. The necessary bridge between micro- and nanotribology, as well as atomistic [15, 16] and continuum models [17, 18] has not yet been addressed convincingly. Both experimental (tribology) and theoretical (simulations) approaches suffered until recently from limitations that prevented a unified understanding.

On the basis of atomic force microscopy (AFM) [19], as one of the more prominent members of the family of proximal probe techniques, a number of highly interesting approaches has been developed in the last ~10 years to start to *quantitatively* address friction and in particular surface dynamics of polymers at the true nanoscale [1, 2, 20]. In general, AFM is attractive for studies at the fundamental level of single asperities, since the method is suitable for the detection of friction forces of nanometer scale contacts of real surfaces with high spatial resolution under pressures of up to several GPa [21]. With these new approaches at hand, one of the main challenges of modern tribology can be tackled, namely to develop a fundamental understanding of nanoscale friction. For polymers additional challenges arise due to the complexities of the time–temperature superposition principle [22] and the fact that the instruments utilized in nano- and microtribology until recently operated on different time and length scale regimes. In addition, polymers can easily be deformed plastically, thus giving rise to altered contact areas and pressures, as well as friction mechanisms other than interfacial friction.

The ability of controlling friction (of polymers), once achieved, will be highly advantageous in new technological developments, such as magnetic storage devices [23, 24], and applications, such as in microelectromechanical systems (MEMS) and nanoelectromechanical systems (NEMS) [25], biosystems [26], and many others. In this review we aim at a concise treatment of friction and its relation to polymer (chain) surface dynamics. On the basis of a rudimentary introduction of polymer viscoelasticity and (nano)tribology, we review the recent progress in the use of AFM technology to explore friction of polymers on the nanoscale. In this review we rely on work published in the literature, as well as on the work performed in our laboratory to provide a broad overview of the topic both for the expert as well as the non-expert readers who want to enter this exciting field.

1.1 Polymer Dynamics and Viscoelasticity

Amorphous polymers show a distinct change in mechanical properties when passing through the glass–rubber transition at the glass transition tempera-

ture (T_g) [27, 28]. As a result of frozen chain motions, the Young's modulus is ~3 orders of magnitude higher at temperatures below T_g than for temperatures above T_g. In addition, amorphous polymers deform in a first approximation elastically below T_g, while polymer melts at temperatures above T_g are best described as viscoelastic non-Newtonian fluids. Even below T_g polymers may show relaxation phenomena, such as the slow recovery after the application of a temporary stress, that are attributed to molecular scale motions. These include the rotation of pending side groups or the crankshaft motion of the polymer backbone. In particular in the light of polymer ageing, these processes are of great importance.

In addition to temperature, all these phenomena depend, as will be briefly alluded to below on the rate (frequency) of the experiment, e.g. the rate at which the stress is applied. For a dynamic-mechanical experiment, we can define the loss tangent $\tan(\delta)$ as the ratio of the dynamic loss modulus E' and the dynamic storage modulus E'' [29]:

$$\tan(\delta) = \frac{E''}{E'} \,. \tag{1}$$

The relationship of $\tan(\delta)$ vs. frequency generally displays several broad peaks corresponding to different classes of molecular relaxations labeled α, β, γ and δ. These relaxation processes are ascribed to the glass–rubber transition and different rotations of side groups, respectively (vide infra). As mentioned, dramatic changes in various material properties are associated with this transition.

The variation of rate (time) and temperature causes similar effects in polymer relaxation processes. For viscoelastic properties the interplay between relaxation time and temperature is well-known [30–33]. The so-called time–temperature superposition principle states that the same molecular relaxation requires longer time at lower temperatures. For instance, a polymer, which displays rubbery characteristics under a given set of testing conditions, can be induced to show glassy behavior by either reducing the temperature (to below T_g) or by increasing the testing rate (or frequency). According to the time–temperature superposition principle (higher $T \Leftrightarrow$ lower frequency), the $\tan(\delta)$ vs. frequency relation can be reduced to a master curve at an arbitrary chosen reference temperature T_o, by multiplying the velocity (or frequency) data with the Williams–Landel–Ferry (WLF) shift factor a_T [22]. The Arrhenius relationship

$$\ln a_T = \frac{E_a}{R}\left(\frac{1}{T} - \frac{1}{T_o}\right) \tag{2}$$

between the shift factor a_T and the temperature T, and the activation energy E_a, is commonly used to analyze relaxation phenomena below T_g. The activation energies represent the potential barrier that is continuously overcome, e.g. for the rotation of dipolar moieties in macromolecules.

For instance, the relaxation processes in bulk poly(methyl methacrylate) (PMMA) are well characterized using a variety of techniques, including dielectric [34, 35] and dynamic mechanical analyses [36–38], NMR spectroscopy [39], positron annihilation [40], and fluorescence spectroscopy [38]. In PMMA the highest relaxation temperature, the α relaxation, is the glass transition temperature ($T_g = 95–110\,^{\circ}C$, $E_a^{\alpha} = 334–460\,kJ\,mol^{-1}$) [29] and is ascribed to long-range conformational changes of the polymer backbone (see Fig. 1). The secondary β, γ, and δ relaxations are attributed to the side chain motions of the ester group and rotations of the methyl groups attached to the main chain and side chain, with characteristic relaxation temperatures $T_{\beta} = 10–40\,^{\circ}C$, $T_{\gamma} = -100–170\,^{\circ}C$, and $T_{\delta} = -180\,^{\circ}C$, and activation energies $E_a^{\beta} = 71–96\,kJ\,mol^{-1}$, $E_a^{\gamma} = 10–29\,kJ\,mol^{-1}$, $E_a^{\delta} = 3\,kJ\,mol^{-1}$, respectively [29, 38, 41].

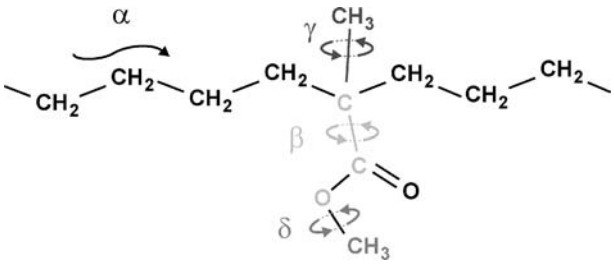

Fig. 1 Schematic of the relaxations in PMMA

In general, the dependence of polymer relaxations on various parameters can be schematically captured in the form of tan(δ)–frequency or tan(δ)–temperature diagrams (Fig. 2). In the tan(δ) vs. frequency relation, the bell-shape curve characteristic for a relaxation with maximum at f_o (relaxation frequency) is shifted to lower frequency values for increasing pressure. By contrast, increasing the temperature results in a shift to higher frequency

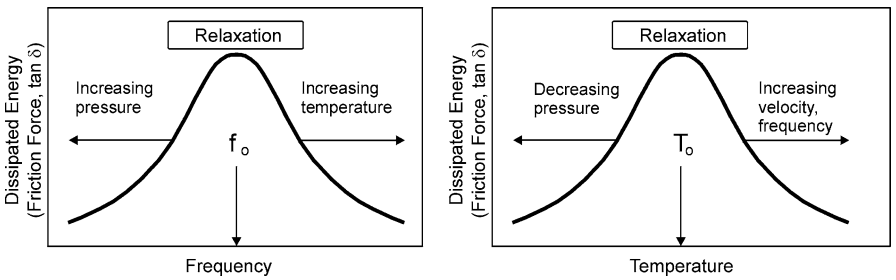

Fig. 2 Schematic diagrams of a relaxation probed in a friction force–frequency (*left*) and a friction force–temperature experiment (*right*) of a polymer

values. As will be discussed in Sect. 3.2 in detail, dynamic friction of polymers has a large contribution from internal viscoelastic dissipation. Hence plots of the friction force, determined e.g. by AFM, vs. f_o are qualitatively similar to plots of tan δ vs. f_o.

1.2 Static and Dynamic Friction Force, Single vs. Multi Asperity Contacts

Friction forces and (surface) dynamics of polymers are intimately related, as already alluded to above. By measuring, for instance, dynamic friction forces under well-controlled conditions, the dynamics of a given polymer can be directly probed at the free surface of a sample specimen. Before discussing the proximal probe techniques and approaches that have been applied to the study of friction and surface dynamics of polymers at the nanoscale, some fundamental aspects of (nano)tribology will be briefly reviewed.

When a lateral force, or shear stress, is applied to two surfaces in adhesive contact, the surfaces initially remain "pinned" to each other until some critical shear force is reached. At this point, the surfaces begin to slide past each other either smoothly or in jerks. The friction force needed to initiate sliding from the rest position is known as the *static friction force*, denoted by F_s (see Fig. 3). The force needed to maintain smooth sliding is referred to as the *kinetic* or *dynamic friction force*, denoted by F_k or F_f. In general, $F_s > F_k$ [42]. Two sliding surfaces may also move in regular jerks, known as "stick-slip" sliding, which is discussed in more detail in Sect. 3.4. The friction force between two bodies in the absence of lubrication is often called *dry friction*.

In the most common situation *normal friction* (kinetic friction accompanied by wear and/or plastic deformation) takes place when two rough surfaces slide with respect to each other. The surface asperities may deform elastically or plastically. When a strong force is applied to the surfaces, damage (or wear) of the shearing substrates occurs. Under certain conditions (low load, completely elastic interactions, smooth tip shape, atomically flat substrate, unreactive surfaces, etc.) a single-asperity contact may be formed and wear-less friction can be observed. This situation is often referred to as *interfacial* or *boundary friction* [43]. In this regime it has been observed that

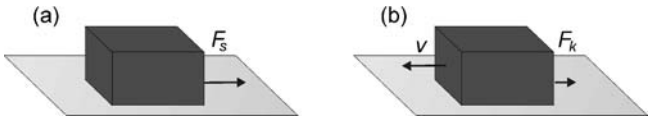

Fig. 3 **a** The friction force needed to initiate sliding from rest is known as the static friction force, denoted by F_s. **b** The force needed to maintain smooth sliding is referred to as the kinetic or dynamic friction force, denoted by F_k or F_f. v stands for velocity

friction is proportional to the contact area. This type of friction can be probed using the surface forces apparatus (SFA) or by AFM.[1]

A general form of the normal friction force (also called lateral force) is given by [1]:

$$F_f = \mu F_N = \mu(L + A)\,, \tag{3}$$

where μ is the friction coefficient and F_N denotes the *normal force*, which is calculated as the sum of externally applied load L and the contribution from *adhesion forces* or *adhesion* A (the maximum force needed to separate two bodies).

On the basis of various studies by Amontons and Coulomb, three laws of friction have been formulated [1]:

1. The friction force is independent of the apparent area of contact.
2. The friction force (F_f) is proportional to the applied load (L): $F_f = \mu L$. The ratio L/F_f is called coefficient of friction μ. Its value is usually larger for static friction than for kinetic friction ($\mu_s > \mu_k$).
3. Kinetic friction is independent of the velocity.

These three macroscopic phenomenological laws of friction are still not fully understood in terms of the corresponding fundamental microscopic processes. However, these laws apply surprisingly well on the macroscopic scale for dry friction.

1.2.1 Multiple and Single Asperity Tribology

The modern study of friction started in the 1950s, when Bowden and Tabor presented a simple model of friction on the micrometer scale [44]. They found that friction force, although independent of apparent microscopic contact area, is in fact proportional to the true contact area (A_R). Surfaces are rough on the microscopic scale, hence the microscopic irregularities of the surfaces touch and push into one another (Fig. 4). The real area of contact is therefore a few orders of magnitude smaller than the apparent area of contact. In the Bowden and Tabor model, the friction force between two unlubricated (dry) surfaces arises from two main factors (Eq. 4). The first, and usually the most important factor is the interaction between the asperities of the contacting surfaces. It is assumed that this part of the friction force is proportional to both the real area of contact A_R and the interfacial shear strength τ^*. The second factor, called the deformation term D, arises from

[1] SFA and AFM are among the most prominent instruments for performing micro- and nanotribological studies. While the SFA is limited to mica as a substrate and affords atomic resolution only in the vertical direction and has limited lateral resolution (several micrometers), AFM is suitable to detect friction forces with atomic resolution in all three dimensions of nanometer-scale contacts of real surfaces under pressures of several GPa.

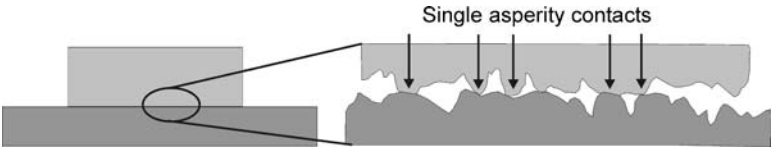

Fig. 4 Surfaces are rough on the microscopic scale. The irregularities of the surfaces touch and push into one another. The real area of contact is a few orders of magnitude smaller than the apparent area of contact

the ploughing, grooving or cracking of one surface by asperities on the other surface.

$$F_f = \tau^* A_R + D\,. \tag{4}$$

Since the friction force is proportional to the real area of contact, as is adhesion (see Sect. 2.3), and since the energy loss in the friction mechanism is ascribed to plastic deformation of the asperities, the model is often called *adhesion model* or *plastic junction model* [44].

For purely plastic deformation, the area of contact A_R is proportional to the load (which simplifies Eq. 4 to the second law by Amontons)[2]. However, totally plastic deformation during sliding provokes huge damage in a short time, which is usually not observed. Thus, elastic processes must play an important role in friction processes and other dissipation mechanisms must exist, which do not change the structure of the surfaces in contact [44].

Different length scales are relevant for microscopic experiments. The surface roughness will determine the size of the asperities. The smallest asperities are plastically deformed at very low loads, whereas larger asperities are still in the elastic regime (interfacial friction). On the micrometer scale the friction force has contributions from different phenomena, such as wear-less friction, plastic deformation of asperities, lateral forces to move debris particles, viscous forces and ploughing terms [1]. To understand the behavior of such a complex contact, it is hence desirable to learn about the properties of single asperity contacts under conditions of interfacial friction. In this case, the friction force was found to be proportional to the real area of contact, hence in good agreement with the Bowden and Tabor model. As will be shown below, a non-linear friction force–load dependence is expected for single asperity contacts, which is in contradiction to Amontons' friction law.

In macroscopic contacts, the interface consists of many micrometer and submicrometer size asperities, where real contact occurs. Contact continuum mechanics describe the elastic deformation of single asperities. All theories described below are based on the following assumptions: the deformations

[2] If the deformation is totally plastic, the asperities are compressed until the pressure becomes equal to a certain yield pressure p^*, which is usually smaller than the yield pressure of the bulk material.

are purely elastic, the contacting materials are elastically isotropic, Young's modulus and Poisson's ratio are not load dependent, the atomic structure is not considered, and the contact radius a is small compared to the radius R of the sphere.

1.2.2 Hertz Model

The Hertz theory [45] assumes that no attractive forces act between the two materials. For a sphere–sphere contact, the contact area A_R depends on load L:

$$A_R = \pi \left(\frac{R \cdot L}{K} \right)^{\frac{2}{3}} \tag{5}$$

$$\frac{1}{R} \equiv \frac{1}{R_1} + \frac{1}{R_2} \tag{6}$$

$$K \equiv \frac{4}{3} \left(\frac{1 - \nu_1^2}{E_1} + \frac{1 - \nu_2^2}{E_2} \right)^{-1}, \tag{7}$$

where R is the composite radius and R_1, R_2 are the radii of curvature of the lower and upper body, respectively, K is the reduced elastic modulus, E_1, E_2 and ν_1, ν_2 are the Young's moduli and Poisson's ratios for the lower and upper body, respectively (Fig. 5).

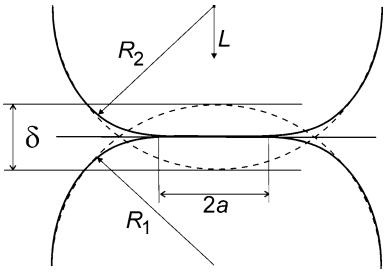

Fig. 5 Geometry of a contact between two elastic spheres (R_1 and R_2) under applied load L for the Hertz theory; a denotes the contact radius, δ is the indentation depth

1.2.3 Johnson, Kendall and Roberts (JKR) Model

The JKR model [46, 47] is the extension of the Hertz model, in which the work of adhesion γ is taken into account (γ is defined as the energy per unit area to separate two flat surfaces in vacuum from contact to infinity). It assumes that the adhesive forces are confined to the inside of the contact area. The contact

area is described by:

$$A(L) = \pi \left(\frac{R}{K}\right)^{\frac{2}{3}} \left(L + 3\pi\gamma R + \sqrt{6\pi\gamma RL + (3\pi\gamma R)^2}\right)^{2/3} . \quad (8)$$

Even at zero applied load there is a finite contact area of $A_R(0) = \pi(6\pi\gamma R^2/K)^{2/3}$. Hence, load has to be applied to break the contact. In the limit of work of adhesion equal to zero ($\gamma \to 0$) and also for large forces compared to γR, the JKR result coincides asymptotically with the Hertzian result. The derivative of R_A with respect to load yields the minimum for the contact area (area at pull-off, see Sect. 2.3.1 for AFM pull-off force), which can be transformed to equation:

$$F_{\text{Pull-off}}^{\text{JKR}} = -\frac{3}{2}\pi R W_{12} . \quad (9)$$

The work of adhesion $\gamma = W_{12}$ can be expressed as a function of the surface energies of the tip γ_1, the sample γ_2, and the corresponding interfacial energy γ_{12}:

$$W_{12} = \gamma_1 + \gamma_2 - \gamma_{12} . \quad (10)$$

The JKR model can be applied when the surface forces are short range in comparison to the elastic deformations they cause (i.e. compliant materials, strong adhesion force, large tip radii).

1.2.4
Derjaguin, Muller, Toporov (DMT) Model

The DMT model includes adhesion outside the contact area by considering long-range attractive forces of van der Waals type [48–51]. Maugis provided an analytical solution for the model [52]. In this case, the real area of contact A_R varies with load L in a simple fashion:

$$A_R = \pi \left[\frac{R}{K}(L + 2\pi R\gamma)\right]^{2/3} . \quad (11)$$

The pull-off force is given by:

$$F_{\text{Pull-off}}^{\text{DMT}} = -2\pi R W_{12} . \quad (12)$$

The JKR and DMT models apply for two extreme cases: for compliant materials with large, short-range attractive forces and for stiff materials with small, long-range attractive forces, respectively. The parameter λ is used to determine which of the two models is most appropriate.

$$\lambda = \left(\frac{9RW_{12}^2}{4\pi K^2 z_0^3}\right)^{1/3} , \quad (13)$$

where z_o is the equilibrium separation between the contacting surfaces. If $\lambda > 5$, the JKR theory should be valid, while for $\lambda < 0.1$ the DMT theory should describe the relation between A_R and L [17, 53]. The most frequently used description covering the JKR–DMT transition regime is the Maugis–Dugdale (MD) theory [52]. The model is relatively difficult to use because it is presented in two coupled analytical equations that must be solved numerically through iteration.

Recently, Carpick, Ogletree and Salmeron [17], as well as Schwarz [54] proposed a general analytical model for the elastic deformation of an adhesive contact in the intermediate regime between JKR and DMT limits as an alternative.

The application of the elastic contact continuum models for viscoelastic materials is limited. For instance, the models can be used only for materials that possess a glass transition temperature well above ambient temperature. For a viscoelastic material the size of the contact zone depends on the loading history. Several attempts have been made to modify the JKR theory with some relaxation functions. A combination model of classical JKR theory with a fracture mechanics model of crack initiation and growth in linear viscoelastic materials has been proposed by Johnson [55, 56]. The major assumption of the model is that viscoelastic effects are limited to the periphery of the contact. Longer-range creep effects are ignored. Hui et al. extended the JKR theory for the contact radius which is a non-decreasing function of time (describing the bonding process). The presented models are complex and often necessitate the use of numerical calculations [57–59].

1.2.5
The Greenwood and Williamson Model of Multiasperity Contact

Realistic surface interactions are influenced not only by the nominal apparent or contact areas A_n, but also by the individual asperity/roughness interactions. Greenwood and Williamson modeled surface roughness using a statistical model, where the roughness of two approaching surfaces is combined into an infinitely smooth surface and a surface with spherically shaped asperities having a uniform mean radius R and following a Gaussian height distribution. A linear dependence between the real contact area and the applied load was obtained independently of the mode of deformation of the asperities (i.e. whether it is elastic, plastic or something in-between) or the shape of asperities [60–62]. In this case, the Greenwood model leads to Amontons' law, as well as to the plastic junction model [44].

2
Techniques to Measure Friction and to Probe Surface Dynamics of Polymers on the Nanoscale and Illustrative Examples

As mentioned in the introduction, the length scales over which energy is dissipated can be directly linked to relaxation processes in the polymer and in the case of the glass transition to the corresponding clustering processes. Hence it is not surprising that a large number of proximal probe techniques has been developed to measure friction and to probe surface dynamics of polymers on the nanoscale.

We focus in the following on a brief description of the rudimentary aspects of the most commonly applied AFM-related techniques, in particular lateral force microscopy (friction force microscopy). In addition, all relevant techniques will be introduced that have been applied to acquire the data reviewed and discussed in Sect. 3. It is important to note that different techniques rely on the detection and quantification of different physicochemical parameters. In addition, among these techniques other factors or parameters may or may not have been maintained constant. Sometimes even identical techniques were applied in different ways. Thus, even though various authors report the same "quantity", e.g., a surface glass transition temperature, for nominally identical polymers, the absolute numbers, but also the trends observed may differ widely.

2.1
Friction Force Microscopy

One of the very prominent techniques to measure friction on the nanoscale is the so-called friction force microscopy (FFM) or, more generally, lateral force microscopy (LFM) [63, 64]. This technique is a contact mode atomic force microscopy (AFM) technique, in which both normal and lateral forces are measured simultaneously. In contact mode AFM a sharp tip (with a typical radius of 10–100 nm and a typical probe material of Si and Si_3N_4) mounted to the end of a flexible cantilever (with a normal spring constant of $k_N = 0.01–1\ N\,m^{-1}$) is brought into contact with the surface. While scanning either by the tip or by the sample (Fig. 6), forces acting between atoms of the AFM tip and atoms of the sample surface will result in a measurable deflection of the cantilever. The cantilever bends vertically (i.e. towards or away from the sample) in response to attractive and/or repulsive forces acting on the tip (see Sect. 2.3). Using, for instance, a feedback loop to maintain a constant cantilever deflection, while scanning the sample surface, a topographic image of the surface can be obtained by plotting the feedback signal vs. tip position.

When the sample is scanned perpendicular to the main cantilever axis in the constant force mode, lateral forces acting on the tip result in twist-

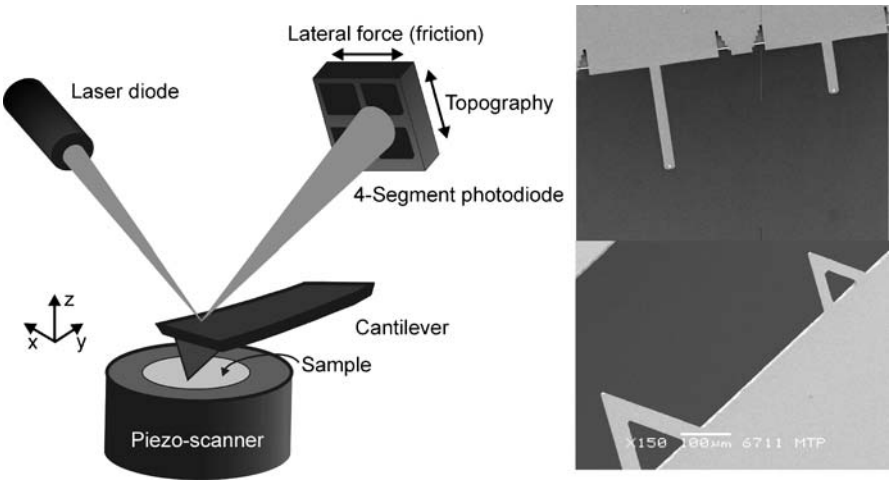

Fig. 6 *Left*: Schematic diagram of contact mode AFM; *right*: SEM images of single beam and V-shaped cantilevers

ing of the cantilever [65]. The magnitude of the cantilever torsion (lateral deflection) is proportional to the friction forces of the tip–sample contact. Simultaneous measurements of the normal and lateral deflections can be performed using several techniques, including a four-segment photodiode (also called optical beam deflection method) [66]. The optical deflection method as the most frequently utilized technique to monitor forces in AFM is based on detection of laser beam position reflected from the back of the cantilever into a position sensitive four-segment photodiode. The voltages measured on the four segment photodiode in normal and lateral direction are defined as the difference voltage between top and bottom photodiode output: $\Delta U_N = ((A + B) - (C + D))/(A + B + C + D)$ and difference voltage between left and right photodiode output: $\Delta U_L = ((A + C) - (B + D))/(A + B + C + D)$, and are labeled *difference normal signal* and *difference friction signal*, respectively. The method, in fact, measures the deflection angles and bending angles of the cantilever, which are linearly proportional to the cantilever deflections (normal and lateral, respectively) for small angles.

Lateral forces acting on the cantilever tip in a direction perpendicular to the cantilever main axis will twist the cantilever. Typical AFM friction measurements are recorded in the form of friction loops, as shown in Fig. 7. In the friction loop, the difference friction signal (also called friction signal) is plotted against the trace (forward scan) and retrace (backward scan) lateral sample displacement. At the beginning of each trace and retrace, the sample remains in static contact until the shear force increases and overcomes the static friction force. The signal changes sign for the retrace with respect to the trace scan. For a given load (normal force), the friction force can be deter-

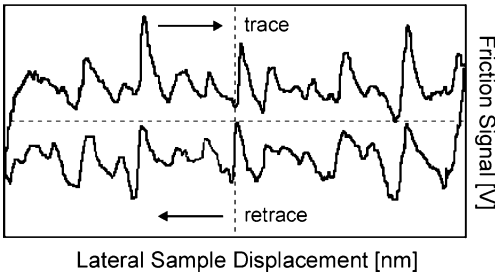

Fig. 7 Typical friction loop in which the differential photodiode output signal for cantilever torsion is recorded for forward (trace) and backwards (retrace) scans along the same scan line

mined as one half of the difference between the corresponding friction signals for trace and retrace scans.

The friction loop may contain information originating from topographic features [67]. Most of this topographic component (i.e. the local slope of the sample surface)[3] is removed from the difference friction signals by subtracting the data for trace and retrace scan directions. However, thermal drift and hysteresis in the lateral scan system may prevent an exact match of trace and retrace data. For quantitative analyses a correction (off-set) of trace and retrace data may be required. In addition, a fundamental requirement for quantitative LFM are symmetric, i.e. spherical tip apex shapes. The friction force can also be determined from trace and retrace lateral force images, as the difference image (also called friction map). By creating histograms of the force maps, the friction forces can be quantified [30].

In order to obtain quantitative data from force microscopy, a reliable and accurate force calibration must be performed [21]. This requires, both the calibration of the normal and lateral force constants of the cantilevers and of the photodiode sensitivity [68]. The normal and lateral forces acting on the cantilever can be expressed as:

$$F_N = k_N S_N \Delta U_N \tag{14}$$

$$F_L = k_L S_L \Delta U_L = \alpha \cdot \Delta U_L \,, \tag{15}$$

where α denotes the lateral calibration factor, which transforms the measured lateral difference signal [V] into friction force [nN]. As the values of S_N and S_L are very sensitive to the position of the laser beam on the cantilever apex [68–70], and the corresponding spot shape [71], the sensitivities must be determined for each cantilever and also for each position of the laser beam on the cantilever [72, 73].

[3] The reaction force from a tilted surface (with respect to the horizontal) will impose a lateral force on the tip, even in a case of zero friction.

The force constants of *single beam* cantilevers (normal spring constant k_N, torsional spring constant k_φ, and lateral spring constant k_L) can be calculated, assuming levers of constant thickness, based on measured cantilever dimensions, from continuum elasticity mechanics of isotropic solids [74–76]:

$$k_N = \frac{Ewt^3}{4l^3} \tag{16}$$

$$k_\varphi = \frac{Gwt^3}{3l} \tag{17}$$

$$k_L = \frac{k_\varphi}{h^2} = \frac{Gwt^3}{3lh^2}\,, \tag{18}$$

with cantilever length l, cantilever thickness t, cantilever width w, tip height h, Young's modulus E, Poisson's ratio ν, and shear modulus $G = E/2(1 + \nu)$.

For Si cantilevers the material properties (Young's modulus and Poisson's ratio) are known in any crystal orientation [77].[4] By contrast, the material properties of the Si_3N_4 cantilevers are not well defined and may vary significantly due to differences of the chemical vapor deposition processes [78–80]. For instance, Young's moduli and Poisson's ratios of Si_3N_4 cantilevers in the range of 120–200 GPa and 0.22–0.27, respectively, have been reported.

Procedures for the reliable calibration of normal forces (i.e. k_N) are well established. Several methods can be used, such as the thermal fluctuation method [81–83], the reference lever [84] or the added mass technique [85]. The calibration of the lateral force constant of a given cantilever and the photodiode sensitivity for measurements of lateral forces remained until recently challenging.

The conventional calibration techniques proposed for the calibration of LFM can be grouped into (1) reference methods [86] and (2) two-step [68, 78, 87] procedures. The challenges mentioned arise from the fact that the reference methods suffer from systematic errors introduced by contaminations on the reference samples and that a separate calibration of the lateral force constant k_L and the photodiode sensitivity for lateral deflection S_L is hampered by a number of problems, respectively. The accuracy of the determined value of k_L is limited due to large errors in the determination of the cantilever dimensions and the uncertainty in the values for Young's moduli and Poisson's ratios for Si_3N_4 (if applicable). The unavailability of a reliable in situ method to calibrate the photodiode sensitivity S_L and its dependence on factors, including laser beam position on the lever, spot size and asymmetry etc., represent additional complications.

A third group of calibration procedures, (3) the direct (single step) techniques avoids (many of) these problems [88–90]. In particular, the so-called

[4] The values of Young's modulus in the [100], [110] and [111] directions are $E[100] = 130$ GPa, $E[110] = 168$ GPa, and $E[111] = 187$ GPa, respectively [77].

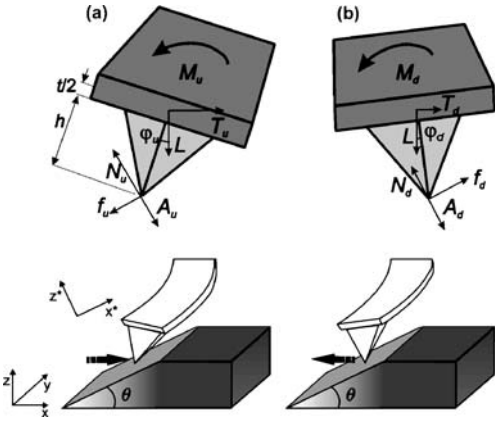

Fig. 8 Schematic illustration of cantilever torsion while **a** sliding up and **b** sliding down on a sloped surface (in the x direction). While sliding across a sloped surface with angle θ, the acting forces (the applied load L, the horizontal tractive force T, the adhesion force A, the reaction force from the surface acting on the tip with a component N in the surface normal direction and a component f (friction force) parallel to the surface) and the torsion momentum M are in equilibrium and depend on the direction of motion—uphill and downhill, denoted here with subscripts u and d, respectively. φ represents the torsion angle of the cantilever, which is proportional to the friction force. h and t stand for tip height and cantilever thickness, respectively. (Reprinted with permission from [91]. © (2006) American Chemical Society)

improved wedge-calibration method, in which a tip/cantilever is scanned across a calibration sample with two well-defined slopes (see Fig. 8), allows one to calculate the calibration factors with an error of ca. 5% [91].

It can be shown that

$$\sin\theta(L\cos\theta + A)\cdot\mu_s^2 - \frac{\Delta_s - \Delta_f}{W_s}(L + A\cos\theta)\cdot\mu_s + L\sin\theta\cos\theta = 0 \qquad (19)$$

$$\mu_f = \frac{\alpha W_f}{(L + A)}\,, \qquad (20)$$

where μ denotes the friction coefficient, W denotes the half width of the friction loop $W = (M_u - M_d)/2)$, Δ denotes the friction loop offsets ($\Delta = (M_u + M_d)/2$) and the subscripts s and f denote sloped and flat surfaces, respectively (see also Fig. 9 below). By solving Eq. 9 for μ_s two possible mathematical solutions are provided (for any given load and adhesion), corresponding to two values of the friction calibration factor α. Since α must be identical for sloped and flat surfaces, we obtain μ_f from Eq. 20. The physical solution stands for μ_s and $\mu_f < 1/\mathrm{tg}\theta$.

In Fig. 9, topographic and lateral force data obtained on a universally applicable standard specimen is shown that enables one to accurately calibrate

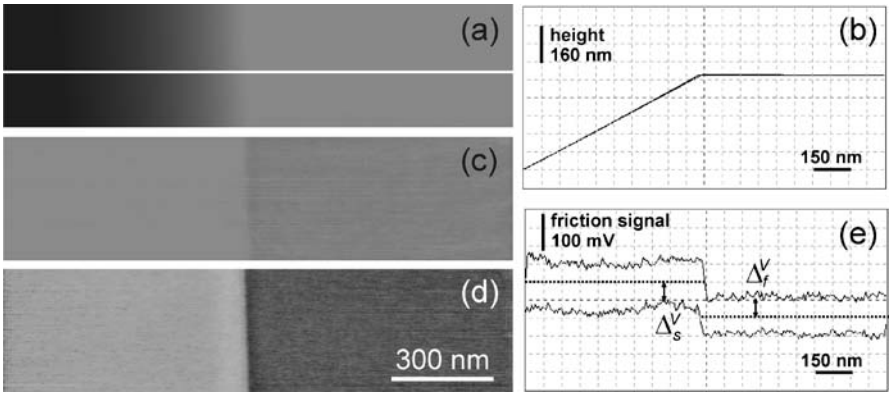

Fig. 9 Example of experimental data measured with a Si_3N_4 tip on both sloped and flat surfaces: **a** topography image (vertical scale from *black* to *white* 800 nm), **b** cross-section of topography (vertical scale 800 nm), **c** difference friction image (trace – retrace, vertical scale 0.5 V), **d** off-set of the friction loops (trace + retrace, vertical scale 0.5 V) and **e** friction loop corresponding to cross-section shown in *panel b* (the off-sets for sloped and flat surface, Δ_s and Δ_f, respectively, have been marked). (Reprinted with permission from [91]. © (2006) American Chemical Society)

all types of AFM cantilevers and tips for quantitative friction force measurements.

Using this standard and the improved wedge calibration method, calibration factors can be calculated with an error of ca. 5%. The approach is not affected by an additional small sample tilt, different feedback settings, and a possible tip position off the central cantilever axis, as is frequently observed. Only laser light interference and non-spherical tip apex shapes must be taken into account. To illustrate the accuracy of the calibration procedure, nanotribological results obtained on well-defined micropatterned monolayer surfaces are shown in Fig. 10. Despite the fact that the tips/cantilevers used had a different geometry (V-shaped and single beam) and were microfabricated using different materials (Si_3N_4 and Si, respectively), the friction coefficients determined under identical conditions are to within the experimental error the same.

Another important aspect of LFM for its application studies of polymer relaxations and surface dynamics is the controlled variation of temperature and scan velocity, which is related to the frequency of the experiment (see Sect. 1.1) [30]. Temperature and the environment can be controlled and/or modulated using environmental chambers purged with thermostatted gasses of controlled composition and relative humidity (%RH). In addition, heatable sample stages have been applied to control the sample temperature (heatable probe tips are treated in Sect. 2.4). Typical piezoelectric materials used in the AFM scanner withstand temperatures of <60 °C and %RH < 65% (see specifications of the particular material used), which limits the range of at-

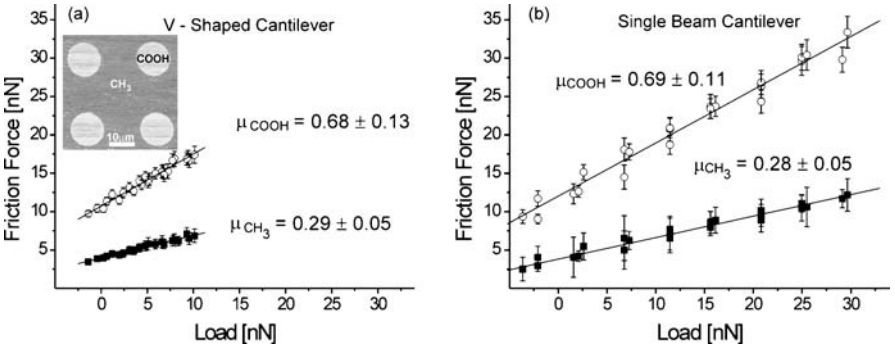

Fig. 10 Friction force versus load for a micropatterned SAM sample (exposing $-CH_3$ and $-COOH$ head groups, respectively, see *inset* in **a**) measured using two different Si_3N_4 cantilevers: **a** V-shaped and **b** single beam, with scanning velocity of 40 $\mu m\,s^{-1}$ at 50% RH and 25 °C. The *solid lines* correspond to linear least squares fits. The *error bars* indicate the standard deviation ($n = 128$) of the data analyzed for a given load (Adapted and reprinted with permission from [91]. © (2006) American Chemical Society)

tainable conditions. The frequency can typically *not* be varied over a broad range while keeping nanoscale resolution using the piezo transducer of the AFM, due to increased noise level, inaccurately operating feedback loop and decreasing pixel resolution as a result of large scan sizes. As an alternative, additional sample actuation stages based on stacked shear piezos [92] or other actuators, such as quartz crystal microbalances [93], have been reported, which allow one to achieve scan velocities of >1.0 $\mu m\,s^{-1}$ and $\sim 10^{-1}$ $m\,s^{-1}$, respectively (for an example, see Fig. 11).

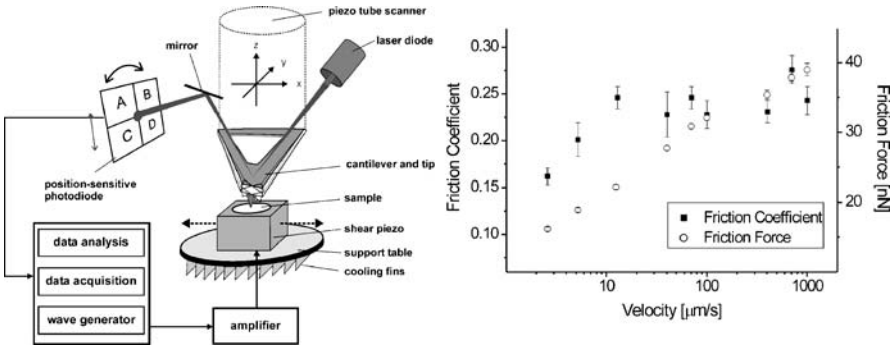

Fig. 11 **a** Schematic of a high velocity AFM set-up comprising a commercial stand-alone atomic force microscope, the high velocity accessory and peripheral devices for accessory operation, data acquisition and signal processing (not to scale). **b** Friction coefficient for oxidized Si(100) and Si_3N_4 tip as a function of velocity measured in a nitrogen atmosphere (<3% RH) at room temperature (25 °C). (Reprinted with permission from [92]. © (2005) American Institute of Physics)

According to Sect. 1, the investigation of friction and surface dynamics of polymers requires careful control of the temperature and the frequency (rate) of the experiment. In addition, the acquired data must be quantitative and hence robust calibration methods must be applied (see above). On top of these requirements a number of important aspects must be considered in the analysis of friction force microscopy data. Comparisons among data from different labs is only viable, if all these points have been taken into account.

One crucial issue is the difference between the *load* applied with the LFM cantilever and the total force in the surface normal direction in the nanoscale contact, the so-called *normal force*. The normal force is defined as the sum of load and adhesion force (e.g. assessed in a f–d experiment, see Sect. 2.3.1). Since friction force and contact area are directly related for single asperity contacts, it is important to take this effect into account, as well as the effect of different contact pressure. The forces due to capillary condensation between tip and sample can be avoided by operation of the AFM in vacuum or under conditions of dry inert gas.

The pressure is given by the normal force divided by the (experimentally not determined, i.e. unknown) true tip–sample contact area. The latter quantity is critically related to the radius of curvature of the probe tip. The value of this radius, which must be carefully calibrated, also determines the time during which tip and sample interact. Such a calibration can be performed by analyzing electron microscopy images or AFM images taken on a reference grating exposing very sharp spikes of known radius of curvature (Fig. 12).

Finally, although noted by various authors to be difficult, care must be taken to ensure an operation in the elastic regime. Local plastic deformation of the polymer sample specimen must be avoided, because in this case ploughing terms (Eq. 4) must be considered as well.

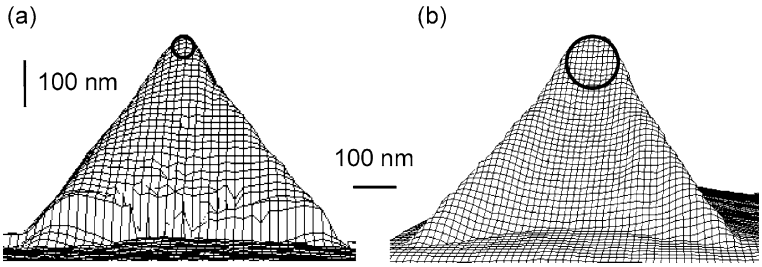

Fig. 12 Images (obtained by contact mode AFM on a calibration grating) of **a** a sharp and **b** a flat tip apex. The tip radii r determined for **a** and **b** were 25 nm and 60 nm, respectively. (Reprinted with permission from [91]. © (2006) American Chemical Society)

2.2
Other Scanned Probe Methods to Assess Polymer Relaxation Phenomena

2.2.1
Shear Modulation Force Microscopy (SM-FM)

In shear modulation force microscopy (SM-FM) a sharp probe tip, which is kept in contact with the sample (typically applied load is on the order of nN to tens of nN), is laterally modulated with a nanometer scale amplitude Δx_i (Fig. 13). This amplitude is chosen such that any tip–sample slipping is avoided. Therefore SM-FM is considered a non-scanning technique. Non-scanning conditions are important to avoid significant scanning-induced changes in the tip–sample contact area. Using lock-in techniques, the modulation response, Δx_R, is analyzed relative to Δx_i. For a small (in-plane) lateral displacement for a sphere-plane geometry (assuming the absence of slip), the lateral stiffness of the contact $k_{c,x}$ is provided as [94–96]:

$$k_{c,x} = 8aG^* \tag{21}$$

with

$$G^* = \left(\frac{2 - \nu_1^2}{G_1} + \frac{2 - \nu_2^2}{G_2} \right)^{-1}, \tag{22}$$

with the radius of the contact area a, the shear moduli of the sample and the probing tip G_1 and G_2, respectively, and the corresponding Poisson's ratios ν_1

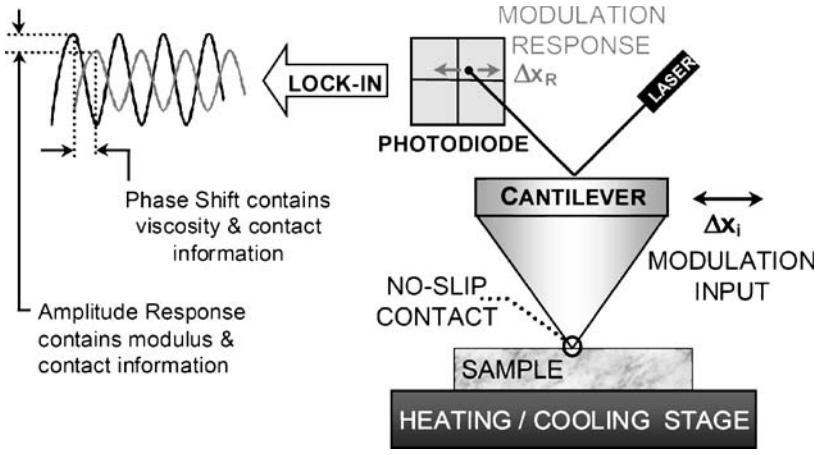

Fig. 13 Schematic diagram of a shear modulation force microscopy experiment. (Reproduced with kind permission of Springer Science and Business Media from [96]. © (2005) Springer)

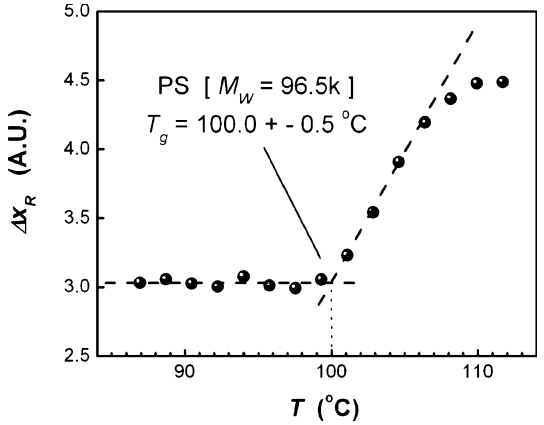

Fig. 14 Determination of the glass transition temperature of polystyrene by SM-FM: modulation amplitude response vs. temperature plot. (Reproduced with kind permission of Springer Science and Business Media from [96]. © (2005) Springer)

and ν_2 [17]. The total lateral elastic constant $k_{\mathrm{tot,x}}$ can be written as:

$$\frac{1}{k_{\mathrm{tot,x}}} = \frac{1}{k_{\mathrm{c,x}}} + \frac{1}{k_{\mathrm{T}}}, \tag{23}$$

where $k_{\mathrm{c,x}}$ and k_{T} denote the lateral contact stiffness and the torsional cantilever stiffness, respectively.

As for most AFM approaches, the true contact area (radius a in Eq. 21) is difficult to assess and the precise determination of the cantilever stiffness k_{T} limits the overall accuracy of the data. Sills and Overney pointed out that these shortcomings are not relevant for simple thermorheological studies (e.g. the determination of T_{g}). In a typical experiment, the stationary AFM tip rests on the polymer (with a pre-set load). The sample temperature is increased in small increments and following equilibration the response Δx_{R} is measured. The tip–sample contact area thus changes only as a consequence of temperature-induced changes, e.g., in the polymer's modulus. A plot of Δx_{R} versus temperature exhibits a "kink" at a temperature assigned to T_{g} (Fig. 14).

2.2.2 Scanning Viscoelasticity Microscopy (SVM)

A related technique, termed scanning viscoelasticity microscopy (SVM) was introduced by Kajiyama and co-workers (Fig. 15). SVM is a (scanning) contact mode AFM technique; similar to SM-FM (Sect. 2.2.1) the sample is modulated with several kHz, albeit in surface *normal* direction [97]. When the tip exerts a force on the surface (corresponding to a deflection characteristic for

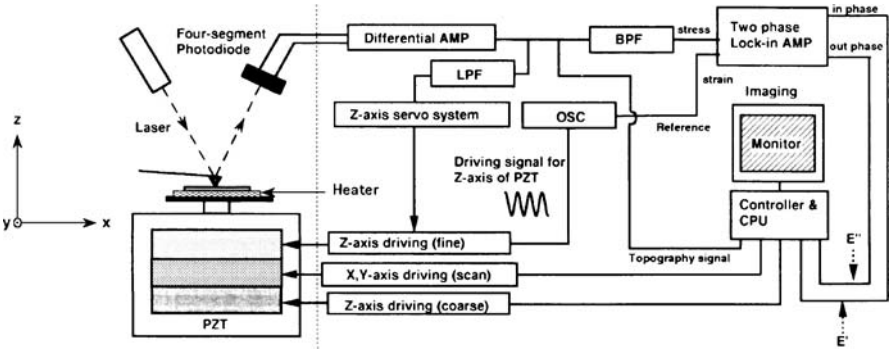

Fig. 15 Schematic of scanning viscoelasticity microscopy used for imaging of dynamic viscoelasticity by AFM. (Reprinted with permission from [97]. © (1994) American Chemical Society)

the repulsive force region of a f–d curve), the sample surface is deformed by the tip. The vertical modulation of the sample position results in a concomitant modulation of the cantilever deflection, which depends on viscoelastic properties of the sample. The phase difference between the modulation signal of the sample position and the modulated response of the tip corresponds to the mechanical loss tangent, $\tan\delta$, of the probed surface region.

2.2.3
Force Modulation Microscopy (FMM)

Force modulation mode (FMM) AFM is a contact mode technique that allows one to resolve lateral differences in modulus [98, 99]. In FMM AFM, the cantilever is excited by a bimorph to oscillate at a frequency of tens of kHz (which is below its resonance frequency), while it scans the surface in contact mode. By monitoring the oscillation amplitude, the elastic modulus of the surface can be mapped with high resolution. Depending on the corresponding moduli, the contrast in the amplitude image reveals high modulus (i.e. large amplitude) and low modulus (i.e. lower amplitude) areas [100]. Recently, the use of frequency dependent FMM AFM has been described, where selective contrast can be achieved in heterogeneous systems [101, 102]. A practical limitation for the approach in the field of polymers is the fact that shear forces, similar to contact mode, may cause sample damage or distortion of the underlying morphology.

2.2.4
Scanning Local Acceleration Microscopy (SLAM)

In scanning local acceleration microscopy (SLAM) the position of the sample is modulated at frequencies *above* the highest system resonance [103].

This provides, as shown in the literature, the clearest difference in cantilever response for the variations in elastic modulus of stiff samples. Experimentally, to a standard AFM set-up a high-frequency transducer is added, which is positioned underneath the sample. The ultrasonic vibrations, generated by a high frequency function generator connected to the transducer, are transmitted through the sample and are detected via the AFM cantilever. The signal is sent to a lock-in amplifier and the output of the lock-in is utilized to generate an image simultaneously captured with the conventional AFM (height) image. Using a small-amplitude continuous sine wave, to which the cantilever responds sinusoidally, provides access to spatially resolved variations in the interaction stiffness, which is related to the elastic modulus of a stiff sample.

2.2.5
Torsional Resonance (TR) Mode AFM

Torsional resonance (TR) mode AFM is a recently introduced AFM mode that exploits the torsional resonance amplitude (or phase) of a stiff cantilever to control the feedback loop (i.e. to maintain the tip/surface relative position through lateral interaction) [104]. This mode provides complementary information to intermittent contact (tapping) mode for surface imaging and studies. The nature of tip/surface interaction of the TR mode facilitates phase measurements to resolve in particular the in-plane anisotropy of materials, as well as measurements of dynamic friction at nanometer scale. Recently, various models have been proposed to extract useful physicochemical parameters, thus paving the route to quantitative measurements of contact stiffness, elastic moduli and friction, from the data [105, 106].

2.3
Normal Force Techniques

2.3.1
Force–Distance Curves and Determination of Pull-Off Forces

The interactions between the tip and the sample surface can be measured using the force spectroscopy mode of AFM [107, 108]. In the experiment the sample is moved up and down (in and out of contact with the tip). A schematic force–displacement curve ("force curve") thus obtained is shown in Fig. 16.

During the approach (loading) part (position 1–2), no interactions occur between the tip and the sample surface. As the tip-surface distance becomes sufficiently small, the gradient of the attractive force overcomes the cantilever spring constant and brings the tip in contact with the sample surface (position 3). Further approaching causes a deflection of the cantilever (position 3–4). The unloading part of the force–displacement curve starts from pos-

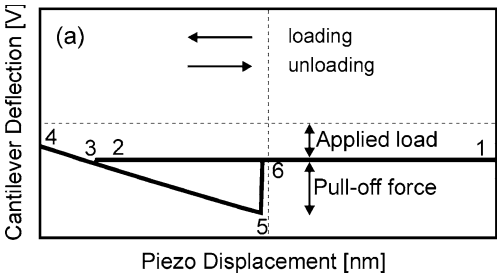

Fig. 16 Schematic AFM force-displacement curve

ition 4, the deflection of the cantilever is decreased as the sample surface retracts from the tip. When the sample surface is further withdrawn from the tip, the cantilever is deflected owing to adhesive forces. At position 5, the elastic force in the cantilever overcomes the force gradient and the tip snaps off

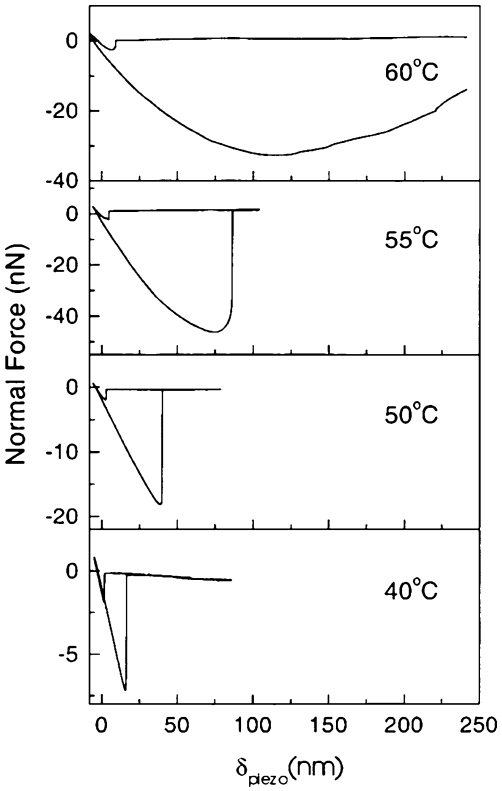

Fig. 17 *f*–*d* curves obtained at different temperatures on a poly(*tert*-butyl acrylate) film at constant probe rate $f = 125$ Hz. (Reprinted with permission from [109]. © (2000) American Chemical Society)

from the surface (position 6). From position 6 to 1, the cantilever returns to its equilibrium position. The adhesion between tip and sample is characterized by the so-called pull-off or pull-out force (snap off). The pull-off force is related in current continuum contact mechanics models to the work of adhesion, which may, in the case of polymers, be temperature and rate-dependent (compare Eqs. 9 to 12). In addition, neck formation between the polymer and the retracting probe may alter the f–d curves in a characteristic manner (see Fig. 17) [109].

2.3.2 Indentation Measurements

In the f–d measurements discussed in the previous section one can also analyze the part of the curves corresponding to tip–sample contact. Using these so-called AFM indentation measurements the Young's modulus of the underlying polymer sample can be determined as a function of temperature and loading rate (∼frequency). As alluded to above, one records f–d curves employing a cantilever with appropriate spring constant (stiffness lever ∼ stiffness sample). The f–d curves can be analyzed according to various indentation models, e.g. the Hertz model (Sect. 1.2), to calculate the Young's

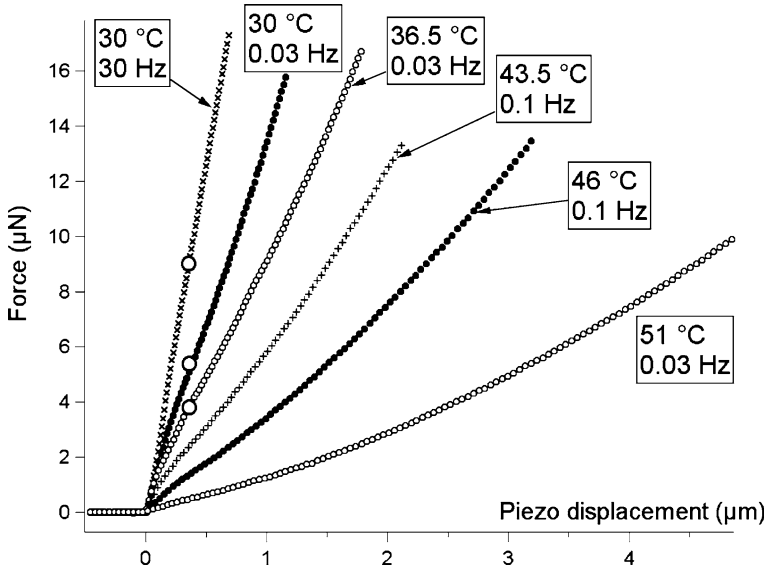

Fig. 18 Approach parts of the f–d curves recorded on poly(n-butyl methacrylate) samples at various rates and temperatures. The different slopes of the indentation curves represent different moduli of the polymer (T_g = 22 °C). (Reprinted with permission from [110]. © (2005) American Chemical Society)

modulus. At the glass transition temperature, the modulus will change by several orders of magnitude, as mentioned. Hence the T_g in polymer films and its possible dependence on various factors, including film thickness, relative humidity (with water as a plasticizer) etc. can be quantitatively captured [110].

2.4
Scanning Thermal Microscopy

In scanning thermal microscopy a heatable probe tip is used. Early examples include relatively blunt probes (the area of this heat source is approx. 1 μm × 0.25 μm) comprising a Wollaston wire (Fig. 19a). More recently, microfabricated heatable cantilever/probe tip assemblies have become commercially available that push the resolution to the sub-100 nm scale due to their sharp integrated tips (Fig. 19b) [111, 112]. Using such probes, the indentation of the probe into the polymer can be recorded as a function of temperature. Hence, transitions, such as the glass transition, can be inferred from the softening of the polymer. However, as has been noted, tip penetration and polymer expansion may, depending on the load and the contact area, lead to an upwards bending of the lever [113].

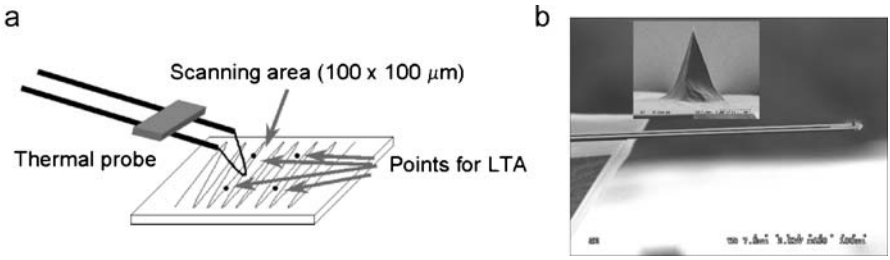

Fig. 19 **a** Schematic of a local thermal analysis experiment using a Wollaston wire probe equipped with a mirror. Within the scanned area the probe may record phase changes in the polymer film via heated tip-induced changes in modulus. (Reprinted with permission from [113]. © (2005) American Chemical Society). **b** SEM image of the microfabricated thermal probes for high resolution thermal analysis (*inset*: SEM image of the actual probe tip). (Reproduced with kind permission from Anasys Instruments Inc.)

3
Friction and Surface Dynamics of Polymers on the Nanoscale

Dynamic friction on polymers has a large contribution from internal viscoelastic dissipation, which is ultimately related to polymer relaxation processes. Using the experimental approached briefly introduced in Sect. 2, var-

ious aspects of friction and surface dynamics ranging from fundamental studies of chain dynamics and glass temperatures in ultrathin polymer films to the mapping of multiphase systems can be addressed.

In particular, one can differentiate friction and chain dynamics at the surface of polymers vs. the bulk, relaxations in (ultra)thin film systems (confinement effects), interface effects such as pinning and possible effects of sample history. Despite a large body of literature the current view on these issues is still controversial, thus known approaches must be refined and new approaches must be developed to provide additional insight to contribute to solve the open questions (for suggested behavior see Fig. 20).

In this context it is important to reiterate that relevant data can only be obtained if the measured quantities are assessed quantitatively (i.e. proper calibration is required) and that all important external factors are controlled and have been taken into consideration. This refers to the elastic vs. plastic contact regime, the load vs. normal force issue, the contact pressure (incl. tip radius) as well as control of both temperature and true frequency (scan rate and tip–sample contact length) etc. In particular, it is also necessary to consider the penetration or information depth of a particular method. To be able to assess, e.g., the proposed 1–2 nm thin surface layer of reduced density (Fig. 20), care must be taken to probe this very layer and not the film interior. In parts, these requirements mandate new technical developments, such as the mentioned velocity control using external high rate actuators, that became only recently available.

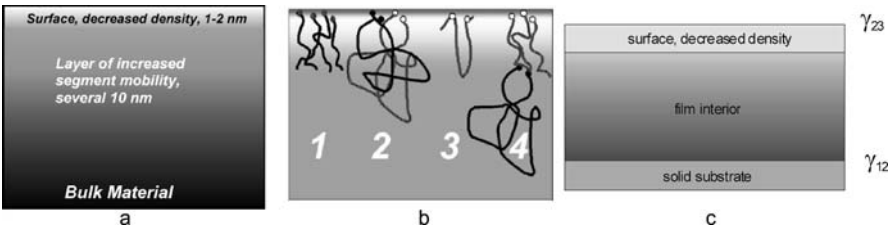

Fig. 20 **a** Schematic of the surface of a glassy polymer that possesses a thin layer of reduced density at the surface followed by a layer of increased mobility of polymer segments changing smoothly to the bulk material. **b** Schematic depicting possible mechanisms of lowering the T_g close to surfaces: (*1*) excess free volume induced by surface enrichment of end groups, which causes an enhanced mobility of chain segments and a lower polymer segment density, (*2*) confinement of polymer chains for polymers with high M_n which causes a break in symmetry at polymer surfaces (flattened chain conformation) and chain confinements in films with $d < R_g$, (*3*) increased collective motions along the chain (loop motions), which require a weaker free volume and does not involve chain ends, (*4*) enrichment of low molecular weight fraction at the surface. (Reprinted with permission from [113]. © (2005) American Chemical Society). **c** Interfacial interactions in (ultra)thin films characterized by the substrate–polymer interfacial free energy and the polymer–air interfacial free energy

3.1 Mapping of Multiphase Systems

An obvious application area of AFM that relies on friction and surface dynamics is the study of heterogeneous systems. While there are many AFM modes that combine high spatial resolution with a contrast mechanism that is sensitive to a particular polymeric phase in a multiphase system (e.g. intermittent contact mode phase imaging, which is sensitive to differences in energy dissipation) [114], LFM, SVM, f–d curve acquisition as well as other AFM modes provide in some cases better access to maps of the local viscoelastic properties. These maps in turn yield access to estimates of surface coverages, morphologies and localization of particular components in complex multiphase systems.

In the so-called chemical force microscopy (CFM) approach [115, 116], in which AFM tips exposing defined surface chemistry are utilized to assess differences in surface chemical composition using e.g. local friction differences (related to interactions between functional groups or atoms exposed on both tip and sample surface as contrast), different polymers have been successfully differentiated. Examples include the differentiation of polyamide-rich regions from poly(ethylene glycol)-rich regions in a blocky segmented copolymer using self-assembled monolayer-coated tips reported by Sinniah et al. [117] and differentiation of a phase-separated blend of polystyrene (PS) and poly(methyl methacrylate) imaged with gold-coated and silicon oxide coated tips in perfluorodecalin [118]. In this latter work Feldman et al. exploited the selective amplification of the dispersive van der Waals interactions in perfluorodecalin to obtain predictable interactions and thus contrast.

Werts et al. reported on successful CFM imaging of the microphase-separated domain structure in PS-poly(vinyl pyridine) hetero-arm star copolymer, thus implying a lateral resolution of better than $\sim$30 nm [119]. The friction contrast measured in an argon atmosphere was well-pronounced with a carboxylic acid-functionalized tip, as shown in Fig. 21.

Using conventional LFM, phase-separated blends of PMA and PMMA, i.e. components possessing T_g's that are close to (287 K) and far above (390 K) the temperature at which the experiment was carried out (295 K), were studied by Lee [120]. While PMMA did not show a dependence of lateral force on scan rate (at a constant load of 5 nN), PMA showed a monotonically decreasing behavior. These observations are consistent with the interpretation that in the glassy state the elastically deformed surface is immediately recovered and the dissipated energy is small. By contrast, for the PMA, at a temperature close to its bulk T_g, a substantial fraction of the energy involved in the deformation at the contact is dissipated. Thus, in phase-separated blends, the two phases were distinguished in scan rate-dependent measurements.

Cappella and Kaliappan measured force–displacement (f–d) curves on PS/PnBMA blends (sandwich of PS and PnBMA) as a function of tempera-

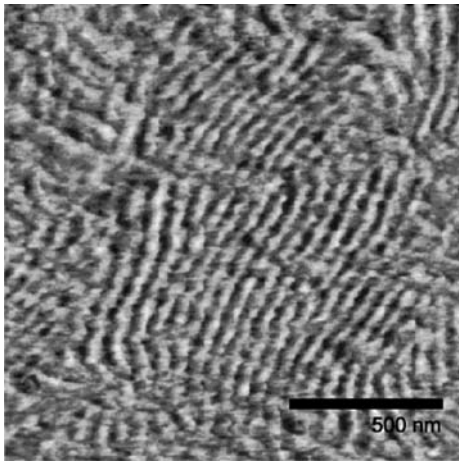

Fig. 21 Friction force image (1.5 μm×1.5 μm) obtained by means of CFM with a COOH tip. Using this tip functionality the friction coefficient is higher for the PVP part of the copolymer, which reveals the morphology as the alternating *bright* (high friction, PVP) and *dark* (low friction, PS) areas. (Reprinted with permission from [119]. © (1998) Wiley-VCH)

ture. In their experiments these authors focused on the determination of local mechanical properties (Young's modulus) of these polymers with a spatial resolution of 800 nm, i.e. on the influence of morphology on the mechanical properties of the model blend/sandwich structure in the vicinity of the interface. Exploiting a new analysis technique based on Hertz theory (Sect. 1.2), the corresponding moduli were obtained. A transition region was revealed (Fig. 22), where the Young's modulus decreases gradually from the value of PS to the value of PnBMA [121].

On bilayer films composed of PS (top layer) and PI (lower layer) Satomi and coworkers studied how far buried layers influence the surface viscoelasticity as assessed by scanning viscoelasticity microscopy (SVM). The surface dynamic storage modulus, E', decreased with decreasing thickness of the upper PS layer due to the contribution from the soft underneath PI layer once the upper layer thickness fell short of 70 nm. On the contrary, surface E' was invariant for the bilayer with a thicker upper layer. These results indicate that the stimulus displacement imposed propagates to a depth of at least 70 nm along the surface normal at room temperature [122].

The elastic and viscoelastic properties blends of PP and ethylene-propylene (EP) were investigated with the force modulation technique by Nysten et al. In addition to a mapping of the distribution of the rubbery nodules of EP at the surface, the sub-surface distribution of these nodules could be estimated [123, 124]. While the FMM data yielded qualitative data, more recent indentation mapping based on force-displacement curves al-

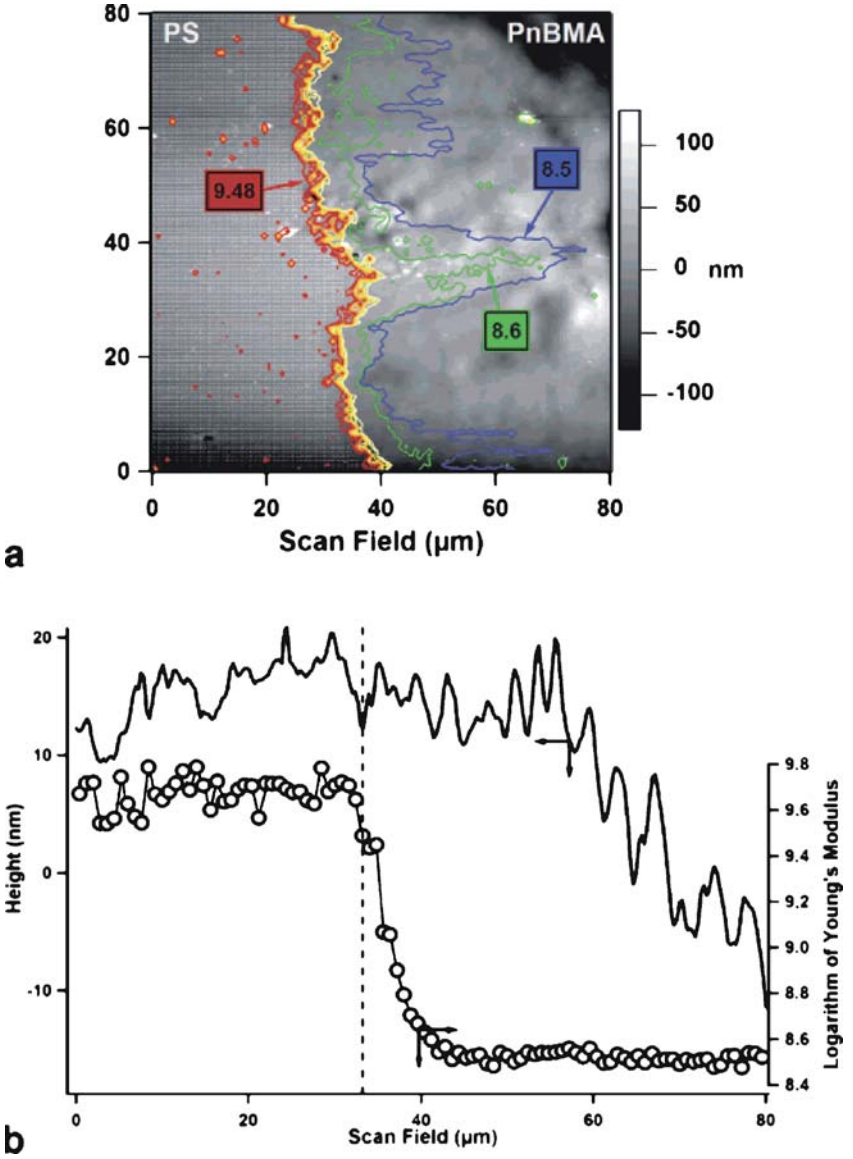

Fig. 22 **a** Topographic image (*gray scale*) of the model blend at the interface at 57.4 °C and superimposed profiles of $\log(E) = 9.48$ (*dark red line*), down to $\log(E) = 9$ (*light yellow line*), in steps of 0.08 (*lines of increasing brightness*, very close to each other and bunched together at the interface). Also the profiles of $\log(E) = 8.6$ (*green line*) and of $\log(E) = 8.5$ (*blue line*) are shown. **b** Line profile of the topography (referred to *left axis*) and of $\log(E)$ (referred to the *right axis*) of the model blend across the interface. It can be seen that there is no discontinuity in the topography at the interface and also that the topography does not influence the determined Young's modulus. (Reprinted with permission from [121]. © (2006) American Chemical Society)

lowed Nysten et al. to obtain quantitative information of the surface elastic modulus [125].

The application of different AFM modes to measure the nanoscale elastic and viscoelastic properties of PMMS/rubber nanocomposites was reported by Cuberes et al. [126] In particular, heterodyne force microscopy (HFM) with ultrasonic force microscopy, FFM and force modulation microscopy were compared. The authors concluded that the combination of different AFM-related techniques helped to interpret the images with respect to the rather complex local structure of the polymer blend in rubber toughened PMMA. Amplitude-HFM resolved differences in local sample stiffness due to the presence of rubber in the near-surface region, while phase-HFM distinguished small differences in viscoelastic and/or adhesion hysteresis response time of PMMA on top of the rubber.

Oulevey et al. discussed dynamic mechanical analysis at sub-micrometer scales based on experiments with local DMA and variable temperature scanning local acceleration microscopy (SLAM) [127]. Primary and secondary relaxations in various polymer materials (PES/SAN and PS/PMMA blends, also PMMA, PS and PTFE) were observed as a function of temperature. The lateral resolution of SLAM was reported to be better than 100 nm.

3.2
Polymer Relaxations, Chain Dynamics and Viscoelasticity

One important fundamental question to be answered is related to the difference of chain dynamics among the bulk and the surface. Using various LFM and related approaches polymers can indeed be probed at the surface and down to various depths; thus this and other related issues can be directly addressed. Depending on the operation conditions and thus indentation depth, AFM probes a given polymer sample always at the surface and may sample into the near-surface region of reduced density (Fig. 20). These measurements have immediate practical relevance as in polymer films, for instance, the structural, material, and transport properties become increasingly dominated by interfacial, conformational, and dimensional constrains, when the thickness is reduced to the sub-100 nm scale (see Sect. 3.3) [1–3]. In addition, rheological gradients near the interfaces can lead to a behavior that deviates from the bulk. Relaxation properties can be influenced and enhanced conformational stability may be achieved through control of the interfacial conditions, molecular weight, crosslinking density, and film thickness [3, 28].

On the basis of fluorescence microscopy data obtained on sandwich samples [128, 129] or in single-molecule fluorescence measurements [130] an improved understanding of the dynamics in thin and ultrathin polymer films, and in particular the role of the interfaces (compare Fig. 20) has emerged. The depression or increase in glass transition temperature, as a confinement ef-

fect of thin substrate-supported polymer films (discussed in more detail in Sect. 3.3), has been attributed by various authors to effects that stem from the substrate–polymer and polymer–vacuum interface, respectively. These studies revealed that the enhancement of dynamics at the free film surface may affect T_g several tens of nanometers into the film [128]. These observations of enhanced mobility of macromolecules at the film surface also point to lowered activation energies and increased frequencies of the relaxation processes involved (compare Figs. 1 and 2).

Studies of polymer relaxations, chain dynamics and viscoelasticity at the surface by AFM-based approaches rely on different types of experiments, in which, depending on the authors, different parameters were determined and different effects that interfere with the interpretation of the data were taken into account. In the following we will review the central results obtained in investigations that targeted mainly the α-transition (T_g), but also various sub-T_g transitions (β, γ). To exclude effects of the underlying solid substrate, films with thicknesses of 100 nm or larger are considered.

Pu et al. studied PS films on silicon with shear modulation force microscopy (SMFM) and concluded that the surface T_g, determined in amplitude vs. temperature plots (Fig. 23), is not different from the bulk under the conditions investigated [131]. In addition, these authors show that the values of the T_g's obtained for samples of various thicknesses do not depend to a noticeable extent on the load applied, which was varied by a factor of 3, the modulation frequency and drive amplitude over a substantial range.

These data are supported by work of Sills et al. who determined surface T_g values in LFM measurements by analyzing friction force-velocity isotherms

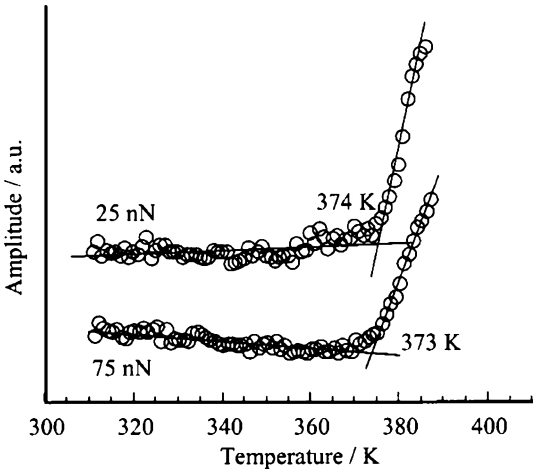

Fig. 23 ΔX vs. temperature curves for PS (M_w = 1230 k) in a thick film on silicon at applied loads of 25 and 75 nN. The T_g was determined from the analysis of the kinks shown (reproduced from [131]. © (2001) American Chemical Society)

and application of the time–temperature superposition principle. From the master plot and an Arrhenius plot of the shift factors an activation barrier of 81 kcal mol^{-1} was determined that coincides with the (bulk) value 80–90 kcal mol^{-1} for the α-transition in PS (96.5 kg mol^{-1}) [132]. In a different study the γ-relaxation (rotation of phenyl groups) was interrogated by Sills and Overney in atactic PS by LFM at different temperatures and scanning velocities (Fig. 24). The activation energy thus determined (E_a = 7 kcal mol^{-1}) was similar to reported bulk data [133].

A similar conclusion was reached by Kaliappan and Cappella, who also studied PS, albeit in force–displacement measurements. From data acquired at different temperatures and tip approach/retraction rates the Young's moduli and the yielding forces were determined. The calculated WLF coefficients for temperatures above T_g and the activation energy below T_g exhibited good agreement with published (bulk) literature values [134].

Similarly, Bliznyuk et al. determined the glass transition of PS (M_n from 3900 to 1 340 000, polydispersity 1.05–1.15) via the acquisition of f–d curves at various temperatures [135]. The values of the surface glass transition reported by these authors for the samples with $M_n > 30\,000$ were also consistent as the corresponding bulk values. However, low molecular mass polymers were concluded to behave differently. Chain entanglement variations were held responsible for the observed surface T_g depression effect rather than the end group localization at the free surface.

Hence several independent measurements concluded that the glass transition temperature in PS (except for possibly low molar mass) is *not* altered in the probed surface-near region. The probed depth is in all these studies a function of the tip radius and, more importantly, the applied load. The load, as shown in Fig. 23, was for the SFMM experiments substantial. Similarly, in the studies of Sills and co-workers, as well as Kaliappan and Cappella a sig-

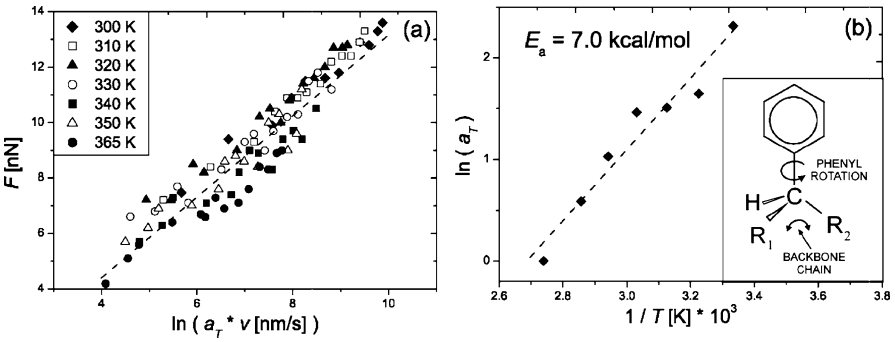

Fig. 24 **a** Superposed friction master curve; **b** thermal shift factor a_T. An activation energy E_a of 7.0 kcal mol^{-1} is deduced from the slope of the regression line, corresponding to the activation of phenyl rotation in atactic PS (*inset*). (Reprinted Figure with permission from [133]. © (2003) by the American Physical Society)

nificant contribution of the adhesive force to the normal force of 91 nN and loads of several μN, respectively, were reported.

Similar to these data on PS, several groups reported unaltered surface T_g values for PtBuA and PnBMA, relying on adhesion measurements at different temperatures and probe rates, and the subsequent application of the time–temperature superposition principle on the one hand [109], and the determination of the Young modulus and yielding force in the vicinity of T_g, as a function of temperature and/or probe rate, on the other hand [110]. These reports thus also support the notion that the molecular relaxation of the polymer sample at the free surface, under the conditions probed, is not noticeably different than that of the bulk.

In contrast to these reports, the group of Kajiyama has reported in numerous publications on the enhanced macromolecular mobility observed at the surface of polystyrene films and the dependence of the observed decreased surface T_g on factors, including molar mass, chain-end chemistry and structure, entanglements and polydispersity [136–139]. For example, in 200 nm thick films of monodisperse PS (M_n from 4900–1 460 000, and binary PS blends with different M_n) on silicon measurements of the lateral force (under an applied load of 10 nN) vs. temperature at a given scan rate indicated that the surface T_g of the PS films was markedly lower than the corresponding bulk T_g over the entire molecular weight range. The surface T_g was determined from the maximum observed in friction force vs. temperature plots (Fig. 25a). In addition, the apparent activation energy of the surface segmental motion in PS was determined as 230 ± 10 kJ mol^{-1}, which is significantly smaller than the reported bulk value that ranges from 360 to 880 kJ mol^{-1} (Fig. 25b,c). Finally, these authors showed a surface enrichment of the shorter chain component in the blend films that becomes more pronounced with an increasing molar mass dispersity between the two components due to entropic effects [140]. Consistent observations of depressed surface T_g values as assessed by the same group using SVM were also reported [139], as well as direct SVM observation of a softening in monodisperse PS films on Si that were partly scratched by a blade [141].

The results of Kajiyama et al. are in line with the data of Hammerschmidt et al. who concluded, based on velocity and temperature-dependent LFM measurements, a lowered surface T_g for PS [30]. These authors also measured the friction force between a Si tip and a PMMA surface for four different velocities between 2 and 220 μm s^{-1}. A peak in friction force was observed for measurements at 25 °C, which shifted towards higher velocities at increasing temperatures. This peak was attributed to the β-relaxation process (compare Fig. 1). These authors also observed a lower activation energy for this process as compared to reported bulk values (50 kJ mol^{-1} vs. 71–96 kJ mol^{-1}). However, this process attributed to the β-relaxation occurred at a similar temperature and a similar frequency as in the bulk, which is apparently inconsistent with the concluded higher mobility at the surface (compare Fig. 2).

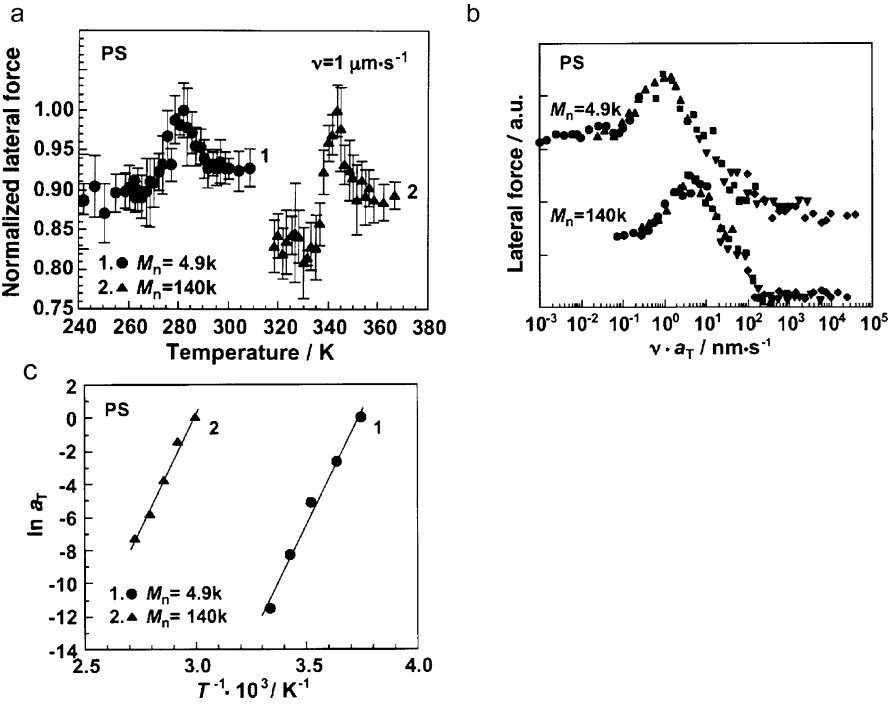

Fig. 25 **a** Typical lateral force/temperature curves at a given scanning rate. Curves for PS with $M_n = 4900$ or $M_n = 140\,000$ at a scanning rate of $1\,\mu m\,s^{-1}$ are displayed. The bulk T_g values measured by DSC are 348 and 376 K, respectively. **b** Master curves of the scanning rate/lateral force relationship for PS films drawn from each curve in Fig. 4. Reference temperatures of 267 and 333 K have been used for PS with $M_n = 4900$ and for PS with $M_n = 140\,000$, respectively. **c** Semi-logarithmic plots of a_T versus the reciprocal absolute temperature (T^{-1}) for PS films with $M_n = 4900$ or $M_n = 140\,000$. (Reprinted with permission of John Wiley & Sons Inc. from [140]. © (2004) John Wiley & Sons Inc.)

The experimental work in this early report may have been restricted by the small range of attainable scan velocities and the limited number of data points. More recent work, in which among others the rigorous calibration of the LFM setup, an enhanced range of scan velocities without compromised noise and data resolution, and the control of all relevant experimental parameters have been implemented, confirm some of these early observations (see below).

Importantly, the paper by Hammerschmidt and co-workers successfully utilized a means to convert the scan velocities to frequencies by considering the tip–sample contact length [142, 143]. For temperatures below T_g this approach can be applied to normalize the scan velocities by simple division of the velocity by this contact length. This approach also implies that the tip radius is a decisive factor in determining the ***frequency*** of the experiment for

constant experimental conditions (temperature, velocity etc.). In fact, by systematic variations in tip radius, a large range of frequencies can be covered with a given range of scan velocities. For comparisons with bulk data the knowledge of the corresponding frequencies is crucial.

As shown in Fig. 26, the friction force vs. velocity relationship assessed for a 125 nm thick PMMA film depends on the temperature of the experiment, as reported by Tocha, Schönherr and Vancso. In these experiments the applied normal forces were limited to $\leq$1 nN to ensure that the surface of the film to a depth of $\leq$2 nm was probed. In addition, care was taken to confirm the absence of ploughing. A clear maximum is observed that shifts to higher velocities with increasing temperature, in accordance with the time–temperature superposition principle (see also Fig. 2).

Data acquired with probes that possessed different tip radii showed a markedly different behavior. This is evident for selected data shown in Fig. 27, in which the data was converted to interfacial shear stress vs. frequency by considering the contact area (estimated according to the JKR model) and the contact length, respectively [46]. Before the conversion to frequency (data not shown), the data showed no consistent monotonic (or other behavior). Only after the mentioned transformation is it obvious that the data acquired with probes with widely different radii belong to different parts of the friction force–velocity phase space. From these data it becomes evident that a large range of frequencies from Hz to MHz was probed using tips with different radii. Low frequencies were accessed in experiments with large tip radii, whereas high frequencies were characterized using sharp probes.

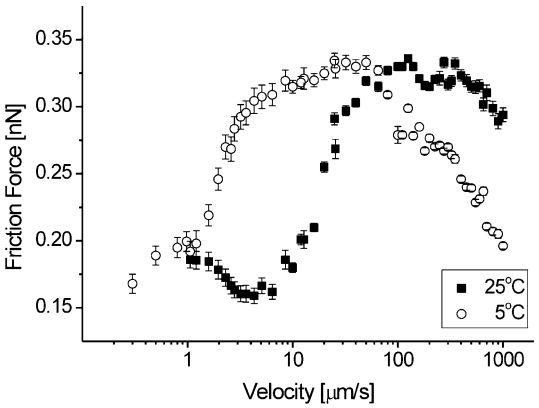

Fig. 26 Semi-log plot of friction force vs. velocity for PMMA film on oxidized silicon (thickness 125 nm) measured with an oxidized silicon tip (R = 20 nm) in nitrogen atmosphere (<5% RH) at various temperatures: 25 °C and 5 °C. A load of 0.2 nN was maintained constant during the measurements. The error bars indicate the standard deviation of the data analyzed for a given velocity (n = 150)

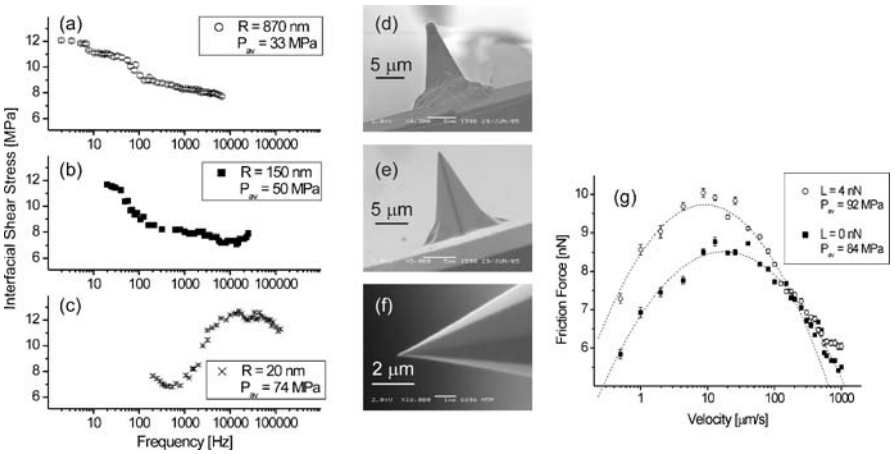

Fig. 27 Effect of different tip radii on interfacial shear stress vs. frequency for PMMA film on oxidized silicon (thickness 125 nm) measured in nitrogen atmosphere (<5% RH) at 26 °C (tip radii: **a** 870 nm, **b** 150 nm, and **c** 20 nm). In **a**, **b**, and **c** loads of 2 nN, 2 nN, and 0.2 nN, respectively, were maintained constant during the measurements. The error bars indicate the standard deviation of the data analyzed for a given velocity ($n = 150$). SEM images of the tips with radii (**d** $R = 870$ nm, **e** 150 nm, and **f** 20 nm). **g** Observed effect of different contact pressure on friction force vs. velocity for PMMA films on oxidized silicon (thickness 125 nm) measured with a Si_3N_4 tip ($R = 35$ nm) in nitrogen atmosphere (<5% RH) at 26 °C. The error bars indicate the standard deviation of the data ($n = 150$) analyzed for a given velocity. The transformation of velocity to frequency was performed using the procedure introduced in the previous section

In addition to these corrections, the effect of the different contact pressures (as a consequence of the different tip radii) on the measured relaxations must be accounted for (Fig. 27g). As shown, for increased load the peak observed was shifted horizontally to lower velocities. This observation is ascribed to the effect of the contact pressure exerted by the tip, which hinders locally the motion of the chain and rotation of the side groups (see below). Thus, the relaxation shifts to lower frequencies, which is similar to the effect observed with decreasing temperature (compare Fig. 2). The influence of pressure on the relaxation temperature was estimated from the value of the activation energy, assuming a value of 35 kJ mol^{-1} (for a tip with 20 nm radius). The approximated increase of the relaxation temperature of 0.5 °C MPa^{-1} is in good agreement with the effect of hydrostatic pressure (~0.35 °C MPa^{-1}) [41, 145]. Therefore, an increase as high as 20 °C can be expected for the same relaxation probed with the sharp tip ($R = 20$ nm), as compared to the large tip ($R = 870$ nm) at the same applied force.

The presence or absence of pressure induced shifts in LFM and related experiments has similar to the question of altered surface T_g's been a controversial issue in the literature. Dinelli et al. argued that pressure-induced

changes in the determined T_g can be excluded [146]. The local pressure applied by an LFM tip was thought to be insufficient to generate a pressure effect that results in an increase in the apparent T_g. In fact, at a constant velocity, the apparent T_g was found to decrease and to approach the bulk value with increasing load. At a fixed load, the apparent T_g was found to decrease, as expected, and to approach the bulk value with decreasing velocity. Dinelli et al. assigned the shift in T_g to "the dynamic nature of the experiment" and not to an actual change in material property, as would be the case for a hydrostatic pressure. In addition, for very thin PS films (thickness 17–50 nm) no pressure effects were observed in SMFM measurements [147].

By contrast, an elevation in the apparent glass transition temperature for PS was reported by Schmidt et al. [148, 149]. This finding was attributed by the authors to a reduction of the free volume in the polymer due to large compressive stress beneath the sliding probe. Similarly, for PP, Gracias et al. reported a T_g that was 20 °C higher for a sharp probe as compared to a large probe due to greater pressure, in accordance with PVT data [150]. In these experiments, the authors did not correct for changes in the contact length which in turn affect the velocity (see above).

Selected friction force vs. velocity master curves constructed from data obtained in experiments with tips with different radii are displayed in Fig. 28. The data were shifted according to the time–temperature superposition principle to a reference temperature of 26 °C to afford the corresponding activation energies. When compared to bulk relaxations, two relaxations can be distinguished: one of lower frequency (higher temperature) and one of higher frequency (lower temperature). These relaxations are attributed to the α and the β processes in panels (b) and (a), respectively.

The observed peak in Fig. 28a is located in the MHz range, as is evident after the conversion of velocity to frequency (compare Fig. 27 and [144]) and

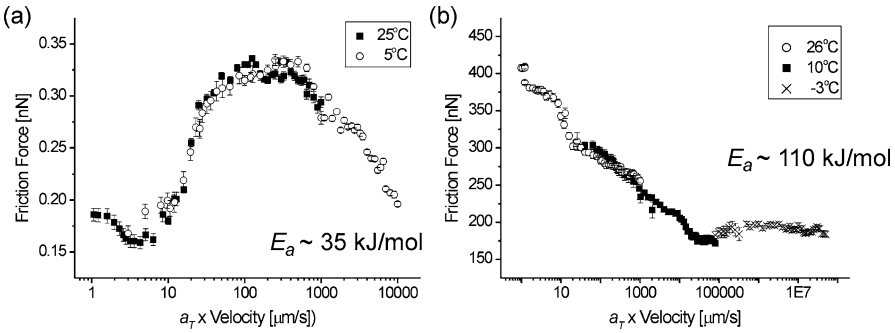

Fig. 28 Masterplot constructed according to the time–temperature superposition principle of friction force vs. velocity for PMMA film on oxidized silicon (thickness 125 nm) measured **a** with an oxidized silicon tip (R = 20 nm) and **b** with an oxidized silicon tip (R = 870 nm) in nitrogen atmosphere (<5% RH) at various temperatures

was assigned to the β-relaxation of PMMA. This relaxation is the result of the rotation of the $-(CO)OCH_3$ side groups around the C – C bonds linking the side groups to the main polymer chain [41]. The value of the corresponding activation energy of $\sim$35 kJ mol^{-1} is significantly lower than the bulk value (71–96 kJ mol^{-1}) determined by mechanical and dielectric methods [29]. Furthermore, the frequency of the β-relaxation is significantly higher (10^6 Hz) than the frequency detected in bulk measurements (10–100 Hz) at room temperature [144]. Both the higher frequency and lower activation energy indicate greater free volume and correspondingly higher mobility at the polymer surface.

The part of the relaxation curve detected at lower frequencies (1–10^4 Hz) is attributed to the α-transition. From the changing slope of the curve, the maximum can be anticipated at around 1 Hz. The curve is expected to possess a bell shape. However, due to increasing ploughing and plastic deformation it was impossible to measure the bend at low velocities (frequencies). This additional component to friction force is known to change the shape of the relaxation curve [33]. In other LFM experiments published in the literature these effects have mostly not been appropriately taken into account.

The estimated activation energy of 110 kJ mol^{-1} observed is significantly lower than the bulk value (334–460 kJ mol^{-1}) and the relaxation frequency is noticeably higher compared to the bulk (f = 1 Hz, T = 26 °C and f = 1 Hz, T = 100 °C, respectively) [29]. The overlap of curves characteristic for the α and β relaxations was observed at a frequency of about 2×10^4 Hz at 26 °C [144], which is noticeably lower in temperature in comparison with bulk mechanical studies ($f = 2 \times 10^4$ Hz, T = 50 °C) [29]. The determined activation energy of 60 kJ mol^{-1} is influenced by both α and β processes due to their different activation energies and shift factors. Thus, the resultant shift factor (activation energy) will be a superposition of α and β processes. These observations of low activation energies and higher relaxation frequencies are consistent with the reported greater free volume at the polymer–air interface [151].

The combined approach of a high velocity actuator and control of tip–sample contact length allowed Tocha et al. to probe the α and the β relaxations of PMMA at 26 °C, which is significantly below the bulk T_g [144]. The central advantage of this method, as compared to the friction force studies carried out at variable temperature only, is that significant artifacts due to changes in the materials properties (Young's modulus, adhesion, scratch resistance) associated with the glass transition can be circumvented. For PMMA a fully consistent picture has thus emerged, in which significantly lowered activation barriers and increased frequencies coincide, as expected based on the time–temperature superposition principle.

Consistent with this interpretation is the report by Hammerschmidt et al. who studied the effect of water on the friction force measured, among other materials, on PVOH films. The friction data acquired at different scan veloci-

ties was converted to frequency as discussed above by dividing the velocity by the tip–sample contact diameter. Water was found to act as a plasticizer for PVOH, as expected. The temperature at which a particular relaxation occurred was lowered with increasing water content, which is equivalent to decreasing relaxation times [143].

Deviations from behavior that would be expected on the basis of the time–temperature superposition principle were attributed to triboheating effects. The energy dissipated in the contact between tip and sample was assumed to locally increase the temperature, which explains the observed decrease in friction force with increasing scan size (0.2–150 μm) for the scan rates less than ~500 $\mu m\, s^{-1}$ in LFM measurements on gelatin films. It was further demonstrated that the heating effect could cause position shifts in a friction peak (which was presumed to be the glass transition of the gelatin film) [152].

Similarly, in PtBuA, the friction vs. velocity peak observed in LFM experiments was found to shift towards higher scan rates as the external load was increased. Similar friction peaks shifted to the low-temperature side when the external load was increased or the scan size decreased. In all cases, the observed shifts in the friction peak are consistent with an effect from heating [153].

3.3
Thin Films and Confinement Effects

As mentioned in Sects. 1 and Sect. 3.2, polymer relaxations can be affected by confinement effects and the presence of interfaces. Depressed or elevated T_g's in ultrathin films exemplify this effect [10, 11]. In addition, it has been reported, for instance, that the structural, material, and transport properties become increasingly dominated by interfacial, conformational, and dimensional constrains, when the thickness is reduced to the sub-100 nm scale [146, 154, 164]. For such ultrathin films, depending on the thickness, crystallization kinetics and degree of crystallinity [8, 155, 156], phase behavior [157–159], morphology [160], permeability [7], or dewetting [9] may be altered, among other properties.

The interface of polymer films with vacuum or air results according to Torkelson and coworkers in increased mobility at this interface [128]. The depth to which this effect can be detected inside the film depends on nanoconfinement, as elucidated in detailed fluorescence spectroscopy studies with layered polymer thin films systems. AFM measurements have also provided novel insight into thin film and confinement effects, i.e. to unravel how far the behavior of polymers is changed when polymer chains reside for instance near interfaces or are confined in ultrathin films.

In a detailed study on the effect of film thickness on the glass transition temperature, Fryer et al. acquired data with scanning thermal probe microscopy and compared these with ellipsometry measurements. The ad-

vantage of using different methods is obvious since changes in complementary properties are being detected. In ellipsometry the thermal expansion of the film is assessed, while scanning thermal probe microscopy probes e.g. the change in film modulus via the cantilever deflection induced by the thermal probe [161]. As shown in Fig. 29, the cantilever deflects markedly when the PS film softens, hence the onset of the T_g can be assessed [161].

In Fig. 30, two different scenarios are compared: PS (left) and PMMA (right) on SiO_2 and hydrophobized SiO_2. For film thicknesses below ~50 nm an altered T_g was detected. In accordance with the ellipsometry data (and reported literature data), non-interacting surfaces and interacting surfaces led to the depression and the increase in T_g, respectively.

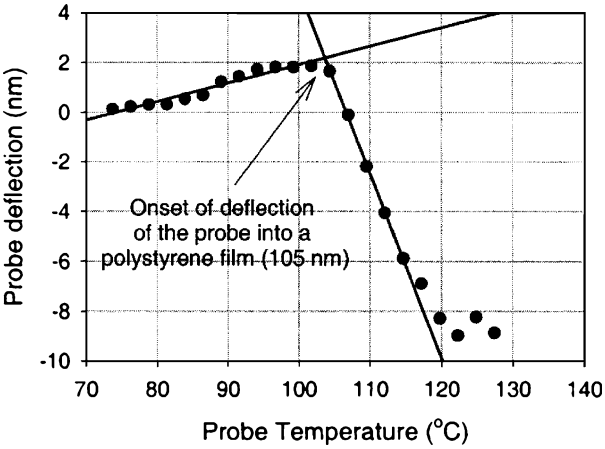

Fig. 29 Plot of the thermal probe deflection vs. temperature measured on a 105 nm thick film of PS on a hydrophobized substrate. (Reproduced with permission from [161]. © (2000) American Chemical Society)

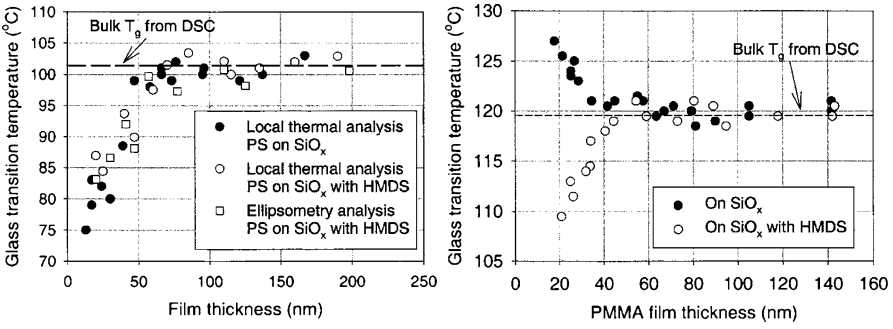

Fig. 30 Values of T_g determined for PS (*left*) and PMMA (*right*) ultrathin films on various substrates. (Reprinted with permission from [161]. © (2000) American Chemical Society)

The group of Kajiyama reported, as already mentioned in Sect. 3.2, indications of a lowered T_g at the film surface. In LFM experiments, a lateral force peak corresponding to the surface α-relaxation process of segmental motion was observed at a temperature much lower than the bulk T_g. For thinner films (3–4 the radius of gyration of the unperturbed chain) the peak on the lateral force vs. temperature curve broadened out with decreasing film thickness and eventually split into two peaks. The T_g determined was independent of the film thickness. On the other hand, the apparent activation energy was altered [162].

By contrast, Ge et al. observed by SMFM for PS films with a thickness between 17 and 500 nm that the value of T_g is equal to the bulk value and is independent of the film thickness for thicknesses exceeding 17 nm. In addition, the strength of the substrate-polymer interactions was shown to play no role. Even a free standing film on a 10 μm hole did not show a different T_g according to these data [147], even though ellipsometry data on free-standing films suggested substantial depressions [163].

Overney and coworkers investigated PS films on hydrogen passivated Si, as well as on OTS and PVP coated Si. These latter surfaces were chosen as model surfaces for low interaction interfaces. The reported LFM and shear modulation mode AFM data suggested that T_g for thick films corresponds to the bulk value. However, for film thickness below 200 nm, confinement effects due to the close substrate and the film preparation technique can significantly alter the phase of polymer. For films thinner than 150 nm, T_g was found to be elevated. Below 20 nm, no T_g was found. For low interaction interfaces, PS on PVP and OTS, T_g was independent of film thickness [164]. As shown in Fig. 31 (left), the friction force measured at constant load decreased when the film thickness is less than a critical thickness t_{c1}. The adhesive forces (data not shown here) did not depend on film thickness. The authors show that

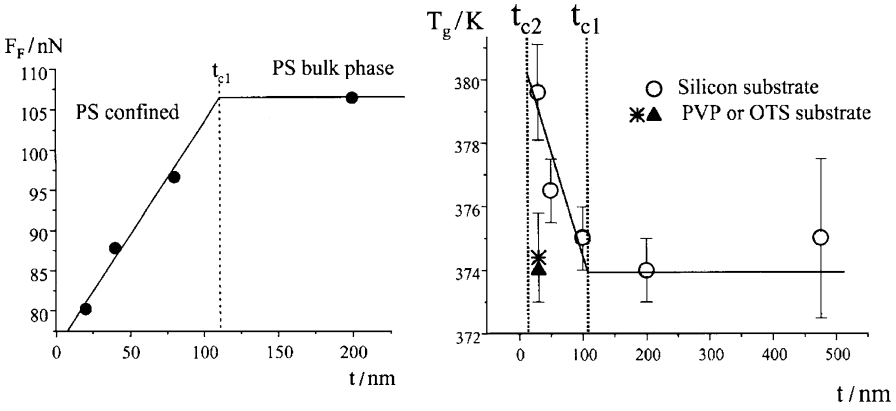

Fig. 31 Values of friction force (*left*) and T_g (*right*) vs. film thickness determined for PS on various substrates. (Reproduced with kind permission of Springer Science and Business Media from [164]. © (2000) Kluwer Academic Publishers)

such a decrease in friction goes along with an increase in the elastic modulus, i.e. the PS film is constrained within a boundary regime of thickness t_{c1} towards the substrate surface. For films with a thickness between t_{c1} and t_{c2} (boundary regime) the glass transition was found to be elevated (Fig. 31, right). Below t_{c2} no glass transition was detected (sublayer regime).

Another example of interfacial confining effects, observed for spin-coated films of PnBMA was reported by these authors (Fig. 32). For film thicknesses below 50 nm the T_g was found to be elevated.

These data were rationalized by the occurrence of an increased lateral disentanglement of polymer chains that is caused during the spin-coating process. Temperature-driven annealing was deemed to be not successful in the case of interactive interfaces. Thus, the heterogeneous structure is established normal to the substrate and effectively creates a property gradient in the polymer matrix. For films with a thickness below 150 nm, the T_g increases with decreasing distance to the substrate interface, while for thicknesses of 20 nm and less a transition is no longer observable.

Work by Wang and Ishida on PVME (thickness 5–400 nm) employing LFM and adhesion measurements as a function of scanning rate and film thickness also demonstrated confinement effects. When the film thickness falls below 200 nm, the lateral force of the PVME films decreases with decreasing film thickness, consistent with the data by Overney et al. on PS (see above), and becomes less dependent on the scanning rate. Local adhesion measurements indicate that the adhesion force per unit area increases with the decreasing film thickness. These results are consistent with each other and point to an increased polymer stiffness and decreased polymer chain mobility due to the confinement in the ultra-thin films [165].

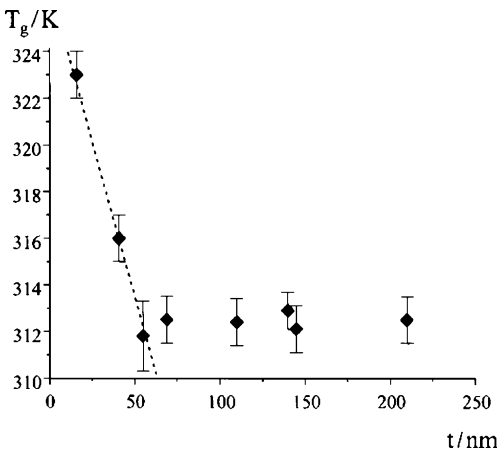

Fig. 32 Values of T_g vs. film thickness determined for poly(*n*-butyl methacrylate). (Reproduced with kind permission of Springer Science and Business Media from [164]. © (2000) Kluwer Academic Publishers)

For PtBuA (thickness 10–133 nm) Wang et al. reported negligible differences in the dynamic behavior between the bulk and the free surface of ultrathin films $d > 15$ nm. These authors analyzed f–d curves acquired at different temperatures and different probe rates. The adhesion master curves and shift factors thus obtained showed no dependence on the film thickness. However, for $d < 15$ nm samples, a suppression in shift factors was found that becomes more pronounced as d decreases. These data are consistent with the existence of an immobile component in the layer of polymer next to the substrate wall and long-range effects from the substrate that influence the surface segmental mobility [166].

These different reports clearly show that the range of the effects mentioned may differ depending on the interaction of the polymer with the substrate, the overall film thickness, but also the sample history and chain entanglements.

3.4 Anisotropy of Friction and Different Wear Modes and Tribological Behavior

Many examples in the literature show that plastic deformation even of glassy polymers, such as polystyrene, may occur under relatively modest loads in CM-AFM experiments. As summarized in Fig. 33, the formation of more or less regularly spaced ridges perpendicular to the fast scan direction is observed in a typical contact mode AFM scan (here the slow scan axis was disabled). The amplitude of the ridges increases over time (from top to bottom) and it is obvious that instead of analyzing the underlying amorphous polymer, the surface is being modified by the scanning AFM tip [167].

The time–temperature dependence of the patterns is well described by the WLF equation, which is typically used to describe viscoelastic behavior of polymers. The detailed analysis of the data further suggested an increased T_g

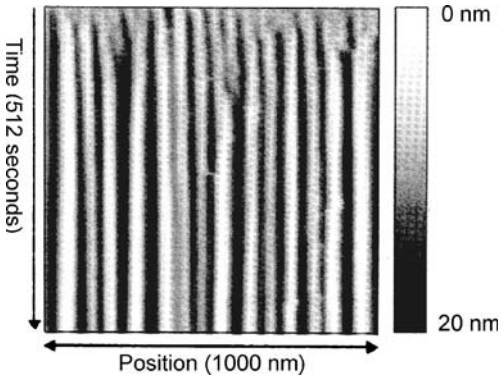

Fig. 33 Formation of parallel ridges on PS imaged by CM-AFM under a load of 30 nN. The slow scan axis (down scan) was disabled hence the vertical axis corresponds to time. (Reprinted from [167] with permission from Elsevier. © (1999) Elsevier)

derived from elevated pressure beneath the tip [8]. As alluded to in previous sections, the onset of plastic deformation may complicate the analysis of friction forces as ploughing terms need to be considered in addition to interfacial friction.

On the molecular level, stick-slip motion has been observed, similar to atomic-scale stick slip on e.g. mica [168] and graphite [169]. An illustrative example of molecular stick slip for polymers has been reported for friction forces measured on PTFE [170, 171]. As shown in Fig. 34, the stick-slip motion corresponds to the molecular corrugations of the PTFE chains. Similar observations have been reported for polyethylene [172]. For such extended-chain crystals maximum friction was observed perpendicular to and minimum friction for scan parallel to the chain direction, respectively. This friction anisotropy can be rationalized in terms of the cobblestone model (interlocking asperity model) of interfacial friction described e.g. by Israelachvili and coworkers [173, 174].

The tip–sample frictional interaction as measured by AFM may also depend upon the molecular/atomic orientation and structure of the interface in a measurable fashion for materials other than atomically smooth atomic or molecular crystals [175, 176]. An impressive example of friction anisotropy was found for a thiolipid monolayer on mica by Liley et al. [177]. These authors observed a flower-shaped structure, formed by domains with different molecular orientation. The dependence of friction force on scanning direction suggested that molecules possess a radial tilt, which is directed towards the center of the "flower".

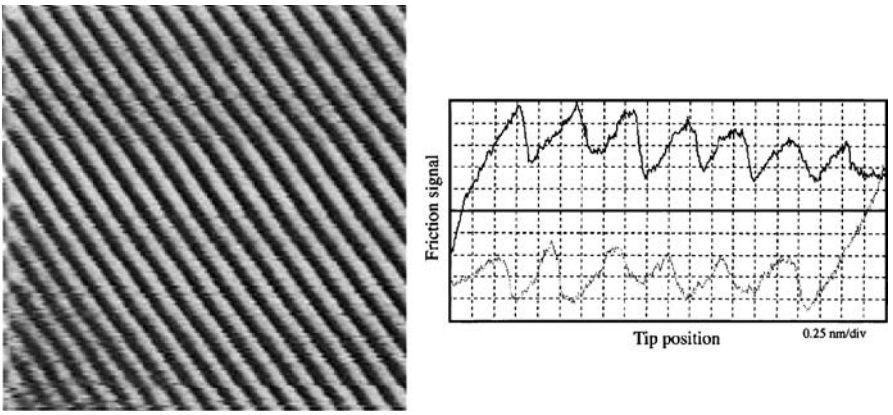

Fig. 34 *Left*: lateral force microscopy image of PTFE deposited on muscovite mica showing molecular resolution. Scan size: 10.7 nm × 10.7 nm; (scan direction: 55° with respect to the chain direction); *right*: a typical LFM scope trace showing a friction loop. Scanning proceeds from left to right on the *top line* (trace) and from *right* to *left* following the *bottom line* (retrace). Scanning was performed at 66.3° with respect to the chain direction. (Reprinted with permission from [170]. © (1996) American Chemical Society)

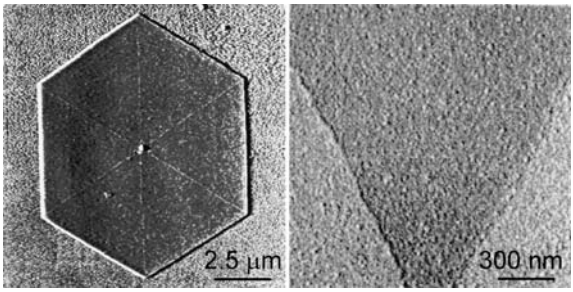

Fig. 35 Lamellar crystals of poly(oxymethylene) with clearly resolved chain fold domains at the surface of the lamellae defined by the diagonals and the edges of the crystals. The frictional force within the domains, obtained in AFM experiments, was found to depend on the relative scan direction. (Reprinted from [180] with permission from Elsevier. © (1994) Elsevier)

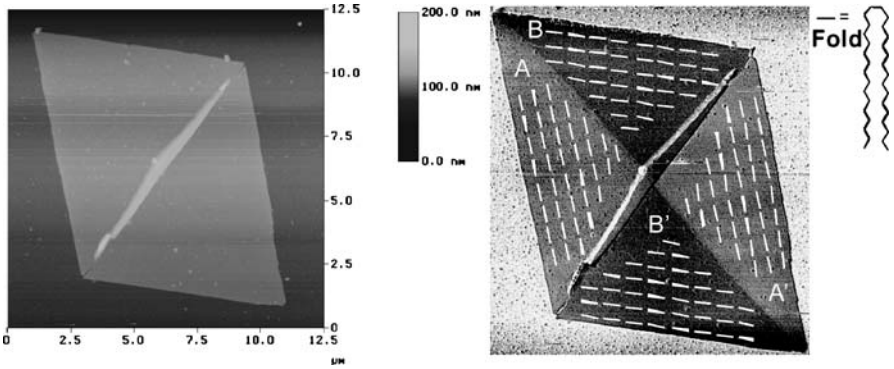

Fig. 36 *Left*: height image of a collapsed PE lamella; *right*: friction image of the same PE crystal including schematic drawing of fold direction. (Reprinted with permission from [174]. © (1999) American Chemical Society)

For polymers anisotropic friction was in particular unveiled at the surface of lamellar polymer crystals (see Figs. 35 and 36), including poly(oxymethylene) [174, 178] and polyethylene [174, 179, 180], as well as on oriented PTFE and PE films [170, 174]. The anisotropic friction for lamellar crystals is explained by the occurrence of chain-folding oriented preferentially in planes parallel to the corresponding growing crystal face.

4 Outlook

The recent results and reports in the area of friction of polymers and its relation to polymer chain dynamics and relaxations, as reviewed above, do

not only show the renewed interest in important fundamental aspects of polymer science, but reflect the challenges met and to be addressed in current and future technology. This refers in particular to (ultra)thin polymer films and coatings, as well as polymer-based devices and processes with submicrometer to nanoscale dimensions. As alluded to throughout this article, interfacial and confinement effects play an increasingly important role on these length scales. These may become determining factors that are critical for reliable device performance or error-free fabrication processes, hence the corresponding effects and phenomena become part of the engineering of polymer materials in these areas.

It is thus fair to conclude that precise material engineering with polymers on the nanoscale is only possible with an understanding of the polymer dynamics near interfaces. Hence, the characterization and control of thin films and interfacial boundary layers become vitally important for nanotechnological applications, such as nano-electromechanical systems (NEMS) for terabit thermomechanical storage, protective coatings, adhesives and lubricants that rely on very specific relaxation and transition properties in sub-100 nm systems [23, 24, 181]. As shown, the widespread application of proximal scanning probe methods also underlines the importance of (local) probing of (macro)molecular dynamics, e.g. near the glass transition.

The recent significant progress regarding the instrumental and technical sophistication of these measurements, including truly quantitative measurements and analyses of the acquired data, controlled tip–sample interactions, and the realization of a broad range of temperatures and scan rates (also considering the relation of tip radius and actual frequencies) promise rapidly progressing insight. These developments are and will be complemented by implementing increasingly realistic experimental conditions (to be able to relate nanoscale and macroscale tribology for instance), including, for example, controlled chemistry (tribochemistry) and controlled media.

Similarly important are advances and progress in modeling and simulations, which are not within the scope of this review. In general, complementary AFM experiments and molecular dynamics (MD) simulations now facilitate the study of contact areas of similar dimensions (since MD recently increased the number of atoms or molecules involved in the contact), but still differ drastically in the time scale of the measurements. MD simulations are currently limited to timescales no greater than tens of nanoseconds and length scales of tens of nanometers, which are insufficient for analyzing many tribological systems [182]. Similarly, a gap can be identified between molecular or atomistic models on the one hand, and continuum (e.g. contact mechanics) approaches that describe the deformation between elastic single asperities on the other hand. Consequently, fundamental aspects of friction and the mechanisms of energy dissipation are poorly understood on a first-principles level. Multi-level experiments (from micrometer to nanometer scale) are clearly required to advance the understanding of tribology.

Work on the necessary bridge between micro- and nanotribology, as well as atomistic and continuum models has only recently begun to emerge.

It is beyond doubt that the mentioned combination of experiment and theory is critically important to reach any of the targets and aims named above. The problem of bridging the gap of length and time scales thus not only refers to AFM-type approaches in relation to polymer dynamics and friction, but also refers to simulations and the development of a congruent picture that encompasses both experimental and theoretical results.

Acknowledgements This work has been financially supported by the Dutch Technology Foundation STW (STW-project 5287, Nanoscale wear-resistant ceramic materials with low friction) and the European Office of Aerospace Research & Development (EOARD) of US-AF.

References

1. Bhushan B (ed) (1999) Handbook of Micro/Nano Tribology. CRC Press, New York, p 371
2. Meyer E, Overney RM, Dransfeld K, Gyalog T (1998) Nanoscience: Friction and Rheology on the Nanometer Scale. World Scientific, Singapore
3. Williams ML, Landel RF, Ferry JD (1955) J Am Chem Soc 77:3701
4. Kato T, Kawaguchi M, Sajjad MM, Choi J (2004) Wear 257:909
5. Soles CL, Lin EK, Lenhart JL, Jones RL, Wu WL, Goldfarb DL, Angelopoulos M (2001) J Vac Sci Techn B 19:2690
6. Alcoutlabi M, McKenna GB (2005) J Phys Cond Matter 17:R461
7. Pfromm PH, Koros WJ (1995) Polymer 36:2379
8. Despotopoulou MM, Frank CW, Miller RD, Rabolt JF (1996) Macromolecules 29:5797
9. Reiter G (1993) Europhys Lett 23:579
10. Keddie JL, Jones RAL, Cory RA (1994) Europhys Lett 27:59
11. Forrest JA, DalnokiVeress K, Stevens JR, Dutcher JR (1996) Phys Rev Lett 77:2002
12. Roth CB, McNerny KL, Jager WF, Torkelson JM (2007) Macromolecules 40:2568
13. Jones RAL, Richards RW (1999) Polymers at Surface and Interfaces. Cambridge University Press, Cambridge, UK
14. Sillescu H (1999) J Non-Crystalline Solids 243:81
15. McClelland GM, Glosli JN (1992) In: Singer IL, Pollock HM (eds) Fundamentals of Friction: Macroscopic and Microscopic Processes. Kluwer, Dordrecht, p 405
16. Colchero J, Meyer E, Marti O (1999) In: Bhushan B (ed) Handbook of Micro/Nano Tribology. CRC Press, New York, p 273
17. Johnson KL (1985) Contact Mechanics. Cambridge University Press, Cambridge
18. Carpick RW, Ogletree DF, Salmeron MJ (1999) Coll Interf Sci 211:395
19. Binnig G, Quate CF, Gerber C (1986) Phys Rev Lett 56:930
20. Colton R J, Engel A, Frommer J E, Gaub H E, Gewirth A A, Guckenberger R, Rabe J, Heckl W M, Parkinson B (1998) Procedures in Scanning Probe Microscopies. Wiley, New York
21. Carpick RW, Salmeron M (1997) Chem Rev 97:1163
22. Ferry JD (1980) Viscoelastic Properties of Polymers. Wiley, New York
23. Lutwyche MI, Despont M, Drechsler U, Dürig U, Häberle W, Rothuizen H, Stutz R, Widmer R, Binnig GK, Vettiger P (2000) Appl Phys Lett 77:3299

24. Dürig U, Cross G, Despont M, Drechsler U, Häberle W, Lutwyche MI, Rothuizen H, Stutz R, Widmer R, Vettiger P, Binnig GK, King WP, Goodson KE (2000) Tribol Lett 9:25
25. Cagin T, Che JW, Gardos MN, Fijany A, Goddard WA (1999) Nanotechnology 10:278
26. Granick S, Lin Z, Bae SC (2003) Nature 425:467
27. Flory PJ (1969) Statistical Mechanics of Chain Molecules. Interscience Publishers, New York
28. Sperling LH (1985) Introduction to Physical Polymer Science. Wiley, New York
29. McCrum NG, Read BE, Williams G (1967) Anelastic and Dielectric Effects in Polymeric Solids. Wiley, London
30. Hammerschmidt JA, Gladfelter WL, Haugstad G (1999) Macromolecules 32:3360
31. Young RJ, Lovell PA (1991) Introduction to Polymers. Chapman & Hall, London
32. Cherry BW (1981) Polymer Surfaces. Cambridge University Press, Cambridge
33. Grosch KA (1963) Proc R Soc London Ser A—Math Phys Sci 274:21
34. Ardi MS, Dick W, Kubat J (1993) Coll Polym Sci 271:739
35. Bergman R, Alvarez F, Alegria A, Colmenero JJ (1998) Chem Phys 109:7546
36. Sane SB, Knauss WG (2001) Mech Time-Depend Mater 5:293
37. Sane SB, Knauss WG (2001) Mech Time-Depend Mater 5:325
38. de Deus JF, Souza GP, Corradini WA, Atvars TDZ, Akcelrud L (2004) Macromolecules 37:6938
39. Schmidt-Rohr K, Kulik AS, Beckham HW, Ohlemacher A, Pawelzik U, Boeffel C, Spiess W (1994) Macromolecules 27:4733
40. Dubek G, Lupke T, Stejny J, Alam MA, Arnold M (2000) Macromolecules 33:990
41. Gedde UW (1999) Polymer Physics. Kluwer Academic Publishers, Dordrecht
42. Israelachvili JN, Berman AD (1999) In: Bhushan B (ed) Handbook of Micro/Nano Tribology. CRC Press, New York, p 371
43. Homola AM, Israelachvili JN, McGuiggan PM, Gee ML (1990) Wear 136:65
44. Bowden FP, Tabor D (1966) Brit J Appl Phys 17:1521
45. Hertz HJ (1882) Reine Angew Math 92:156
46. Johnson KL (1997) Proc R Soc London Ser A—Math Phys Eng Sci 453:163
47. Johnson KL (1996) Langmuir 12:4510
48. Muller V, Derjaguin BV, Toporov YP (1983) Coll Surf 7:251
49. Derjaguin BV, Muller V, Toporov YP (1980) J Coll Interf Sci 73:293
50. Derjaguin BV, Muller V, Toporov YP (1978) J Coll Interf Sci 67:378
51. Derjaguin BV, Muller V, Toporov YP (1978) J Coll Interf Sci 53:314
52. Maugis DJ (1992) Coll Interf Sci 150:243
53. Tabor DJ (1977) Coll Interf Sci 58:2
54. Schwarz UD (2003) J Coll Interf Sci 261:99
55. Johnson KL (1999) In: Tsukruk VV, Wahl KJ (eds) Microstructure and Microtribology of Polymer Surfaces. ACS Symp Ser Vol 741. American Chemical Society, Washington, p 24
56. Giri M, Bousfield DB, Unertl WN (2001) Langmuir 17:2973
57. Hui CY, Baney JM, Kramer EJ (1998) Langmuir 14:6570
58. Lin YY, Hui CY, Baney JM (1999) J Phys D Appl Phys 32:2250
59. Lin YY, Hui CY (2002) J Polym Sci B-Polym Phys 40:772
60. Greenwood JA, Williamson JB (1966) P Proc R Soc London A 295:300
61. Greenwood JA, Tripp JH (1967) Trans ASME Ser E, J Appl Mech 34:153
62. Greenwood JA (1967) Trans ASME Ser F, J Lubrication Technol 89:81
63. Overney R, Meyer E (1993) MRS Bull 18:26
64. Liu YH, Wu T, Evans DF (1994) Langmuir 10:2241

65. Perry SS (2004) MRS Bull 29:478
66. Meyer G, Amer NM (1990) Appl Phys Lett 57:2089
67. Binggeli M, Christoph R, Hintermann HE (1995) Tribol Lett 1:13
68. Schwarz UD, Köster P, Wiesendanger R (1996) Rev Sci Instrum 67:2560
69. Warmack RJ, Zheng XY, Thundat T, Allison DP (1994) Rev Sci Instrum 65:394
70. Proksch R, Schaffer TE, Cleveland JP, Callahan RC, Viani MB (2004) Nanotechnology 15:1344
71. D'Costa NP, Hoh JH (1995) Rev Sci Instrum 66:5096
72. Gibson CT, Watson GS, Myhra S (1997) Wear 213:72
73. Burnham NA, Chen X, Hodges CS, Matei GA, Thoreson EJ, Roberts CJ, Davies MC, Tendler SJB (2003) Nanotechnology 14:1
74. Landau LD, Lifshitz EM (1986) Theory of Elasticity, vol 7. Pergamon Press, Oxford
75. Albrecht TR, Akamine S, Carver TE, Quate CF (1990) J Vac Sci Technol A—Vac Surf Films 8:3386
76. Sader JE (1995) Rev Sci Instr 66:4583
77. Wortman JJ, Evans RA (1965) J Appl Phys 36:153
78. Noy A, Frisbie CD, Rozsnyai LF, Wrighton MS, Lieber CM (1995) J Am Chem Soc 117:7943
79. Kiesewetter L, Zhang JM, Houdeau D, Steckenborn A (1992) Sens Actuator A—Phys 35:153
80. Schneider D, Tucker MD (1996) Thin Solid Films 291:305
81. Levy R, Maaloum M (2002) Nanotechnology 13:33
82. Ma HL, Jimenez J, Rajagopalan R (2000) Langmuir 16:2254
83. Butt HJ, Jaschke M (1995) Nanotechnology 6:1
84. Tortonese M, Kirk M (1997) Proc SPIE 3009:53
85. Cleveland JP, Manne S, Bocek D, Hansma PK (1993) Rev Sci Instrum 64:403
86. Buenviaje CK, Ge SR, Rafailovich MH, Overney RM (1998) Mat Res Soc Symp Proc 522:187
87. Liu E, Blanpain B, Celis JP (1996) Wear 192:141
88. Feiler A, Attard P, Larson I (2000) Rev Sci Instrum 71:2746
89. Ogletree DF, Carpick RW, Salmeron M (1996) Rev Sci Instrum 67:3298
90. Varenberg M, Etsion I, Halperin G (2003) Rev Sci Instrum 74:3362
91. Tocha E, Schönherr H, Vancso GJ (2006) Langmuir 22:2340
92. Tocha E, Stefański T, Schönherr H, Vancso GJ (2005) Rev Sci Instrum 76:083704
93. Lubben JF, Johannsmann D (2004) Langmuir 20:3698
94. Mindlin RD (1949) J Appl Mech 16:259
95. Pietrement O, Beaudoin JL, Troyon M (1999) Tibol Lett 7:213
96. Sills S, Overney RM (2006) In: Bhushan B, Fuchs H (eds) Applied Scanning Probe Methods III. Springer, Berlin Heidelberg New York, p 83
97. Kajiyama T, Tanaka K, Ohki I, Ge SR, Yoon JS, Takahara A (1994) Macromolecules 27:7932
98. Maivald P, Butt H-J, Gould SAC, Prater CB, Drake B, Gurley JA, Elings VB, Hansma PK (1991) Nanotechnology 2:103
99. Chi L-F, Anders M, Fuchs H, Johnston RR, Ringsdorf H (1993) Science 259:213
100. Chen JT, Thomas EL (1996) J Mater Sci 31:2531
101. Anczykowski B, Krüger D, Babcock KL, Fuchs H (1996) Ultramicroscopy 66:251
102. Jourdan JS, Cruchon-Dupeyrat SJ, Huan Y, Kuo PK, Liu G-Y (1999) Langmuir 15:6495
103. Burnham NA, Kulik AJ, Gremaud G, Gallo P-J, Oulevey F (1996) J Vac Sci Technol B 14:794

104. Huang L, Su CM (2004) Ultramicroscopy 100:277
105. Song YX, Bhushan B (2005) J Appl Phys 97:083533
106. Reinstadtler M, Kasai T, Rabe U, Bhushan B, Arnold W (2005) J Phys D, Appl Phys R269
107. Cappella B, Dietler G (1999) Surf Sci Rep 34:1
108. Butt H-J, Cappella B, Kappl M (2005) Surf Sci Rep 59:1
109. Tsui OKC, Wang XP, Ho JYL, Ng TK, Xiao X (2000) Macromolecules 33:4198
110. Cappella B, Kaliappan SK, Sturm H (2005) Macromolecules 38:1874
111. Binnig G, Despont M, Drechsler U, Haberle W, Lutwyche M, Vettiger P, Mamin HJ, Chui BW, Kenny TW (1999) Appl Phys Lett 74:1329
112. King WP, Kenny TW, Goodson KE, Cross G, Despont M, Durig U, Rothuizen H, Binnig GK, Vettiger P (2001) Appl Phys Lett 78:1300
113. Fischer H (2005) Macromolecules 38:844
114. Garcia R, Perez R (2002) Surf Sci Rep 47:197
115. Noy A, Vezenov DV, Lieber CM (1997) Annu Rev Mater Sci 27:381
116. Vancso GJ, Hillborg H, Schönherr H (2005) Adv Polym Sci 182:55
117. Sinniah SK, Steel AB, Miller CJ, ReuttRobey JE (1996) J Am Chem Soc 118:8925
118. Feldman K, Tervoort T, Smith P, Spencer ND (1998) Langmuir 14:372
119. Werts MPL, Van der Vegte EW, Grayer V, Esselink E, Tsitsilianis C, Hadziioannou G (1998) Adv Mater 10:452
120. Lee WK (1999) Polymer 40:5631
121. Cappella B, Kaliappan SK (2006) Macromolecules 39:9243
122. Satomi N, Tanaka K, Takahara A, Kajiyama T (2001) Macromolecules 34:6420
123. Nysten B, Legras R, Costa J-L (1995) J Appl Phys 78:5953
124. Tomasetti E, Nysten B, Legras R (1998) Nanotechnology 9:305
125. Nysten B, Meerman C, Tomasetti E (1999) In: Tsukruk VV, Wahl KJ (eds) Microstructure and Microtribology of Polymer Surfaces. ACS Symp Ser Vol 741. American Chemical Society, Washington, p 304
126. Cuberes MT, Assender HE, Briggs GAD, Kolosov OV (2000) J Phys D, Appl Phys 33:2347
127. Oulevey F, Burnham NA, Gremaud G, Kulik AJ, Pollock HM, Hammiche A, Reading M, Song M, Hourston DJ (2000) Polymer 41:3087
128. Ellison CJ, Torkelson JM (2003) Nature Mater 2:695
129. Priestley RD, Ellison CJ, Broadbelt LJ, Torkelson JM (2005) Science 309:456
130. Tomczak N, Vallee RAL, van Dijk EMHP, Kuipers L, van Hulst NF, Vancso GJ (2004) J Am Chem Soc 126:4748
131. Pu Y, Ge SR, Rafailovich M, Sokolov J, Duan Y, Pearce E, Zaitsev V, Schwarz S (2001) Langmuir 17:5865
132. Sills S, Gray T, Overney RM (2005) J Chem Phys 123:134902
133. Sills S, Overney RM (2003) Phys Rev Lett 91:095501
134. Kaliappan SK, Cappella B (2005) Polymer 46:11416
135. Bliznyuk VN, Assender HE, Briggs GAD (2002) Macromolecules 35:6613
136. Tanaka K, Takahara A, Kajiyama T (1997) Macromolecules 30:6626
137. Kajiyama T, Tanaka K, Takahara A (1997) Macromolecules 30:280
138. Kajiyama T, Tanaka K, Takahara A (1998) Polymer 39:4665
139. Satomi N, Tanaka K, Takahara A, Kajiyama T, Ishizone T, Nakahama S (2001) Macromolecules 34:8761
140. Kajiyama T, Tanaka K, Takahara A (2004) J Polym Sci Polym Chem 42:639
141. Tanaka K, Hashimoto K, Kajiyama T, Takahara A (2003) Langmuir 19:6573
142. Briscoe B, Smith AC (1982) J Phys D: Appl Phys 15:579

143. Hammerschmidt JA, Moasser B, Gladfelter WL, Haugstad G, Jones RR (1996) Macromolecules 29:8996
144. Tocha E, Schönherr H, Vancso GJ (2007) (submitted)
145. Schmidt M, Maurer FHJ (2000) Macromolecules 33:3879
146. Dinelli F, Buenviaje C, Overney RM (2000) J Chem Phys 113:2043
147. Ge S, Pu Y, Zhang W, Rafailovich M, Sokolov J, Buenviaje C, Buckmaster R, Overney RM (2000) Phys Rev Lett 85:2340
148. Schmidt RH, Haugstad G, Gladfelter WL (2003) Langmuir 19:10390
149. Schmidt RH, Haugstad G, Gladfelter WL (1999) Langmuir 15:317
150. Gracias DH, Zhang D, Lianos L, Ibach W, Shen YR, Somorjai GA (1999) Chem Phys 245:277
151. Mansfield KF, Theodorou DN (1991) Macromolecules 24:6283
152. Haugstad G, Gladfelter WL, Weberg EB, Weberg RT, Jones RR (1995) Langmuir 11:3473
153. Wang XP, Tsui OKC, Xiao XD (2002) Langmuir 18:7066
154. Sills S, Overney RM, Chau W, Lee VY, Miller RD, Frommer J (2004) J Chem Phys 120:5334
155. Sutton SJ, Izumi K, Miyaji H, Miyamoto Y, Miyashita S (1997) J Mater Sci 32:5621
156. Schönherr H, Frank CW (2003) Macromolecules 36:1199
157. Meuse CW, Yang XZ, Yang DC, Hsu SL (1992) Macromolecules 25:925
158. Tao HJ, Meuse CW, Yang XZ, Macknight WJ, Hsu SL (1994) Macromolecules 27:7146
159. Krausch G, Dai CA, Kramer EJ, Marko JF, Bates FS (1993) Macromolecules 26:5566
160. Fasolka MJ, Banerjee P, Mayes AM, Pickett G, Balazs AC (2000) Macromolecules 33:5702
161. Fryer DS, Nealey PF, de Pablo JJ (2000) Macromolecules 33:6439
162. Akabori K, Tanaka K, Kajiyama T, Takahara A (2003) Macromolecules 36:4937
163. Forrest JA, DalnokiVeress K, Dutcher JR (1997) Phys Rev E 56:5705
164. Overney RM, Buenviaje C, Luginbuhl R, Dinelli F (2000) J Therm Anal 59:205
165. Wang D, Ishida H (2006) CR Chimie 9:90
166. Wang XP, Xiao XD, Tsui OKC (2001) Macromolecules 34:4180
167. Pickering JP, Vancso GJ (1999) Appl Surf Sci 148:147
168. Hirano M, Shinjo K (1993) Wear 168:121
169. Sasaki N, Tsukada M, Fujisawa S, Sugawara Y, Morita S, Kobayashi K (1998) Phys Rev B 57:3785
170. Vancso GJ, Förster S, Leist H (1996) Macromolecules 29:2158
171. Vancso GJ, Förster S, Leist H, Liu G, Trifonova D (1996) Trib Lett 2:231
172. Schönherr H, Vancso GJ (1997) Macromolecules 30:6391
173. Israelachvili JN, Chen Y-L, Yoshizawa H (1995) In: Rimai DS, DeMejo LP, Mittal KL (eds) Fundamentals of Adhesion and Interfaces. VSP, Utrecht, p 261
174. Vancso GJ, Schönherr H (1999) In: Tsukruk VV, Wahl KJ (eds) Microstructure and Microtribology of Polymer Surfaces. ACS Symp Ser Vol 741. American Chemical Society, Washington, p 317
175. Overney RM, Takano H, Fujihira M, Paulus W, Ringsdorf H (1994) Phys Rev Lett 72:3546
176. Schönherr H, Kenis PJA, Engbersen JFJ, Harkema S, Hulst R, Reinhoudt DN, Vancso GJ (1998) Langmuir 14:2801
177. Liley M, Gourdon D, Stamou D, Meseth U, Fischer TM, Lautz C, Stahlberg H, Vogel H, Burnham NA, Duschl C (1998) Science 280:273
178. Nisman R, Smith P, Vancso GJ (1994) Langmuir 10:1667
179. Smith PF, Nisman R, Ng C, Vancso GJ (1994) Polym Bull 33:459

180. Vancso GJ, Nisman R, Snétivy D, Schönherr H, Smith P, Ng C, Yang H (1994) Coll Surf A 87:263
181. Sills S, Overney RM, Gotsmann B, Frommer J (2005) Tribol Lett 19:9
182. Urbakh M, Klafter J, Gourdon D, Israelachvili J (2004) Nature 430:525

Top Curr Chem (2008) 285: 157–202
DOI 10.1007/128_2007_25

Published online: 28 February 2008

Exploring Electronic Transport in Molecular Junctions by Conducting Atomic Force Microscopy

Jeffrey M. Mativetsky[1] · Matteo Palma[1] · Paolo Samorì[1,2] (✉)

[1]Institut de Science et d'Ingénierie Supramoléculaires (ISIS) – CNRS 7006, Université Louis Pasteur, 8 Allée Gaspard Monge, F-67000 Strasbourg, France
samori@isis-ulp.org

[2]Istituto per la Sintesi Organica e la Fotoreattività, Consiglio Nazionale delle Ricerche, via Gobetti 101, I-40129 Bologna, Italy

Abstract Measuring the electronic transport properties of single molecules and molecular nanostructures is an interesting and challenging new frontier from both a fundamental as well as technological perspective. Conducting atomic force microscopy (C-AFM) represents an attractive line of approach given its ability to position a sharp electrical probe with nanometer-scale precision and a controlled nano-Newton-range force. Moreover, the combination of AFM imaging and C-AFM electrical characterization enables investigation of the relationship between structure and function in molecular architectures. The aim of the present review is twofold: (1) to introduce the C-AFM method, alongside a discussion of experimental practices, capabilities and limitations, and (2) to provide an overview of the application of C-AFM to different types of molecular systems. These include alkane-based and oligomer-based self-assembled monolayers, molecular crystals, conducting polymer films, molecular wires (e.g. carbon nanotubes), and electrically active biomolecules. We will also discuss C-AFM approaches that allow single molecule measurements as well as other recent developments.

Keywords Charge transport · Conducting atomic force microscopy · Molecular electronics · Molecular wires · Self-assembled monolayers

Abbreviations

AFM	Atomic force microscopy
C-AFM	Conducting atomic force microscopy
CNT	Carbon nanotube
I–V	Current-voltage
HOMO	Highest occupied molecular orbital
LUMO	Lowest unoccupied molecular orbital
MWCNT	Multi-walled carbon nanotube
NC-AFM	Non-contact atomic force microscopy
NDR	Negative differential resistance
RMS	Root mean squared
SAM	Self-assembled monolayer
STM	Scanning tunneling microscopy
SWCNT	Single-walled carbon nanotube
UHV	Ultrahigh vacuum
UPS	Ultraviolet photoemission spectroscopy
XPS	X-ray photoelectron spectroscopy

1 Introduction

The current drive towards alternative and smaller electrical components has spawned a great interest in molecule-based electronics [1–6]. Nevertheless, performing quantitative and reliable measurements of the electrical properties of molecular nanostructures and single molecules remains a great challenge. Several approaches have emerged in recent years and notable progress has been made in the last decade in understanding transport processes in molecular systems [2, 7]. This progress is a result of advances along three main fronts:

(1) The development of a broad range of complementary experimental approaches for electrically interfacing with molecules, including conducting atomic force microscopy (C-AFM), mechanical break junctions [8, 9], mercury drop experiments [10–13], nanopore junctions [14–16], crossed nanowires [17–19], nanoparticle bridges [20, 21] and electromigration-induced junctions [22–26].

(2) The demonstration of different transport behaviours, such as tunneling [13, 16, 19, 21, 27, 28], negative differential resistance [14, 29], Coulomb blockade [22, 23], Kondo behaviour [24–26], and switching [30, 31].

(3) The increased convergence of experimental results with each other [19, 21, 28] and with theory [7, 32, 33].

In this review, we will focus on one method in particular, C-AFM, and its application to the study of electronic transport in molecules. The aim of the review is to provide an introduction to the C-AFM method (Sect. 2.1), a discussion of experimental practices, and an outline of the capabilities and

limitations of the technique (Sect. 2.2). Furthermore, we will present illustrative examples of the application of C-AFM to different types of molecular systems. With this scope in mind, the review is not meant to be exhaustive in nature, but to be instructive and to provide some perspective about progress in the field. The discussion will be limited throughout most of the review to organic systems. Moreover, as self-assembled monolayers (SAMs) of molecules chemisorbed on metallic surfaces, and alkanethiol SAMs in particular, have been studied most, these topics will be given greater attention (Sects. 3.1 and part of 3.2). Other systems that will be considered are short conjugated molecules, in SAM and nanocrystal configurations (Sect. 3.2), conducting polymer films (Sect. 3.3), molecular wires (Sect. 4), and electrically active biomolecules (Sect. 5). In the last section (Sect. 6), we will offer an outlook for upcoming progress in the field.

First, consider the case of measuring electrical resistance in a macroscopic sample, and how this relates to C-AFM. For a macroscopic sample, the resistance can be measured by using a multimeter with probes or alligator clips to contact the sample. In its simplest configuration, the multimeter applies a small voltage between the two probes. The resulting current through the sample is measured and converted to a resistance via Ohm's law, $R = V/I$. C-AFM represents an extension of this basic concept, where a sharp probe with a contact area of about 15 nm^2 is used to electrically connect to nanostructures on a sample surface. The counter-electrode is normally a microfabricated wire on the sample surface or a conducting substrate. A voltage is applied between the electrodes, and the current is measured. With this approach, the surface topography can be visualized by atomic force microscopy (AFM) imaging and the probe can be positioned with nanometer-scale precision. In this manner, C-AFM can be used to interrogate small groups of molecules (e.g. 30–100), and in some cases, individual molecules.

Similar to the macroscopic case, a further consideration during the measurement is the force applied by the probe. It is important that the force is strong enough such that electrical contact is established, but soft enough so that the sample is not damaged. This is achieved in C-AFM by using the force-feedback electronics which are normally used for maintaining a constant force during AFM imaging. This makes it possible to apply forces in the nano-Newton range, thus enabling contact to molecular structures without incurring damage.

The quality of the contact to the sample can also play a role in the measurement. For example, in the case of macroscopic measurements, soldering may offer a lower resistance and more stable contact than a mechanical contact. At the molecular scale, contacts play a critical role in determining the transport behaviour [34–36]. The alignment of the electrode Fermi levels with the HOMO-LUMO levels of the molecules and the nature of the bond between molecules and electrodes largely determine the magnitude of the energetic barriers which exist at the molecule–electrode interfaces. For instance,

alkane molecules with thiol-gold chemicontacts at either end offer a resistance which is two to three orders of magnitude smaller than that for a similar molecule with a single chemical bond to one electrode and a physical contact to the other [5, 37, 38]. C-AFM readily allows for comparisons between molecules with different molecule–electrode couplings. In addition, the electrode materials can be varied and their influence on transport studied. The above described assets make C-AFM a valuable tool for investigating electronic transport in organic materials.

It should be noted that C-AFM also goes by several other names including: conducting probe AFM (CP-AFM), current sensing AFM (CS-AFM), scanning resistance microscopy (SRM), and nano spreading resistance profiling (nano-SRP); nevertheless, the terms C-AFM and CP-AFM are most commonly used in the context of molecular electronics. Unfortunately, the lack of consensus can be a source of confusion and a barrier for finding literature in the field. Throughout this review, we will refer to the technique by the name C-AFM.

2
Conducting Atomic Force Microscopy

2.1
Basic Principles

Atomic Force Microscopy. As suggested by its name, C-AFM is closely related to AFM. AFM was first developed in 1986 [39] and is now widely used for high-resolution measurements of surface structure on a broad range of materials, from solid-state systems to biomolecules [40–43]. Although the method is employed to visualize structures on the nanometer scale, the approach is more akin to touching than it is to seeing. Generally, a microfabricated silicon or silicon nitride cantilever with a sharp tip at the end is used to sense the surface (Fig. 1a). In the most basic mode, the contact mode, the tip is scanned over the surface and the cantilever is deflected as it passes over topographic features. The movements of the cantilever are normally monitored by reflecting a laser off the backside of the cantilever and measuring the laser position with a photodetector. Electrical feedback is used to control a piezo which maintains a constant cantilever deflection, and hence, according to Hooke's law, a constant force between the tip and the sample. As a result, the tip follows the contours of the sample surface and provides a map of the surface topography.

Although the contact mode works well on hard surfaces, unwanted damage can sometimes be incurred on more delicate samples such as organic and biological systems. For soft materials, an alternative imaging mode called tapping mode [44], or intermittent contact mode, is often employed. In this case, the cantilever is driven to oscillate, and the amplitude of the oscillation is

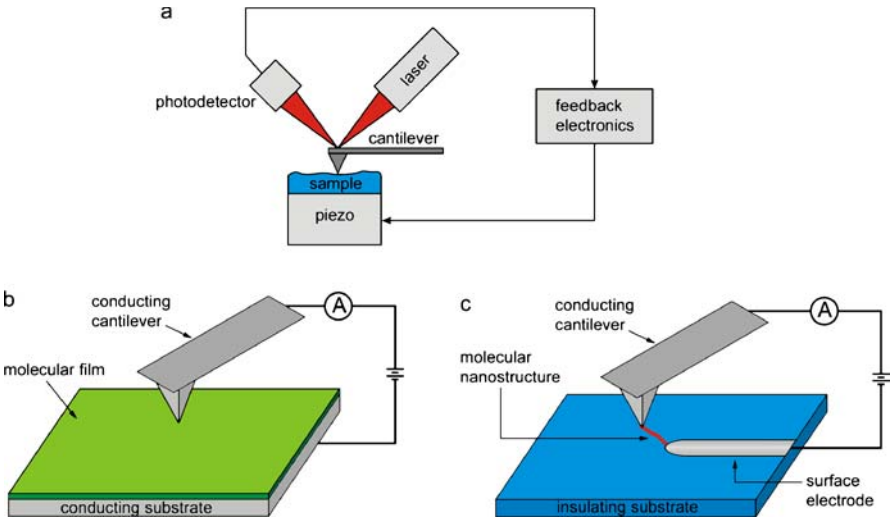

Fig. 1 **a** A schematic diagram of the basic setup used for AFM. **b** The arrangement used for C-AFM measurements in the vertical configuration, and **c** in the horizontal configuration

monitored. In response to tip–sample interactions, the amplitude decreases when it is brought sufficiently close to the surface. To measure topography, the cantilever oscillation amplitude is maintained at a constant value while the tip is scanned over the sample surface.

Conducting Atomic Force Microscopy. In C-AFM, an AFM tip with an electrically conducting coating is used as a movable electrode in a conventional AFM setup. The tip is brought into contact with the surface at a position of interest with a user-specified applied force, which is maintained by the AFM's feedback electronics. Current-voltage (I–V) characteristics are acquired at fixed points on the surface by applying a voltage between the AFM tip and a fixed counter electrode, and measuring the resulting current between the electrodes. Depending on the system under study, the measured currents can range from pico-Amperes to hundreds of nano-Amperes. The resistance of the tip–sample junction is often calculated from the inverse slope of the I–V trace, according to Ohm's law, at small voltages where the I–V behaviour is normally linear.

There are two basic configurations for performing C-AFM measurements: the vertical configuration (Fig. 1b) and the horizontal configuration (Fig. 1c). In the vertical configuration, a conducting substrate is used as a counter-electrode. This is normally used for measuring currents through thin films, especially SAMs. The advantage of this approach is that it does not require any microfabrication, and is therefore relatively simple to implement. This approach is used to compare the I–V characteristics of different molecules, often with only small structural variations between molecules, in order to

study the influence of the molecular structure on transport. It is also possible to vary the materials used for the back-electrode and tip in order to study the role of the contacts in the transport behaviour.

In the horizontal configuration, currents are measured between the AFM tip and a metallic contact pad on an insulating substrate surface. The nanostructure of interest bridges the electrode gap between the movable AFM tip and the contact on the surface. This approach is used for studying nanostructures such as individual molecular nanocrystals and carbon nanotubes (CNT). The contact pad normally consists of a microfabricated wire, though simpler macroscopic contacts with a well-defined edge produced by shadow masking can also be used. Because of the need for patterned surface electrodes, the horizontal configuration is more challenging to implement than the vertical one. However, given that the method only requires having a nanostructure contacted by a single surface electrode, it is normally simpler than other types of electrical measurements where the nanostructure of interest must bridge two or more electrodes with a nanometer-scale spacing on a surface. In the horizontal configuration, it is also possible to measure the I–V characteristics as a function of a gate voltage.

It should be noted that C-AFM can also be used for imaging. In this mode, a constant voltage is applied between the tip and the counter electrode and the current is recorded while the tip is scanned over the sample surface. This provides a spatial map of the local sample conductivity. The sample topography can also be measured simultaneously, making it possible to correlate spatial variations in the conductivity with the topography. Since C-AFM imaging of this type is based on the contact mode of imaging, it is not suitable for all types of samples.

Advantages and Disadvantages. One of the strengths of C-AFM is the ability to image a sample's structure using conventional AFM, and then use the AFM tip as a movable electrode to perform I–V measurements selected areas. The sample can then also be imaged again, following the I–V measurement, to verify that the sample structure was not perturbed during the measurement. This capability of visualizing structure and measuring I–V characteristics makes it possible to measure the I–V properties of specific nanostructures and to study the relationship between physical structure and electronic behaviour. The ability to measure local electronic properties offers an advantage over the mercury drop method where very large ensembles of molecules are contacted. In addition, unlike scanning tunneling microscopy (STM), samples with insulating regions can be used. The use of the tip as a second contact also precludes the need for closely spaced contact pairs on a surface [20–26], which can be challenging to nanofabricate, or for depositing a fixed top electrode [15, 31], which may damage the intervening molecular layer.

A further advantage of C-AFM is the use of force feedback for controlling the tip–sample separation. As a result, the vertical positioning of the tip is de-

coupled from the electrical measurements. This is not the case in STM, where the tunneling current is used for regulating the position of the tip: owing to the typically unknown electrical properties of the material under investigation, the precise vertical position of the tip with respect to the sample is often ambiguous. A second advantage of using force feedback for regulating the force is the possibility of measuring electrical properties as a function of applied load. This allows for the investigation of the connection between mechanical and electrical contact, and the effect of compression and deformation on molecular transport.

The greatest disadvantage of C-AFM is the generally unknown atomic-scale structure of the conducting tip apex. This results in a certain level of ambiguity about the nature of the probe-molecule contact, which often plays an important role in electronic transport through molecules. It should be noted that this drawback is shared with most other approaches, since the precise structure of the contact electrodes at the molecule–electrode interface is normally not known. This and other challenges associated with C-AFM will be addressed in the next section.

Intrinsic and Extrinsic Properties. Finally, an important concept to keep in mind when performing C-AFM measurements is the idea of extrinsic and intrinsic properties. Extrinsic properties depend on the amount of material being measured while intrinsic properties do not. When measuring a sample's properties, one normally tries to convert an extrinsic measurement to an intrinsic one so that it is independent of the quantity of material under consideration. For example, when measuring the resistance of a sample, one is normally interested in the resistivity. This measured quantity is converted by accounting for the cross-sectional area and length of the sample.

Central to all C-AFM experiments is the measurement of current, usually as a function of voltage. However, the magnitude of the current itself is not normally of primary interest since it depends directly on the contact area which varies from tip to tip. One can estimate the tip's contact area in order to convert the measurement to a current per unit area, or current per contacted molecule. However, owing to the difficulty in accurately quantifying contact areas, this is not always reliable. For example, a comparison of recent measurements [5] has shown a spread of up to four orders of magnitude for the estimated current per molecule for the same type of molecule. In addition, efforts to correlate tip dimensions with junction resistance have not been successful, suggesting that tip contamination plays a large role in tip to tip variance, at least when performing measurements in air [45].

Instead of estimating the tip–sample contact area, other properties of the system which are independent of the contact area should be sought. This normally means measuring the resistance as a function of a controllable parameter such as the molecular chain length in the vertical configuration, the distance from the patterned electrode in the horizontal configuration, or the applied force in either configuration. This makes it possible to extract param-

eters from the slopes, such as the tunneling decay parameter β which will be discussed in more detail in Sect. 3.1.

It should also be noted that although the current or resistance depends on the contact area, useful comparisons can be drawn between measurements performed with the same tip, provided that the tip structure does not change significantly, or between sets of experiments with large statistical ensembles. Such experiments do not provide absolute or intrinsic quantities, but allow the determination of the relative behaviours of different systems. In this manner, C-AFM is also useful for screening and comparing the electronic properties of molecular junctions.

2.2 Experimental Procedures and Practical Considerations

Experimental Challenges. Although C-AFM is conceptually simple, it can be tricky to apply in practice. There are several reasons for this. Firstly, it is often desirable to image a sample prior to (and after) I–V measurement, or to image in the C-AFM mode. Because the optimal choice of cantilever and tip material for imaging and I–V acquisition are often different, such measurements can be problematic. Secondly, once the tip is located over a region of interest, the tip's position must remain stationary. Thirdly, one must have good control over the force applied. And finally, since the current measured largely depends on the nature of the contact between the tip and sample, the tip's chemical composition, size, and shape should be controlled as much as possible. While some of these challenges are readily addressable, others are not.

One of the distinct advantages of the C-AFM technique is the ability to visualize surface structures by AFM imaging and then probe the electrical properties of specific features on the surface. Nevertheless, in practice, there are limited examples in the literature where AFM imaging has been used in conjunction with I–V measurement. Instead, many studies use a "blind approach" method, where a sample is approached at various random locations, without imaging the area. The latter method is limited to measurements in the vertical configuration with relatively uniform films such as SAMs. The difficulties related to imaging and performing I–V measurements in sequence are largely related to the choice of cantilever spring constant and tip material for the measurements.

Cantilever Selection. The choice of cantilever depends on the range of forces that will be applied and the mode of imaging that will be performed. During C-AFM measurements, it is important that the force applied by the AFM tip is sufficiently large, so that the there is a stable electrical contact. Empirically, this usually means applying a force of at least 1–2 nN for monolayers [27, 37, 46], although larger loads up to about 50 nN are sometimes needed for other systems [47]. On the other hand, since the electrical properties and the state of a system can depend on the amount of force applied,

it is desirable not to apply too large a force during measurement (unless the force-dependence itself is under study). One must also be careful not to push through the molecular film or structure of interest. In the case of the vertical geometry, this is usually marked by a sharp increase in current if the conductive substrate is contacted. To avoid these problems, minimal loads are typically used in C-AFM measurements. Small applied forces require a small spring constant in order to have a relatively large, measurable deflection during application of the force. Cantilevers with spring constants in the range of 0.01–0.1 N/m, commonly used for contact mode imaging, can readily be used to apply forces in the nN range.

However, "soft" cantilevers of this type are only suitable for contact mode operation. Tapping mode imaging, which is normally necessary for non-destructive imaging of organic materials calls for a relatively high spring constant (20–50 N/m). This is to avoid "jump-to-contact" problems due to attractive forces, which may cause instabilities in the cantilever oscillation. Therefore, the choice of cantilever depends greatly on the application. In cases when tapping mode imaging is needed, a compromise must be reached where an intermediate spring constant is used (e.g. 1–5 N/m). This makes it possible to image in the tapping mode, and still apply sufficiently small forces during I–V acquisition. However, given the reduced force sensitivity, small deflections correspond to relatively large forces. Therefore, one must carefully measure the force applied during I–V measurement. This entails frequently monitoring the offset in the measured cantilever deflection when the tip is far away from the sample. The offset depends on the alignment of the laser onto the photodetector, and can drift over time. Alternatively, C-AFM measurements can be performed with contact mode cantilevers using the blind approach. In this case, the force sensitivity during the measurements is improved, but the ability to image the sample is sacrificed.

Sample Drift. One advantage of imaging before and after I–V measurement is the ability to monitor sample drift. Drift is characterized by the shift in position of the AFM tip relative to the sample over time and depends on the instrument design, thermal effects, and sometimes the manner in which the sample is mounted. Drift can be reduced dramatically by performing measurements at low temperatures. Benefiting from this increased stability, low-temperature STM spectroscopy [48] and AFM force versus distance measurements [49] have been performed over specific atomic sites on a surface. However, to date, low-temperature C-AFM measurements have not yet been reported. At room temperature, drift effects can rarely be avoided, but can be minimized by imaging more quickly, at the cost of signal to noise, and by waiting for the sample and cantilever to reach thermal equilibrium after laser alignment. By imaging before and after I–V measurement, one can verify whether the feature of interest remained at the same position.

Using the blind approach to C-AFM measurement, one cannot directly monitor the drift. In this case, sample uniformity is highly important. In

a study of variability in C-AFM measurements, Frisbie and co-workers compared the resistance measured over a 5 minute period for a decanethiol monolayer on smooth (RMS roughness = 0.28 nm) and rough gold (RMS roughness = 1.33 nm) [45]. They found that as the tip drifted over the surface, the resistance of the rough substrate varied by as much as 2 orders of magnitude while the resistance on the flat substrate was considerably more stable. Furthermore, it was observed that the variations in resistance for the rough substrate were mainly where the piezo height changed significantly, i.e., where there were large topographic variations. The different resistances are probably the result of increased disorder in the SAM on the rough substrate, lateral forces between the tip and sample as the tip drifts over the rough surface, and possibly, contact with different parts of the tip while probing the peaks and valleys of the rough surface.

Variability and Procedures for Reducing Variability. The primary source of variability in C-AFM measurements is the difference in the tip–sample contact from tip to tip. This can arise due to variations in contact area, wear, and contamination. Frisbie et al. showed that resistance measurements on decanethiol SAMs vary within an order of magnitude for single tips, while measurements with 32 different tips yield a spread in resistance of over 4 orders of magnitude [45]. This variability is quite large; however, one should bear in mind that the absolute magnitude of the resistance (or current) is often not of primary interest, unless an estimated contact area is to be used to calculate a resistance (or current) per area, or per molecule. Generally, the resistance of different samples is measured with the same tip, and the relative resistances are compared. Provided that there are no significant changes to the tip structure during the experiments, the tip–sample contact area should remain nearly constant; or, put in other terms, the measurements are normalized to the same contact area. Experiments with different tips are expected to have different magnitudes of resistance. Nevertheless, if multiple sets of experiments are performed, where each set is done with one tip, then, despite having different magnitudes of resistance, the sets should produce similar sample to sample trends. Therefore, it is generally thought that it is best to perform sets of experiments with one tip, and then do many sets of experiments to verify reproducibility and reduce the statistical error. To obtain improved statistics, some experiments have involved performing as many as several thousand I–V curves [38, 50].

Care must also be taken, however, not to use the same tip for too many experiments since it has been shown that junction resistance can increase by up to 2 orders of magnitude during extensive use (e.g. 30 experiments, each comprised of 20 I–V traces) [45]. Nevertheless, more moderate use (e.g. less than 100 I–V traces) shows little change in resistance. It is likely that the increase in resistance is due to increased tip contamination over time. To avoid this problem, it is therefore best to reduce the number of times that the tip comes in contact with the surface, while at the same time having reasonable statistics.

This typically means measuring sets of 5–20 I–V curves on a given sample, potentially at different sample locations, and using the same tip for several samples. The measurements are then repeated with other tips.

Tip Material Selection. The choice of conducting tip material is also important. Several types of materials have been used to date, including doped silicon, metal coatings, doped-diamond coatings, and carbon nanotubes. Studies have also been performed with chemically modified tips. A summary of the tip characteristics is provided in Table 1.

Doped silicon tips, although they are reasonably conductive, do not work well for C-AFM because they readily oxidize in air. This results in an additional tunneling barrier and a large contact resistance [51, 52]. This is not a problem for non-contact AFM methods which require a conducting probe, such as Kelvin probe force microscopy [53], since these methods only require that the tip can be used to apply a voltage. However, because C-AFM relies on having a direct electrical contact to the substrate, the silicon tips are not suitable.

Metal coatings, primarily gold and platinum, are the most frequently used tip materials for C-AFM measurements. This is mainly because they are chemically well defined and easy to prepare. The coating is usually deposited by evaporating a 5–10 nm adhesion layer of chromium or titanium and then a 100–200 nm film of the desired metal onto a silicon cantilever. The coating process increases the tip radius from about 5–10 nm to 10–50 nm [27, 45, 54–56]. Cantilevers with metal-coated tips are also commercially available.

Table 1 C-AFM tip characteristics

Tip material	Stability during imaging	Electrical contact	Refs.
Doped silicon	Stable	Poor – readily forms oxide in air	[51, 52]
Metal coating	Contact mode – tip wears easily on hard surfaces	Excellent	[51, 52, 56]
	Tapping mode – reduced tip wear		[52, 56–58]
Doped diamond coating	Stable	Good	[51, 56, 63]
SWCNT	Some stability issues Stable for SWCNT bundles	Poor	[64, 65]
Metal coated SWCNT bundles	Stable	Excellent	[65]
Short chain alkanethiol on gold coating	Not tested	Excellent, resistant to contamination in air	[45]

Metal-coated tips generally form good, low-resistance contacts (hundreds of Ohms on a metallic substrate) [52, 56]. However, these types of tips wear easily during contact mode imaging on hard substrates, rendering the tips insulating [51, 52, 57]. As a result, metal-coated tips are frequently used for studies where the sample is approached at random locations, without imaging. On the other hand, there are reports of experiments where metal-coated tips were successfully used for tapping mode imaging and I–V characterization, suggesting that tip wear is less of an issue in the tapping mode [52, 56–58]. Platinum-iridium is sometimes chosen over gold or other metals because of its relatively high durability. It should be noted that contact mode and C-AFM imaging of certain soft, yet robust surfaces such as polymers is possible with metal-coated tips [59–62].

Boron-doped diamond coatings exhibit a good electrical conductivity and are highly resistant to wear, making it possible to reliably alternate between imaging and electrical measurement [51, 63]. However, the contact resistance associated with these tips (about 100 kΩ on a metallic substrate) is higher than that for metallic tips [56]. This does not pose a problem for resistive samples, but can be an issue for highly conducting samples such as carbon nanotubes (CNTs), where the sample's electrical characteristics may be hidden by the large contact resistance. During imaging, tip contamination, resulting in insulating behaviour, may sometimes occur; nevertheless, conducting behaviour can usually be restored by pulsing the bias, inducing large feedback oscillations, or by rinsing the tip in acetone and ethanol. Conducting diamond-coated tips are commercially available. Still, despite the advantages related to these tips, they are not widely used owing to their high costs.

Single walled carbon nanotube (SWCNT) [64] and metal coated SWCNT [65] tips have also been tested. Both types of tips were produced by a "pick-up" technique, where vertically oriented SWCNTs are attached to an AFM tip by van der Waals attraction during tapping-mode imaging [66]. Bare SWCNT tips were at first thought to have good electrical properties for C-AFM measurements based on I–V traces recorded during immersion in liquid mercury [64]. However, it was later found that the ends of the SWCNT tips do not form good contacts with solid metallic surfaces [65]. In addition, although imaging is possible with SWCNT tips, stability can be an issue. SWCNT bundles, produced by picking up multiple SWCNTs, show greatly improved stability during imaging, but suffer from the same electrical contact problems as individual SWCNTs. On the other hand, metal-coated SWCNT bundles provide a stable, low-resistance electrical contact (about 2.5 kΩ on a metallic substrate) [65]. Furthermore, unlike metal-coated silicon tips, the metal-coated SWCNT bundles exhibit good contact behaviour even after 5 hours of continuous C-AFM imaging on a gold surface. Other types of carbon nanotube tips have also been developed for AFM applications [67], although their suitability for C-AFM has not yet been tested.

Ethanethiol (C_2) and butanethiol (C_4) modified gold-coated tips were shown to reduce contact resistance and reduce tip to tip variance by a factor of about 2–4 [45]. The improvements were more pronounced for the C_4 modified tips than the C_2 modified tips. It is thought that the improved characteristics are a result of reduced contamination effects, with the aliphatic monolayer displacing existing contaminants and increasing tip hydrophobicity. These results also imply that unmodified tips normally have contamination layers which are thicker than a C_4 layer. This suggests chemical modification as an attractive means of providing a chemically defined tip apex under ambient conditions.

Experimental Conditions. To date most C-AFM measurements have been performed under ambient conditions. In air, a water layer normally forms around the tip. Even under low humidity conditions, this layer can be as thick as 2 nm [68]. The uncontrolled size of the water layer has been cited as a likely cause of the large variations in junction resistance measured for different tips [45]. To reduce contamination effects, some experiments have been performed in low-polarity liquids such as toluene [38, 50, 54, 69], cyclohexane [45, 70], and hexadecane [71]. Measurements on alkanethiol SAMs under cyclohexane have shown a reduction in junction resistance and in tip to tip variation [45]. This was attributed to a more reproducible solvent layer at the interface between the tip and sample. The findings are similar to those for short alkanethiol modified tips operated in air, where the coating of the tip is thought to reduce surface contamination and, owing to the hydrophobic nature of the film, lessen the influence of water layers. A handful of C-AFM experiments have also been performed in vacuum [46, 72–74]. This environment offers reduced contamination and improved interfaces. However, the benefits to C-AFM measurements have not yet been studied in detail. C-AFM experiments may also potentially profit from an inert gas environment. Under all experimental conditions, the transfer of material between tip and sample cannot be entirely avoided, but can be reduced by using minimally invasive procedures (e.g. small forces, tapping mode imaging, etc.).

Adhesion Forces. Finally, an important consideration which is often overlooked is the magnitude of the adhesion forces during C-AFM measurements. Adhesion forces are normally monitored by measuring force as a function of distance. As an AFM tip is pulled out of contact with a surface, adhesion is marked by a negative (attractive) force which occurs just before the tip comes free from the surface. Considering once again the benchmark system of alkanethiols on gold, typical adhesion forces in air are about 10 nN [27, 45]. This means that when a load of 2 nN is applied to the junction, the effective load is in fact about 12 nN. Unfortunately, the adhesion is not cited in many experiments, making it difficult to compare the total load on the sample. In experiments performed under liquids, the adhesion forces are usually much smaller, making adhesion less of an issue. As a result of low adhesion forces, an applied force of 12 nN was required for stable meas-

urements on alkanethiol SAMs in cyclohexane, rather than the 2 nN used in air [45].

An additional source of adhesion is the capacitive force arising from the voltage applied between the tip and sample. Treating the tip–sample system as a capacitor, with capacitance C, the capacitive force $F_C(z)$ is given by

$$F_C(z) = -\frac{1}{2}\frac{\partial C}{\partial z}(V - V_{CPD})^2 , \tag{1}$$

where z is the separation between the tip and the conducting substrate. The quantity V_{CPD} is the contact potential difference between the tip and substrate

$$V_{CPD} = \frac{\phi_{tip} - \phi_{substrate}}{e} \tag{2}$$

with ϕ_{tip} and $\phi_{substrate}$ being the tip and sample work functions, and e being the charge of an electron. The capacitive forces can be approximated by treating the tip apex as a sphere of radius R [27, 75]

$$F_C(z) = \pi\varepsilon\left[\frac{R^2}{z(z+R)}\right](V - V_{CPD})^2 , \tag{3}$$

where ε is the permittivity of the dielectric between tip and the conducting back-electrode. In other words, the capacitive force depends quadratically on the applied bias. For most systems, this contribution is minor. For example at 1 V the capacitive force is about 1 nN. However, at larger voltages, the capacitive forces can amount to several nN.

3 Molecular Layers

3.1 Akane-Based Monolayers

Over the last decade, self-assembled monolayers (SAMs) of alkanethiols [76] have served as the main test bed for studying electrical transport in molecule-metal-molecule junctions. This is largely because of the ease of preparation of the SAMs and their well-characterized structure, by various surface analysis techniques [76–79]. Furthermore, the simple structure of the molecules facilitates the interpretation of the results as well as the theoretical modeling of the system [80, 81].

In terms of electronic properties, it is generally accepted that transport through alkanethiols and similar aliphatic chains occurs via coherent non-resonant tunneling [15, 37, 82]. This type of transport takes place when the energy of the electrons traversing the metal-molecule-metal junction is far from the molecular energy levels. In the case of alkanethiols, the molecules

have a large HOMO-LUMO gap (∼7–11 eV) [16, 18, 80, 81], with the Fermi energy of the electrical contacts lying within the gap. Coherent nonresonant tunneling is common in molecular junctions since the Fermi energy of the electrodes does not line up with the HOMO or LUMO levels in most cases.

In C-AFM measurements, SAMs of molecules are electrically contacted by approaching a conducting tip to a SAM-covered metal surface. Generally, SAMs form when a molecule's headgroup has a strong affinity for a substrate, resulting in a chemisorption of the molecule on the substrate surface. Thiol groups are commonly used to bind molecules to metal surfaces, although many other binding groups such as selenium, isocyanide or amine can be used as well. In the case of alkanethiols on gold, reasonably well-ordered SAMs are formed with the molecules standing up with a tilt angle of about 30°. It should be noted that the uniformity of the SAM is highly dependent on the roughness of the substrate, as well as the cleanliness of the substrate and solution. Consequently, SAMs, though often ordered on a local scale, can have defects, grain boundaries, and limited long-range order, resulting in a more complex structure than is commonly assumed [76, 77].

Sample Preparation. In the C-AFM experiments on aliphatic SAMs, a thin film (40–250 nm) of metal, such as gold, is deposited by evaporation onto mica [54, 71], silicon [27, 37], or glass [16, 55, 83]. For the latter two substrates, an adhesion layer of chromium or titanium (3–20 nm) is normally employed. Ultraflat gold substrates [84–88] were recently used by Frisbie et al. [45, 70]. These are made according to the template-stripping method outlined by Blackstock et al., where gold is deposited onto a clean silicon wafer, glued to another piece of silicon, cured, and then separated from the initial silicon surface [88].

The SAMs are prepared by incubating the sample in ethanol, toluene, or hexane solution for at least a few hours. To ensure that the SAM quality is satisfactory, some studies have also included a characterization of the SAMs by water contact angle measurements [37], ellipsometry [37, 54], STM [38, 54], and XPS analysis [83]. Evidence that the molecules are upright and not hairpinned to the surface was also provided by the electrical measurements which showed characteristics which scale with molecular length [37]. This is primarily a concern for dithiolated molecules where both ends of the molecule have an affinity for the surface.

Current-Voltage Behaviour. The first detailed study of metal-supported alkanethiol SAMs was performed by Wold and Frisbie in 2001 [27]. This work demonstrated many of the salient features of the system. Firstly, it was shown that over the ±1.5 V range, the I–V characteristics follow a sigmoidal shape, with nearly linear behaviour over ±0.3 V (Fig. 2a). Secondly, the resistance of the junction, calculated from the slope in the linear I–V region, increased exponentially with the chain-length of the molecule (Fig. 2b). This behaviour is typical of transport by nonresonant tunneling.

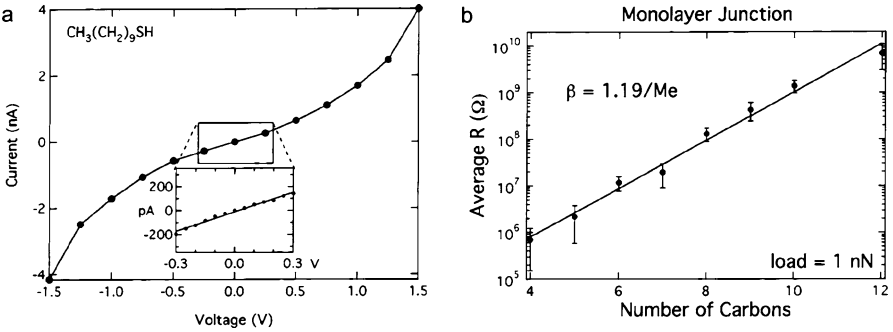

Fig. 2 **a** A typical *I–V* trace for a decanethiol SAM. The *inset* shows the nearly linear behaviour at low voltages. **b** Semilog plot of the alkanethiol junction resistance as a function of chain length. Reprinted with permission from [27]. © 2001 American Chemical Society

The basic *I–V* behaviour is often described in terms of the Simmons model for coherent nonresonant tunneling through a square potential barrier [89]:

$$I = \frac{eA}{4\pi^2\hbar s}\left\{\left(\phi - \frac{eV}{2}\right)\exp\left(-\frac{2s\sqrt{2m}}{\hbar}\sqrt{\phi - \frac{eV}{2}}\right) - \left(\phi + \frac{eV}{2}\right)\exp\left(-\frac{2s\sqrt{2m}}{\hbar}\sqrt{\phi + \frac{eV}{2}}\right)\right\}, \quad (4)$$

where s is the barrier width, ϕ is the barrier height, V is the applied bias, A is the junction area, e is the electron charge, and m is the electron mass. This equation is sometimes modified by including a dimensionless parameter α in the exponential terms to account for the effective mass of the electron [16, 21]. In the case of a SAM, the barrier width s is normally taken as the molecular length [16, 90]. This treatment assumes through-bond tunneling, where the current flows along the alkane chain, rather than through-space tunneling, where the tunneling is along the shortest path between the metal surfaces. These two situations differ since molecules in a SAM have a tilt angle with respect to the vertical. It is generally accepted that through-bond tunneling dominates in the alkanethiol system, though through-space tunneling from chain to chain can contribute, especially for large tilt angles (e.g. during compression) [91].

Although the Simmons model provides a good fit to the data, care should be taken in the interpretation of the obtained parameters [37]. Owing to the simplified nature of the model, the parameters can take on non-physical values. The problem is thought to lie in the differences between the model, which only considers a single energy barrier, and the real situation, which is expected to involve a density of states in the junction, due to mixing between

molecule and electrode states [34, 92]. The broadening of the molecular states results in a reduced barrier for transport. Therefore, the barrier ϕ determined from the Simmons model is best thought of as an effective barrier [37].

At low voltages, the Simmons model (Eq. 4) reduces to

$$I = \frac{e^2 VA\sqrt{2m\phi}}{4\pi^2\hbar s} \exp\left(-\frac{2s\sqrt{2m\phi}}{\hbar}\right) . \tag{5}$$

This equation is linear in voltage V and therefore reproduces the linear I–V behaviour in the low bias regime. In addition, the dependence of the current on the molecular chain length (barrier width) s is predominantly exponential (the s dependence of the prefactor being slowly varying compared to the exponential dependence). It is common to write this equation in a simpler form, in terms of resistance as

$$R = R_0 \exp\left(\beta s\right) , \tag{6}$$

where

$$\beta = 2\sqrt{\frac{2m\phi}{\hbar^2}} . \tag{7}$$

The prefactor R_0 is the effective contact resistance and β is the tunneling decay factor. Experimentally, these parameters are extracted by measuring the junction resistance for several alkanethiol chain lengths and plotting the logarithm of the resistance as a function of the molecular length (Fig. 2b). The tunneling constant β is given by the slope of the linear fit while the contact resistance R_0 is given by the y-intercept, i.e. the extrapolated resistance at a chain length of zero.

Based on this analysis, several groups have measured β. A summary of β values obtained by C-AFM for alkanethiols, alkanedithiols, and alkylamines is provided in Table 2. Although there are greater disagreements between some of the early experiments, later experiments produce similar β values of about 0.8–1/Å (∼1–1.25 per carbon atom), which is in agreement with the results of complementary techniques [10, 12, 15, 16, 21, 28]. The increased convergence of the results over time is probably in part due to progressively refined experimental practices (see Sect. 2.2). In addition, the very low β value in the 2002 study of alkanedithiols [93] is now understood to stem from the use of small gold nanoparticles as intermediate contact points between the tip and the molecules. The approach, which will be discussed in more detail at the end of the section, initially produced some discrepancies because of size effects in the gold nanoparticles [50, 94]. Nevertheless, more recent measurements with larger nanoparticles have produced results which are in line with other experiments, thus demonstrating the validity of the method.

Effect of End Groups. To study the influence of the molecule–electrode bonding on transport, several molecular end-group configurations have been considered. When performing C-AFM measurements on alkanethiol SAMs,

Table 2 Compilation of β values for alkanethiols, alkanedithiols, and alkylamines measured by C-AFM

Molecule type	β (/Å)	Experimental conditions	Refs., year
Alkanethiol 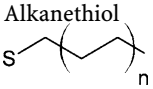	1.16[a]	Ambient	[201], 2000
	0.96[a]	Ambient	[27], 2001
	0.64[a]	Under toluene	[54], 2002
	0.94	Ambient	[90], 2002
	1.04	Ambient	[16], 2004
	0.88	Ambient	[37], 2004
	1.07, 0.98[b]	Ambient	[55], 2006
	0.9[c]	Ambient	[70], 2006
	0.76	Ambient	[21], 2007
Alkanedithiol 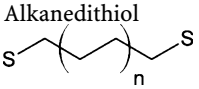	0.46	Au nanoparticle contact, under toluene	[93], 2002
	0.88	Ambient	[37], 2004
	0.84 (LC), 0.77 (HC)[d]	Au nanoparticle contact, under toluene	[50], 2007
Alkylamine 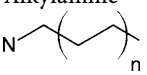	0.97	Ambient	[21], 2007

[a] Converted based on 1.25 Å/methylene [90]
[b] Based on fitting to the Simmons model (see [55])
[c] Estimated from a graph and converted based on 1.25 Å/methylene [90]
[d] LC = low conductance, HC = high conductance. These terms are discussed in the presentation of the gold nanoparticle contact method at the end of the section.

there is one chemical contact, between the thiol and the substrate, and one physical contact, between the terminating CH_3 and the AFM tip. It has been shown that alkanedithiols, which can form chemical molecule–electrode bonds at either end of the molecule, have a contact resistance which is two to three orders of magnitude smaller than that for singly thiolated alkane chains [5, 37, 38]. Furthermore, the estimated current per molecule for alkanedithiols measured in air and in liquids is comparable [5]. This has not been the case for measurements on singly thiolated alkanes. These observations have led to the suggestion that chemical contacts provide a more reliable electrical connection to molecules than physical ones [5, 38].

Other types of chemical contacts have also been considered. Amine-terminated alkanes were shown to have resistances which are 1 to 2 orders of magnitude smaller than those in alkanethiols of similar length [21]. On the other hand, isonitrile terminated alkanes showed a reduction in the contact resistance of only 10% in comparison with alkanethiols [95]. Another study considered alkanethiol SAMs with various end groups opposite the thiol bond [71]. It was found that hydroxyl terminated alkanethiols had a con-

tact resistance which is about 10 times smaller than methylene terminated alkanethiols, while amine terminated alkanethiols had a contact resistance which is about 10 times larger. It should be considered, however, that differences in the structures of the SAMs, which have not been characterized in detail, may also contribute to the measured resistance [71].

Recent experiments have shown that β is similar for alkanethiols and dithiols (see Table 2). The alkylamines produced a slightly higher β value, although the reason for this is unclear, especially in light of the improved conductivity, which would seem to indicate an increased tunneling efficiency [21].

Effect of Electrode Material. The choice of electrode material was also shown to have a large influence on contact resistance. Alkanethiol and alkanedithiol SAMs contacted by different combinations of gold, platinum, and silver electrodes were considered by the Frisbie group. It was found that the contact resistance varied over about 2 orders of magnitude, depending in the electrode material, with the contact resistance decreasing with increasing metal work function (Fig. 3a) [37, 95]. This result indicates that higher electrode work functions give rise to lower transport barriers. It also suggests that the Fermi level of the electrodes is closer to the molecule's HOMO than LUMO, which implies hole tunneling as a likely mechanism [37, 95]. This can be understood in terms of an energy level diagram (Fig. 3b). Junctions with two different electrode materials did not depend on whether the tip metal or substrate metal were interchanged. In either configuration, the contact resistance took on an intermediate value in between those for the two related single metal junctions. This result is surprising in the case of the singly thiolated alkanes since it suggests that physical and chemical contacts are similarly affected by changes in electrode work function. The tunneling parameter β was found not to vary with electrode material.

Force Dependence. The dependence of the junction resistance on applied load has also been studied [27, 54, 70]. Wold and Frisbie showed that there

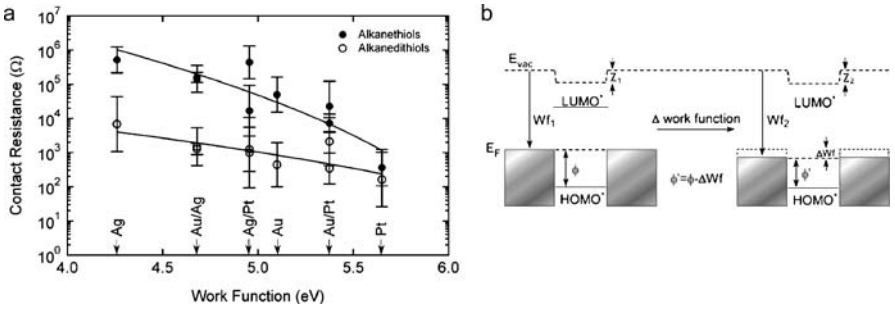

Fig. 3 **a** A plot of the dependence of contact resistance on electrode work function for alkanethiol and alkanedithiol SAMs. **b** An energy diagram showing how a change in electrode work function results in a change in the effective tunneling barrier ($\phi \rightarrow \phi'$). Reprinted with permission from [37]. © 2004 American Chemical Society

are two force regimes which are characterized by different slopes in a log-log plot of resistance versus applied force. For small loads (e.g. less than 70 nN), a slope of –0.83 was found, which is roughly in accordance with the Hertzian contact mechanics model which predicts a slope of –2/3. In the Hertz model, a spherical tip of radius r indented with a force F into a uniform elastic medium of elastic modulus K has a contact area given by [96]

$$A = \pi \left(\frac{rF}{K} \right)^{2/3} . \tag{8}$$

Since the resistance is inversely related to the contact area, a dependence of

$$R \propto F^{-2/3} \tag{9}$$

is therefore expected. At larger loads, the slope was about –7.5. The changed behaviour at high loads has been attributed to a structural transition in the SAM, most likely an increase in disorder via the creation of defects [27]. A more in-depth study of the relationship between resistance and force was recently conducted by the same group [70]. Analysis based on contact mechanics was used to estimate the tip indentation depth as a function of load, and the film modulus (∼50 GPa). The tip–sample contact area during C-AFM measurement can be estimated by using this value for the modulus in Eq. 8. For typical tip radii of 10–50 nm [27, 45, 54–56], and a total load of 12 nN (2 nN applied +10 nN due to adhesion), the contact area is about 6–20 nm^2, which corresponds to 30–100 alkanethiol molecules (based on a complete alkanethiol coverage of about 5 molecules/nm^2 [27]).

In experiments performed under toluene, Cui et al. confirmed the behaviour in the low load regime [54]. Interestingly, the resistance in alkanedithiols was independent of the applied force, within the range of forces considered in the study (2–18 nN). This further demonstrates the importance of the electrode–molecule bonding on molecular junction properties.

Single Molecule Measurements. Finally, we will consider the topic of single molecule measurements. The Lindsay group has developed a clever method for probing single molecules embedded in a monolayer film [38, 50, 93]. Their approach involves inserting isolated dithiolated molecules into a relatively insulating alkanethiol matrix and then using the protruding thiols as anchors for attaching gold nanoparticles, which act as electrical contact pads. A schematic of the configuration is shown in Fig. 4a. To prepare the samples, an alkanethiol SAM is first formed on a gold surface. The SAM is then immersed in a dithiol solution, which results in the insertion of the dithiols at defect sites in the monothiol SAM. In the final step, the sample is incubated in a gold nanoparticle suspension and then rinsed. The resulting samples show isolated gold nanoparticles at the surface (see Fig. 4b). C-AFM measurements on the alkanedithiols were performed by contacting the tethered gold nanoparticles and measuring the I–V characteristics.

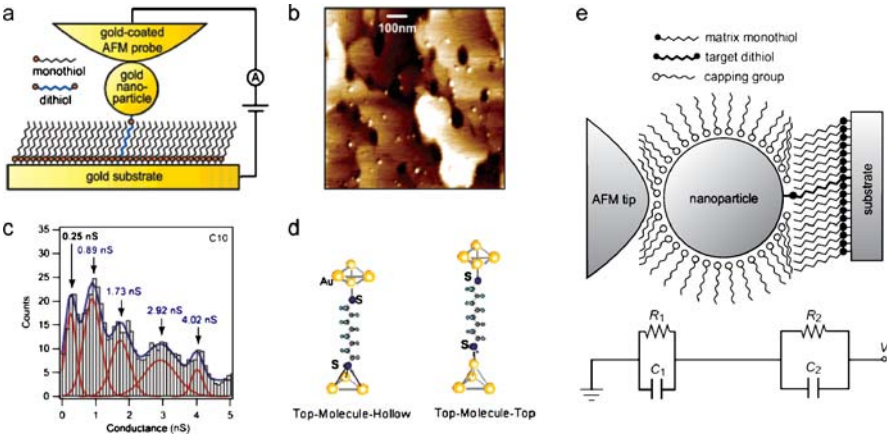

Fig. 4 **a** A schematic diagram of the basic setup for the nanoparticle contact method. **b** A representative AFM image of an alkanethiol SAM on gold, with isolated gold nanoparticles anchored to the surface by alkanedithiols. **c** A histogram of the conductance. **d** Two proposed bonding configurations which are thought to result in the high and low single molecule conductances. **e** A more detailed schematic of the experimental system, including the capping layer around the gold nanoparticle, and the equivalent electric circuit. Reprinted with permission from [28, 50]. © 2006 and 2007 American Chemical Society

In this manner, measurements over hundreds of individual nanoparticles produced families of I–V curves in which most of the curves correspond to a multiple of a fundamental curve [50]. This behaviour is more easily seen in a histogram of the conductance (the inverse of the resistance) (see Fig. 4c). The second peak is in fact the fundamental curve, which is interpreted as the conductance from a single molecule. The higher conductance peaks, which are multiples of the second peak, are taken to be due to integer numbers of molecules in the junction. The first peak, which is not a multiple of the others, has been interpreted as the conductance from a single molecule in an alternate sulphur-gold contact configuration (see Fig. 4d). The high conductance (HC) peak is thought to correspond to adsorption on the hollow site of the gold (111) lattice, and low conductance (LC) peak is thought to correspond to adsorption on the top site of the gold (111) lattice [28]. Break junction studies (described below) have shown similar HC and LC conductances [28, 97]. However, in the case of the break junction measurements, it was possible to observe integer multiples of both HC and LC peaks. In the nanoparticle contact C-AFM study, higher multiples of the LC peaks were not resolved. Based on the C-AFM measurements, separate β values were obtained for the LC and HC configurations (see Table 2).

The use of nanoparticles as contacts to molecules is appealing since it provides a way to contact single molecules reproducibly. However, there are some difficulties to consider, which are specific to this approach. In

the first nanoparticle junction experiments, nanoparticles with diameters of less than 2 nm were used [38, 93]. This led to a very small β value (see Table 2), which has been attributed to distortions in the I–V traces, caused by both energy quantization and charging effects (Coulomb blockade) in the nanoparticles [50, 94]. The most recent work (presented above) showed that these problems can be reduced by using 5.4 nm diameter nanoparticles [50]. Nevertheless, there still remains a contact resistance associated with the tip–nanoparticle interface. It was at first assumed that the tip–nanoparticle contact represents a metallic (ohmic) contact. However, the situation is complicated by the fact that the nanoparticles, in order to prevent coalescence in solution, have a capping layer of molecules (see Fig. 4e).

An additional concern is stress on the SAM. Since the nanoparticles (5.4 nm diameter) are small compared to a metal-coated tip ($\sim$40–100 nm diameter), the pressure (force per area) exerted during the measurement is relatively large. The experiments are normally performed under toluene, which reduces adhesion and allows the application of small total forces. However, to produce appreciable currents, forces of at least 5 nN are required. This is presumably in order to displace the capping molecules around the gold nanoparticle. On the other hand, at forces above about 15 nN, the current increases rapidly, possibly due to the nanoparticle pushing through the SAM. At intermediate forces (5–15 nN), which is the range used for I–V acquisition, the current remains fairly constant, although it is estimated that the film is distorted by as much as 0.45 nm. Some variability in the measurements is also expected to arise from the fact that the dithiolated molecules under investigation are mainly inserted at defect sites of the SAM, which may allow for conformational fluctuations [50].

It is also worth considering the current contribution from the surrounding alkanethiol molecules. This contribution is expected to be small, given that the current through the singly thiolated alkanes is about 100–1000 times smaller than that in the dithiolated alkanes [5, 37, 38]. Based on the Hertzian contact model (Eq. 8), a 5.4 nm nanoparticle has a contact area of about 2 nm^2. This corresponds to about 10 molecules which contribute to the current (estimated using Eq. 8 with a total force of 10 nN, an elastic modulus of 50 GPa [70] and an alkanethiol coverage of 5 molecules/nm^2 [27]). The use of larger particles would increase this "background signal".

Another technique which provides information about single molecule conductance is the C-AFM break junction approach (see Fig. 5) [28, 69, 97]. In this type of experiment, the tip is brought into and out of contact with an alkanedithiol SAM under toluene while the conductance (the inverse of resistance) and force are monitored. As the tip is pulled away from the substrate, the bonds between the tip and the molecules sequentially break down, until the contact is entirely broken. Figure 5b shows the resulting conductance and force curves which are obtained. The conductance decreases in discrete steps, while the force decreases in a sawtooth manner. Each discrete decrease

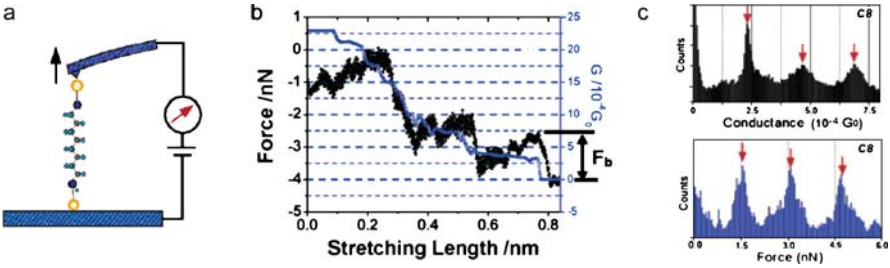

Fig. 5 **a** An illustration of the C-AFM break junction concept. **b** Simultaneously recorded conductance and force curves with jumps corresponding to molecular breakdown events in the junction. **c** Histograms of the conductance and force jumps. Reprinted with permission from [69, 97]. © 2003 and 2006 American Chemical Society

in conductance, and accompanying sharp decrease in force, is interpreted as a bond breaking event between a single molecule (or small numbers of molecules), and the tip. A histogram of the conductance, taken from several hundred measurements, shows two sets of peaks which are multiples of a two fundamental peaks (one set is shown in Fig. 5c). This is in accordance with STM break junction studies [28, 98] and the recent C-AFM nanoparticle junction study [50]. The fundamental peaks are thought to be single molecule conductances due to different bonding configurations. The jumps in force, called the breakdown force, also produce a histogram with peaks which are multiples of a fundamental peak. The fundamental peak is therefore interpreted as the force required for rupturing a single molecule–electrode bond. The peak position of 1.5–1.6 nN is consistent with the force required to break an Au – Au bond, indicating that the thiolated molecules strip off gold atoms from the electrodes during the bond breaking [28, 69, 97].

3.2
Short Conjugated Molecules and Oligomers

As we have seen in the previous section, two important features which influence electronic transport in a metal-molecule-metal junction are: the relative alignment of the electrode Fermi level with the molecular energy states, and the nature of the bonding between the molecule and electrodes. The former determines whether the transport is via resonant or nonresonant tunneling, and also affects the magnitude of the energetic barriers between electrode and molecule. The latter largely determines the coupling strength between the molecule and the adjoining electrodes. In this section, we will explore how a third feature, the use of conjugated molecular structures, affects transport. The presence of π-conjugation generally results in an increased delocalization of the electronic structure and a reduced HOMO-LUMO gap. States which span the molecule may act as conduits for electronic transport, espe-

cially if the state is near the electrode Fermi energy [34]. As a result, notwithstanding electrode–molecule coupling considerations, conjugated molecules are expected to exhibit higher conductivities than unconjugated molecules.

Conjugated Molecule SAMs. To date, less work has been done on conjugated molecules compared to alkanethiols. Most efforts have focussed on the SAM configuration. The sample preparation is similar to that used for alkanethiol SAMs, as outlined in Sect. 3.1. Much like the alkanethiol SAMs, most of the investigated conjugated molecules exhibit behaviour which is consistent with nonresonant tunneling. In other words, the molecules produce sigmoidal I–V curves and exponential length dependencies. It is not obvious that such behaviour should be expected, however. For example in oligoacenes, the HOMO-LUMO gap decreases with increasing number of rings. This should increase the tunneling efficiency as the molecular length is increased. However, this is not observed, suggesting that the Fermi level of the electrodes is too far from the molecular levels to significantly affect β [99].

Wold and Frisbie showed that a benzylthiol molecule has a resistance which is about 10 times smaller than an alkanethiol of similar length [27]. Later studies measured the dependence of the resistance on molecule length by considering families of oligophenylenes [19, 46, 72–74, 90] and oligoacenes [19, 99]. The tunneling decay factor β obtained for the conjugated oligomers are shown in Table 3. These values are significantly smaller than (about half) those found for alkanethiol SAMs (see Table 2), indicating a higher tunneling efficiency. A single methylene spacer was used in some of the studies since this was observed to result in improved monolayer order [46]. Intriguingly, the inclusion of as few as 2 or 3 methylene spacers in phenylene oligomers resulted in a dramatic increase in the SAM resistance and the β value (see Table 3). It was suggested that the decrease in tunneling efficiency is not just because of the additional barrier posed by the methylene spacers, but also due to an overall increase in the localization of the HOMO and LUMO levels in the entire molecule [46]. The use of an isocyanide surface linker rather than a thiol was found to increase the contact resistance by a factor of 3 in oligoacenes [99]. This is unlike the case of alkanes where isocyanide linkers decrease the resistance by 10% compared to thiols [95]. The higher resistance in the isocyanide-bonded versus thiol-bonded oligoacenes was proposed to be due to a larger offset between the molecular HOMO level and the metal Fermi energy, as revealed by ultraviolet photoemission spectroscopy (UPS) [99].

In a recent study, a transition from tunneling to field-emission behaviour was observed in phenylene oligomers at sufficiently high voltages (ranging from 0.6–1 V depending on the molecule) [19]. The change in mechanism is marked by an inflection point in a $\ln(I/V^2)$ versus $1/V$ plot (for more details see [19]). The transition voltage was observed to scale linearly with the offset between the molecule's HOMO level and the electrode's Fermi energy. This suggests that the C-AFM measurement of the transition voltage can be used to gauge the tunneling barrier height.

Table 3 Compilation of β values for various oligomers measured by C-AFM

Molecule type	β (/Å)	Experimental conditions	Reference, year
Oligophenylene-*S* 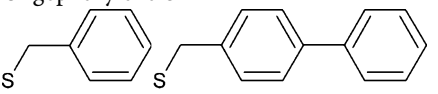	0.42	Ambient	[90], 2002
	0.42[a]	Vacuum	[46], 2002
	0.55	Vacuum	[73], 2002
	0.77, 0.54[a]	Vacuum	[74], 2003
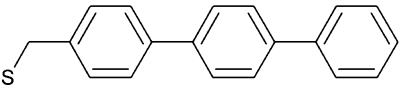			
Oligophenylene-*S* with methylene spacers 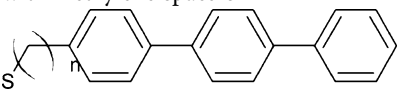	1.05[a]	Vacuum	[46], 2002
Oligoacene-*S* 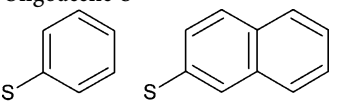 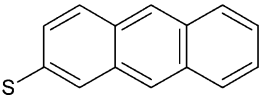	0.51	Ambient	[99], 2006
Oligoacene-CN 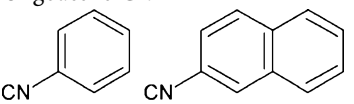 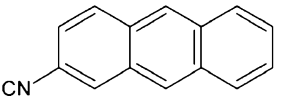	0.45	Ambient	[99], 2006

[a] Taken from an average of β values for different lengths, estimated by assuming a contact resistance of 4×10^4 Ω (see [46])

Single Molecules Experiments. Measurements on individual dithiolated molecules containing an electroactive nitro moiety, using the nanoparticle contact method (see Sect. 3.1), showed negative differential resistance (NDR) behaviour (see Fig. 6) [29]. NDR is characterized by a region in an I–V trace where the current decreases with increasing voltage. The NDR peak is at about 1 V with a peak to valley ratio of 2 : 1. Conversely, similar molecules without the nitro functionalization did not show NDR behaviour. It has been proposed that the NDR behaviour results from alignment between the incoming electron energy and the potential for a redox process [29, 100].

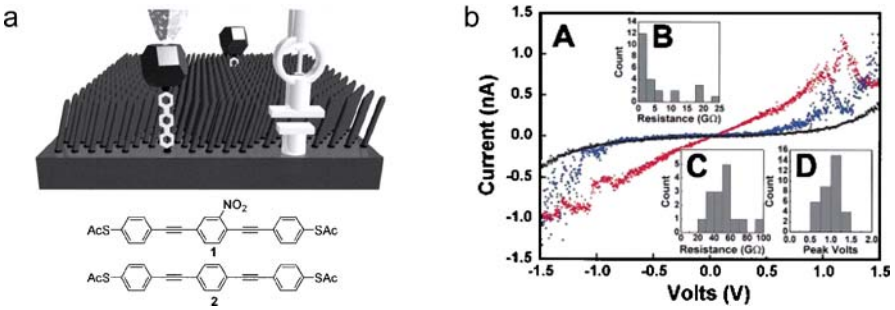

Fig. 6 **a** A schematic of the experimental system, with a dithiolated test molecule contacted by a gold nanoparticle in an alkanethiol matrix, along with the chemical structures of the test molecules. **b** Representative *I–V* curves for molecule 1 (in *red* and *blue*), showing a negative differential resistance (NDR) peak, and molecule 2 (in *black*). The *insets B* and *C* show histograms of the junction resistance for molecules 1 and 2, respectively. *Inset D* shows the spread of NDR peak voltages. Reprinted with permission from [29]. © 2002 American Institute of Physics

Further single molecule measurements were performed on a range of dithiolated oligo(phenylenevinylene)s (see Fig. 7a) [101]. The nanoparticle contact method was found to be advantageous since not all of the molecules formed well-ordered monolayers. In the nanoparticle contact approach, the molecules are inserted at alkanethiol SAM defect sites, which is thought to force the inserted molecules to stand upright. In agreement with the conventional C-AFM measurements on phenylene oligomers (presented above), single molecule measurements showed a 30 fold increase in resistance when two methylene spacer units were included. Comparison between C-AFM and STM results showed that the presence of a direct electrical contact at both ends (in the case of C-AFM) and at one end (in the case of STM) can have an effect on the transport properties. This was evident for molecule 2 (see Fig. 7a), a dithi-

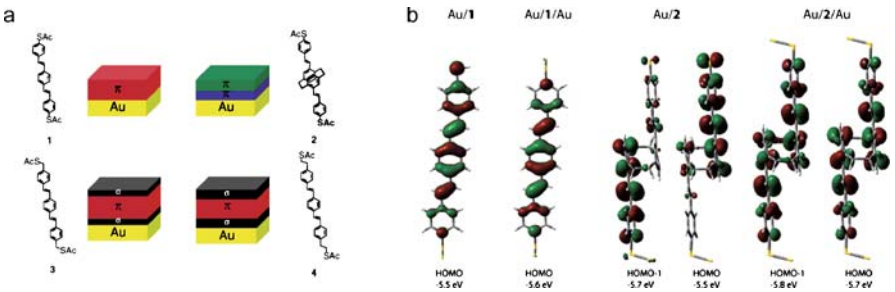

Fig. 7 **a** The chemical structures and corresponding bonding structure of four test molecules. **b** Charge density plots of HOMO and HOMO-1 levels for molecules 1 and 2 attached to one or two gold contacts. Reprinted with permission from [101]. © 2006 American Chemical Society

olated oligo(phenylevinylene) with a [2.2]paracyclophane core, where C-AFM showed a high conductivity and STM showed a low conductivity. This was supported by electronic structure calculations which showed that the single contact results in HOMO and HOMO-1 levels which are localized on the upper and lower halves of the molecule, respectively (see Fig. 7b). In the case where the molecule is contacted at both ends, the molecular orbitals span

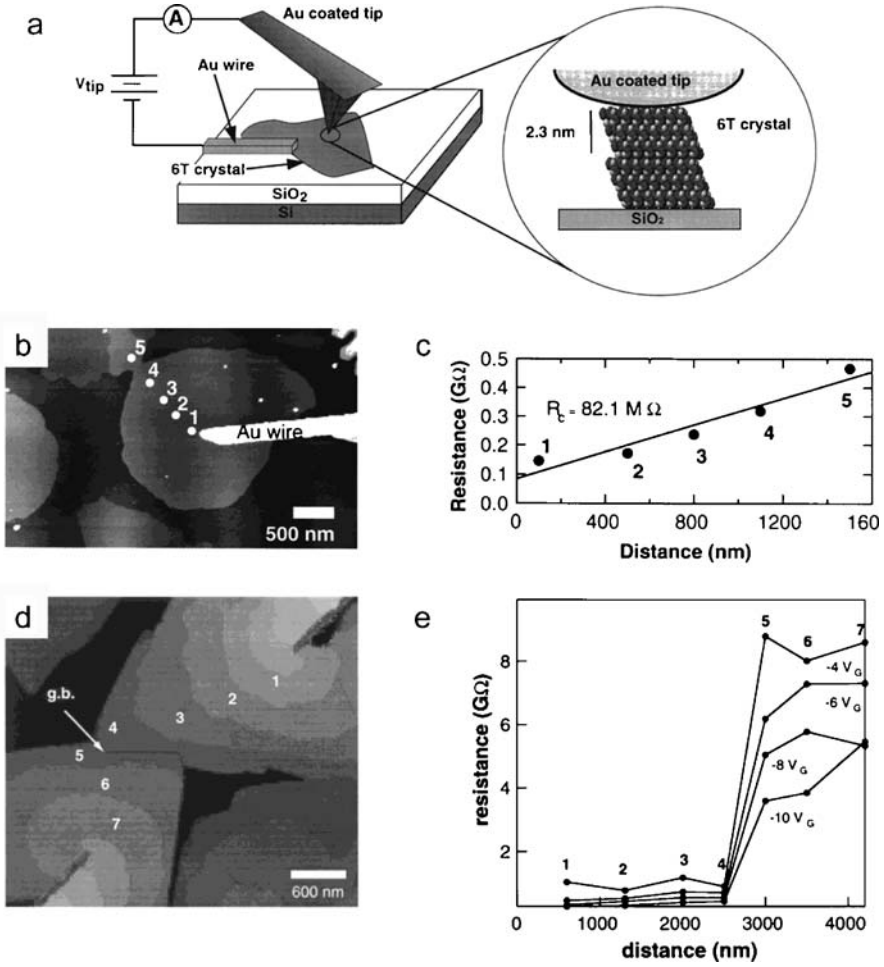

Fig. 8 **a** An illustration of the experimental setup used to contact sexithiophene nanocrystals. **b** An AFM topography image of a sexithiophene nanocrystal contacted by a gold electrode. **c** The resistance a function of distance from the surface electrode. **d** AFM topography image of two sexithiophene grains separated by a grain boundary. **e** The resistance as a function of distance from the surface electrode, showing a sharp change in resistance at the grain boundary. Reprinted with permission from [57, 102]. © 1999 Wiley-VCH and 2001 American Chemical Society

over the entire molecule. This points to the importance of contacts in defining the properties of molecular junctions. In other words, contacts do not just act as an interface to molecular systems, they are an integral part of the system.

Molecular Nanocrystals. The electronic properties of individual molecular nanocrystals were also studied by C-AFM [47, 57, 58, 102, 103], using the horizontal configuration (described in Sect. 2.1). Silicon wafers with a 150–250 nm silicon oxide layer were used as substrates. Gold or platinum electrodes were patterned by photolithography and electron beam lithography.

To date, this type of measurement has been predominantly performed on sexithiophene nanocrystals (Fig. 8). Sexithiophene [104–108] is a p-type semiconductor with a hole mobility similar to that of amorphous silicon [109]. Because of this, it is seen as a candidate material for organic thin film transistors [109] and all-plastic electronics applications [110]. Figure 8b shows a sexithiophene grain contacted by a gold nanowire. The molecules were deposited by vacuum sublimation and were found to preferentially nucleate around the gold structures [47, 58]. Measurements of the resistance as a function of distance from the electrode (Fig. 8c) make it possible to estimate the system's contact resistance, by extrapolating to zero length [47, 57]. It should be noted that the system's contact resistance is due to both the tip-nanocrystal and nanocrystal-contact wire junctions. Interestingly, when similar measurements are performed across a crystal grain boundary (Fig. 8d), there is a large change in resistance (about an order of magnitude) across the boundary (Fig. 8e) [57, 102]. These results demonstrate that grain boundaries are likely to be the main bottleneck to electronic transport in polycrystalline organic semiconductors. The grain boundary resistance was also found to depend on the gate voltage. This is consistent with the presence of trapped charge at the boundaries which acts as an electrostatic barrier to hole transport [102]. The I–V characteristics of copper phthalocyanine nanocrystals were also measured as a function of gate voltage [103]. The charge carrier mobility was determined based on the slope of current versus gate voltage plots.

Measurements on single sexithiophene crystals in the vertical configuration on a sulphur-treated gold substrate were considered as well [58]. This made it possible to study the conductance as a function of grain thickness. These measurements showed, surprisingly, that three layer crystals conduct about 600 and 30 times more than one and two layer films, respectively.

3.3 Conducting Polymers

Conducting polymers have gathered a great deal of attention for applications in organic electronics because of their easy processibility, their stability, and the possibility of tailoring the structure with high precision using cheap and scalable methodologies [110, 111]. As a result, thin films of conducting polymers

are promising materials for applications such as thin-film transistors [112, 113], solar cells [114, 115], light-emitting diodes (LEDs) [116–119], light-emitting electrochemical cells [120, 121], and light-emitting transistors [122, 123]. Various AFM techniques, including C-AFM, have been employed to simultaneously map the electronic and morphological properties of such systems with a resolution down to the nanoscale [53, 124, 125].

Conducting Polymer Films. Lee and Park employed C-AFM in the vertical configuration to study the electrical properties of poly(3-methylthiophene) (P3MeT) films with varying doping levels [126]. The conducting properties of the polymer films were also correlated with their absorption spectra as measured by near-normal incidence reflectance spectroscopy (NNIRS) [126]. In particular, the conductivity of P3MeT films, as calculated from the I–V slopes measured by C-AFM, the film thickness, and the tip–sample contact area, was shown to decay as the doping level was decreased by electrochemical dedoping. In accordance with this, the P3MeT films' absorption spectra varied from a fully doped state with a strong polaron/bipolaron peak to a fully undoped state for which only a band–gap transition was observed.

In a similar way, the same group has studied the I–V characteristics as a function of doping in polypyrrole films [127]. As the film's doping level was decreased, the I–V curves varied from ohmic to semiconducting, and eventually to insulating behaviour [127]. Furthermore, studies of polypyrrole film conductivity and morphology during growth were used to optimize film preparation conditions. It was found that growth and doping in acetonitrile proceeded in a more homogeneous and efficient manner with the addition of a small amount of water [62]. Furthermore, degradation as a result of exposure to air was monitored and shown to result in a gradual decrease in measured current over the course of days and months. In a separate study, the electrical conductivity through polypyrrolyl conjugated bonds was estimated to be at least 5.0×10^5 S/m. This result was obtained by studying monolayers of *N*-[11-(trichlorosilyl)undecyl]pyrrole (PNN) chemically adsorbed on glass through the trichlorosilyl groups [128]. After the monolayer adsorption, an electro-oxidative polymerization was performed by applying a bias between two parallel platinum surface electrodes, creating paths of polypyrrolyl conjugated bonds which were examined by C-AFM [128].

The effect of doping on conductivity has been studied in polyaniline films as well [129, 130]. Varying the pH revealed that polyaniline films prepared under acidic conditions exhibit an average conductivity of about 50 S/cm, while at pH 5.0 the average conductivity was found to be around 1.5×10^{-4} S/cm. These studies demonstrate that the degree of protonation of the monomers significantly affects the chemical nature of polyaniline films, and consequently their morphologies and electronic properties [131].

C-AFM has also been used to gain insight into the transport properties of contacts formed by dispersing noble metal nanoparticles on various conducting polymer films. Such studies revealed that contacts exhibiting

ohmic characteristics can be formed between gold or silver nanoparticles and sulphur-containing polymers by simple immersion of polymer films in colloidal solutions of the particles [132].

Organic Devices. C-AFM has been employed to study organic LEDs, in an effort to scale them down for applications such as ultrahigh density displays. In one study, Hersam and co-workers used C-AFM to address individual pixels in OLED arrays [133]. Simultaneous images of topography, current, and light emission were obtained by using the tip to inject and measure current, and a photomultiplier to collect the generated light. Lin and co-workers have explored, with nanoscale spatial resolution, hole transport in the electroluminescent polymer, poly[2-methoxy,5-(2′-ethyl-hexyloxy)-*p*-phenylene vinylene] (MEH-PPV) [134]. From space-charge-limited current analysis of the I–V curves, mobility values were obtained and fitted to the Poole–Frenkel equation. Interestingly, the zero-field mobility was found to be two orders of magnitude larger than that obtained from macroscopic measurements.

In view of its sensitivity to spatial variations in resistance at the nanometer scale [59], C-AFM has been shown to be a valuable tool for studying conducting polymer blends which hold promise, for example as charge-injecting electrodes, for optoelectronic devices. The combination of AFM topography and phase imaging (in the tapping mode) with C-AFM conductivity maps (in the contact mode) allowed Lal and co-workers to correlate the local charge transport properties of poly(3,4 ethlyenedioxythiophene) (PEDOT)/poly(styrene sulfonate) (PSS) blends with the molecular superstructure of the blends (see Fig. 9) [60]. Phase imaging, which involves measuring the shift in phase between the cantilever excitation and oscillation signals, provides contrast between materials with different visco-elastic properties [135, 136]. This structural information can then be correlated with the local electrical transport behaviour obtained by C-AFM analysis. It has in this way been demonstrated that the blends have a lamellar structure with charge transport occurring mainly along the lamella. These results suggest that the efficiency of charge

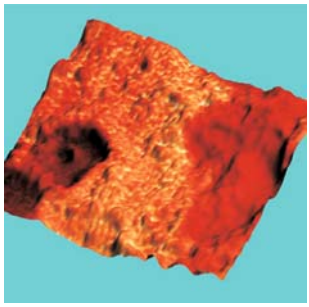

Fig. 9 A three-dimensional representation of surface topography, with the colour scale representing current (0–60 pA), for a PEDOT-PSS blend. Reprinted with permission from [60]. © 2004 Wiley-VCH

injection at the polymer–metal interface can be enhanced by controlling the lamellar orientation [60].

An electron donor-acceptor polymer blend of two phase-separated semiconductor polymers was also studied by C-AFM, in view of the potential use of this type of material as the active layer in plastic photovoltaic devices [61]. The electronic properties of the blends were measured by mapping the current distribution with nanoscale spatial resolution, and by recording current-distance (I–z) and I–V characteristics under illumination. In addition, the capacity of C-AFM to electrically sense phase separated electron donor and acceptor regions has been demonstrated in reference blends used in organic bulk heterojunction solar cells, such as films consisting of a C_{60} derivative blended with either poly(2-methoxy-5-(3′,7′-dimethyloctyloxy)-1,4-phenylene vinylene) (MDMOPPV) or poly(3-hexylthiophene) (P3HT) [137].

More recently Ginger and co-workers demonstrated a method for studying photocurrent distributions with 20 nm resolution. This was accomplished by aligning a C-AFM probe at the centre of a diffraction-limited laser spot, which generates enough photocurrent signal to allow imaging at small current levels (see Fig. 10) [138]. This technique was employed in the study of a donor/acceptor solar cell blend of the conjugated polymer MDMOPPV with the fullerene (6,6)-phenyl-C_{61}-butyric acid methyl ester (PCBM) [138]. Charges were shown to collect mostly at the domain interfaces and, most interestingly, domains that appeared almost identical in the AFM topographical image would sometimes have a different appearance in the photocurrent images. The authors state that such differences result from variations in the detailed film structure. These findings confirm that the enhancement of device performance can be reached through a better control of the film morphology.

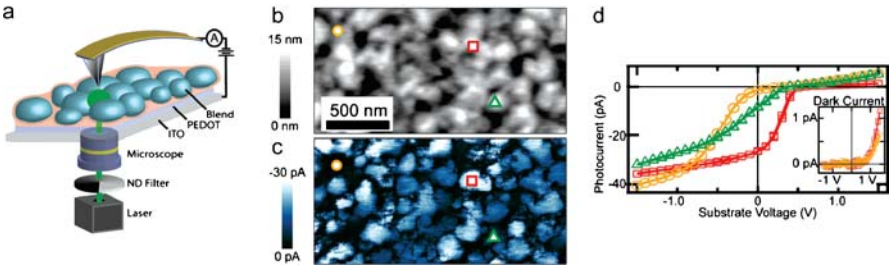

Fig. 10 **a** A diagram of the experimental set-up used by Ginger et al. for measuring photocurrents. The photovoltaic blend film is illuminated by a laser which is focused through a transparent electrode. **b** The surface topography and **c** a simultaneously recorded photocurrent map measured with zero external bias. **d** The local I–V characteristics recorded at the three sample locations (indicated in **b** and **c**). The inset shows the local I–V characteristics in the absence of illumination, showing much smaller currents. Reprinted with permission from [138]. © 2007 American Chemical Society

Polymer-fullerene blends have been studied for applications such as memory devices as well [139]. In bulk devices, the measured I–V hysteresis of poly-vinyl-phenol (PVP)-C_{60} blends was used to perform read, write, and erase memory operations at high and low frequencies. C-AFM was used to show that the hysteretic behaviour, which provides the high and low conductance states used for memory operations, is also exhibited at the nanoscale [139].

4 Molecular Wires

The electrical properties of molecular wires, which for our purposes can be defined as anisotropic molecular objects whose lengths are more than ten times their widths, have been extensively studied using different methodologies in recent years [4, 6, 140]. There is much interest in these types of architectures due to their potential to act as quasi-one-dimensional pathways for charge transport [141–144]. AFM approaches have played a major role in this field, not only for exploring morphological properties on the nanoscale, but also to study the electronic properties of the objects under investigation [53, 145]. C-AFM has enabled the measurement of electrical transport in molecular wires, in a configuration where the tip is used to probe the nano-object, which is in contact with a surface electrode, i.e. the horizontal configuration (see Sect. 2.1 and Fig. 11).

Carbon Nanotubes. Among quasi-1D nanostructures, individual carbon nanotubes (CNTs) have been investigated most, in view of their interesting

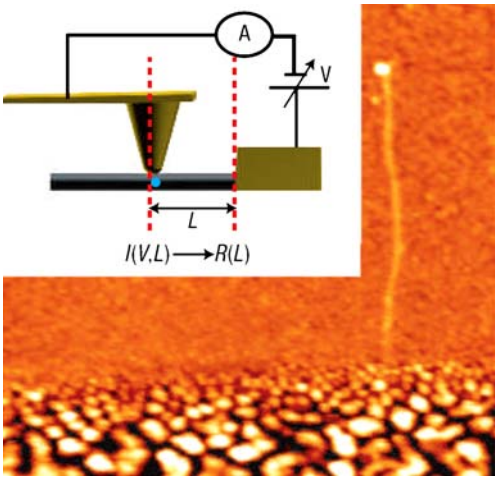

Fig. 11 An AFM image (1 μm×1 μm) of a carbon nanotube contacted by a gold electrode on an insulating substrate. The *inset* shows a schematic of the experimental setup. Reprinted with permission from [151]. © 2005 Nature Publishing Group

electrical properties and their consequent potential use as active components in electronic devices [56]. To locate the CNTs for I–V measurements, intermediate spring constant cantilevers and dynamic AFM modes were used, providing minimal friction between tip and sample [146]. This is often important when studying organic or biological architectures at surfaces since perturbations of the object under investigation can induce structural deformations that in turn will affect electrical behaviour [147].

I–V measurements have been performed at different locations along SWCNTs [147, 148]. A small number of SWCNTs exhibited low resistances ($\sim$10 kΩ), with highly similar values measured at positions 500 nm apart. The low resistance and weak distance dependence suggests ballistic transport [147]. On the other hand, most SWCNTs showed a nonlinear dependence of resistance on the distance from the surface electrode. This indicates that the charge transport is neither ohmic, where a linear dependence is expected, nor entirely ballistic. It was suggested that the behaviour may be a result of elastic scattering at defect sites [148]. This situation differs from the case of ohmic transport, where the behaviour is due to inelastic scattering (e.g. via interactions with phonons). Experiments in the high-bias regime show a linear relationship between resistance and distance, which is consistent with an increased contribution to resistance due to electron–phonon interactions [56, 149].

The role of defects has been highlighted in other studies as well [147, 150, 151]. Gomez-Herrero and co-workers have investigated the influence of defects on the low-bias electrical properties of CNTs by irradiating SWCNTs with an Ar^+ ion beam [151]. Previous molecular dynamic simulations suggested that Ar^+ collisions create both mono-vacancies and di-vacancies along the nanotube [152]. However, it was shown, through a combination of density-functional simulations and Green's function techniques, that di-vacancies are the main contribution to the increase in resistance induced by irradiation. The low voltage resistance was also calculated and shown to follow a similar exponential length dependence compared to the C-AFM data. These results point to the potential use of ion irradiation as a new way to tailor the electrical characteristics for future CNT-based devices [151].

The electrical and mechanical properties of the contact between a C-AFM tip and a SWCNT were also studied, showing that once the electrical contact is established, the high voltage conductance does not depend on the applied load [153, 154]. In contrast, for large loading forces (>50 nN), a decrease in the low voltage conductance is observed. The drop in conductance has been attributed to a gap opening in the molecule's band structure as the SWCNT is radially deformed [154]. Similar experiments on multi-walled carbon nanotubes (MWCNTs) showed no significant dependence of the conductance on applied load, even at loads up to 3000 nN [154].

Other Nanowire Systems. CNTs are widely considered to be good candidates for future device applications. Nevertheless, at present, the degree of control over the synthesis and processing of CNTs is limited. Consequently,

the controlled positioning of isolated nanotubes on a surface with well defined and tuneable electrical characteristics is highly challenging. Some alternative quasi-1D systems have recently been considered. For example, V_2O_5 nanowires have been shown to posses high structural definition [155]. The electrical transport in V_2O_5 nanowires has been probed with C-AFM as a function of their length and compared to studies performed with complementary techniques. The non-linear response of the resistance as a function of length suggested a non-ohmic transport regime [156]. Furthermore, semiconductor and metallic nanowires, have also been studied by C-AFM [118, 157]. The electrical properties of selectively modified CdTe nanowires, for example, have been investigated. Thinning of the nanowires was accomplished by applying a sufficiently high voltage between a conducting AFM tip and a CdTe nanowire, such that local field-assisted evaporation of the CdTe would occur. Using this approach, the widths and lengths of CdTe nanowires were decreased, resulting in increased quantum confinement behaviour [157].

Anisotropic conducting polymer nanostructures have also been of interest, given their easy processability and potential for organic electronic applications. C-AFM has been employed to investigate individual nanowires and nanotubes of conjugated polymers, such as polypyrrole [158, 159]. The nanostructures are prepared by the template synthesis technique, where the pores of a nanoporous membrane are filled with a desired material by chemical synthesis or electrodeposition [160, 161]. The nanostructures can be freed by dissolving the membrane. Conductivity measurements were performed by probing isolated nanotubes on a surface [158], or by contacting the ends of nanotubes which are embedded in the templating membrane [159].

By and large, C-AFM can be employed to study the electrical properties of isolated anisotropic nanostructures, allowing a better understanding of their characteristics and paving the way towards their application as active components in electronic devices.

5 Bioelectronics

C-AFM has been also used to study biological molecules. The capability to form of a junction at a precise sample location with a quantifiable contact force makes C-AFM a valuable tool to cast light on fundamental issues related to charge flow. Additionally, the notion of incorporating biological molecules into electronic devices has stimulated great interest due to the wealth of functional building blocks found in nature [162].

Conjugated Biomolecules. Carotenoids, which are known to be responsible for colour in plants, animals and microorganisms, were one of the first biological molecules to be studied by C-AFM. These molecules are considered to be prototypical molecular wires because of the delocalization of the elec-

tronic states responsible for their optical properties. It has been demonstrated that a carotenoid molecule chemisorbed on gold and physically contacted to a conducting AFM tip in a vertical configuration exhibits ohmic electrical properties with a resistance of approximately 4.2 GΩ, being therefore over 10^6 times more conductive than an alkane chain having a similar length [163].

Proteins. Charge transport plays a key role in various protein-based biological processes; the redox-active centres of metallo-proteins, for example, are involved in photosynthesis and respiration. C-AFM offers a complementary approach to photochemistry and electrochemistry-based techniques for studying electron transfer in proteins. Protein-based junctions have also been investigated by STM [164, 165], in view of the potential for switchable and diode characteristics of redox-accessible electronic states. The main drawback of the STM approach is the lack of control over the electrical contact and the potential for mechanical perturbations. C-AFM overcomes such limitations through force feedback control, which allows conductivity measurements of protein-electrode junctions under specific applied loads. To avoid problems with sample drift when locating the proteins on a surface, some studies used protein-modified tips rather than protein-modified surfaces (Fig. 12). Using C-AFM, it was shown that the charge flow in the blue copper metallo-protein, azurin, can be well described by a nonresonant electron transfer process by applying a modified Simmons formula to the experimental data in the low voltage regime [166]. In addition, a model for protein mechanical deformation was suggested and simulated by molecular dynamics in order to interpret the variation of tunneling barrier height.

Similar kinds of studies have been carried out on single ferritin molecules. Ferritin is a highly stable iron storage protein found in animals, plants and bacteria. It has generated interest because of its magnetic, electrochemical and directed assembly properties, and it is currently being investigated as a material for nanoscale batteries based on electrochemical reduction in the ferritin core [167]. Ferritin molecules are composed of 24 subunits which are

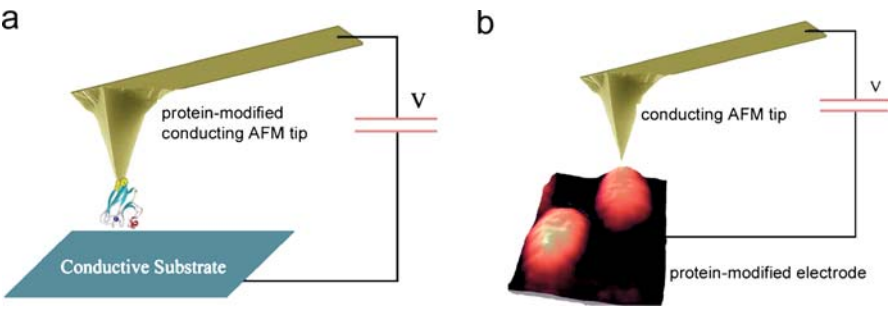

Fig. 12 A schematic of the two configurations used for protein studies: **a** using a protein-modified tip, and **b** using a protein-modified surface. Reprinted with permission from [162]. © 2005 Royal Society of Chemistry

arranged in a spherical configuration, with an 8 nm diameter interior, which is normally filled with anhydrous ferric oxide-phosphate mineral. The filled ferritin molecule is referred to as holoferritin, whereas a ferritin molecule with an empty core is called apoferritin. Electrical conductivity measurements have been performed on single holoferritin and apoferritin molecules by C-AFM. It was found that holoferretin is 5–15 times more conductive than apoferritin, which suggests that the core is significantly more conductive than the shell [168]. A Fowler–Nordheim tunneling model was shown to better describe the probed electron tunneling when compared to the low voltage Simmons theory [89]. Fowler–Nordheim tunneling theory is applicable when the bias applied is larger than the barrier height, while the Simmons model applies when the applied voltage is less than the barrier height. Therefore the better fitting of the Fowler–Nordheim model is an indication of a low barrier height between the gold contacts and the ferritin molecules [168].

DNA. A great effort in the field has been devoted to the investigation of electron transport in DNA [169]. Such studies are important because of issues related to radiation damage and repair [170], as well as for the potential use of double-stranded DNA in molecular electronics [171] and biosensor applications [172]. In recent years, double-stranded DNA has been described as an insulator [173], a semiconductor [174] and a conductor [175] as well as a superconductor [176]: C-AFM has helped cast light onto this highly debated issue.

The ability of short strands of DNA (26 base pairs, 8 nm long) to transport electrical current under appropriate conditions has been confirmed by C-AFM, although an unambiguous mechanism for charge transport has not yet been identified [177, 178]. Measurements were performed in two configurations: on a monolayer of dithiolated double-stranded DNA, and on gold nanoparticle-linked dithiolated double-stranded DNA, embedded in a single-stranded DNA monolayer. This latter approach is similar to that employed by Lindsay and co-workers for measuring the I–V properties of single alkanedithiols inserted into alkanethiol SAMs (see Sect. 3.1) [50]; however, in the case of the DNA studies, up to 10 molecules are contacted at a time [178]. It was found that covalent bonding to the electrodes played an essential role, with physical rather than chemical contacts showing no significant measurable currents. Similarly, single-stranded DNA was not conductive. By measuring the influence of DNA base pair sequence on its charge transport properties it was shown that double-stranded DNA behaves as a wide band-gap semiconductor, with the width of the gap decreasing, and the current increasing, with increasing guanine-cytosine base pair content [179].

The effect of the conformation of DNA bundles (containing from a few molecules up to 10^6 molecules) adsorbed on various substrates and the nature of the DNA-electrode contact on the measured conductivity have been investigated as well [180]. Under most conditions it was found that the DNA bundles conduct, but are highly resistive. Measurements have also been per-

formed as a function of applied load [181], and photoinduced conductivity has been analyzed in self-assembled dye-DNA networks [182]. Overall, C-AFM has proved its potential as an important technique which can play a key role in studies of the electronic properties of biological molecules, and is likely to play a role in the screening of biomolecules for applications in the emerging field of nanobioelectronics.

6
Conclusions and Future Directions

6.1
Conclusions

Although C-AFM has only been in use for about 10 years, it has already been applied to many types of molecular systems and has provided a great deal of insight into the mechanisms governing electronic transport. This versatility is a result of the fact that minimal microfabrication is required for contacting nanostructures in the horizontal configuration, and no microfabrication at all is needed for measurements in the vertical configuration. Furthermore, the electrode materials, the molecular structures, and the molecule–electrode interactions can all be readily varied and their effects on transport studied.

On the other hand, it should be recognized that C-AFM experiments can be difficult to perform and often require large sets of measurements in order to reduce the effects of trace to trace variability. As stated by Reed and co-workers, "it is easy to perform an 'incorrect' measurement" [16]. Nevertheless, as we have seen in Sect. 2, experimental practices are evolving over time, and with a certain amount of caution, reproducible measurements can be carried out. It must also be kept in mind that molecular electronics is still a nascent field, and that measuring electrical transport in molecular nanostructures remains difficult by any means. In this context, C-AFM provides unique and valuable information about local electronic properties under a controlled load, which is complementary to the information provided by other techniques. Thus, together with these other approaches, C-AFM is helping to put together different pieces of the molecular electronics puzzle.

In the benchmark system of alkanethiol SAMs, C-AFM showed behaviour which is consistent with coherent nonresonant tunneling. Furthermore, it was possible to determine the tunneling decay parameter β and to compare the contact resistances associated with different electrode materials and molecular end groups. Based on these studies, it was shown that the contact resistance decreases substantially with increasing work function, indicating hole tunneling as a likely mechanism [37, 95]. The choice of end group also had a large effect of the transport, with alkanedithiols conducting 100–1000 times more than alkanethiols [5, 37, 38]. While the above experiments typ-

ically involved 30 to 100 molecules, the conductance of single alkanedithiol molecules was provided by the nanoparticle contact method [38, 50, 93] and the C-AFM break junction approach [28, 69, 97].

SAMs of short conjugated molecules, owing to their delocalized electronic structure, showed higher conductances and lower β values than alkanethiols. Interestingly, the inclusion of only 2 or 3 methylene spacers in phenylene oligomers resulted in substantially lower conductances, presumably due to changes in the overall electronic structure of the molecule [46]. It was also shown that the conductivity of certain molecules is different when the molecule is in direct electrical contact with 2 electrodes (in a vertical C-AFM configuration) or 1 electrode (in an STM configuration) [101]. This was supported by theoretical simulations which showed that the electrodes can play a large role in defining the molecule's electronic structure in the junction. C-AFM measurements also revealed interesting effects, such as NDR behaviour [29].

Horizontal configuration measurements on sexithiophene nanocrystals showed a large resistance associated with grain boundaries, suggesting that these are the main bottleneck to transport in sexithiophene films [102]. A similar configuration was employed to investigate the electrical behaviour of quasi-1D systems, such as CNTs and nanowires, in view of the increasing interest for their application as active components in electronic devices. C-AFM has been also used to simultaneously map the electrical and morphological properties, as well as the photocurrent response, of conducting polymers with a resolution down to the nanoscale. Furthermore, C-AFM has proved to be a reliable tool to cast light on fundamental issues in biology, allowing the investigation of charge flow across individual biological macromolecules.

6.2 Future Directions

Advances related to C-AFM are expected in two main areas: (1) improvements in the techniques used, and (2) a move towards the investigation of increasingly complex systems and phenomena.

Methods. The greatest difficulty, and source of variability, in C-AFM is the lack of control over the microscopic details of the tip–sample interface. In order to have clean and well-defined surfaces, surface science experiments are often performed under ultrahigh vacuum (UHV) conditions (see e.g. [183]). Nevertheless, to date there are no reports, to our knowledge, where the sample preparation and C-AFM characterization were performed entirely in UHV.

Clean metallic surfaces with atomically flat terraces can be prepared in UHV by sputtering and annealing, or evaporation [183]. In addition, the deposition of molecules can be done by gas phase dosing or by sublimation.

Sufficiently hydrophobic surfaces may potentially remain sufficiently clean if they are prepared ex-situ and promptly transferred into UHV [184]. Furthermore, tips can be heated in order to remove water layers, or be coated in situ. Although more challenging, measurements in the horizontal configuration can potentially be performed by depositing electrodes by shadow masking [185–188], in situ, onto an insulating substrate. As discussed in Sect. 2.2, measurements in liquids, inert gases, and with chemically modified tips, also offer a more controlled tip–sample interface than ambient conditions, and should be considered further as well.

An additional advantage of using UHV is the possibility of performing high-resolution AFM imaging in the non-contact mode (NC-AFM) [189]. NC-AFM is a type of AFM measurement where the tip is oscillated and the frequency of oscillation is used to regulate the tip–sample separation. NC-AFM in UHV has been used to measure the surface structure of metals [190], semiconductors [191], and insulators [192] with atomic resolution. It has also been possible to resolve molecules such as alkanethiols [184], C_{60} [193] and PTCDA [194]. Switching between NC-AFM and C-AFM modes may offer the possibility of approaching specific sample locations with molecular-scale resolution. This would make it possible to correlate the detailed sample structure with transport properties. It should be noted, however, that the tip–sample contact area would remain similar to that in other C-AFM experiments, i.e. about 6–20 nm^2. The NC-AFM imaging mode is also highly non-invasive, even less so than the tapping mode. Therefore, it is expected that the tip and sample structure will remain largely unperturbed during imaging.

In addition to the cleanliness of the tip, the structure of the tip is also important. It is essential that the structure remains constant throughout the experiment and it is desirable, for the sake of quantifying the contact area, to know what the structure is. A nanolithography method called nanografting [195, 196] provides an attractive approach which helps address these issues. Nanografting is used to insert a second type of SAM at defined locations on a SAM coated surface. This is accomplished by dragging a SAM coated tip at sufficiently high loads, in order to displace the original SAM and allow the new molecules to adsorb onto the surface. Using this approach, Scoles and co-workers showed that it is possible to have two types of SAMs on the same surface, side by side [197]. They were then able to compare the I–V characteristics of the two molecules with the same tip conditions. Nanografting has also been used to create lines of alkanethiols which are imaged and used to estimate the size and geometry of the tip apex [198], thus providing a tool for quantifying contact areas in situ.

Variable temperature measurements are another important direction for future experiments. This type of experiment will help elucidate transport mechanisms, and may also reveal different and unexpected behaviour. At low temperatures (e.g. 4.2 K), many molecular systems have been shown to be-

have as quantum dots, showing single electron charging (Coulomb blockade) behaviour [22, 23], and in magnetic systems, spin-dependent (Kondo) [24–26] behaviour. Experiments at low temperatures are also less prone to problems with sample drift.

Systems. Advances related to C-AFM will also come from applying C-AFM to new types of systems. As we have seen in Section 3, a large proportion of C-AFM studies were done on alkanethiol SAMs. These experiments are valuable for determining the effects of specific aspects of the molecular junction, such as molecule length, electrode material, and end groups. Further experiments also considered conjugated cores. Ultimately, it was seen that the electrodes and the electrode–molecule coupling are integral parts of molecule-metal-molecule junctions, which have an important effect on the junction properties. Moreover, the effect of using certain electrode materials or molecular end groups can be different for different molecules. For example, isocyanide surface linkers were shown to increase the resistance in oligoacenes by a factor of three compared to thiols [99], but reduce the resistance by only 10% in alkanes [95]. Similarly, different electrodes may have different alignments of their Fermi energies with the molecular levels of different molecules. Therefore, when studying new molecules, it is desirable to consider a range of end groups and electrode materials, in order to understand and optimize the system behaviour. This type of study can be readily done by C-AFM, making C-AFM a valuable approach for screening the effects of different junction components. In addition, single molecule approaches such as the nanoparticle contact method and the break junction approach are promising and have only been applied to a few systems to date.

C-AFM can also play an important role in unravelling the electronic properties of more complex molecular, supramolecular, and biological architectures. Phenomena triggered by external stimuli or agents are also of great potential interest. For instance, C-AFM could offer direct information on the dependence of the I–V characteristics of a nanostructure on doping levels. Alternatively, the use of photoexcitations and charge transfer can also be explored in electron acceptor-donor systems. Furthermore, in nature, many complex systems are still poorly understood. One can, for example, foresee the use of C-AFM to address single enzymes or ion channels.

Finally, the main, largely untapped, advantage of C-AFM is the ability to correlate structural and electronic properties of nanoscale architectures. This is highly important given that it is well established that the electrical properties of molecule-based nanostructures strongly depend on their order at the supramolecular level. Thus, C-AFM can play a fundamental role in the optimization of the performance of molecule-based devices. In view of this, C-AFM, and other quantitative scanning probe approaches which go beyond imaging [125, 199, 200], will ultimately provide an important contribution to nanoelectronics, and more generally to nanoscience and nanotechnology.

Acknowledgements This work was supported by the EU Marie Curie through the EST project SUPER (MEST-CT-2004-008128) as well as the RTN projects PRAIRIES (MRTN-CT-2006-035810) and THREADMILL (MRTN-CT-2006-036040), the ERA-Chemistry project SurConFold, the ESF-SONS2-SUPRAMATES project, the Regione Emilia-Romagna PRIITT Nanofaber Net-Lab and the EU-ForceTool (NMP4-CT-2004-013684) project.

References

1. Joachim C, Gimzewski JK, Aviram A (2000) Nature 408:541
2. Tao NJ (2006) Nat Nanotechnol 1:173
3. Weibel N, Grunder S, Mayor M (2007) Org Biomolec Chem 5:2343
4. Nitzan A, Ratner MA (2003) Science 300:1384
5. Salomon A, Cahen D, Lindsay S, Tomfohr J, Engelkes VB, Frisbie CD (2003) Adv Mater 15:1881
6. Carrol RL, Gorman CB (2002) Angew Chem Int Ed 41:4378
7. Lindsay SM, Ratner MA (2007) Adv Mater 19:23
8. Reed MA, Zhou C, Muller CJ, Burgin TP, Tour JM (1997) Science 278:252
9. Kergueris C, Bourgoin JP, Palacin S, Esteve D, Urbina C, Magoga M, Joachim C (1999) Phys Rev B 59:12505
10. Slowinski K, Chamberlain RV, Miller CJ, Majda M (1997) J Am Chem Soc 119:11910
11. Haag R, Rampi MA, Holmlin RE, Whitesides GM (1999) J Am Chem Soc 121:7895
12. Holmlin RE, Haag R, Chabinyc ML, Ismagilov RF, Cohen AE, Terfort A, Rampi MA, Whitesides GM (2001) J Am Chem Soc 123:5075
13. Selzer Y, Salomon A, Cahen D (2002) J Phys Chem B 106:10432
14. Chen J, Reed MA, Rawlett AM, Tour JM (1999) Science 286:1550
15. Wang WY, Lee T, Reed MA (2003) Phys Rev B 68:035416
16. Lee T, Wang WY, Klemic JF, Zhang JJ, Su J, Reed MA (2004) J Phys Chem B 108:8742
17. Kushmerick JG, Holt DB, Yang JC, Naciri J, Moore MH, Shashidhar R (2002) Phys Rev Lett 89:086802
18. Kushmerick JG, Holt DB, Pollack SK, Ratner MA, Yang JC, Schull TL, Naciri J, Moore MH, Shashidhar R (2002) J Am Chem Soc 124:10654
19. Beebe JM, Kim B, Gadzuk JW, Frisbie CD, Kushmerick JG (2006) Phys Rev Lett 97:026801
20. Dadosh T, Gordin Y, Krahne R, Khivrich I, Mahalu D, Frydman V, Sperling J, Yacoby A, Bar-Joseph I (2005) Nature 436:677
21. Chu C, Na J-S, Parsons GN (2007) J Am Chem Soc 129:2287
22. Park H, Park J, Lim AKL, Anderson EH, Alivisatos AP, McEuen PL (2000) Nature 407:57
23. Kubatkin S, Danilov A, Hjort M, Cornil J, Bredas JL, Stuhr-Hansen N, Hedegard P, Bjornholm T (2004) Curr Appl Phys 4:554
24. Liang WJ, Shores MP, Bockrath M, Long JR, Park H (2002) Nature 417:725
25. Park J, Pasupathy AN, Goldsmith JI, Chang C, Yaish Y, Petta JR, Rinkoski M, Sethna JP, Abruna HD, McEuen PL, Ralph DC (2002) Nature 417:722
26. Pasupathy AN, Bialczak RC, Martinek J, Grose JE, Donev LAK, McEuen PL, Ralph DC (2004) Science 306:86
27. Wold DJ, Frisbie CD (2001) J Am Chem Soc 123:5549
28. Li XL, He J, Hihath J, Xu BQ, Lindsay SM, Tao NJ (2006) J Am Chem Soc 128:2135
29. Rawlett AM, Hopson TJ, Nagahara LA, Tsui RK, Ramachandran GK, Lindsay SM (2002) Appl Phys Lett 81:3043

30. Ramachandran GK, Hopson TJ, Rawlett AM, Nagahara LA, Primak A, Lindsay SM (2003) Science 300:1413
31. Lau CN, Stewart DR, Williams RS, Bockrath M (2004) Nano Lett 4:569
32. Heimel G, Romaner L, Zojer E, Brédas JL (2007) Nano Lett 7:932
33. Long DP, Lazorcik JL, Mantooth BA, Moore MH, Ratner MA, Troisi A, Yao Y, Ciszek JW, Tour JM, Shashidhar R (2006) Nat Mater 5:901
34. Xue YQ, Datta S, Ratner MA (2001) J Chem Phys 115:4292
35. Nazin GV, Qiu XH, Ho W (2003) Science 302:77
36. Samorì P, Severin N, Simpson CD, Müllen K, Rabe JP (2002) J Am Chem Soc 124:9454
37. Engelkes VB, Beebe JM, Frisbie CD (2004) J Am Chem Soc 126:14287
38. Cui XD, Primak A, Zarate X, Tomfohr J, Sankey OF, Moore AL, Moore TA, Gust D, Harris G, Lindsay SM (2001) Science 294:571
39. Binnig G, Quate CF, Gerber C (1986) Phys Rev Lett 56:930
40. Takano H, Kenseth JR, Wong S-S, O'Brien JC, Porter MD (1999) Chem Rev 99:2845
41. Sheiko SS, Möller M (2001) Chem Rev 101:4099
42. Samorì P (2005) Chem Soc Rev 34:551
43. Samorì P, Surin M, Palermo V, Lazzaroni R, Leclère P (2006) Phys Chem Chem Phys 8:3927
44. Zhong Q, Innis D, Kjoller K, Elings VB (1993) Surf Sci Lett 290:L688
45. Engelkes VB, Beebe JM, Frisbie CD (2005) J Phys Chem B 109:16801
46. Ishida T, Mizutani W, Aya Y, Ogiso H, Sasaki S, Tokumoto H (2002) J Phys Chem B 106:5886
47. Kelley TW, Frisbie CD (2000) J Vac Sci Technol, B 18:632
48. Manoharan HC, Lutz CP, Eigler DM (2000) Nature 403:512
49. Lantz MA, Hug HJ, Hoffmann R, van Schendel PJA, Kappenberger P, Martin S, Baratoff A, Guntherodt HJ (2001) Science 291:2580
50. Morita T, Lindsay S (2007) J Am Chem Soc 129:7262
51. O'Shea SJ, Atta RM, Welland ME (1995) Rev Sci Instr 66:2508
52. Thomson RE, Moreland J (1995) J Vac Sci Technol, B 13:1123
53. Palermo V, Palma M, Samorì P (2006) Adv Mater 18:145
54. Cui XD, Zarate X, Tomfohr J, Sankey OF, Primak A, Moore AL, Moore TA, Gust D, Harris G, Lindsay SM (2002) Nanotechnology 13:5
55. Song H, Lee C, Kang Y, Lee T (2006) Coll Surf a-Physicochem Eng Aspects 284:583
56. Gomez-Navarro C, de Pablo PJ, Gomez-Herrero J (2006) J Mater Sci-Mater Electron 17:475
57. Kelley TW, Granstrom EL, Frisbie CD (1999) Adv Mater 11:261
58. Loiacono MJ, Granstrom EL, Frisbie CD (1998) J Phys Chem B 102:1679
59. Planes J, Houze F, Chretien P, Schneegans O (2001) Appl Phys Lett 79:2993
60. Ionescu-Zanetti C, Mechler A, Carter SA, Lal R (2004) Adv Mater 16:385
61. Alexeev A, Loos J, Koetse MM (2006) Ultramicroscopy 106:191
62. Lee HJ, Park SM (2005) J Phys Chem B 109:13247
63. Munuera C, Barrena E, Ocal C (2007) Nanotechnology 18:125505
64. Wilson NR, Cobden DH, Macpherson JV (2002) J Phys Chem B 106:13102
65. Wilson NR, Macpherson JV (2003) Nano Lett 3:1365
66. Hafner JH, Cheung CL, Oosterkamp TH, Lieber CM (2001) J Phys Chem B 105:743
67. Hafner JH, Cheung CL, Woolley AT, Lieber CM (2001) Prog Biophys Molec Biol 77:73
68. Jarvis SP, Oral A, Weihs TP, Pethica JB (1993) Rev Sci Instr 64:3515
69. Xu BQ, Xiao XY, Tao NJ (2003) J Am Chem Soc 125:16164
70. Engelkes VB, Frisbie CD (2006) J Phys Chem B 110:10011

71. Gosvami N, Lau KHA, Sinha SK, O'Shea SJ (2006) Appl Surf Sci 252:3956
72. Ishida T, Mizutani W, Azehara H, Miyake K, Aya Y, Sasaki S, Tokumoto H (2002) Surf Sci 514:187
73. Wakamatsu S, Akiba U, Fujihira M (2002) Jap J Appl Phys Part 1 – Regular Papers Short Notes & Review Papers 41:4998
74. Ishida T, Mizutani W, Liang TT, Azehara H, Miyake K, Sasaki S, Tokumoto H (2003) Molec Electron III 1006:164 (Ann NY Acade Sci)
75. Hudlet S, Saint Jean M, Guthmann C, Berger J (1998) Eur Phys J B 2:5
76. Love JC, Estroff LA, Kriebel JK, Nuzzo RG, Whitesides GM (2005) Chem Rev 105:1103
77. Schreiber F (2000) Prog Surf Sci 65:151
78. Ulman A (1996) Chem Rev 96:1533
79. Tao F, Bernasek SL (2007) Chem Rev 107:1408
80. Kaun CC, Guo H (2003) Nano Lett 3:1521
81. Zahid F, Paulsson M, Polizzi E, Ghosh AW, Siddiqui L, Datta S (2005) J Chem Phys 123:064707
82. Ratner MA, Davis B, Kemp M, Mujica V, Roitberg A, Yaliraki S (1998) Molec Electron: Sci Technol 852:22 (Ann NY Acad Sci)
83. Alamarguy D, Schneegans O, Noel S, Boyer L (2004) Appl Surf Sci 225:309
84. Samorì P, Diebel J, Lowe H, Rabe JP (1999) Langmuir 15:2592
85. Hegner M, Wagner P, Semenza G (1993) Surf Sci 291:39
86. Stamou D, Gourdon D, Liley M, Burnham NA, Kulik A, Vogel H, Duschl C (1997) Langmuir 13:2425
87. Wagner P, Hegner M, Guntherödt HJ, Semenza G (1995) Langmuir 11:3867
88. Blackstock JJ, Li ZY, Freeman MR, Stewart DR (2003) Surf Sci 546:87
89. Simmons JG (1963) J Appl Phys 34:1793
90. Wold DJ, Haag R, Rampi MA, Frisbie CD (2002) J Phys Chem B 106:2813
91. Song H, Lee H, Lee T (2007) J Am Chem Soc 129:3806
92. Tian WD, Datta S, Hong SH, Reifenberger R, Henderson JI, Kubiak CP (1998) J Chem Phys 109:2874
93. Cui XD, Primak A, Zarate X, Tomfohr J, Sankey OF, Moore AL, Moore TA, Gust D, Nagahara LA, Lindsay SM (2002) J Phys Chem B 106:8609
94. Tomfohr J, Ramachandran GK, Sankey OF, Lindsay SM (2005) In: Cuniberti G, Fagas G, Richter K (eds) Introducing Molecular Electronics. Springer, Berlin Heidelberg New York, p 301
95. Beebe JM, Engelkes VB, Miller LL, Frisbie CD (2002) J Am Chem Soc 124:11268
96. Johnson KL (1987) Contact mechanics. Cambridge University Press, Cambridge
97. Huang ZF, Xu BQ, Chen YC, Di Ventra M, Tao NJ (2006) Nano Lett 6:1240
98. Chen F, Li XL, Hihath J, Huang ZF, Tao NJ (2006) J Am Chem Soc 128:15874
99. Kim B, Beebe JM, Jun Y, Zhu XY, Frisbie CD (2006) J Am Chem Soc 128:4970
100. Mazur U, Hipps KW (1995) J Phys Chem 99:6684
101. Seferos DS, Blum AS, Kushmerick JG, Bazan GC (2006) J Am Chem Soc 128:11260
102. Kelley TW, Frisbie CD (2001) J Phys Chem B 105:4538
103. Nakamura M, Yanagisawa H, Kuratani S, Iizuka M, Kudo K (2003) Thin Solid Films 438:360
104. Biscarini F, Zamboni R, Samorì P, Ostoja P, Taliani C (1995) Phys Rev B 52:14868
105. Horowitz G, Garnier F, Yassar A, Hajlaoui R, Kouki F (1996) Adv Mater 8:52
106. Horowitz G, Peng XZ, Fichou D, Garnier F (1990) J Appl Phys 67:528
107. Servet B, Ries S, Trotel M, Alnot P, Horowitz G, Garneir F (1993) Adv Mater 5:461
108. Torsi L, Dodabalapur A, Rothberg LJ, Fung AWP, Katz HE (1996) Science 272:1462
109. Dimitrakopoulos CD, Malenfant PRL (2002) Adv Mater 14:99

110. Forrest SR (2004) Nature 428:911
111. Friend RH, Gymer RW, Holmes AB, Burroughes JH, Marks RN, Taliani C, Bradley DDC, Dos Santos DA, Bredas JL, Logdlund M, Salaneck WR (1999) Nature 397:121
112. Huitema HEA, Gelinck GH, van der Putten JBPH, Kuijk KE, Hart CM, Cantatore E, Herwig PT, van Breemen AJJM, de Leeuw DM (2001) Nature 414:599
113. Sirringhaus H, Brown PJ, Friend RH, Nielsen MM, Bechgaard K, Langeveldvoss BMW, Spiering AJH, Janssen RAJ, Meijer EW, Herwig P, De Leeuw DM (1999) Nature 401:685
114. Cravino A, Sariciftci NS (2002) J Mat Chem 12:1931
115. Schmidt-Mende L, Fechtenkötter A, Müllen K, Moons E, Friend RH, MacKenzie JD (2001) Science 293:1119
116. Friend RH, Gymer RW, Holmes AB, Burroughes JH, Marks RN, Taliani C, Bradley DDC, Dos Santos DA, Brédas JL, Logdlund M, Salaneck WR (1999) Nature 397:121
117. Cacialli F, Wilson JS, Michels JJ, Daniel C, Silva C, Friend RH, Severin N, Samorì P, Rabe JP, O'Connell MJ, Taylor PN, Anderson HL (2002) Nat Mater 1:160
118. Gustafsson G, Cao Y, Treacy GM, Klavetter F, Colaneri N, Heeger AJ (1992) Nature 357:477
119. Mitschke U, Bäuerle P (2000) J Mater Chem 10:1471
120. Pei QB, Yu G, Zhang C, Yang Y, Heeger AJ (1995) Science 269:1086
121. Wilson JS, Frampton MJ, Michels JJ, Sardone L, Marletta G, Friend RH, Samorì P, Anderson HL, Cacialli F (2005) Adv Mater 17:2659
122. Muccini M (2006) Nat Mater 5:605
123. Zaumseil J, Friend RH, Sirringhaus H (2006) Nat Mater 5:69
124. Chiesa M, Burgi L, Kim JS, Shikler R, Friend RH, Sirringhaus H (2005) Nano Lett 5:559
125. Samorì P (2006) Scanning Probe Microscopies Beyond Imaging: Manipulation of Molecules and Nanostructures. Wiley-VCH, Weinheim
126. Lee HJ, Park SM (2004) J Phys Chem B 108:16365
127. Lee HJ, Park SM (2004) J Phys Chem B 108:1590
128. Yamamoto SI, Ogawa K (2006) Surf Sci 600:4294
129. Han DH, Park SM (2004) J Phys Chem B 108:13921
130. Wu CG, Chang SS (2005) J Phys Chem B 109:825
131. Hong SY, Park SM (2005) J Phys Chem B 109:9305
132. Park SM, Cho SH (2006) J Phys Chem B 110:25656
133. Pingree LSC, Hersam MC, Kern MM, Scott BJ, Marks TJ (2004) Appl Phys Lett 85:344
134. Lin HN, Lin HL, Wang SS, Yu LS, Perng GY, Chen SA, Chen SH (2002) Appl Phys Lett 81:2572
135. Brandsch R, Bar G, Whangbo MH (1997) Langmuir 13:6349
136. Magonov SN, Elings V, Whangbo MH (1997) Surf Sci 375:L385
137. Douheret O, Lutsen L, Swinnen A, Breselge M, Vandewal K, Goris L, Manca J (2006) Appl Phys Lett 89:032107
138. Coffey DC, Reid OG, Rodovsky DB, Bartholomew GP, Ginger DS (2007) Nano Lett 7:738
139. Paul S, Kanwal A, Chhowalla M (2006) Nanotechnology 17:145
140. Zhong ZH, Wang DL, Cui Y, Bockrath MW, Lieber CM (2003) Science 302:1377
141. Hoeben FJM, Jonkheijm P, Meijer EW, Schenning APHJ (2005) Chem Rev 105:1491
142. Leclère P, Surin M, Brocorens P, Cavallini M, Biscarini F, Lazzaroni R (2006) Mater Sci & Eng R-Reports 55:1

143. Samorì P, Engelkamp H, de Witte PAJ, Rowan AE, Nolte RJM, Rabe JP (2005) Adv Mater 17:1265
144. Samorì P, Francke V, Müllen K, Rabe JP (1999) Chem Eur J 5:2312
145. Samorì P, Rabe JP (2002) J Phys – Cond Mater 14:9955
146. de Pablo PJ, Colchero J, Luna M, Gomez-Herrero J, Baro AM (2000) Phys Rev B 61:14179
147. de Pablo PJ, Gomez-Navarro C, Martinez MT, Benito AM, Maser WK, Colchero J, Gomez-Herrero J, Baro AM (2002) Appl Phys Lett 80:1462
148. de Pablo PJ, Gomez-Navarro C, Colchero J, Serena PA, Gomez-Herrero J, Baro AM (2002) Phys Rev Lett 88:036804
149. Park JY, Rosenblatt S, Yaish Y, Sazonova V, Ustunel H, Braig S, Arias TA, Brouwer PW, McEuen PL (2004) Nano Lett 4:517
150. Dai H, Wong EW, Lieber CM (1996) Science 272:523
151. Gomez-Navarro C, De Pablo PJ, Gomez-Herrero J, Biel B, Garcia-Vidal FJ, Rubio A, Flores F (2005) Nat Mater 4:534
152. Krasheninnikov AV, Nordlund K, Sirvio M, Salonen E, Keinonen J (2001) Phys Rev B 63:245405
153. de Pablo PJ, Martinez MT, Colchero J, Gomez-Herrero J, Maser WK, Benito AM, Munoz E, Baro AM (2000) Adv Mater 12:573
154. Gomez-Navarro C, de Pablo PJ, Gomez-Herrero J (2004) Adv Mater 16:549
155. Livage J (1998) Coord Chem 178:999
156. Gomez-Navarro C, de Pablo PJ, Colchero J, Fan Y, Burghard M, Gomez-Herrero J, Baro AM (2003) Nanotechnology 14:134
157. Tan SS, Tang ZY, Liang XR, Kotov NA (2004) Nano Lett 4:1637
158. Park JG, Lee SH, Kim B, Park YW (2002) Appl Phys Lett 81:4625
159. Saha SK, Su YK, Lin CL, Jaw DW (2004) Nanotechnology 15:66
160. Martin CR (1994) Science 266:1961
161. Mativetsky JM, Datars WR (2002) Phys B – Cond Matter 324:191
162. Davis JJ, Morgan DA, Wrathmell CL, Axford DN, Zhao J, Wang N (2005) J Mater Chem 15:2160
163. Leatherman G, Durantini EN, Gust D, Moore TA, Moore AL, Stone S, Zhou Z, Rez P, Liu YZ, Lindsay SM (1999) J Phys Chem B 103:4006
164. Gittins DI, Bethell D, Schiffrin DJ, Nichols RJ (2000) Nature 408:67
165. Tao NJ (1996) Phys Rev Lett 76:4066
166. Zhao JW, Davis JJ, Sansom MSP, Hung A (2004) J Am Chem Soc 126:5601
167. Watt GD, Frankel RB, Papaefthymiou GC (1985) Proc Natl Acad Sci USA 82:3640
168. Xu DG, Watt GD, Harb JN, Davis RC (2005) Nano Lett 5:571
169. Xu B, Zhang P, Li X, Tao N (2004) Nano Lett 4:1105
170. Dandliker PJ, Holmlin RE, Barton JK (1997) Science 275:1465
171. Malyshev AV (2007) Phys Rev Lett 98:096801
172. Boon EM, Ceres DM, Drummond TG, Hill MG, Barton JK (2000) Nat Biotechnol 18:1096
173. Dunlap DD, Garcia R, Schabtach E, Bustamante C (1993) Proc Natl Acad Sci USA 90:7652
174. Porath D, Bezryadin A, de Vries S, Dekker C (2000) Nature 403:635
175. Fink HW, Schonenberger C (1999) Nature 398:407
176. Kasumov AY, Kociak M, Gueron S, Reulet B, Volkov VT, Klinov DV, Bouchiat H (2001) Science 291:280
177. Cohen H, Nogues C, Naaman R, Porath D (2005) Proc Nat Acad Sci USA 102:11589

178. Cohen H, Nogues C, Ullien D, Daube S, Naaman R, Porath D (2006) Faraday Discuss 131:367
179. Nogues C, Cohen SR, Daube S, Apter N, Naaman R (2006) J Phys Chem B 110:8910
180. Heim T, Deresmes D, Vuillaume D (2004) J Appl Phys 96:2927
181. Tanaka S, Cai LT, Tabata H, Kawai T (2003) Jap J Appl Phys Part 1 – Regular Papers Short Notes & Review Papers 42:2818
182. Gu JH, Tanaka S, Otsuka Y, Tabata H, Kawai T (2002) Appl Phys Lett 80:688
183. Oura K (2003) Surface Science: an Introduction. Springer, Berlin Heidelberg New York
184. Uchihashi T, Ishida T, Komiyama M, Ashino M, Sugawara Y, Mizutani W, Yokoyama K, Morita S, Tokumoto H, Ishikawa M (2000) Appl Surf Sci 157:244
185. Luthi R, Schlittler RR, Brugger J, Vettiger P, Welland ME, Gimzewski JK (1999) Appl Phys Lett 75:1314
186. Zahl P, Bammerlin M, Meyer G, Schlittler RR (2005) Rev Sci Instr 76:023707
187. Egger S, Ilie A, Fu YT, Chongsathien J, Kang DJ, Welland ME (2005) Nano Lett 5:15
188. Gartner C, Hoffmann R, Perez-Willard F, Sauter M, Surgers C, von Lohneysen H (2006) Rev Sci Instr 77:099901
189. Morita S, Wiesendanger R, Meyer E (2002) Noncontact Atomic Force Microscopy. Springer, Berlin Heidelberg New York
190. Loppacher C, Bammerlin M, Guggisberg M, Schar S, Bennewitz R, Baratoff A, Meyer E, Guntherodt HJ (2000) Phys Rev B 62:16944
191. Sugimoto Y, Pou P, Abe M, Jelinek P, Perez R, Morita S, Custance O (2007) Nature 446:64
192. Bennewitz R, Schar S, Barwich V, Pfeiffer O, Meyer E, Krok F, Such B, Kolodzej J, Szymonski M (2001) Surf Sci 474:L197
193. Burke SA, Mativetsky JM, Hoffmann R, Grutter P (2005) Phys Rev Lett 94:096102
194. Mativetsky JM, Burke SA, Fostner S, Grutter P (2007) Nanotechnology 18:105303
195. Xu S, Liu GY (1997) Langmuir 13:127
196. Amro NA, Xu S, Liu GY (2000) Langmuir 16:3006
197. Liang J, Sun Q, Selloni A, Scoles G (2006) J Phys Chem B 110:24797
198. Xu S, Amro NA, Liu GY (2001) Appl Surf Sci 175:649
199. Samorì P (2004) J Mater Chem 14:1353
200. Palermo V, Liscio A, Palma M, Surin M, Lazzaroni R, Samorì P (2007) Chem Comm, p 3326
201. Wold DJ, Frisbie CD (2000) J Am Chem Soc 122:2970

Top Curr Chem (2008) 285: 203–267
DOI 10.1007/128_2008_2

Published online: 10 April 2008

Two-Dimensional Nanotemplates as Surface Cues for the Controlled Assembly of Organic Molecules

Fabio Cicoira[1,2] · Clara Santato[3,4] · Federico Rosei[5] (✉)

[1]Department of Materials Science and Engineering, Bard Hall, Cornell University, Ithaca, NY 14853-1501, USA

[2]Institute of Photonics and Nanotechnology, Consiglio Nazionale delle Ricerche, Via alla Cascata 56/C, 38050 Povo (Trento), Italy

[3]Département de génie physique, Ecole Polytechnique de Montréal, C.P. 6079, Succ. Centre-ville, Montréal, QC H3C 3A7, Canada

[4]ISMN-CNR, via Gobetti, 40129 Bologna, Italy

[5]Centre Énergie Matériaux et Télécommunications, Institut National de la Recherche Scientifique (INRS), Université du Québec, 1650 Boul. Lionel-Boulet, Varennes, QC J3X 1S2, Canada
rosei@emt.inrs.ca

Abstract Controlled two-dimensional assembly of organic molecules can be successfully realized by means of surface nanotemplates that provide surface cues for assembly upon adsorption. Examples of such templates are nanostructured surfaces and organic porous networks. In this review, we discuss the formation and use of such templates for controlled molecular assembly. The formation of the organic porous network is typically based on non-covalent interactions, e.g., hydrogen bonds, dipole–dipole interactions, metal-organic coordination bonds together with substrate-mediated molecular interactions. The pores of the network can act as hosts for specific organic molecules. The chemical structure of the molecular building blocks of the porous network has a primary effect on the shape, size, and chemical reactivity of the cavities. Long-range mesoscale

reconstructions can also be employed as surface nanotemplates based on the selective adsorption of atomic or molecular species at specific surface sites. Scanning tunneling microscopy is the key tool to study the formation of the nanotemplates as well as the effect of the template in the growth of the ordered organic structures. The reported studies contribute to build the rationale in the design and fabrication of two-dimensional organic networks. The topic covered in this review represents an important challenge in nanotechnology since these findings might have a wide range of applications, e.g., in electronics, sensing, and bio-recognition.

Keywords Bottom-up approach · Nanostructured surface · Nanotemplate · Organic porous network · Self-assembly · Surface cues

Abbreviations

AQ	Anthraquinone
BTB	1,3,5-Benzenetribenzoic acid
CA	Cyanuric acid
c[12]T	Cyclo[12]thiophene
DPDI	4,9-Diaminoperylene-quinone-3,10-di-imine
HBC	Hexabenzacoronene
HOMO	Highest occupied molecular orbital
HOPG	Highly oriented pyrolytic graphite
HT	High temperature
I_t	Tunneling current
LT	Low temperature
LUMO	Lowest unoccupied molecular orbital
M	1,5,3-Triazine-2,4,6-triamine (melamine)
ML	Monolayer
MOCN	Metal-organic coordination network
NEXAFS	Near edge X-ray absorption fine structure
OPE	Oligomer of phenylene-ethynylene
PTCDI	3,4,9,10-Perylene tetracarboxylic diimide
RT	Room temperature
SAMN	Self assembled molecular network
STM	Scanning tunneling microscopy
STS	Scanning tunneling spectroscopy
TAB	Tetraaminobenzene
TDA	4,1′,4′,1″-Terphenyl-1,4″dicarboxylic acid
TMA	1,3,5-Benzenetricarboxylic (trimesic acid)
TMLA	1,2,4-Benzenetricarboxylic acid (trimellitic acid)
TPA	Terephthalic acid
TPT	1,3,5-Tris(4-pyridil)-2,4-triazine
T5	α-Quinquethiophene
UHV	Ultra high vacuum
V_s	Bias voltage
XPS	X-ray photoelectron spectroscopy
ZnOEP	Zinc-octaethylporphyrin

1 Introduction

One of the most challenging issues in nanotechnology is the design and fabrication of arrays of functional nanostructures with controlled size and shape, precisely positioned on a substrate of choice [1, 2]. In this context, the bottom–up approach is emerging as a truly promising method for the controlled growth and processing of nanostructured materials. This approach is based on the concept of (organic) self-assembly [3] or (inorganic) self-organization [4, 5].

In a typical self-assembly process [6], non-covalent interactions, such as hydrogen bonds, guide the formation of ordered, well-defined structures under equilibrium conditions. In crystal engineering, supramolecular chemists exploit non-covalent interactions to organize molecules within a three-dimensional crystal lattice [7–9]. To confine the self-assembly process to two dimensions, it is best to use a fairly inert crystalline surface (e.g., gold or graphite) so that the substrate itself does not strongly influence the interactions between molecules. In this sense, the substrate is expected to act as a "spectator", or simply as a "static template" that does not heavily influence molecular ordering, since it only provides a regular lattice of atoms on which to physisorb. The fairly weak lateral and periodic forces exerted by the surface of choice on the physisorbed molecules guide molecule–molecule interactions in such a way as to form long-range aggregates. Once the desired ordered monolayer is formed, it may serve as the starting point to build a 3D molecular crystal [10–14].

Surface *nanotemplates* [15] are substrates that are artificially or naturally patterned at the nanoscale, where specific functionalities provide suitable surface cues that are able to drive the controlled assembly of atomic or molecular species [16]. By surface cues, we mean either extended defects (e.g., steps) or other relatively periodic surface features that can locally influence molecular adsorption, thus effectively steering the formation of long-range ordered patterns.

In our description, there are two main groups of surface nanotemplates, organized as follows: porous networks (often referred to as "nanomeshes") and nanostructured surfaces. These two groups differ in the mechanism used to realize the "templating" effect. Porous networks are able to drive the assembly of guest atoms or molecules into the cavities or at the rims of the pores. Depending on the size, a single pore can accommodate an individual molecule or clusters of several molecules. The templating effect of nanostructured surfaces is based on the selective adsorption of atomic or molecular species at specific surface sites. Examples of templates based on nanostructured surfaces are the striped periodic nanograting produced by the partial nitrogen reconstruction on Cu(001) and oxygen reconstruction of Cu(110) (discussed in Sect. 3), the self-organization of semiconductor islands on step-

bunched Si(111) [17, 18], and the ordered growth of magnetic dots on stepped surfaces [19, 20]. The most powerful and versatile technique to study the assembly of organic molecules at surfaces is scanning tunneling microscopy (STM). STM allows in situ investigations under a wide range of experimental conditions, attaining molecular and atomic resolution [21–43].

While the field of self-assembly at surfaces is fairly well established, the use of surface cues to guide the formation of ordered constructs is still in its infancy.

The review attempts to describe recent work on the controlled assembly of organic building blocks, driven by surface templates and investigated by STM. While we have strived to make it comprehensive, it is by no means exhaustive. The review is organized in two main sections: the first deals with porous network templates and the second with nanostructured surface templates.

2
Porous Molecular Networks at Surfaces

Organic molecular porous networks, the analogue of inorganic *nanomeshes* [44–48], are ordered structures with cavities formed by organic molecules on top of a solid crystalline substrate. The porous structure can act as host for other organic molecules. For this reason, these systems are often named host-guest systems. The building blocks of the pores are held together by non-covalent interactions, such as hydrogen bonding, Van der Waals forces, and metal-organic coordination. The pores can be formed by a single species or by different species. The size of the pores can be tuned by changing the building blocks so that molecules with different size can be accommodated within the pores. One of the most common host-guest system is based on the self-assembly of 1,3,5-benzenetricarboxylic (trimesic) acid (TMA), usually into a porous network with threefold symmetry. However, in recent years many other kinds of porous networks have been introduced. Such pores are smaller than any other feature that can be obtained by other approaches (e.g., e-beam lithography) and in principle can combine chemical functionality with spatial control.

2.1
Hydrogen-Bonded Networks

2.1.1
TMA and Other Benzoic Acids

TMA consists of a phenyl ring with three carboxylic groups disposed in the threefold 1,3,5 positions (see Fig. 4), and is therefore considered a model system for self-assembly in two dimensions. In fact, its molecular struc-

ture allows the formation of supramolecular architectures, such as two-dimensional porous networks via hydrogen bonding. After the first pioneering studies on the self-assembly of TMA performed in ultra high vacuum (UHV) on graphite [49] and Cu [50] surfaces, porous networks of TMA were also obtained at the solid/liquid interface [51], and the role of the solvents in addressing self-assembly was also investigated [52]. TMA adlayers were studied by electrochemical STM on Au(111) [53]. A potential-induced phase transition, attributed to the interfacial deprotonation/protonation of the TMA molecules [54], was observed between flat lying molecules organized into a (4×4) structure and vertically oriented molecules giving rise to a $(2\sqrt{3}\times4\sqrt{3})$ adlayer structure. Porous networks at the liquid/solid interface were obtained also with TMA analogues, such as 1,3,5-tris (ethoxycarbonylmethoxybenzene) on HOPG in a mixture of toluene and ethanol [55].

The first works on the self-assembly of TMA in two dimensions date back to 2002. Griessl et al. [49] studied the self-assembly of TMA on graphite in UHV. STM investigations carried out at 25 K revealed that TMA can form two different network structures that are named *chicken wire* (or *honeycomb*) and *flower* (Fig. 1), both exhibiting threefold symmetry. The two structures can coexist on the surface, with a coverage ratio that depends on the deposition conditions, and are found to be stable up to room temperature (RT).

The *chicken-wire* structure (Fig. 2a) is modeled as composed of sixfold rings of TMA molecules with a perfect arrangement of the hydrogen bonds. Each molecule is part of three neighboring rings; a double hydrogen bond forms between two adjacent molecules. In the *flower* structure (Fig. 2b), the hydrogen bonds are formed in the same way within the rings as in the *chicken wire* structure, yet in this structure the hydrogen bonds are formed between three molecules. This results in a close packed structure. Both structures consist of sixfold rings with a hole in the centre. The diameter of the larger holes is about 1.5 nm. The smaller holes, present in the *flower* structure into the rectangles on each side of the hexagon, have a diameter of 0.75 nm.

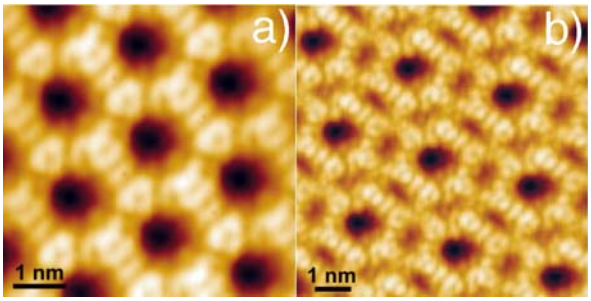

Fig. 1 STM images of TMA on graphite. **a** *Chicken wire* structure ($5.4\times5.4\,nm^2$, $U = -1.4$ V, $I = 126$ pA) and **b** *flower* structure ($8.2\times8.2\,nm^2$, $V_s = -1.4$ V, $I_t = 126$ pA). Reprinted with permission from [49]. © 2002 Wiley

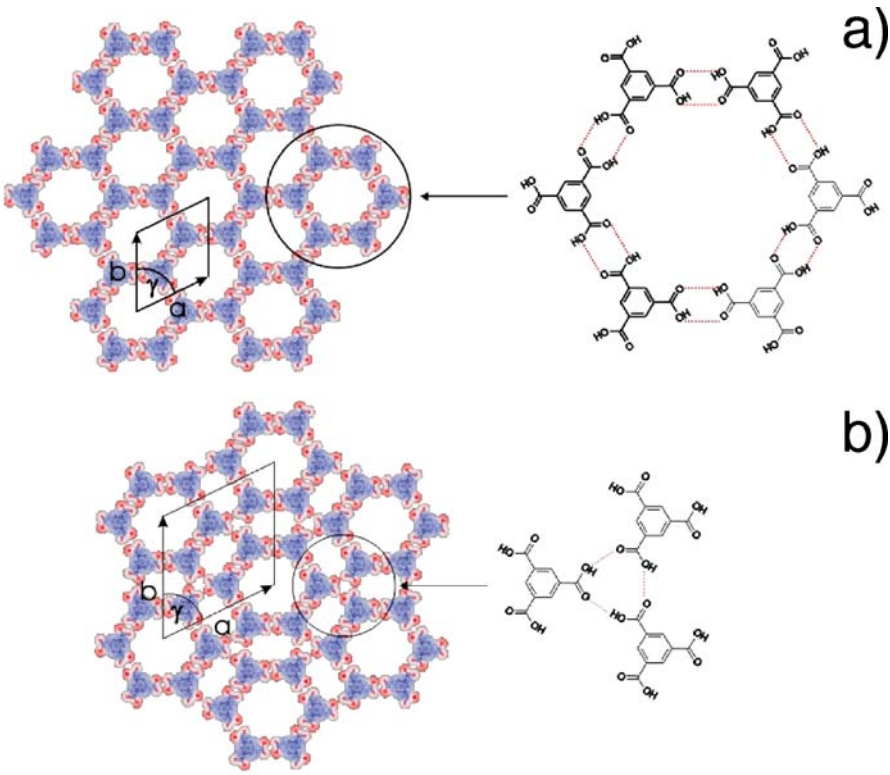

Fig. 2 Schematic pictures of the *chicken wire* (**a**) and the *flower* (**b**) structures. Reprinted with permission from [49]. © (2002) Wiley

Interestingly, both TMA networks can act as host systems for guest TMA molecules, which can be adsorbed on the larger pores. The position of the guest molecules is different for *chicken wire* or *flower* structures. In *chicken wire* networks, the TMA guest lies flat on the substrate being placed in an a-centric position within the pores and bound with two hydrogen bonds to the molecules constituting the pore. In the *flower* structure, the guest can be also placed in an upright position above the ring.

Dmitriev and co-workers reported on the self-assembly of TMA on the (100) surface of copper in UHV at variable substrate temperature [50]. TMA was found to assemble into two different structures, depending on substrate temperature. At low temperature (LT, 200 K), the molecules lie flat on the substrate, with their phenyl rings oriented parallel to the surface. In small islands (20×20 nm^2 sized) most of the molecules assemble into the *chicken wire* structure. Other structures, i.e., close-packed islands or pentagonal meshes, were also found. The difficulty to obtain large islands with *chicken wire* structure was attributed to substrate corrugation experienced by the adsorbed TMA

molecules and to kinetic limitations. At RT, TMA assembles into a *striped* phase. The stripes can have four distinct orientations (Fig. 3). In this phase, TMA is present in the carboxylate form due to the catalytic activity of copper towards the deprotonation reaction. The molecules adsorb with an upright geometry and are anchored at the surface via the carboxylate. Therefore the substrate–molecule interactions are stronger, as compared to the LT phase.

Similar results have been recently obtained for TMA on the (111) surface of silver [56]. On this surface, the *honeycomb* structure (Fig. 4a) was obtained by evaporating TMA on a substrate held at 100 K and subsequently annealed at 300 K. Performing further annealing at 420 K led to an irreversible transformation in a denser structure (*quartet*, Fig. 4b). Scanning tunneling spectroscopy (STS), X-ray photoelectron spectroscopy (XPS), and near-edge X-ray absorption fine structure (NEXAFS) proved that the *honeycomb* phase is made of weakly physisorbed molecules whereas the denser phase is made up of deprotonated molecules, tightly bound to the substrate.

TMA porous networks and TMA/C_{60} *host-guest* systems on graphite were studied at the liquid–solid interface in ambient conditions, using heptanoic acid as solvent [51]. Heptanoic acid is an ideal solvent for STM studies in solution because of its low conductivity and low vapor pressure. In a first step, a TMA *chicken wire* structure was self-assembled on the surface and, subsequently, a saturated solution of C_{60} was added. The C_{60} molecules were found to adsorb preferentially on the open pores of the template (Fig. 5). A nearly perfect geometric match was achieved, since the dimensions of C_{60} are close to the pore diameter of the TMA network (about 1 nm). Only a low density of occupied cavities was observed, probably due to the low solubility of C_{60} in heptanoic acid. The presence of the TMA network stabilizes the adsorption of C_{60} on graphite. In fact, C_{60} by itself does not self-assemble on this surface. The C_{60} molecules are found exactly in the centre of the pores, since this conformation maximizes the interaction with both the TMA network and the

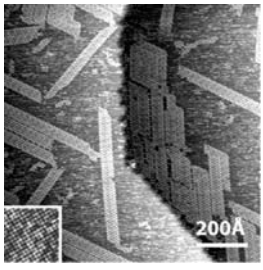

Fig. 3 STM micrograph of stripes of TMA adsorbed on Cu(100) having four different orientations. Tunneling parameters: $V_s = 0.752$ V, $I_t = 0.54$ nA. *Inset*: pristine Cu(100) imaged with atomic resolution. Reprinted with permission from [50]. © (2002) American Chemical Society

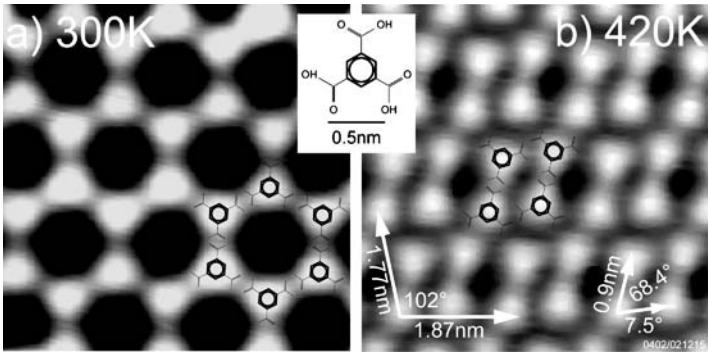

Fig. 4 STM images of **a** *honeycomb* and **b** *quartet* structure of TMA on Ag(111) formed after annealing at 300 K and 420 K, respectively. $V_s = 0.5$ V, $I_t = 0.5$ nA. Reprinted with permission from [56]. © (2002) Wiley

graphite substrate. The relatively low resolution of the STM images suggests that the C_{60} molecules are rotating within the pores.

Interestingly, the TMA/C_{60} system was used to demonstrate RT manipulation of single molecules. Using the STM tip under appropriate biasing conditions, C_{60} could be moved from one pore to the adjacent one, leaving the TMA network unperturbed (*nanosoccer* experiment, Fig. 5).

A similar approach was used to obtain TMA/coronene host-guest systems in the liquid phase using highly oriented pyrolytic graphite (HOPG) as surface [58] (for coronene molecular structure, see Fig. 48). After forming and imaging the *chicken wire* network (the diameter of the cavities is about 1 nm) a saturated solution of coronene in heptanoic acid was added. As shown in Fig. 6, coronene fills all the pores, with the exception of few vacancies. The molecules adsorb with the molecular plane parallel to the substrate and have a disk-like appearance with a diameter of about 1 nm. Six TMA molecules of the *chicken-wire* structure surround each coronene molecule. The coronene molecules hosted in the network are imaged with two very distinct contrasts, as highlighted in Fig. 6A. Molecule **1** appears as six bright lobes, i.e., the six outer benzene rings of the coronene molecule, arranged around a depression, whereas molecule **2** appears as two concentric rings. In the former case, a comparable contrast was observed for coronene molecules directly deposited on HOPG, whereas in the latter case the rings resemble the highest occupied molecular orbital (HOMO) and the lowest unoccupied molecular orbital (LUMO) of an isolated coronene molecule, as found from first principle calculations [58]. These different shapes of the molecule are the result of a periodic modulation of the adsorbate–substrate interactions within the cavities, due to a Moiré-like superstructure arising from the superposition of the HOPG substrate and the TMA host network lattices, that leads to variation in the distance between graphite and the planar coronene molecules.

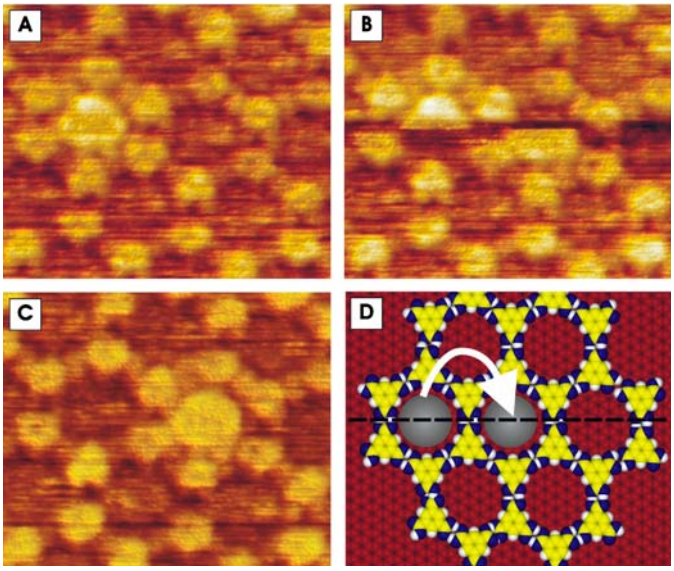

Fig. 5 STM images (**A**–**C** $4.6 \times 4.6\,nm^2$). **A** Single C_{60} molecule on a TMA network; **B** manipulation step: after half the molecule was scanned, the current was switched from 70 to 150 pA; **C** final result of the manipulation with the molecule moved into the adjacent cavity. **D** Illustration of the manipulation experiment. Reprinted with permission from [51]. © (2004) American Chemical Society

The molecules that are bound less tightly to the substrates (type 2 molecules) were found to be free to rotate within the TMA network. The latter acts as a molecular bearing that stabilizes coronene adsorption from solution: in the absence of the TMA network "template", coronene does not form ordered structures when dissolved in heptanoic acid. The TMA network was found to be stable upon manipulation of the guest molecules by the STM tip. The manipulation consisted of removing a molecule from an occupied site (Fig. 6A,B). Differently from what was shown for C_{60}, it was not possible to transfer a molecule from one site to another since most of the sites were occupied.

The steric aspects of the hydrogen bonding were investigated studying the self-assembly of three isomers of the benzene-dicarboxylic acid: terephthalic acid, isophthalic acid, and phthalic acid (see Fig. 7) [59]. The experiments were carried out on HOPG from a heptanoic acid solution. Terephthalic and isophthalic acid are planar whereas phthalic acid is not (the proximity of the two carboxylic groups results in out of plane tilting of the benzene core).

For terephthalic and isophthalic acids it was possible to routinely observe ordered monolayers. Differently from what was observed for trimesic acid networks, where two-dimensional hydrogen bonds are present, the hydrogen bond stabilization in this case occurs only in one dimension. No adsorption

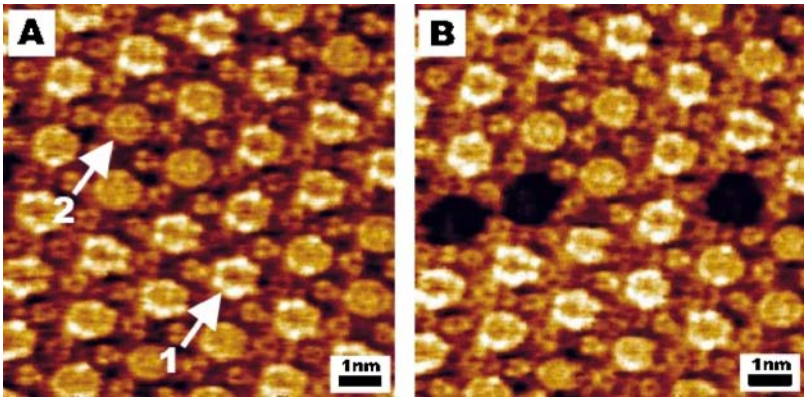

Fig. 6 STM images of coronene guests in a TMA network. **A** Molecules showing different appearance: (*1*) still standing coronene molecule; (*2*) rotating (disk-like) molecule. **B** Same area after removal of some guest molecules. $V_s = 0.8$ V, $I_t = 147$ pA. Reprinted with permission from [57]. © (2004) American Chemical Society

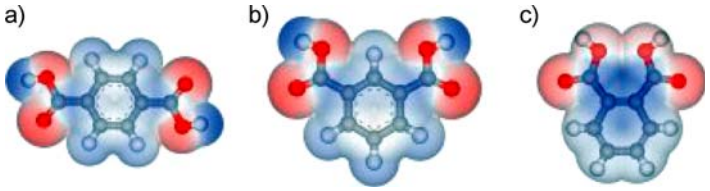

Fig. 7 Molecular structures of **a** terephthalic acid (1,4-benzenedicarboxylic acid), **b** isophthalic acid (1,3-benzene-dicarboxylic acid), and **c** phthalic acid (1,2-benzene-dicarboxylic acid); the surface is given by the van der Waals radii of the atoms. Reprinted with permission from [59]. © (2004) American Chemical Society

was observed for the non-planar phthalic acid. Self-assembly was instead observed from solution of the non-planar 1,2,4,5-benzene-tetracarboxylic acid (pyromellitic acid), revealing that the non-planar structure was not the only element responsible for the behavior of phthalic acid, which was explained by the close proximity of the two carbonyl groups. For steric reasons, only two or three molecules can be connected in a circular bonding scheme, saturating all the carboxylic groups of the molecules involved.

TMA self-assembly was investigated on HOPG at the solid–liquid interface using several fatty acids as solvents: butyric, pentanoic, hexanoic, heptanoic, octanoic, and nonanoic acids, in order to understand the effect of the solvent [52]. Depending on the solvent used, both the *chicken wire* and the *flower* structure were observed. The *chicken wire* structure was found for octanoic and nonanoic acids, whereas the *flower* structure was observed for butyric, pentanoic, and hexanoic acids. Both structures were observed when TMA was dissolved in heptanoic acid. So the general conclusion is that short-chain acids may stabilize the trimer species in solution, thus, leading to a *flower*

structure. On the other hand, long-chain acids stabilize the TMA dimer leading to a *chicken wire* structure. The polymorphs structure seems to correlate with the solubility of TMA in the solvent series, which decreases by increasing the number of C atoms in the acid. Examples of *chicken wire* and *flower* structures formed at the interface of a saturated solution of TMA in heptanoic and pentanoic acids are shown in Fig. 8a,b. In both structures, all the carboxylic groups participate in the hydrogen bond. The main difference is that in the *chicken wire* structures the hydrogen bonds always involve two molecules, leading to a packing density of 0.8 molecule/nm^2 for the *chicken wire* structure, whereas in the *flower* structure one third of the bonds involve three molecules, leading to a packing density of 1.1 molecule/nm^2. The pore diameter is about 1 nm for both structures. However, the center-to-center distance between circular cavities is larger for the *flower* structure. In the *chicken-wire* structure the basic unit is a TMA dimer, whereas in the *flower* structure it is a TMA trimer.

Porous networks similar to those obtained from TMA were also built from 1,3,5-benzenetribenzoic acid (BTB) [60]. Also these studies were carried out on graphite substrates at the solid/liquid interface. To investigate solvent-induced polymorphism, BTB self-assembly on graphite was carried out from several solvents: butanoic, pentanoic, hexanoic, heptanoic, octanoic, and nonanoic acids, 1-octanol, 1-nonanol, 1-decanol, 1-phenyloctane, and dodecane.

BTB consists of three benzoic acid groups arranged with threefold symmetry around a central benzene core and can be considered a phenyl-extended version of TMA. Depending on the solvent, BTB was found to assemble into two different motifs, differing in packing density and hydrogen bond pattern. Nonanoic acid and 1-phenyloctane led to an interconnected six-membered ring structure with a hexagonal cell, similar to the TMA *chicken wire* struc-

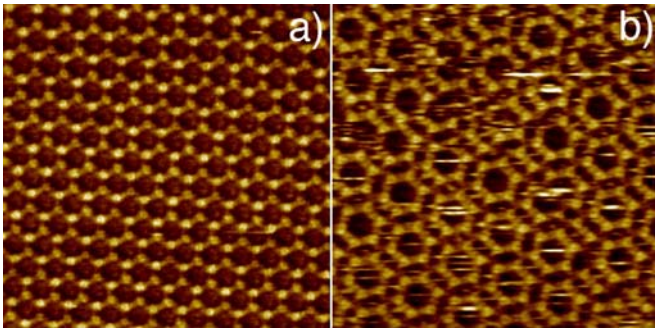

Fig. 8 15×15 nm^2 constant current STM image of a TMA monolayer on HOPG in heptanoic acid (**a**) where the *chicken-wire* pattern forms, and in pentanoic acid (**b**), where the *flower* structure forms. Reprinted with permission from [59]. © (2004) American Chemical Society

ture. In this network, the pores are larger than those of the TMA network (2.8 nm vs. 1 nm). Butanoic, pentanoic, hexanoic and heptanoic acid, 1-octanol, 1-nonanol and 1-decanol lead to a network structure with an oblique cell, where four molecules define a rectangular cavity. The two motifs are shown in Fig. 10. Both polymorphs are found with octanoic acid and dodecane. The packing densities of the rectangular and hexagonal structures are 0.39 and 0.23 molecules/nm^2.

As already observed for TMA, fatty acid solvents with a long chain length stabilize the *chicken wire* structure. For solvents with functional groups able to form hydrogen bonds with the solute, a dependence on the dielectric constant was found. The less dense hexagonal structure was found only for solvents with a relative dielectric constant lower than 3.

BTB self-assembly was also investigated on Ag(111) in UHV at 250 K [61]. The networks were obtained by sublimation of BTB followed by annealing. As shown in Fig. 11, depending on the annealing temperature, three different phases were observed: a *honeycomb* network (phase I, at 270–300 K), *1D ribbons* (phase II, at 300 K) and *close-packed 2D adlayers* (phase III, at 420 K). STS revealed that the *honeycomb* network is composed of uncharged species, weakly physisorbed at the surface. The other two phases are made of negatively charged adsorbates, whose surface concentration increases with increasing annealing temperature. Phase I is a *honeycomb* porous network very similar to the TMA network but with much larger pores (2.95 nm vs. 1.1 nm). This pore diameter provides the space to accommodate a single or several guest molecules. This possibility was explored using the macrocycle mt-33 (which contains a terpyridine and a phenantroline component) as a guest. Mt-33 was evaporated on the porous network and the surface was subsequently imaged at 5 K. STM micrographs revealed that the mt-33 was confined within the BTB pores. Only single species were accommodated in the cavities, with a flat lying geometry. The guest molecules showed a tendency

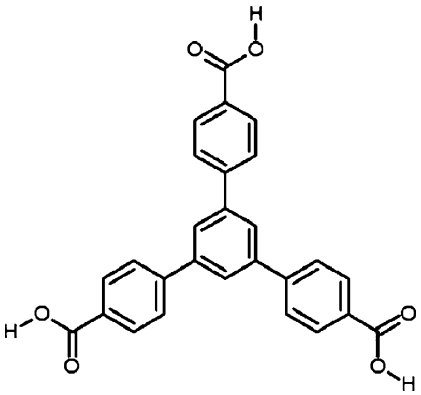

Fig. 9 Chemical structure of BTB

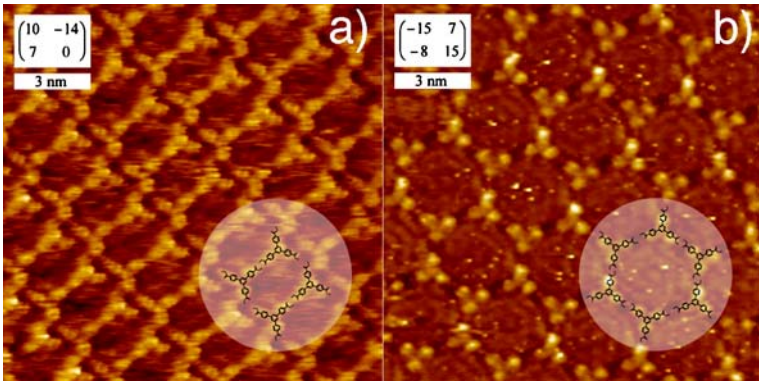

Fig. 10 STM images of the BTB monolayers on HOPG(0001). The superstructure matrices (referred to the hexagonal lattice of every second graphite atoms, lattice constant 0.246 nm and 60° as visible in atomically resolved STM images, are given in the *insets* and the positions of individual BTB molecules are indicated). **a** oblique unit cell as obtained in butanoic through heptanoic acid, 1-octanol, 1-nonanol, and 1-decanol, and **b** chicken-wire modification as obtained in nonanoic acid and 1-phenyloctane. For octanoic acid and dodecane both modifications were observed. $0.3\ \text{V} \leq V_s \leq 1.5\ \text{V}$, $0.1\ \text{nA} \leq I_t \leq 0.9\ \text{nA}$. Reprinted with permission from [60]. © (2006) American Chemical Society

to lie close to the rim of the cavities, so as to maximize π–π interactions. Annealing of the BTB template containing mt-33 determined a transition to phase II (close packed structure) with release of the macrocycles that formed dimers, trimers and tetramers. This result is interesting, since it demonstrates the controlled release of a guest molecule from the BTA network.

Recently, Nath and co-workers showed that the threefold symmetry patterns (*flower* or *chicken-wire*), which TMA forms on threefold symmetry substrates (HOPG in this case), can be broken by introducing an alcohol to the solution [10, 62]. For example, when using 1-undecanol, the well-known *flower* structure is found to be surrounded by a linear pattern, which is a novel TMA polymorph. This is an interesting type of self-assembled molecular network (SAMNs), in which TMA and the alcohol co-adsorb on the surface by exploiting hydrogen bonds and Van der Waals interactions with two rows of TMA molecules facing each other (*ribbon*) separated by an alcohol lying flat on the surface. The *flower* pattern is found to be less stable than the TMA double-ribbon linear pattern, as it slowly disappears during scanning (Fig. 12).

Besides the already noted aspect of symmetry breaking and co-adsorption, this pattern is also interesting because it represents a nanoscale structure with alternating hydrophobic and hydrophilic regions. Changing the length of the alcohol was expected to modulate the spacing between the TMA tapes. However, using hexadecanol the distance between the chains decreased by

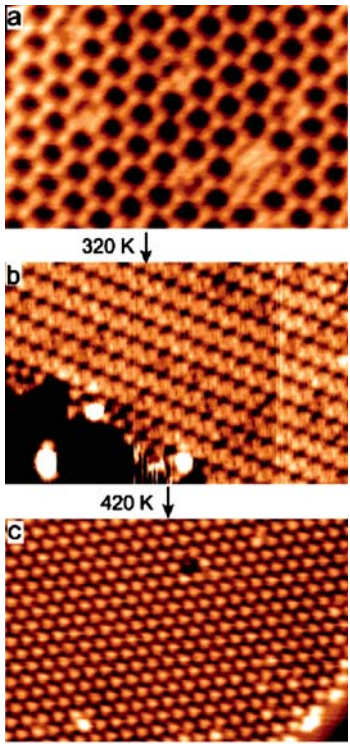

Fig. 11 Three different hydrogen-bond motifs resulting from the deposition of BTB on Ag(111) at different temperature: **a** phase I (open *honeycomb* network), **b** phase II (1D *ribbons*), **c** phase III (close-packed 2D adlayer). Image size: $30 \times 20\ nm^2$. $V_s = 0.5$ V, $I_t = 0.5$ nA. Reprinted with permission from [61]. © (2006) American Chemical Society

0.14 nm. Indeed, STM images showed that the orientation of the long axis of the alcohols tilts from ∼90° (undecanol) to ∼60° (hexadecanol). This result suggested that not only the length of the alcohol but also the parity of carbon atoms in the alcohol chain plays a role in the co-adsorption process. The latter hypothesis was confirmed testing other solvent pairs: odd alcohols always formed an almost perpendicular pattern, whereas even alcohols always formed a tilted pattern. The origin of the parity effect depends on the molecular structure of the assembly [63–65]. The alkyl chains adsorb with the zig-zag plane perpendicular to the surface, with every second C atom lying on the top of the surface. To achieve dense packing, the carbon atoms of neighboring chains should be staggered, with each up atom in one chain next to a down atom in each of the two neighbors. This condition is achieved only for odd-numbered alcohols where the two ends point in different directions. Even-numbered alcohols need to shift by one carbon atom along the chain to achieve efficient packing. This shift results in the tilt of the alcohol chains (Fig. 13).

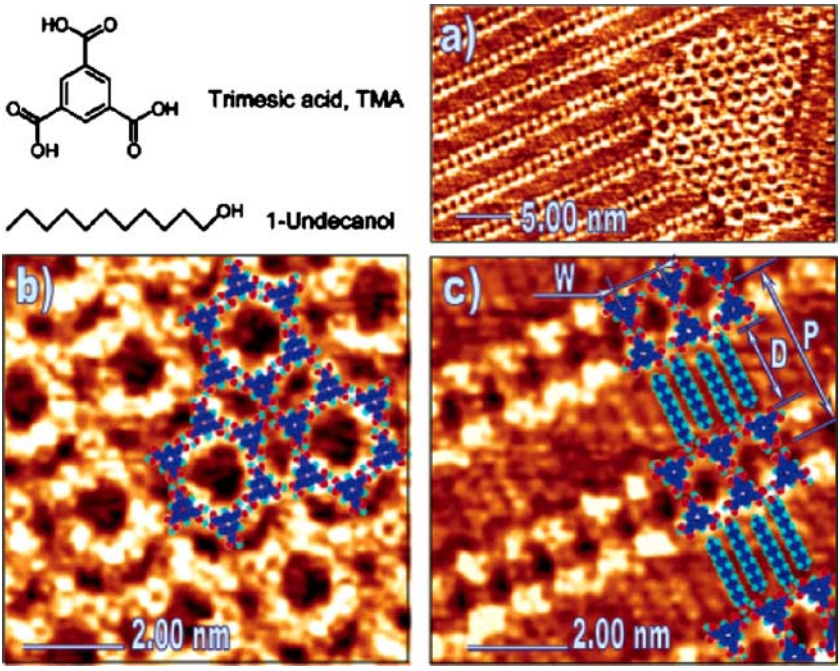

Fig. 12 **a** STM images of SAMNs formed by deposition of 1-undecanol and TMA from a heptanoic acid solution on HOPG. **b** TMA flower pattern with molecular model. **c** TMA linear pattern with molecular model. $V_s = -0.8$ V, $I_t = 150$ pA. Reprinted with permission from [62]. © (2006) American Chemical Society

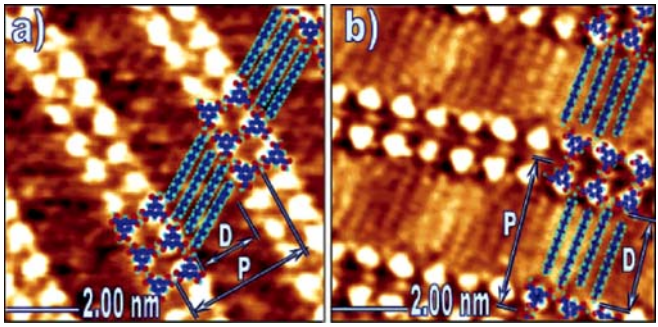

Fig. 13 STM images of SAMNs obtained by mixing TMA with 1-hexadecanol (**a**) and 1-heptadecanol (**b**) in heptanoic acid solution. $V_s = -1.4$ V, $I_t = 200$ pA (a), $V_s = -1.1$ V and $I_t = 200$ pA (**b**). Reprinted with permission from [62]. © (2006) American Chemical Society

Recently, TMA polymorphs different from the *chicken wire* and the *flower* have been observed, both in UHV on the Au(111) surface and at the liquid/solid interface on highly oriented pyrolytic graphite (HOPG) sur-

face [66, 67]. Such polymorphs had been predicted previously [52] but were never experimentally observed.

A recent UHV STM study of TMA self-assembly on Au(111)-(22$\times\sqrt{3}$) at RT has shown that a high number of TMA structures (at least 9) can be formed (depending on surface coverage) and that the *chicken wire* and *flower* structures are only two special cases [66]. Self-assembly was observed to start with the formation of the *chicken wire* structure, followed by the formation of the *flower* structure. Further increase of the coverage up to 13.4×10^{13} molecules/cm^2 led to seven more structures characterized by an increasing packing density (Fig. 14a–i). All the structures appear as hexagonal porous networks, and could be used as templates to control the adsorption and positioning of new molecules. The pore diameter for all structures remained 1.1 nm, in agreement with previous results. The interpore distance increased gradually with the surface coverage from 1.65 to 8.16 nm in steps of 0.93 nm.

All the structures could be described by a unified model, in which the TMA molecules inside the half unit cells are bound via trimeric hydrogen bonds

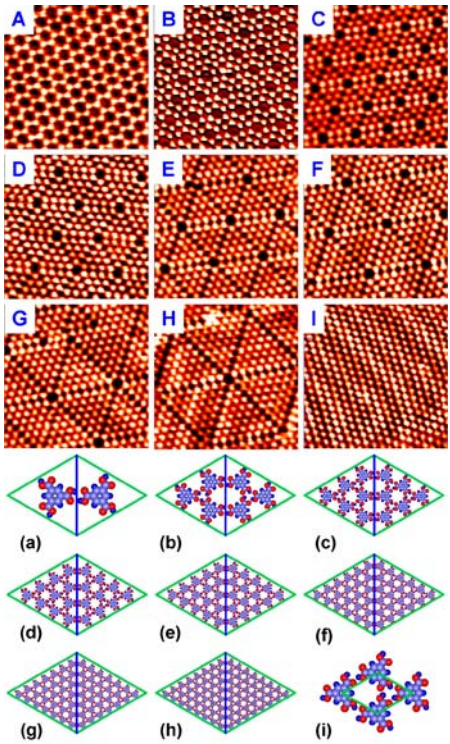

Fig. 14 Coverage induced evolution of TMA self-assembling structures on Au(111)-(22$\sqrt{3}$). Image size: 16.5×16.5 nm^2. Reprinted with permission from [66]. © (2007) American Chemical Society

and half unit cells connect to each other through dimeric hydrogen bonds. The ultimate structure, at 1 monolayer (ML) coverage, consists of a close packed network where all the molecules are bound together with a trimeric hydrogen bond. An energetic analysis indicated that the minimization of the energy of the TMA networks at submonolayer coverage was driven by the maximization of the number of dimeric hydrogen bonds per unit area, which are lower in energy and then more stable compared to the trimeric ones.

TMA structures other than the *chicken wire* and the *flower* have been recently observed at solution/HOPG interface, in pure TMA metastable phases segregated at the domain boundaries of TMA-alcohol self-assembled molecular networks (SAMNs) [67]. The evolution of the TMA-alcohol SAMNs,

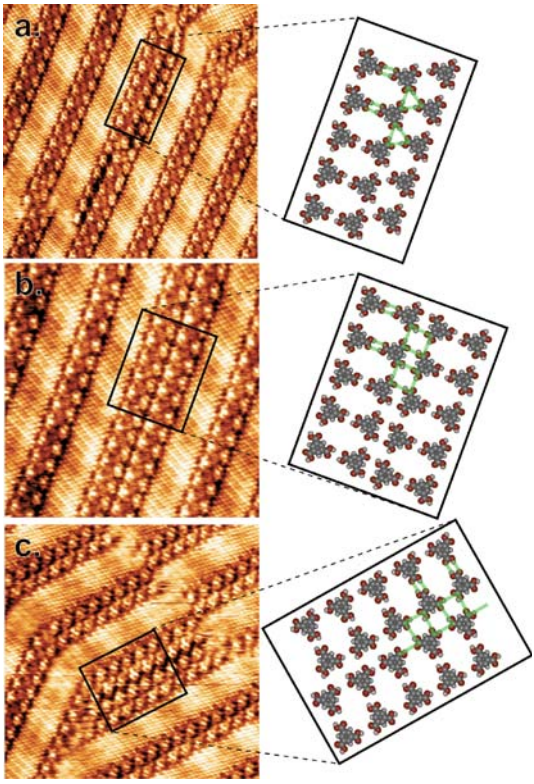

Fig. 15 Triple- and quadruple-TMA tapes observed at aligned boundaries between TMA/$C_{17}H_{35}OH$ domains at the heptanoic acid/HOPG interface, with schematic illustration of the hydrogen-bonding motifs. Image **a** shows a triple-TMA row. Image **b** shows a doubled-dimer row where the TMA dimers are aligned with one another, and image **c** shows a quadruple-TMA (doubled-dimer) row where the dimers are staggered with respect to one another. Image areas: $17\times17\,nm^2$ (**a**), $14\times14\,nm^2$ (**b**), $14.2\times14.2\,nm^2$ (**c**). Tunneling parameters: $V_s = -0.8$ V, $I_t = 200$ pA for all images. Reprinted with permission from [67]. © (2007) Institute of Physics Publishing

through dynamic exchange with the solution or lateral dynamics on the surface, accompanies the evolution of the domain boundaries thus fostering the formation of exotic motifs. Remarkably, triple and quadruple TMA *tapes* have been observed where combined dimeric and trimeric, or dimeric and tetrameric, or dimeric and possibly polymeric bonds exist among the TMA units (Fig. 15).

The differences in the stability of the TMA *tapes* have been investigated. The most stable of the two quadruple tapes is reported in Fig. 15b: it is based on the doubling of thermodynamically stable TMA dimers [10], in an eclipsed manner. In the less stable quadruple-TMA (Fig. 15c) doubled dimers have a staggered configuration. Novel polymorphs, such as the *second generation flower* and the previously predicted *superflower* [52], were found to be located in enclosed spaces between domains of the TMA-alcohol SAMNs (Fig. 16). Such polymorphs are stabilized by the geometries created by the boundaries between non-aligned domains. The TMA/alcohol network stabilized the formation of the *superflower* structure because of the exact lattice match be-

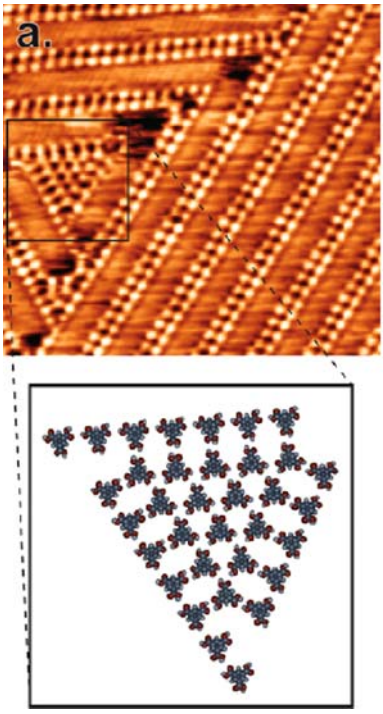

Fig. 16 TMA *Superflower* structure observed within TMA/$C_{16}H_{33}OH$ SAMNs at the octanoic acid/HOPG interface. A triangular domain boundary stabilizes the *superflower* structure. Image area: $15.2 \times 15.2\ nm^2$. Tunneling parameters: $V_s = -1.0\ V$, $I_t = 300\ pA$. Reprinted with permission from [67]. © (2007) Institute of Physics Publishing

tween the dimer *tape* and the *superflower* (lattice constant 0.97 nm). There is an infinite number of mathematically possible 2D periodic TMA polymorphic structures. If only dimeric and trimeric hydrogen bonds are considered, the possible structures can be organized in a homologic order, where the *chicken wire* and the *superflower* structures are the two extremes in terms of order of generation, i.e., the *chicken wire*, where only dimeric bonds are present, is the 0th generation and the *superflower*, where only trimeric bonds are present, the ∞ generation. Within this homologic order, every subsequent generation has a larger repetitive unit, i.e., a larger unit cell and, as a consequence, high generation order structures are less likely to form. The interesting point is that there is an exception to this scaling law for the homologic order we are discussing: the unit cell of the ∞ generation is actually smaller than that of the 0th one. This explains why it was possible to observe the *superflower* structure in a structure locked by domain boundaries.

The relevance of the study is that relatively unstable polymorphs of self-assembled molecular networks can be prepared taking advantage of the stabilizing effect of more stable neighboring phases.

2.1.2 Bi-Component Networks

Honeycomb networks can also be constituted by binary systems. The adsorption of 1,3,5-tris(4-pyridil)-2,4,-triazine (TPT), that consists of a triazine ring with three pyridil substituents (see Fig. 17) on HOPG in the liquid phase (heptanoic acid solution) was observed in binary solutions with TMA or terephthalic acid (TPA) [68]. TPT by itself provides only a functional group acting as a hydrogen bond acceptor (thus rendering intramolecular TPT-TPT hydrogen bonding impossible). TMA and TPA both act as hydrogen bond linkers. In absence of the linkers, the molecule does not assemble on HOPG.

TMA and TPA both have the possibility to form homo-molecular hydrogen bonding via the carboxylic groups and are able to self-assemble from solution into 2D porous networks. A stable co-adsorption of TPT with TMA or TPA, where TPT acts as a proton acceptor and TMA or (TPA) as a proton donor is

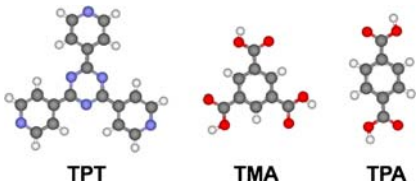

Fig. 17 Molecular structures of 1,3,5-tris(4-pyridil)-2,4,-triazine (TPT), TMA and terephthalic acid (TPA). *Gray* corresponds to C atoms, *red* to O atoms, and *blue* to N atoms. Reprinted with permission from [68]. © (2005) American Chemical Society

achieved through N···H–OH bonds. The networks formed by TPT with the two different linkers are rather different (Fig. 18). Co-adsorption with TMA leads to a loosely packed structure with sixfold symmetry similar to the TMA *chicken wire* structures but with larger pores (2.0 nm vs. 1.6 nm). This network can be considered as a 2D molecular host system with reactive walls, due to the presence of the free carbonyls of the TMA. Co-adsorption with TPA leads to a denser packing with a *bone-shaped* packing motif. In the case of the TPT-TMA, all the outer nitrogens of the TPT are involved in hydrogen bonds, resulting in an actual network. In the TPT-TPA network only the basic unit, consisting of two TPT and one TPA molecules, is strongly hydrogen bonded. The binding energy for the TMA network is probably larger, since it forms three hydrogen bonds versus the two of TPA, as highlighted in Fig. 18.

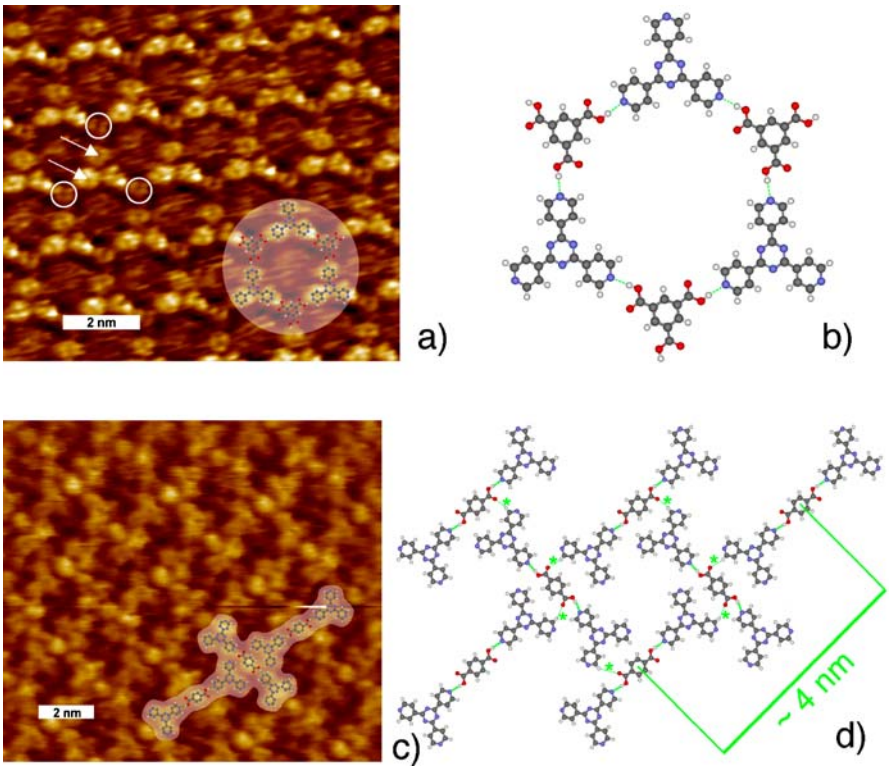

Fig. 18 **a** STM image of the 2D TPT-TMA network on HOPG. The *white circles* indicate TMA molecules, the *arrows* mark the center-to-center distance between two pyridil groups of TPT. **b** molecular model of the structure. **c** STM image of the 2D TPT-TPA network. **d** molecular model of the structure. The *dashed line* indicate N···H–OH networks. Bias voltage: between + 0.3 V and 1.6 V, tunneling current 100 pA. Reprinted with permission from [68]. © (2005) American Chemical Society

One of the most thoroughly investigated binary systems is perylene tetracarboxylic di-imide (PTCDI) and 1,5,3-triazine-2,4,6-triamine (melamine). The structure formed by PTCDI and melamine (M) is shown in Fig. 19. The system was chosen because each PTCDI·M pair can form three hydrogen

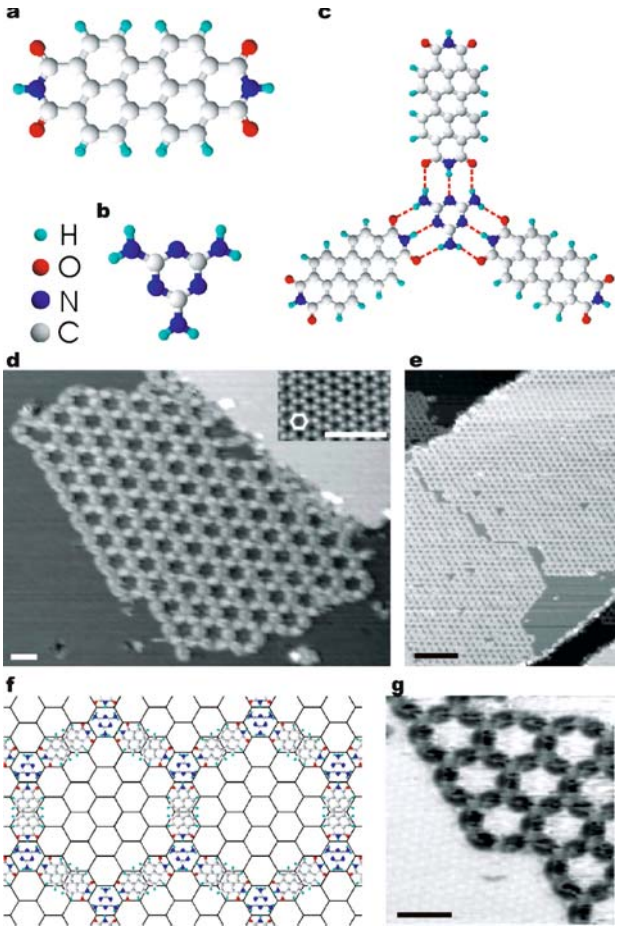

Fig. 19 Self-assembly of a PTCDI-melamine supermolecular network. Chemical structure of **a** PTCDI and **b** melamine. **c** Schematic diagram of PTCDI-melamine junction. *Dotted lines* represent the hydrogen bonds between the molecules. **d** STM image of a PTCDI-melamine network. *Inset*: Ag/Si(111)-$\sqrt{3}\times\sqrt{3}R30°$ surface. The vertices and centres of hexagons correspond, respectively, to the bright (Ag trimers) and dark (Si trimers) features in the STM image. *Scale bars*: 3 nm. **e** STM image of large-area network, with domains extending across terraces of the Ag/Si(111)-$\sqrt{3}\times\sqrt{3}R30°$. *Scale bar*: 20 nm. **f** Schematic diagram showing the registry of the network with the surface. Imaging parameters for all STM images: $V_s = -2$ V, $I_t = 100$ pA. Reprinted with permission from [69].

bonds that can lead to highly stable networks (see Fig. 19c). The samples were prepared under UHV conditions on a Ag/Si(111)-$\sqrt{3}\times\sqrt{3}$ 30° surface. The latter was chosen based on previous studies indicating that molecules such as napthalene tetracarboxylic di-imide diffuse freely on the Ag/Si(111)-$\sqrt{3}\times\sqrt{3}$ 30° surface and form islands where the order is based only on molecular interactions [69]. The preparation of the network started with deposition of PTCDI at RT followed by deposition of melamine while the sample was heated at 375 K. The highly ordered network shown in Fig. 17d,e was obtained. Melamine is a molecular unit with threefold symmetry and forms the vertices of the *honeycomb* network, whereas PTCDI molecules constitute the straight edges. The pores of the network, larger than those of the TMA *chicken-wire* structure, could accommodate up to seven C_{60} guest molecules. Increasing the C_{60} coverage led to an increasing fraction of pores filled with heptameric clusters. Interestingly, after saturation of the pores, a C_{60} honeycomb network formed on the PTCDI/melamine lattice. A further increase of C_{60} coverage did not induce any change in the structure, indicating that the C_{60} honeycomb network acts as a termination layer. This work demonstrates that large pore areas can induce the co-location of molecules in *nanoscale vessels*.

The same network on the same surface was used as a host for C_{84}, a molecule 10% larger than C_{60} [70]. The pores are able to accommodate clusters made up of a number of C_{84} molecules ranging from 2 to 7, depending on the coverage. Porous networks of melamine/PTCDI were obtained also on the Au(111) surface [71]. High resolution images of the pores (Fig. 20a) revealed that PTCDI molecules appear as bright rectangles and melamine as

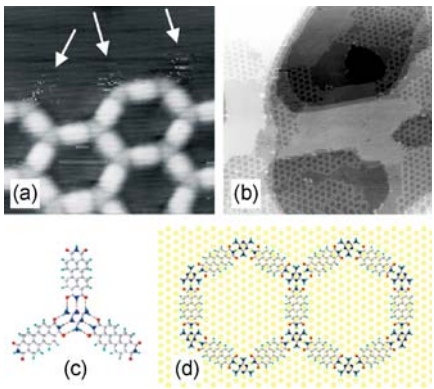

Fig. 20 **a** 8.8×8.8 nm^2 STM image of the hexagonal PTCDI/melamine network. V_s = −1.4 V, I_t = 0.05 nA. **b** Larger area (98.4×98.4 nm^2) STM image showing different areas on different Au terraces. **c** Schematic of the PTCDI/melamine network. **d** Hexagonal network overlaid on Au(111) substrate. Reprinted with permission from [71]. © (2006) American Chemical Society

lower contrast triangular vertices. The preparation of the network is similar to that described in previous references [69, 70]. The pores are hexagonal and have common edges (Fig. 20d) and more rarely common vertices. The network is able to host C_{60} dimers, hexamers, and heptamers, with the hexamers being the prevalent structures because of their kinetic stability.

Another interesting bimolecular system able to generate a hexagonal porous network is based on cyanuric acid (CA) and melamine [72]. The first cyanuric acid-melamine (CA·M) network was created on Ag/Si(111)-$\sqrt{3}\times\sqrt{3}$ 30° under UHV conditions. The CA·M complex is stabilized by three hydrogen bonds, as shown in Fig. 21. The CA·M network can be prepared either by sequential deposition or by simultaneous deposition of the two components. The network has pore dimensions smaller than those of the PTCDI·M network. This result is particularly important, because it demonstrates that the characteristic dimensions of the network can be systematically tailored through the appropriate selection of the component molecules. The approach has the potential to form a wide range of template structures, with varying pore dimensions, which are able to trap (host) different molecular species.

The CA·M network was later obtained on the long-range herringbone reconstruction of the Au(111) surface [73]. In the same work, the self-assembly of single component CA acid and M monolayers was reported. Combining the two components on the surface leads to two distinct intermixed phases. One phase is a *honeycomb* structure where CA and M are stabilized by triple hydrogen bonds and form hexagons containing 3 CA and 3 M molecules (see Fig. 21). The second structure is composed of smaller *honeycomb* domains with different orientations. This work is particularly important since it proves that the CA·M pattern, as the PTCDI·M one, can be formed both on semiconductor and metal surfaces.

Novel cyanuric acid/melamine networks formed on Au(111) in UHV were demonstrated [74] and imaged with submolecular resolution. Both CA and M, when deposited individually, form large islands on gold that are stable up to 300 K. The two molecules are clearly distinguished in the STM images in Fig. 22a (CA) and c (M). Simultaneous evaporation of CA and M leads to the formation of a 1 : 1 network (Fig. 22e). Interestingly, sub-stoichiometric networks with M to CA ratio of 3 : 1 were found if CA was deposited after M. These networks are only present as locally ordered structures. The CA_1M_3 structure has a lower binding energy compared to that of CA_1M_1 and can be considered a step towards the formation of the thermodynamically stable CA_1M_1 network. A theoretical model was proposed to explain the hierarchy of interactions in the bi-component system thus contributing to the rational synthesis of complex self-assembled systems.

An intermixed adsorbed phase has been recently obtained by sequential deposition of perylene tetracarboxylic acid (PTCDA) and tetraamminobenzene (TAB) (see Fig. 23) [75]. The structure is not a porous network, yet it is

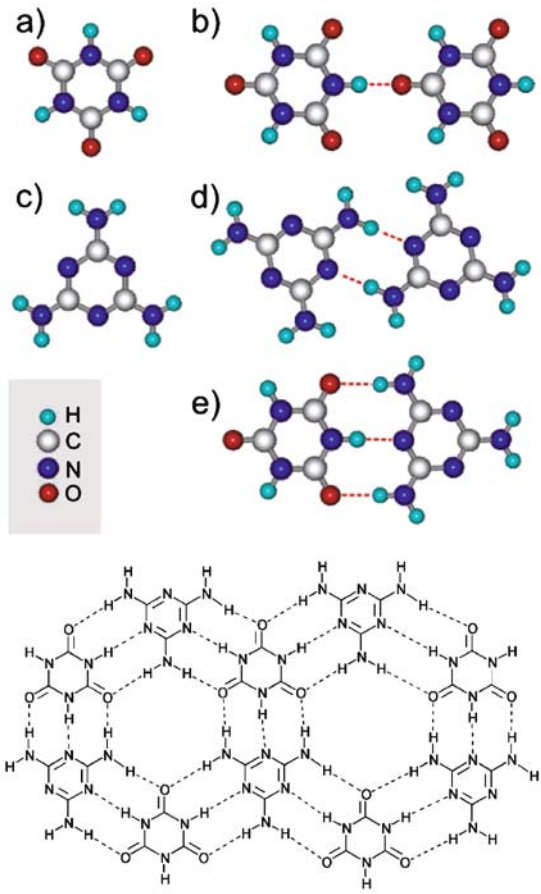

Fig. 21 **a** Molecular structure of cyanuric acid (CA); **b** single hydrogen bonding (*dotted line*) between CA molecules; **c** molecular structure of melamine (M); **d** hydrogen bonds between melamine molecules; **e** hydrogen bonds between a CA and a M molecule (**f**); portion of the 2D CA·M network. Reprinted with permission from [72]. © (2006) Royal Society of Chemistry

very important because it is the first demonstration that a 2D hydrogen bond complex formed between a diamine and an andhydride group can stabilize intermixed phases of organic molecules.

An organic template network constituted of an end-functionalized oligomer of phenylene-ethynylene (OPE, see inset Fig. 24a) has been employed to realize the controlled arrangement of single molecules (coronene) and peptides (enkephalin 1-3 with a sequence TGG) on HOPG surfaces [76]. The self-assembly of the oligomer leading to the template was previously reported [77]. The stability of the template is based on the balance between

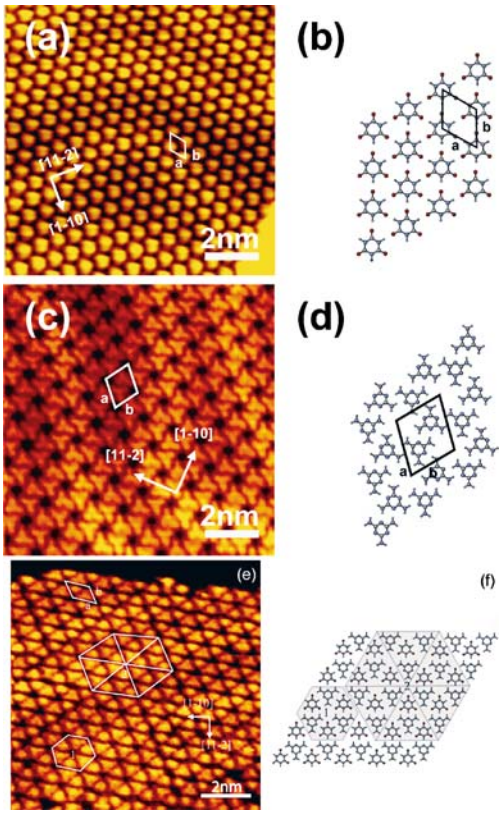

Fig. 22 STM images of **a** CA ($V_s = 1.25$ V, $I_t = 0.72$ nA); **b** M ($V_s = 1.486$ V, $I_t = 0.57$ nA); **c** CA_1M_1 ($V_s = 1.25$ V, $I_t = 0.56$ nA). The image size for **a**–**c** 10.2×10.2 nm^2. **b**, **d**, and **f**: corresponding optimized models of the structures in **a**, **c** and **e**. Adapted with permission from [74]. © (2007) Wiley

two intervening factors: (i) hydrogen bonding between head-to-head carboxyl groups, enabled by the linear packing mode of the conjugated backbones in the assembling monolayer; and (ii) the space-filling properties of alkoxyl chains and planar conjugated backbones that minimize the free space per unit area within the monolayer, thus resulting in a maximum of the intermolecular and molecule–graphite interactions.

Various molecular patterns with different distributions of the molecules were prepared on HOPG as a function of the molar concentration ratio of coronene and the OPE template: (i) for the 1 : 2 ratio, coronene molecules are dispersed in the vacancies of the template and have an available space larger than their size; (ii) for the 1 : 1 ratio, coronene is present as dimer and the available space is almost fully occupied; (iii) for a 3 : 2 ratio, both structures discussed in (i) and (ii) are observed. The TGG peptide was uniformly positioned on the template (Fig. 24): two peptide molecules are located be-

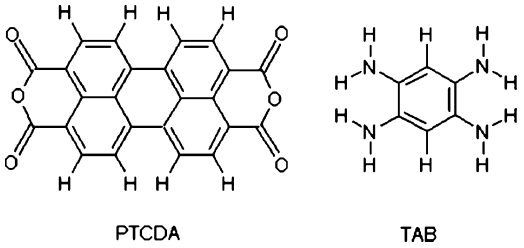

Fig. 23 Molecular structure of PTCDA and TAB

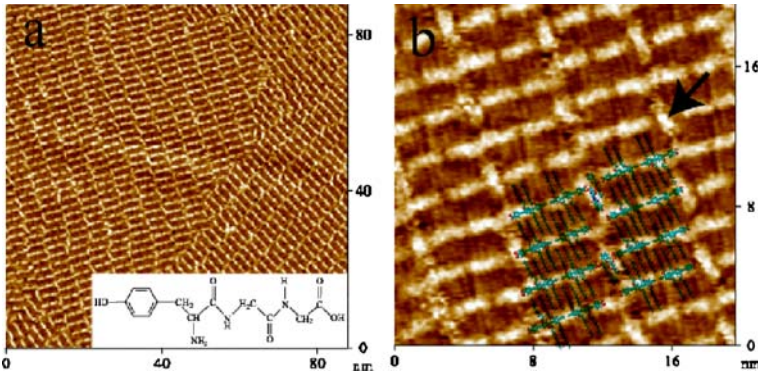

Fig. 24 Peptide dispersed within an OPE network. **a** Large scale image (V_s = 880 mV, I_t = 663 pA); **b** high resolution image (V_s = 784 mV, I_t = 729 pA). Structural formulas of OPE and the peptide in the inset of part a. Reprinted with permission from [76]. © (2006) American Chemical Society

tween neighboring conjugated backbones. The hydrogen bonds between OPE backbones and TGG molecules are responsible for the stability of the ordered molecular array.

2.1.3 Quinone and Quinone-Like Porous Networks

Quinone and quinone-like molecules have been employed to form extended regular *honeycomb* patterns, stabilized by hydrogen bonds. Anthraquinone (AQ) networks were obtained by evaporating AQ molecules onto Cu(111) in UHV (see Fig. 25) at substrate temperatures ranging between 10 and 200 K and at substrate coverage of one molecule per several tens of substrate unit cells [78]. The side of the hexagon is constituted of three parallel AQ molecules (adsorbed with a configuration similar to that of the isolated molecules). Interestingly, the pore diameter is of about 5 nm, which is five times the size of the AQ molecule.

Hydrogen bonds between a carbonyl oxygen atom of one molecule and an arene hydrogen of another molecule are responsible for the geometric

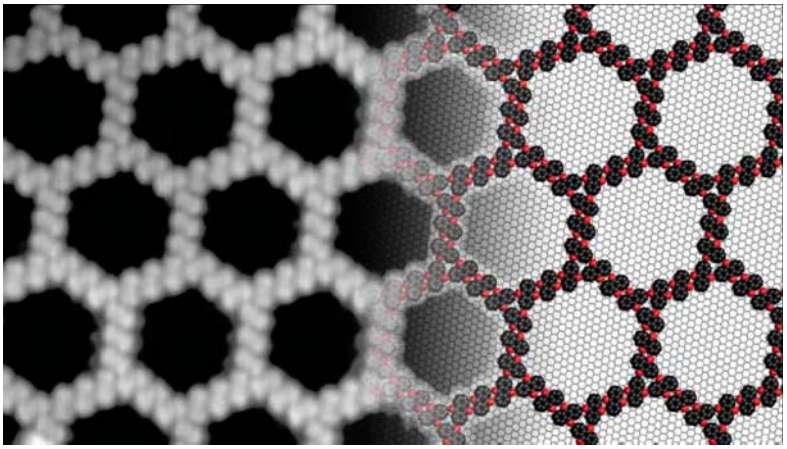

Fig. 25 (*Left*) $25 \times 16\ nm^2$ STM image of the *honeycomb* AQ network on Cu(111). $V_s = 1.3$ V, $I_t = 0.73$ nA. (*Right*) Model of the unit cell. *Red spheres*: O atoms, *black spheres*: C atoms. Reprinted with permission from [78]. © (2006) American Association for the Advancement of Science

motifs (trimers) determining the *honeycomb* structure. Substrate mediated long-range repulsive interactions are possibly responsible for the number of molecules (three) arranged in rows, constituting the side of the hexagon. The honeycomb pattern is in fact the result of a compromise between short-range attractive forces that lead to molecular rows at very low coverages and long-range repulsive forces that prevent the proximity of parallel molecular rows. The engineering of short-range and long-range interactions opens the possibility to tailor the dimension of the *honeycomb* pattern.

In a different context, AQ molecules were found to act as *molecular carriers* which are able to transport one or two CO_2 molecules, reversibly attached to them in a linear and guided fashion across an isotropic Cu(111) surface [79]. In this sense, the AQ molecules act as "dynamic" surface cues, which can selectively pick up molecules and transfer them on a surface.

Quinone-like molecules were used as precursors for the formation of organic porous networks. Honeycomb patterns were obtained from the quinone-like molecule 4,9-diaminoperylene-quinone-3,10-di-imine (DPDI) by thermally induced 2D aggregation on Cu(111) in UHV [80]. The most stable form of DPDI is the semiquinoidal structure (structure **1** displayed in Fig. 26). DPDI was evaporated on Cu(111), then the surface was annealed in UHV at 575 K. Dehydrogenation induced by the catalytic activity of the Cu surface at high temperature (575 K) converted DPDI to the quinoidal state 1b (Fig. 26). In this structure, the modified hydrogen functions can act as both hydrogen-bonding donors and acceptors. The molecules form hydrogen bonds with each DPDI unit, binding four neighboring molecules to form the *honeycomb* network.

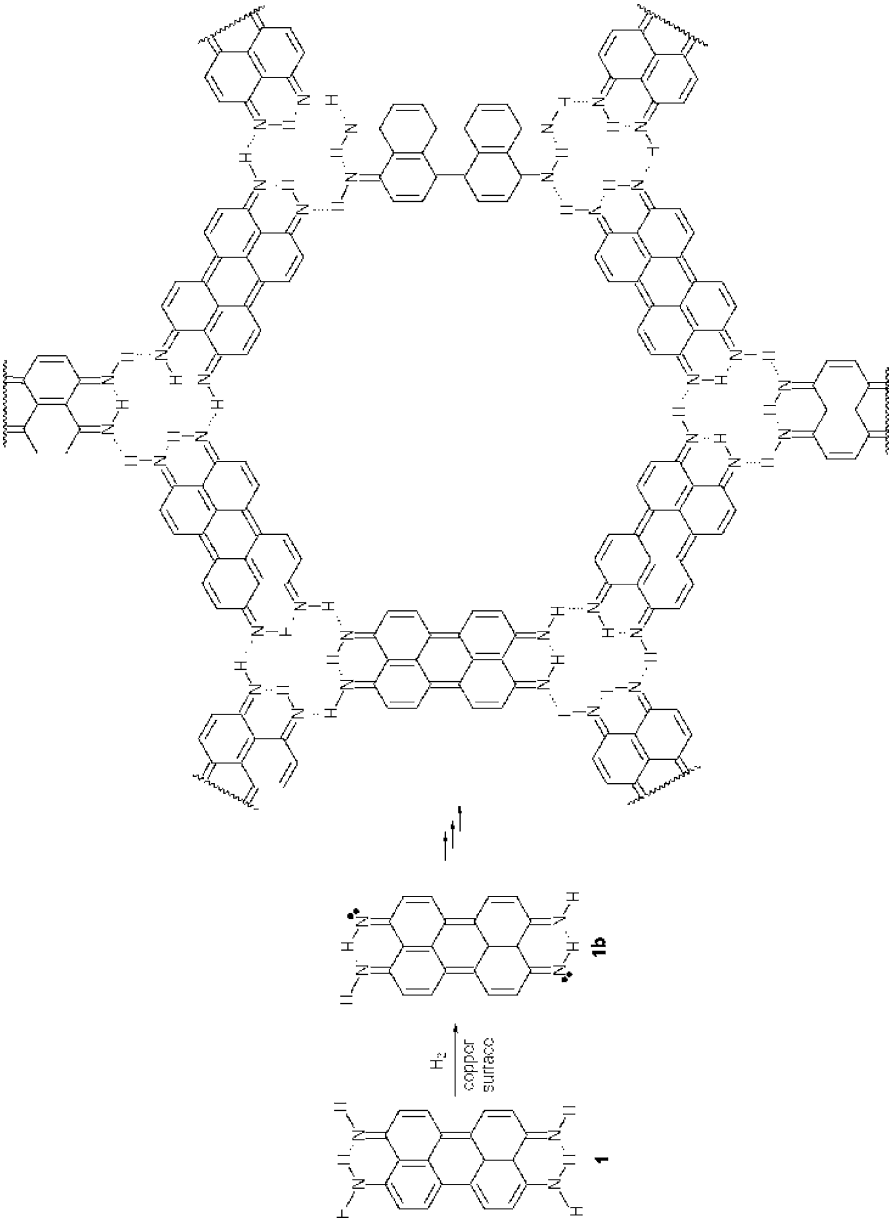

Fig. 26 Hexagonal *honeycomb* network of thermally generated 1b on Cu(111). Reprinted with permission from [80]. © (2005) Wiley

The network exhibits a commensurate structure with respect to the Cu(111) surface (see Fig. 27). One of the requirements for the formation of such a *honeycomb* 2D network is low surface coverage (0.1–0.7 ML) before the

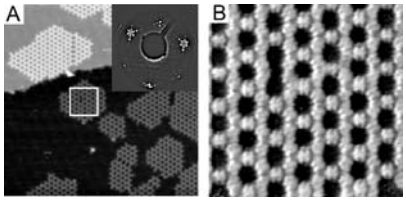

Fig. 27 Self-assembly of 0.3 ML of DPDI on Cu(111) annealed at 575 K. **A** $100\times100\ nm^2$ STM image ($I_t = 25$ pA, $V_s = -1.5$ V) of DPDI islands with *honeycomb* structures. Inset: LEED pattern corresponding to the overlayer, as obtained at 52 eV primary energy representing a Cu(111)-$p(10\times10)$ DPDI lattice registry of the *monomeric* components. **B** High resolution STM image ($15\times15\ nm^2$) of the marked region ($I_t = 25$ pA, $V_s = -2$ V), showing details of the *honeycomb* network. Reprinted with permission from [80]. © (2005) Wiley

annealing step, since the monomer species need to be mobile at the surface to arrange into large hexagonal cavities. Higher coverage is observed to lead to more compact, non-porous structures.

The dehydro-DPDI porous network, with *holes,* which have a vertex-to-vertex diameter of 1.63 nm, is interesting as host for other molecular species. Its extraordinary stability towards manipulation of individual monomers with the STM tip and towards temperature (> 575 K) renders it suitable for the realization of hierarchical structures by self-assembly of subsequently deposited material.

The dehydro-DPDI network was used as a host for the molecule zinc-octaethylporphyrin (ZnOEP) [81]. The ZnOEP molecule has a fourfold symmetry. It fits in the pores of the honeycomb network such that its translational motion is hindered. ZnOEP/dehydro-DPDI system was studied by STM at various temperatures: RT, 77 K, and 5 K (Fig. 28). At RT (Fig. 28a), the ZnOEP molecules appear as rings due to rotation within the pores. At 77 K (Fig. 28b),

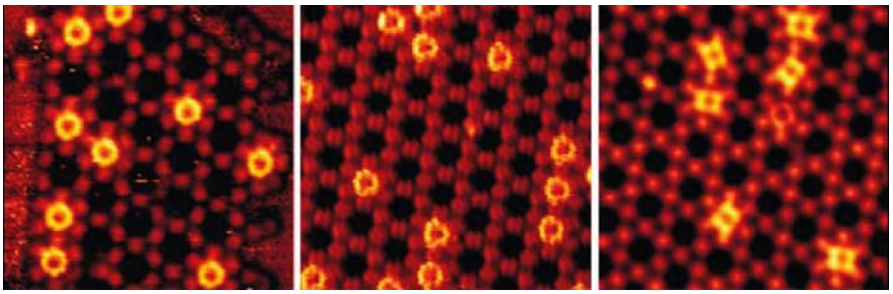

Fig. 28 STM images ($16\times16\ nm^2$) showing different thermal behaviors of the ZnOEP molecules, which are trapped inside the hexagonal pores of the dehydro-DPDI honeycomb network. The *left image* was recorded at RT, the *middle one* at 77 K and the *right one* at 5 K. Reprinted with permission from [81]. © (2007) Royal Society of Chemistry

the rings become noisy, indicating a lower rotational symmetry. At 5 K, the rotation is *frozen* and the molecules appear as rectangles. Indeed, at RT the eight ethyl groups point upwards leading to an eight-lobed structure with fourfold symmetry, whereas at very LT (5 K) the ethyl groups arrange themselves flat on the substrate in pair wise opposite directions distorting the molecular square to a rectangle. The reorganization energy between the rotational potential minima was monitored as a *switching* between different tunnel currents at a given spot (off-centered above the guest molecule). A bi-state signal between two approximately fixed heights was observed. From the measurements of the switching between two states carried out at different temperatures (77 and 84 K), it was possible to obtain a value of the activation energy between the local rotational potential minima of 0.17 ± 0.03 eV. The possibility to locally manipulate the rotation of the guest molecules by the STM tip was also demonstrated.

The highly stable dehydro-DPDI network is suitable for the fabrication of ordered structures based on hierarchical interactions, i.e., complex structures where the first structural level requires a stronger interaction energy than the second one, and successive levels requiring always weaker interaction energies. C_{60} and ZnOEP have been subsequently deposited on the highly stable dehydro-DPDI network, considered as the starting point of the molecular hierarchical structure. At 77 K, C_{60} molecules do not exhibit any mobility within the pores, whereas ZnOEP still exhibit thermally activated rotation [82]. At RT, trapped C_{60} molecules display a translational mobility within the pore whose magnitude depends on the adsorption of the C_{60} on the copper surface (if C_{60} is adsorbed via a five-membered ring, six-membered ring or a C=C double bond) and on the di-hydro DPDI network. C_{60} cannot jump from one pore to the other due to the high-energy barrier of the cavity walls. The difference in the behavior of the two molecules in the network is paralleled by the different behavior outside the *honeycomb* network. Indeed, C_{60} forms a close packed hexagonal structure whereas ZnOEP gives rise to a mobile two-dimensional fluid phase. Through a so-called *constant-height manipulation mode* [83], a *ball bearing* experiment was attempted where a C_{60} molecule was moved on top of a ZnOEP molecule to form a bimolecular system that can be seen as a solid ball (C_{60}) on top of a porphyrin (the position of C_{60} vs. the porphyrin is slightly off-centered, because of the presence of attractive π interactions in this position) and suspended by the eight ethyl legs. Upon attempting to move the bimolecular system towards another pore, the molecules separate to occupy different pores. A different experiment, based on vertical manipulation was also attempted: a C_{60} molecule was transferred to the STM tip apex and then, by positioning the tip above an empty pore it was placed back on the surface. The manipulation and the positioning experiments were enabled by the superior stability of the dehydro-DPDI network that provide for a reliable spatial grid.

2.2
Dipole–Dipole Bonded Networks

2.2.1
Porphyrin Networks

Porphyrins are a class of molecules that can be used to construct 2D supramolecular porous networks [84]. In particular, bis(3-cyano-phenyl)-substituted porphyrins were throughly investigated on Ag(100) and Ag(111) surfaces in UHV (see Fig. 29). The self-assembly of porphyrin networks is likely to be driven by both Van der Waals and dipole–dipole interactions involving the polar cyano-phenyl residues. The nature of the bonding responsible for the formation of the network is then the main difference with the previously discussed networks that were stabilized by hydrogen bonds. Porphyrin porous networks were investigated as hosts for several guest molecules, e.g., fullerene C_{60}.

The system fullerene-porphyrin is of relevance because of the redox- and photo-activity of the two molecules. The affinity between C_{60} and the porphyrin molecules is due to Van der Waals and donor–acceptor interactions. Before the preparation of the host-guest system, a detailed STM investigation of the adsorption properties of the porphyrins on Ag(100) and Ag(111) was carried out. On both surfaces, the molecule shown in Fig. 29a lies flat on the metal. On Ag(100), no ordered C_{60} phase was observed on the porphyrin network. On Ag(111), porphyrin molecules at 1 ML coverage form an ordered phase after annealing at 450 K [85]. On this phase, deposition of 0.14 ML of C_{60} followed by annealing at 450 K led to the self-assembly of fullerene dimers in a *dumb-bell* shape, with intrapair distance of 2.3 nm. Most importantly, on Ag(111) at lower coverages (0.5–0.7 ML) porphyrin molecules are organized in a network with a hexagonal superstructure [86] (Fig. 30). The superstructure is constituted of discrete pores and rotated by $15 \pm 4^\circ$ with respect to the [1–10] direction of the underlying Ag(111) surface and shows a periodicity of 3.3 nm. The pores have a diameter of 1.2 nm and a depth of 0.12 nm (these dimensions are underestimated because of the tip-surface convolution due to the tip finite size).

In the tentative model to interpret the hexagonal structure (Fig. 30c), the polar cyano-phenyl substituents form trimeric units leading to a central cavity, by both Van der Waals and dipole–dipole interactions. Deposition of C_{60} on the top of the network leads to a structure where the fullerenes are confined into the pores (Fig. 31). The C_{60} molecules are able to diffuse to adjacent empty pores. At 0.01 ML coverage, the pore-to-pore hopping rate was as high as 10^{-3} s, at RT. A detailed study of the dynamics of C_{60} and C_{70} fullerene molecules on the 2D nanoporous network of porphyrins on Au(111) is provided in [87]. Here, by time-lapsed STM imaging, the mobility of the fullerenes was investigated as a function of the molecular structure (C_{60} and

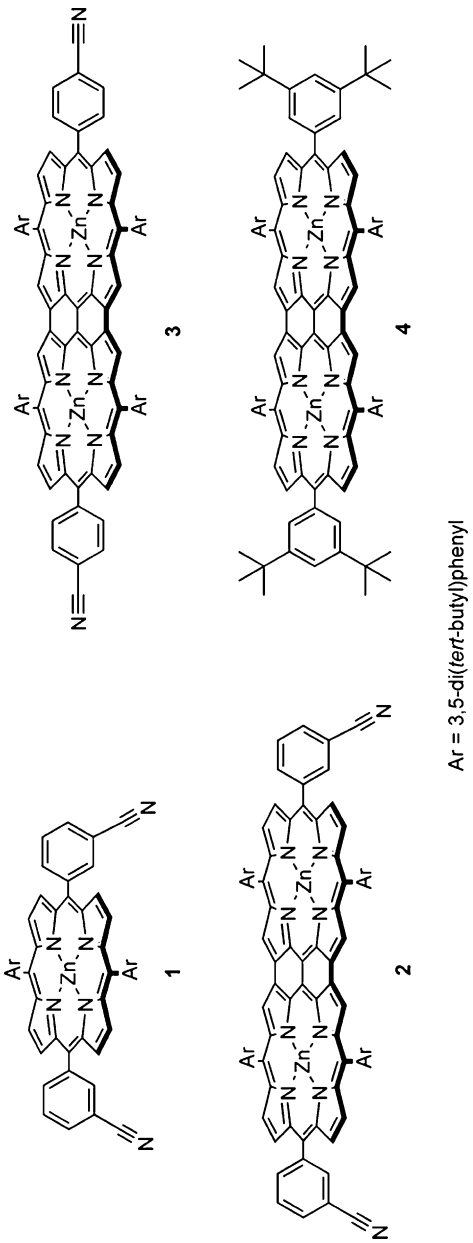

Fig. 29 Chemical structure of two porphyrin derivatives investigated as building block for 2D organic porous networks

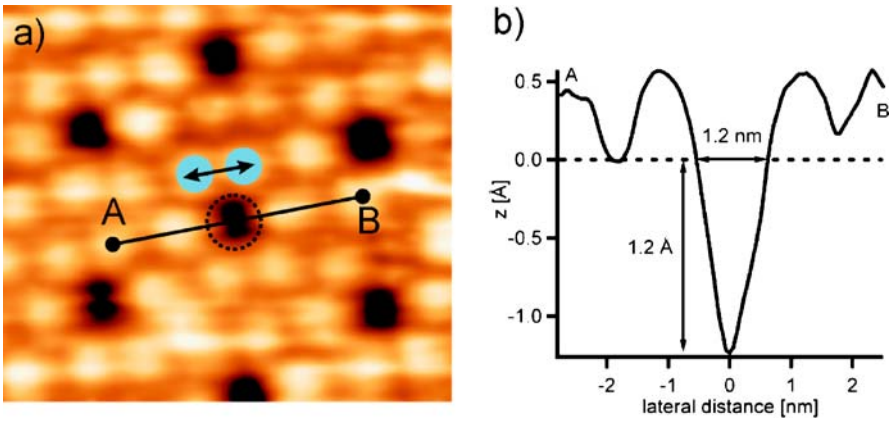

Fig. 30 **a** STM image ($9.1 \times 8.0\,\mathrm{nm}^2$, $V_s = 2.9\,\mathrm{V}$, $I_t = 25\,\mathrm{pA}$, $T = 298\,\mathrm{K}$) of the porous porphyrin-based network on Ag(111). Each porphyrin molecule appears as two bright lobes (*double arrow*). **b** Cross-section profile of a single pore (from *A* to *B*). **c** Proposed model of the self-assembled porous network ($\alpha \approx 15°$). The *blue spheres* indicate the molecular fragments which largely contribute to the image, i.e., tunneling current. Reprinted with permission from [86]. © (2006) Wiley

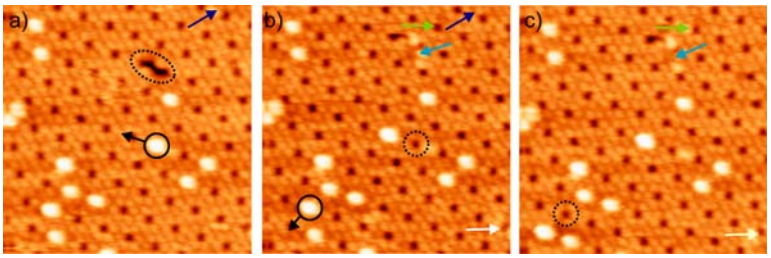

Fig. 31 **a**, **c**, **d** Three sequential STM images (scan range: $30 \times 30\,\mathrm{nm}^2$, $V_s = 2.9\,\mathrm{V}$, $I_t = 12\,\mathrm{pA}$, $T = 298\,\mathrm{K}$; the time difference between each image is 62 s). **b** Proposed molecular model of a C_{60} molecule (*bright spots* in the STM images) hosted inside a supramolecular porphyrin-based pore. Reprinted with permission from [86]. © (2006) Wiley

C_{70}) and the degree of coverage of the guest. The results revealed interactions between the fullerene guest molecules at distances longer than the Van der Waals radii of the molecules. The investigation of the supramolecular structure of porphyrin-fullerene molecules on silver surfaces was extended to di-porphyrins, in particular to the compound shown in Fig. 29b. This compound, when deposited on Ag(100) at coverages in the range of 0.2–0.5 ML, forms 2D ordered islands where individual molecules appear as four bright lobes due to preferential tunneling through the four 3,5-di-terbultyl substituents. A coverage of 0.02 ML of C_{60} deposited onto a complete monolayer of this molecule on Ag(100) gives chains of C_{60} where each molecule is represented by a bright protrusion [85]. The tentative model for the adsorption of

C_{60} on the di-porphyrin network is that fullerenes are adsorbed where three porphyrin molecules meet, on top of the electronegative 3-cyanophenyl substituents. Porphyrin mediated coupling via local modifications of the hosting layer by the fullerenes through conformational or electronic adaptation and electronic interaction via the metal substrate are proposed as rationale to interpret the formation of ordered fullerene assemblies on Ag(100) and Ag(111) surfaces.

Molecular assemblies where the controlled switch between different molecular states can be realized are of interest for molecular devices. Porphyrins self-trapped into the pores of a porphyrin network were observed to rotate into distinguishable positions, defined by the geometry of the porphyrin host. The system can be described as a molecular multiposition rotary device [88]. The porous network was obtained by thermal evaporation on Cu(111) in UHV of the porphyrin whose molecular structure is reported in Fig. 32.

The pores of the network (diameter of 1.8 nm) appear as windmill structures with six wings (Fig. 33). Each wing, attributed to a flat lying porphyrin, can be resolved into two lobes, each of which in turn is attributable to two *tert*-butyl residues. At 77 K, it was observed that pores can trap porphyrins, the latter appearing as bright four-lobe structures. The guest molecules can have three different positions (the hexagonal symmetry of the pore would allow six different positions but because of the C_{2h} symmetry of the guest only three of these positions are distinguishable). STM sequences demonstrated that at 112 K the guest molecules can thermally switch from one stable position to the other (see Fig. 33). The activation energy for the switching was estimated to be 0.24 eV (Fig. 33g). Switching by the STM tip was also investigated where single switching events could be triggered.

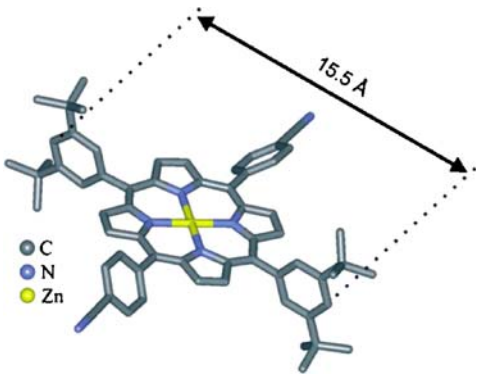

Fig. 32 Chemical structure of the porphyrin discussed in [88]. Reprinted with permission from [88]. © (2007) Wiley

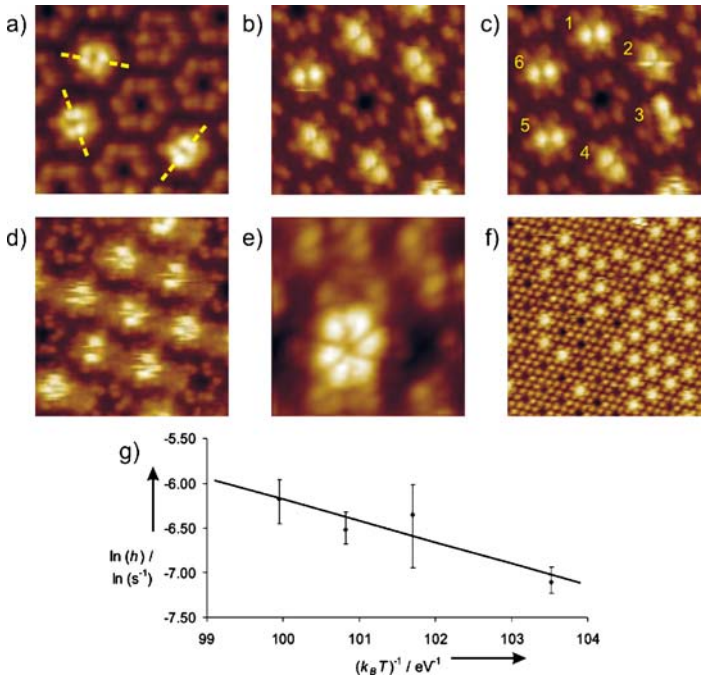

Fig. 33 **a**–**f** STM images of the porphyrin network (I_t = 20 pA, V_s = –1.5 V). Sample coverage 10% (**a**–**c**) and 30–40% (**a**–**f**). **a** 77 K, 10.2×10.2 nm^2, **b** and **c** 112 K (7.4×7.4 nm^2); **d** 115 K, 8.8×8.8 nm^2, **e** 150 K, 3.0×3.0 nm^2, **f** RT, 29.9×29.9 nm^2. **g** Arrhenius plot for the determination of the activation energy needed to switch between two neighboring positions. Reprinted with permission from [88]. © (2007) Wiley

2.3 Metal-Organic Coordination Networks

Metal-organic coordination networks (MOCNs) offer a valuable route towards the fabrication of 2D porous networks. Most MOCNs networks are based on the attractive interaction between carboxylic acids and transition metals. The lateral metal-organic coordination bonds give a high chemical stability to this type of network compared to those stabilized by hydrogen bonds or Van der Waals forces.

One of the first MOCN systems to be investigated was TMA/Cu [89]. The metal-organic complexation was observed on Cu(100) in the temperature range 250–300 K, after deposition at RT. In this temperature range, TMA is completely deprotonated due to the catalytic activity of surface Cu adatoms that continuously evaporate from atomic steps [50]. Two different complexes were identified at the surface, namely $[Cu(TMA)_4]^{n-}$ and $[Cu_2(TMA)_6]^{n-}$. In the former complex, a Cu atom is surrounded by four TMA ligands, resulting in a cloverleaf shaped arrangement in the STM images. In the latter, two

Cu atoms are bound by six TMA molecules. Extended TMA/Cu networks were not formed because of the pinning of the reactive species in a certain position and orientation to the surface.

Highly organized networks driven by metal-organic coordination could be achieved by sequential deposition of TMA and Fe on Cu(100) in UHV [90] (Fig. 34). The deposition was carried out at 300 K, where TMA is present in the deprotonated form [50, 56]. During deposition at 300 K, the TMA ligands react with the Fe atoms forming chiral tetra-coordinated complexes (clover-leaf phase) [91]. Upon annealing at 350 K the system evolves to an assembly consisting of 16 TMA molecules arranged in square patterns like molecular

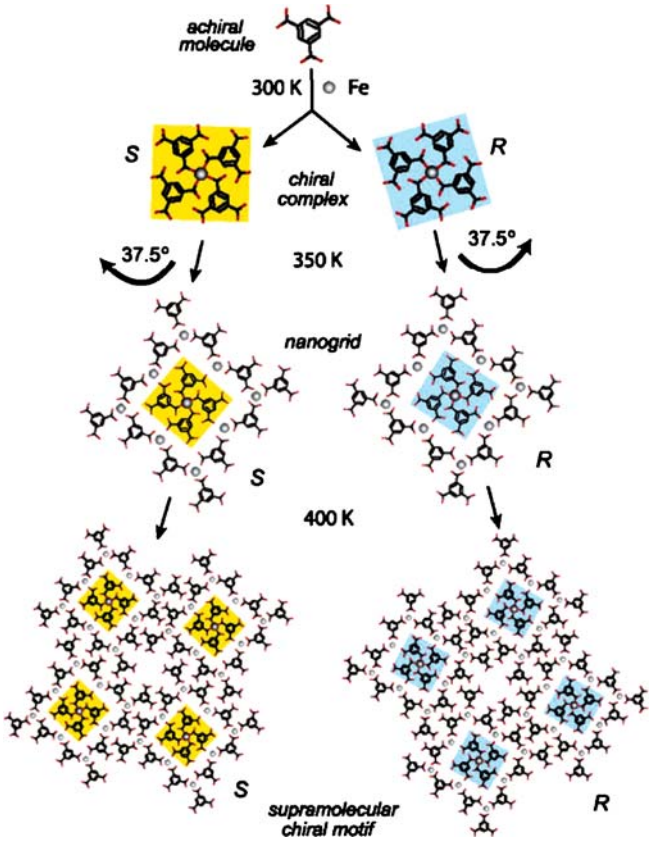

Fig. 34 1,3,5-tricarboxylic benzoic acid (trimesic acid, TMA) molecules and Fe atoms represent the primary units employed for the formation of secondary chiral mononuclear ($Fe(TMA)_4$) complexes. The complexes are antecedents for tertiary polynuclear nanogrids which are in turn the supramolecular motifs for the assembly of homochiral nanocavity arrays. The respective mirror-symmetric configurations (labeled *S* and *R*) are indicated with *yellow* and *turquoise background*. Reprinted with permission from [90]. © (2003) American Chemical Society

nanogrids, the core of which is a cloverleaf unit. The final stage of the structure is achieved upon further annealing at 400 K, which leads to homochiral extended regular metal-organic superstructures.

The system TMA/Cu was also used to prepare in situ 1D metal-organic coordination chains on the anisotropic Cu(110) surface [92]. TMA was deposited on Cu(110) at 300 K, a temperature high enough to ensure the presence of mobile Cu adatoms that catalyse the deprotonation of carboxylate groups. The deposition resulted in 1D [–Cu–TMA–Cu–] chains running along the [1–10] direction of Cu(110). The 1D anisotropy of the substrate is transferred to the resulting 1D chains.

Another example of a metal organic surface supported porous network was obtained by sequential deposition of 1,2,4-benzenetricarboxylic acid (trimellitic acid, TMLA, Fig. 35) and Fe atoms on clean Cu(100) at a substrate temperature of 400 K [93]. By varying the ratio between the constituents of the network, it was possible to obtain different metal-carboxylate architectures.

The precursor for the MOCNs is an ordered phase of TMLA, with a superstructure oriented along the high-symmetry directions of Cu(100). The TMLA molecules are likely to be deprotonated, due to the high preparation temperature. Upon Fe deposition onto the TMLA layer, the carboxylate groups react with the metal adatoms forming a regular network, oriented along the high symmetry directions of the substrate. Two different networks were obtained depending on the coverage ratio of one or two Fe atoms per TMLA molecule, namely the *double row MOCN* (Fig. 36), for a ratio of one Fe atom per TMLA molecule and the *single row MOCN* (Fig. 37), for a ratio of two Fe atoms per TMLA molecule. In the *double row MOCN*, paired rows are interconnected by individual molecules oriented in the direction perpendicular to the substrate and Fe atoms are located at the points of intersections. The *para* carboxylate groups of TMLA point towards the Fe atoms. The *single row MOCN* contains two phases comprising different cavities which are close in composition and energy (α and β, see Fig. 36d,e), and whose main difference is in the symmetry of the iron-carboxylate bonds: in the α phase, each TMLA molecule has either two bidentate or four unidentate bonds to iron atoms, whereas in the β phase each TMLA has a bidentate and an unidentate bond.

Stepanow and coworkers explored MOCNs formed by the sequential deposition of three different carboxylic acids (structures in Fig. 35), namely

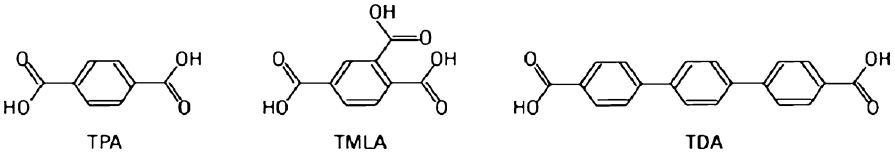

Fig. 35 Structure of TPA, TMLA and TDA

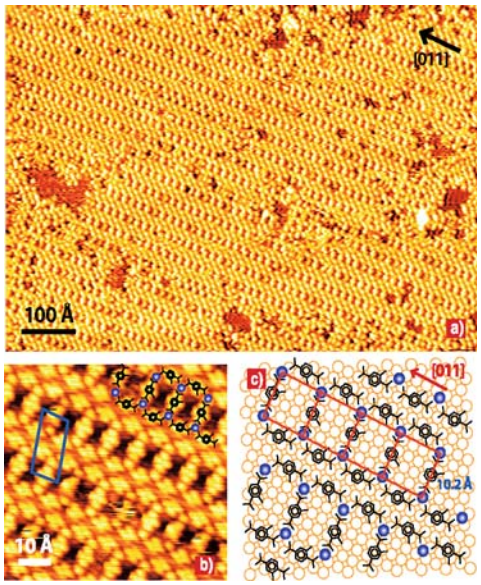

Fig. 36 A *double row MOCN*. **a** Large-scale STM topography showing the ordered network structure; **b** high-resolution STM image revealing the four-lobe molecular structure; **c** tentative model for the double row Fe–carboxylate MOCN. Fe atoms (*green*) are arranged in a ladder-type structure with a $1.02 \times 1.02\,\mathrm{nm}^2$ repeat unit. Reprinted with permission from [93]. © (2003) Wiley

TPA, TMLA and 4,1′,4′,1″-terphenyl-1,4″dicarboxylic acid (TDA), and Fe on Cu(100) [94]. All the three acids, after complexation form ladder-type porous 2D networks that are stable up to 500 K. The dimensions of the pores can be tuned by changing the length of the backbone of the carboxylic acid group, which is 0.7 nm for TPA and TMLA and 1.4 nm for TDA. Pores in the TMLA network are expected to have a different chemical functionality due to the presence of an additional carboxylic group. The arrangement of the molecules at the surface is driven by the symmetry of the underlying copper lattice. The dimensions of the pores range from those of a small molecule to the nanometer range. The suitability of the MOCNs to act as guests for supramolecular structures was tested studying the co-adsorption of C_{60} molecules (Fig. 38). The Fe/TPA network has three types of cavities (A, B, and C in Fig. 38b) differing in shape and size. All the three cavities can accommodate only single C_{60} molecules. Moreover, C_{60} molecules have a preference to occupy larger cavities (B type), where the interactions with the underlying Cu surface are stronger. Fe/TPA networks are also a means to keep C_{60} molecules separated, since on Cu(100) they normally tend to form large hexagonal clusters (Fig. 38a, areas not covered by the network). Individual C_{60} molecules also can be accommodated in Fe/TMLA networks (Fig. 39a,b). A different scenario is found for the larger Fe/TDA network, where the cavities are so large

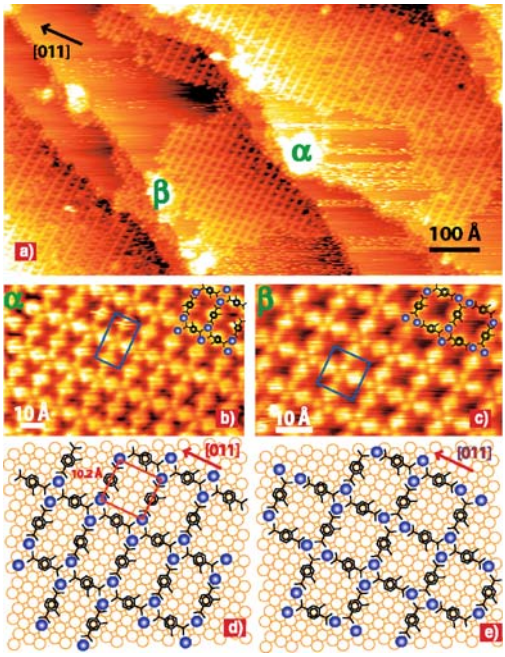

Fig. 37 A *single-row MOCN*: **a** STM topography showing the two types of ordered networks, designated as α and β phases. In the inset, both 90° rotational domains of the α phase are depicted; **b**, **c** high-resolution STM images of Fe and TMLA in both the α and β phases. **d**, **e** tentative models that identify the α and β phases as MOCN isomers. Reprinted with permission from [93]. © (2003) Wiley

as to host C_{60} monomers, dimers, trimers and, rarely, tetramers (Fig. 39b,c). The possibility of a reversible C_{60} adsorption was explored. Thermal annealing experiments showed that C_{60} is ejected from the pores at temperatures between 370 and 420 K for the various cavities of the Fe/TPA network and at temperatures higher than 500 K from the TDA network. However, it was impossible to desorb C_{60} from the TMLA network. The explanation is that the carboxylic group in the *orto* position, likely present in the deprotonate form and not involved in the network formation, modifies the chemical functionality of the pores leading to stronger host–guest interactions. This work demonstrates that MOCNs can be used as template for the patterning of functional species.

2D networks with threefold metal-organic coordination symmetry can be fabricated based on Fe centers with linear bi-phenol ligands or Co centers with linear terphenyl-dicarbonitrile ligands on Ag(111) and Cu(100) [95]. The local threefold coordination mode is kept even on a substrate with fourfold symmetry, indicating that the self-assembly process is driven mainly by intermolecular interactions. Nearly perfect *honeycomb* networks were formed.

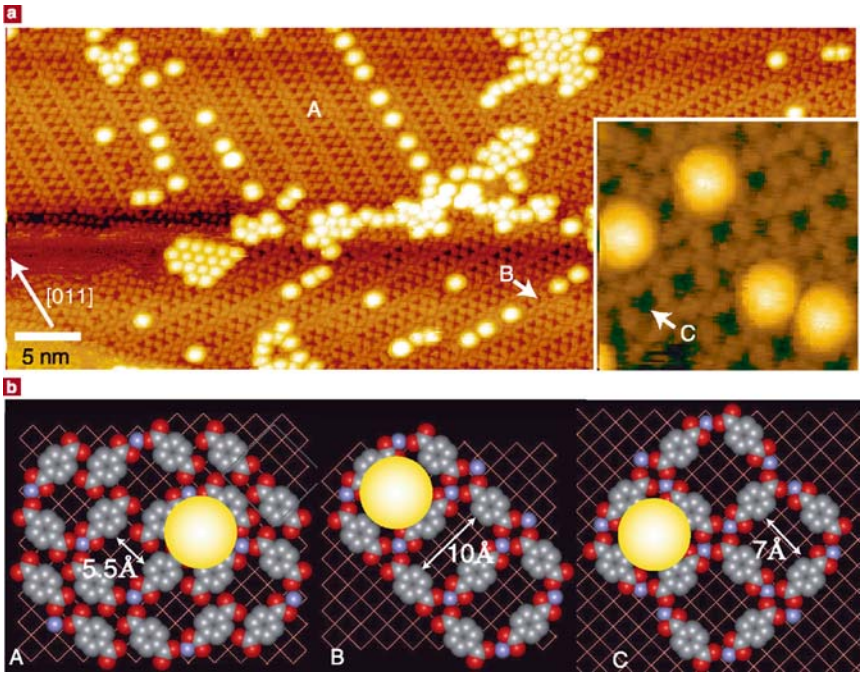

Fig. 38 Adsorption of single C_{60} in Fe-TPA host networks. **a** As seen in the STM image, ladder-type MOCNs account for linear arrangements of single C_{60} (*yellow spheres*) with preferential occupation of larger cavities available (C_{60} clusters are on areas with bare Cu substrate). *Inset*: C_{60}-monomer accommodation in cavities of type-C network. **b** Top-view models for C_{60} adsorption in the cavities encountered in **a** with molecules drawn to scale. Possible configurations are labeled in the model and data by *A*, *B*, and *C*. In the Van der Waals geometries used for modeling, the molecules appear smaller than in the STM images. Reprinted with permission from [94]. © (2005) Nature Publishing Group

A combination of metal nanopatterning and controlled metal-organic assembly was employed to mesoscopically organize supramolecular architectures on surfaces [96]. Fe or Co nanodot arrays, whose formation was enabled by the preferential nucleation of metal islands at the elbow sites of the reconstructed Au(111) surface, decorated the Au(111) surface providing for the nanopatterned surface. The deposition of 1,4-benzenedicarboxylic acid (TPA) on the nanopatterned surface led to the formation of metal-organic nanostructures (via an irreversible reaction with elimination of molecular hydrogen). Using a stoichiometry of about one Fe atom per one TPA molecule with the sample maintained at 355 K during deposition, the growth of TPA on a Fe nanoarray on Au(111) resulted in the complete dissolution of the Fe nanodots and the formation of irregular islands constituted of nanogrids sized 1×1.2 nm^2. To interpret the STM images, a model was proposed, whereby diiron centers were surrounded by four molecules (inset of Fig. 40a). Since the

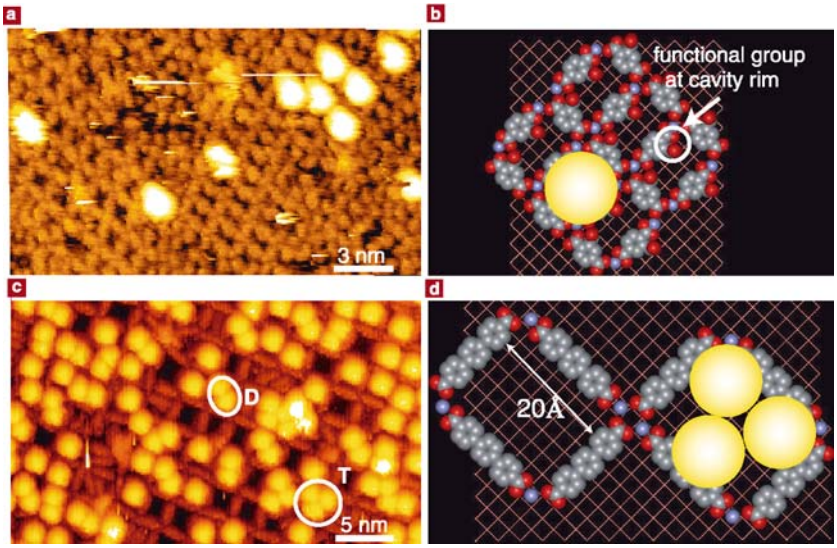

Fig. 39 Adsorption of C_{60} in Fe-TMLA and Fe-TDA network hosts. **a** Similar to the Fe-TPA networks, Fe-TMLA networks host C_{60} monomers. **b** Model of accommodation of a C_{60} monomer in Fe-TMLA MOCN cavities. **c** The cavities in 2D reticulated Fe-TDA networks can host C_{60} monomers, dimers (*D*), or trimers (*T*). **d** Model of rectangular cavity and accommodation of a C_{60} trimer. Reprinted with permission from [94]. © (2005) Nature Publishing Group

quasi-hexagonal structure of the Au(111) surface does not match with the rectangular structure of Fe-TPA nanogrid, the size of the islands did not exceed 10 to 15 nm. Mesoscopically ordered metallosupramolecular ribbons of Fe-TPA were observed keeping the Fe nanopatterned surface at 325 K and employing a fourfold Fe excess, compared to the ideal 1 : 1 nanogrid geometry (Fig. 40b). The partial dissolution of the Fe nanodots provided for anchoring sites localized along the elbow sites of the Au(111) surface for the reticulated metal-organic assemblies. The ribbons are 5–10 nm large and their length can be hundreds of nanometers.

The possibility to monitor with submolecular resolution the non-covalent bonding between a surface-supported metallosupramolecular network and C_{60} and molecules of biological interest, such as cysteine or diphenylalanine, has been demonstrated [97]. The metallosupramolecular host structure, a square lattice array with a 3.4 nm periodicity, results from the hierarchical assembly of Fe atoms and trimesic acid molecules on Cu(111). In the case of the cysteine guest molecule the two protrusions, in some cases three, appearing in the nanocavity were attributed to cysteine molecules standing upright inside the cavity and bound to the Cu surface via the carboxylic end group. Individual adsorption of C_{60} molecules at each nanocavity was observed due to the good size fit between C_{60} and the nanocavity. The 1.3 nm

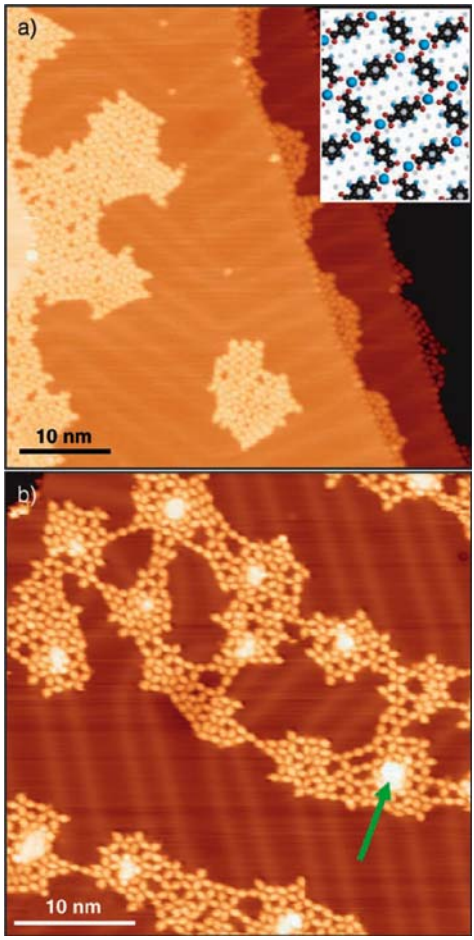

Fig. 40 Fe–TPA complexation reaction. **a** Complete dissolution of Fe islands for a Fe–TPA stoichiometry of about 1 : 1 following deposition of TPA on the Fe nanoarrays at 355 K (image size $51 \times 51\ nm^2$, $V_s = 2.5$ V, $I_t = 0.5$ nA, 5 K). The *inset* shows a tentative model for an ideal Fe–TPA nanogrid where at each di-iron center the end groups of four molecular linkers come together. **b** Localized reaction with TPA deposition at 325 K and 10 min post-deposition annealing at 330 K, with Fe–TPA stoichiometry of ca. 4 : 1. The resulting nanogrid structure reflects selective growth of metal–organic islands at residual Fe dots (Fe island indicated by *arrow*; 0.1 ML Fe, 0.25 ML TPA; image size $38 \times 38\ nm^2$, $V_s = 1.5$ V, $I_t = 0.2$ nA, 5 K). Reprinted with permission from [96]. © (2005) Wiley

long diphenylalanine contains bulky phenyl groups, so that it cannot be completely included in the nanocavity. The fuzzy protrusions appearing in the STM image of the diphenylalanine molecules was attributed to the different conformations that are accessible to the flexible molecular backbone. The

investigated guest molecules are reversibly bound to the host structure as demonstrated by their thermal removal.

Another strategy for the growth of metal-organic nanostructures made use of a Au(111) surface patterned with Fe islands arrays [98]. The Fe arrays were formed spontaneously upon Fe deposition via strain relief nucleation at the elbows of the herringbone reconstructed Au surface. The template was able to drive the formation of PTCDA molecular chains or nanodots. On this template, PTCDA molecules aggregated in close proximity of the Fe islands, forming structures different than those formed on pristine noble metal surfaces. The presence of Fe nucleation centers stabilizes aggregates that are typically not observed at RT. Two different structures are observed: *molecular chains* at high temperature and *nanodots* (round structures) at LT. This result suggests that the key parameter controlling the growth of PTCDA structures is the amount of free Fe adatoms diffusing at the surface. This number increased at high temperature, leading to a chain formation, where PTCDA molecules were linked by Fe atoms. At low T most of the Fe atoms were localized close to the reconstruction corners thus favoring the formation of rounded structures. Therefore, it was possible to switch from one structure to another tuning the deposition conditions. Annealing at temperature as high as 420 K resulted in a structure with the herringbone phase characteristic of PTCDA on Au(111). STS revealed that the PTCDA nanostructures nucleated at the Fe sites possess a local density of states different from that deposited on pristine Au(111).

A porphyrin nanoarray was employed as the key component of a novel reaction scheme for the formation of metalloporphyrin nanoarrays, with the metal being provided by an atomic beam [99]. Iron atoms react with tetrapyridyl-porphyrin (TPyP) molecules ordered in a staggered arrangement on Ag(111) surface, to give the compound Fe-TPyP. The structure of the TPyP layer was preserved upon Fe deposition. The synthesis of metallo porphyrins at surfaces by this method gives high purity products (usually metalloporphyrins are thermally unstable and reactive). Metalloporphyrins prepared using this method exhibit an available axial position for the binding of ligands of biological interest.

2.4 Macrocycle Networks

A very smart approach for the synthesis of highly ordered host-guest systems is based on macrocycles which are typically used as building blocks for molecular machines [100]. In this context an interesting host-guest system is the couple cyclo [12]thiophene (c[12]T) and C_{60} fullerene, respectively a ring-shaped p-type and a spherical n-type organic semiconductor [101]. Cyclothiophenes are a well-known class of macrocycles [102], whose self-assembly has been extensively studied by STM [103, 104]. The porous network was

constituted by a close packed monolayer of c[12]T (Fig. 41a) where the macrocycles are held together by Van der Waals forces and present cavities with a diameter of about 1.2 nm. The network is not stabilized by hydrogen bonds. In consecutive steps, c[12]T and C_{60} are self-assembled on HOPG from a 1,2,4-trichlorobenzene solution. The STM experiments were performed at the air/solid or air/liquid interface. Due to its pronounced electron-accepting properties, C_{60} forms a 1 : 1 donor-acceptor (D/A) complex with the electron donor c[12]T (Fig. 41b). At low coverage, two complexation sites for C_{60} are found: at the rim (R-type) of the macrocycle (in six different positions, in agreement with the sixfold symmetry of the macrocycle) and in the cavity (C-type), as shown in Fig. 41c. The complex at the rim is expected to be more stable since it provides the maximal π–π interaction. R-type and C-type fullerenes are imaged differently with the STM. R-type fullerenes appear brighter and with a shorter apparent diameter: 1 nm vs. 1.6 nm for the C-type. This indicates that C-type fullerenes are not immobilized within the cavity, but rather rotate around an axis perpendicular to it. The c[12]T to fullerene ratio is 1 : 1 at any surface coverage since after complexation of one molecule the electron density of the c[12]T LUMO is modified so that complexation of a second molecule is unfavored. At high coverage, close to 1 ML, the complexed fullerenes form an ordered 2D crystal structure. In this structure, the distance between neighboring fullerenes (2.3 nm) is much larger than that reported for pure adsorbates or bulk fullerenes (1 nm) since the network hinders short-range intermolecular interactions.

Another cyclothiophene (structure **1** in Fig. 42) was used to build supramolecular structures with C_{60} [105]. Trichlorobenzene solutions of **1** or **1** plus fullerene were deposited in solution on HOPG. After drying of the solvent, STM imaging was performed in an air-tight chamber. STM images show the cavities of the macrocycles in the self-assembled layer (Fig. 42). Subsequently, the self-assembly of the two components system **1**/C_{60} was studied. The co-deposition leads to a highly ordered array of fullerene molecules. Due to weak bonding between fullerene and **1**, the structures were not stable during STM imaging. Interestingly, even in this case, the C_{60} molecules were found to adsorb preferentially at the rim of the macrocycle, in agreement with the n- and p-character of the two compounds. Due to the larger dimensions of the macrocycle compared to c[12]T, two C_{60} molecules were found on each macrocycle. For this network, the driving force to adsorption was the

Fig. 41 (*Left*) Conjugated macrocycle C[12]T. **a** STM image of a monolayer of C[12]T on HOPG, including a C[12]T/C_{60} R-type complex (*white arrow*). *Image area*: 11.6×8.7 nm^2; tunneling conditions: $V_s = -700$ mV, $I_t = 44$ pA. **b** Calculated model of a closely packed monolayer of C[12]T with a hexagonal arrangement including the unit cell parameters. *Side view* of the calculated energy minimum conformation of a C[12]T/C_{60} complex (*inset*, *upper right*). Adapted with permission from [103]. © (2006) Wiley ►

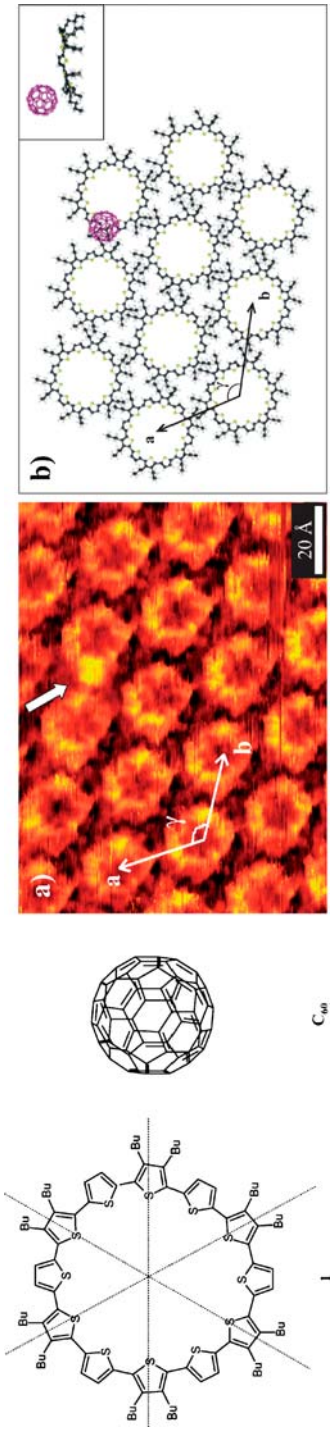
b)
a
b
a)
20 Å
a
b
c
C_{60}
Bu
S

donor–acceptor interaction between the host and the guest rather than the guest–graphite interaction.

The non-planar tetralactam macrocycle (TLM) shown in Fig. 43 was able to form 2D highly ordered supramolecular networks [106]. It contains four amide groups, which are involved in hydrogen bonds. The system had already been investigated as receptor for benzoquinone [107] and as a active component in sensors for the detection of trans-2-hexanal and acrylamide, where it was proposed that these molecules adsorb in the cavity of the macrocycle [108].

The macrocycle was deposited on Au(111) in UHV. After deposition, two ordered phases (α and β) were found at the surface. The α phase is believed to be the most thermodynamically stable one since it prevails at RT, whereas the β phase prevails after annealing at 400 K. The monolayers decompose if

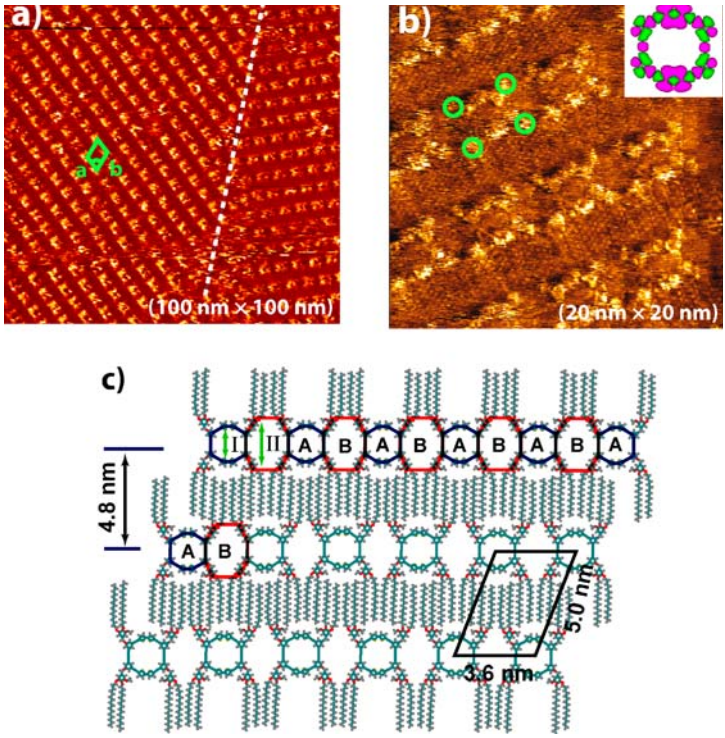

Fig. 42 Networks of **1** on HOPG under ambient conditions. **a** Typical large-scale STM image (100×100 nm^2). $V_s = 0.35$ V; $I_t = 0.6$ nA. An oblique unit cell is indicated in *green*. **b** Higher resolution STM image (20×20 nm^2) $V_s = 0.41$ V; $I_t = 0.5$ nA. The four extra-annular groups are indicated with *green circles*. The *inset* is the HOMO of the cyclic backbone of **1**. **c** Proposed structural model. The *blue* and *red octagons* indicate the two types of nanoscale holes, A and B. Reprinted with permission from [105]. © (2006) American Chemical Society

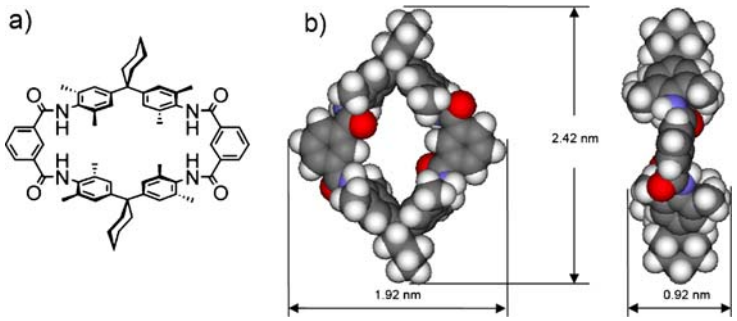

Fig. 43 Tetralactam macrocycle: **a** molecular structure; **b** sphere model of the molecule, obtained using DFT calculations. Reprinted with permission from [106]. © (2007) Wiley

a tunneling current higher than 1 pA is used for imaging. In both phases, self-organization occurs through intramolecular hydrogen bonds formed between the –NH and the carbonyl group of two neighboring macrocycles. In phase β, the number of hydrogen bonds per molecule is by one third smaller than in phase α, thus explaining the lower stability of phase β. This work demonstrated that hydrogen bonded 2D ordered networks can be formed also by large non-planar molecules.

The self-assembly of OBOCMC8, a calyx [8]arene derivative, and of the host-guest system OBOCMC8/C_{60} (see scheme in Fig. 44) supported on the Au(111) surface was investigated by electrochemical STM [109], leading to submolecular resolution of the self-assembly of calyxarenes molecules. Calyxarenes are suitable to fabricate nanoscale electronic devices because of their ability to host fullerene molecules. OBOCMC8 molecules adsorb on Au(111) by carboxyl-, phenyl-, and *tert*-butyl-gold interactions [110, 111]. OBOCMC8 molecules appear in the STM images as ordered arrays of dark depressions (*calixes*). When a saturated solution of C_{60}/OBOCMC8 is introduced into the STM cell, STM images show an ordered array of bright spots surrounded by circular protrusions, corresponding to the C_{60}/OBOCMC8 assembly. The C_{60}/OBOCMC8 complex has an upright orientation on the Au(111) surface, the carboxyl groups being responsible for this arrangement. The bright spots and circular protrusions can be assigned as C_{60}, *tert*-butyl, and phenyl units. The contents of the calix could be changed to other fullerenes, clusters, and organic molecules.

Coronene monolayers also act as macrocycle-type host systems. C_{60} molecules, C_{120} and C_{130}, were epitaxially deposited onto an Au(111) surface covered by an ordered layer of electron donating coronene molecules [112]. This study was carried out in the context of the investigations on the growth of organic films onto substrates modified with organic *buffer* layers. The latter is an interesting approach to improve the electronic properties of organic films. Indeed, it has been recently demonstrated that the electron field-effect

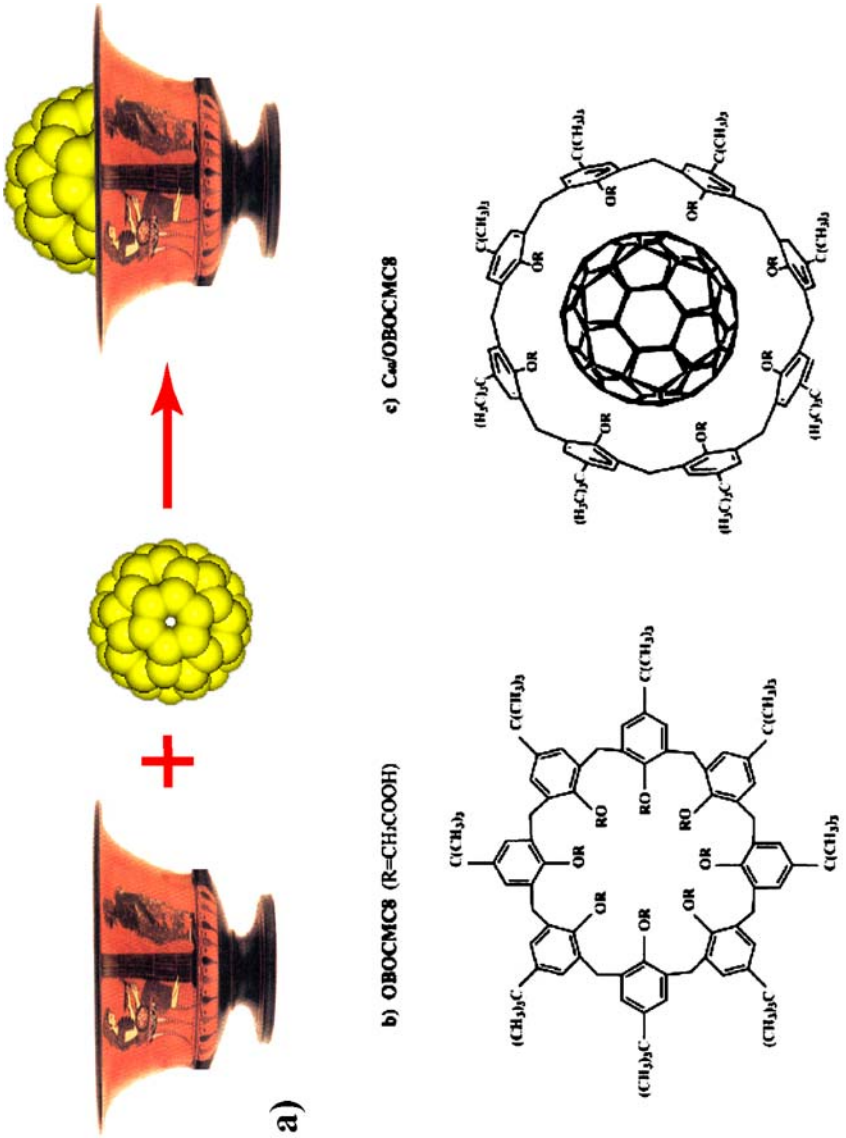

Fig. 44 **a** Schematic representation of the formation of the C_{60}/OBOCMC8 complex; molecular structures of OBOCMC8 (**b**) and C_{60}/OBOCMC8 (**c**). Reprinted with permission from [109]. © (2003) Wiley

mobility in C_{60} films grown on a pentacene *buffer* layer is 4–5 times higher compared to when the buffer layer is absent [113]. On the *buffer* layer, fullerene molecules have a low surface mobility, thus having the possibility to form an ordered array of molecules. The coronene modified Au(111) was ob-

tained by immersing gold in a coronene-containing benzene solution and the modified surface was immersed in a fullerene-containing benzene solution to obtain the fullerene layer on the coronene *buffer* layer. In STM images, coronene molecules appear as hexagonal donuts and give an ordered array with (4×4) symmetry. The molecular rows go along the [110] direction and the intermolecular spacing is 1.17 ± 0.03 nm, which correspond to 4 Au atoms. C_{60} molecules deposited on the coronene adlayer give a *honeycomb* structure and are aligned with coronene molecular rows positioned between them. The *honeycomb* array could originate by a relaxed coronene adlattice (4.3×4.3), observed in the presence of C_{60} molecules. The *honeycomb* structure was tentatively explained by the adsorption of the C_{60} molecules in the threefold sites of the (4×4) coronene adlayer, which are exposed to Au. Indeed, C_{60} has high adsorption energy for gold ($40-60\,\mathrm{kcal\,mol^{-1}}$) and Au has enhanced electron donating properties after the adsorption of the electron donating coronene molecules. The adsorption of C_{70} molecules on the coronene modified Au(111) surface is different. 1D domains are present and they have a metastable structure, with C_{70} arrays oriented along the three directions of the underlying coronene layer or Au(111) substrate. Fullerene dimers, such as C_{120} (homodimer) and C_{130} (heterodimer), were also studied as adlayers on the coronene modified Au(111) surface. Two bright spots (*dumb-bell* shaped) characterize C_{120} molecules that are organized in stripes having the same direction or crossing each other at 60° or 120°. The packing arrangement and the molecular distances of the C_{130} array were almost identical to those of the C_{120} array on the coronene modified Au(111). The different behavior of the fullerene molecules suggests that the *buffer* coronene layer selectively recognizes the different fullerenes, thus indicating that the *buffer* layer plays an important role in the formation of supramolecular assemblies of fullerenes.

2.5 Flexible Porous Networks

A novel class of surface templates is represented by *flexible porous networks*, i.e., non-porous networks that turn porous as a response to the addition of a guest.

Flexible networks can be based on benzoannulene derivatives [114, 115]. Several types of benzoannulene derivatives were tested, differing in the length of the of alkyl chains at the periphery of the triangular cores (Fig. 45a). STM observations were carried out on HOPG and 1,2,4-trichlorobenzene (TCB) was used as solvent.

On one hand, benzoannulene compounds with short alkyl chains form *honeycomb* networks. On the other hand those with long alkyl chains form linear *non-porous* structures (Fig. 45b). The latter compounds prefer to pack in a compact structure since large pores would lead to unstable low-packing

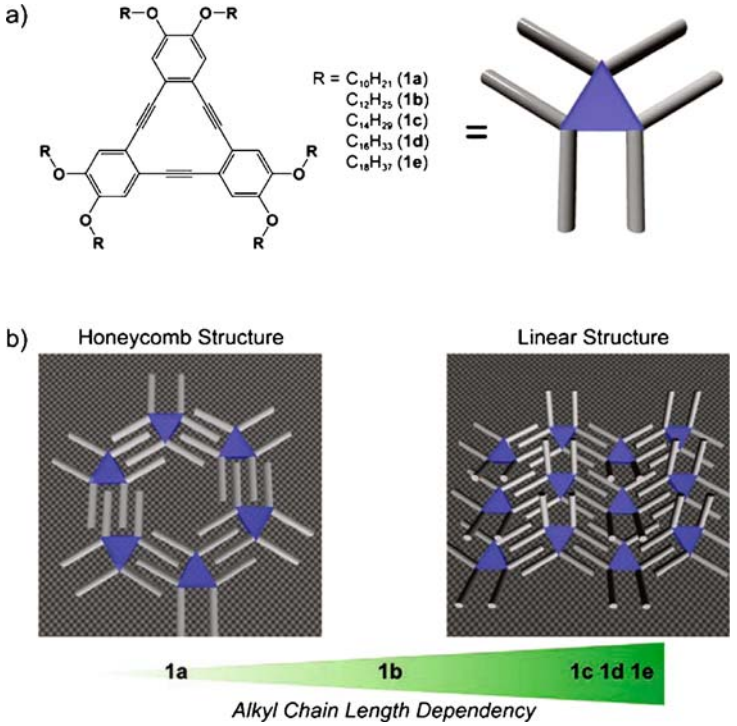

Fig. 45 **a** Molecular structure of annulenes; **b** alkyl chain length dependence of the 2D networks formed. Reprinted with permission from [114]. © (2007) Wiley

density structures. The host properties of benzoannulenes were initially probed introducing a coronene guest on the *honeycomb* pattern of compound 1a (Fig. 45a). The result was a network where coronene guests occupy the cavities of the pattern. Based on pore dimensions, the number of coronene molecules in each pore was estimated to range from one to three. Surprisingly, adding a tenfold excess of coronene on a solution of 1c (Fig. 45a) resulted in a porous structure, with coronene guest molecules positioned in the cavities (see Fig. 46). The number of coronene molecules was estimated to be about seven, based on pore dimensions. A *honeycomb* network was formed also upon application of a mixed solution of the two compounds

Fig. 46 **a** Tentative models of the surface patterns of 1c. *Left*: linear structure of 1c without coronene; *right*: honeycomb structure capturing at most seven coronene molecules. **b** Plot of the area fraction of the honeycomb structure versus the guest/host molecular ratio (G/H). **c–f** Large-area STM images ($96 \times 96\ nm^2$) of the network structures of 1c with or without coronene ($V_s = 0.7$ V, $I_t = 0.04$ nA): **c** guest/host = 0 : 1; **d** guest/host = 2 : 1; **e** guest/host = 4 : 1; **f** guest/host = 7 : 1. Reprinted with permission from [114]. © (2007) Wiley ►

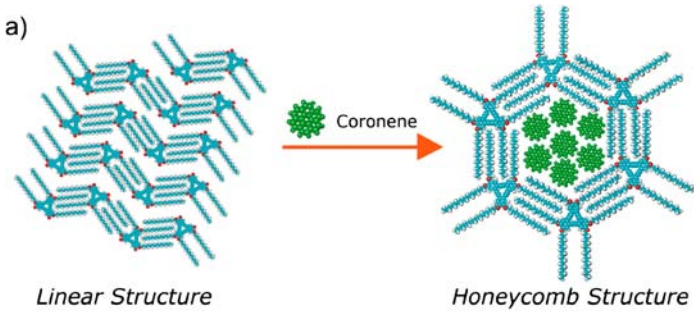
a)
Coronene
Linear Structure
Honeycomb Structure

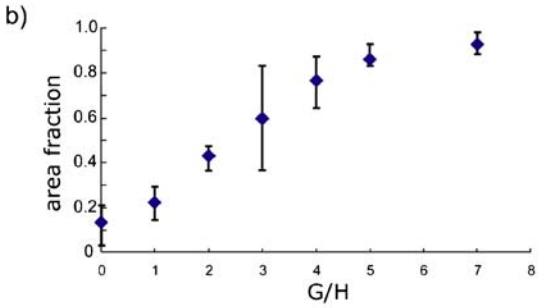
b)
area fraction
1.0
0.8
0.6
0.4
0.2
0
0 1 2 3 4 5 6 7 8
G/H

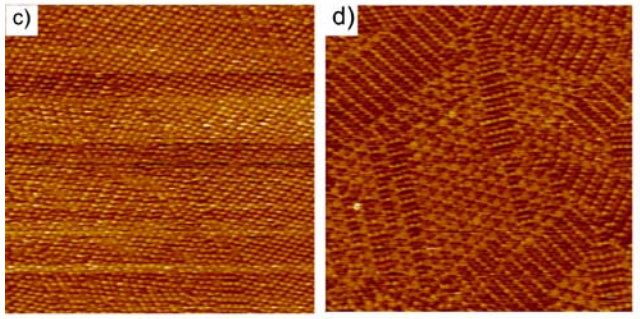
c)
d)
G/H = 0:1
G/H = 2:1

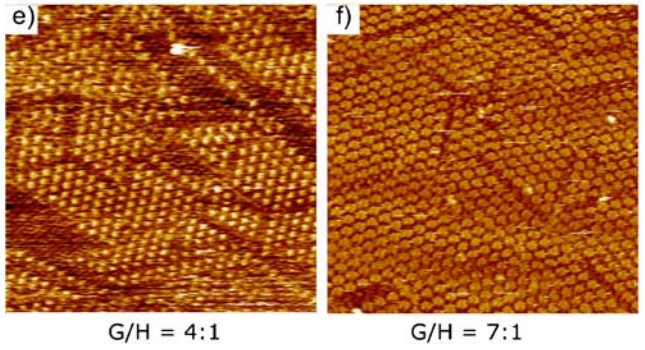
e)
f)
G/H = 4:1
G/H = 7:1

(coronene and 1c), indicating that the porous structure was thermodynamically favored in presence of a coronene guest. Molecules with longer alkyl substituents did not form porous networks since the strong adsorption energy of long alkyl chains on graphite did not favor the coadsorption of coronene.

A titration experiment was carried out to understand the mechanism of the transformation of the linear non-porous network into a porous one. Coronene was gradually added to a layer of 1c molecules and the area fraction of the *honeycomb* pattern was measured as a function of the guest to host molecular ratio (see Fig. 46b). The results suggest that the transformation into a honeycomb network is initiated by coronene molecules captured at the boundaries between linear structures. To investigate the selectivity of the network, six different guest molecules were studied: coronene, hexakis(phenylethynyl)benzene (hpeb), C_{60}, 9–10 diphenylanthracene (dpa), hexaiodobenzene (hib), chrysene, and phthalocyanine (pc) (see Fig. 47). Adding a tenfold excess of the guest to a 1c solution showed that large π-conjugated cores (coronene, hpeb, and pc) led to the formation of porous networks, whereas small π-conjugated molecules leave the system unperturbed. This result reveals that the adsorption energy of the guest on graphite is a key issue. Large π-systems with higher adsorption energy reside in the cavities and stabilize the porous network.

Another example of flexible networks are 2D molecular sieves, obtained using a purposely designed star-shaped stilbenoid compound (1,3,5-tris[(*E*)-2-(3,5-didecycloxyphenyl)-ethenyl]-benzene, whose structure is shown in Fig. 48A [116, 117]. Star shaped stilbenoids are known to self-assemble on graphite leaving empty cavities [118]. Self-assembly on HOPG from a phenyloctane solution led to *honeycomb* cavities with a diameter of $\sim$1.3 nm (see Fig. 48B). The cavities were able to host both coronene and hexabenzocoronene (HBC) that, despite the different dimensions (1 nm for coronene and 1.3 for HBC), appeared similar in the STM image, probably due to motion within the pores. The mass transport within the network was investigated on incompletely filled matrixes obtained from diluted coronene and HBC solutions (10^{-7} M) at variable temperature. For coronene, at LT and fast scanning rates, filled and empty cavities were found to coexist. Coronene molecules were able to move in and out of the cavities due to 2D diffusion confined into the matrix. On the other hand, HBC molecules tended to keep their position in the network due to their larger size.

The size and shape selectivity of the 2D molecular sieve was also investigated. STM investigations of a TSB35 network were carried out before and after addition of an excess of different polycyclic aromatic hydrocarbon (PAHs) on graphite [117], namely: benzo[*rst*]perylene (BPL), coronene, benzo[*rst*]pentaphene (BPP) or HBC, BPP, and pentacene (see Fig. 48A). After addition of BPL, coronene, BPP, and HBC (Fig. 48C–E) a bright spot appears

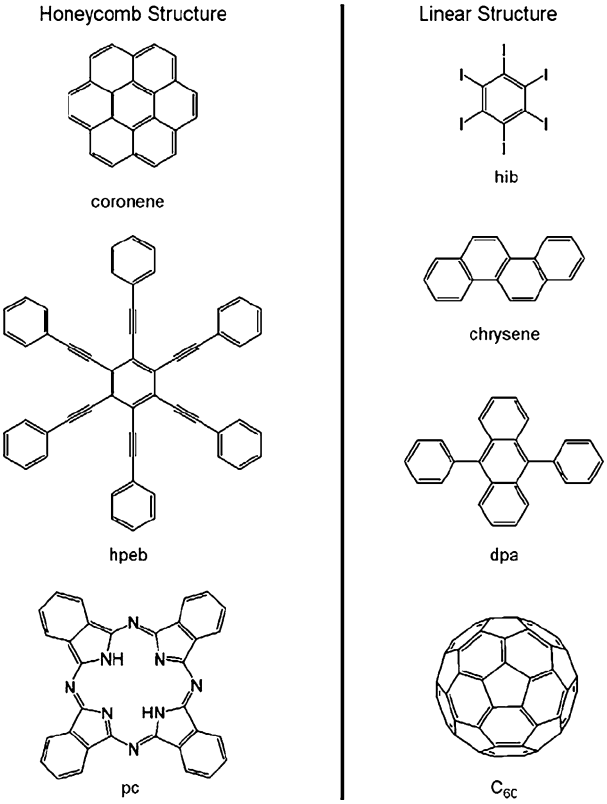

Fig. 47 Guest molecules used in [114]. Reprinted with permission from [114]. © (2007) Wiley

in the centre of the cavities of the TSB35 *honeycomb* pattern. Pentacene never adsorbs on the cavities due to its longer dimensions. Despite the difference in size and chemical structure, the other four macrocycles appear identical when adsorbed in the pores. This is described in terms of fast molecule translational and rotational diffusion inside the cavity. To understand the guest molecule dynamics, the observation of incompletely filled matrices was carried out from dilute solutions at variable temperature. The results showed that BPL, coronene, and BPC are able to diffuse in and out from the cavities, whereas HBC remains sequestered up to 320 K.

A flexible porous network was observed based on the porphyrin derivative 5,15-bis(4-carboxyphenyl)-10,20-bis(3,5-di-*t*-butylphenyl)porphyrin(trans-BCaTBPP, Fig. 49) adsorbed on Au(111) [119]. The initial network consisted of close packed porphyrin molecules and did not contain any pores, yet pore formation is induced by the adsorption of C_{60} molecules at RT. STM images obtained at 63 K show that the porphyrin network is made up of wires stabi-

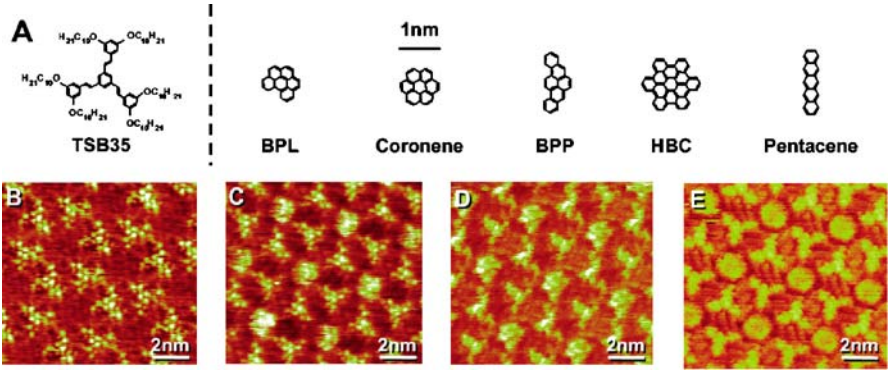

Fig. 48 **A** Molecular structure of the star-shaped stilbenoid compound (1,3,5-tris[(*E*)-2-(3,5-didecycloxyphenyl)-ethenyl])-benzene (TSB35) and of the guest molecules benzo(*rst*)perylene (BPL), coronene, benzo[*rst*]pentaphene (BPP), hexabenzocoronene (HBC), and pentacene; **B** porous network of TSB35, porous network of TSB35 after addition of **C** coronene, **D** HBP and **E** HBC. $V_s = -1$ V, $I_t = 21–46$ pA. Reprinted with permission from [117]. © (2006) Wiley

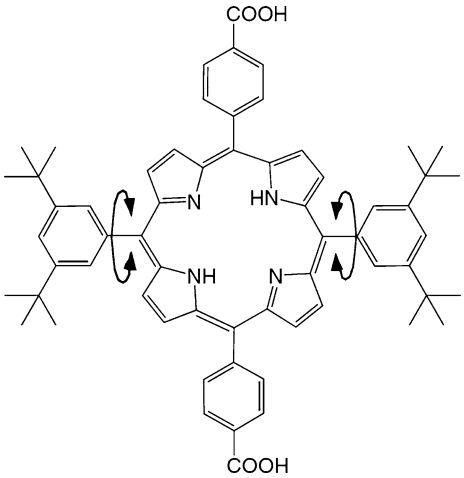

Fig. 49 Molecular structure of trans BCaTBPP

lized by hydrogen bonds. When C_{60} is deposited on the network, linear C_{60} chains form along the porphyrin wires and the distance of the C_{60} molecules in the wire is about 2.1 nm (as the distance between the porphyrins within the supramolecular wire). Interestingly, the adsorbed C_{60} resides between the wires and apparent height measurements indicate that C_{60} molecules are adsorbed directly on Au(111). The shift of the supramolecular porphyrin wires along the wire direction determines the formation of nanopores with a 0.92 nm size.

3
Nanostructured Surfaces

The nanostructured surfaces that can be used as templates for the self-assembly of organic molecules are long-range reconstructions and vicinal surfaces. In this section, we will focus mainly on long-range surface reconstructions. For an overview of the templating effect of vicinal surfaces on organic self-assembly, we refer to a recently published review [120]. We briefly mention that vicinal Au surfaces have been mainly used to drive the self-assembly of C_{60} and PTCDA into nanodots or nanowires. The most studied surfaces are Au(788) and Au(433) [121, 122], although higher index surfaces have also been recently investigated [123, 124].

3.1
Long-Range Mesoscale Reconstructions

A long-range reconstruction that results in an interesting one-dimensional nanotemplate is the (2×1)oxygen-induced reconstruction of the Cu(110) surface [125]. The template is formed by exposing the Cu(110) surface to relatively high pressures of oxygen at elevated temperatures under UHV conditions. Early studies on this system revealed that the reaction between chemisorbed oxygen and surface Cu atoms leads to the formation of O–Cu rows running along the [001] direction of the Cu(110) surface. The rows organize in islands, separated by two [1–10] lattice spacings ($\sim$0.512 nm) [126–128]. A successive study demonstrated that, under appropriate substrate temperature and oxygen pressure, the islands arrange themselves into stripes running along the [001] direction [129]. The (2×1)O–Cu (oxygen-passivated) stripes are separated by regularly spaced clean copper areas and form a periodic grating (Fig. 50). The width of the stripes can be adjusted by varying the oxygen pressure and the substrate temperature during the oxidation process [130]. The O–Cu nanotemplate can be used to drive highly ordered patterns of organic molecules based on their higher affinity for the clean Cu areas rather than the oxygen passivated stripes. The template represents an ideal tool for studying the self-assembly of organic molecules since metallic stripes with a width approaching molecular dimensions can be used to explore the effect of spatial confinement on the adsorption geometry and molecular patterning. Moreover, adsorption geometries and self-assembled patterns of organic molecules can be simultaneously studied on two different surfaces, namely, the metallic and the oxygen-passivated Cu(110). The template has been employed to pattern one-dimensional and two-dimensional nanostructures of organic molecules, including fullerenes [131], the so-called *Lander* molecules [130–134] and the organic semiconductors α-quinquethiophene (T5) [135] and rubrene [136]. The same system has been used to study the electronic properties and the

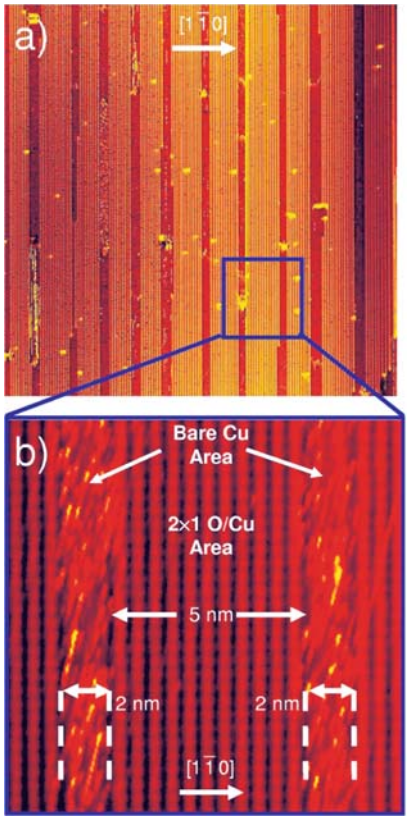

Fig. 50 **a** $70\times70\,nm^2$ STM image of the Cu–O/Cu periodic nanopattern resulting from O_2 exposure. A certain fraction of the derived image has been added to enhance the resolution; **b** $14\times14\,nm^2$ STM image of a partially oxidized Cu(110) surface recorded at RT. 2×1 reconstructed oxidized areas can clearly be distinguished, separated by bare Cu stripes running along the [001] direction. The image is rotated so that the [001] direction is vertical. The original scan direction can be easily recognized as the direction of the spike noise originated from the fast diffusion of kink atoms in the Cu–O edges at RT. Reprinted with permission from [132]. © (2004) Wiley

self assembly of oligophenylenes by means of ultraviolet photoelectron spectroscopy (UPS) [137] STM and NEXAFS [138] and, in a different context, to study adsorbate-induced surface stress [139].

The system was used as template for the self-assembly of two molecules of the so-called *Lander* family [130]: the *single lander* and the larger *violet lander*. Lander molecules adsorb exclusively on the Cu stripes, forming ordered 1D chains stabilized by Van der Waals interactions (Fig. 51). No adsorption was observed on the Cu–O stripes since the oxygen partially withdraws the charge density of underlying metal, thereby reducing the sticking coefficient. The *single lander* molecules in the stripes aligned as on bare Cu(110). The

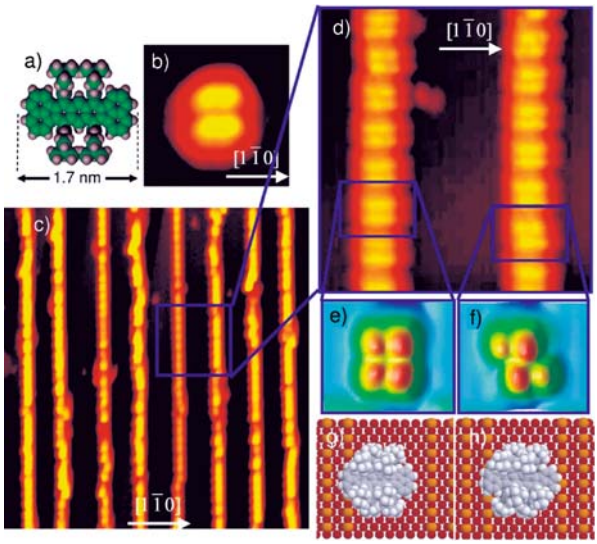

Fig. 51 **a** Filled-space model of the Single Lander (SL) molecule; **b** typical 3×3 nm^2 STM image of the SL molecule on a clean Cu(110) surface revealing the SL as four lobes corresponding to the spacer legs; **c** 60×60 nm^2 STM image showing the molecular chains formed after the deposition of SL on the nanopatterned Cu–O surface. The molecules adsorb exclusively on bare Cu stripes; **d** 14×14 nm^2 high-resolution STM image. The individual SL molecules can be individually resolved, and their conformation can be extracted thereby; **e**, **f** Simulated STM images of the SL on the bare Cu stripes, with two different conformations; **g**, **h** ball models of the SL adsorbed on the nanopatterned Cu–O surface from which the simulated STM images **e** and **f** were extracted. These models show that the SL adsorbs on bare Cu areas with the board perpendicular to the direction of the stripes. Reprinted with permission from [132]. © (2004) Wiley

longer *violet lander* molecules which on bare Cu have the same orientation as the *single lander*, were adsorbed with their board oriented along the nanotemplate stripes. For the smallest possible Cu stripe (1.8 nm in width) all the molecules were aligned along the stripe direction (Fig. 52). If the width of the stripes was increased, the molecules changed their orientation forming a certain angle with respect to the [1–10] direction. These results showed that the supergrating stripe not only provides an adsorption site but also steers the orientation of the molecules.

The O–Cu template was used to study the self-assembly of T5 [135], an organic semiconductor with great potential as active layer in organic field effect transistors [136]. T5 self-assembly was studied for increasing coverage (Fig. 53). At low coverage, the molecules adsorbed preferentially on the Cu(110) stripes (Fig. 53b), in agreement with the observations with *Lander* molecules. In the middle of the Cu(110) stripes, the molecules aligned along the close packed direction of the surface (as seen for the majority of the molecules on the pristine Cu(110) surface). At the Cu/O–Cu interface, the

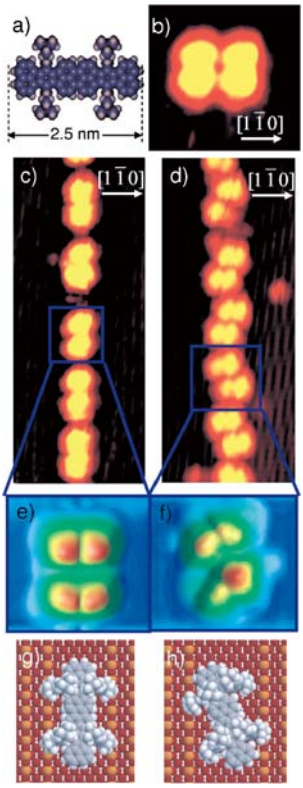

Fig. 52 **a** Filled-space model of the Violet Lander (VL) molecule; **b** typical $3\times3\,nm^2$ STM image of the VL molecule on a clean Cu(110) surface, which reveals the VL as four lobes corresponding to the spacer legs; **c**, **d** $8\times20\,nm^2$ STM images showing the molecular chains formed after the deposition of VL on the nanopatterned O–Cu surface. The molecules adsorb exclusively on bare Cu stripes, but their orientation is no longer perpendicular to the direction of the stripes. The molecules are found either perfectly aligned with the direction of the stripes (**c**) or forming an angle of 20° with respect to that direction (**d**); **e**, **f** Simulated STM images of the VL on the bare Cu stripes, with two different adsorption geometries; **g**, **h** ball models of the VL adsorbed on the nanopatterned Cu–O surface from which the simulated STM images **e** and **f** were extracted. Reprinted with permission from [132]. © (2004) Wiley

molecules tended to align parallel with respect to the direction of the stripes (see insets). This observation indicates that the molecules also adsorbed on the O–Cu regions. To investigate this topic more deeply, the nanopattern was exposed to a higher dose of T5. This resulted in the adsorption of T5 molecules even towards the center of the oxygenated stripes (Fig. 53c). Here, the molecules aligned along the closed-packed direction of the O–Cu surface (i.e., perpendicular to the majority of the molecules adsorbed on Cu(110)) and lied flat on the substrate as on Cu(110). The adsorption of T5 molecules

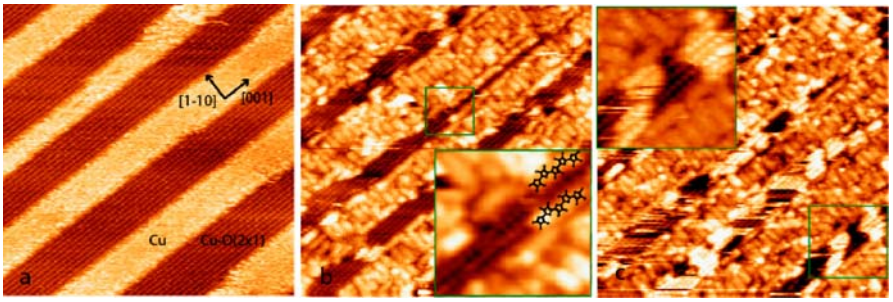

Fig. 53 **a** STM image of the Cu/O–Cu nanopattern (partial 2×1 reconstruction) obtained by exposing the Cu(110) surface to 0.5 Langmuir (L) of oxygen at 623 K ($34\times34\ nm^2$). Imaging parameters: $V_t = -645$ mV, $I_t = 1.06$ nA. **b** 0.4 ML T5 coverage of the nanopattern ($34\times34\ nm^2$). The *inset* ($5.9\times5.4\ nm^2$) shows a high-resolution image of T5 adsorbed on the border between the Cu(110) and the O–Cu regions. Image parameters: $V_s = -2866$ mV, $I_t = 1.06$ nA. **c** Increasing the coverage of T5 to 0.8 ML, the molecules begin to adsorb in the middle of the O–Cu regions ($34\times34\ nm^2$). A highly resolved image of the islands is shown in the inset ($8.1\times8.1\ nm^2$). Imaging parameters: $V_s = 526$ mV, $I_t = 1.06$ nA. Reprinted with permission from [135]. © (2006) Wiley

on O–Cu occurred after saturation of the pristine Cu rows and started on the border with the Cu(110) rows. This happens because the molecules impinging on the O–Cu surface diffuse until they find an energetically favorable adsorption site that is provided by the molecules adsorbed on pristine Cu(110).

Self-assembly of T5 was also studied on a fully (2×1) oxygen-reconstructed Cu(110) surface. T5 has a lower chemical affinity for O–Cu compared to Cu(110). For this reason, a dose a factor of 2.5 times higher than on pristine Cu(110) was required to achieve full monolayer coverage. As seen for the case of T5 adsorbed onto a Cu/O–Cu nanopattern, the molecules aligned with their axis along the closed packed direction of the (2×1)O–Cu reconstructed surface. At monolayer coverage, the molecules assembled with a high degree of order over several hundred square nanometers, with the driving force for assembly being weak Van der Waals attractive interactions. Such interactions are favored by the presence of the oxygen layer that reduces the interaction between the metallic *d* orbitals and the molecular π orbitals. A high-resolution image for complete monolayer coverage is shown in Fig. 54a. Molecular models are superimposed on the image for clarity. A higher degree of order was achieved compared to Cu(110), since all T5 molecules lied along the close packed direction. This observation suggests that the registry of the molecules with respect to the surface was improved on the (2×1)O–Cu reconstructed surface with respect to the pristine Cu(110) surface. The T5 molecules are clearly interdigitated. A model for their orientation within the layer is proposed in Fig. 54b. The molecules within a column are aligned in the same direction, such that the sulphur atoms of the thiophenes at each end of the molecule point in the same di-

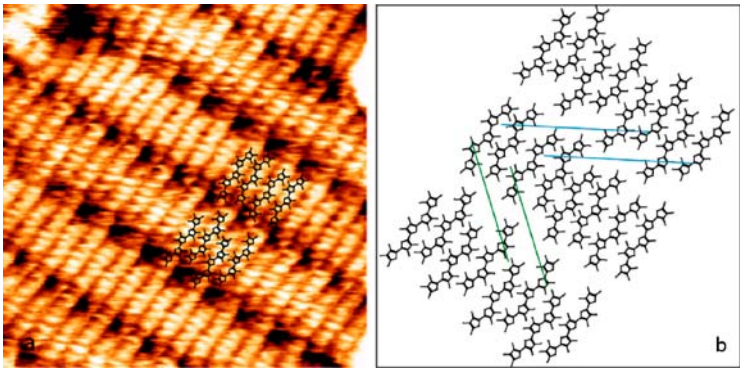

Fig. 54 **a** Saturation coverage of T5 on the (2×1)O–Cu reconstructed surface (12×12 nm^2). Tunneling parameters: V_s = –0.526 V, I_t = 0.659 nA. **b** Proposed adsorption geometry of T5. *Blue* and *green lines* show the direction of tilt of the holes. Reprinted with permission from [135]. © (2006) Wiley

rection. In this scenario, steric interactions are reduced as T5 molecules within a column are shifted by approximately a single thiophene ring (or 0.7 nm) with respect to one another. In neighboring columns, the molecules adsorb such that the sulphur atoms of the end thiophene rings point in the opposite direction. The ordered assembly of molecular layers on the copper oxide surface is particularly interesting for applications in organic electronics since oxide layers are often an essential component in devices. In perspective, the selective affinity of T5 for Cu(110) and O–Cu paves the way to the improved fabrication of electrode/organic semiconductor interfaces.

4 Conclusions and Perspectives

STM studies have recently demonstrated the possibility to control the assembly of organic building blocks, exploiting surface nanotemplates that provide suitable surface cues which can drive the formation of ordered structures upon adsorption. In this review, we described most known studies of the adsorption properties of organic molecules deposited on nanotemplates, demonstrating the exciting opportunity of controlling molecular assembly with nanoscale precision and at fairly long ranges on nanostructured single crystal surfaces.

When using molecular porous networks, the key concept for the templating effect is to realize a hierarchical stability of the components of the desired, complex system, typically using intermolecular interactions, such as hydrogen bonds and metal-organic complexation. The component of highest

stability should be the nanotemplate, on top of which structures of increased complexity and lower stability can be built.

We also described how novel polymorphs of bi-dimensional assemblies of organic molecules have been self-assembled by the stabilization of pure phases of the molecule of interest at the domain boundaries of more stable, ordered, multi-component systems.

Finally, we discussed the use of long-range surface reconstructions as templates to steer the adsorption of functional organic molecules. A classic example is the partial (2×1)O–Cu reconstruction obtained by exposing a Cu(110) surface to oxygen at high temperature, leading to a one-dimensional nanoscale supergrating which acts as a template upon adsorption of organic molecules.

These studies open interesting perspectives both for fundamental studies and for possible applications. With respect to basic research, they are providing new insight into the mechanisms that govern self-assembly, and ways to control it by balancing molecule–molecule versus molecule–surface interactions. In terms of applications, controlled molecular patterning with nanoscale precision will offer new opportunities for developing molecular writing, chemical and biological sensors, molecular electronic devices, and improved biocompatible materials.

Acknowledgements F.C. and C.S. acknowledge CBIE for partial financial support. F.R. is funded by NSERC of Canada and the Canada Foundation for Innovation. F.R. is grateful to FQRNT and the Canada Research Chairs program for partial salary support. We acknowledge funding from the Petroleum Research Fund of the American Chemical Society and the International Office of the Air Force Office of Scientific Research (U.S.A.). The authors acknowledge J.V. Barth, P.H. Beton, M. Lackinger, R. Otero, M. Stöhr, N. Wintjes, S. De Deyter, S. Furukawa, Ge-Bo Pan, Li-Jun Wan, Kai Wu, M. Sokolowski for supplying original figures.

References

1. Barth JV, Costantini G, Kern K (2005) Nature 437:29
2. Rosei F (2004) J Phys Condens Matter 16:S1373
3. Whitesides GM, Mathias JP, Seto CT (1991) Science 254:1312
4. Pohl K, Bartelt MC, De La Figuera J, Bartelt NC, Hrbek J, Hwang RQ (1999) Nature 397:238
5. Weaver JH, Antonov VN (2004) Surf Sci 557:1
6. Whitesides GM, Grybowski B (2002) Science 295:2418
7. Lehn JM; Desiraju GR (1995) Angew Chem Int Ed 34:2311
8. Williams JH (1993) Acc Chem Res 26:593
9. Desiraju GR (1989) Crystal Engineering: The Design of Organic Solids. Elsevier, Amsterdam
10. Nath KG, Ivasenko O, McLeod JM, Miwa JA, Wuest JD, Nanci A, Perepichka DF, Rosei F (2007) J Phys Chem C 111:16996

11. Eichhorst-Gerner K, Stabel A, Moessner G, Declerq D, Valiyaveettil S, Enkelmann V, Müllen K, Rabe JP (1996) Angew Chem Int Ed 35:1492
12. Mena-Osteritz E, Bäuerle P (2001) Adv Mater 13:243
13. Grave C, Lentz D, Schäfer A, Samorí P, Rabe JP, Franke P, Schlüter AD (2005) J Am Chem Soc 125:6907
14. Stabel A, Heinz R, Rabe JP, Wegner G, De Schryver FC, Corens D, Dehaen W, Süling C (1995) J Phys Chem 99:8690
15. Brune H, Giovannini M, Bromann K, Kern K (1998) Nature 397:238
16. Cicoira F, Rosei F (2006) Surf Sci 600:1
17. Sgarlata A, Szkutnik PD, Balzarotti A, Motta N, Rosei F (2003) Appl Phys Lett 83:4002
18. Men FK, Liu F, Wang PJ, Chen CH, Cheng DL, Lin JL, Himpsel FJ (2002) Phys Rev Lett 88:096105
19. Gambardella P, Rusponi S, Veronese M, Dhesi SS, Cabria I, Zeller R, Dederichs PH, Dallmeyer A, Grazioli C, Kern K, Carbone C, Brune H (2003) Science 300:1130
20. Gambardella P, Dallmeyer A, Maiti K, Malagoli MC, Eberhardt W, Kern K, Carbone C (2002) Nature 416:301
21. Barth JV (2000) Surf Sci Rep 40:75
22. Barth JV (2007) Annu Rev Phys Chem 58:375
23. Rosei F, Schunack M, Naitoh Y, Jiang P, Gourdon A, Laegsgaard E, Stensgaard I, Joachim C, Besenbacher F (2003) Prog Surf Sci 71:95
24. Otero F, Rosei F, Besenbacher F (2006) Annu Rev Phys Chem 57:497
25. De Feyter S, De Schryver F (2005) Top Curr Chem 258:205
26. De Feyter S, De Schryver F (2005) J Phys Chem B 109:4290
27. De Feyter S, De Schryver F (2003) Chem Soc Rev 32:139
28. Ernst KH (2006) Top Curr Chem 265:209
29. Elemans JAAW, van Hameren R, Nole RMJ, Rowan A (2006) Adv Mater 18:1251
30. Bohringer M, Schneider WD (2000) Surf Rev Lett 7:661
31. Schunack M, Linderoth TR, Rosei F, Laegsgaard E, Stensgaard I, Besenbacher F (2002) Phys Rev Lett 88:156102
32. Lopinski GP, Wayner DDM, Wolkow RA (2000) Nature 406:48
33. Miwa JA, Eves BJ, Rosei F, Lopinski GP (2005) J Phys Chem B 109:20055
34. Ruben M, Lehn JM, Müller P (2006) Chem Soc Rev 35:1056
35. Hipps KW, Scudiero L, Barlow DE, Cooke JR MP (2002) J Am Chem Soc 124:2126
36. Scudiero L, Hipps KW, Barlow DE (2003) J Phys Chem B 107:2903
37. Pokrifchak M, Turner T, Pilgrom I, Johnston M, Hipps KW (2007) J Phys Chem C 111:7735
38. Gyargas BJ, Wiggins B, Zosel M, Hipps KW (2005) Langmuir 21:919
39. Ogunrinde A, Hipps KW, Scudiero L (2006) Langmuir 22:5697
40. Katsonis N, Marchenko A, Fichou D (2003) J Am Chem Soc 125:13682
41. Piot L, Marchenko A, Wu J, Müllen K, Fichou D (2005) J Am Chem Soc 125:13682
42. Jiang P, Nion A, Marchenko A, Piot L, Fichou D (2006) J Am Chem Soc 128:12390
43. Yokoyama T, Yokoyama S, Kamikado T, Okuno Y, Mashiko S (2001) Nature 413:619
44. Chen W, Loh KP, Xu H, Wee ATS (2004) Appl Phys Lett 84:281
45. Chen W, Loh KP, Xu H, Wee ATS (2004) Langmuir 20:10779
46. Chen W, Xu H, Liu L, Gao X, Qi D, Peng G, Tan SC, Feng Y, Loh KP, Wee ATS (2005) Surf Sci 596:176
47. Chen W, Zhang HL, Xu H, Tok ES, Loh KP, Wee ATS (2006) J Phys Chem 110:21873
48. Corso M, Auwärter W, Muntwiler M, Tamai A, Greber T, Osterwalder J (2004) Science 303:217

49. Griessl S, Lackinger M, Edelwirth M, Hietschold M, Heckl WM (2002) Single Mol 3:25
50. Dmitriev A, Lin N, Weckesser J, Barth JV, Kern K (2002) J Phys Chem B 106:6907
51. Griessl S, Lackinger M, Jamitsky F, Markert T, Hietschold M, Heckl WM (2004) J Phys Chem B 108:11556
52. Lackinger M, Griessl S, Heckl WM, Hietschold M, Flynn GW (2005) Langmuir 21:4984
53. Su GJ, Zhang HM, Wan LJ, Bai CL, Wandlowski T (2004) J Phys Chem B 108:1931
54. Ishikawa Y, Ohira A, Sakata M, Hirayama C, Kunitake M (2002) Chem Commun 2652
55. Lu J, Zeng QD, Wang C, Zheng QI, Wan L, Bai C (2002) J Mater Chem 12:2856
56. Payer D, Comisso A, Dmitriev A, Strunskus T, Lin N, Woll C, De Vita A, Barth JV, Kern K (2007) Chem Eur J 13:3900
57. Griessl SJH, Lackinger M, Jamitzki F, Markert T, Hietschold M, Heckl WM (2004) Langmuir 20:9403
58. Walzer K, Sternberg M, Hietschold M (1998) Surf Sci 415:376
59. Lackinger M, Griessl S, Markert T, Jamitzky F, Heckl WM (2004) J Phys Chem B 108:13652
60. Kampschulte L, Lackinger M, Maier AK, Kishore RSK, Griessl S, Schmittel M, Heckl WM (2006) J Phys Chem B 110:10829
61. Ruben M, Payer D, Landa A, Comisso A, Gattinoni C, Lin N, Collin JP, Sauvage JP, De Vita A, Kern K (2006) J Am Chem Soc 128:15644
62. Nath KG, Ivasenko A, Miwa JA, Dang H, Wuest JD, Nanci A, Perepichka DF, Rosei F (2006) J Am Chem Soc 128:4212
63. Hibino M, Sumi A, Tsuchiya H, Hatta I (1998) Phys Chem B 102:4544
64. Wintgens D, Yablon DG, Flynn GW (2003) J Phys Chem B 107:173
65. Wei Y, Kannappan K, Flynn GW, Zimmt MB (2004) J Am Chem Soc 126:5318
66. Ye Y, Sun W, Wang Y, Shao X, Xu X, Cheng F, Li J, Wu K (2007) J Phys Chem C 111:10138
67. McLeod JM, Ivasenko O, Perepichka DF, Rosei F (2007) Nanotechnology 18:424031
68. Kampschulte L, Griessl S, Heckl WM, Lackinger M (2005) J Phys Chem B 109:14074
69. Theobald JA, Oxtoby NS, Phillips MA, Champness NR, Beton PH (2003) Nature 424:1029
70. Theobald JA, Oxtoby NS, Champness NR, Beton PH, Dennis TJS (2005) Langmuir 21:2038
71. Perdigao LMA, Perkins EW, Ma J, Staniec PA, Rogers BL, Champness NR, Beton PH (2006) J Phys Chem B 110:12539
72. Perdigao LMA, Champness NR, Beton PH (2006) Chem Commun 538
73. Staniec PA, Perdigao LMA, Rogers BL, Champness NR, Beton PH (2007) J Phys Chem B 111:886
74. Xu W, Dong M, Gersen H, Rauls E, Vasquez-Campos S, Crego-Calama M, Reinhouldt DN, Stensgaard I, Laegsgaard E, Linderoth TR, Besenbacher F (2007) Small 3:854
75. Ma J, Rogers BL, Humphry MJ, Ring DJ, Goretzki G, Champness NR, Beton PH (2006) J Phys Chem B 110:12207
76. Gong JR, Yan H, Yan QH, Xu LP BO ZS, Wal LJ (2006) J Am Chem Soc 128:12384
77. Gong JR, Zhao JL, Lei SB, Wan LJ, Bo ZS (2003) Langmuir 19:10130
78. Pawin G, Wong KL, Kwon KY, Bartels L (2006) Science 313:961
79. Wong KL, Pawin G, Kwon KY, Lin X, Jiao T, Solanki U, Fawcett RHJ, Bartels L, Stolbov S, Rahman TS (2007) Science 315:1391

80. Stöhr M, Wahl M, Galka CH, Riehm T, Jung TA, Gade LH (2005) Angew Chem Int Ed 117:7560
81. Wahl MA, Stohr M, Spillmann H, Jung TA, Gade LH (2007) Chem Commun 13:1349
82. Stöhr M, Wahl M, Spillmann H, Gade LH Jung TA (2007) Small 3:1336
83. Moresco F (2004) Phys Rep 399:175
84. Bonifazi D, Kiebele A, Stöhr M, Cheng F, Jung TA, Diederich F, Spillmann H (2007) Adv Funct Mater 17:1051
85. Bonifazi D, Spillmann H, Kiebele A, De Wild M, Seiler P, Cheng F, Güntherodt J, Jung TA, Diederich F (2004) Angew Chem Int Ed 43:4759
86. Spillmann H, Kiebele A, Stöhr M, Jung TA, Bonifazi D, Cheng F, Diederich F (2006) Adv Mater 18:275
87. Kiebele A, Bonifazi D, Cheng F, Stöhr M, Diederich F, Jung TA, Spillmann H (2006) Chem Phys Chem 7:1462
88. Wintjies N, Bonifazi D, Cheng F, Kiebele A, Stöhr M, Jung TA, Spillmann H, Diederich F (2007) Angew Chem Int Ed 46:4089
89. Lin N, Dmitriev A, Weckesser J, Barth JV, Kern K (2002) Angew Chem Int Ed 41:4779
90. Spillmann H, Dmitriev A, Lin N, Messina P, Barth JV, Kern K (2003) J Am Chem Soc 125:10725
91. Messina P, Dmitriev A, Lin N, Spillmann H, Abel M, Barth JV, Kern K (2002) J Am Chem Soc 124:1400
92. Classen T, Fratesi G, Costantini G, Fabris S, Stadler F, Kim C, De Gironcoli S, Baroni S, Kern K (2005) Angew Chem Int Ed 44:6142
93. Dmitriev A, Spillmann H, Lin N, Barth JV, Kern K (2003) Angew Chem Int Ed 42:2670
94. Stephanow S, Lingenfelder M, Dmitriev A, Spillmann H, Lin N, Deng X, Cai C, Barth JV, Kern K (2004) Nat Mater 3:229
95. Stepanow S, Lin N, Payer D, Schlickum U, Klappenberger F, Zoppellaro G, Ruben M, Brune H, Barth JV, Kern K (2007) Angew Chem Int Ed 46:710
96. Clair S, Pons S, Brune H, Kern K, Barth JV (2005) Angew Chem Int Ed 44:7294
97. Stepanow S, Lin N, Barth JV, Kern K (2006) Chem Commun 2153
98. Méndez J, Caillard R, Otero G, Nicoara N, Martin-Gago JA (2006) Adv Mater 18:2048
99. Auwärter W, Weber-Bargioni, Brink S, Riemann, Schiffrin A, Ruben M, Barth JV (2007) Chem Phys Chem 8:250
100. Balzani V, Venturi M, Credi A (2003) Molecular Devices and Machines. Wiley-VCH, Weinheim, Germany
101. Mena-Osteritz E, Bäuerle P (2006) Adv Mater 18:447
102. Bäuerle P, Ammann M, Wilde M, Götz G, Mena-Osteritz E, Rang A, Schalley CA (2007) Angew Chem Int Ed 46:383
103. Mena-Osteritz E (2002) Adv Mater 14:609
104. Krömer J, Rios-Carreras I, Fuhrmann G, Musch C, Wunderlin M, Debaerdemaeker T, Mena-Osteritz E, Bäuerle P (2000) Angew Chem Int Ed 39:3481
105. Pan GB, Cheng XH, Hoger S, Freyland W (2006) J Am Chem Soc 128:4218
106. Kossev I, Reckien W, Kirchner, Felder T, Nieger M, Schalley CA, Vögtle F, Sokolowski M (2007) Adv Funct Mater 17:513
107. Hunter CA (1992) J Am Chem Soc 114:5303
108. Herrmann U, Jonischkeit T, Bargon J, Hahn U, Li QY, Schalley CA, Vogel E Vögtle F (2002) Anal Bioanal Chem 372:611
109. Pan GB, Liu JM, Zhang HM, Wan LJ, Zheng QY, Bai CL (2003) Angew Chem Int Ed 42:2747

110. Pan GB, Wan LJ, Zheng QY, Bai CL (2003) Chem Phys Lett 367:711
111. Sakai T, Ohira A, Sakata M, Hirayama C, Kunitake M (2001) Chem Lett 782
112. Yoshomoto S, Tsusumi E, Narita R, Murata Y, Murata M, Fujiwara K, Komatsu K, Ito O, Itaya K (2007) J Am Chem Soc 129:4366
113. Itaka K, Yamashiro M, Ymaguchi J, Haemori M, Yaginuma S, Matsumoto Y, Kondo M, Koinuma H (2006) Adv Mater 18:1713
114. Furukawa S, Tahara K, De Schryver F, Van der Auweraer M, Tobe Y, De Feyter S (2007) Angew Chem Int Ed 46:2831
115. Tahata K, Furukawa S, Uji-i H, Uchino T, Ichikawa T, Zhang J, Mamdouh W, Sonoda M, De Schryver, De Feyter S, Tobe Y (2006) J Am Chem Soc 128:16613
116. Schull G, Douillard L, Fiorini-Debuisschert C, Charra F, Mathevet F, Kreher D, Attias AJ (2006) Nano Lett 6:1360
117. Schull G, Douillard L, Fiorini-Debuisschert C, Charra F, Mathevet F, Kreher D, Attias AJ (2006) Adv Mater 18:2954
118. Xu S, Zeng Q, Lu J, Wang C, Wan L, Bai CL (2003) Surf Sci 538:L451
119. Nishiyama F, Yokoyama T, Kamikado T, Yokoyama T, Mashiko S, Sakaguchi K, Kikuchi K (2007) Adv Mater 19:117
120. Kröger J, Néel N, Jensen H, Berndt R, Rurali R, Lorente N (2006) J Phys: Condens Matter 18:S51
121. Néel N, Kröger J, Berndt R (2006) Adv Mater 18:174
122. Néel N, Kröger J, Berndt R (2006) Appl Phys Lett 88:163101
123. Xiao W, Ruffieux P, Ait Mansour K, Gröning O, Palotas K, Hofer WA, Gröning P, Fasel R (2006) J Phys Chem B 110:21395
124. Cañas-Ventura ME, Xiao W, Wasserfallen D, Müllen K, Brune H, Barth JV, Fasel R (2007) Angew Chem Int Ed 46:1814
125. Ertl G (1967) Surf Sci 6:208
126. Jensen F, Besenbacher F, Laesgaard E, Stensgaard I (1990) Phys Rev B 41:10233
127. Coulman DJ, Wintterlin J, Behm RJ, Ertl G (1990) Phys Rev Lett 64:1761
128. Besenbacher F, Jensen F, Lægsgaard E, Mortensen K, Stensgaard I (1991) J Vac Sci Technol B 9:874
129. Kern K, Niheus H, Schatz A, Zeppenfeld P, Goerge J, Comsa G (1991) Phys Rev Lett 67:855
130. Otero R, Naitoh Y, Rosei F, Jiang P, Thostrup P, Gourdon A, Laegsgaard E, Stensgaard I, Joachim C, Besenbacher F (2004) Angew Chem Int Ed 43:2092
131. Pedersen MØ, Murray PWH, Lægsgaard E, Stensgaard I, Besenbacher F (1997) Surf Sci 389:300
132. Otero R, Rosei F, Naitoh Y, Jiang P, Thostrup P, Gourdon A, Laegsgaard E, Stensgaard I, Joachim C, Besenbacher F (2004) Nano Lett 4:75
133. Schunack M, Rosei F, Naitoh Y, Jiang P, Gourdon A, Lægsgaard A, Stensgaard I, Joachim C, Besenbacher F (2002) J Chem Phys 117:6259
134. Rosei F, Schunack M, Jiang P, Gourdon A, Laegsgaard E, Stensgaard I, Joachim C, Besenbacher F (2002) Science 296:328
135. Cicoira F, Miwa JA, Melucci M, Barbarella G, Rosei F (2006) Small 2:1366
136. Cicoira F, Miwa JA, Perepichka DF, Rosei F (2007) J Phys Chem A 111:12674
137. Koller G, Winter B, Oehzelt M, Ivanco J, Tetzer FP, Ramsey MG (2007) Organic Electronics 8:63
138. Oehzelt M, Grill L, Berkebile S, Koller G, Netzer FP, Ramsey MG (2007) Chem Phys Chem 8:1707
139. Bombis C, Moiseva M, Ibach H (2005) Phys Rev B 72:245408

Top Curr Chem (2008) 285: 269–312
DOI 10.1007/128_2007_23

Published online: 8 April 2008

STM, STS and Bias-Dependent Imaging on Organic Monolayers at the Solid–Liquid Interface

Shengbin Lei · Steven De Feyter (✉)

Division of Molecular and Nanomaterials, Katholieke Universiteit Leuven (K.U.Leuven), INPAC – Institute for Nanoscale Physics and Chemistry, Celestijnenlaan 200 F, 3001 Heverlee, Belgium
Steven.DeFeyter@chem.kuleuven.be

Abstract This chapter deals with various aspects of scanning tunneling spectroscopy (STS) and in particular it reviews STS investigations on organic films. Though this chapter addresses in particular those systems which have been probed under ambient conditions and at the solid–liquid interface, a significant part deals with studies under UHV conditions. Some key principles of STS are highlighted and various molecular systems are reviewed, ranging from prototypical dyes or conjugated systems such as phthalocyanines, over conjugated polymers and multi-component covalent and non-covalent systems.

Keywords Scanning tunneling microscopy · Scanning tunneling spectroscopy · Bias dependence · Solid–liquid interface

Abbreviations

CITS	Current imaging tunneling spectroscopy
CoPor	Cobalt(II) 5,15-bis-(4-octadecyloxyphenyl)porphyrin
C[12]T	Cyclo[12]thiophene
CV	Cyclic voltammetry
DAD	Donor–acceptor–donor
15DA	1,5-Di(octyloxy)anthracene
DMA	9,10-Dimethoxyanthracene
DOS	Density of states
FBPor	5,15-Bis-(4-octadecyloxyphenyl)porphyrin
HBC	Hexabenzocoronene
HOMO	Highest occupied molecular orbital
HOPG	Highly ordered pyrolytic graphite
IETS	Inelastic tunneling spectroscopy
IPES	Inverse photoemission spectroscopy
LDOS	Local density of states
LUMO	Lowest unoccupied molecular orbital
Nc	Naphthalocyanine
OMTS	Orbital-mediated tunneling spectroscopy
OPV	Oligo-*p*-phenylene vinylene
Pc	Phthalocyanine
P3DDT	Poly(3-dodecylthiophene)s
PDI	Perylene bisimide
PTCDA	3,4,9,10-Perylene tetracarboxylic dianhydride
STM	Scanning tunneling microscopy
STS	Scanning tunneling spectroscopy
TPP	Tetraphenylporphyrin
TpyP	Tetrapyridylporphyrin
TTF	Tetrathiafulvalene
UHV	Ultra-high vacuum
UPS	Ultra-violet photoelectron spectroscopy
VOPc	Vanadyl phthalocyanine
WKB	Wentzel–Kramers–Brillouin
ZnPor	Zinc(II) 5,15-bis-(4-octadecyloxyphenyl)porphyrin

1 Introduction

Seeing molecules is no longer a dream. Since the invention of the scanning probe microscopes, it is almost a trivial exercise to visualize molecules on surfaces. Scanning tunneling microscopy (STM) [1, 2] is especially equipped for the job, under a variety of conditions such as ultra-high vacuum (UHV), ambient conditions and at the interface between a solid and a liquid. Atomic force microscopy [3] has a somewhat inferior resolution, at least under ambient conditions, as it has been demonstrated that submolecular and true atomic resolution, including chemical identification of individual surface

atoms [4] can be achieved by non-contact imaging under UHV conditions. Imaging, though, is only part of the problem. The main goal is to extract properties, including for instance electronic, spectroscopic, magnetic, and mechanical properties on the molecular to submolecular scale. Often, these features are of relevance when it comes to integration of molecules in devices.

STM is the technique of choice when it comes to high-resolution imaging of molecules on conductive surfaces. Over the past two decades, numerous examples have been reported, and clearly this technique is very versatile, allowing for the investigation of a wide range of molecular systems (liquid crystals, self-assembled monolayers (both chemisorbed and physisorbed), conductive molecular crystals, proteins) in a variety of different experimental environments ranging from UHV conditions, ambient conditions, to a variety of liquids (organic solvents, aqueous electrolytes, ionic liquids) [5]. This broad scope has definitely contributed to the success and popularity of STM. A main requirement though is that the sample must be conductive, typically allowing the detection of tunneling currents on the order of a few picoamps (10^{-12} A) to a few nanoamps (10^{-9} A). However, as we will see, it is also possible to use thin isolating surfaces as the substrate.

In STM, a metallic tip is brought very close to a conductive substrate and by applying a voltage between both conductive media, a tunneling current through a classically impenetrable barrier results between the two electrodes. The direction of the tunneling depends on the bias polarity. The exponential distance dependence of the tunneling current leads to excellent control of the distance between the probe and the surface and very high resolution (atomic) on atomically flat conductive substrates can be achieved. For imaging purposes, the tip and substrate are scanned precisely relative to one another and the current is accurately monitored as a function of the lateral position. In the constant height mode, the absolute vertical position of the probe remains constant during raster-scanning and the tunneling current is plotted as a function of the lateral position. In the constant current mode, the absolute vertical position of the probe (or sample) is adjusted to maintain a constant tunneling current. An image can be constructed by assigning every pixel in the probed 2D area a gray scale or color code reflecting the height of the probe or the tunneling current, depending on the approach used.

Of particular interest for this review is the fact that the contrast in STM images reflects both topography and electronic effects. In fact, STM can be used to locally probe the electronic properties of the systems under investigation, transforming it to a real spectroscopy tool, which is often referred to as scanning tunneling spectroscopy (STS). Indeed, a constant current image will only reflect true height changes if the local density of states (LDOS) of the surface is constant across the surface. More often than not, the LDOS for a give system is not constant and as a result, electronic information is mixed in with topographic information.

In this review, we will focus on the power of STM and STS to reveal the electronic properties of molecules adsorbed on surfaces. We restrict ourselves to those systems where molecules are physisorbed (or weakly chemisorbed) on surfaces. We do not report on charge transport studies through the backbone of single molecules which are linked at two different sites to the electrodes (such as transport measurements using mechanically controlled break junctions [6, 7]), nor do we discuss the interesting field of charge transport through chemisorbed self-assembled monolayers (typically alkyl thiols on gold) [8]. Charge transport studies at electrified interfaces [9–12] or involving proteins [13] are also not described in this review.

We highlight recent studies on bias-dependent imaging and STS in UHV and in particular at the solid–liquid interface and in ambient conditions. Where appropriate, we will compare results obtained in the different media. We start with a brief introduction into scanning tunneling spectroscopy and will discuss then various chemical systems ranging from prototypical aromatic molecules such as perylenediimide and phthalocyanines, over polymers to complex multi-component systems.

There are a number of excellent reviews on scanning tunneling spectroscopy, but highly recommended is the review by K.W. Hipps [14].

2
Scanning Tunneling Spectroscopy: Some Basics

Tunneling is a quantum mechanical effect and the probability of transmission through a barrier decreases exponentially with the thickness of the barrier (the distance between tip and sample) and the square root of the potential (barrier height) relative to the electron energy [15, 16]. Assuming that the bias voltage is small compared to the barrier height, the tunneling current between two metals in vacuum is roughly proportional to

$$\mathrm{I} \sim \mathrm{V} \exp(-\,\mathrm{d}\sqrt{\Phi})\,,$$

where I (current), V (applied bias), d (distance between tip and sample), and Φ (the work function).

However, this simple formula (reflecting the exponential tunneling transmission probability) does not take into account the contribution of the density of states of the tip and sample as a function of the position along the surface plane. Therefore, the tunneling process is better represented by the following formula, based on the Wentzel–Kramers–Brillouin (WKB) method:

$$\mathrm{I} = \int_0^{eV} \rho_\mathrm{s}(r, E)\rho_\mathrm{t}(r, -eV + E)T(E, eV, r)\,\mathrm{d}E\,,$$

where I is the tunneling current, $\rho_s(r, E)$ and $\rho_t(r, E)$ are the density of states of the sample and tip at location r and the energy E, measured with respect to their individual Fermi levels. $T(E, eV, r)$ is the tunneling transmission probability for electrons with energy E and applied bias voltage V.

Figure 1 reflects in a schematic way the experimental approach and the key electronic properties of tip and sample (substrate + adsorbate) of concern in this review. Typically, the spacing between the tip and substrate is a few angstrom. It is already important to note at this stage that the tip–molecule distance is typically larger than the molecule substrate distance. The diagram shows the filled conduction bands of metallic tip and substrate, and the density of states (DOS) of the adsorbate, simplified by the presentation of its frontier orbitals (highest occupied molecular orbital (HOMO), lowest unoccupied molecular orbital (LUMO)). "Adsorbate" refers to an adsorbed molecule on a surface. For simplicity, the density of states of the metal tip and substrate are ignored. Or in other words, it is assumed that the density

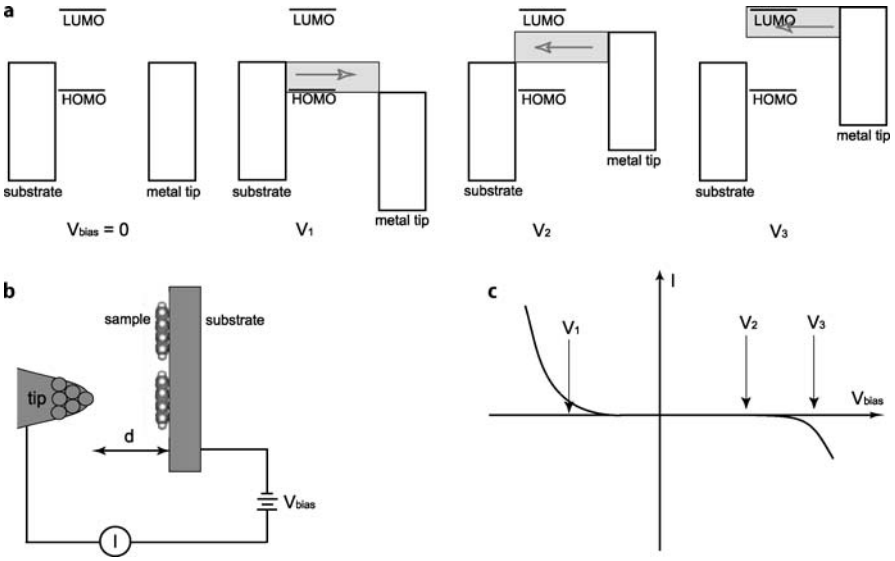

Fig. 1 Schematic diagram of orbital mediated tunneling spectroscopy and the STM/STS setup. In this example, the HOMO of the adsorbed molecule is closer to the Fermi level of the substrate than the LUMO. V is the applied tip bias. The *arrow* indicates the current flow. At positive tip bias (or negative sample bias) electrons tunnel from filled states of the substrate into the tip. At negative tip bias (or positive sample bias) electrons tunnel from the tip into empty states of the substrate. At certain potentials, the molecular orbitals may mediate the tunneling process. A resulting asymmetric I–V plot is shown in (**c**). The asymmetry is due to the asymmetric position of the molecular frontier orbitals versus the Fermi level of the substrate combined with the asymmetric position of the molecule in the tunneling gap. dI/dV–V spectroscopy typically reveals peaks if molecular orbitals are involved. For examples, see text

of states of tip and substrate are rather smooth and that any spectroscopic features are dominated by the properties of the adsorbate.

Upon applying a positive bias voltage to the sample, electrons will tunnel from filled states of the tip into empty states of the sample. Upon applying a negative bias voltage to the sample, electrons will tunnel from filled states of the sample into empty states of the tip. Electrons close to the Fermi energy of the "electron source" will contribute most to the tunneling current.

Typically, in STS experiments current (I)–voltage (V) curves are recorded on top of a given *x*, *y* coordinate while the feedback loop is turned off. In imaging, the feedback loop is necessary to adjust the height of the tip in order to satisfy a certain set point tunneling current (in constant current mode). As can be seen in Fig. 1, by ramping the sample bias voltage to more positive values, higher empty states of the sample (e.g., the LUMO) should be addressed. By ramping the sample bias voltage to more negative values, lower lying filled states of the sample (e.g., the HOMO) could contribute to the tunneling process. However, the current (I)–voltage (V) curves look often rather smooth and featureless and do not reveal at first sight the involvement of adsorbate states.

Therefore, to probe the electronic properties of molecular adsorbates often dI/dV–V spectroscopy is carried out, either under UHV and ambient conditions or even at the liquid–solid interface. The dI/dV–V plot, also called the differential conductance curve, is proportional to the LDOS. Sometimes the normalized differential conductance curve [dI/dV/(I/V)–V] or [dlnI/dlnV–V] is shown. Transitions reflected in the appearance of peaks in these dI/dV–V curves are the result of the elastic tunneling process (no energy loss during tunneling) and the bands are typically not temperature-dependent, which is due to their large intrinsic width. The spectroscopy associated with the detection of such transitions is called *orbital-mediated tunneling spectroscopy* (OMTS). Apparently, various mechanisms can contribute to the observed transitions: in true resonance tunneling the effective residence time of the tunneling electrons on the molecule is negligible with respect to nuclear motion. Other processes involve oxidation or reduction of the molecule, followed by relaxation to the original state via charge hopping, or the redox process can be so fast that such relaxation cannot occur. The latter situation is also the case in ultra-violet photoelectron spectroscopy (UPS) or inverse photoemission spectroscopy (IPES) [14].

Therefore, STS can be used to probe electronic states of the entities investigated as a function of energy within the range of a few electron volts around the Fermi level.

Among the many variants, *current imaging tunneling spectroscopy* (CITS) is of special interest. In CITS, both topography and current–voltage characteristics are recorded simultaneously. While the normal STM topography image is being recorded with constant tunneling current I, at any pixel the feedback (current control) is released for a short time and the I–V characteristics

are measured. Typically, the data are displayed as a series of current images (CITS maps) representing the tunneling current I as a function of the lateral x, y coordinates for a given voltage. The contrast of such images may change significantly at certain bias voltages when new energy levels are addressed. Therefore, CITS is a technique which makes energy-resolved spectroscopy possible with spatial resolution. The density of states of the molecules can be visualized as a function of energy and position.

CITS is related to *bias-dependent imaging*. In bias-dependent imaging, no I–V curves are obtained but images are compared which are obtained for a given constant set point current but variable values for the bias (V). Most often, such images are taken sequentially but also other options have been reported, where for instance the forward trace is obtained at bias 1 and the return trace at bias 2. CITS has the advantage that in addition to recording a large amount of information in a short time, images (CITS maps) can be obtained for certain extreme current–voltage settings which would be hard to achieve in traditional imaging mode because of instabilities.

Another related technique is dI/dV maps. The dI/dV maps are obtained by recording the dI/dV intensity at selected bias voltages simultaneously with the topography images. As mentioned above dI/dV is proportional to the LDOS. The dI/dV maps therefore show the spatial distribution of the LDOS of the surface structure [17, 18].

Some other variants (e.g., current–distance spectroscopy) will be introduced and discussed in the coming sections.

In general, I–V curves could contain both information on elastic and inelastic tunneling processes. In contrast to elastic tunneling processes, in inelastic tunneling spectroscopy (IETS), the moving electronic charge interacts with the time varying molecular dipoles to induce excitation of the molecule in the barrier, e.g., to excite vibrational modes of a molecule, with loss of energy by the electron. However, such experiments require UHV at low temperature. We will focus on the elastic part of the tunneling process, where electrons do not lose energy during the tunneling process, as in OMTS.

3 Technical Aspects and UHV Versus Liquid–Solid Interface and Ambient Conditions

In order to carry out scanning tunneling spectroscopy measurements, a few technical requirements have to be taken into account. An important point is the fact that one should be able to shut off the feedback loop during data acquisition, in order to decouple sample–distance effects from the spectroscopy data. Typically, the faster one can record a STS curve the better, in order to eliminate instabilities or temperature-induced drift effects while running the spectroscopy experiments. A critical point is the capacitance in

the tip–sample assembly and the wires leading to the preamplifier circuit. The preamplifier should be as close as possible to the tip. Both tip and sample need to be electrically isolated and as small as possible [14]. The acceptable drift will depend on the spatial resolution needed. Of course, the price to pay for taking the spectra as fast as the electronic bandwidth allows is signal-to-noise quality. Therefore, one often finds in literature that I–V curves have been averaged, sometimes after a "selection" of the raw data. To directly obtain dI/dV–V curves, it must be possible to add a modulation to the bias (or position voltage). Sometimes, the dI/dV–V curves are calculated from the I–V curves [19] or "noisy" I–V data are fitted by an appropriate polynomial before constructing the dI/dV–V curves.

It is clear that UHV conditions provide optimum control to carry out STS as solvent is an extra factor of noise. The bias range, which can be used, will be affected by the properties of the solvent which to begin with should be very dry (unless one uses coated tips as done at electrified interfaces). If not, Faraday processes will come into play. Even so, the solvent itself can become electrochemically active at high biases leading to an unstable tunneling junction. Therefore, it is hard in solution to access the direct energetic positions of the molecular states with respect to the Fermi level of the substrate. Due to the absence of solvent, in UHV one can use a much larger bias window.

Other effects which hamper "error"-free STS are molecular conformational changes or desorption. Therefore, it is advisable to take an STM image after recording the STS data in order to detect eventual changes during the spectroscopy events.

An unanticipated problem in taking STS curves in solution is the fact that the tunneling barrier height might oscillate. By carrying out in situ distance

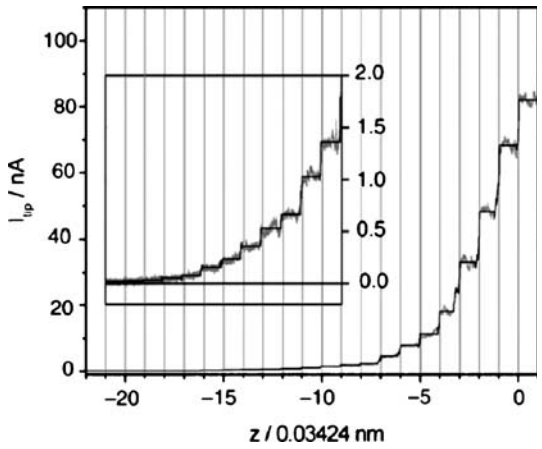

Fig. 2 Current–distance curve (I–z) at the Au(111)/0.02 M $HClO_4$ interface

tunneling spectroscopy, it was revealed that the exponential decay of the tunneling current with the gap is modulated with oscillations of a period of 0.35 nm (Fig. 2), which coincides with the theoretically predicted spacing of the interfacial water layers at the charged solid–water interface [20]. Both tunneling current and local barrier height oscillate with the gap width. Such results indicate that tunneling spectroscopy in liquids could be sensitive to electronic states of solvent molecules. However, the limitations set by the solvent does not mean that spectroscopy at the liquid–solid interface is useless. As we will show, it allows systems to be probed, which would be hard to access under UHV conditions.

Throughout this chapter, a number of examples will illustrate the issues discussed here.

4 Spectroscopy on Electronically Decoupled Systems

As we will see, on metallic substrates it is often a problem that the electronic structure of the molecules is strongly perturbed by the presence of the substrate electrons. Therefore, an electronic decoupling from the supporting substrate is highly desirable. This decoupling can be achieved for instance by using an insulating film (e.g., a few layers of NaCl) on top of a Cu(111) surface as the substrate. Electrons can still tunnel through such a thin insulating film facilitating imaging with a low-temperature STM in UHV conditions. Differential conductance spectroscopy (dI/dV–V) on an individual pentacene molecule adsorbed on such an insulating film reveals distinct features: two peaks at –2.4 and +1.7 V, respectively, separated by a broad region of low conductance [21]. Bias-dependent imaging at the peak potentials and in the broad gap region clearly show intramolecular differences. The molecular images obtained at –2.4 and +1.7 V are clearly much broader and have a large apparent height compared to those obtained for potentials in the broad gap region (Fig. 3). In addition, more intramolecular features are resolved at the peak potentials, especially for a STM tip which carries a pentacene molecule at its apex. Strikingly, in the latter case, the STM images are very similar to the native HOMO and LUMO of the free molecule. The lifetime of an electron or a hole on the pentacene molecule is strongly increased by the presence of the insulating layer. As a result, an electron or a hole is localized within the molecule before it can tunnel away into the substrate. So the peak positions correspond to the negative and positive ion resonances of the adsorbed molecule which are related to the ionization energy and the electron affinity of the free molecule.

Another interesting observation is that the position of the LUMO peak is only weakly shifted upon decreasing the tip–sample distance by about 0.2 nm. In the current range from 7.5 pA to 1100 pA, the influence of the

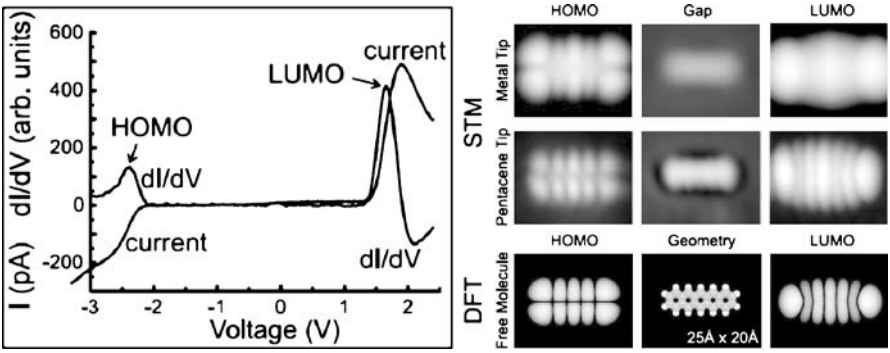

Fig. 3 (*Left*) dI/dV–V spectroscopy at the center of a pentacene molecule on NaCl. (*Right*) From top to bottom: STM images acquired with a metal and a pentacene tip, and contours of constant orbital probability distribution of the free molecule. The geometry of the pentacene molecule is displayed in the lower center image

applied electric field on the peak positions is rather small. In addition, by changing the metal substrate orientation from Cu(111) to Cu(100), an identical gap between the frontier orbital peaks is observed, while the peaks are shifted by 0.35 eV to lower voltages, which could be nicely explained by the difference in work functions of the clean surfaces, again supporting the claim that the pentacene molecule is electronically decoupled from the substrate. This is in contrast to the situation where π-conjugated molecular films are directly adsorbed onto a metal surface where a variety of interface phenomena are observed that can cause the breakdown of the vacuum level alignment [22].

5 Spectroscopy on Perylenediimides

PTCDA (3,4,9,10 perylene tetracarboxylic dianhydride) has been extensively studied. PTCDA films present semiconducting behavior, strong anisotropy in electronic transport and interesting optical properties [23]. Its growth mode and structural properties have been investigated on different metallic substrates such as silver, copper and gold [24–28]. On Au(111) a layer-by-layer growth has been reported for the first several layers, followed by island formation for multi-layer coverage. PTCDA typically assembles in a herringbone structure on most substrates. For Au(111), a less dense square assembly also can be obtained.

Highly ordered ultra-thin PTCDA films have been prepared by organic molecular beam epitaxy on Au(100) (Fig. 4). The molecules form large domains of well-known herringbone structures resembling the (102) bulk plane within a one-monolayer thick film. A striped superstructure has been ob-

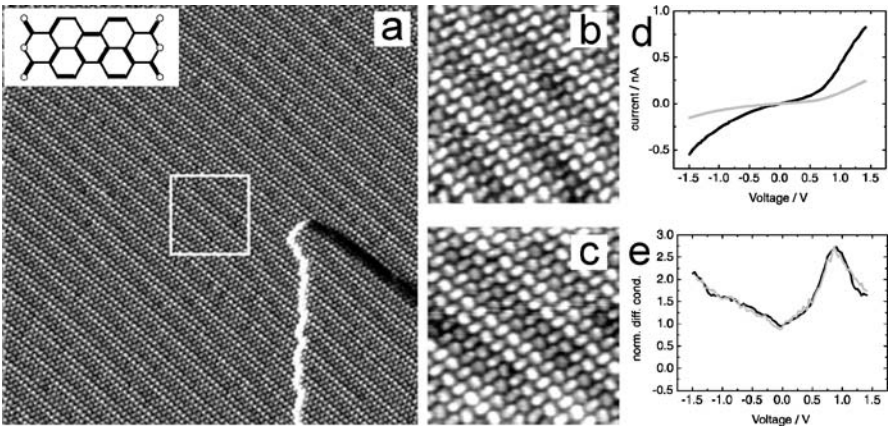

Fig. 4 **a** STM image of a monolayer of PTCDA on Au(100) ($80 \times 80\ nm^2$, 0.05 nA, 0.65 V) showing the well-known herringbone structure. **b**,**c** The images obtained at the area marked by the white square in (**a**) before and after recording the STS data. **d**,**e** Show I–V and normalized differential conductance ((dI/dV)/(I/V)) curves recorded at fixed tip–sample distance. The *black* and *gray curves* are recorded at different tip–sample distance

served due to the position of the molecules relative to the underlying reconstructed Au(100) surface. The electronic structure of PTCDA has been probed with STS [29]. Normalized derivatives of the I–V curves obtained on such assembly clearly reveal a peak at approximately 0.9 eV, which is independent of the tip–sample distance. By comparing the normalized derivatives of I–V curves taken consecutively on PTCDA islands and uncovered areas of the Au(100) surface, the peak at 0.9 eV was attributed to the LUMO of PTCDA.

No peak was detected in the negative sample bias region, which was attributed to the limited voltage range probed (± 1.5 V) while the position of the HOMO for PTCDA is expected approximately at –1.9 V relative to the substrate Fermi level. Good agreement was found with inverse photoemission spectroscopy (IPES) and UV photoemission spectroscopy (UPS) data.

STS experiments on a monolayer and a 2–3 layer PTCDA film on Au(111) show peaks representing the density of filled and empty states (Fig. 5) [30]. The energy difference between these peaks is measured to be 3.3 eV for the monolayer and in contrast a 0.25 eV increase of this value is observed for the 2–3 layer spectrum. IPES/UPS measurements confirm this increase of the transport gap for the multi-layer. In addition a broad feature has been revealed in the STS spectrum of the PTCDA monolayer and this has been attributed to the surface state of the Au(111) substrate, which is not eliminated by the deposition of PTCDA molecules.

The above hypothesis has been further addressed using a combination of STS and UPS techniques. The STS dI/dV–V curves obtained on one mono-

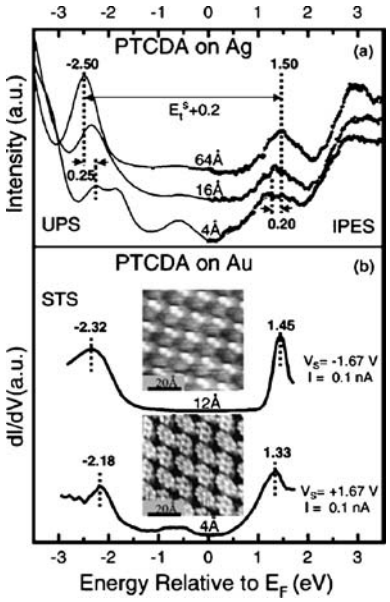

Fig. 5 Composite UPS/IPES spectra as a function of PTCDA thickness on Ag (**a**) and STS spectra recorded for a monolayer (*bottom*) and a 2–3 molecular layer (*top*) film of PTCDA deposited on Au (111). The corresponding STM images are also shown

layer of PTCDA reveal similar broad features in the range of –0.4 V to 0.2 V (Fig. 6) [31]. The position of this feature is in good agreement with the Shockley-type surface state observed in the STS curve obtained on clean Au(111) surface. Only a slight shift of about 40 meV toward the Fermi level is detected in presence of the PTCDA monolayer. This shift is attributed to the interaction between the PTCDA molecules with the gold substrate and its small value points to a weak interaction in this case. The HOMO and LUMO states of PTCDA could also be resolved in these spectra at around +1.0 V and –1.9 V, respectively. The transport gap is thus detected to be 2.9 eV. At high PTCDA coverage, a slight broadening of the energy gap is detected. The feature close to the Fermi level was no longer detectable, suggesting that the gold surface state could only tunnel through the first PTCDA layer.

6
Spectroscopy on Phthalocyanines and Porphyrins

Phthalocyanines and porphyrins belong to the most promising candidates to form ordered organic thin films with applications in organic electronics due to their chemical stability and electronic properties. Both *p*- and

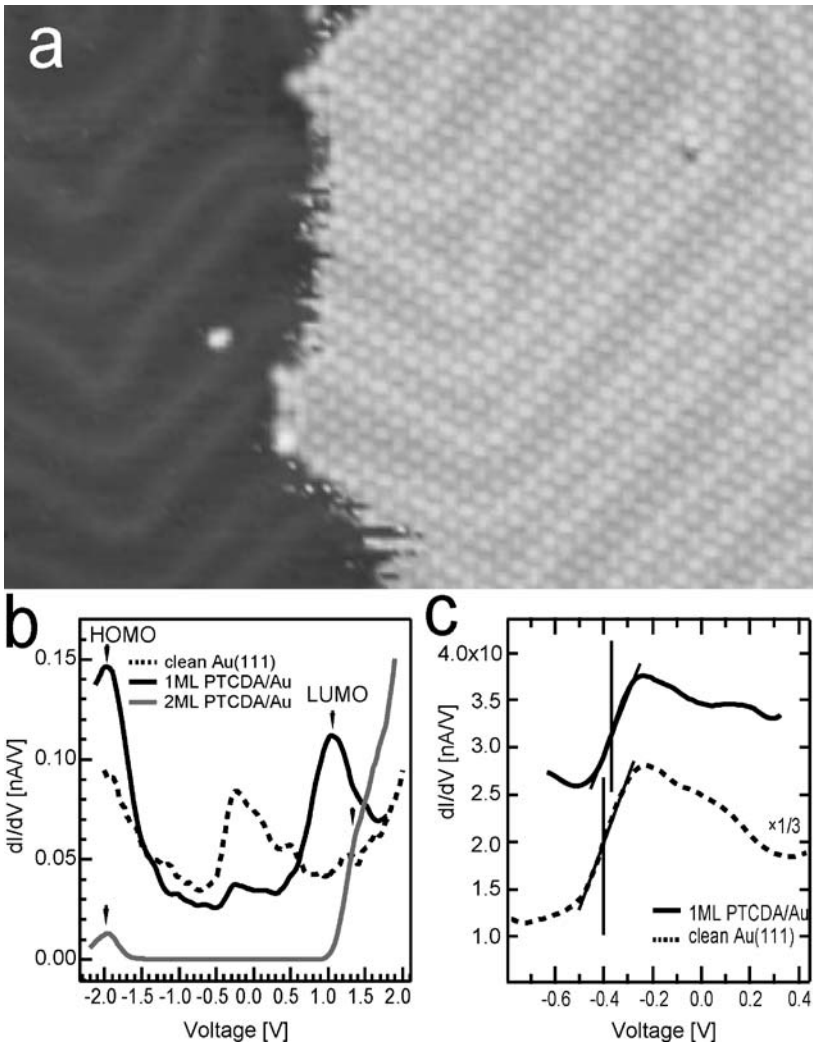

Fig. 6 **a** STM image of submonolayer PTCDA film on Au(111) ($57 \times 40\ nm^2$, V = –2.0 V, I = 0.16 nA). **b** STS performed at room temperature on clean Au(111) and 1 ML PTCDA. The onset of Shockley surface states is identified for clean gold (*dashed line*) at –0.4 V. A similar peak and molecular related features (HOMO and LUMO) are detected in the dI/dV–V spectra recorded on the PTCDA monolayer. For 2 ML PTCDA only the molecular related HOMO and LUMO appear. **c** Detail of the gold surface state region where a shift of ~40 meV can be observed

n-type conductivity can be attained in this class of compounds by proper chemical modifications. This is of special importance for the realization of complementary logic circuits [32]. The presence of metal, ring and peripheral group centered electron transport processes makes porphyrins and

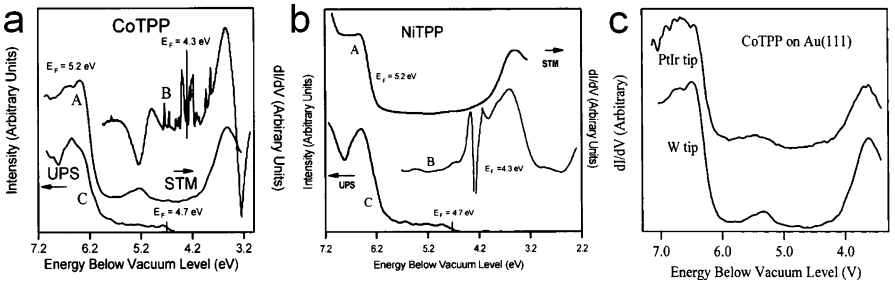

Fig. 7 Combined results of UPS, STM dI/dV–V OMTS, and tunnel junction IETS and OMTS of CoTPP (**a**) and NiTPP (**b**) thin films. Curve positions on the *x*-axis are adjusted for differences in device work function. **c** Comparison of STM dI/dV–V spectra of CoTPP on Au (111) as obtained with Pt/Ir and W tips

phthalocyanines exciting model systems for scanning tunneling microscopy and orbital-mediated tunneling spectroscopy studies.

Hipps et al. have carried out a series of investigations on OMTS of porphyrin and phthalocyanine derivatives on Au(111) surface with STM (Fig. 7). In one of their reports the STS results obtained on Co-tetraphenylporphyrin (CoTPP) and NiTPP were compared with that from conventional tunnel diode structures and UPS. Their studies show STM-OMTS could determine the position of both the HOMO and LUMO, while UPS could only give out information of the HOMO and conventional IETS-OMTS on the LUMO. Thus they concluded that STM-OMTS could give out more information than both UPS and IETS-OMTS, and could do so with submolecular resolution [33, 34].

The OMTS spectra of a porphyrin derivative TPP with different metal ions, CoTPP and NiTPP, reveal one remarkable difference. There is an apparent band at about 5.3 eV relative to the vacuum level for CoTPP while this feature is absent for NiTPP. This band is attributed to ionization from the half filled d_z^2 orbital of Co. The determination of the HOMO and LUMO levels with STM-OMTS is consistent with the UPS and IETS-OMTS data.

The difference in the work functions of W (4.6 eV) and Pt (5.6 eV) should cause a significant difference in the internal field experienced by the molecules in the Au–W and Au–Pt junction. However, within the accuracy of experiments, there was no discernible shift in peak positions despite the 1 V difference in the internal potential expected. This apparent lack of sensitivity is attributed to the relatively small thickness of the adsorbate layer in comparison with the tunneling gap between the tip and substrate. Thus the internal potential field created by the work function difference between tip and substrate has little effect on the positions of adsorbate electronic energy levels. A comparative study using UPS, XPS and STM-OMTS on Ni(II)-octaethylporphyrin adsorbed on Au(111) led to the same conclusion.

Most reports on STM-OMTSs assume that STM-OMTS is independent of tip–sample separation. The excellent agreement between the observed en-

ergies of frontier orbitals and those reported by UPS and electrochemistry justified the interpretations. However, previous theoretical and experimental studies proved the possibility that changing the distance between the tip and the molecular film might change the OMT peak positions [35–37]. The tip–sample distance dependence observed in STS studies of quantum dots is an example [38, 39]. The tip–sample distance dependence is understood to be related to the resistance between tip–sample and sample–substrate. For adsorbates such as porphyrin and phthalocyanine, the dependence of STS with the tip–molecule separation has not yet been proven experimentally.

In one report, the OMTS of NiTPP is measured as a function of tip–substrate separation in a range of tip motion of 0.42 nm (Fig. 8). In this report the tip–sample separation is varied by changing the set point, the 0.42 nm increase in separation approximately corresponds to a decrease in 20 fold of the current. Using the logarithmic derivative, dlnI/dlnV, it was possible to determine the peak positions and shapes. For all the spectra measured with different tip–sample separation the LUMO is determined at 1.52 V above the Fermi level, while the HOMO is determined at 1.17 V below the Fermi level (5.2 eV for gold). In this range of tip–sample separation the splitting between the HOMO and LUMO bands does not change with tip–sample separation. The tip–sample distance dependence could be interpreted with a double-tunneling-barrier mechanism, in which the interaction between the sample and substrate is weak [38, 39]. For the NiTPP/gold system the HOMO–LUMO separation independent of the tip–sample distance is attributed to the fact that the resistance between tip and molecule is always significantly larger than that between the molecule and gold substrate, which indicates the molecule–substrate interaction is relatively strong [40].

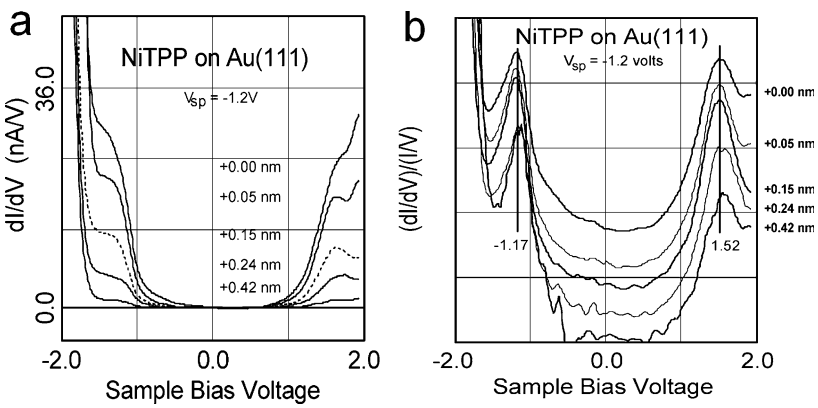

Fig. 8 OMTS dI/dV–V (**a**) and dlnI/dlnV (**b**) curves acquired from a NiTPP monolayer at –1.2 V sample bias and varying tip–sample distance. A different constant was added to each data set in (**b**) to allow them to be better distinguished. The distances given are relative to the closest tip–sample separation (–1.2 V, 2.0 nA)

STS is also ideal to distinguish between structurally alike but electronically different molecules. A composite film of CoPc and CoTPP has been formed by sequential deposition of these compounds (Fig. 9) [41]. An approximately 1:1 CoTPP/CoPc structure is observed to form spontaneously on Au(111) at low coverage irrespective of which species is deposited first. In the 1:1 structure nearly pure molecular rows of CoPc or CoTPP are seen to arrange alternatively on the surface. This structure is highly defective in comparison with the structure formed by F_{16}CoPc and NiTPP, which is generated through the H–F hydrogen bonding. The transient oxidation of the Co d_z^2 orbital is identified in STM dI/dV–V curves just negative of the 0 V sample bias for both molecules, while the HOMO orbital of the aromatic ring is observed in different positions (5.8 eV for CoPc and 6.5 eV for CoTPP). This allows identification of these molecules from each other in the mixed phase. Nearly identical constant current contours are observed over the central Co^{2+} ions of CoTPP and CoPc, indicating the different structure of TPP and Pc ligands do not cause significant difference in the d_z^2 orbital-mediated tunneling current of the central Co^{2+} ion.

In addition to the "traditional" phthalocyanines, also more exotic derivatives have been investigated. Non-planar vanadyl phthalocyanine (VOPc) has been assembled on the Au(111) surface and this molecule is observed to show nodal planes running through the center of the molecule (Fig. 10) [42]. The dark central region is attributed to the oxygen atom that is considered to reduce the number of available states near the Fermi energy. The apparent height of the Pc is highly bias-dependent. dI/dV–V curves of this molecule

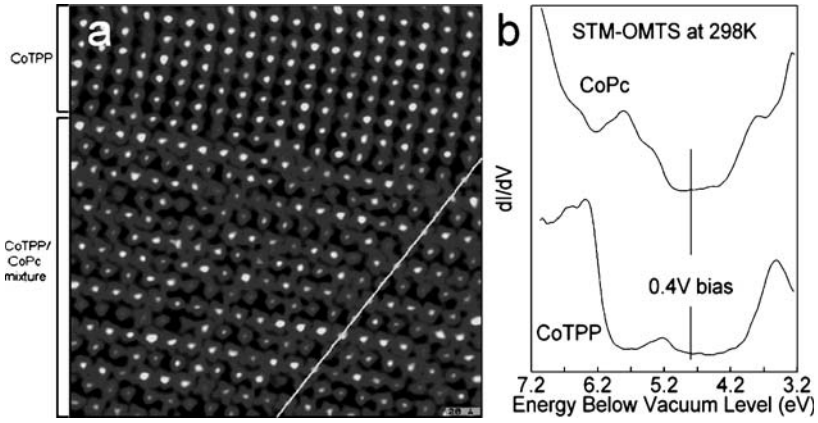

Fig. 9 **a** High-resolution constant current STM image of CoTPP and CoPc on Au(111). The CoTPP/CoPc film was made by first depositing 0.25 ML of CoTPP on Au(111) and followed by 0.3 ML of CoPc. Acquired with 0.4 sample bias, 0.1 nA. **b** STM-OMTS of CoPc and CoTPP. Zero bias is taken as 5.2 eV relative to the vacuum level. The bias at which the image was acquired is indicated

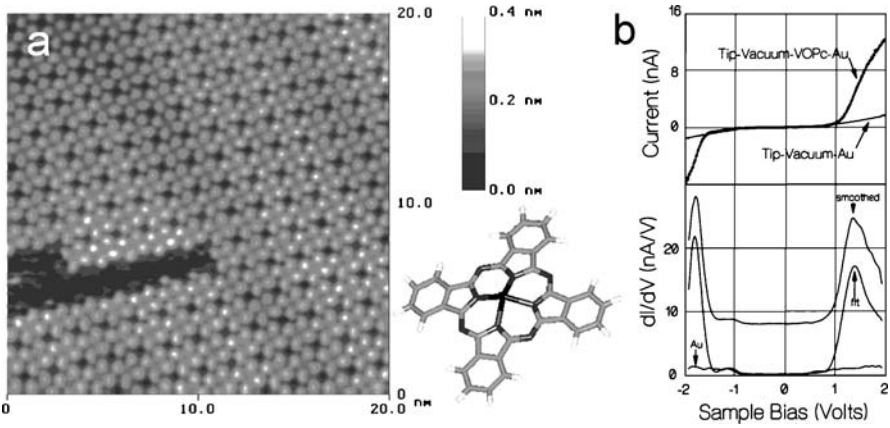

Fig. 10 **a** High-resolution STM image of a VOPc monolayer on Au(111). The image was acquired at 600 mV sample bias and 300 pA. A model of the VOPc molecule is shown in the *lower right*. **b** Area averaged I–V curves and generated dI/dV–V. The dI/dV–V was generated in two ways: the I–V curve was fit by a polynomial and the exact derivative of the polynomial was taken (indicated as fit), or the raw I–V data was smoothed and then a numerical derivative was taken (indicated as smoothed)

show apparent peaks at +1.4 and –1.8 V sample bias, corresponding to 3.9 and 7.1 eV with respect to the vacuum level. The +1.4 V peak is assigned to OMT through the LUMO. The peak at –1.8 V bias was assigned to the HOMO.

On the other hand, in case of naphthalocyanine (Nc) a pronounced tip–sample distance effect was observed: the highest occupied orbital is pinned to the filled band of the substrate while the electron affinity states show a shift in their relative energy position toward the Fermi energy with decreasing tip–sample distance [43, 44]. In contrast no HOMO–LUMO gap shrinking has been detected for SnNc (2.29 eV) in comparison with Nc (2.59 eV). The different tip–sample distance dependence of these two molecules is attributed to their different interaction with the substrate. The interaction between the Nc molecule and substrate is considered to be weak and the molecule–substrate interface is considered to be pure capacitive. On the other hand, the interaction between the non-planar SnNc molecule and substrate is strong and the interface is purely ohmic. This affects the tunneling process in the following way: as the tip–sample distance decreases to a critical value the transmission rate of electrons to the molecule will become greater than that from the molecule to the substrate, inducing a residence time of the electron on the molecule. If the interface has more capacitive character, the electron will have a longer residence time in comparison with a pure ohmic interface. Thus in a capacitive interface, electrons partially fill the unfilled levels near the Fermi level and partially charge the molecule. The charging will cause a lowering of the energy of the unfilled levels. Thus the shift of electron affinity states of Nc is assigned to the charging of these levels during the tunneling process.

STS also turns out to be fruitful in distinguishing between reagent and product formed on a surface. A metal-free tetrapyridylporphyrin (H_2-TpyP) was preorganized on Ag(111) surface under vacuum by evaporation (Fig. 11) [45]. Upon evaporation of Fe atoms onto this well-defined H_2-TPyP precursor layer a dramatic change in image contrast happens to some of the molecules in the lattice, indicating emergence of a new species. The number of modified molecules shows a direct correlation with the Fe dose. The STM observation clearly reveals a preserved 2D TPyP layer structure, where exclusively the central porphyrin moieties undergo dramatic changes.

The STS measurements on the precursor and reacted product elucidate significant differences in the electronic properties before and after reaction with Fe atoms. The LUMO position of the new species appeared at 0.99 V, while the LUMO position of H_2-TPyP was observed at 0.74 V. To confirm the anticipated formation of Fe-TPyP, the organization and electronic properties of Fe-tetraphenylporphyrin (Fe-TPP) have been studied with STM and STS as control experiments. Indeed, a similar contrast in the central porphyrin core was observed in the STM image, and the dI/dV–V curves of this compound showed a pronounced feature at 1.02 V, associated with its LUMO position. This approach may provide a novel pathway to realize low-dimensional metal–organic architectures and patterned surfaces, which cannot be achieved by conventional means.

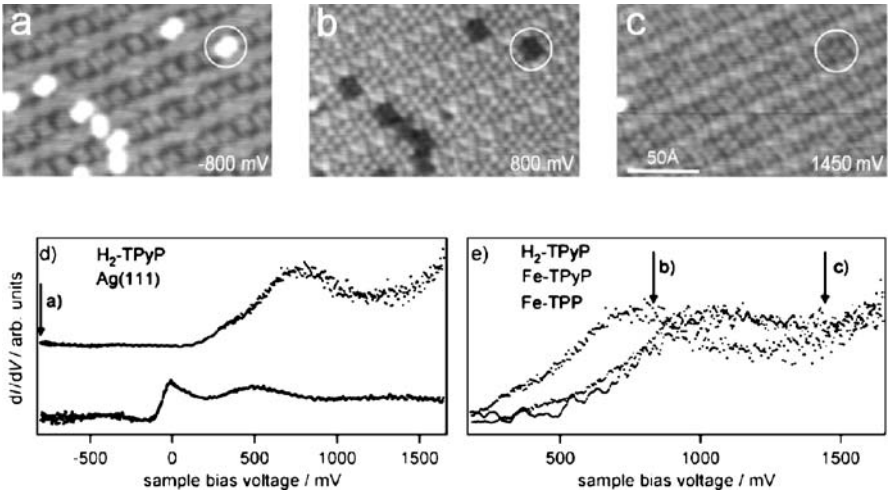

Fig. 11 **a–c** Chemical sensitivity through bias-dependent imaging of H_2-TpyP and Fe-TpyP. All three images are taken at a set point current of 0.71 nA. The *white circle* highlights the position of one specific Fe-TpyP molecule. **d** Tunneling spectra taken on bare Ag(111) and H_2-TpyP. **e** Comparison of the spectrum taken on H_2-TpyP with those on Fe-TpyP and Fe-TPP. The *gray arrows* indicate the bias voltages where the images in (**a**), (**b**) and (**c**) are taken, respectively

All of the examples above were obtained in UHV. Now, some examples will be provided on STS under ambient conditions or at the liquid–solid interface. For instance, the effect of substituent polarity on the charge transfer of adsorbed CuPc molecules on the graphite surface has been studied with STM/STS in air (Fig. 12) [46]. STM results indicate a dramatic change in the two-dimensional assembly of halogenated CuPc and this change is attributed to the change in the electronic structure of CuPc by the large electron affinity of fluorine atoms. STS investigations on these CuPcs demonstrate that they all show an apparent energy gap of about 2 eV, in good agreement with UPS/IPES data. Upon increasing the substituent polarity, a shift of the HOMO/LUMO bands towards negative sample bias was observed as well as a slight narrowing of the band gap. Interestingly, the LUMO bands seem to be more sensitive to the substituent polarity and show a more apparent shift than the HOMO bands. The observed shifts of the valence bands are considered to be associated with the charge transfer between the adsorbate and substrate.

In another study the doping effect of oxygen from the air for titanylphthalocyanine (TiOPc) has been investigated with a combination of STM/STS and cyclic voltammetry (CV) method [47]. STS spectra taken on a well-assembled monolayer of TiOPc on graphite shows that the HOMO and LUMO edges are at –0.94 V and 1.10 V, with an apparent energy gap estimated to be 2.04 eV. The slight positive shift of the energy gap center relative to the Fermi level of the substrate indicates that the molecule shows a *p*-type semiconductor behavior in air. As a control experiment, the first oxidation and reduction potential were estimated with CV either with or without N_2 protection. Without N_2 protection the TiOPc molecules show an energy gap and semiconducting behavior in good agreement with the results from STS, while with N_2 protection, a smaller energy gap and opposite semiconducting behavior was observed. This result is in good agreement with a previous report where TiOPc changes its electronic behavior before and after being exposed to oxygen [48, 49]. These differences in electronic characteristics are attributed to a charge transfer process between TiOPc and O_2.

Though there have been significant advances in understanding electron transmission through a single molecule, few studies deal with electron transmission from one molecule to another. Recently, a fullerene-modified gold STM tip was used to detect the electron transmission in a single fullerene-porphyrin molecular pair (Fig. 13) [50]. The functionalized fullerene was attached to the tip through thiolate-gold interaction, and a single fullerene-porphyrin molecular pair was realized by approaching the fullerene-modified tip to a self-assembled monolayer of porphyrin at the HOPG/trichlorobenzene interface. By comparing STM images obtained with modified and unmodified tips it was concluded that the electron tunneling through the fullerene-porphyrin pair occurs from the electron donating porphyrin to the electron accepting fullerene via a charge transfer interaction. I–V curves showed a clear rectifying behavior with a large current at negative sample bias while the

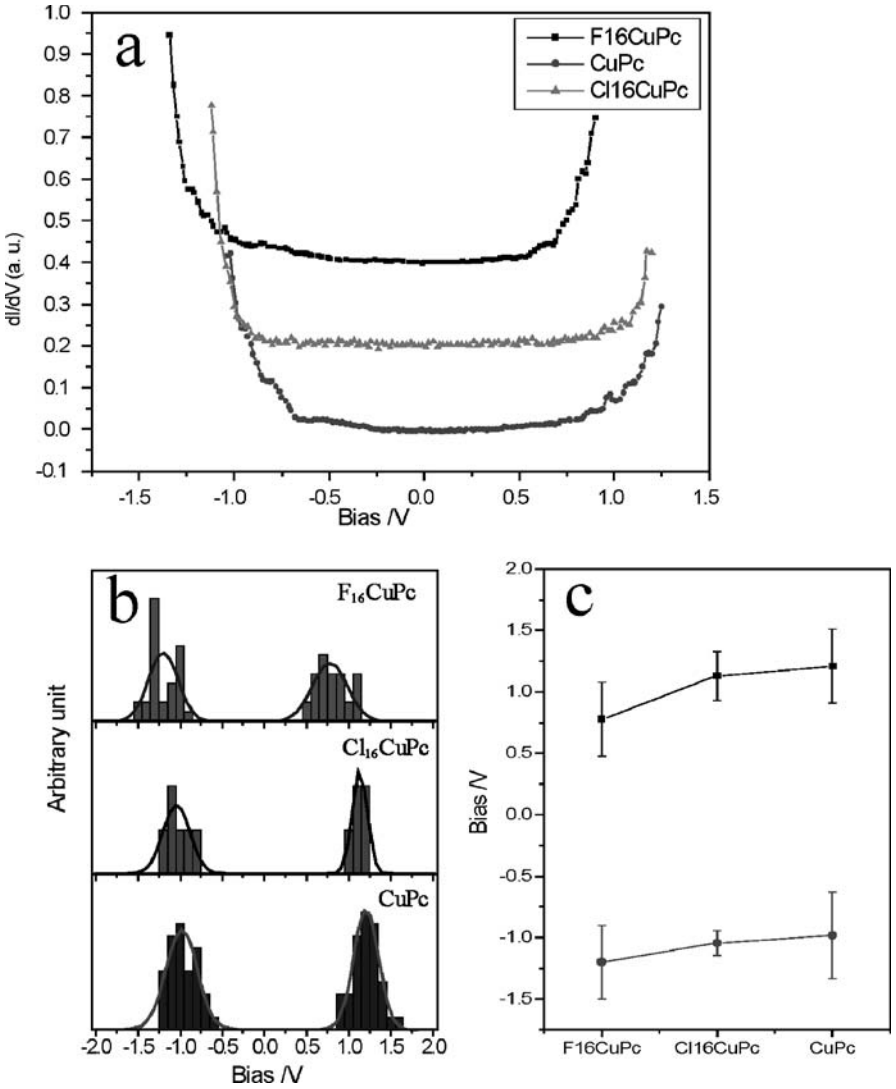

Fig. 12 **a** Typical dI/dV–V curves obtained on differently substituted CuPcs. These dI/dV–V spectra were acquired at a fixed height with given set point current and sample bias, –1.00 V, 380 pA for CuPc, –1.02 V, 350 pA for Cl_{16}CuPc and –1.08 V, 220 pA for F_{16}CuPc, and shifted for clarity. **b** Histogram of the gap edges of differently substituted Pcs. The *solid lines* show a Gauss fit of the columns. **c** Variation of the averaged gap edge with the changing substituents

current flow is significantly smaller at positive bias. The asymmetric current is consistent with the polarity dependence in STM imaging and a rectification ratio of 12 is estimated. STS curves obtained with an unmodified

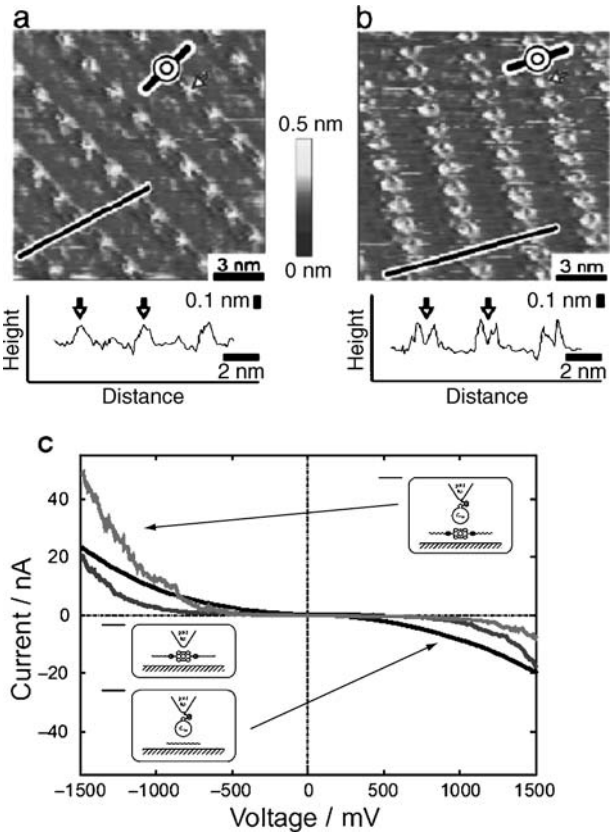

Fig. 13 STM images of CoPor monolayers physisorbed on HOPG observed with an unmodified gold tip (**a**) and the fullerene molecular tip (**b**). Tunneling conditions: –1.30 V, 0.30 nA for (**a**) and –1.25 V, 0.30 nA for (**b**). The *insets* schematically show the molecular arrangement in the images. Cross-sectional profiles measured along the lines marked in the images are shown under the images. **c** The I–V curves measured with the fullerene tip at the porphyrin ring of CoPor, with an unmodified gold tip at the porphyrin ring of CoPor, and with the fullerene tip at $C_{33}H_{68}$, in an argon atmosphere

tip on cobalt(II) 5,15-bis-(4-octadecyloxyphenyl)porphyrin (CoPor) and with a modified tip on $C_{33}H_{68}$ both show symmetric curves, demonstrating the rectification is really reflecting the behavior of the fullerene-porphyrin junction rather than the fullerene-tip or porphyrin–substrate junctions.

A mixed monolayer of zinc(II) 5,15-bis-(4-octadecyloxyphenyl)porphyrin (ZnPor) and 5,15-bis-(4-octadecyloxyphenyl)porphyrin (FBPor) has been imaged with bare gold and fullerene-modified tips to test the chemical sensitivity of the modified tip (Fig. 14). These two porphyrins appear with identical contrast when imaged with a bare gold tip in which the centers of all of the porphyrin rings were observed as depressions compared with the sur-

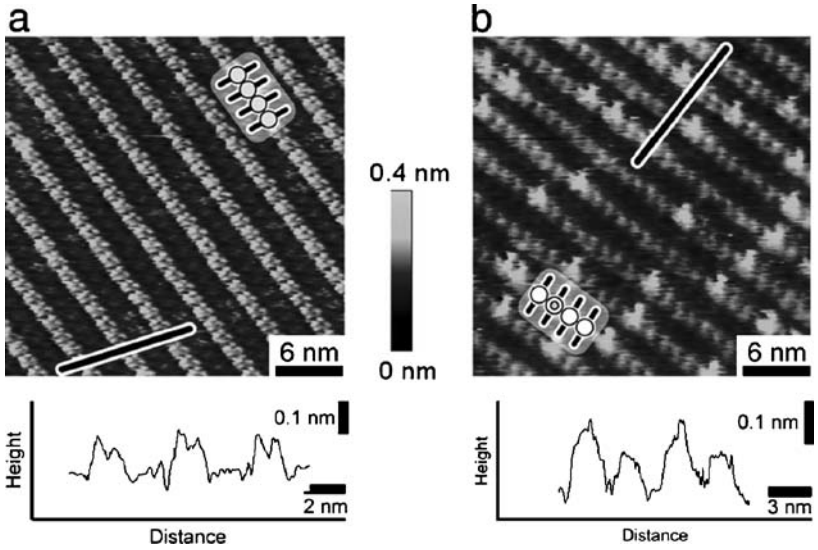

Fig. 14 STM images of mixed monolayers of FBPor and ZnPor physisorbed on HOPG observed with an unmodified gold tip (**a**) and a fullerene-modified tip (**b**). Tunneling conditions: −1.2 V, 0.35 nA for (**a**) and −1.30 V, 0.45 nA for (**b**). Below the images the cross-sectional profiles along the lines in the images are shown

rounding pyrrole moieties. However, when imaged with a fullerene-modified tip, some of the porphyrins are observed to be much brighter than the others. A statistical study of the number of molecules with bright and dim contrast in a large area reveal a ratio which is consistent with the molar ratio of these two compounds in the sample solution, thus proving that the bright and dim porphyrin rings correspond to ZnPor and FBPor, respectively. This difference in contrast is attributed to a different degree of charge transfer between both porphyrins and the fullerene tip.

7 Spectroscopy on Other Related Aromatic Systems

The group of Rabe et al. was the first to report on reliable STS at the liquid–solid interface with submolecular resolution [51]. The self-assembly and the electronic properties of an alkylated hexabenzocoronene (HBC) were studied by STM and STS (Fig. 15). These molecules formed highly ordered 2D crystals. The bright features, which reflect a high tunneling probability, were attributed to the aromatic part of the HBC molecules while the darker areas were attributed to the place the (mobile) alkyl chains were adsorbed. These authors recorded STS curves on top of the aromatic HBC cores, the alkyl chains and graphite, and clearly showed that STS with a resolution bet-

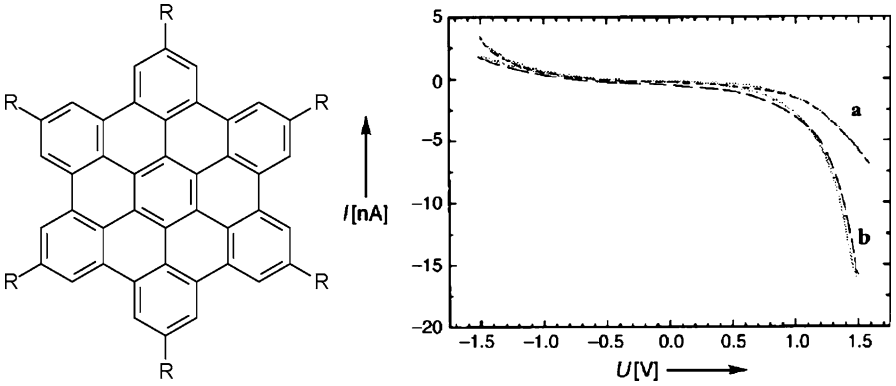

Fig. 15 (*Left*) Chemical structure of an alkylated hexabenzocoronene (HBC). (*Right*) I–V through alkyl chains (**a**) and through the aromatic cores (**b**)

ter than 1 nm is possible, even at the liquid–solid interface. The diode-like structure of the STS curve on top of the aromatic HBC moieties (a higher tunneling probability at negative sample bias) was attributed to resonant contributions of the HOMO of HBC. Using the same model of resonant tunneling (orbital-mediated tunneling), the symmetric featureless I–V curves on top of the alkyl chains were attributed to the lack of a resonant contribution as the HOMO and LUMO levels of these alkyl chains are too far from the Fermi energy.

Typically, STS experiments reveal the participation of the frontier orbitals in the tunneling process (HOMO–LUMO). It is a rare event that also lower lying filled states and higher lying empty states are measured. This has been achieved for bilayers of hexabenzocoronene on Au(111), where at room temperature the dlnI/dlnV–V curves have been recorded in an extended voltage range ($\pm$2.5 V) (Fig. 16) [52]. The normalized differential conductance reveals for peaks at +2.2 V, +1.8 V, –1.4 V, and –2.0 V. The STS results were independent of the tip material. It has been assumed that the applied potential dropped entirely between the molecule and the tip, so, with the assumption that there is no voltage drop at the molecule–substrate interface: indeed, the obtained HOMO position was in perfect agreement with the value obtained in the UPS measurements. The absence of a bias-dependent bias drop is also supported by the fact that the peak positions in the normalized differential conductance curves are not affected by the tip–sample distance. These authors argued that if there is a fraction of the bias voltage which is dropped at the molecule–substrate interface, this fraction should change when increasing the tip–molecule separation.

Monolayers and bilayers of hexabenzocoronene have also been investigated at the liquid–HOPG interface. In contrast to the previous report, it was shown for the HBC molecules in the second layer that their electronic prop-

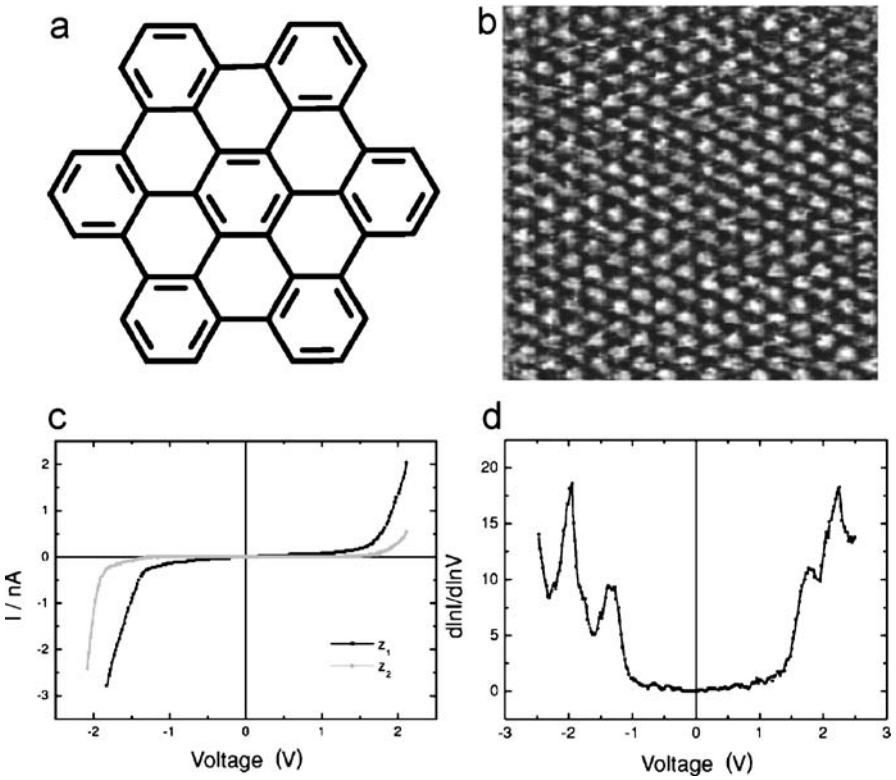

Fig. 16 **a** Chemical structure of hexabenzocoronene. **b** Constant height STM image of a double layer of hexabenzocoronene on Au(100). (Image size is 100 nm × 100 nm, V = 0.65 V, I = 0.05 nA.) **c** I–V curves at two different tip–sample distances measured on the same site with a tungsten tip. The distance z_2 is nominally 0.25 nm larger. The separation z_1 is determined by the tunneling parameters I = 0.05 nA and V = 0.7 V. **d** Normalized differential conductance curve calculated from an I–V curve obtained at 0.2 nA/–1.5 V with a gold tip

erties are site-dependent, e.g., bias-dependent imaging revealed differences in contrast based upon the relative orientation of the HBCs in the second layer with respect to the ones in the first layer [53]. The selective visualization of the first or second layer could be realized by adjusting the tunneling impedance. Interestingly, controlled "bilayer" formation at the level of a single molecule, i.e., tuned stacking of two HBC moieties, could be induced in a hexabenzocoronene cyclophane [54, 55].

Another recent example is the bias-dependent imaging and tunneling spectroscopy of 1,5-di(octyloxy)anthracene (15DA) in UHV, solid–air and solid–liquid conditions [56]. Monolayers of this compound on graphite were prepared from a vast range of different conditions (Fig. 17). For experiments at the liquid–solid interface, solutions of 15DA in phenyloctane (1 mg/ml)

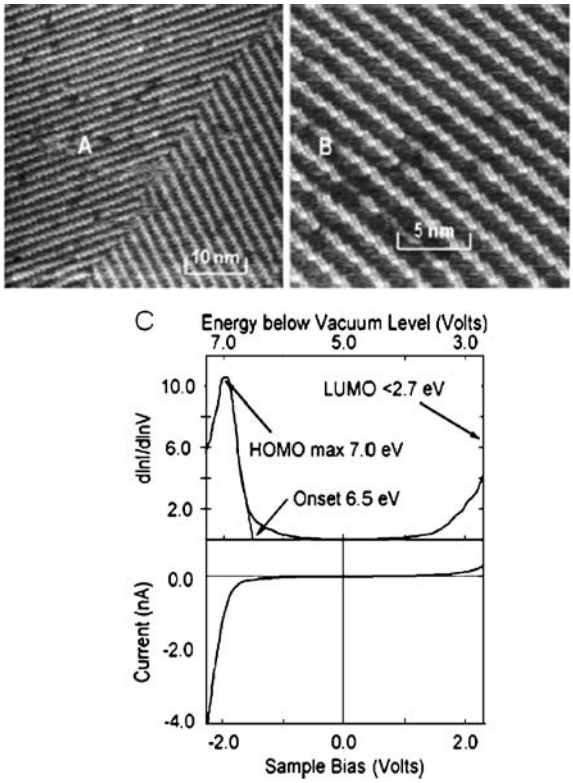

Fig. 17 Constant current STM images of a monolayer region at the air–solid interface of 15DA spin coated on HOPG from (**A**) octane (–700 mV, 50 pA) and (**B**) dichloromethane (–700 mV, 50 pA). **C** Current–voltage curve and OMTS recorded under UHV conditions at 295 K of a monolayer region of 15DA spin coated from octane on HOPG

were prepared and a few drops were applied on HOPG. 1-Phenyloctane has a very low vapor pressure so this experimental setup allows imaging and spectroscopy experiments for a few hours while the tip is immersed in solution. In order to prepare dry monolayers films, solutions of 15DA in dichloromethane or octane were prepared and again a few drops were placed on the substrate, followed by spinning the sample at several thousand rpm for a few minutes. In contrast to the liquid–solid interface, monolayers in these spin-doped samples contained defects and also areas with multi-layer formation could be observed. Monolayer defects are expected for spin coated samples as under these conditions "self-healing" is limited. Multi-layers are less likely to be observed in liquid due to the solvating power of the liquid. Such spin-doped samples were also transferred to UHV. The same molecular ordering was observed under all experimental conditions. 15DA self-assembles in rows and the alkyl chains between adjacent rows are interdigitated, which is typical for

this kind of molecule: intermolecular interactions (van der Waals interactions between alkyl chains) dominate the molecular packing.

Under all conditions, the tunneling efficiency through the aromatic units is higher than through the alkyl chains: actually, the alkyl chains are hardly visible. The data indicate orbital-mediated tunneling involving the HOMO of 15DA. In fact, the apparent molecular height is largest at negative voltages (tunneling from occupied states), at least on spin-coated samples. Bias-dependent imaging showed that there is a clear drop in the total tunneling current and the apparent corrugation as the sample bias is varied from –1 to +0.5 V. However, at the liquid–solid interface, a high corrugation is still observed at high positive voltages, which has been attributed to solvent-induced surface work function changes, increased coupling between substrate and tip orbitals, and weak but non-zero solvent-mediated electronic state mixing between empty surface states of graphite and the 15DA HOMO. However, it is not clear at all what is the role of the solvent in enhancing such processes.

STS experiments confirmed the dominant role of the HOMO in the orbital-mediated tunneling process, both under ambient conditions as well as in UHV. Typically, those obtained under UHV conditions were characterized by a larger signal-to-noise ratio. An intense band at –2 V dominates the dlnI/dlnV–V spectrum, which must be an occupied orbital. This strong resonance near 7 V below the vacuum level can therefore be assigned to the first ionization of 15DA.

The spectroscopic abilities of STM are often crucial in order to provide the submolecular resolution needed especially to unravel the structural details of complex supramolecular systems. Tunneling spectroscopy is especially helpful in those cases if there are energy regions where the molecular levels exclusively arise from some functional subgroups, allowing a selective screening of parts of the molecule. Such a situation can arise for systems where transition metal centers are embedded into a set of organic ligands via coordination bonds. This has been demonstrated for supramolecular transition metal assemblies of grid-type architecture which comprise two-dimensionally ordered arrays of metal ions interconnected by sets of organic ligands (Fig. 18) [57, 58]. Due to their geometry, flat deposition of such grid-

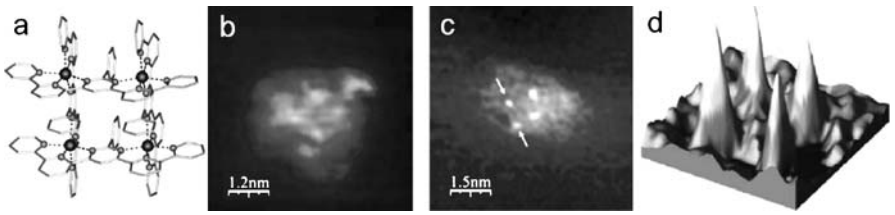

Fig. 18 **a** Molecular structure of the grid containing four Co atoms. **b** Experimental topography map of a single complex. **c,d** Experimental CITS map at –0.942 V with 3D representation

like complexes onto solid surfaces delivers large domains of highly ordered ions. Room temperature STM topography images do not show any submolecular structure. CITS experiments (obtaining I–V curves in combination with topography experiments) were carried out for the grid on HOPG and in order to avoid redox processes only potentials in the negative sample bias regime were applied, so exclusively probing occupied molecular energy levels. The experimental CITS map (the measured current is plotted for a selected voltage) at –0.942 V shows four local peaks. The distance between these maxima correspond with the location of the Co atoms in the grid. Therefore, CITS maps reveal the submolecular details of the grid. Different kinds of grids, star-like supramolecular metal ion assemblies, coordination polymers and polyoxoanions have been analyzed in the same way [58].

Also the tunneling spectroscopy of fullerenes and endohedral metallofullerenes [59] has been investigated, even at the liquid–solid interface [60].

8
Spectroscopy on Conjugated Oligomers and Polymers

Not only small molecules or oligomers have been investigated by STS, the electronic properties of conjugated polymers can also be revealed by this approach. Polydiacetylenes are a special kind of polymer in the sense that they can be "synthesized" on a graphite substrate. Irradiation of preorganized diacetylene monolayers on a surface can lead to their topochemical polymerization [61, 62]. Interestingly, not only far-field illumination but also near-field approaches allow the local polymerization [63, 64]. It has been demonstrated that the polymerization reaction can be induced by a scanning tunneling microscope tip by applying a voltage pulse. Such ability of STM to induce chemical bond formation at atomically precise positions has also been demonstrated by Hla et al., in which the whole process of an Ullmann reaction was demonstrated on a single molecular scale [65]. These fabricated polydiacetylene wires grow in straight lines and their length is typically only restricted by the domain size. These polydiacetylene nanowires are expected to be electrically conducting, especially upon doping and STS could explore the conductivity of these nanowires. STS experiments were both carried out under UHV conditions and in air [66]. Typically, the STS spectra on the diacetylene units of unreacted monomer and the alkyl chains produced noisy spectra which were almost indistinguishable and which varied from experiment to experiment. STS curves on the UV-irradiated surface lead to the higher signal to noise spectra. It turned out to be difficult to correlate the position of the data acquisition and the monolayer structure. Hundreds of curves were obtained arbitrarily on the surface. Apparently, many of these experiments actually destroyed locally the monolayer. The obtained STS curves could be grouped into three classes. The dI/dV–V spec-

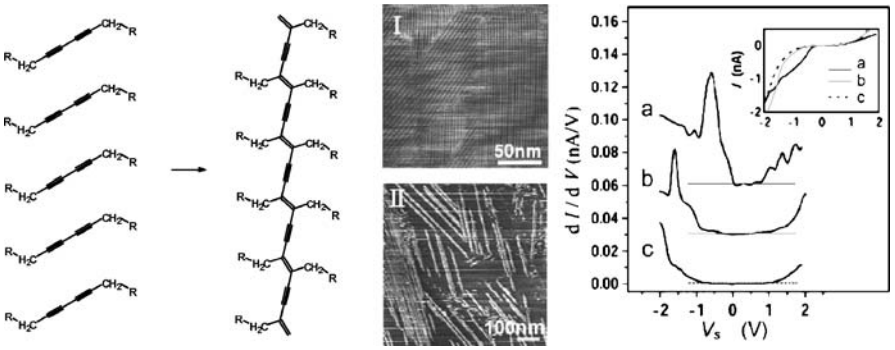

Fig. 19 (*Left*) Chemical structure: topochemical polymerization of diacetylenes. (*Center*) Topographic STM image of a diacetylene self-assembled monolayer before (I) and after (II) UV irradiation for 10 min, taken in air with V = –1 V and I_t = 40 pA. (*Right*) dI/dV–V spectra (a–c) acquired on the UV-irradiated sample using a lock-in amplifier with bias modulation (f = 4 kHz, V_{ac} = 50 mV). The I–V curves are shown in the *inset*

tra are shown in Fig. 19. Experiments not following UV-irradiation showed a different population. The authors identified the three STS classes to originate from polydiacetylene wire, the unreacted diacetylene moiety and the alkyl chain, respectively. The normalized differential conductance spectra (V/I)dI/dV–V show a semiconducting gap and peaks at Vs = –0.5 and 0.8 V, assigned to the density of states of the linear polydiacetylene wire adsorbed on a HOPG surface.

Polydiacetylenes are a special case as they are prepared in situ, on the surface. Also more "traditional" polymers have been investigated. Regioregular poly(3-dodecylthiophene)s (P3DDT) are of special interest because of their semicrystalline properties and high carrier mobilities in organic field effect transistors. These polymers are shown to self-organize on HOPG [67]. Given that it is possible to visualize the topographic features of these self-assembled layers, the simultaneous acquisition of spectroscopic images should shine light on the local conformational and electronic properties. Such films could be obtained by drop-casting from a chloroform solution. The STM experiments were carried out under UHV conditions. In the current imaging tunneling spectroscopy mode (CITS), topographic images in the variable height mode were recorded simultaneously with the I–V curves (Fig. 20). The STM topographs show the polymer chains which are organized in three-fold ordered domains, a result of the molecule–substrate interaction: the alkyl chains tend to align along one of the main symmetry axes of graphite and are interdigitated, stabilizing the self-assembled structure. Interestingly enough, polymer molecules could also be visualized on top of the first layer. Apparently, these "layer 2" polymers are not in registry with the first layer. The topographs suggest an increased electronic density above the second layer (the layer 1–layer 2 height is larger than the

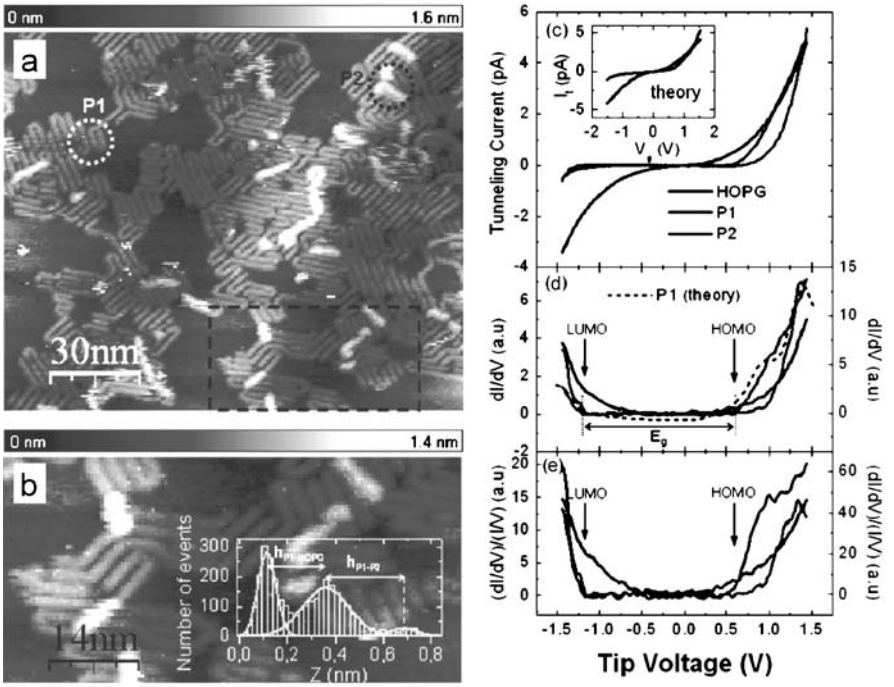

Fig. 20 **a**,**b** STM images of P3DDT film on HOPG with submonolayer coverage obtained in the low-current mode (I_t = 2.5 pA, V_g = 1.4 V). Histogram in the lower figure reflects the monolayer and bilayer stacking heights. (*Right*) Experimental and calculated STS spectra: **c** Experimental I–V curves recorded during a CITS measurement (I_t = 4.6 pA, V_g = 1.42 V) over the bare substrate (HOPG), the first polymer monolayer (P1) and the second layer (P2). **d** Differential conductance dI/dV–V spectra. **e** Normalized differential conductance spectra

HOPG–layer 1 height). Interestingly, the height of these conjugated polymers is smaller than that obtained for π-conjugated cycles on HOPG. For the polymers, the I–V curves and conductance spectra show an extended plateau (or conductance gap) with zero current. A much higher current is obtained at positive then negative sample bias, which has been attributed to tunneling through asymmetrically positioned "screened electron affinity and ionization potential" levels [68], respectively related to HOMO and LUMO molecular levels of the polymer. The authors concluded that on HOPG no noticeable charge transfer effects take place. The apparent band gap reduction (1.7 eV) compared to solution has been attributed to extrinsic screening effects in the tunneling region. However, a similar analysis reveals a band gap of 2 eV on top of a second layer, which is counterintuitive given that the anticipated π-stacking interactions would rather give rise to a decrease in the band gap. This has been attributed to polarization effects.

9
Spectroscopy on Multi-Component or Multi-Interacting Systems

9.1
Covalent Systems

Thus far, most of the systems discussed contain only one spectroscopically active part. An appealing feature of STS though is the fact that it can distinguish between electronically different moieties, for instance in multi-component systems. A first example of a multi-component covalent system is a donor–acceptor–donor molecule (DAD). It combines an electron donor (D = oligo-*p*-phenylene vinylene (OPV)) and electron acceptor part (A = perylene bisimide (PDI)), covalently linked to each other. The donor and acceptor parts are relatively large and well-separated in space, allowing to address them individually. DADs form well-ordered 2D patterns when physisorbed from 1-phenyloctane on HOPG at the liquid–solid interface, as measured by STM in the constant height mode (Fig. 21) [69]. The tunnel path through the aromatic core is tip-D-graphite or tip-A-graphite and not tip-D-A-D-graphite. Of course, the tunneling direction (tip-graphite or graphite-tip) depends on the bias polarity. Alkyl chains occupy the dark regions between the rows of bright rods. From the high-resolution images it appears that the bright rods consist of three parts: the central part is attributed to the location of the PDI part, the outermost parts correspond to the OPV moieties.

At high negative voltages (–1.19 to –1.06 V), the OPV parts appear brighter compared to the central PDI moiety. By changing the bias voltage from negative to positive, the PDI part gradually becomes brighter (from –0.77 to +0.80 V). Upon further increasing the positive bias voltage, the PDI parts become brighter than the OPV units. The bias-dependent contrast changes can be explained by the schematic energy diagrams proposed in Fig. 21, which are based upon a number of assumptions: (1) The tunneling junction is asymmetric with the molecules closer to the substrate than to the tip. (2) The interaction between the molecules and the substrate is weak; physisorption does not significantly affect the energy levels of HOMO and LUMO. (3) The molecular orbital that is closer in energy to the Fermi level of the negatively biased electrode (the electron source), affects the tunneling process stronger. (4) OPV and PDI moieties are electronically decoupled or only weakly coupled as indicated by the absorption spectrum.

As depicted in the left scheme, at negative sample bias, the $HOMO_{OPV}$ level is located close to the Fermi level of graphite. Therefore, electrons tunneling from graphite to the tip couple stronger to the $HOMO_{OPV}$ level than to the other energy levels. At high positive bias voltages (right scheme), the $LUMO_{PDI}$ level is closer to the Fermi level of the tip than other states and accordingly is expected to affect the tunneling process, from tip to substrate, to a greater extent. This simplified model is in line with experimental obser-

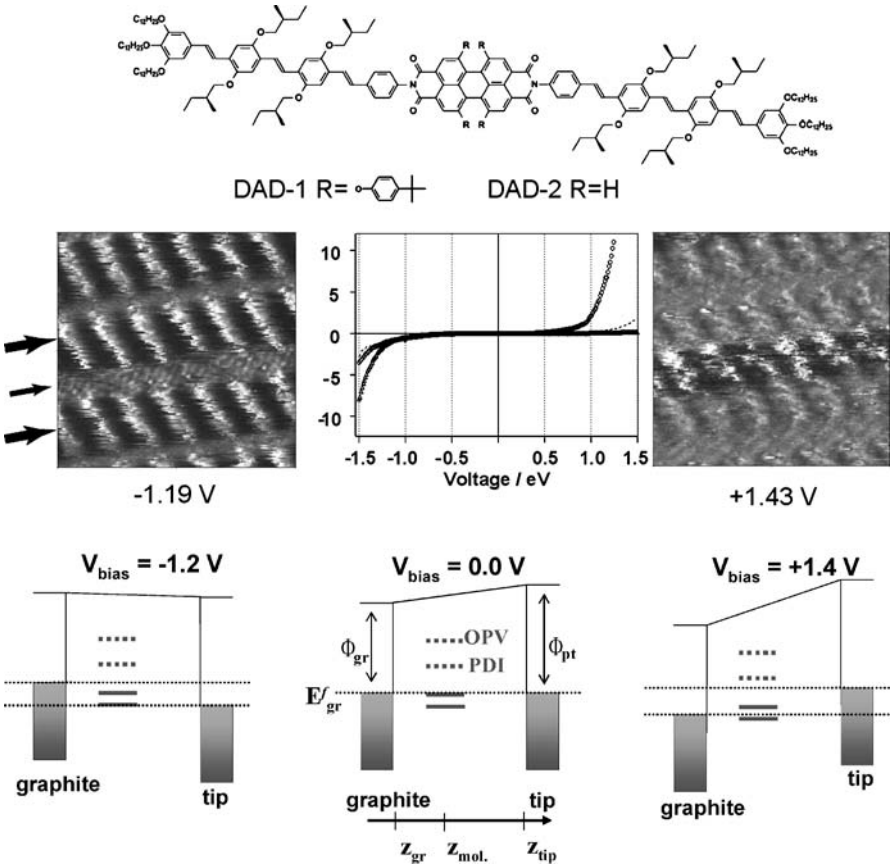

Fig. 21 (*Top*) Chemical structure of the donor-acceptor-donor triad (DAD). (*Middle left* and *right*) Bias dependent imaging of DAD-1 at the 1-phenyloctane/graphite interface. The applied sample bias is indicated below each image. Image size is $10.1 \times 10.1\ \mathrm{nm}^2$. $I_{set} = 0.40$ nA. *Arrows* outside the images refer to OPV (*heavy solid arrow*) and PDI moieties (*thin solid arrow*). (*Middle center*) I–V curves recorded on top of the alkyl chains (*dashed line*), the electron donor moiety (*triangle*) and electron acceptor moiety (*circle symbols*) of DAD-2. (*Bottom*) Tentative energy level diagrams illustrating the relative position of the HOMO (*solid lines*) and LUMO levels (*dashed lines*) of OPV and PDI (of DAD-1) with respect to the graphite and Pt/Ir tip Fermi levels upon applying a bias on the sample. (*Left*) Negative sample bias. (*Right*) Positive sample bias. Fermi levels of graphite ($E_{f,S}$) and STM tip ($E_{f,T}$) are indicated with *black dotted lines*

vations: OPV moieties appear brighter (higher tunneling current) at negative sample bias while the PDI moiety appears brighter at high positive sample bias.

Such behavior can also be confirmed by scanning tunneling spectroscopy (STS) as illustrated for DAD-2 which shows qualitatively the same features as DAD-1 [70]. Figure 21 shows I–V curves over the PDI core, OPV moiety, and

alkyl chains of DAD-2 measured at the 1,2,4-trichlorobenzene/graphite interface. The I–V curve of the alkyl group is relatively symmetric under both bias voltage polarities. Any observed asymmetry could be related to the asymmetry of the tunneling gap. On the other hand, I–V curves of PDI-1 and OPV-1 exhibit diode-like curves, though with an inversed asymmetry: the current on the OPV moiety is larger for negative sample bias while over the PDI part a large current was observed at positive sample bias.

OPV4UT-PERY is a related molecule. It is a diad molecule with an electron donor (OPV) and electron acceptor (perylenediimide) part. The OPV unit is decorated with an ureido-s-triazine moiety which favors dimer formation. OPV4UT-PERY was dissolved in 1,2,4-trichlorobenzene, and a drop of the solution was brought onto a freshly cleaved HOPG surface [71]. After a while, the STM images revealed a particular contrast which indicated the presence of immobilized molecules. Figure 22b represents such a large-scale STM image. The image shows relatively ordered domains with parallel bright rods, which are not equally spaced. They indeed appear to dimerize as the end-to-end distance between these rods changes in an alternating fashion, leading to small and broad "gaps". However, such a rod does not reflect the complete molecule but only the OPV part. The width of the bright rods often exceeds the expected OPV width, indicating that the PERY units are adsorbed between the dimers rather than on top of the OPV units. It proved to be extremely difficult to image the perylene bisimide unit, probably since it does not absorb so strongly on the graphite surface, hence giving it a high mobility. We tentatively assign the low-contrast features between adjacent OPV dimers as observed in Fig. 22 to the perylene bisimide units. Based upon the experience with the covalent DAD triad (bias-dependent imaging and STS spectroscopy), it was anticipated that it should be possible to locate the perylene bisimide units and to distinguish them from the OPV rods. There is a clear bias-dependent reversal of the image contrast. In analogy with the compounds previously studied, the bright areas in negative sample bias were assigned to the OPV rods while the more square-like bright spots to the location of the PERY units. The images suggest that perylene bisimide moieties of adjacent hydrogen-bonded dimers are in close proximity, since on average a single bright spot is observed for every hydrogen-bonded OPV4UT-PERY dimer. Attempts to record reproducible STS curves on top of these molecules failed, since the monolayers are relatively unstable and especially the PERY units are not strongly adsorbed.

Another example is the tunneling microscopy and spectroscopy of an electron donor (hexa-peri-hexabenzocoronene) covalently linked to six acceptors (anthraquinone) in self-assembled layers at the graphite-liquid interface [72]. In the STM images, the bright circular features at the corners of the indicated unit cell are attributed to the conjugated cores of the HBC, while the slightly less bright features are attributed to the anthraquinone molecules. Due to spatial constraints, only four of the six anthraquinone molecules adsorb on

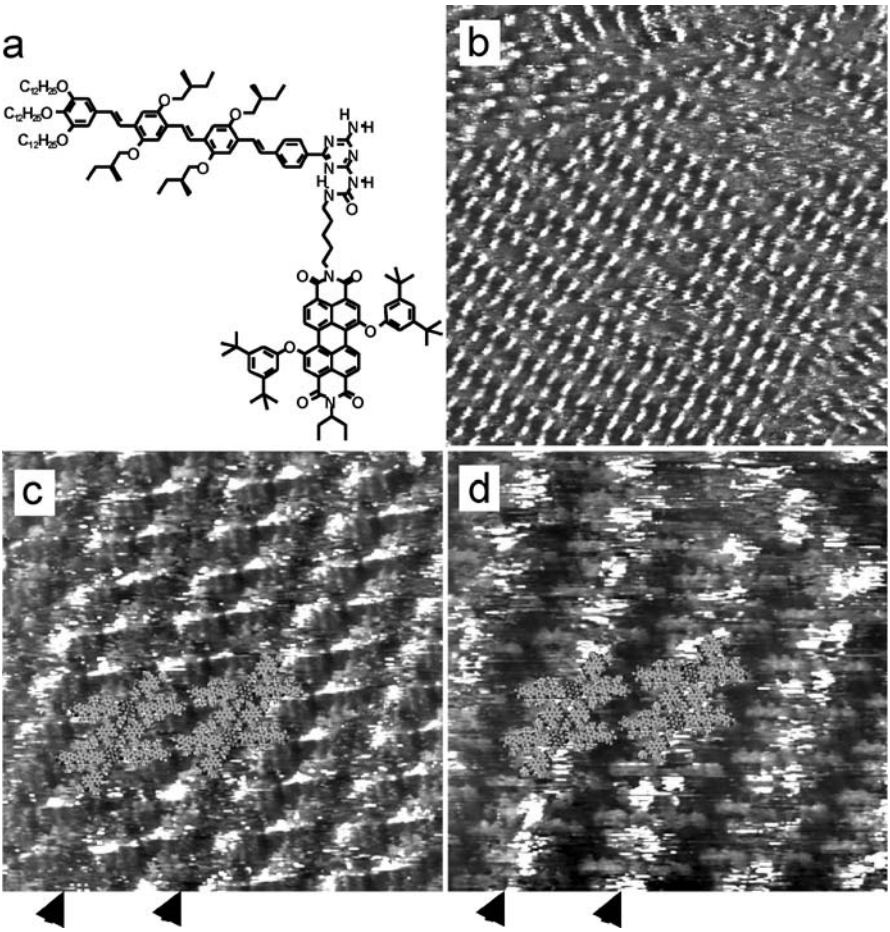

Fig. 22 **a** Chemical structure of OPV4UT-PERY. **b** Large scale STM image (58×58 nm) of OPV4UT-PERY physisorbed from a 1,2,4-trichlorobenzene solution on the basal plane of HOPG. (*Bottom*) Bias-dependent imaging of the same area (except for a small drift) of an OPV4UT-PERY monolayer at the 1,2,4-trichlorobenzene-graphite interface. **c** I_{set} = 115 pA, V_{bias} = –1.37 V, showing the OPVs part brighter, and (**d**) I_{set} = 115 pA, V_{bias} = +1.22 V, showing the perylene bisimide part brighter. Image sizes are 25×25 nm. Models on *top* illustrate the molecular arrangement

the surface while the other two are most likely solubilized in the supernatant solution. Bias-dependent experiments reveal interesting differences (Fig. 23): at positive sample bias, both hexabenzocoronene and the anthraquinone moieties appear almost equally bright while at negative sample bias the tunneling probability is much higher for the HBCs than for the anthraquinones. So, the electron donors appear brighter at negative sample bias while the electron acceptors show the highest tunneling efficiency at positive sample bias. This

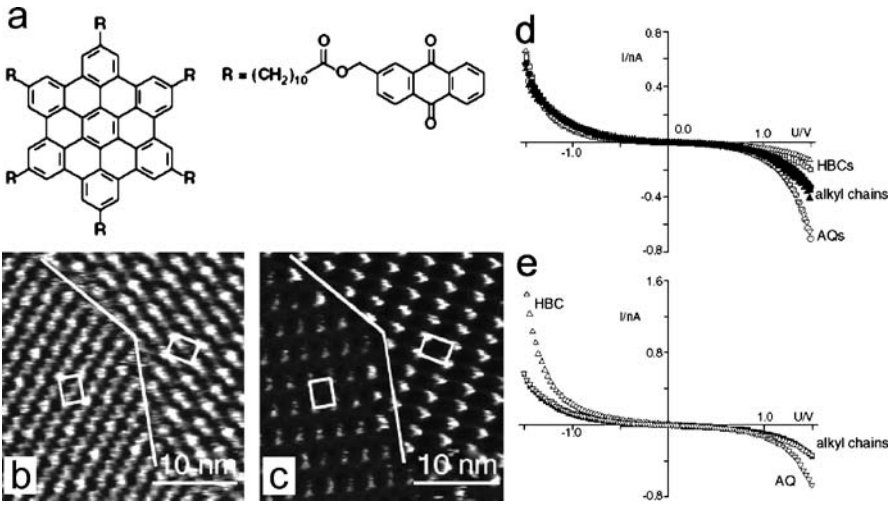

Fig. 23 **a** Chemical structure of the hexabenzocoronene (HBC) derivative with six anthraquinone groups. **b,c** Simultaneously recorded STM images with positive and negative sample bias, respectively, for the two scan directions. **d** I–V curves through the HBC cores, the anthraquinone moieties, and the alkyl chains. **e** Normalized I–V curves. The I–Vs were normalized at positive and negative sample bias for the HBC- and anthraquinone regions, respectively, assuming that resonant contributions for HBC at positive – and for anthraquinone at negative sample bias – can be neglected

trend in bias-dependent imaging was also confirmed in the STS experiments. STS experiments reveal that the tunneling current through the HBC-cores is larger than through the anthraquinones. This difference is bias-dependent and much smaller at positive sample bias. In the I–V experiments, the current is larger for hexabenzocoronene regions at negative sample bias while over anthraquinone regions larger currents are observed at sufficiently large positive sample bias. Thus hexabenzocoronene regions exhibit higher tunneling probability at negative than at positive sample bias whilst anthraquinone regions exhibit an opposite behavior. The different asymmetries of the I–Vs of hexabenzocoronene and anthraquinone, respectively, can be explained by resonant tunneling through the HOMO of hexabenzocoronene and the LUMO of anthraquinone, respectively.

As for the DAD triad, this molecular design – covalent linking of the HBC and the anthraquinone parts – avoids the phase separation of the donor and acceptor parts in different areas. A very nice further development is the integration of this hexabenzocoronene-anthraquinone system with 9,10-dimethoxyanthracene (DMA) [73]. DMA is an electron donor which is known to form a charge transfer complex with anthraquinone. Upon mixing DMA with the compound discussed above, two types of self-assembled structures were observed (Fig. 24). The first one was indistinguishable from the patterns formed by the HBC-anthraquinone molecule. The second one, though

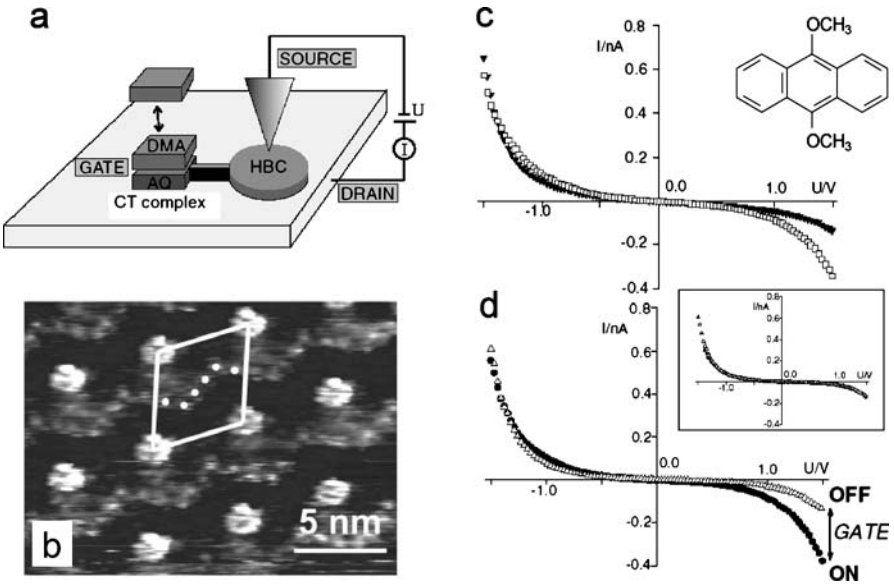

Fig. 24 **a** Schematic of the prototypical single-molecule field-effect transistor. **b** High resolution STM image of a monolayer formed from a mixed solution of the HBC-anthraquinone molecule and DMA. The DMA molecules, indicated by *small white dots*, are adsorbed on top of the anthraquinone molecules and form a charge transfer complex. I–V curves through the (**c**) HBC cores (*solid triangles*) and alkyl chains (*open squares*) in monolayers of the HBC-anthraquinone molecule. The *inset* is the chemical structure of 9,10-dimethoxyanthracene (DMA). **d** STS curves through HBC cores in monolayers with DMA recorded in areas where charge transfer complexes are adsorbed (*solid circles*) or not adsorbed (*open triangles*). The *insets* are the shifted and normalized data

– the one with the larger unit cell – showed six additional bright spots per unit cell which were attributed to charge transfer complexes between anthraquinone and DMA. Interestingly, upon recording I–V curves on top of the HBC units, two distinct sets were obtained depending on whether or not charge transfer complexes between anthraquinone and DMA were formed. Strikingly, these two sets of I–V curves could be superimposed by shifting the one in the presence of the charge transfer complexes by 120 mV to more positive sample bias and normalizing with an appropriately chosen constant. A number of control experiments were carried out to verify that the effect observed was indeed due to the presence of the charge transfer complexes, and not for instance the presence of DMA or the charge transfer complexes in solution. The shift in the I–V curve was attributed to an electric field effect induced by the oriented charge transfer complexes, with the anthraquinone in contact with the HOPG surface and DMA adsorbed on anthraquinone. The so-formed interface dipole was believed to cause a potential drop at the interface. For resonantly tunneling electrons this potential drop shifts the

molecular orbitals of the adsorbate with respect to the Fermi level of the substrate. Assuming a dipole strength of 3 D (based upon ab initio calculations), the dipole density determined from the STM images and a dielectric constant of 3, a relative shift of 130 meV was calculated which is in good agreement with the experimental value of 120 meV. In fact, a prototypical single-molecule field-effect transistor with nanometer-sized gates was realized: the source and the drain are the graphite and tip electrodes, the channel is the aromatic hexabenzocoronene and the gate is a charge transfer complex, formed between anthraquinone, the acceptor, covalently linked to the "channel" and DMA, the donor, provided from solution.

9.2 Non-Covalent Systems

STS measurements have also been carried out to shine light on the electronic properties of non-covalent multi-component systems. Highly organized monolayers of hexagonally packed ring-shaped cyclo[12]thiophene (C[12]T) are formed upon adsorption from a 1,2,4-trichlorobenzene solution on top of HOPG [74]. On top of such a modified template surface, C_{60} fullerene are adsorbed to form a 2D crystalline layer. The nature of the interaction between C[12]T and C_{60} is the formation of 1:1 π–donor–π–acceptor complexes. The C_{60} molecules adsorb on top of the oligothiophene ring rather than in the void of the macrocycle despite the fact that the size of that void is large enough to accommodate a C_{60} molecule (Fig. 25). Therefore, the bicomponent surface is composed of ring-shaped *p*-type organic semiconductors with complexing sites for *n*-type materials. Again the high tunneling efficiency through the macrocycle ring can be attributed to orbital-mediated tunneling via the HOMO. Despite the fact that there is room to do so, multiple complexes by more than one fullerene per macrocycle are never seen. This has been attributed to the intrinsic dipole formation upon complexation of one C_{60} molecule, rendering the opposite site of the macrocycle less electron donating. STS measurements on top of C[12]T are slightly asymmetric and the differential conductance curves indicate two frontier orbitals at –0.7 and +0.95, leading to a HOMO–LUMO gap of 1.65 V. At negative bias, the shape of the I–V curve for the complex is quite different from the non-complexed system. The saturation of the current at negative bias was attributed to the special spectroscopic characteristic of the D–A complex.

Thus far, a number of systems were presented where the π-rich parts interact with each other in the direction normal to the surface. It is also a challenge to make such structures stack parallel to the substrate. The self-assembly of a series of oligothiophene derivatives was reported at the liquid–solid interface [75]. These bis(urea)-substituted thiophene derivatives form extended domains of lamellar structures. The bright features have been attributed to the thiophene units. The intermolecular spacing along the lamella was de-

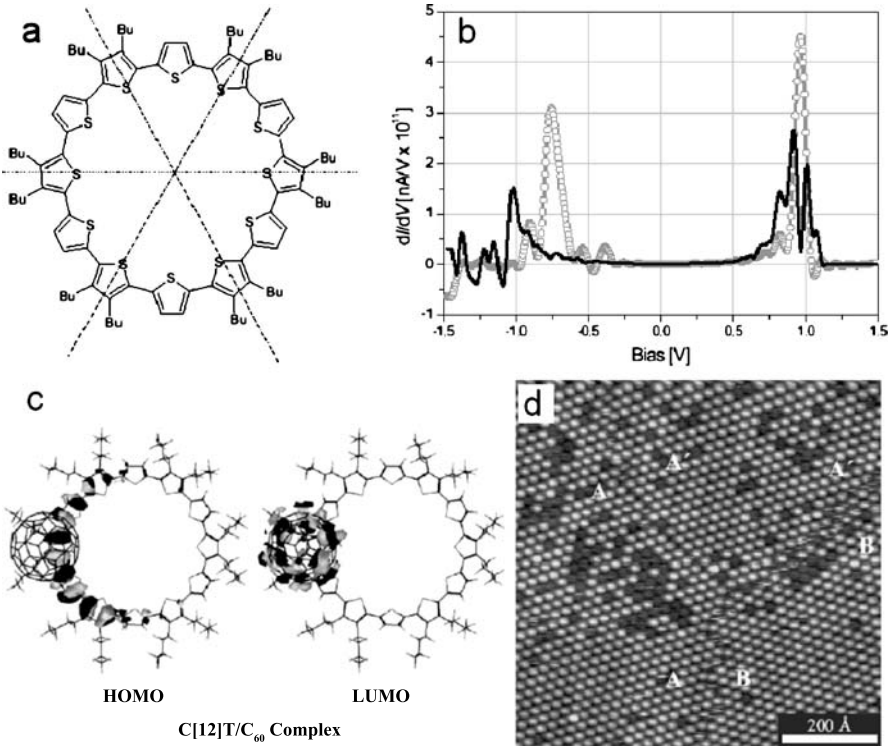

Fig. 25 **a** Molecular model of C[12]T. **b** Differential conductance (dI/dV) versus bias voltage (V) measured on top of a C[12]T-macrocycle (*circles*) and a C[12]T-C_{60} complex (*solid line*). **c** Calculated molecular orbitals of complexed C[12]T molecule derived from an energy-minimized geometry. **d** STM image of C[12]T-C_{60} complexes, including some non-complexed macrocycles

termined to be 0.462±0.005 nm: the packing is controlled by intermolecular hydrogen bonds between the urea groups. As a result, the thiophene moieties must be tilted with respect to the surface which provides electronic coupling between the thiophene rings along the lamella. Therefore, such an arrangement is interesting to study π–π interactions. In order to compare the STS data recorded on top of thiophene stacks with those of isolated molecules, T2 was co-adsorbed in a matrix of C12–U–C14–C12. In these mixed layers, single T2 molecules could be identified.

Current–voltage curves measured through the π-stacked T2 were attributed to a semiconductor-like behavior with a band around zero bias (Fig. 26) [76]. This observed gap increased from about 0.45±0.08 eV for T2 to about 0.65±0.11 eV for single T2 molecules. These results are qualitatively in line with the expectation that for π-stacked molecules the HOMO–LUMO gaps should narrow due to the HOMO and LUMO splittings of the interacting molecule.

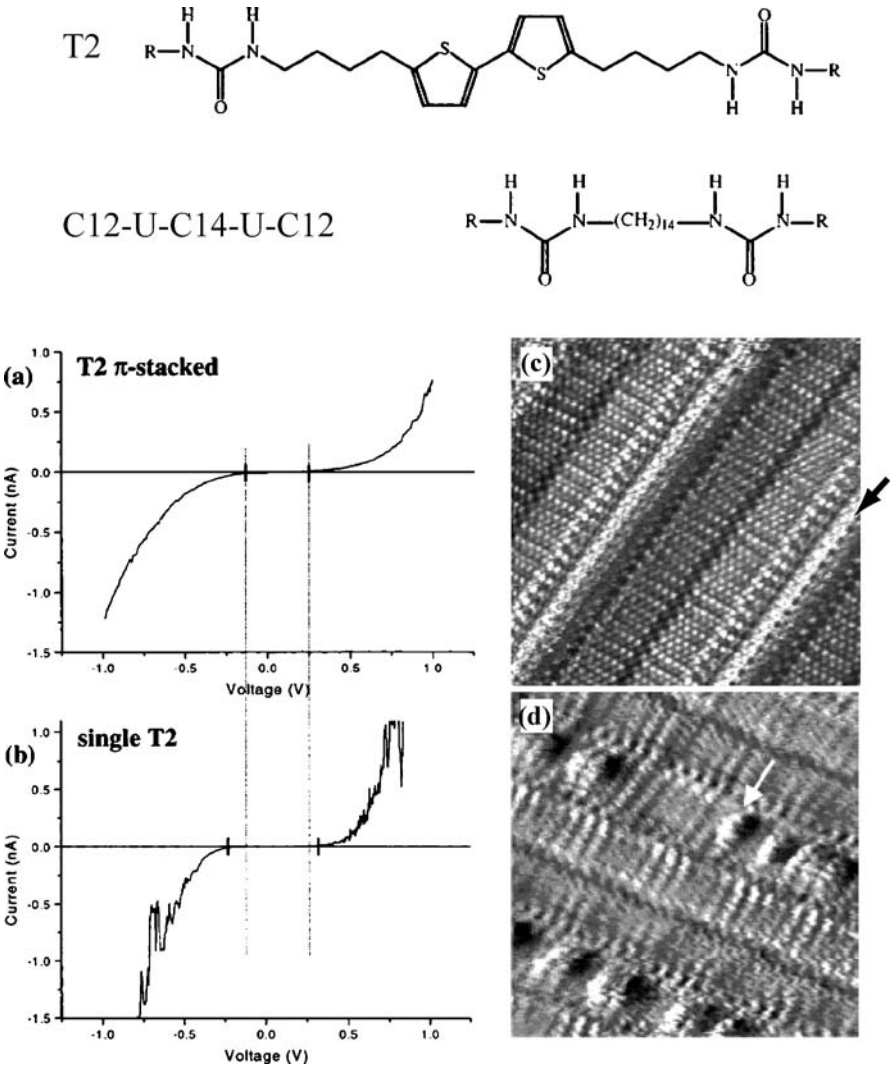

Fig. 26 (*Top*) Chemical structures of bis(urea)-substituted thiophene derivative T2 and the matrix molecule C12–U–C14–U–C12. (*Center* and *bottom*) Current voltage curves (*left*) and corresponding STM images (*right*) of bis(thiophene) stacks (*black arrow*) and isolated bis(thiophene) moieties (*white arrow*). The image size is 10×10 nm

Not only oligothiophenes but also TTF derivatives are an interesting class of molecules due to their electronic properties. By tuning the substitution pattern of the TTF molecules, i.e., by introducing hydrogen bonding groups such as amides in the alkyl chains, the TTF moieties were forced to be tilted with respect to the surface and to interact via π–π stacking as revealed by the STM images (Fig. 27) [77]. Also molecular modeling and molecular dynamics re-

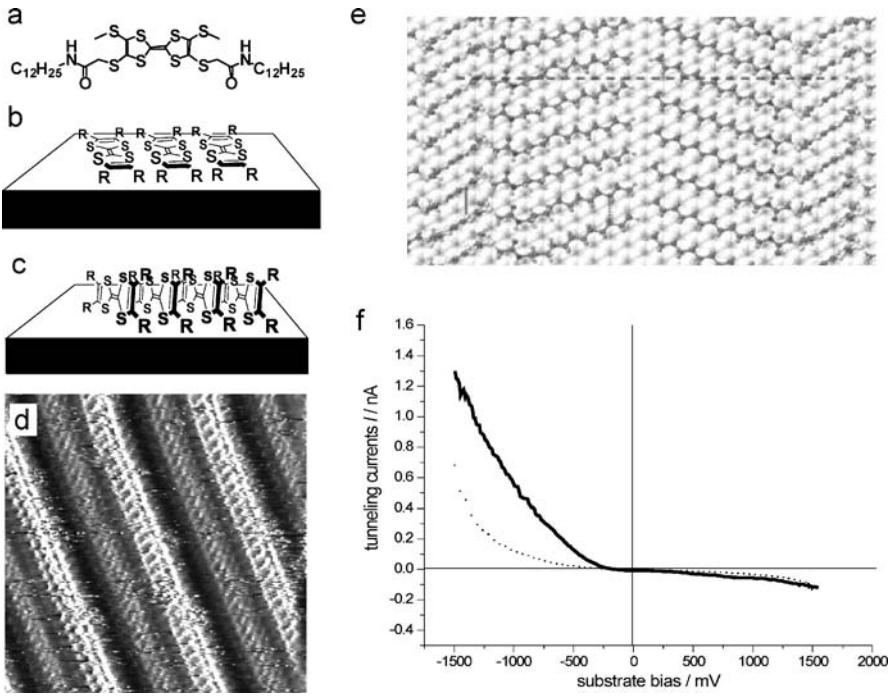

Fig. 27 Molecular structure (**a**) and schematic illustration of the flat (**b**) and tilt alignment (**c**) of the TTF derivative. High-resolution STM image (**d**) and molecular dynamic simulation (**e**) both confirms the tilt conformation of the TTF moieties. **f** The STS curve (*solid line*, average of 56 spectra recorded with the set point value I_{set} = 0.5 nA, V_{bias} = –1.03 V) obtained on those TTF stacks at the octanoic acid/graphite interface reveals a small conductance gap. The *dotted line* shows a curve recorded in the solvent alone

vealed the crucial role of the hydrogen bonding units creating the TTF stacks. Quantum-chemical calculations were performed to quantify the electronic coupling between two adjacent molecules in the stack. The transfer integral for the HOMO, which is related to the capacity for hole transport, was computed to be 134 meV and for the LUMO, which is related to electron transport, 111 meV. This indicates a strong interaction between the π-systems of the two molecules. According to Hückel theory, for an infinite one-dimensional stack, the width of the valence band and conduction band is equal to four times the transfer integral associated to the HOMO and LUMO levels, respectively, i.e., 0.54 eV and 0.44 eV. These large bandwidths show that those TTF stacks can act as molecular wires both for hole and electron transport.

Another example is π-stacked pyrenes. At the graphite–1-phenyloctane interface, STM clearly reveals that 1-pyrenehexadecanoic acid adsorbs with the pyrene unit parallel to the surface (Fig. 28) [78]. When 4,4′-dipyridyl units are co-adsorbed, the 1-pyrenehexadecanoic acid molecules adsorb with their

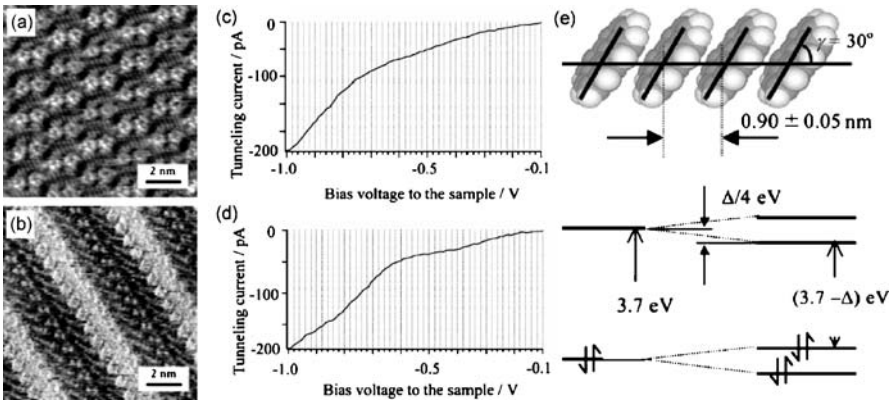

Fig. 28 STM images of 1-pyrenehexadecanoic acid (**a**) (11×11 nm^2) and 1-pyrenehexadecanoic acid-4,4-dipyridyl (**b**) (11×11 nm^2) monolayers at the 1-phenyloctane/graphite interface. Imaging condition was I = 0.15 nA, V = 0.80 V and I = 0.13 nA, V = 1.00 V, respectively. **c**,**d** I–V curves taken above the isolated pyrene unit within the one-component monolayers and the π-stacked pyrene units within the two-component monolayers, respectively. **e** Schematic structural model of the π-stacking of pyrene units and energy diagrams of the HOMO and LUMO levels for isolated and π-stacked pyrene units

pyrene units tilted with respect to the graphite surface. They overlap with each other in the same lamella and form π-stacks. I–V curves recorded on isolated and π-stacked pyrene units show inflection points around –0.80 and –0.65 V, respectively, indicating an about 0.15 V narrowing of the energy gap due to π-stacking. This energy gap narrowing was attributed to the π electron delocalization in the π-stacked lamella.

10
Molecules Tuning Surface Properties

Finally, it is appropriate also to pay attention to some physical phenomena which are affected by the presence of molecules and which can be probed by STS. The "Kondo" effect is the realignment of the electron spins below a critical temperature due to spin–electron interactions, when a magnetic impurity is surrounded by free electrons. The Kondo effect has been observed for a wide range of systems, including single atoms or molecules, quantum dots, and carbon nanotubes [79]. In a recent report, a two-dimensional molecular Kondo system was reported [80]. The molecules were porphyrins with a cobalt atom in its center. Most of these molecules assembled with a planar conformation on the Cu(111) surface under UHV conditions. By measuring the local density of states around the Fermi level, the spin–electron interaction could be determined (Fig. 29). Therefore, dI/dV–V spectra were recorded by positioning the STM tip above the Co-site of a porphyrin molecule which was part of a two-dimensional

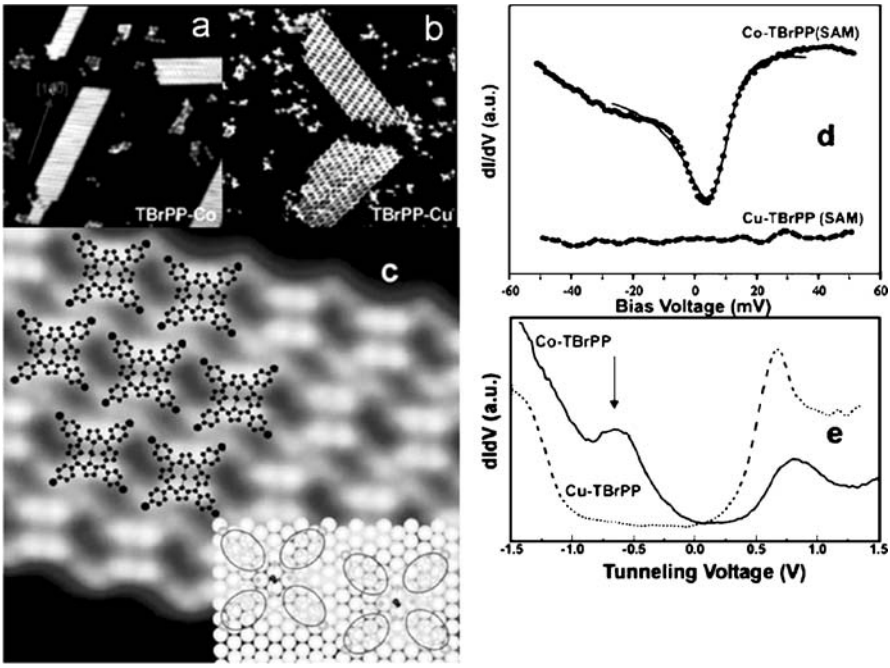

Fig. 29 STM images of the Co-porphyrin (**a**) and the Cu-porphyrin (**b**) arranged in ribbon-like self-assembled molecular assemblies. The differential conductance spectrum of the Co-porphyrin inside the ribbon shows a dip (Kondo resonance). The peak located at –0.7 V is assigned to the HOMO from the Co d_z^2 orbital. This peak is absent in the orbital-mediated tunneling spectrum of the Cu analogue. The peaks at positive bias voltages are the lowest unoccupied orbitals

molecular layer. In contrast to Cu-porphyrins, a resonance located around the substrate Fermi level was obtained in case of the Co-porphyrins, assigned to the Kondo effect. In addition, the dI/dV–V spectra also revealed an occupied molecular orbital located at –0.7 V assigned to the ionization of the d_z^2 orbital of the Co atom. In addition, it was shown that the spin–electron coupling strength could be manipulated by varying the nearest neighbor coordination number of molecules inside a 2D molecular self-assembly.

11
Conclusions and Outlook

Scanning tunneling spectroscopy is an established technique. With unprecedented spatial resolution, the electronic properties of individual molecules or their assemblies can be probed, even with submolecular resolution. Although STS and bias-dependent imaging were originally implemented under UHV

conditions, the versatility of these approaches has been demonstrated under ambient conditions too, and even at the liquid–solid interface. However, the specific experimental conditions put some constraints on the general applicability, mainly in terms of bias range which can be applied and the response of the solvent to the changing electric field.

What's the future of tunneling spectroscopy? In order to learn more about the limitations set by or the opportunities offered by the different experimental environments (UHV, ambient conditions, liquid solid), it is absolutely necessary that identical systems be compared on identical substrates in the various experimental environments. The first attempts in this direction have recently been made. As far as the liquid–solid interface is concerned, the solvent should be selected carefully and the effect of different solvents on the tunneling spectroscopy should be probed. Experiments under ambient conditions would benefit from a rigorous environmental (humidity) control.

The potential of visualizing molecular orbitals is definitely a very appealing one, given that the molecule–substrate coupling can be limited, which is the case for molecules adsorbed on non-conductive films: a chemist's dream come true. The effects of substituents or particular molecular conformations on the electronic fingerprint of single molecules will be addressed. Thus far, STS has not been used extensively to exploit its potential to probe differences between individual molecules. Being a single-molecule technique, it is perfectly suited to map the profile of a heterogeneous population.

In the future, definitely more complex functional (supramolecular) systems will be probed. STS will be indispensable for differentiating between the individual units of complex multi-component systems and will be the technique of choice to unravel the effects arising from the interaction between different components.

For sure, the integration of STS with other techniques, such as optical microscopy, will open many new possibilities. Spatially resolved tunneling spectroscopy awaits a bright future.

References

1. Binnig G, Rohrer H, Gerber C, Weibel E (1982) Phys Rev Lett 49:57
2. Binnig G, Rohrer H (1982) Helv Phys Acta 55:726
3. Binning G, Quate CF, Gerber C (1986) Phys Rev Lett 56:930
4. Sugimoto Y, Pou P, Abe M, Jelinek P, Pérez R, Morita S, Custance O (2007) Nature 446:64
5. De Feyter S, De Schryver FC (2003) Chem Soc Rev 32:139
6. Xu B, Tao NJ (2003) Science 301:1221
7. Schröter U, Scheer E, Arnold R, Bacca C, Böhler T, Grebing J, Konrad P, Kunej V, Kang N, Pernau HF, Schirm C (2005) Adv Eng Mater 7:795
8. Reed MA, Zhou C, Muller CJ, Burgin TP, Tour JM (1997) Science 278:252
9. Hugelmann M, Hugelmann P, Lorenz WJ, Schindler W (2005) Surf Sci 597:156

10. Schindler W, Hugelmann M, Hugelmann P (2005) Electrochim Acta 50:3077
11. Li Z, Han B, Meszaros G, Pobelov I, Wandlowski T, Blaszczyk A, Mayor M (2006) Faraday Disc 131:121
12. Albrecht T, Moth-Poulsen K, Christensen JB, Hjelm J, Bjornholm T, Ulstrup J (2006) J Am Chem Soc 128:6574
13. Andolfi L, Canters GW, Verbeet M, Cannistraro S (2004) Biophys Chem 107:107
14. Hipps KW (2006) Scanning tunneling spectroscopy. In: Vij DR (ed) Handbook of applied solid state spectroscopy. Springer, Berlin Heidelberg New York
15. Doyen G, Drakova D (1997) Prog Surf Sci 54:249
16. Tsukada M, Kobayashi K, Isshiki N, Kageshima H (1991) Surf Sci Rep 13:265
17. Nazin GV, Qiu XH, Ho W (2003) Science 302:77
18. Tanaka H, Kawai T (2006) Appl Surf Sci 252:5474
19. Hulsken B, Gerritsen JW, Speller S (2005) Surf Sci 580:95
20. Huglemann M, Schindler W (2003) Surf Sci 541:L643
21. Repp J, Meyer G, Stojkovic SM, Gourdon A, Joachim C (2005) Phys Rev Lett 94:026803
22. Kahn A, Koch N, Gao W (2003) J Polym Sci B 41:2529
23. Forrest SR (1997) Chem Rev 97:1793
24. Seidel C, Awater C, Liu XD, Ellerbrake R, Fuchs H (1997) Surf Sci 371:123
25. Glöcker K, Seidel C, Soukopp A, Sokolowski M, Umbach E, Böhringer M, Berndt R, Schneider WD (1998) Surf Sci 405:1
26. Wagner T, Bannani A, Bobisch C, Karacuban H, Möller R (2007) J Phys Condens Matter 19:056009
27. Stöhr M, Gabriel M, Möller R (2002) Surf Sci 507–510:330
28. Chizhov I, Kahn A, Scoles G (2000) J Cryst Growth 208:449
29. Toerker M, Fritz T, Proehl H, Sellam F, Leo K (2001) Surf Sci 491:255
30. Tsiper EV, Soos ZG, Gao W, Kahn A (2002) Chem Phys Lett 360:47
31. Nicoara N, Román E, Gómez-Rodríguez JM, Martín-Gago JA, Méndez J (2006) Org Electron 7:287
32. Bao Z, Lovinger AJ, Brown J (1998) J Am Chem Soc 120:207
33. Scudiero L, Barlow DE, Mazur U, Hipps KW (2001) J Am Chem Soc 123:4073
34. Scudiero L, Barlow DE, Hipps KW (2002) J Phys Chem B 106:996
35. Zhang J, Chi Q, Kuznetsov AM, Hansen AG, Wackerbarth H, Christensen HEM, Andersen JET, Ulstrup J (2002) J Phys Chem B 106:1131
36. Han W, Durantini EN, Moore TA, Moore AL, Gust D, Rez P, Letherman G, Seely GR, Tao N, Lindsay SM (1997) J Phys Chem B 101:10719
37. Muller AD, Muller F, Hietschold M (1999) Appl Phys Lett 74:2963
38. Bakkers EPAM, Hens Z, Kouwenhoven LP, Gurevich L, Vanmaekelbergh D (2002) Nanotechnology 13:258
39. Katz D, Millo O, Kan SH, Banin U (2001) Appl Phys Lett 79:117
40. Deng W, Hipps KW (2003) J Phys Chem B 107:10736
41. Barlow DE, Scudiero L, Hipps KW (2004) Langmuir 20:4413
42. Barlow DE, Hipps KW (2000) J Phys Chem B 104:5993
43. Lackinger M, Müller T, Gopakumar TG, Müller F, Hietschold M, Flynn GW (2004) J Phys Chem B 108:2279
44. Gopakumar TG, Müller F, Hietschold M (2006) J Phys Chem B 110:6060
45. Auwärter W, Weber-Bargioni A, Brink S, Riemann A, Schiffrin A, Ruben M, Barth JV (2007) ChemPhysChem 8:250
46. Lei SB, Deng K, Yang DL, Zeng QD, Wang C (2006) J Phys Chem B 110:1256
47. Kong XH, Wang M, Lei SB, Yang YL, Wang C (2006) J Mater Chem 16:4265
48. Nishi T, Kanai K, Ouchi Y, Willis MR, Seki K (2005) Chem Phys Lett 414:479

49. Tada H, Touda H, Takada M, Matsushige K (2000) Appl Phys Lett 76:873
50. Nishino T, Ito T, Umezawa Y (2005) PNAS 102:5659
51. Stabel A, Herwig P, Müllen K, Rabe JP (1995) Angew Chem Int Ed 34:1609
52. Toerker M, Fritz T, Proehl H, Gutierrez R, Großmann F, Schmidt R (2002) Phys Rev B 65:245422
53. Jäckel F, Watson MD, Müllen K, Rabe JP (2006) Phys Rev B73:045423
54. Watson MD, Jäckel F, Severin N, Rabe JP, Müllen K (2004) J Am Chem Soc 126:1402
55. Jäckel F, Rabe JP (2006) Scanning tunneling spectroscopy of complex molecular architectures at solid/liquid interfaces: toward single-molecule electronic devices. In: Samori P (ed) Scanning probe microscopies beyond imaging. Wiley-VCH, Weinheim, p 36
56. Pokrifchak M, Turner T, Pilgrim I, Johnston MR, Hipps KW (2007) J Phys Chem C 111:7735
57. Alam MS, Strömsdörfer S, Dremov S, Müller P, Kortus J, Ruben M, Lehn JM (2005) Angew Chem Int Ed 44:7896
58. Ruben M, Lehn JM, Müller P (2006) Chem Soc Rev 35:1056
59. Taninaka A, Shino K, Sugai T, Heike S, Terada Y, Hashizume T, Shinohara H (2003) Nano Lett 3:337
60. Katsonis N, Marchenko A, Fichou D (2003) Synt Met 137:1453
61. Grim PCM, De Feyter S, Gequière A, Vanoppen P, Rücker M, Valiyaveettil S, Moessner G, Müllen K, De Schryver FC (1997) Angew Chem Int Ed 36:2601
62. Takami T, Ozaki H, Kasuga M, Tsuchiya T, Mazaki Y, Fukushi D, Ogawa A, Uda M, Aono M (1997) Angew Chem Int Ed 36:2755
63. Okawa Y, Aono M (2001) Nature 409:683
64. Miura A, De Feyter S, Abdel-Mottaleb MMS, Gesquière A, Grim PCM, Moessner G, Sieffert M, Klapper M, Müllen K, De Schryver FC (2003) Langmuir 19:6474
65. Hla SW, Meyer G, Rieder KH (2001) ChemPhysChem 2:361
66. Akai-Kasaya M, Shimizu K, Watanabe Y, Saito A, Aono M, Kuwahara Y (2003) Phys Rev Lett 91:255501
67. Scifo L, Dubois M, Brun M, Rannou P, Latil S, Rubio A, Grévin B (2006) Nano Lett 6:1711
68. Dubois M, Latil S, Scifo L, Grévin B, Rubio A (2006) J Chem Phys 125:034708
69. Miura A, Chen ZJ, Uji-I H, De Feyter S, Zdanowska M, Jonheim P, Schenning APHJ, Meijer EW, Würthner F, De Schryver FC (2003) J Am Chem Soc 49:14968
70. Uji-I H, Miura A, Schenning APHJ, Meijer EW, Chen ZJ, Würthner F, De Schryver FC, Van der Auweraer M, De Feyter S (2005) ChemPhysChem 6:2389
71. Zhang J, Hoeben FJM, Pouderoijen MJ, Schenning APHJ, Meijer EW, De Schryver FC, De Feyter S (2006) Chem Eur J 12:9046
72. Jäckel F, Wang Z, Watson MD, Müllen K, Rabe JP (2004) Chem Phys Lett 387:372
73. Jäckel F, Watson MD, Müllen K, Rabe JP (2004) Phys Rev Lett 92:188303
74. Mena-Osteritz E, Bäuerle P (2006) Adv Mater 18:447
75. Gesquière A, Abdel-Mottaleb MMS, De Feyter S, De Schryver FC, Schoonbeek F, van Esch J, Kellog RM, Feringa BL, Calderone A, Lazzaroni R, Brédas JL (2000) Langmuir 16:10385
76. Gequière A, De Feyter S, De Schryver FC, Schoonbeek F, van Esch J, Kellog RM, Feringa BL (2001) Nano Lett 1:201
77. Puigmarti-Luis J, Minoia A, Uji-I H, Rovira C, Cornil J, De Feyter S, Lazzaroni R, Amabilino DB (2006) J Am Chem Soc 128:12602
78. Uji-I H, Nishio S, Fukumura H (2005) Chem Phys Lett 408:112
79. Choi MS (2006) Int J Nanotech 3:216
80. Iancu V, Deshpande A, Hla SW (2006) Phys Rev Let 97:266603

Subject Index